Intra-caldera rhyolitic eruptions: lithostratigraphy and pyroclast textures to reconstruct the ~1314 CE Kaharoa eruption of Mt Tarawera, New Zealand

A thesis presented in partial fulfilment
of the requirements for the degree of
Doctor of Philosophy
in Earth Science
at Massey University,
Palmerston North, New Zealand

Andrea Todde

2022

To Lina, Paolo, Betti and Fabrizio

Abstract

Rhyolitic eruptions are commonly sourced from silicic caldera systems and display a great variety of eruptive styles and magnitudes, ranging from the extrusion of lava domes to catastrophic caldera-forming eruptions. The different types of eruptions associated with rhyolitic volcanism can result in severe impacts to the environment and society, varying from a local to a global scale. Yet, due to their typically longer recurrence times compared to volcanic events of less evolved magmas, only a very limited number of rhyolitic eruptions have been documented in historical accounts or recorded through geophysical monitoring. This lack of direct records limits the current understanding of the main processes controlling the dynamics of rhyolitic volcanism and hinders the construction of robust eruption scenarios.

This study presents new insights into the eruptive behaviour of rhyolitic eruptions using the Kaharoa eruption from the Taupō Volcanic Zone (TVZ) of New Zealand as a case study. The TVZ is one of the most frequently active regions of rhyolitic volcanism on Earth with the 1314±12 CE Kaharoa eruption being the most recent rhyolitic event in the TVZ. This eruption is sourced from multiple vents along the Tarawera dome complex, within the Okataina caldera system, and erupted up to 9 km^3 of magma. By investigating the Kaharoa pyroclastic succession, this research contributes to constraining the key factors controlling the dynamics of moderate- to large-scale rhyolitic eruptions occurring in intra-caldera settings. The approach used in this research combines geological field investigations and quantification of the sedimentological and componentry characteristics of the deposits with the analyses of single-clast features (e.g., bulk density and textures of vesicles in pumice clasts).

Field-stratigraphic relationships of 24 lithostratigraphic units for the Kaharoa deposit elucidate the intra-eruption chronology, placing time constraints on the numerous, discrete explosive episodes, while revaluating previous stratigraphic schemes. From variations within the stratigraphy in sedimentary structures, grain size and particle content of the pyroclastic beds, an array of deposit types is identified and linked to temporal changes in transport and depositional patterns as well as eruptive styles. Five distinct explosive eruptive phases are established for the Kaharoa eruption. These include multiple phases of repeated subplinian-type, fall-dominated episodes, alternating with phases characterised by overall sustained pyroclastic density currents and episodes of ash emission. A final sixth phase places the main lava dome building sequence within the proposed reconstruction and eruption model.

Following constraints on the eruption from field-derived data, an in-depth investigation of the Kaharoa pumice microtextures is performed using Scanning Electron Microscopy, which revealed complex and anisotropic vesicle textures. To characterise the observed complex vesicle

features of the Kaharoa pumices, a methodology is developed providing guidelines for the 2D quantification of tube-like vesicles. The integration and interpretation of the pumice textural results along the stratigraphic sequence indicates that the main processes that regulate the evolution of the magma during ascent in the shallow conduit region are magma shearing, bubble coalescence and outgassing. These factors provide bounding conditions for magma ascent dynamics and indicate cyclical variation in the eruption behaviour. Furthermore, by combining textural, sedimentological and componentry data, this study suggests that the inferred dike-shaped geometry of the conduit, together with conduit-vent wall instabilities, are primary factors in controlling: (i) the intrinsic responses of the magma to ascent and decompression to the surface and (ii) the characteristics of the ejected gas-pyroclasts mixtures, influencing the transport-sedimentation regime. The dynamic magma-conduit interrelationships ultimately govern the changes in eruptive styles and overall dynamics of the Kaharoa eruption.

This research defines a framework to relate depositional and textural characteristics to eruptive processes and provides critical insights into the types of eruptive sequence and eruptive style changes of intra-caldera rhyolitic eruptions. The scenario depicted for the Kaharoa eruption highlights the complex episodic, multi-phase, explosive to dome-forming nature of dike-fed rhyolitic eruptions. Furthermore, it provides crucial information for scenario-based volcanic hazard assessments of a Kaharoa-type eruption at Okataina and at other rhyolitic centres within the TVZ. Finally, comparing with available datasets from other volcanic events of similar magnitudes, magma composition, and geological settings, this research suggests that this type of rhyolitic eruption behaviour is common at other silicic caldera systems worldwide, making it of great relevance for future volcanic hazard studies.

Acknowledgements

The firm commitment, the healthy working discipline and the unbreakable passion that go into any years-long research project cannot serve alone to achieve the project goals. The support, at different levels, along with the friendship and love of fellow humans are equally needed. This section tries to warmly acknowledge the many that, in different ways, have contributed in these past years to make this doctoral thesis possible.

My utmost gratitude goes to my family and lifelong friends in my home country for their incessant support, love, and encouragement. The completion of this project simply would have not been possible without each one of them. Although these few lines will never fill the cosmos of gratitude I owe to them, I do hope this will provide grounds to forgive my absence during these years of unforeseen global changes.

I would like to take this opportunity to express my deepest gratitude to Raffaello Cioni (Università di Firenze). I would not have been here today without his teachings during the formative years of Bachelor and Master studies. His enthusiasm and knowledge, coupled with humility and outstanding work ethic have no equivalent and have been a source of inspiration for many years. I am greatly indebted for his mentoring and encouragement, and I would also like to thank him for discussions on some of the topics presented in this thesis.

I wish to sincerely thank my doctoral supervisors Jonathan Procter and Gábor Kereszturi (Massey University) for having provided the opportunity to pursue my research interests in such a fascinating area of volcanology, and for enabling me to work autonomously. I thank Gábor for discussions and for timely commenting on submitted chapter drafts and I thank Jonathan for discussions and for reading the thesis before submission. For their involvement at a very early stage of this project, I send my thanks to Károly Németh (Massey University) and Phil Shane (Auckland University).

I would like to greatly thank Rebecca Carey (University of Tasmania), Ben Kennedy (University of Canterbury) and Gert Lube (Massey University) for examining this thesis in depth and for their many helpful comments and stimulating discussions.

During these years I had the opportunity to meet numerous researchers at conferences and field trips who kindly shared their knowledge and passion for volcanology with me and provided valuable scientific discussions for which I am very grateful. I would like to thank in particular Nobuo Geshi (Geological Survey of Japan), Geoff Kilgour (GNS Science), Federico Lucchi (Università di Bologna), Yasuo Miyabuchi (Kumamoto University) and Mitsuhiro Nakagawa (Hokkaido University). Furthermore, I would like to extend my sincere gratitude to Georg Zellmer

and Mark Bebbington (Massey University) for inviting me in taking part at some of these conferences and for covering travel and lodging expenses.

Many are the people within Massey University, especially at the School of Agriculture and Environment (SAE), that I would like to thank. I would like to thank Kate Arentsen for her irreplaceable support on the administrative aspects of the PhD and for helping with logistics during field work. I am grateful to Anja Moebis for discussion on many laboratory-related topics and for her kind assistance during grain size analyses with laser diffraction techniques. Many thanks to Alan Palmer for discussion on soil development around Mt Tarawera. I also wish to extend my thanks to Matthew Savoian and Raoul Solomon of the Massey Microscopy Imaging Centre for their assistance while operating the Scanning Electron Microscope. Furthermore, I would like to send special thanks to Aniek Hilkens and Hannah Tokona from the Graduate Research School for their support during the final stages of this PhD.

To Diane Pearson (Massey University), I am extremely grateful for her help and support during the many steps of the PhD processes. I would also like to thank her for the numerous discussions and for always be willing to provide invaluable advice on the troubled waters of doctoral and early career research paths in academia.

I thank all the fellow colleagues at the Volcanic Risk Solutions of Massey University. I am grateful to Gert Lube for discussion on many topics related to this research and for his encouragement, to Charline Lormand for discussion and help with image analysis of pumice textures, and to Stuart Mead, together with Nicolás De Francesco (National Scientific and Technical Research Council, Argentina) for initial assistance with image analysis programming. Furthermore, I would like to acknowledge James Ardo and Michael Morgan for their initial assistance during thin section preparation.

The field work component of this research conducted around Tarawera has benefited from the interactions with many colleagues. I wish to warmly thank Federico Lucchi (Università di Bologna), Roberto Sulpizio (Università di Bari) and Matteo Roverato (Université de Genève) for dedicating time in the field together and for their numerous and valuable advice. Rich and insightful field discussions were also provided by Mitsuhiro Nakagawa (Hokkaido University), who is kindly thanked for having shared his expertise. For assistance and discussion in the field I would like to express my gratitude also to Marija Voloschina (now at Università di Pisa), Aliz Zemeny (now at the University of Copenhagen), Gabriel Ureta (Universidad Católica del Norte), and to Ermanno Brosch, Szabolcs Kósik and Sarah Tapscott (Massey University). Furthermore, I wish to send my thanks to the many landowners around Tarawera that have allowed me access to "geologise" in their properties. Finally, I would like to kindly thank Hancock Forest Management Ltd., as well as Timberland Ltd., and PF Olsen for granting me access to their respectively manged

land areas in the Tarawera and Rotoiti Forests. Even if during this research field work within the Makatiti Dome Scenic Reserve was not undertaken, I wish to sincerely thank Rotoiti 15 Ngā Rawa E Tupu Trust for granting me access at this location.

I wish to send special thanks to Ian Nairn for his kind hospitality, for discussions on the Okataina Volcanic Centre and for providing old field photos and maps produced during his research at Tarawera.

I will never be able to thank Clel Wallace and Nicky Banks enough for their enormous generosity and help during this final PhD year. Thank you for welcoming me in your family, for offering a place to stay in complicated times, for the support you have generously given me, as well as for the numerous motivating scientific and non-scientific discussions.

The invaluable friendship and support during these years of Aliz Zemeny, Marija Voloschina and Ermanno Brosch are immensely thanked. Their enthusiastic scientific curiosity, brilliant minds and warm hearts have enriched every moment of this experience. The many discussions on the topics presented in this thesis as wells as their on-point comments on submitted abstracts and conference presentations are also warmly thanked.

Finally, I would like to extend my thanks to the many musicians that have provided a pleasant escape from the tedious and meticulous work that goes with completing a doctorate. Moreover, I thank them for supplying melodies in which performing laboratory works and driving long hours to field sites were an absolute pleasure. Special mentions go, in a not so random order, to Vangelis, Mike Oldfield, Neil Ardley, Klaus Schulze, The Moody Blues, The Who, Uriah Heep, Led Zeppelin, Rush, Neil Young, Tracy Chapman, PJ Harvey, Nick Cave, Lucio Dalla and Kenze Neke.

Funding information

The funding necessary to support this research was provided by the New Zealand Natural Hazards Research Platform programme "Quantifying Exposure to Specific and Multiple Volcanic Hazards" (2015-MAU-PC-01) and by the Resilience to Nature's Challenges programme (GNS – RN047), funded by the New Zealand Ministry of Business, Innovation and Employment.

Furthermore, I would like to acknowledge a Massey University Conference Presentation Grant which enabled the participation at some scientific conferences during these years. Lastly, I wish to express my gratitude to the SAE for providing additional funding that helped in covering living expenses in late 2020.

Table of contents

Abstract ..... *i*
Acknowledgment ..... *iii*
Table of content ..... *vii*
List of Figures ..... *xi*
List of Tables ..... *xix*

CHAPTER 1 – Introduction *1–24*
1.1 Project definition **2**
1.1.1 Research motivations 2
1.1.2 Aim of this research and specific objectives 4
1.1.3 Thesis structure and overview 5
1.2 Background concepts: silicic volcanism **10**
1.2.1 Silicic caldera systems and their post-collapse activity 11
1.2.2 Plinian-type eruptions 13
1.2.3 Lava dome and Vulcanian eruptions 16
1.2.4 Magma dynamics during ascent in the conduit 18
1.3 Background geology: New Zealand and Taupō Volcanic Zone **20**
1.3.1 Regional settings of New Zealand 20
1.3.2 The Taupō Volcanic Zone 22

CHAPTER 2 – The Okataina Volcanic Centre *25–47*
2.1 Introduction **26**
2.2 Volcano-tectonic settings **27**
2.3 Eruptive history **31**
2.3.1 Early volcanism (~625-557 ka) 31
2.3.2 Caldera-forming eruptions (~557, ~322 and ~54 ka) 32
2.3.3 Activity between major caldera collapse events (>54 ka) 33
2.3.4 Post-Rotoiti volcanisms: The Mangaone eruptions (<54–31 ka) 36
2.3.5 Recent intra-caldera volcanism (~25 ka to present) 37
2.3.5.1 Rhyolitic eruptions from the Haroharo vent lineament *39*
2.3.5.1 Rhyolitic eruptions from the Tarawera vent lineament *43*
2.4 Summary **45**

CHAPTER 3 – Deposit and stratigraphy of the Kaharoa eruption *49–121*
3.1 Introduction **50**
3.2 Geological and volcanological background **51**
3.2.1 Geological setting and eruptive history of Okataina caldera and Mt Tarawera 51
3.2.2 Previous studies on the Kaharoa eruption 55
3.3 Methods **58**

3.3.1 General field terminology 58
3.3.2 Field and interpretation approach 59
3.3.3 Analytical methods 61
3.4 Results 62
3.4.1 Deposit features and stratigraphy 62
3.4.1.1 General characteristics of the Kaharoa deposit 62
3.4.1.2 Kaharoa units and deposit types 65
3.4.1.3 Resedimented volcaniclastic deposits 83
3.4.1.4 Lateral correlations and spatial distribution 84
3.4.2 Grain size 87
3.4.3 Componentry 92
3.4.3.1 Types of components of the Kaharoa deposit 92
3.4.3.2 Characteristics of component types 93
3.4.3.3 Componentry variation along the pyroclastic succession 96
3.5 Interpretations 100
3.5.1 Eruptive and depositional processes 100
3.5.2 Reworking and resedimentation of pyroclastic units 105
3.5.3 Key stratigraphic relationships and chronology of depositional events 105
3.6 Discussion 107
3.6.1 Comparison with previous stratigraphic reconstructions 107
3.6.2 Constraints on intra-eruption time breaks 109
3.6.3 Insights into the vent system 112
3.6.4 Evolution of the eruption 114
3.7 Conclusions 119

CHAPTER 4 – An approach to quantify complex and anisotropic vesicle textures in pumice clasts 123–158
4.1 Introduction 124
4.1.1 The importance of microtextural studies of pyroclasts 124
4.1.2 Tube pumice clasts 125
4.1.3 Study motivations 126
4.2 Materials and methods 130
4.2.1 Sample selection and description 130
4.2.2 Image acquisition 132
4.2.3 Image adjustments 134
4.2.4 Image analysis of vesicle features 134
4.2.4.1 Vesicle shape analysis 135
4.2.4.2 Vesicle size and number density analysis 137
4.3 Results 138
4.3.1 Variability of 2D vesicle shape 138
4.3.1.1 Variation of vesicle shape with thin section orientation 138
4.3.1.2 Variation of vesicle shape with magnification and vesicle size 139

4.3.1.3 Vesicle aspect ratio vs. vesicle size *143*
4.3.1.4 Vesicle shape and texture type *144*
4.3.2 Variability of 2D vesicle size and number density 145
4.3.2.1 Vesicularity *145*
4.3.2.2 Vesicle number density *145*
4.3.2.3 Vesicle size distribution *147*
4.4 Discussion and implications 150
4.4.1 Representativeness and uncertainties in vesicle textures analysis 150
4.4.2 The importance of thin section orientation 150
4.4.3 Optimal image magnification(s) for vesicle analysis 151
4.4.4 Effects of manual "decoalescence" of interconnected vesicles 154
4.4.5 Combination of vesicle shape and size data 155
4.5 Conclusions 157

CHAPTER 5 – Magma conduit dynamics during the explosive phases of the Kaharoa eruption 159–219
5.1 Introduction 160
5.2 Background 162
5.2.1 Geological and volcanological settings 162
5.2.2 General features of the Kaharoa eruption 163
5.2.3 Deposit features and eruptive phases of the Kaharoa eruption 165
5.3 Methods 167
5.3.1 Sampling and clast frequency 167
5.3.2 Bulk density and vesicularity measurements 168
5.3.3 Image analysis of vesicle textures 169
5.4 Results 172
5.4.1 Macroscopic observations of pumice clasts 172
5.4.2 Bulk density and vesicularity 176
5.4.3 Characteristics of vesicle textures in pumice clasts 180
5.4.3.1 Type 1 texture (MHP clasts) *180*
5.4.3.2 Type 2 and 3 textures (TP clasts) *182*
5.4.3.3 Vesicles interactions and coalescence features *182*
5.4.3.4 Qualitative vesicle observations and stratigraphic context *185*
5.4.4 Quantitative vesicle data from pumice clasts 188
5.4.4.1 Vesicle number density and size distribution *188*
5.4.4.2 Area-based vesicle size distribution and 2D vesicularity *188*
5.4.4.3 Cumulative vesicle size distribution *191*
5.4.4.4 Comparison in vesicle size data between white and grey pumices *192*
5.4.4.5 Vesicle shape distributions *195*
5.4.5 Crystal content in pumice clasts 198
5.4.6 General features of obsidian microtextures 199
5.5 Interpretations and discussion 201
5.5.1 Insights into conduit processes during magma ascent 201

5.5.1.1 Bubble nucleation, growth and coalescence *201*
5.5.1.2 Shear stress, bubble deformation and outgassing *204*
5.5.2 Pyroclast textural heterogeneity 206
5.5.2.1 Formation of different pumice type and associated vesicle textures *206*
5.5.2.2 Effects of additional syn-ascent and post-fragmentation processes on pumice vesicle textures *209*
5.5.2.3 Insights into the origins and significance of obsidian pyroclasts *210*
5.5.3 Implications for conduit geometry 213
5.5.4 Evaluating the role of conduit processes for deposit pattern and eruptive styles 214
5.6 Conclusions 218

CHAPTER 6 – Synthesis: an integrated view of intra-caldera, dike-fed, rhyolitic eruptions 221–239
6.1 A model for the ascent and degassing dynamics of the Kaharoa magma in the conduit 222
6.1.1 The dike nature of the shallow Kaharoa feeding system 222
6.1.2 Magma dynamics during the subplinian explosive episodes 223
6.1.3 Temporal variations and cyclicity in magma conduit dynamics 224
6.1.4 Obsidian plug formation: aborted transition to effusive activity 225
6.1.5 Transition to the final dome-building phase 226
6.2 Controlling factors on eruption dynamics 226
6.2.1 Variation in eruptive style 226
6.2.2 Episodic behavior of the eruption 228
6.3 Kaharoa eruption model 230
6.4 Comparison with similar rhyolitic eruptions 235
6.4.1 Comparison with other eruptions at Okataina 235
6.4.2 Comparison with post-Oruanui eruptions at Taupō 236
6.4.3 Comparison with similar rhyolitic eruptions worldwide 237
6.5 Eruption classification 239

CHAPTER 7 – Conclusions and future work 241–253
7.1 Research summary 242
7.2 Objectives and key findings 243
7.3 Broader impact of this research 248
7.4 Directions for future work 250

REFERENCES 255–301

List of Appendices 302–303

List of figures

Figure 1.1 – Location of New Zealand in the Australian-Pacific plate boundary. Tectonic settings follow Mortimer and Scott (2020). Bathymetry data from NIWA (https://www.niwa.co.nz) 21

Figure 1.2 – Map of the TVZ modified after Spinks et al. (2005) showing modern and old TVZ boundaries, locations and approximative topographic boundaries of the eight silicic caldera systems within the central TVZ and the main andesitic-dacitic composite volcanoes on the southern and northern segments of the TVZ. Inset shows position of the TVZ in the North Island. 23

Figure 2.1 – Aerial view of the Okataina Volcanic Centre. © Institute of Geological & Nuclear Science Limited 2002. The photo is the front cover of Nairn (2002) and was taken by D.L. Homer. The photo is reproduced here with their permission and modified to add descriptions of main volcanological features of the centre. Dashed black line is approximative border of the OVC. Location of the IAVCEI 2023 Scientific Assembly is also shown 27

Figure 2.2 – (a) Map of the OVC showing topographic margins of Okataina caldera system, including the main Okataina caldera structure, subsidiary basins, and the inferred position of the Okataina Ring Structure, after Nairn (2002). White lines represent the approximate length and width of the two post-25 ka lineaments of eruptive vents. Vent locations associated with the eruptive activity from Haroharo and Tarawera dome complexes are also shown. (b) is modified after Fig. 3b of Cole et al. (2010) and shows location and geometry of the OVC within the Okataina "transfer zone" segment of Spinks et al. (2005) within the TVZ of the Taupō Rift. Dashed thin black lines display the inferred continuation of the axes of the Kapenga (to the south) and Whakatane (to the north) rift segments into OVC, which broadly correspond to the Haroharo and Tarawera vent lineaments 29

Figure 2.3 – Figure 2 of Cole et al. (2010) showing the main Okataina caldera topographic borders and spatial distribution and ages of the intra-caldera and peripheral lava dome complex, with eruptive vent locations. Inset shows negative gravity anomaly (contours in mGals). 30

Figure 2.4 – Map of the post-25 ka intra-caldera rhyolitic lavas and domes of the OVC, modified after Villamor et al. (2007) 41

Figure 3.1 – Map of the OVC showing topographic settings, borders of the Okataina caldera and subsidiary basins (Puhipuhi basin, Okareka and Rotoma embayments) and approximate margins of the intra-caldera Haroharo and Tarawera dome complexes. Location of eruptive vents active at the OVC during the past 25 kyr along the Haroharo (HVL) and Tarawera vent lineaments (TVL) are also shown. The OVC structural features and borders of neighbouring calderas are drawn following Nairn (2002). The inset shows tectonic settings of the southern Hikurangi-Kermadec (HK) subduction margin and locations of the OVC in the TVZ within the North Island of New Zealand. 52

Figure 3.2 – (a) Photo of Mt Tarawera with the three summit domes emplaced during the Kaharoa eruption (Wahanga, Ruawahia and Tarawera). The photo is taken from the NW shore of Lake Tarawera. (b) Map of the Tarawera dome complex with the distribution of lavas (following Nairn, 2002) erupted during the four rhyolite eruptions that built the dome complex. W, R, CD and T indicate Wahanga, Ruawahia, Crater and Tarawera domes (Crater dome is buried beneath Ruawahia and Tarawera domes). Stars show the locations of the inferred seven vents active during the Kaharoa eruption (following Nairn et al. 2001). The vents are numbered from SW to NE (no temporal order is implied): 1 is Green Lake Plug vent, 2 is Tarawera dome vent, 3 is Crater dome vent, 4 is Ruawahia dome vent, 5 is Ruawahia crater vent, 6 is Wahanga dome vent and 7 is Northeast crater. The white arrows indicate the distributions of the Kaharoa block-and-ash flow fans 54

Figure 3.3 – Distribution of the Kaharoa fall deposits in the North Island of New Zealand showing isopach map of the deposits total thickness (in cm) redrawn after Sahetapy-Engel et al. (2014). Individual fall deposit isopach maps are reported in Sahetapy-Engel et al. (2014). Inset show the distribution of the visible distal limit of the Kaharoa deposit reported as ~1-3-cm isopach (Pullar and Birrell,1973).....57

Figure 3.4 – Shaded relief map of the studied area with locations of the investigated stratigraphic sections. Stars indicate the position of the Kaharoa eruptive vents inferred by Nairn et al. (2001), with the yellow start marking the position of Ruawahia vent. The shaded relief map and drainage system of the studied area are obtained from Land Information New Zealand - LINZ, data component of the Topo50 and Topo250 map series (https://data.linz.govt.nz) 59

Figure 3.5 – Field photos of the studied pyroclastic succession. (a) Panoramic view of the Kaharoa deposit at reference section 2 (Fig. 3.4), at 6.7 km south from the vent. (b) Zoom on section 2. (c) Reference section 24 (Fig. 3.4), at 7.4 km north from the vent. Subdivision of the deposit in units (A1 to BS) is indicated in (b) and (c) (spade is 1 m long in both sections). Note erosional gully at the contact between units A3 and L3.....64

Figure 3.6 – Representative field photos showing the different deposit features of the Kaharoa units at key sections in proximal and medial sites (refer to Fig. 3.4 for location of outcrops). Solid red lines indicate sharp and erosive units contacts; solid black lines indicate sharp unit contacts with non to minor erosion/reworking; dashed black lines indicate gradual unit contacts; bold, black lines indicate the basal contact of the Kaharoa deposit. (a) Massive lapilli unit L3 at S18 (S=stratigraphic section) south form the vent, overlain by the laterally discontinuous ash unit A4. Note the characteristic features of the top bed of unit A3 in proximal sites having plane-parallel- to cross-laminations (see also f and g) with few laminae being oxidized. (b) Massive lapilli unit L7S at S28, east form the vent. (c) Weakly stratified lapilli unit L5 at S1, south from the vent. (d) Stratified lapilli unit L6 at S18, south from the vent. The poorly sorted ash beds within L6 deposit have a limited distribution and rapidly fade away from the vent. (e) Stratified lapilli unit L4 at S2, south from the vent. (f) Deposit features of unit A3 at S2, with alternation of massive, fine to coarse, ash beds. Note the cm-size scours on top of A3 (see also dm-size erosional gullies at A3-L3 contact in Fig. 3.5). (g) Characteristics of A3 at S18. (h) Massive lapilli unit L1 at S2 south from the vent and gradual contact with overlaying massive fine ash unit A2. Note the increase in fine ash content on the top part of unit L1 towards the contact with A2. Basal contact of the pyroclastic succession and underlying P-layer and soil are also shown. (i) Top ~3 m of S18, south from the vent with proximal facies of unit A7 lapilli-bearing ash deposits. Note the alternation between massive, dm-thick lapilli-bearing ash beds with dispersed carbonised tree logs and the massive to cross-laminated medium-to-fine, ash beds. Lapilli lenses within A7 are indicated with thin dotted black lines. Unit A7 is overlain by the laterally discontinuous unit A11 and the coarse ash unit Af. The base of the BAF deposit of unit BS is exposed at this section. BS is separated from the underlying units by a thin red, oxidized ash layer. (j) Massive coarse ash unit A1 at the base of the Kaharoa deposit at S17. (k) Zoom on the variably consolidated unit A8 at S26, north from the vent, showing distinctive very fine ash beds (bottom and top) and cross-stratified, coarser ash beds (middle). Additional field photos are reported in Appendix A.....71

Figure 3.7 – Reconstructed stratigraphy and proposed unit subdivision of the Kaharoa pyroclastic succession. The composite stratigraphic log illustrates the stratigraphic relationship between units and summarized the main sedimentological and lithological features of individual beds. Units' thickness is only representative of main unit differences, and it is not to scale. For each unit the associated deposit type is indicated as follow: 1-ML is massive lapilli deposit; 2-SL is stratified lapilli deposit; 3-MCA is massive coarse ash deposit; 4-MFA is massive fine ash deposit; 5-ldA is laterally discontinuous, ash deposit; 6-LbA lapilli-bearing, ash-supported deposit; 7-vcA is variably consolidated ash deposit. Solid red lines indicate sharp and erosive units contacts (A3-L3 and L6-A7) and contacts marked by thin laterally continuous, oxidized ash layer (Af-BS); solid black lines indicate sharp unit contacts with non to minor reworking; dashed black lines indicate gradual units contacts. Stars indicate reconstructed unit contacts, based on units' correlation among different outcrops. All other unit contacts have been directly observed in the field. Grain size and sorting based on visual estimations on the field: F–fine, M–medium, C–coarse and B–bomb; ws–well sorted, ms–moderately sorted and ps–poorly sorted 77

Figure 3.8 – Isopach maps of individual ash units (thickness in centimetres). Black solid lines represent well constrained isopachs, while black dashed lines represent tentative isopachs based on the available thickness data of this study. Thickness measured at each stratigraphic section (value next to black dots) is also reported; tr indicates sections where the unit is found as trace. Blue stars indicate the inferred positions of the Kaharoa eruptive vents after Nairn et al. (2001), while the area occupied by the Kaharoa lava domes is highlighted in orange 80

Figure 3.9 – Isopach maps of individual lapilli units (thickness in centimetres). Black solid lines represent well constrained isopachs based on the available thickness data of this study, while black dashed lines represent tentative isopachs. Thickness measured at each stratigraphic section (value next to black dots) is also reported; tr indicates sections where the unit is found as trace. Isopachs from Sahetapy-Engel et al. (2014) are shown as red dashed lines for equivalent stratigraphic units (refer to Table 3.1). Blue stars indicate the inferred positions of the Kaharoa eruptive vents after Nairn et al. (2001), while the area occupied by the Kaharoa lava domes is highlighted in orange 82

Figure 3.10 – Photograph of section 21 at ~15 km from the vent along the Tarawera river floodplain (see Fig. 3.4), showing deposit features of interpreted RV deposits (RV1 and RV2) and pyroclastic units A8 and L8 at the bottom of the section. A medium ash bed at the top of RV1 is tentatively correlated with unit Af at more proximal sites. Spade 1 m long. Peat horizon might represent accumulation of organic material (e.g., leaves) from the surrounding, partially buried, vegetation..... 84

Figure 3.11 – Stratigraphic correlations of Kaharoa units among selected key sections (S) along four different transects in both S and N sector. Note that the deposit's thickness in section 18 is not to scale. Reliable correlations are marked with solid black lines, while few tentative correlations are marked with dashed black lines. Inset shows the locations of key sections (white dots) and transects (AA′, BB′, CC′ and DD′) relatively to the Kaharoa domes (dark grey) and vents (stars; the yellow star indicate the reference vent for source-to-outcrop distances) 86

Figure 3.12 – Grain size characteristics of units at reference sections 2 and 24. (a) Stratigraphic logs of the two sections with position and ID of samples (e.g., K100). T1886 in section 24 indicates scoria deposits from the 1886 CE Tarawera eruption. (b) Variation with stratigraphic height in median diameter (Mdϕ) and sorting coefficient (σϕ) of individual beds sampled within each unit. (c) Selected grain size distributions organized by deposit type (symbol on top left corner of each histogram): massive lapilli deposit (light grey circles); stratified lapilli deposit (dark grey circles); massive coarse ash deposit (white circles); massive, fine ash deposit (dark grey squares); laterally discontinuous, ash deposit (yellow triangles); lapilli-bearing, ash deposit (red triangles); variably consolidated ash deposit (blue diamonds)..... 88

Figure 3.13 – Results of grain size analyses of representative samples analysed in this work plotted as (a) median diameter (Mdϕ) versus sorting coefficient (σϕ) and (b) as weight % of sample <1 mm (F1) versus weight % of sample <63 μm (F2). Deposit type of individual samples is indicated as follow: 1-ML is massive lapilli deposit (light grey circles); 2-SL is stratified lapilli deposit (dark grey circles); 3-MCA is massive coarse ash deposit (white circles); 4-MFA is massive, inter-lapilli, fine ash deposit (dark grey squares); 5-ldA is laterally discontinuous, ash deposit (yellow triangles); 6-LbA lapilli-bearing, ash-supported deposit (red triangles); 7-vcA is variably consolidated ash deposit (blue diamonds)..... 89

Figure 3.14 – Representative clasts photographs of juvenile (a to f) and lithic (g and h) materials of the Kaharoa deposit: (a) white pumice; (b) grey pumice; (c) obsidian; (d) dense juvenile: (e) banded pumice; (f) basaltic material as free clasts and coated with pumice; (g) lava fragments with variable degree of oxidation: (h) hydrothermally altered clasts. White and black scale bars are 1 cm long in each picture ... 95

Figure 3.15 – Componentry characteristics of units and variations in the relative abundance of different components with stratigraphic height at reference sections 2 (a) and 24 (b). In (c) are reported the variations in the relative abundance of obsidian and total lithic (lave fragments + hydrothermally altered clasts) through the reconstructed whole pyroclastic sequence 98

Figure 4.1 – SEM-BSE images at 50× magnification of the three different Kaharoa pumice vesicle textures investigated in this study. Top images are from thin sections parallel (PA) to main vesicle elongation and bottom images are thin sections orthogonal (OR) to main vesicle elongation 131

Figure 4.2 – Shape variation captured by the shape parameters used in this study. The eleven hypothetical vesicle geometries are reproduced from Moitra et al. (2013). See text for more details and equations of individual shape parameters 136

Figure 4.3 – (a) Relationship between Aspect Ratio (AR) and Deformation (D) parameters, with nomenclature for elongated vesicles used in this study: subspherical (AR = 1 to 1.5 and D = 0 to 0.2), elongated (AR = 1.5 to 5 and D = 0.2 to 0.67), very elongated (AR = 5 to 10 and D = 0.67 to 0.82), extremely elongated (AR = 10 to 100 and D = 0.82 to 0.98) and thread-like vesicle (AR > 100 and D > 0.98). Schematic example of vesicles at different elongations are reported in the graph (AR = 1.5, AR = 5, AR = 10, AR = 50 and AR = 100). To the right side, two SEM-BSE images at 200× magnification (processed and binarized) from PA (b) and OR cuts (c) are reported for comparison, with mean values of AR and ± standard deviation 137

Figure 4.4 – Boxplots of the 2D vesicle shape parameters quantified from images acquired at 20×, 50×, 100× and 200×, along two mutually perpendicular thin sections (PA and OR to main direction of vesicle elongation) in the three vesicle textures analysed: (a) Type 1, (b) Type 2 and (c) Type 3. The shape parameters are dimensionless and are indicated as C = circularity, R = regularity, SF = shape factor, D = deformation, E = eccentricity and FLT = flatness. C, R and SF measure the complexity of the 2D vesicle, while D, E and FLT measure the elongation of the 2D vesicle. See text for shape parameters equations and examples in Fig. 4.2. Inset in each graph indicate the number of vesicles analysed (N), the number of images taken (in brackets) and the vesicle size range (VSR, in mm) per each magnification 140

Figure 4.5 – Frequency distributions of the Deformation (D) (vesicle elongation) and Regularity (R) (vesicle complexity) parameters among the vesicle texture types 1, 2 and 3 from both PA and OR cuts to main vesicle elongation. The distributions resulting from the images acquired at 20x, 50x, 100x and 200x are reported in different colours (grey, blue, yellow and orange, respectively) in each graph for comparison 141

Figure 4.6 – Variation in vesicle AR with vesicle size among the three texture types. To simplify data visualization, upper limits for both vesicle size and vesicle AR are set in each graph to contain >95% of vesicles analysed. For maximum AR values see Table 4.3. Vesicles tend to maintain steady AR for size >250 µm 146

Figure 4.7 – Variation in 2D vesicularity (corrected for crystal content) with image magnification and thin section orientation among the three texture types, type 1 to type 3. Values in brackets indicate the average of 2D vesicularity across all the magnifications per thin sections. Error bars are reported as standard deviation from the results of images at the same magnification 145

Figure 4.8 – NA-VSDs. Vesicle number density per area (NA) as a function of vesicle size (expressed as the diameter of the circle of equivalent area) for the three texture types and thin section cut: (a) and (b) are type 1, PA and OR cuts, respectively; (c) and (d) are type 2, PA and OR cuts, respectively; (e) and (f) are type 3, PA and OR cuts, respectively. The plotted NA are per melt area as they are corrected for crystal content of individual images. In each graph, NA vs vesicle size plots resulting from the images acquired at 20×, 50×, 100× and 200× magnifications are displayed in different colours (grey, blue, yellow and orange, respectively) for comparison. The average NA calculated across individual magnification are reported in each graph. Note the change in the y-axis scale from PA to OR cuts 146

Figure 4.9 – Area-VSDs. Vesicle size distributions per melt area (corrected for crystal content) of images acquired at 20× (grey), 50× (blue), 100× (yellow) and 200× (orange) magnifications. VSDs are plotted for the three texture types and two thin section cuts: (a) and (b) are type 1, PA and OR cuts, respectively; (c) and (d) are type 2, PA and OR cuts, respectively; (e) and (f) are type 3, PA and OR cuts, respectively. Vesicle size (diameter of the circle of equivalent area) are reported across 30 geometric bin size classes (geometric bin factor is 100.1, see text for detail) from 1.84 µm (diameter of smallest vesicle analysed) 148

Figure 4.10 – Comparison of vesicle shape and size distributions obtained from the combination of 20× and 200× images (dark grey) and obtained from the combination of images at all magnifications used in this study (light grey), 20×, 50×, 100× and 200×. Texture type 2 is used as an example for the comparison, where (a) and (b) are vesicles shape and size distributions from the PA cut, while (c) and (d) are from the OR cut. Boxplots of shape parameters report median, interquartile range and min and max (outliers excluded). The area-VSDs are per melt area express the vesicle area fraction as a function of vesicle equivalent circular diameter in 30 geometric bin size classes. The total NA resulted from the two magnification combinations are reported in (b) and (d) for PA and OR cuts, respectively..... 153

Figure 4.11 – Comparison of vesicle shape and size distributions obtained from the minimal decoalescing approach (Approach 1) and from the maximal decoalescing approach (Approach 2) for images of texture type 2 in PA (a and b) and OR (c and d) cuts. See text for more details on the two image editing approaches 155

Figure 5.1 – (a) Map of the OVC showing topographic settings, borders of the Okataina caldera and subsidiary basins (Puhipuhi basin, Okareka and Rotoma embayments) and approximate margins of the intra-caldera Haroharo and Tarawera dome complexes (dashed lines). Triangles indicates active eruptive vents during the past 25 kyr of the centre, along the Haroharo (HVL) and Tarawera vent lineaments (TVL). Structural features, caldera border and vent location are drawn following Nairn (2002). Inferred vents active during the Kaharoa eruption are indicated with red triangles following Nairn et al. (2001). The inset displays the tectonic settings of the southern Hikurangi-Kermadec (HK) subduction margin and locations of the Okataina caldera (OC) in the Taupō Volcanic Zone (TVZ) within the North Island of New Zealand. (b) Zoom in the Tarawera dome complex with distributions of pre-Kaharoa and Kaharoa lavas (following Nairn, 2002) and locations of the outcrops sampled for this work (white dotes). RV indicates position of Ruawahia vent 164

Figure 5.2 – Representative Kaharoa pumice clast typologies according to their vesicle surface textures: (a) microvesicular heterogeneous pumice (MHP) and (b) tube pumice (TP)..... 174

Figure 5.3 – Relative frequency of MHP (orange) and TP (blue) clasts in the studied units in upward succession along the stratigraphic sequence. Pumice type frequency is measured from clasts in the 16-32 mm grain size interval. (b) and (t) in units L4 and L8 indicate samples collected from the bottom and top parts of the units, respectively..... 175

Figure 5.4 – Bulk density distributions of pumice clasts in the investigated units from the Kaharoa deposit. White pumice and grey pumice clasts (the latter occurring only in unit L7S, L7N and L8) are indicated in light and dark grey, respectively. Graphs are in stratigraphic order from left to right panels. Two blue dashed lines at clasts densities of 1000 kg/m3 and 1500 km/m3 (corresponding to bulk vesicularity of 58 and 36%, respectively) are reported in the figure to facilitate comparison between units 177

Figure 5.5 – Bulk density distributions for MHP (orange) and TP (blue) clasts from the entire pumice sample collections (~1300 clasts in total) 178

Figure 5.6 – Bulk density distributions for lava dome fragments collected from block-and-ash flow units BS (light red) and BN (dark red) and for obsidian pyroclasts (OBS in black) collected from unit L3 and A7 178

Figure 5.7 – Representative SEM-BSE images at 20× and 100× of vesicle texture type 1 in MHP clasts. (a) to (f) and are taken from PA cuts (parallel to main direction of vesicle elongation), while (g) to (l) are taken from OR cuts (perpendicular to main direction of vesicle elongation). Dashed line in (c) shows the sharp boundary between texturally different domains having deformed (left in f) and undeformed vesicles (right in f)..... 181

Figure 5.8 – Representative SEM-BSE images at 20× and 100× of vesicle texture type 2 from TP clasts. (a) to (d) are taken from PA cuts (parallel to main direction of vesicle elongation), while (e) to (h) are taken from OR cuts (perpendicular to main direction of vesicle elongation) 183

Figure 5.9 – Representative SEM-BSE images at 20× and 100× of vesicle texture type 3 from TP clasts. (a) to (d) are taken from PA cuts (parallel to main direction of vesicle elongation), while (e) to (h) are taken from OR cuts (perpendicular to main direction of vesicle elongation) 184

Figure 5.10 – Examples of vesicle coalescence features from SEM-BSE images at 200× from OR cuts of TP (a and c) and MHP (b and d) clasts. Red arrows indicate thinning of the glass walls separating adjacent vesicles prior to rupture and coalescence, with the thin walls varying from planar to curvilinear; Blue and yellow arrows indicate retraction and wrinkling, respectively, of glass walls after rupture. Scale for all images is reported at the bottom of (c) and (d) 185

Figure 5.11 – Representative SEM-BSE images at 50× and 200× of vesicle textures type 1 from MHP clasts (a) and type 2 from TP clasts (b) for the studied units along the stratigraphic sequence. For the same sample within a unit, both textures from PA and OR cuts are shown. Scale for each image is indicated by a red bar on the bottom right corner, having length of 1 mm and 150 µm for 50× and 200× images, respectively 186

Figure 5.12 – (a) Variation of the total vesicle number density per unit area of melt (NA) of white pumice clasts along the stratigraphic sequence. Total NA are reported as average results from type 1 texture (orange) and average results from type 2 texture (blue). (b) and (c) show the distributions of NA as a function of vesicle size (equivalent diameter in µm) for type 1 texture and for type 2 texture among the different Kaharoa units 189

Figure 5.13 – Vesicle size distributions as area fraction vs vesicle equivalent diameter (in mm) for white pumice clasts from fall lapilli units (L1 to L8) and the PDC unit A7 of the Kaharoa stratigraphy. Vesicle size distributions are obtained from sets of 200× images from OR cuts of three clasts per each unit. Results are corrected for crystal content and normalized for the average 2D vesicularity (value in % on the top right corner of each graph). Vesicle size distributions are plotted as average results from type 1 texture (orange), average results from type 2 texture (blue) and as average results from type 3 textures (dark grey). Two black dashed lines at vesicle size 0.009 and 0.09 mm are reported to facilitate comparison between units in each panel 190

Figure 5.14 – Cumulative vesicle size distributions of white pumice clasts as a function of vesicle number density (number of vesicles per unit area of melt larger than a given vesicle diameter L, left panel) and vesicle area fraction (right panel), corrected for crystal content. Vesicle number densities and area fraction for the different Kaharoa units are plotted as average results from type 1 texture (a and b), average results from type 2 texture (c and d) and as average results from type 3 (e and f; only units L5 and L7N). For comparison, orange and blue fields in e and f represent ranges of cumulative size distributions for type 1 and type 2 textures 191

Figure 5.15 – Vesicle size distributions as area fraction vs vesicle equivalent diameter (in mm) for grey pumice clasts in unit L7N for type 1 (a) and type 2 (b) textures. Results are corrected for crystal content and normalized for the average 2D vesicularity (value in % on the top right corner in a and b). Cumulative vesicle size distributions as number densities (number of vesicles per unit area of melt larger than a given vesicle equivalent diameter L) and vesicle area fraction are reported in c and d respectively, for type 1 (solid black line) and type 2 (dashed black line) textures. Orange and blue fields in c and d represent ranges for type 1 and type 2 cumulative size distributions from white pumice clasts in the analysed Kaharoa units 193

Figure 5.16 – Distributions of the vesicle shape parameters quantified from white pumice clasts among the investigated Kaharoa units along the stratigraphic sequence. Boxplots show median and quartiles. Results are from type 1 texture (a) and type 2 texture (b) 196

Figure 5.17 – Phenocryst content and crystal-vesicle interactions in SEM-BSE images of white (a and b) and grey (c) pumice clasts. The main crystal phases are indicated as plg, qtz and bt for plagioclase, quartz and biotite crystals, respectively. Arrows in (a), (b) and (c) indicate examples of tube vesicles bend in the proximity of crystals (red arrows), vesiculation of equant vesicles around crystals (yellow arrows) and formation of large cavities around crystals (blue arrows) 198

Figure 5.18 – SEM-BSE images of obsidian pyroclast microtexture from unit L3 (a, b, c and d) and from unit A7 (e, f, g and h). Images are taken at 20× (a, b, d and e) and at 50× (c, d, g, and h). qtz, pl, bt and ox in (e) indicate abbreviations for quartz, plagioclase, biotite and oxides (titanomagnetite) crystals, respectively; the same mineral assemblage is found in the remaining pictures 200

Figure 5.19 – Conceptual model of magma ascent in the conduit through time and origin of different microtextures observed in this study. The conduit width is not to scale, and sizes of bubbles are exaggerated. (a) Schematic representation of the evolution of the bubble fraction within the ascending magma column in the conduit at progressively shallower levels and associated sequential and overlapping processes (i to v). (b) Schematic representation of magma in the conduit approaching and at fragmentation (vi) during explosive events. The figure shows variation in magma ascent velocity laterally across the conduit leading to the development of areas at different shear. Within the central region of the conduit, magma shearing and bubble deformation is localized in narrow zones. Towards the marginal regions of the conduit, the magma experiences high and pervasive shear with formation of networks of tubular bubbles. Near the conduit walls, longer residence time and efficient outgassing promote collapse of tubular bubbles and magma densification. This model is proposed to explain the origins within the conduit of the different microtextures (indicated by the arrows) observed in the later erupted juvenile pyroclasts. SEM-BSE photos are reported as examples; MHP is microvesicular heterogeneous pumice, TP is tube pumice, and DJ is dense juvenile clasts 207

Figure 5.20 – Combined pumice textures and componentry changes throughout the eruption stratigraphy (i.e., time) within the studied units. (b) and (t) in units L4 and L8 indicate samples collected from the bottom and top parts of the units, respectively. (a) Relative frequency of MHP (orange) and TP (blue) clasts. (b) and (c) relative abundances of dense juvenile (DJ, grey), obsidian (black) and lithic clasts in componentry analysis (expressed in weight percent) at sections 2 and 24. Obsidian clasts in unit A7 is up to ~27 wt.% in section 28. (d) Proportion of obsidian to lithic clasts 211

Figure 5.21 – Schematic model illustrating the main changes through time in shallow conduit dynamics and eruption styles with examples for Phases B to C. Development of a laterally stratified magma approaching fragmentation follows Fig. 5.19, with light grey indicating the source area of later microvesicular heterogeneous pumice clasts (MHP), dark grey indicating the source area of tube pumice clasts (TP), and blue indicating the source area of dense and outgassed magma forming dense juvenile clasts (DS) and obsidian plug/clasts (OBS). The fragmentation level is kept at the same depth for visualisation purposes; however, it is noted that the depth of the fragmentation zone likely varied during the eruption sequence (e.g., deepening of the fragmentation depth is expected during L4, L5 and L6 episodes). (i) onset of Phase B is characterised by the disruption of a previously formed obsidian plug obstructing the conduit-vent system, with obsidian clasts being incorporated in the L3 column. Efficient clearing of the conduit ensures steady mass discharge rate and stable column leading to deposition of massive lapilli fall deposits. (ii) Conduit-vent instabilities result in repeated wall collapses an incorporation of a higher proportion of lithic clasts in the L4, L5 and L6 plumes, favouring a shift from stable to oscillating eruptive columns and deposition of stratified lapilli fall deposits. Continued partial outgassing during Phase B leads to magma densification at the conduit walls and production of denser juvenile clasts at fragmentation which further impacted the L6 column stability. (iii) The protracted and efficient magma outgassing, and slower ascent rates culminate with the formation of a second obsidian plug, resulting in a pause in the eruption between phases B and C. (iv) Phase C starts with the disruption of the second obsidian plug by the ascending and degassing A7 magma within narrower conduit, leading to an elevated production of TP clasts upon fragmentation. Widening of the vent during eruption favours slower exit velocity of the gas-pyroclast mixture and incorporation of a larger proportion of obsidian clasts. These processes triggered the shift from buoyant plume to boiling-over conditions and production of PDCs 217

Figure 6.1 – Schematic representation of the Kaharoa eruption model and magma dynamics in the conduit. (a) Composite stratigraphic log of the Kaharoa pyroclastic succession with lithostratigraphic units and eruptive phases. The log is not to scale; however, it gives indication on the mean deposit gain size (horizontal axis; finer to coarser is left to right). The colour of each unit in the log are coded according to

their deposit type with: 1ML = massive lapilli deposit, 2SL = stratified lapilli deposit, 3MCA = massive coarse ash deposit, 4MFA = massive, fine ash deposit, 5ldA = laterally discontinuous, ash deposit, 6LbA lapilli-bearing, ash-supported deposit, 7vcA = variably consolidated ash deposit; BAF indicates deposit from block-and-ash flows. (b) Schematic visualisation of the seven aligned vents (triangles; positions of vents follow Nairn et al., 2001) active (red triangles) during the eruption, with main distribution of the pyroclastic deposits associated to each eruptive phase. Vent numeration follows Figure 3.2 (D=dome; V=vent). (c) Summary of the eruption timeline with style of eruptive activity and main deposition mechanisms of the erupted products. For the sake of simplicity, the black bars are drawn with equal lengths, however the duration of each activity varied (i.e., activity during Phase E and later F was possibly prolonged for months to years). The subplinian activity is further subdivided to incorporate the observed variations in deposits and interpreted processes: a indicates stable sustained columns, b indicates oscillating sustained columns, c indicates partial column collapses from sustained columns and d indicates the fine ash settling mainly occurring when the column had ceased. (d) Schematic visualisation of conduit dynamics. (d1) and (d2) show variation of conduit characteristics and magma at fragmentation with example for Phase A and Phase B, respectively. The fragmentation level (dashed grey line) is kept at the same depth for visualisation purposes; however, it is here noted that the depth of the fragmentation zone likely varied during the eruption sequence. In (d1) the evolution of the conduit is shown for the entire Phase A: in A1 (eruption onset) the conduit paths are poorly connected from bottom to surface; in L1 (first subplinian column) erosion and widening of the conduit walls occur with lithic clasts carried by the eruptive column; in L2, the well-developed conduit ensure stable column condition and higher mass discharge rate; in A3 the outgassing and slower magma ascent result in a low-intensity ash activity with initiation of conduit occlusion by formation of dense magma at the conduit walls; the protracted magma outgassing culminates with the formation of an obsidian plug in the conduit-vent. In (d2) two examples are represented: in L3, disruption of the obsidian plug by new gas-rich ascending magma leads to onset of Phase B and subplinian activity; in L5 a case is made for conduit-vent instabilities (wall collapses) leading to oscillating subplinian columns (see text for more details). (d3) Illustration of magma ascending through a dike-shaped conduit (modified after Gonnermann and Taisne 2015) showing cross-conduit velocity gradient and magma densification at the conduit walls. (d4) Illustration of the inferred variable conduit diameter between eruptive episodes depositing the L fall unit and the A7 PDC unit. The colour gradient gives indication of the areas of magma in the conduit from which MHP and TP clasts are produced at fragmentation. The magma TP portion extends to more central area of the conduit as conduit diameter decrease (e.g., Mitchell et al., 2019) 234

List of tables

Table 1.1 – Simplified scheme of explosive eruptions of silicic and intermediate magmas with New Zealand examples..... 8

Table 1.2 – Definition of eruptive activity and classification of temporal units used in this thesis to characterise volcanic eruptions and their intra-eruption sequences. The subdivision of eruptive activity into eruption, phase and event/episode/pulse follows (1) a temporal hierarchy (i.e., an eruption contains one or more eruptive phases; an eruptive phase contains one or more eruptive events/episodes/pulses) based on the length of quiescence period between two consecutive intervals of eruptive activity. The subdivision also incorporates (2) changes in eruptive styles to separate two consecutive units (e.g., between consecutive eruptive phases or between consecutive eruptive events/episodes/pulses). 20

Table 2.1 – Summary of the eruptive history of the OVC with names, ages and volumes (DRE) of the erupted and emplaced pyroclastic deposit and lava domes. Sbg and S indicate subgroup and sequence, respectively used in Nairn (2002) and Leonard et al. (2010), which used typically to group a package of successive pyroclastic deposits of different ages interlayered by soils 35

Table 2.2 – Summary of the main characteristics of the post-25 ka intra-caldera rhyolitic eruptions from the OVC. Note: all eruptions are multi-phase, multi-vent and mixed explosive to effusive. see Sections 2.3.5.1 and 2.3.5.2 for more details. Key for location: LV = vent lineament; H = Haroharo; T = Tarawera; HDC = Haroharo Dome Complex; TDC = Tarawera Dome Complex; OB = Okareka basin; RB = Rotoma basin. Recognized type of discrete magmas erupted during individual eruption (number of discrete magmas erupted is also indicated): R = rhyolitic magma; B = basaltic magma; RD = rhyodacitic (mixed and mingled compositions). PDC = pyroclastic density current; co-PDC = PDC-derive buoyant plume; BAF= block-and-ash flow; PM = inferred phreatomagmatic activity. 38

Table 3.1 – Tentative correlations between the stratigraphic units of the Kaharoa deposit identified in this study and those proposed in previous works. See Section 3.6.1 for discussions on the stratigraphic changes adopted in this work compared to previous stratigraphic reconstructions..... 67

Table 3.2 – Summary of the distinctive deposit characteristics of the seven recognised deposit types for the units in the studied pyroclastic succession. 68

Table 3.3 – Grain size data of representative samples analysed in this work. Mdϕ and $\sigma\phi$ are the median diameter and sorting coefficient of the obtained grain size distributions, following Inman (1952). F1 and F2 represent the weight % of the sample <1 mm and <63 μm, respectively (Walker, 1971). Deposit type for each unit sampled are abbreviated as follow: (1) massive lapilli deposit; (2) stratified lapilli deposit; (3) massive, coarse ash deposit; (4) massive, fine ash deposit; (5) laterally discontinuous, ash deposit; (6) lapilli-bearing, ash deposit; (7) variably consolidated ash deposit. Location (N=north and S=south) indicates the position of the sampled stratigraphic sections with respect to Mt Tarawera. 90

Table 3.4 – Results of componentry analyses expressed in weight percent of samples collected from coarse-grained units (coarse ash to lapilli units). H.A. lithic indicates hydrothermally altered lithic clasts. Deposit type for each unit sampled are abbreviated as follow: (1) massive lapilli deposit; (2) stratified lapilli deposit; (3) massive, coarse ash deposit; (4) massive, fine ash deposit; (5) laterally discontinuous, ash deposit; (6) lapilli-bearing, ash deposit; (7) variably consolidated ash deposit..... 99

Table 3.5 – Summary of the suggested intra-eruption time breaks and their lengths during the Kaharoa eruption 111

Table 3.6 – Summary of intra-eruption Phases (A to F) and Episodes (I to XI), associated lithostratigraphic units with interpreted eruptive activity and inferred time breaks (1^{st} to 3^{rd} order; see Table 3.5)..... 118

Table 4.1 – Summary of studies on pumice vesicle textures. Ref. = references; N. = number; Mag. = microscopy magnification used; n/a = not available; S&P (1998) = Sahagian and Proussevitch (1998); C&L (1983) = Cheng and Lemlich (1983) 128

Table 4.2 – Summary of the magnifications and resolutions of SEM-BSE images used in this study and minimum vesicle size thresholding applied in quantitative image analyses. Eq.D = equivalent circular diameter of the vesicle. The image widths and heights are 6827µm and 6292µm for 20× images, 2990µm and 2755µm for 50× images, 1495µm and 1378µm for 100× images, and 745µm and 686µm for 200× images. (*) Due to the large area of 20× images (width of the image is ~7 mm) which would result in extensive manual image editing (see Section 4.2.3), the minimum vesicle size for quantitative analyses is set at vesicle area of >700 pixels (i.e., vesicle with Eq.D = 50 µm). Vesicles <50 µm are largely captured by all the other three magnifications. If an 80-pixel vesicle area thresholding was to be also maintained for the 20× images, it would have resulted in a minimum vesicle size of ~17 µm. 133

Table 4.3 – Summary of 2D vesicle shape parameters quantified for the three different pumice microtextures investigated in this study. Results of each thin sections consist of the vesicle shape data collected over 10 (OR thin sections) to 12 (PA thin sections) images acquired at four magnifications (20x, 50x, 100x, 200x). STD = Standard deviation 142

Table 4.4 – Summary of 2D vesicularity, number density (NA) and area vesicle size distribution (area-VSD) quantified for the three different pumice microtextures investigated in this study at PA and OR cuts. Values reported in the table are average of three images per magnification 149

Table 5.1 – Summary of the main features of the Kaharoa pumice clasts, surface texture and vesicle texture types. 173

Table 5.2 – Bulk density and vesicularity data of pumice clasts from the analysed units (L1 to L8) of the Kaharoa deposit and additional data for juvenile obsidian and lava dome fragments. Data on pumice clast types from the whole sample population are also reported, as well as data on obsidian and lava dome fragments. (SD) indicates the standard deviation for mean density and vesicularity values. Mode 1 indicates the mode of the density and vesicularity distributions, while Mode 2 indicates secondary, minor peaks in the distributions when present 179

Table 5.3 – Summary of vesicle size data quantified from set of 200× images acquired from OR cuts of pumice clasts for each unit along the stratigraphic sequence. 2D vesicularity is the average total area of vesicles per melt area; NA is the total number of vesicles per unit melt area; mode and median vesicle size are derived from the area-VSD and cumulative area-VSD plots, respectively. All parameters are corrected for the image crystal content.....194

Table 5.4 – Median values for the 2D vesicle shape parameters quantified from set of 200x images acquired from OR cuts of pumice clasts for each unit along the stratigraphic sequence 197

Table 5.5 – Summary of crystallinity data as phenocryst content of white pumice clasts in the studied units of the Kaharoa stratigraphic sequence, calculated from 2D analysis of images at 20× (14 to 19 images over 3 clasts per units). Crystallinity for grey pumice clasts were calculated from three selected clasts from unit L7N. Additional crystallinity data are provided for two obsidian pyroclasts from unit L3 and A7 199

Chapter 1

Introduction

1.1 Project definition

1.1.1 Research motivations

Volcanic eruptions are among the most spectacular phenomena occurring on Earth. Fundamental research is needed to continuously improve the current understanding on the nature and dynamics of eruptions and how volcanic systems work and evolve over time (Cashman and Sparks, 2013; Acocella, 2014). Along with the investigations of volcanic processes and their products, over the last forty years (post-1980 eruption of Mount St. Helens, USA) the focus of research in volcanology has increased towards eruption scenario forecasting (e.g., Newhall and Hoblitt, 2002; Marzocchi et al., 2004) and on how to quantify the impacts of numerous volcanic hazards (e.g., Barberi et al., 1992; Bebbington et al., 2008; Del Negro et al., 2016; Biass et al., 2017; Sandri et al., 2018; Lube et al., 2020). Volcanic eruptions can have devastating effects on the communities and infrastructures near active volcanoes (Wilson et al., 2014; Deligne et al., 2017) and might have global scale consequences on the environment (therefore on modern society), as volcanic ash particles can travel over wide areas from the eruptive vents and can remain suspended in the atmosphere for prolonged times (Mackie et al., 2016).

Typically, moderate- to large-scale explosive eruptions, here defined as eruptions depositing a total volume of pyroclasts between 0.1 and 100 km^3 (**Table 1.1**), consist of a composite succession of individual eruptive phases (see Fisher & Schmincke 1984; Cioni et al., 2015; Martí et al., 2018). Eruptive phases represent a discrete time-interval during the sequence of a single eruption (Cioni et al., 2008; Bebbington and Jenkins, 2019) characterised by: (i) specific dynamics of the subvolcanic and volcanic processes determining the modes of magma ascent and discharge to the surface, (ii) a dominant range of intensities and magnitudes (*sensu* Pyle, 2015), and (iii) styles of the resulting eruptive activity and transport-deposition mechanisms of the erupted products (see **Table 1.2**). Similar eruptive phases may repeat sequentially during an eruption or may alternate with eruptive phases of different styles, separated or not by short (hours/days to months) time breaks (e.g., Askja 1875, Sparks et al., 1981; Novarupta 1912, Fierstein and Hildreth, 1992; Mount St. Helens 1980, Sarna-Wojcicki et al., 1981; Pinatubo 1991, Wolfe and Hoblitt, 1996; Chaitén 2008, Lara, 2009). Usually, a *climactic* or *paroxysmal* explosive phase (i.e., the magnitude- and intensity-largest phase in a single-eruption sequence) is preceded and/or followed by phases of lower magnitude and intensities (Siebert et al., 2015).

Recent documented and instrumentally recorded eruptions at monitored volcanoes, as well as historical chronicles of past eruptions, can provide a dataset to understand eruption dynamics and scale future volcanic events a region may face. For historically documented eruptions, these data

rely on the accuracy of the observations made during the eruption and may give useful insights to constrain the temporal changes in eruptive activity, from the onset to the end of an eruption. Although they represent invaluable source of information, limitations and uncertainties may arise on their sole application to the interpretations of volcanic phenomena and to hazard assessments (see Cashman and Biggs, 2014). Extensive written historical accounts are restricted to eruptions that occurred at volcanoes located close to large cities, usually describing only the largest-scale phase(s) within an eruption (notable examples from some historically active Italian volcanoes – e.g., Somma-Vesuvius and Etna, Rosi et al., 1993; Branca and Del Carlo, 2004; Mulas et al., 2016 – and Japanese volcanoes – e.g., Sakurajima, Fuji, Asama, Imura, 1998; Yasui and Koyaguchi, 2004; Miyaji et. al, 2011). Whereas data from mid-20th century to present of monitored volcanoes are representative of the more frequent, but usually smaller-scale, eruptions (see Global Volcanism Program database, http://www.volcano.si.edu).

Characterising the intra-eruption sequence and dynamic of eruptions and their phases at volcanoes with limited or not available historical records present many challenges, since few to no spatial and temporal evidence have been constrained by direct observations. This is usually the case at rhyolitic-dominated caldera systems. Due to their generally longer repose time compared with volcanoes fed by less evolved magmas (e.g., Bebbington, 2020), rhyolitic eruptions are underrepresented in the catalogue of historic volcanic events (White et al., 2006; Crosweller et al., 2012). The limited number of well-documented cases of rhyolitic eruptions (i) hampers a comprehensive understanding of their eruption dynamics and physical processes and consequently (ii) limits the ability to formulate eruption scenarios in volcanic hazard studies (e.g., Marzocchi and Bebbington, 2002), both for the smaller-scale events and for the super eruption case (**Table 1.1** for eruption scale terminology).

Field geology of volcanic terrains and eruption deposits, along with textural and petrological investigations of the erupted products, remain paramount tools even in modern volcanology to understand volcanic eruptions and volcanic systems (Cioni et al., 2021). Geological investigations are required to develop more comprehensive knowledge on the dynamics of rhyolitic eruptions and to build more robust eruption scenarios, accessing the information from past, non-instrumentally recorded, volcanic events preserved in the geological record (see Groppelli et al., 2019).

Of great significance to gain a better understanding on rhyolitic eruptions and to better constrain the magmatic and eruptive dynamics at active silicic caldera volcanoes are the studies of moderate- to large-scale eruptions, not associated with extensive caldera-collapse events. These eruptions, althought smaller than the super eruption endmember for which caldera systems are usually known for (Wilson, 2008), are capable to erupt substantial volumes of magma, reaching

Plinian-type explosive intensities and might have regional to global environmental impacts. This study is designed to bring further attention and expand the knowledge on this type of rhyolitic activity which characterise the more recurrent style of volcanism at silicic caldera systems (e.g., Nairn, 2002; Hildreth, 2004; Hildreth et al., 2010; Barker et al., 2021; Sourisseau et al., 2020).

1.1.2 Aim of the research and specific objectives

The central aim of this research is to provide a better understanding of rhyolitic eruptions. Particularly, this research focuses on the eruptive dynamics and physical processes of moderate- to large-scale rhyolitic eruptions sourced from intra-caldera settings. *Intra-caldera eruptions* are defined here as those eruptions having eruptive vents located within or immediately outside silicic caldera systems (e.g., Heiken, 1990; Hildreth, 2004; Sourisseau et al., 2020), and occur after a major caldera-collapse event (VEI≥7 eruptions) or in-between major caldera-collapse events for polycyclic caldera systems (Lipman, 2000; Cole et al., 2005; Bouvet de Maisonneuve et al., 2021).

The field area chosen for this research is the Okataina Volcanic Centre (Lat. 38°11′S, Long. 176°30′E), the northernmost and active rhyolitic centre of the Taupō Volcanic Zone, in the North Island of New Zealand, which hosts the Okataina caldera system (Nairn, 2002; Wilson and Rowland, 2016). The Okataina caldera is widely known in the volcanological literature for comprising Mt Tarawera, a NE-trending, cluster of rhyolitic lava domes and coulees from which the historic basaltic Plinian eruption of 1886 CE took place (Walker et al., 1984; Keam, 1988; Rowe et al., 2021).

During the past 25 kyr, nine moderate- to large-scale rhyolitic eruptions occurred from multiple vents within the Okataina caldera (Nairn, 2002). The most recent rhyolitic event of the centre occurred at ~636±12 cal. yr BP (calendar date 1314±12 CE; Hogg et al., 2003; Lowe et al., 2013) and it is known as the Kaharoa eruption (Grange, 1937; Pullar et al., 1973; Froggatt and Lowe, 1990; Nairn et al., 2001). This eruption represents to date the youngest volcanic events involving rhyolitic magmas in New Zealand and is the largest volume eruption since the 232 CE "Y" eruption of Taupō volcano, the other active caldera system of the Taupō Volcanic Zone (Wilson and Walker, 1985; Wilson, 1993).

Using the pyroclastic succession emplaced during the Kaharoa eruption, this study investigates the eruptive styles, sequences and dynamics of intra-caldera rhyolitic eruptions. The goals of this research are accomplished through field investigations of the pyroclastic deposits and by the quantification and evaluation of the textural characteristics of the erupted juvenile pyroclasts. The overarching aim of this thesis is achieved by addressing the following specific objectives:

Objective 1 – *Characterisation of the pyroclastic succession emplaced during the Kaharoa eruption to define the timing of events and the temporal changes in eruptive and depositional and patterns*.

Objective 2 – *Development of an approach to quantify complex and anisotropic vesicle textures from pumice clasts using Scanning Electron Microscope – backscattered electron (SEM-BSE) images*.

Objective 3 – *Constrain the dynamics of magma ascent in the shallow conduit and evaluate how conduit processes influenced the observed variations in deposit characteristics and pyroclasts textures*.

Objective 4 – *Define the factors controlling the changes in eruptive styles and the overall eruption dynamic to provide a general model for the Kaharoa eruption*.

1.1.3 Thesis structure and overview

This thesis is comprised of seven chapters designed around the central aim of better understanding the dynamics of rhyolitic eruptions from intra-caldera settings. The thesis also includes appendices of the complete dataset produced and used during this research.

Following this introductory chapter and a review chapter on the Okataina Volcanic Centre, each of the chapters forming the main body of this thesis is self-contained and structured in the form of journal research articles. These chapters include an introduction to the topic investigated, a methodology section detailing approaches and analytical techniques used, a result section reporting the data obtained, a discussion around the data and topic of the study and conclusive remarks summarising the main findings. Therefore, some repetitions can be found in the thesis (e.g., the introductory and background sections of Chapters 3, 4 and 5). A separate methodology chapter is not provided in this thesis, instead the methodologies used to achieve individual research objectives are included in each of the pertinent chapter. References for the cited published works and list of appendices are reported at the end of the thesis, following Chapter 7. The statement of originality and contribution to Chapters 3, 4 and 5 is reported in the format of the Massey University *DRC16* form in **Appendix G**.

Chapter 1 – Introduction

This chapter highlights the research motivations and defines the overarching aim and the specific objectives of this study. It further gives indications on the general thesis structure and content of individual sections. The chapter concludes by providing backgrounds on the regional geology of

New Zealand, on the volcanism of the Taupō Volcanic Zone and on concepts inherent in silicic volcanism.

Chapter 2 – The Okataina Volcanic Centre

This chapter details the geological background and volcano-tectonic settings of the study area. The chapter further reviews the eruptive history of the Okataina Volcanic Centre based on the available data, focusing on the intra-caldera rhyolitic volcanism following the Rotoiti/Rotoehu major caldera-forming eruption.

Chapter 3 – Deposits and stratigraphy of the Kaharoa eruption

This chapter presents a detailed field study of the Kaharoa pyroclastic succession. Coupling field observations with the quantification of the main sedimentological and lithological characteristics of the deposits, this chapter addresses Objective 1 of this research. This study revaluates the stratigraphic sequence of the Kaharoa deposit, placing more constraints on timing of eruptive events and on intra-eruption time-breaks. The sedimentary structures of the identified lithostratigraphic units, together with their main grain size and componentry features, allows to recognize an array of deposit types, which are linked to different eruptive and transport-depositional mechanisms.

Chapter 4 – An approach to quantify complex and anisotropic vesicle textures in pumice clasts

Following the discovery and description made during fieldwork and componentry analyses regarding vesicle textural features of the Kaharoa pumices, this chapter gives guidelines and presents an approach on how to quantify vesicle attributes (e.g., vesicle size, shape and number density) from complex and anisotropic vesicle textures in pumice clasts using SEM-BSE images. This chapter addresses Objective 2 of this research.

Chapter 5 – Magma conduit dynamics during the explosive phases of the Kaharoa eruption

This chapters presents the first and thorough characterisation of the vesicle textures of pumice clasts of intra-caldera rhyolitic eruptions from Okataina, addressing Objective 3 of this research. By applying the workflow presented in the previous chapter, systematic vesicle texture analyses of the Kaharoa pumices are here performed. The vesicle analyses are coupled with the estimations of the pumice clasts bulk densities and frequency of different pumice types in the deposit. This dataset is produced for the coarse-grained (lapilli-bearing) units along with the reconstructed stratigraphy and provides constraints onto the dynamics of magma ascent and degassing/outgassing in the conduit during the eruption. Furthermore, the textural data are correlated to the deposit types and componentry characteristics of the investigated units to evaluate the role of shallow conduit processes in controlling the eruption dynamic.

Chapter 6 – Synthesis: an integrated view of dike-fed, intra-caldera, rhyolitic eruptions

This chapter integrates the findings arising from the previous chapters and addresses Objectives 3 and 4 of this research. Furthermore, the studied eruption is here compared to other similar rhyolitic events both locally and globally and its significance in terms of traditional volcanic eruption classifications is discussed.

Chapter 7 – Conclusions and future work

This chapter reviews the work conducted during this research, summarized the main findings in relation to the specific research objectives defined in Chapter 1, and outlines the broader impacts of this research to the topic area. The chapter further provides indications for potential research directions worth exploring for future work.

Table 1.1 – Simplified scheme of explosive eruptions of silicic and intermediate magmas with New Zealand examples (***caption continues next page***).

Eruption group	Pyroclastic deposit volume		Erupted magma volume (DRE)		VEI	Common and/or intensity-largest eruption styles	New Zealand examples	
	(km^3)	(m^3)	(km^3)	(m^3)			Intermediate	Silicic
Small to moderate	10^{-5} – 10^{-3}	10^4 – 10^6	<0.01	<10^7	1	Ash-ballistic outburst	Whakaari [1]	-
	10^{-3} – 10^{-2}	10^6 – 10^7			2	Semi-continuous ash emission / transient Vulcanian pulse	Tufa Trig (T2; T14) [2]	Taupō W [3]
	10^{-2} – 10^{-1}	10^7 – 10^8			3	Multiple Vulcanian pulses/ Violent strombolian / Subplinian	Tufa Trig (T13) [2]	Puketarata[4] Taupō Ψ [5]
Moderate to large	10^{-1} – 1	10^8 – 10^9	~0.01 – 10	~10^7 – 10^{10}	4	Multiple Vulcanian pulses/ Subplinian	Burrell Lapilli [6]	Taupō V [7]
	1 – 10^1	10^9 – 10^{10}			5	Plinian	Bullot Fm. (Mgt; Sw; Our; Ak) [8]	Waiohau [9] Rotorua [10]
	10^1 – 10^2	10^{10} – 10^{11}			6	Plinian / small to int. ignimbrite (minor caldera collapse)	-	Waimihia[11] Kawerau [12]
Very large to super	10^2 – 10^3	10^{11} – 10^{12}	~10 to >450	~10^{10} to >45×10^{10}	7	Int. to large ignimbrite (major caldera collapse)	-	Rotoiti [13]
	>10^3	>10^{12}			8	Large to super ignimbrite (major caldera collapse)	-	Oruanui [14]

References for eruptions cited: **[1]** Whakaari (White Island) post-1976 CE to present (Houghton and Nairn, 1991; Kilgour et al., 2021). **[2]** Tufa Trig (T2; T13; T14) >1.8 ka Ruapehu eruptions (Voloschina et al., 2020; 2021). **[3]** ~2.75 ka "W" eruption, Taupō caldera (Wilson, 1993; Barker et al., 2021). **[4]** ~16 ka Puketarata eruption, Maroa (Brooker et al., 1993; Kósik, 2018; Kósik et al., 2019). **[5]** ~20.5 ka "Ψ" eruption, Taupō caldera (Wilson, 1993; Barker et al., 2021). **[6]** 1655 CE Burrel Lapilli eruption, Taranaki (Platz et al., 2007). **[7]** ~2.8 ka "V" eruption, Taupō caldera (Wilson, 1993; Barker et al., 2021). **[8]** 27-10 ka Bullot Formation, Mangatoetoenui (*Mgt*), Shawcroft (*Sw*), Oruamatua (*Oru*), Akurangi (*Ak*) eruptions from Ruapehu (Pardo et al., 2012). **[9]** ~13.6 ka Waiohau eruption, Okataina caldera (Speed et al., 2002; Nairn, 2002). **[10]** ~15.4 ka Rotorua eruption, Okataina caldera / Okareka embayment (Kilgour and Smith, 2008). **[11]** ~3.4 ka Waimihia ("S") eruption, Taupō caldera (Wilson, 1993; Barker et al., 2020). **[12]** ~33 ka Kawerau/Unit I eruption, Okataina caldera (Jurado-Chichay & Walker 2000; Spinks, 2005; Cole et al. 2010). **[13]** ~61 ka Rotoiti /Rotoehu eruption, Okataina caldera (Charlier et al., 2003; Cole et al. 2010). **[14]** ~ 25.5 ka Oruanui/Kawakawa eruption, Taupō caldera (Wilson, 2001; Barker et al., 2021). "-" not documented.

Table 1.1 (*caption continued*)

Simplified descriptive scheme of explosive eruptions of silicic (>63 wt% SiO2, dacitic to rhyolitic) and intermediate magmas (>53 wt% SiO2, basaltic-andesite to andesitic) according to their scale (total volume of pyroclastic deposit emplaced or erupted magma), with examples from New Zealand's calc-alkaline Taupō Volcanic Zone (TVZ) and Taranaki volcano. Eruption subdivisions by pyroclastic deposit volume follows the VEI (Volcanic Explosivity Index) of Newhall and Self (1982). The main three-fold eruption group nomenclature is adapted from eruption terminology concepts developed by Bonadonna and Costa (2013) for the small to moderate eruptions group, and from Geshi and Nakagawa (2018) and Miller and Wark (2008) for the very large to super eruption group (conventional lower limit of VEI≥8 eruption is >1000 km^3 or >450 km^3 DRE). The moderate to large eruption group represent a midway term between the lower and upper scale eruption groups, where most Plinian-type magnitude eruptions would fall (see Cioni et al., 2015). Range for erupted magma volumes (DRE=Dense Rock Equivalent) are only approximations based on DRE values reported in the literature for eruption of equivalent VEI (e.g., Carey and Sigurdsson, 1989; Carey et al., 2010; Pyle, 2015), and from available data in the eruption databases LaMEVE (Crosweller et al., 2012; Brown et al., 2014) and the Smithsonian's GVP (https://volcano.si.edu/). Boundaries for the three eruption groups are not to be envision as sharp but flexible due to variable preservation status of pyroclastic deposit in the geological record (e.g., Todde et al., 2017; Cutler et al., 2018; 2020; Voloschina et al., 2020) and to different sources of uncertainties in deposit volume estimations (e.g., Scarpati et al., 2014; Bonadonna et al., 2015a; Silleni et al., 2020). Names for the common and/or largest-intensity eruption styles follow traditional eruption style names (e.g., *violent Strombolian; Vulcanian, Subplinian and Plinian*) of Mercalli (1907) and Walker (1973), and less traditional terms (e.g., *ash emission*) from Miyabuchi et al. (2008), Martin-Del Pozzo et al. (2008) and D'Oriano et al. (2011). The terminology for VEI≥6 ignimbrite-style, usually caldera-forming, eruptions and their deposit volume follows Giordano and Cas (2021) (*int.* = intermediate volume ignimbrite). The terms *minor* and *major* preceding caldera collapse give a qualitative description of the extent of the caldera collapse event (see also Lipman, 1997; Cole et al., 2005; 2010; Geshi et al., 2014). The term *ash-ballistic outburst* is introduced to indicate instantaneous explosive events erupting a very limited magma volume, potentially generating a transient and directed pyroclastic density current and/or ash fall and ballistic shower (e.g., activity at Whakaari since 1976, Houghton and Nairn, 1991; Kilgour et al., 2021). If no magma is erupted, the equivalent size "eruption" is a steam-driven, phreatic or hydrothermal explosion.

1.2 Background concepts: silicic volcanism

The term silicic volcanism encompasses a broad range of eruption styles, magnitudes, intensities, and durations, associated with the eruption of high-silica magmas (>63 wt.% SiO_2). Silicic eruptions vary from very large to super explosive eruptions, resulting in major caldera collapses and in the emplacement of extensive ignimbrite deposits, to the mild and slow extrusion of dense magma as lava domes or flows (Eichelberger, 1995). The volumes of magma erupted during silicic eruptions can range thereby significantly up to 8 orders (see **Table 1.1**), with magma discharge rates varying from one to millions of cubic meters per second depending on the type of activity (e.g., Newhall and Melson, 1983; Carey and Sigurdsson, 1989; Mason et al., 2004; Bryan et al., 2010; Pallister et al., 2013).

Despite the extreme case of super eruptions (i.e., eruption producing a volume of the associated pyroclastic deposits ≥ 1,000 km^3, Rampino, 2002; Miller and Wark, 2008; Wilson, 2008; **Table 1.1**), of which 42 are known to have occurred in the past 36 Myr (minimum time-average eruption frequency estimates of 1.1 events/Ma; Mason et al. 2004), more commonly silicic eruptions cluster within the moderate- to large-scale eruption group, in the form of Plinian-type explosive events (see **Section 1.2.2**). On a dataset of 45 Pleistocene and Holocene Plinian-type eruptions compiled by Carey & Sigurdsson (1989), 80% of them are associated to magma of evolved compositions, with SiO_2 higher than 60 wt.% (see also Cioni et al. 2015).

Along with explosive Plinian-type eruptions, effusive dome-forming eruptions are also common during silicic volcanism. These involve the slow extrusion of degassed and highly viscous magmas, which accumulate around the eruptive vent (*lava domes*) and/or spreads downhill out of the vent (*coulees or flows*) (**see Section 1.2.3**). In some cases, lava dome-forming eruptions represent the dominant style of volcanism at some silicic volcanoes (e.g., Soufrière Hills, Montserrat, Lesser Antilles, Sparks and Young, 2002; Smith et al., 2007; Wadge et al., 2014; Maroa volcanic complex, New Zealand, Leonard, 2003). Although lava dome-forming eruptions comprise around 6% of the eruptions worldwide (Calder et al., 2015), silicic eruptions are often characterised by one or more effusive phase(s) which precede, intersperse, or follow the main explosive phase(s) (Newhall and Melson 1983; Heiken and Wohletz 1987; Eichelberger, 1995; Ogburn et al., 2015).

Many historical and older cases of silicic eruptions are characterised by this mixed, explosive-effusive eruption behaviours, including the four most recent (~150 years) moderate to larger scale rhyolitic eruptions: (1) The 1874–1875 CE Askja eruption and rifting episode in Iceland (e.g., Sparks et al., 1981; Sigurdsson and Sparks, 1981; Carey et al., 2009, 2010); (2) the 1912 CE

eruption of Novarupta, Alaska, the magnitude largest eruption of the 20th century (e.g., Fierstein and Hildreth, 1992; Coombs and Gardner, 2001; Houghton et al., 2004; Adams et al., 2006; Gonnermann and Houghton, 2012; Hildreth and Fierstein, 2012); (3) the 2008–2009 CE Chaitén eruption, Chile (Lara, 2009; Watt et al., 2009; Alfano et al., 2011; 2012; Castro et al., 2012a; Pallister et al., 2013; Saubin et al., 2016); the 2011–2012 CE Cordón Caulle eruption, Chile (Castro et al., 2013; Schipper et al., 2013; 2021; Pistolesi et al., 2015; Alloway et al., 2015). The dominant factors determining the transition between explosive to effusive eruptive phases may change from case to case (Cassidy et al., 2018; Schipper et al., 2021), however this mixed eruption behaviour is a central element in silicic volcanism, in particular for eruptions involving rhyolitic magmas (Jaupart and Allegre 1991; Ogburn et al., 2015).

In the following sections, the main types of VEI≤6 eruptions from silicic caldera systems and their conduit-to-surface eruptive processes are outlined. The focus here is therefore placed on the post-collapse caldera volcanism, while the characteristics of very large to super eruptions resulting into caldera collapse events are not reviewed since beyond the scope of this thesis.

1.2.1 Silicic caldera systems and their post-collapse activity

Silicic caldera systems constitute a type of volcano[1] whose chief volcanic-structural element consist of a large (up to tens of km wide and up to few km deep), subcircular to rectilinear depression, resulting from the evacuation of very large magma volumes stored in the upper crust (usually >10 km^3 DRE) (Lipman, 2000; Cole et al., 2005; Geshi et al., 2014; Branney and Acocella, 2015; Acocella, 2021) during VEI≥7 catastrophic caldera-forming, ignimbrite-style eruptions (Wilson, 2008; Geshi and Nakagawa, 2018; Bouvet de Maisonneuve et al., 2021; Giordano and Cas, 2021). These eruptions cause the subvertical collapse of the surface-to-chamber caldera block into the underlying magma reservoir, with the consequent subsidence of the ground surface forming the caldera depression.

Silicic caldera systems can be classified into mono- or polycyclic base on the number (one or more) of caldera-forming eruptions (Bouvet de Maisonneuve et al., 2021). Examples for the former are the Aira (Japan; Geshi et al., 2020) and Long Valley (USA; Hildreth, 2004) calderas, while the Okataina (New Zealand; Cole et al., 2010) and Valles-Toledo (USA; Kennedy et al., 2012) calderas are examples for the latter type. The term c*aldera complex* of Cole et al. (2005), indicating caldera systems constituted by "spatially and structurally associated nested or

[1] Following Poland (2019) the term *caldera system* or simply *caldera* volcano (see also Branney and Acocella, 2015) is preferred to the term *supervolcano* (cf. Rymer et al., 2005; Miller and Wark, 2008; De Silva and Lindsay, 2015).

overlapping calderas of different ages" converge with the meaning of the term *polycyclic caldera systems* introduced by Bouvet de Maisonneuve et al. (2021). The former term highlights the structural evolution of the caldera system while the latter emphasises its volcanic-magmatic time evolution.

The term *silicic* is generally added to typify the dominant geochemical characteristics of the erupted magmas, although eruptions at silicic caldera systems can vary from rhyolitic to basaltic (Branney and Acocella, 2015). In the context of this work, which is centred on rhyolitic eruptions from the TVZ's Okataina caldera system, the term silicic (i.e., magmas with SiO_2>63%) is directly associated to calc-alkaline magmas, although silicic caldera systems of alkaline (and peralkaline) equivalent magmas have been widely known and studied worldwide (e.g., the caldera systems from the Quaternary Roman Magmatic Province of central and southern Italy, Avanzinelli et al., 2008; Acocella et al., 2012; Cashman and Giordano, 2014; Marra et al., 2020; Aluto and Corbetti calderas within the Main Ethiopian Rift, Hutchison et al., 2016).

The volcanic areas hosting dominantly rhyolitic caldera systems have been sometimes referred to as *rhyolitic volcanic centre*, particularly within the New Zealand and Australian volcanological literature (e.g., Cas and Wright, 1987; Sutton et al., 2000; Nairn, 2002; Leonard et al., 2010). However, the extent of the topographic and structural borders of the caldera complex are usually smaller than the designated volcanic area/centre (e.g., the Okataina volcanic and Taupō volcanic centres and associated calderas).

Silicic caldera systems are polygenetic volcanoes that typically lack a principal and continuously active conduit-vent system. After a caldera-forming eruption, the system can undergo to a post-collapse cycle, with eruptive activity occurring from multiple eruptive vents (Cole et al., 2005; Branney and Acocella, 2015). Eruptive vents can form (i) scattered within the entire depression (e.g., Campi Flegrei, Italy), (ii) localize within zones of pre-existing regional structures at depth (e.g., Okataina and Taupō, within the Taupō Rift, New Zealand) or (iii) along the structural border of the caldera (e.g., Kos-Nysiros, Greece; Rabaul, Indonesia; Aira-Sakurajima, Japan). This intra-caldera volcanism often results in the resurgence (magma-related uplift) of part of the caldera floor (Acocella, 2021). The post-collapse eruptive activity at some caldera systems can also continue outside the structural borders of the caldera, forming more extensive volcanic fields (e.g., Long Valley caldera, USA, and La Primavera caldera, Mexico; Hildreth, 2004; Sourisseau et al., 2020). Such distributed volcanism, might reflect regional to local structural and volcano-tectonic features assisting the formation of magma pathways to the surface (e.g., Spinks et al., 2005; Vitale and Isaia, 2014; Di Vito et al., 2016; Rivalta et al., 2019; Kósik et al., 2020), as well as the extensive complexities associated to the magma reservoirs beneath silicic caldera systems (e.g., Hildreth, 2004; Costa, 2008; Giordano and Cashman, 2014; Forni et al., 2018; Kennedy et

al., 2018; Geshi et al., 2020; Barker et al., 2020; Bouvet de Maisonneuve et al., 2021; Sas et al., 2021).

The type of silicic eruptions from the newly open, post-collapse vents can vary in scale from small to moderate up to moderate to large (**Table 1.1**). Accordingly, the type of activity can range widely. Post-collapse eruptions at caldera systems can be characterised by dominantly effusive activity with the extrusions of lava domes and coulees forming in time one or more dome complexes within the caldera system, with associated minor (VEI≤3) explosive activity (e.g., Heiken et al., 1986; Leonard, 2003). In other cases, eruptions can reach Plinian-type intensities with or without phases of lava domes extrusion (e.g., Jurado-Chichay and Walker, 2000; Kilgour and Smith, 2008; Matsumoto and Nakagawa, 2019). During the course of a single eruption, multiple vents are typically active, varying from aligned and connected to a main dike-fissure system (e.g., Heiken, 1978; Nairn, 2001; Bursik et al., 2014) to (apparently) independently distributed within the caldera, few to several km apart (e.g., Roggensack et al., 1996; Pistolesi et al., 2016). This multiple vent activity of intra-caldera eruptions, along with the different eruptive styles and magnitude events can result in variable pyroclast transport-deposition regimes (e.g., various types of eruptive plumes and pyroclastic density currents), typically forming complex pyroclastic succession (see **Chapter 3**).

Eruptive activity can also vary largely depending on the surface water infill of the caldera depression forming lakes of variable sizes (Manville, 2010). This can increase the possibility of efficient magma-water interactions during the openings of new eruptive vents (e.g., Wilson, 2001; Pistolesi et al., 2017). Furthermore, silicic calderas typically host one to several hydrothermal systems (Branney and Acocella, 2015; Wilson and Rowland, 2016), in which the heated and pressurized fluids can result in hydrothermal or phreatic explosions, connected or not to a magmatic eruption (e.g., Kobayashi et al., 2018; Montanaro et al., 2017; 2020; Isaia et al., 2021).

1.2.2 Plinian-type eruptions

The term *Plinian-type* is used here to group the continuum of explosive volcanic eruption styles, from subplinian to ultraplinian, defined by of Walker (1973) based on the dispersal characteristics of the associated fallout deposits. This term is similar to the term *Plinian family* recently used in Giordano and Cas (2021).

Plinian-type eruptions typically occur when the rapid ascent and decompression to the surface of magma hamper the exsolved magmatic volatiles in the conduit (mainly water) to efficiently decouple from the magma itself (Sparks et al., 1994; Cashman, 2004). This causes excess of gas overpressure in bubbles until final brittle break-up (fragmentation) of the bubble-bearing melt

continuum into an expanding mixture of magma particles and gas, violently ejected to the surface (Dingwell, 1996; Gonnermann, 2015; Cashman and Scheu, 2015).

The term *Plinian* has been widely applied to describe explosive eruptive events (**Table 1.2** for eruptive activity terminology) defined by the sustained, quasi-steady, hours-long, high-mass-discharge-rate release of the fragmented magma particles into the atmosphere (Wilson et al., 1980; Woods, 1995; Gonnermann and Manga, 2013; Cioni et al., 2015). This type of volcanic activity results in the formation of a buoyant, vertically ascending eruptive column formed by a mixture of volcanic gas, solid particles and entrained air that can reach heights up to few tens of km above the vent (Sparks, 1986, Carey and Bursik, 2015). Plinian events have high values of eruption intensity and magnitude, ranging between 10-11, and >4-6, respectively (Pyle, 2015; Cioni et al., 2015). The reported volume of erupted magma during a Plinian event ranges typically between 0.01 to 10 km^3 DRE, with reported peak of mass discharge rates from 10^6 to 10^8 kg/s (Carey and Sigurdsson, 1989; Cioni et al., 2015). These very high eruption rates are the cause of the general short duration of individual Plinian event, which generally lasts from few hours up to few days (Walker, 1981; Sparks et al., 1997; Mastin et al., 2009).

Plinian eruptive columns can transport fragmented quenched magma particles in the atmosphere to maximum heights of 20 up to 40 km (Sparks et al., 1992; Cioni et al., 2008; Bonadonna and Costa, 2013). Plinian columns rise until a buoyancy level is reached with the surrounding atmosphere. The ejected material is then carried and dispersed laterally by the dominant winds over wide areas. The fallout deposits resulting from the settlement of the particles from the umbrella region or volcanic cloud of the Plinian column consists of laterally continuous blankets of well sorted pyroclastic fragments (juveniles as vesicular pumice and denser clasts, together with lithics) that mantle the topography (Bursik et al., 1992; Rosi, 1998). Deposit's thickness, maximum and median grain size of the particles decrease exponentially with increasing distance from the source (Pyle, 1989), passing from coarse-grained lapilli deposit in proximal locations to thin beds of fine ash in distal sites.

The convective behaviour of a Plinian column may pass to collapsing behaviour if the buoyancy of the eruptive plume is not maintained (Sparks et al. 1978; Woods et al., 1988; Neri et al., 2003; Di Muro et al., 2004; Giordano and Cas, 2021). The partial or total collapse of the Plinian column can lead to the generation of concentrated to dilute, pyroclastic density currents (PDCs). In a PDC, the eruptive mixture moves horizontally on the ground as a density current (i.e., a fluid spreading in a host environment of different density) driven by gravity, reaching distances up to several kilometres away from the vent (Branney and Kokelaar, 2002; Suplizio et al., 2014; Dufek et al., 2015; Lube et al., 2020; Carazzo et al., 2020). This transition between convective and collapsing behaviours can occur at different times during the course of a Plinian event (Neri and Dobran,

1994), however repeated partial collapses are more common during subplinian events. As a result, proximal fall deposits may be interbedded with PDC deposits and may be locally eroded by the passage of PDCs (e.g., Cioni et al., 1992, Rosi et al., 2001).

The term *subplinian* has been used to describe eruptions of similar eruptive dynamics of Plinian events but characterised by lower values of their associated main eruption parameters (e.g., intensity, magnitude, dispersal power and degree of fragmentation of associated fallout deposits; Walker, 1973). Subplinian events have values of eruption intensity and magnitude of 10 and 4, respectively (Pyle, 2015), and peak mass discharge rate typically between 10^6 and 10^7 kg/s (Cioni et al. 2015). The lower eruption intensity (i.e., mass discharge rate) of subplinian events determines the usually lower heights reached by their convective columns with respect to Plinian events (subplinian columns typically do not cross the tropopause; Cioni et al., 2015). Atmospheric conditions can play an important role in the ascending dynamics of low-intensity subplinian columns which can be bent-over under strong winds, influencing fallout sedimentation (Bursik, 2001, Bonadonna et al. 2015b; 2015c).

In terms of eruptive behaviours, individual and sustained subplinian events are typically characterised by (1) an unsteady mass discharge rate (eruptive intensity), which can oscillate over short (minutes to hours) timescales (Cioni et al., 2015; Bonadonna et al., 2016). The oscillation in discharge rate can often lead to instabilities of the eruptive column and to partial column collapse(s), with the generation of small-volume PDCs (e.g., Rosi, 1996; Cioni et al., 2003; Sulpizio et al. 2005; Pardo et al., 2011; Jenkins et al. 2013). In addition, (2) eruptions dominated by subplinian events are often non-sustained. In this case, magma discharge to the surface is discontinuous during the course of the entire eruption, resulting in an episodic or pulsatory eruption behaviour (Bursik, 1993; Scandone et al. 2007). The eruption sequence can therefore be characterised by repeated, discrete, however short-lived (hours long), events of magma discharge over days to months (e.g., Sarna-Wojcicki et al., 1981; Miller and Chouet, 1994; Paladio-Melosantos et al., 1996; McGimsey et al., 2001; Maeno et al. 2014). Due to this more typical non-sustained (i.e., discontinuous magma discharge) and/or unsteady (i.e., continuous but oscillating magma discharge over short timescales) activity, subplinian fall deposits are usually well bedded, marked by frequent changes in the mean deposit grain size in which coarser- to finer-grained beds alternate (Bursik, 1993; Rosi, 1998; Cioni et al. 2011). These characteristics further distinguished subplinian and Plinian events and their deposits.

Overall, studied eruptions that have been classified as Plinian or subplinian are constituted by a complex succession of multiple eruptive phases of contrasting eruptive styles (Cioni et al., 2015). Phases of dominant Plinian and/or subplinian events can alternate with phases dominated by intermittent Vulcanian explosions (e.g., Matthews et al., 1997), phases of prolonged ash emissions

(e.g., Todde et al., 2017) and effusive phases of lava domes or flows extrusions (e.g., Swanson et al., 1987; Platz et al., 2007; Tuffen et al., 2013; Pallister et al., 2013).

1.2.3 Lava dome and Vulcanian eruptions

The term lava dome eruption refers to volcanic activity dominated by the extrusion of highly viscous magma that piles and accumulates around the vent area forming a dome-shaped mass of lava (Calder et al., 2015). Dome-building eruptions are typical features of silicic volcanism (Eichelberger, 1995; Fink and Anderson, 2000), although the composition of lava domes can span over a wide range, from basaltic-andesite to high-silica rhyolite (Calder et al., 2015; Ogburn et al., 2015). Lava dome eruptions occur as a consequence of the slow magma ascent in the volcanic conduit, where the efficient outflow of the exsolved magmatic volatiles from the rising magma reduces the gas pressure in bubbles preventing volatile-driven, magma fragmentation and explosion to the surface (e.g., Melnik et al., 2005; Mueller et al., 2008; Lavallée et al., 2012; Cassidy et al., 2018).

Lava dome eruptions can occur at the summit crater(s) of stratovolcanoes (e.g., Mount St. Helens, USA; Pinatubo, Philippines; Volcan de Colima, Mexico; Galeras, Colombia; Unzen, Japan; Merapi, Indonesia) or can develop along multiple vents within silicic caldera systems or volcanic fields (Fink, 1990). The latter results in the formation of lava dome complexes that can extend in length from few to several km, consisting in chains of domes and coulees (e.g., Tarawera, New Zealand; Santiaguito, Guatemala; Mono-Inyo volcanic chain, USA). During some lava dome eruptions, the ascending magma can degas at the top of the volcanic conduit forming a plug or cap, which can later be (i) vertically extruded, (ii) spread laterally, or (iii) can be disrupted if eruption continues (Calder et al., 2015). The duration of dome-building eruptions varies largely from days to few decades (Newhall and Melson, 1983; Ogburn et al., 2015). For years-long, dome-building eruptions, the growth of the dome(s) may occur in repeated episodes or cycles (e.g., Barmin et al., 2002; Harris et al., 2003; Rhodes et al., 2018; Bain et al., 2021), with extrusion rates varying widely from 0.01 m^3/s to 100 m^3/s (Newhall and Melson, 1983; Calder et al., 2015).

On a dataset of 156 historical lava dome eruptions, Newhall and Melson (1983) noted that 95% of the eruptions were associated with explosive activity. Different styles of volcanic explosions may occur at different time during a lava dome eruption, passing from the semi-continues ash emission to transient Vulcanian explosions, up to major explosions of Plinian-type intensity and magnitude (Heiken and Wohletz, 1987; Ogburn et al., 2015). Transient Vulcanian explosions are the most frequent form of explosive activity associated with the growth of lava domes (Stix et al., 1997; Formenti et al. 2003; Kennedy et al., 2005; Wright et al., 2007; Clarke et al., 2015),

irrespective of magma composition, from intermediate to silicic (e.g., Galeras, Colombia; Unzen, Japan; Merapi, Indonesia; Soufrière Hills, Montserrat, Lesser Antilles). Whereas Plinian-type events are more common during eruptions involving dacitic and rhyolitic magmas (e.g., 1902 Mt Pelée, Martinique; 1912 Novarupta, Alaska; 1980 Mount St. Helens, USA; 1991 Pinatubo, Philippines; 2008 Chaitén, Chile; 2011 Cordón Caulle; Chile) (Ogburn et al., 2015).

Vulcanian explosions are triggered by the sudden decompression and evacuation of pressurised magma stalling in the shallow volcanic conduit (Alidibirov, 1994; Woods, 1995; Clarke, 2013). High pressures can accumulate (i) in the upper part of the volcanic conduit beneath a plug (a dense magma body obstructing the conduit-vent), (ii) beneath an extruded lava dome or (iii) can develop within the dome interiors (Sparks, 1997). The explosions occur then when it is reached a sufficiently high gas pressure gradient in the underlying magma that cause the disruption of the dome or plug sealing the conduit-vent (Tait et al., 1989, Stix et al., 1997). Alternatively, Vulcanian explosions can result from collapse events of the growing dome (Druitt and Kokelaar, 2002). In both cases, the disruption or collapse of the capping plug or dome causes the rapid decompression, fragmentation and evacuation of the underlying magma in the conduit (Kennedy et al., 2005; Clarke et al., 2015). In addition, hydrothermal alterations on the timescale of months to years at growing lava domes can also trigger Vulcanian explosions by significantly reducing the permeability of the dome-material, hampering gas escape from the magma column in the conduit and causing pressure build-up (Heap et al., 2019). The deposits resulting from individual Vulcanian events are typical of small volumes (**Table 1.1**), since the erupted materials do not usually exceed the volume of the magma in the volcanic conduit and from the partially disrupted dome/plug (Clarke et al., 2015). Fall deposits are usually fine-grained (ash-size) (e.g., Bonadonna et al., 2002) and are characterised in very proximal sites by showers of ballistic materials, often with breadcrust textures (Cas and Wright 1987; Robertson et al., 1998; Wright et al., 2007). Vesicularity of the ash clasts is typically low as they derived from the outgassed and partially solidified magma in the shallow conduit and/or from the dome edifice (Heiken and Wohletz, 1987; Miwa et al., 2013).

Recent and well documented lava dome eruptions (e.g., 1980-1986 Mount St, Helens, USA; 1990-1995 Unzen, Japan; 1995-2015 Soufrière Hills, Montserrat; 1998-2013 Volcan de Colima, Mexico), have also highlighted a variety of processes in generating PDCs (including block-and-ash flows, BAFs) and debris avalanches during the lava dome eruptions (e.g., Miyabuchi, 1999). Instabilities of the dome may lead to gravitational collapse of part of the lava edifice which can trigger explosions and produce BAFs (Ui et al., 1999; Saucedo et al., 2004, Schwarzkopf et al., 2005; Brown and Andrews, 2015). Plume collapse associated with Vulcanian explosions can cause the formation of PDCs (Sato et al., 1992; Cole et al., 2002). Significant release in the confining pressure due to sector collapse of the dome and associated debris avalanches can result

in violent, laterally directed PDCs (Voight et al., 2002; Belousov et al., 2007). Collapses of the dome edifice and production of debris avalanches can occur also when not associated to explosive events and furthermore years after the end of the eruption. The latter is typically due to period of prolonged hydrothermal alteration which can significantly weaken the dome edifice and resulting in collapses and generation of debris avalanches (Siebert, 1984; Calder et al. 2015).

1.2.4 Magma dynamics during ascent in the conduit

The environment where the magma ascends from its last shallow storage region (or magma chamber) in the upper crust (see Edmonds et al., 2019; Sparks et al., 2019) towards the surface is referred to as volcanic conduit. The shape of the conduit can vary largely from dikes (vertically and laterally extend conduit) to cylinders (Tibaldi, 2015; Gonnermann and Taisne, 2015; Aravena et al., 2017; Kavanagh, 2018).

Magma during ascent in the conduit will respond to decompression with a number of processes, such as **(1)** degassing (*the exsolution of melt-dissolved volatiles into gas bubbles*; e.g., Cashman, 2004; Shea, 2017), **(2)** outgassing (*the outflow of gas from the magma column within the conduit*; e.g., Gonnermann et al., 2017) and **(3)** syn-ascent crystallization (*element diffusion into the formation of microlite-to-nanolite-size mineral phases at ascent timescales*; e.g., Hammer et al., 1999; D'Oriano et a., 2005; Cáceres et al., 2020; Di Genova et al., 2020). These processes affect the intrinsic and evolving properties of the magma such as its permeability/porosity (e.g., Blower, 2001; Gonnermann et al., 2017) and viscosity (e.g., Whittington et al., 2009), impacting the overall magma rheology, flow behaviour and the ascent speed (Sparks, 1978; Cashman, 2004; Llewellin and Manga, 2005; Gonnermann and Manga, 2013). Ultimately, these processes will govern the magma ascent dynamics and the resultant eruption style (Cashman and Sparks, 2013; Burgisser and Degruyter, 2015). When silicic magmas rise sufficiently fast and explosive conditions are met while approaching the surface (i.e., the exsolved magmatic volatiles are not able to efficiently decouple from the magma column in the conduit) the magma will undergo **(4)** fragmentation (Cashman and Scheu, 2015; Cassidy et al., 2018): the passage of the magma from a continuous liquid (melt) with dispersed crystals and gas bubbles into a continuous gas with dispersed liquid drops and solid particles (Gonnermann, 2015). The investigation of how and in which extent these processes impact magma rheology and flow conditions is of primary importance in the understanding of how an eruption will unfold.

Silicic melts due to their high content in silica have elevated initial (pre-ascent) viscosity compared to intermediate and mafic melts, with viscosity increasing further by order of magnitudes as magmas decompress and cool towards the surface (Giordano et al., 2008; Lesher

and Spera, 2015). Ascending silicic melts are often modelled as Newtonian fluids (i.e., viscosity is independent of strain rate), however silicic melts bearing gas bubbles and crystals can exhibit non-Newtonian behaviours (Caricchi et al., 2007; Mader et al., 2013; Vona et al., 2016). Of interests here is that the stress to which the magma is subjected while rising to the surface can be accommodated by two main different types of deformation: (i) ductile deformation, with formation of networks of deformed (stretched) bubbles and localised sheared zones (e.g., Martí et al., 1999; Wright and Weinberg 2009; Dingwell et al., 2016); (ii) and/or brittle deformation with the opening and closures of fractures in more denser magmas (e.g., Tuffen et al., 2003; Castro et al., 2012a). The former is typically the result of the development of lateral (cross-conduit) gradients in magma ascent velocity (and shear rates), with magma velocity decreasing from the central portion of the conduit to the conduit walls (e.g., Polacci et al., 2003; Shea et al., 2012). Slower magma ascent velocities (and higher shear rates) towards the conduit margins are typically due to friction and/or cooling of the magma at the conduit walls (Costa et al., 2007; Burgisser and Degruyter, 2015; Acocella, 2021).

The deformation of the bubble-bearing melt and the shape of the deformed bubbles depend on the capillary number, whereby on the balance between shear stress that tends to deform and surface tension that tends round the bubbles into its original spherical shape (Rust and Manga, 2002; Rust et al., 2003; Kilgour et al., 2016; Ohashi et al., 2018; 2020a). If deformation prevails, gas bubbles are deformed into elongated up to tubular shapes (aspect ratio from 1 up to >100; see **Chapter 4**), parallel or subparallel to the direction of shear. Bubble deformation can significantly affect the degree of bubble interconnection and magma permeability (e.g., Okumura et al., 2006; Wright et al., 2006; 2009; Burgisser et al., 2017), in turn impacting the outgassing efficiency of the magma column in the conduit (e.g., Degruyter et al., 2012; Kushnir et al., 2017). This can ultimately influence the ability of the magma to erupt explosively or effusively when approaching the surface (Okumura et al., 2009; Castro et al., 2013). Shear-derived textures, inherited from the deformation of the bubble-bearing melt in the conduit, can be preserved in the erupted and quenched vesicular juveniles (pumice clasts) in (i) localized zones (Wright and Weinberg, 2009) or (ii) within the entire clasts volume, forming tube pumices (Martí et al., 1999). Due to the rheological properties of silicic magmas, tube pumice clasts are common products of rhyolitic eruptions, albeit their complex textures are often not quantified in textural studies of pumice clasts owning to intrinsic complexities in the measurement of anisotropic vesicle fabrics (see Shea et al., 2010; **Chapter 4**).

Table 1.2 – Definition of *eruptive activity* and classification of temporal units used in this thesis to characterise volcanic eruptions and their intra-eruption sequences. The subdivision of eruptive activity into *eruption*, *phase* and *event/episode/pulse* follows (1) a temporal hierarchy (i.e., an *eruption* contains one or more *eruptive phases*; an *eruptive phase* contains one or more *eruptive events/episodes/pulses*) based on the length of quiescence period between two consecutive intervals of eruptive activity. The subdivision also incorporates (2) changes in eruptive styles to separate two consecutive units (e.g., between consecutive *eruptive phases* or between consecutive *eruptive events/episodes/pulses*).

Eruptive activity = the explosive or effusive discharge to the surface of new magma (with or without the expulsion of older rocks) from a volcanic centre.

Eruptive activity unit	Definition
Eruption	A period of continuous to discontinuous eruptive activity usually characterised by the progressive alternation or repetition of one or more different eruptive styles. The separation between two consecutive eruptions is marked by a quiescence period typically long enough (≥ years) to allow, for example, the occurrence of non-volcanic processes such as (i) soil formation or (ii) substantial weathering/erosion and emplacement of epiclastic deposits.
Phase	A period of relatively continuous eruptive activity within an eruption, characterised by a predominant style of eruptive activity. The separation between two consecutive eruptive phases is marked by changes in the dominant eruptive style and/or by a short time break (hours/days to months) between the two phases (*e.g., a phase dominated by repeated Vulcanian-style events*).
Event, episode, or pulse	A period of relatively continuous eruptive activity within an eruption or a phase characterised by a single eruptive style. The separation between two consecutive eruptive events is marked by a change in eruptive style and/or by a very short time break (minutes to hours/days) between the two events (*e.g., a Plinian explosive event or a lava flow event*)

1.3 Background geology: New Zealand and Taupō Volcanic Zone

1.3.1 Regional settings of New Zealand

Straddling the boundary of the Australian and the Pacific plates (**Fig. 1.1**), New Zealand is among the most geologically active areas on Earth. Through New Zealand the active Pacific-Australian plate boundary consists of different tectonic segments, including subduction zones, back-arc rift, transcurrent faulting motion and continental collision (Walcott, 1984; Walcott, 1987; Beaven and Haines, 2001). Such great variety of tectonic environments shaped New Zealand and the

Zealandia continent over the past 85 Myr (Sutherland, 1999; King, 2000; Grobys et al., 2008; Mortimer et al., 2017; Mortimer and Scott, 2020).

The current geological setting of the North Island of New Zealand is affected by the Hikurangi subduction margin, where the Pacific plate subducts obliquely beneath the Australian plate (**Fig. 1.1**). The NNE-SSW Hikurangi Trough, located offshore and to the east of the North Island, represents the southernmost expression of the Tonga–Kermadec subduction system (**Fig. 1.1**), where the Kermadec Trench shallows, with subduction rate decreasing from 60-100 mm/yr to 37-50 mm/yr (DeMets et al., 1994; Parson and Wright, 1996; Henrys et al., 2003; Smith and Price, 2006). A back-arc rift occurs in the central and northern part of the North Island (**Fig. 1.1**) due to the oblique subduction of the Pacific plate beneath the continental crust of New Zealand and in association with the clockwise rotation of the Hikurangi margin (Beanland and Haines, 1998; Beaven and Haines 2001; Wallace et al., 2004). This plate motion caused crustal thinning and formation of the Taupō Rift on continental crust, with associated magmatism and volcanism defining a region named the Taupō Volcanic Zone (TVZ) (**Fig. 1.2**) (Cole et al., 1995; Wilson et al., 1995; 2009; Acocella et al., 2003; Leonard et al., 2010; Seebeck et al., 2014; Mortimer and Scott, 2020; Pittari et al., 2021; Stagpoole et al., 2021).

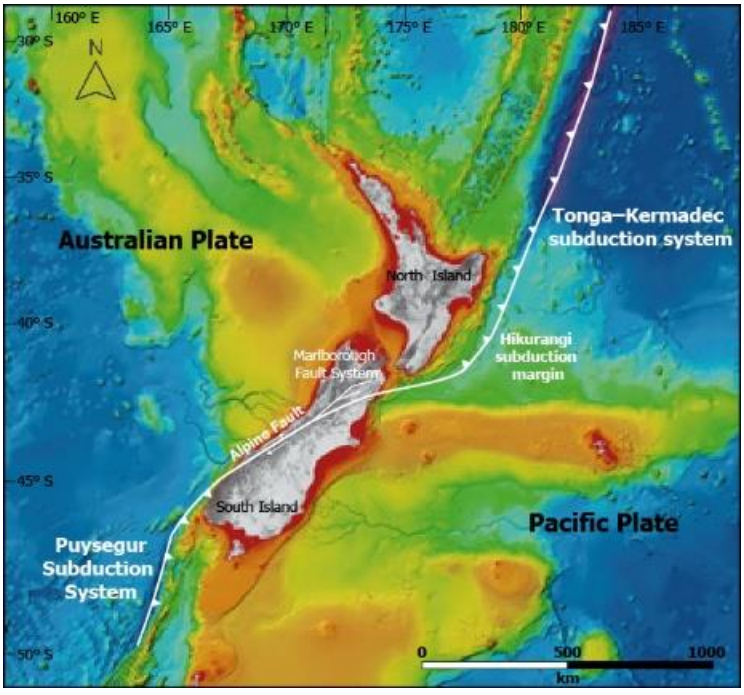

Figure 1.1 – Location of New Zealand in the Australian-Pacific plate boundary. Tectonic settings follow Mortimer and Scott (2020). Bathymetry data from NIWA (https://www.niwa.co.nz)

The on-land convergent Pacific-Australian plate boundary displays strike-slip dominated fault systems in the South Island, including the NE-SW Marlborough Fault System and the Alpine Fault (**Fig. 1.1**). The plates' continent-continent convergence resulted in the formation of the Southern Alps that run for 400 km NE to SW across the South Island, and it is also responsible for the exhumation of deep-seated crustal rocks to the east of the Alpine Fault (Norris et al., 1990; Van Dissen and Yeats; 1991; Holt and Haines, 1995; Beavan et al., 1999; Norris and Cooper, 2001; Mortimer et al., 2014). In the southwest edge of the South Island (SW of the Fiordland region) the continental collision gives way to the Puysegur Subduction System (**Fig. 1.1**) (Melhuish et al., 1999; Beavan et al., 2010). Here the Australian Plate subducts beneath the Pacific Plate at the Puysegur Trench (Lebrun et al., 2000; Lamarche and Lebrun, 2000; Sutherland et al., 2006; Mortimer and Scott, 2020).

1.3.2 The Taupō Volcanic Zone

The TVZ is a zone of Quaternary calc-alkaline volcanism and back-arc rifting developed in association with the oblique subduction of the Pacific Plate along the Hikurangi margin within the New Zealand North Island and a section of off-land continental crust (Cole et al., 1990; Spinks et al., 2005; Pittari et al., 2021). The TVZ extends SSW-NNE for ~300 km from Mt Ruapehu to the south, to Whakaari (White Island) in the Bay of Plenty (**Fig. 1.2**) (Wilson et al. 1995; Leonard et al., 2021). The subduction-related rifting has produced crustal thinning up to 25 and 15 km in this area (Bibby et al., 1995; Price et al., 2012), with a present spreading rate across the onshore TVZ, of <5 mm/y up to 13 mm/y from south to north of Lake Taupō (Villamor and Berryman, 2001; Wallace et al., 2004; Lamarche et al., 2006).

The volcanic activity of the TVZ started at ca. 2 Ma with emplacement of andesite, followed by rhyolitic eruptions from ~1.6 Ma, including at least 34 caldera-forming eruptions (Houghton et al., 1995; Wilson et al., 1995; Pittari et al., 2021). The TVZ eruptive history was divided by Wilson et al., (1995) into two main periods, (i) from 2.0 Ma to 0.34 and (ii) from 0.34 Ma to present. The two periods are separated by the Whakamaru-group eruptions, which consisted of several very large ignimbrite-producing eruptions and associated fall deposits that covered much of the deposits of the older activity (Pittari et al., 2021). The modern TVZ (<0.34 Ma) stretches for ~250 km NE and is 20 to 40 km wide. It can be divided into three sectors (southern, central and northern) along its length based on the dominant magma composition (Wilson et al., 1995; Seebeck et al., 2014; Wilson and Rowland, 2016) (**Fig. 1.2**). The central sector encloses several, dominantly rhyolitic, silicic caldera systems of different ages, from Taupō to Okataina and it has been the main location of silicic volcanism in the TVZ (Wilson et al., 1995; Barker et al., 2021). The southern and northern sectors consist instead in mainly andesitic (to dacitic) composite

volcanoes, including Ruapehu and Tongariro in the south, and Putauaki (Edgecumbe), Moutohora (Whale Island) and Whakaari (White Island) in the north (Leonard et al., 2021; Kilgour et al., 2021).

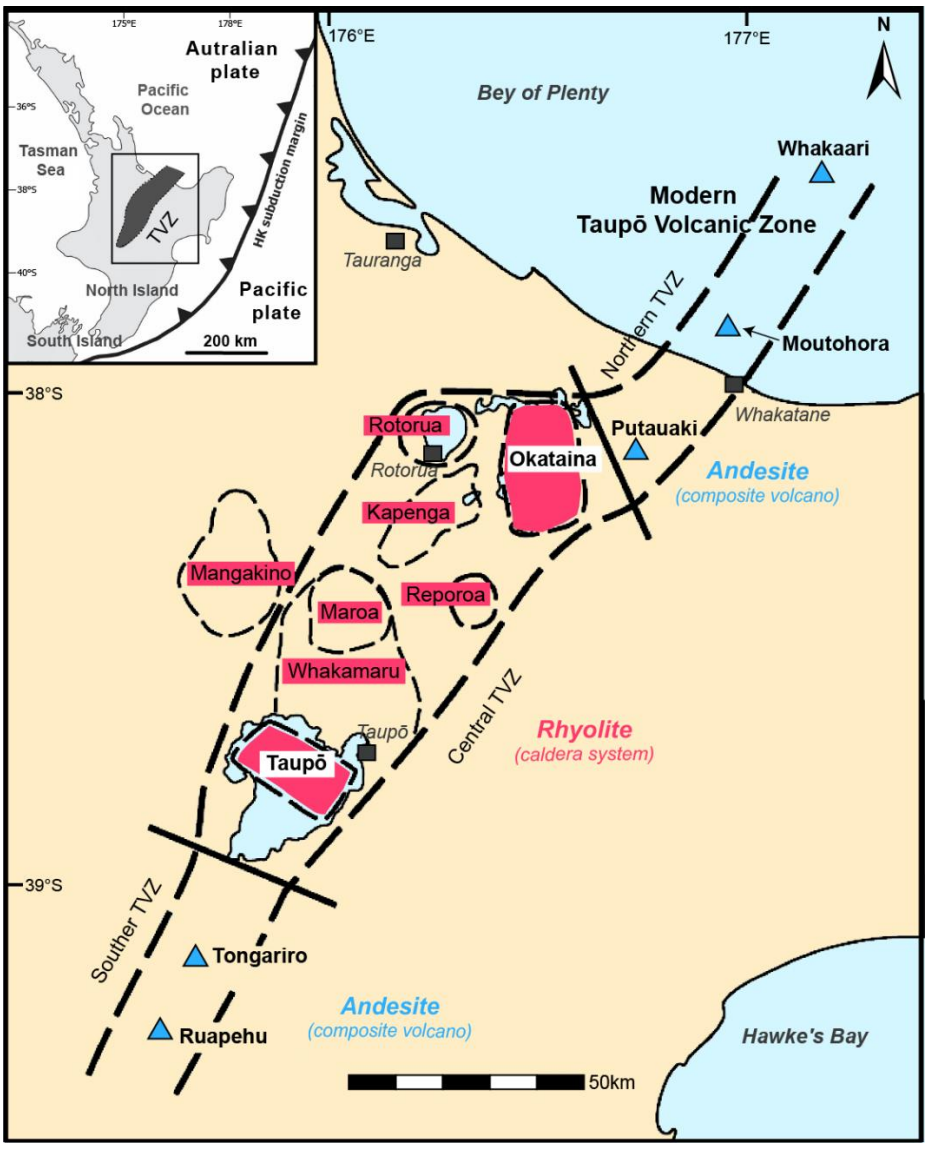

Figure 1.2 – Map of the TVZ modified after Spinks et al. (2005) showing modern and old TVZ boundaries, locations and approximative topographic boundaries of the eight silicic caldera systems within the central TVZ and the main andesitic-dacitic composite volcanoes on the southern and northern segments of the TVZ. Inset shows position of the TVZ in the North Island.

The central TVZ is an extraordinarily productive region of rhyolitic volcanism, with an estimated volume of 15,000–20,000 km^3 of volcanic material erupted over the past 1.6 Myr (Rogan, 1982; Hoguthon et al., 1995; Wilson et al., 2009). The two silicic caldera systems considered to be active to date are the Taupō and the Okataina caldera systems, hosted respectively within the

Taupō Volcanic Centre (TVC) and the Okataina Volcanic Centre (OVC) (Wilson and Rowland, 2016). The two caldera systems produced the largest eruptions to have occurred in New Zealand over the last 2000 years: the 232 ±10 CE Taupō Y eruption (Wilson and Walker, 1985; Wilson, 1993) and the 1314 ±12 CE Kaharoa eruption (Nairn et al., 2001), which erupted a DRE magma volume of 35 and 9 km^3, respectively (Sahetapy-Engel et al., 2014; Barker et al., 2021).

Houghton et al. (1995) compared the frequency and magnitude of the eruptions occurred in the central TVZ with the Yellowstone volcano, as an example of a very large caldera system. The cumulative magma volume erupted over the past 2 Myr is very similar, suggesting comparable magma supply rates between the two regions, however they differ in terms of styles, sizes, and frequencies of individual eruptions (Wilson et al., 2009). In the central TVZ there have been an order of magnitude more, but smaller in size, very large caldera-forming eruptions compare to those at Yellowstone. Furthermore, a significantly greater number of intra-caldera rhyolitic eruptions have occurred within the central TVZ, varying form small to moderate mainly dome-forming eruptions to moderate- to large-scale mixed Plinian-type and dome-forming eruptions (cf. Christiansen, 2001). For these reasons the central TVZ has been recognised as the most frequently active and Quaternary silicic volcanic region on Earth (Wilson et al., 1995; Houghton et al., 1995).

Chapter 2

The Okataina Volcanic Centre

2.1 Introduction

The Okataina Volcanic Centre (OVC) (**Fig. 2.1**) is one of the eight rhyolitic-dominated centres of the Quaternary central TVZ (see **Fig. 1.2**). Okataina represents one of the most scenic locations of the Bay of Plenty region of New Zealand, hosting significant cultural and natural heritage sites (e.g., Molloy and Acland, 2006), with Mt Tarawera (**Fig. 2.1**) in the southern part of the OVC being the archetypal example. The Mountain is held as sacred by the Ngāti Rangitihi and by the Tūhourangi (local Māori iwi) (Ngāti Rangitihi Trust, 2017) and has a significant value in the history of New Zealand both for the early human settlements (Hogg et al., 2003; Lowe, 2008) and for being the location of the historic 1886 CE Plinian basaltic eruption (Rowe et al., 2021). The eruption caused major destruction to the nearby areas and the death of ~120 people (Lowe et al., 2001; Keam, 2016), representing to date the largest volcanic disaster in New Zealand's history.

Okataina is an active volcanic centre and is monitored by the Crown Research Institute GNS Science (www.geonet.org.nz; Scott and Traves, 2009). Although no volcanic eruptions occurred since 1886 and the centre has not exhibited signs of volcanic unrest (cf. volcanic unrest at Taupō, Illsley-Kemp et al., 2021), recent studies on (i) ground deformation at Okataina (Ellis et al., 2014; Hamling et al., 2015; Holden et al., 2015; 2017) and on (ii) recent earthquakes and inferred basaltic dike intrusions near Mt Tarawera (Benson et al., 2021), suggest localized magma movements in the upper crust beneath the centre.

The OVC hosts and borders several geothermal fields (Nairn, 2002; Wilson and Rowland, 2016), with the Waiotapu-Rotomahana-Waimangu geothermal system to the SW of Tarawera being one of the largest (e.g., Hunt et al., 1994; Giggenbach et al., 1994; de Ronde et al., 2016a). The famous silica sinter formation of the Pink (*Otukapuarangi*) and White (*Te Tarata*) Terraces (Martin, 1888; de Ronde et al., 2016b; 2019) within the pre-1886 Lake Rotomahana (**Fig. 2.2**) were the result of the conspicuous hydrothermal activity within the early lake (Keam, 2016). Hydrothermal and/or phreatic explosions connected to magmatic eruptions have been inferred for the 17.6 ka and 9.5 ka rhyolitic eruptions at Okataina (Nairn and Wiradiradja, 1980) and also associated to the ~1314 CE Kaharoa eruption (Nairn et al., 2005; Montanaro et al., 2020; Gallagher er al., 2020). More recent hydrothermal explosions were observed and documented during the 20th century (not related to any magmatic eruptions), creating explosion craters within the Waimangu and Waiotapu areas (Nairn, 2002).

The geology and volcanic history of the OVC are extensively described in Nairn (2002), with works and reviews by Cole et al. (2010; 2014) on the structural and volcanic-plutonic evolution of the centre. The review of the OVC presented in this chapter is built upon these previous works, as well as other studies for individual Okataina eruptions (see **Section 2.3**). The PhD thesis work

of Cole (1966) and Nairn (1981) on Mt Tarawera and Okataina, respectively are praised here, along with early tephra-soil works by Vucetich and Pullar (1963; 1964; 1969), for setting up the foundation for future Okataina-related volcanological and interdisciplinary studies.

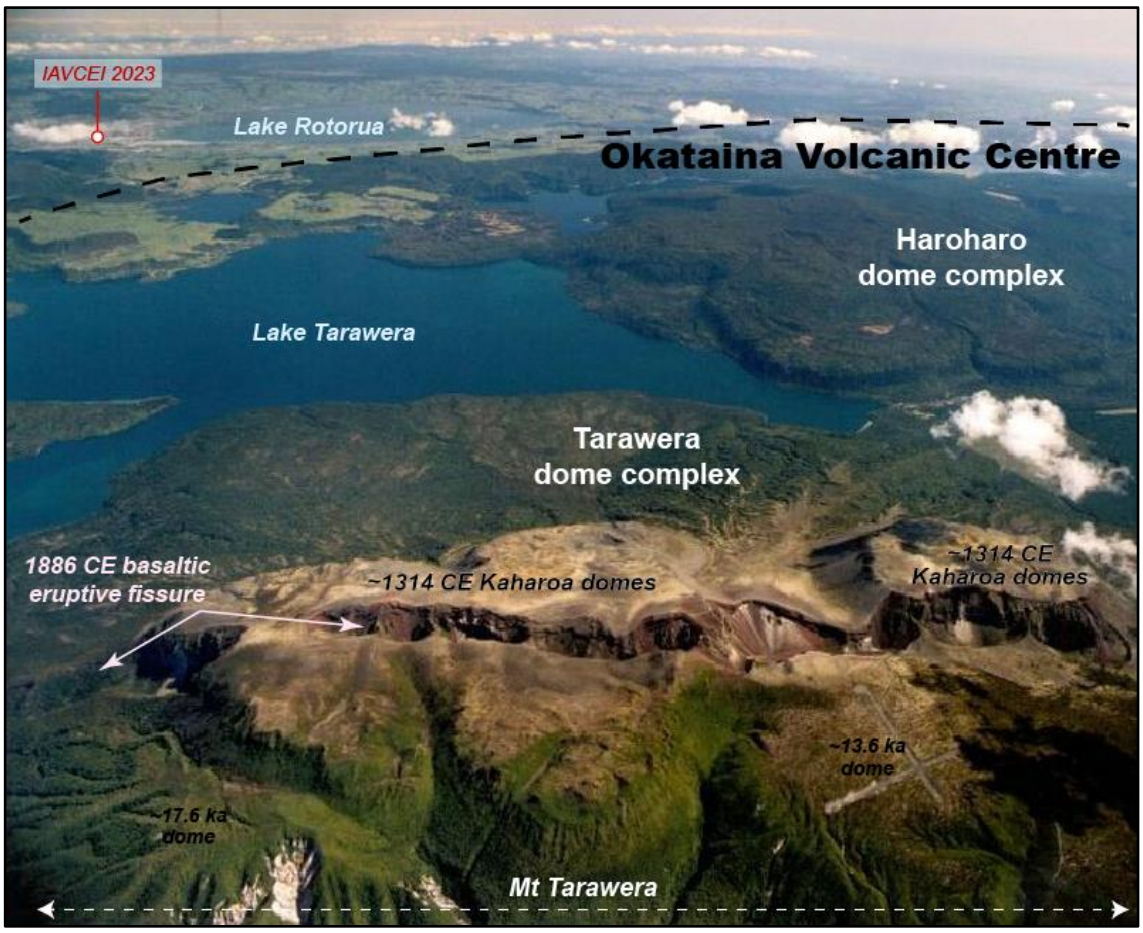

Figure 2.1 – Aerial view of the Okataina Volcanic Centre. © Institute of Geological & Nuclear Science Limited 2002. The photo is the front cover of Nairn (2002) and was taken by D.L. Homer. The photo is reproduced here with their permission and modified to add descriptions of main volcanological features of the centre. Dashed black line is approximative border of the OVC. Location of the IAVCEI 2023 Scientific Assembly is also shown.

2.2 Volcano-tectonic settings

The OVC is the northernmost and most recently active rhyolitic centre of TVZ (see **Fig. 1.2; Fig. 2.2**) (Nairn 2002; Cole et al. 2010). The OVC is part of the modern TVZ (<0.34 Ma), a 20–40 km wide NNE-trending zone of active rifting (Seebeck et al., 2014; Stagpoole et al., 2021), in which the current NW-SE spreading extends at different rates, passing from ~15 mm/y at the Bay of Plenty to <5 mm/y south of Lake Taupō, with extension of ~12 mm/y at OVC (Wallace et al., 2004). The modern TVZ has been further subdivided into five structural segments with variable

components of extension by Acocella et al. (2003) and Spinks et al. (2005). The segments with the largest degree of extension coincide with the highly and most recently active Taupō and Okataina caldera systems. Moreover, the Okataina segment is the locus of a major transfer zone (Acocella et al., 2003; Cole et al., 2010) at the intersection between the Kapenga and Whakatane segments, trending ENE-WSW, offset from the mean NNE-SSW direction of the TVZ (**Fig. 2.2**). The OVC occurs in this structurally complex transfer zone within the Taupō Rift, in which volcano-tectonic interactions are suggested to have played an important role in the eruptive history of the centre, with controls on the caldera geometry and distribution of eruptive vents at the surface (Nairn, 2002; Spinks et al., 2005; Cole and Spinks, 2009; Seebeck et al., 2010; Villamor et al., 2011). Faults around the OVC have a dominant NE direction, consistent with the main active fault trend of the Taupō Rift. Faults extend into the margins of the OVC, however there is a lack of mapped faults within the caldera system. This is possibly due to (i) the caldera-fill deposits (e.g., Branney and Acocella, 2015) from the post-25 ka activity covering older outcrops and/or (ii) because no displacements have actually occurred within the caldera system during this period (Villamor et al. 2011).

The OVC extends for ~700 km^2 and consists of the Okataina caldera system with intra-caldera lava dome complexes, and peripheral (extra-caldera) lava dome complexes (**Fig. 2.2; Fig. 2.3**). The Okataina caldera system represent the main volcano-tectonic structure of the centre and was formed after at least three very large caldera-forming eruptions (individual erupted magma volume >90 km^3 DRE) over the past ~557 kyr, the last of which occurred ~45 or 54 ka (**Table 2.1**; see also **Section 2.3**) (Deering et al., 2011; Danišík et al., 2012; Cole et al. 2014; Flude and Storey, 2016). These eruptions resulted in the formation of a complex system of overlapping and nested collapse structures (Nairn, 2002; Spinks et al., 2005; Cole et al., 2010), with a possible fourth minor caldera-collapse event at ~33 ka associated with the eruption of the Kawerau Ignimbrite (Jurado-Chichay and Walker 2000; Cole et al. 2014).

The Okataina caldera system consists of the N–S Okataina caldera (also refer to as the Haroharo caldera in Nairn, 2002) and includes other three minor basins (**Fig. 2.2**) named Rotoma, Puhipuhi and the Okareka, respectively on the NE, E and W margins of the Okataina caldera. During the post-25ka volcanic activity of the centre, eruptive vents opened at Okataina, Rotoma and Okareka, excluding the Puhipuhi basin which was possibly last active during the Mangaone eruptions (25 to 54ka; see **Sections 2.3.4 and 2.3.5**).

The Okataina caldera has a rectangular geometry (28×16 km wide), with the long axis trending N8°W, nearly perpendicular to the rift axis of the Okataina segments of Spinks et al. (2005). The structure of the caldera floor is obscured by syn-collapse ignimbrite deposits and deposits related to the post-collapse intra-caldera activity of the centre. However, a distinctive large negative

gravity anomaly and magnetic data suggest a maximum depth of the basement of the caldera depression of 5 km, infilled by the low-density volcaniclastic rocks (**Fig. 2.3**) (Rogan, 1982; Davy and Caldwell 1998; Sherburn et al., 2003; Stagpoole et al., 2021). The gravity data also define a N–S depression whose margins are consistent with the mapped topographic boundaries of the Okataina caldera (**Fig. 2.3**) (Nairn, 2002; Spinks et al., 2005). The caldera rim has clear topographic expressions north of lake Tarawera, and at lakes Rotoiti and Okataina, whereas in other areas the caldera margins are often buried beneath younger deposits (Nairn 2002). Where exposed, the caldera rim is strongly scalloped due to repeated slumping of the caldera rim scarps, which have extended the boundaries of the caldera to its present position (Cole et al. 2010). Laterally to the main N–S Okataina caldera structure, the three lateral subsidiary basins (Rotoma Puhipuhi and Okareka) are thought to reflect subsidence events resulting from the lateral movements of the underlying magmas towards the Okataina caldera and their evacuation by subsequent eruptions (Cole et al., 2010).

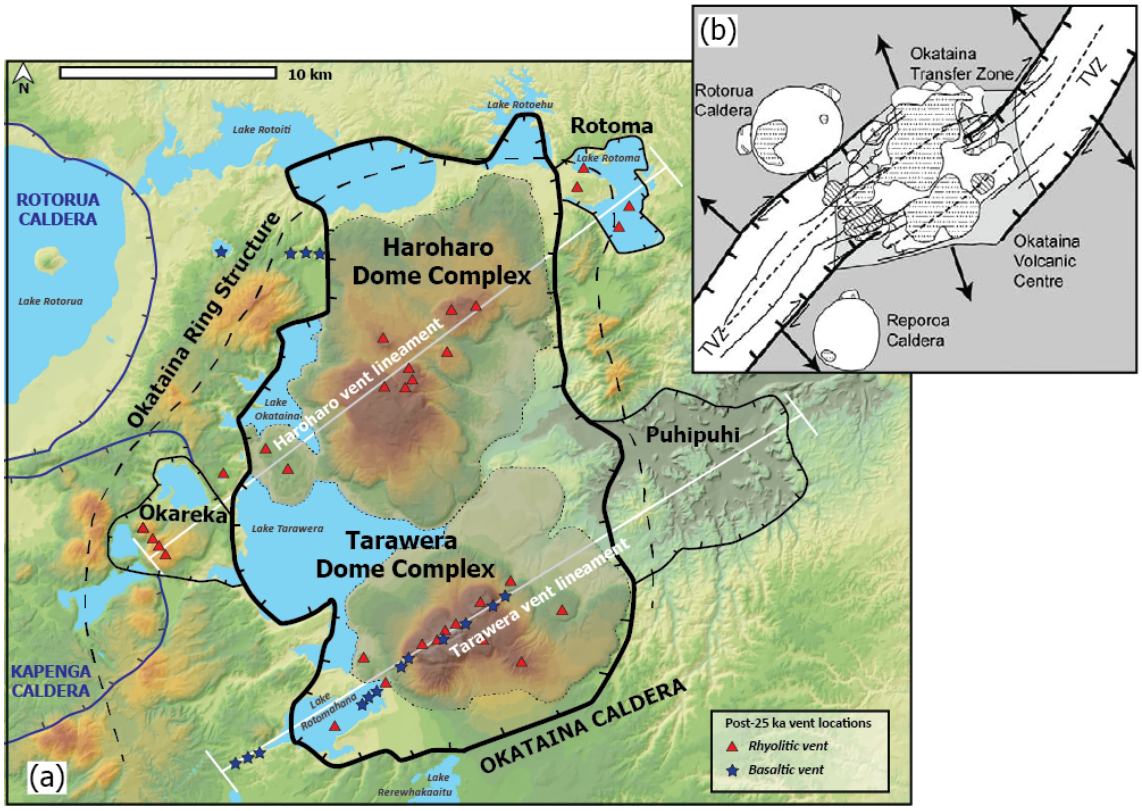

Figure 2.2 – (**a**) Map of the OVC showing topographic margins of Okataina caldera system, including the main Okataina caldera structure, subsidiary basins, and the inferred position of the Okataina Ring Structure, after Nairn (2002). *White lines* represent the approximate length and width of the two post-25 ka lineaments of eruptive vents. Vent locations associated with the eruptive activity from Haroharo and Tarawera dome complexes are also shown. (**b**) is modified after Fig. 3b of Cole et al. (2010) and shows location and geometry of the OVC within the Okataina "transfer zone" segment of Spinks et al. (2005) within the TVZ of the Taupō Rift. *Dashed thin black lines* display the inferred continuation of the axes of the Kapenga (to the south) and Whakatane (to the north) rift segments into OVC, which broadly correspond to the Haroharo and Tarawera vent lineaments.

The peripheral lava dome complexes within the OVC (e.g., Matawhaura, Whakapoungakau, Maungawhakamana, Moerangi and Tutaeheke) are located outside the margins of the Okataina caldera and subsidiary basins and have ages between possibly >557 ka (pre-caldera) to >54ka (Cole et al. 2014). (**Fig. 2.3**). Healy (1962) proposed that these peripheral domes mark a large "ring complex" (see also Cole et al., 2005 for terminology) known as the Okataina Ring Structure within which the OVC developed. The margins of the ring structure are however not well defined and apparently cut across the nearby Kapenga caldera system to the SW (**Fig. 2.2**) (Nairn 2002).

Eruptions related to the post-25 ka activity of the centre occurred from two zones of vent clustering within the caldera system. The alignments of eruptive vents define two, subparallel, lineaments possibly controlled by basement structures (Nairn, 2002; Cole et al., 2010; Seebeck et al., 2010): the Haroharo and the Tarawera linear vent zones or vent lineaments (**Fig. 2.2; Fig. 2.3**). The vent lineaments transect the caldera and have a NE-trending, offset (~10°–20° clockwise) from the main active fault trend around the OVC (Villamor et al., 2011).

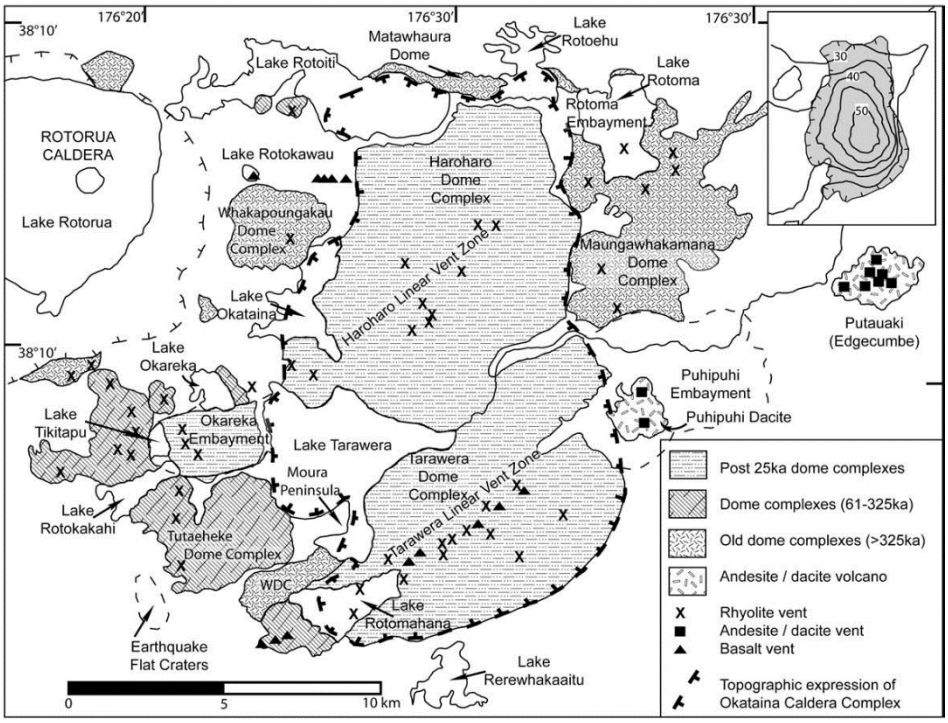

Figure 2.3 – Figure 2 of Cole et al. (2010) showing the main Okataina caldera topographic borders and spatial distribution and ages of the intra-caldera and peripheral lava dome complex, with eruptive vent locations. Inset shows negative gravity anomaly (contours in mGals).

The present-day geomorphology of the OVC is the result of the repeated volcanic activity of the centre, from the major caldera collapse events to the recent intra-caldera activity, and the variable levels of erosion of the erupted and deposited volcanic materials. Today, the Tarawera and the

Haroharo rhyolitic lava dome complexes within the southern and northern parts of the Okataina caldera, respectively, formed during the post-25 ka activity along the two mentioned vent lineaments, are the most prominent volcanic edifices of the centre. Variably eroded ignimbrite deposits cover the OVC outside the topographic caldera borders. These ignimbrites were erupted from both the OVC and from the two nearby silicic caldera systems, Rotorua and Kapenga, to the W and SW, respectively. The depressed area of the caldera system is variably filled by water forming several lakes (clockwise starting NE: Lakes Rotoma, Rotomahana, Tarawera, Okataina, Rotoiti and Rotoehu) between the caldera margins and the intra-caldera lava domes (**Fig. 2.2**).

2.3 Eruptive history

In the following section it is to be noted that the date for the Rotoiti/Rotoehu very large, caldera-forming eruption is debated between ~45 ka (Danišík et al., 2012) and ~54 ka (Flude and Storey, 2016). Previous work by Wilson et al. (2007) also gave a different date for the eruption at ~61 ka. For the sake of simplicity (about halfway between the two endmember dates) here it is used the latest available date published: ~54 ka (Flude and Storey, 2016). No preferences are given on basis of the different dating techniques used by these works. If not otherwise specified, all the pyroclastic deposits and lavas cited below are emplaced by eruptions dominantly or exclusively fed by rhyolitic magmas.

2.3.1 Early volcanism (~625-557 ka)

Volcanic activity from the OVC possibly initiated from 625 ka, based on the finding of rhyolitic tephra layers dispersed on the Bay of Plenty coast, with cummingtonite crystals suggesting an Okataina origin (Manning, 1996; Cole et al. 2010). The age of this cummingtonite-bearing tephra layers is however uncertain: reported ages in the literature range between 420 and 625 ka (Nairn and Beanland, 1989; Manning, 1995). Pre-caldera rhyolitic lava domes (Whakapoungakau and Matawhaura domes, and the Maungawhakanana dome complex) have been possibly extruded during this period (**Table 2.1**) and are likely associated with the Bay of Plenty coastal pyroclastic sequence (Nairn 2002; Cole et al., 2014). These domes might have also formed after 557ka, however the abundant angular rhyolitic lava blocks found within the ~557 ka Utu Ignimbrite, suggests the presence of pre-caldera domes within the OVC (Cole et al., 2010).

2.3.2 Caldera-forming eruptions (~557, ~322 and ~54 ka)

The first voluminous and widespread pyroclastic deposit that appears to be associated with the formation of the Okataina caldera system is the 90 km^3 DRE Utu Ignimbrite (Nairn, 2002; Deering et al., 2011; Cole et al., 2014) (**Table 2.1**). This very large caldera-forming, ignimbrite-producing eruption was thought to have occurred at ~380 ka, preceding the large Whakamaru group ignimbrite from Whakamaru caldera system to the south (see **Fig. 1.2**) (Nairn 2002). However, new dates suggest the Utu eruption and the associated first caldera collapse of the OVC occurred at ~557 ka (Leonard et al. 2010). The extent and thickness distribution of the Utu Ignimbrite is not well constrained due to later structural evolution of the OVC and younger deposits cover both from the Okataina and nearby caldera systems. Important to note is the absence of available topographic evidence for the caldera structure resulting from the Utu eruption, therefore no definitive constraint is placed on this caldera collapse event (Cole et al., 2014). A possible location of this collapse structure is reported in Cole et al. (2010) at the SE edge of the present Okataina caldera. The limited outcrop exposures of the Utu Ignimbrite can be found S and E within the Puhipuhi Basin (Nairn, 1981). The Utu Ignimbrite deposits vary from non-welded to weakly welded with devitrified pumice lapilli, and are occasionally intercalated with fall beds (Nairn, 1981; 2002; Cole et al., 2014). Since the deposits bear large (<cm) crystals of quartz and abundant biotite crystals, the ignimbrite was previously named the *Quartz-biotite tuff* (Nairn 2002; Cole et al., 2010).

A second major caldera collapse event within the OVC is related to the evacuation of ~160 km^3 DRE magma during the 322ka Matahina eruption (Deering et al., 2009) (**Table 2.1**). The emplaced ignimbrite deposits vary from partially to densely welded, light-brown in colour, with characteristic obsidian clasts, and large devitrified pumices (Nairn 1981; Nairn 2002). The ignimbrite deposits are best exposed east of the OVC, with thickness varying from 5 up to 150 m (Nairn, 1981; Bailey and Carr, 1994) and they overlay a Plinian-type, pumice-bearing fall deposit (Cole et al. 2010). The boundaries of the caldera structure resulting from the eruption of the Matahina Ignimbrite are not well defined as they are largely hidden by the products of the later activity of the centre and by the following, ~54 ka, caldera collapse. The possible location of the Matahina caldera structure is given by Cole et al. (2010) in the southern part of the present Okataina caldera.

The last major caldera collapse event to have shaped the caldera complex of the OVC is associated with the emplacement of the ~100 km^3 DRE, Rotoiti Ignimbrite and Rotoehu fall deposits (Nairn and Kohn, 1973; Burt et al. 1998; Nairn 2002; Charlier et al., 2003; Schmitz and Smith, 2004), last dated at 54 ka (Flude and Storey, 2016; see **Section 2.3**). The deposits of the Rotoiti/Rotoehu eruption comprise a 50-100 m thick sequence of non-welded ignimbrite units (the Rotoiti

Ignimbrite) and intercalated fall beds collectively named the Rotoehu Ash or Tephra (Nairn, 1972; Froggatt and Lowe, 1990; Nairn, 2002). The eruption started with the deposition of the subplinian Matahi basaltic scoria fall (Pullar and Nairn, 1972) from suggested eruptive vents within the northern part of the Okataina caldera (Nairn 2002). The eruption progressed with the ejection of rhyolitic magma deposited by magmatic and phreatomagmatic (e.g., Self and Sparks, 1978; Van Eaton et al., 2012) Plinian eruptive columns (Nairn, 2002), which form part of the Rotoehu Tephra. These Plinian-type fall deposits are interbedded by fine-grained PDC deposits (Nairn, 1981), which underly crystal-rich fall beds (Walker, 1979; Nairn, 2002). This fall-dominated sequence is then overlain by the thick (>50m) non-welded flow units of the Rotoiti Ignimbrite. The ignimbrite deposit extends N from the OVC for 30 km up to the Bay of Plenty coast (Nairn 2002). The distribution of the ignimbrite deposit and the locations of thick lithic lag breccia deposits around lakes Rotoiti, Rotoehu and Rotoma are indicative for a caldera collapse to have occurred in the northern part of OVC (Cole et al. 2010). Shortly after the Rotoiti eruption was emplaced the non-welded Earthquake Flat ignimbrite deposit (10 km^3 DRE) from the nearby Kapenga caldera (Nairn and Kohn, 1973; Schmitz and Smith, 2004), with inferred vents on the Okataina Ring Structure (Nairn, 2002).

2.3.3 Activity between major caldera collapse events (>54 ka)

Volcanic activity from the OVC continued during periods between the three major collapse events. Eruptions occurred at vents within the newly formed caldera complex and within the Okataina Ring Structure outside the caldera borders. This activity was characterised by repeated explosive Plinian-type eruptions and extrusion of rhyolitic lava domes and flows, forming ultimately several dome complexes.

Information on the ages for OVC eruptions >557ka and between the Utu and the Matahina Ignimbrites are uncertain (**Table 2.1**). For instance, the >557ka pre-caldera (?) domes (Whakapoungakau and Matawhaura domes, and the Maungawhakanana dome complex) are exposed N, E and W of the OVC (**Fig. 2.3**), by erosion of the overlaying Matahina ignimbrite deposit, indicating an age of the lavas at least of >322 ka (Nairn, 2002; Cole et al., 2010). However, the Whakapoungakau domes have a ferromagnesian mineral assemblage which correlates with the Okataina-sourced Bay of Plenty pyroclastic deposits on the coast, dated at between 420 and 625 ka (Manning, 1995; Nairn and Beanland, 1989), suggesting a possible age of >557ka (pre-Utu ignimbrite) for the extrusion of these domes.

Explosive volcanism occurred after the Utu ignimbrite eruption, with the emplacement of the Murupara Subgroup deposits (Bonisch Subgroup in Nairn 2002) of 30 km^3 DRE of cumulative

volume (Manning, 1995; Deering, 2009; Cole et al., 2010). The activity of the Murupara Subgroup was characterised by several inferred Plinian-type eruptions during a time interval of 340-322 ka (**Table 2.1**), which concluded with the Matahina ignimbrite eruption (Manning, 1996; Cole et al., 2010). The associated Plinian fall deposits are separated by paleosols and their areal distribution is consistent with eruptive vents opened on the southern part of the present Okataina caldera (Nairn 2002).

More constraints are available for the post-Matahina 322 ka eruptions. Activity between the two largest Matahina and Rotoiti Ignimbrites consisted of a series of explosive eruptions that formed the Onuku Subgroup, the Pokopoko pyroclastic sequence and the Te Wairoa pyroclastic sequence (Cole et al., 2010). During this period the Moerangi and Tutaeheke rhyolitic lava dome complexes were also emplaced (Cole et al., 2010). Dacitic volcanism also occurred during this period with lavas emplaced withing the Puhipuhi basin (Nairn 2002).

The Pokopoko pyroclastic sequence comprises alternating PDC and fall deposits (of unspecified eruption styles) containing variable amount of obsidian clasts (Nairn, 2002). The whole sequence is up to 120 m thick in the proximity of Lake Okareka (**Fig. 2.2**), suggesting eruptive vents west from the Okataina caldera (Thompson, 1974; Nairn, 2002). Age of the Pokopoko pyroclastic sequence, not constrained by analytical dating techniques, is >220 ka based on stratigraphic relations as it underlies the Mamaku Ignimbrite from the nearby Rotorua caldera system (Wilson et al., 1995; Nairn, 2002). Extrusion of some lava domes on the NE shore of lake Okareka could be associated with the Pokopoko activity (Cole et al., 2010).

The Onuku Subgroup comprises multiple pyroclastic fall deposits, PDC units with common obsidian and rhyolite lava lithics and interbedded fine ash layers in some cases containing accretionary lapilli (Nairn, 2002). Six paleosols occur within the Subgroup. Mapped Onuku pyroclastic deposits suggest eruptive vents in the southern part of OVC. Although not dated, eruptions occurred possibly between 322 and 240 ka as the Onuku Subgroup units are stratigraphically bracketed by the ~322 ka Matahina and ~240 ka Kaingaroa ignimbrite deposits (the latter was erupted from the Reporoa caldera system) (Cole et al. 2010).

The small volume (>1 km^3 DRE) Te Wairoa pyroclastic sequence consists of stratified PDC deposits containing hornblende-bearing pumice lapilli and rhyolite lava blocks in ash matrix (Bellamy, 1991; Nairn, 2002). The deposits extend north and east from the Moerangi lava dome complex on the western border of the OVC between Lakes Okareka and Rotorua (**Fig. 2.3**) and appear to be related to the emplacement of this dome complex (Cole et al., 2010). Other rhyolitic lavas forming the Tutaeheke Dome Complex were extruded probably during the same period from vents at the SE border of the Okataina caldera, N of Lake Rotomahana (**Fig. 2.3**).

Table 2.1 – Summary of the eruptive history of the OVC with names, ages and volumes (DRE) of the erupted and emplaced pyroclastic deposit and lava domes. *Sbg* and *S* indicate subgroup and sequence, respectively used in Nairn (2002) and Leonard et al. (2010), which used typically to group a package of successive pyroclastic deposits of different ages interlayered by soils.

Okataina Volcanic Centre eruptive history						
Name of pyroclastic *Sbg* or *S*	**Caldera-forming Ignimbrite**	**Lava Dome Complex**	**Age (ka)**	**Magma volume (DRE)**	**Notes**	**Ref.**
Haroharo and Tarawera (Sbg)		Haroharo and Tarawera	<25	80*	Intra-caldera activity	[1]
Mangaone (Sbg)	Kawerau		33	>15	Minor caldera collapse (suspected)	[2] [3] [4]
			54-31	22	Intra-caldera activity	
Rotoehu/Rotoiti (S)	Rotoiti		54	>100	Major caldera collapse	[5] [6]
Te Wairoa (S)			<220	1	Intra-caldera activity	[1] [4]
		Moerangi	<220	-		
		Tutaeheke	<220	-		
Pokopoko (S)			>220	-		
Onuku (Sbg)			322-240	20		
	Matahina		322	>160	Major caldera collapse	[7] [8]
Murupara (Sbg)			340-322	30	Intra-caldera activity	[1] [4]
		?Matawhaura	-	-		
		?Whakapoungakau	-	-		
		?Maungawhakamana	-	-		
	Utu		557	90	Major caldera collapse	[9] [10]
		?Matawhaura	-	-	Pre-caldera (suspected)	[1] [4] [11]
		?Whakapoungakau	-	-		
		?Maungawhakamana	-	-		
Bay of Plenty coastal (S)			620	-		

References cited: **[1]** Nairn (2002), **[2]** Jurado-Chichay and Walker (2000), **[3]** Spinks (2005), **[4]** Cole et al. (2010), **[5]** Nairn and Kohn (1973), **[6]** Charlier et al. (2003), **[7]** Deering et al. (2009), **[8]** Nairn (1981), **[9]** Leonard et al. (2010), **[10]** Cole et al. (2014), **[11]** Manning (1996). See **Section 2.3** for a more details on individual eruptions.

2.3.4 Post-Rotoiti volcanism: The Mangaone eruptions (<54–31 ka)

The Mangaone Subgroup represents the last eruptive activity of the OVC before the recent post-25 ka period of intra-caldera eruptions (Jurado-Chichay and Walker, 2000; Smith et al., 2002). The deposits of the Mangaone Subgroup occupy a stratigraphic position between the ~54 ka Rotoiti Ignimbrite and the Taupō-sourced ~25.5 ka Oruanui Ingmibrite (Wilson, 2001; Vandergoes et al. 2013; Barker et al., 2021).

The Mangaone Subgroup consists of a series of 12 rhyolitic to rhyodacitic Plinian-type eruptions which occurred from several eruptive vents widely dispersed within the Okataina caldera and Puhipuhi basin (Jurado-Chichay and Walker, 2000; Smith et al., 2002; Shane et al., 2005; Cole et al. 2010). The 12 associated fall deposits are named unit A to L, with the largest (>1 km^3) PDC deposits emplaced during the units I (in addition to the Kawerau Ignimbrite) and L eruptions (Jurado-Chichay and Walker, 2000; Cole et al., 2010). The Plinian fall deposits are generally well-sorted and consist of highly vesicular pumice and typically abundant lithic clasts. Some of the deposits are associated with episodes of various level of magma-water interaction during the eruptive activity (Jurado-Chichay and Walker, 2001). The cumulative DRE volume of erupted magma associated with the Mangaone Subgroup (excluding the Kawerau Ignimbrite) is 22 km^3, corresponding to a cumulative deposit volume of ~80 km^3 (Jurado-Chichay and Walker, 2000; Cole et al., 2010).

No lavas have been recognised from this eruptive period; however, many deposits are rich in rhyolite lava lithic fragments, suggesting that lava extrusions might have occurred. Growing lava domes might have in turn been disrupted during the subsequent Mangaone eruptions or buried by the later post-25ka activity at the Tarawera and Haroharo dome complexes (Cole et al., 2010)

The Mangaone eruptive period lasted about 15 kyr until 31 ka (Jurado-Chichay and Walker, 2000, Leonard et al., 2010). During this period, at ~33ka a large eruption occurred emplacing the Kawerau Ignimbrite (Spinks, 2005; Cole et al., 2014) whose deposit volume has been estimated to vary between 15 and 50 km^3 (Spinks, 2005). Vents for the Kawerau ignimbrite are inferred in the southern part of the OVC to the west of the Puhipuhi Basin (Cole et al., 2010). The ignimbrite was correlated with the largest Plinian-type eruptions (Unit I) of Jurado-Chichay and Walker (2000), and it represents the largest eruption at OVC since the 54 ka Rotoiti/Rotoehu eruption (Spinks, 2005; Cole et al., 2010). It has been suggested by Spinks (2005) and Cole et al. (2010) that the eruption of the Kawerau Ignimbrite was accompanied by a possible minor caldera collapse that could have modified the structure of the caldera complex after the Rotoiti Ignimbrite.

2.3.5 Recent intra-caldera volcanism (~25 ka to present)

Eruptive activity of the OVC during the past ~25 ka consisted of a series of nine rhyolitic, mixed explosive (generally described as Plinian or subplinian) to dome-forming eruptions (**Table 2.2**), and by two basaltic eruptions (Nairn, 2002). All these eruptions, with the exception of the basaltic Rotokawau event (see below), occurred from two NE-trending, linear zones of clustering of vents that transect the Okataina caldera in the northern (Haroharo vent lineament) and southern parts (Tarawera vent lineament) (Nairn, 2002; Cole et al., 2010; Seebeck et al., 2010). Five rhyolitic eruptions (Te Rere, Rotorua, Rotoma, Mamaku and Whakatane eruptions) occurred from the northern vent zone (Haroharo), building over time the Haroharo dome complex and emplacing lava also at Okareka and Rotoma (**Fig. 2.3; Fig. 2.4**) (Nairn, 2002; Smith et al., 2005; Smith et al., 2006). Four rhyolitic eruptions (Okareka, Rerewhakaaitu, Waiohau and Kaharoa eruptions) occurred instead at the southern vent zone (Tarawera), which ultimately built the Tarawera dome complex (**Fig. 2.3; Fig. 2.4**) (Nairn, 2002; Shane et al., 2007). During each rhyolitic eruption multiple, aligned eruptive vents were active.

The most recent volcanic event of the centre is the historical 1886 CE Plinian basaltic eruption, which developed from a 17-km-long fissure that cut through the domes of Mt Tarawera (**Fig. 2.1**) and continued SW to Lake Rotomahana and Waimangu valley (Nairn and Cole 1981; Walker et al., 1984; Sable et al., 2006; Carey et al., 2007; Keam, 2016; Rowe et al., 2021). Another basaltic event, the ~3.4 ka Rotokawau maar-forming eruption, occurred instead at vents aligned E–W just west of the Okataina caldera topographic borders, south of lake Rotoiti (**Fig. 2.3**). The Rotokawau eruption consisted of phreatomagmatic and strombolian explosions emplacing fall and small-volume PDC deposits, rapidly thinning away from the vent (Beanland and Houghton, 1991; Houghton and Smith, 1993; Nairn, 2002).

In the following two sections, descriptions of the main characteristics of the nine <25 ka rhyolitic eruptions from the OVC are presented (see also **Table 2.2** for a summary). Eruption ages, if not stated otherwise, are given in ka cal. BP according to Lowe et al. (2008; 2013). For a review on the Kaharoa eruption the reader is referred to **Section 3.2.2** in Chapter 3.

Table 2.2 – Summary of the main characteristics of the post-25 ka intra-caldera rhyolitic eruptions from the OVC. Note: all eruptions are multi-phase, multi-vent and mixed explosive to effusive. see **Sections 2.3.5.1** and **2.3.5.2** for more details**.** Key for location: *LV* = vent lineament; *H* = Haroharo; *T* = Tarawera; *HDC* = Haroharo Dome Complex; *TDC* = Tarawera Dome Complex; *OB* = Okareka basin; *RB* = Rotoma basin. Recognized type of discrete magmas erupted during individual eruption (number of discrete magmas erupted is also indicated): *R* = rhyolitic magma; *B* = basaltic magma; *RD* = rhyodacitic (mixed and mingled compositions). *PDC* = pyroclastic density current; co-PDC = PDC-derive buoyant plume; *BAF*= block-and-ash flow; PM = inferred phreatomagmatic activity.

Eruption general characteristics							
Eruption name	**Age (ka cal. BP)**	**VL**	**Vent position**	**Magma types erupted**	**Deposit volume (bulk)**	**Deposit volume (conv. DRE)**	**Lava volume**
Kaharoa [1]	0.636	T	TDC	2R (minor RD & B)	16.5	8.2	0.84
Whakatane [2]	5.6	H	HDC	3R	6	2.6	8.53
Mamaku [3]	8	H	HDC	1R	1.2	-	12
Rotoma [4]	9.5	H	HDC & RB	3R	5.6	2.2	5
Waiohau [5]	13.6	T	TDC	1R (minor B)	4.5	-	10
Rotorua [6]	15.4	H	OB	2R	2.7	-	1
Rerewhakaaitu[7]	17.6	T	TDC	2R (minor B)	7.6	-	5.7
Okareka [8]	21.8	T	TDC	3R (minor B)	12	-	5
Te Rere [9]	25.2	H	HDC & OB	1R (?)	5	-	10

Inferred type of eruptive and depositional styles during individual eruption									
Eruption name	**Plinian-type**	**Minor explosions (Dry)**	**(PM)**	**PDC**	**co-PDC**	**Lava flow**	**Lava dome**	**BAF**	**Debris avalanche**
Kaharoa	X	X	X	X	X	-	X	X	-
Whakatane	X	X	X	X	-	X	X	-	-
Mamaku	X	-	X	X	-	X	X	-	-
Rotoma	X	X	X	X	-	X	-	-	-
Waiohau	X	X	X	X	-	X	X	X	X
Rotorua	X	X	X	X	-	X	X	X	-
Rerewhak.	X	X	X	X	-	X	X	-	-
Okareka	X	X	X	X	X	X	X	-	-
Te Rere	X	-	X	X	-	X	X	-	-

Reference cited: [1] Sahetapy-Engel et al. (2014); [2] Kobayashi et al. (2005); [3] and [4] Smith et al. (2006); [5] Speed et al. (2002); [6] Kilgour and Smith (2008); [7] and [8] Darragh et al. (2006); [9] Nairn (2002). See text for more details

2.3.5.1 – Rhyolitic eruptions from the Haroharo vent lineament

Te Rere (Nairn 1992; 2002). After a period of quiescence that lasted for ~6 kyr, eruptive activity resumed at the OVC with the **25.2 ka cal. BP** Te Rere eruption. The eruption occurred at two spatially separated (20 km apart) cluster of vents at Haroharo dome complex and at Okareka (**Fig. 2.4**). The duration of the eruption is unknown. It consists of an initial Plinian phase followed by extrusion of lava flows and domes. The initial Plinian event from the Haroharo dome complex emplaced fall beds and PDC deposits that extend out to the northern and eastern caldera margins. Explosive activity is inferred to have occurred simultaneously at the vents within Haroharo and Okareka. Four lava flow units and a dome were extruded during and after the explosive phase (no Te Rere pyroclastic deposits are found overlying the lavas). Characteristic obsidian-rich surge deposits are found around the Haroharo dome complex vent area and are suggested to be originated from minor phreatomagmatic explosions when the extruding lavas entered in contact with abundant external water from perhaps a lake. The eruption deposited up to 5 km^3 of pyroclastic deposits and emplaced 10 km^3 as lava flows and dome (13 km^3 of total magma erupted).

Rotorua (Nairn, 1980; 2002; Smith et al., 2004; Shane et al., 2007; Kilgour and Smith, 2008). The **15.4 ka cal. BP** Rotorua eruption occurred at four vents within Okareka and involved two physically and chemically distinctive magma bodies. The eruption sequence consisted of two main phases. The first phase was characterised by a Plinian style explosive activity that dispersed tephra to the northwest and lasted probably for few hours up to few days. The Plinian phase began with minor phreatomagmatic activity as the rising rhyolite magma possibly intersected shallow groundwater or surface water within the Okareka basin. With increasing in the rate of magma discharge, the eruption transitioned to dominantly magmatic emplacing proximal deposits characterised by multiple bedding with sharp changes in the grain size of the beds vertically along the stratigraphy. These features are suggested as related to significant fluctuations in magma discharge rate over short intervals, possibly caused in response to variable magma ascent rate and degassing dynamics in the conduit. Eruption columns are estimated to have varied between 13 and 20 km. The second phase of the Rotorua eruption consisted of the transition from explosive to dominantly effusive activity with the extrusion of two lava domes that continued for a suggested duration of several years. Dome growth was accompanied by inferred Vulcanian explosions erupting crystal-rich pumice and as well as dome collapses producing locally dispersed PDC deposits. The deposit volume emplaced during the whole Plinian phase was revised by Kilgour and Smith (2008) at 2.6 km^3, plus an estimated 0.1 km^3 volume of pyroclastic deposits associated with the second phase of the eruption. Volumes of the domes are estimated at 1 km^3 (Nairn, 2002).

Rotoma (Nairn, 2002; Smith et al., 2006). The **9.5 ka cal. BP** Rotoma eruption occurred from at least six suspected aligned eruptive vents over a 12-km-long segment of the Haroharo vent lineament, from the subsidiary Rotoma basin into the Okataina caldera. The eruption consists of Plinian-style activity, minor phreatomagmatic explosions and by the extrusion of lavas at the Rotoma vent area as well as from the NE and W part of the Haroharo dome complex. Different vents were inferred as active simultaneously, however the location of the eruptive activity possibly shifted from Lake Rotoma (NE) to two vents within the Haroharo dome complex, tapping three distinct magmas. The eruption possibly commenced with minor explosions of magmatic and suspected phreatomagmatic activity from the Rotoma vent area, with deposition of fall and PDCs beds which resulted in the formation of a tuff ring. Plinian eruptions followed at Rotoma and at the NE margin of the Haroharo dome complex, with pyroclasts dispersed toward the NE. Shortly after, phreatomagmatic activity occurs at a second vent to the W margin of the Haroharo dome complex, which produced PDCs and a tuff cone. During the explosive activity, lavas were extruded from other vents at both Rotoma and at the NE Haroharo dome complex area. The eruption concluded with the emplacement of PDCs deposits at the E margins of Okataina caldera, forming a 200m-thick fan. The total volume of fall deposits is calculated at ~5.15 km^3 (DRE volume = ~2.2 km^3), while PDC units account for 0.5 km^3. The total volume of the lava flows is estimated at >5 km^3.

Mamaku (Nairn, 2002; Smith et al., 2006). The **8 ka cal. BP** Mamaku eruption occurred from several aligned vents (possibly eight) spread over ~10 km from the NE to the SW ends of the Haroharo dome complex, with one vent just outside the western margin of the Okataina caldera. The eruption displayed both explosive and effusive activity, however it was dominantly effusive as estimated 90% of the magma was erupted as lava domes and flows. The eruption sequence began with the extrusion of two lava flows from vents at the NE part of Haroharo dome complex according to Nairn (2002) while it initiated with phreatomagmatic and Plinian activity according to Smith et al. (2006). After a period long enough for the lava surfaces to have cooled, Nairn (2002) suggests Plinian events took place which were preceded by phreatomagmatic explosions. Plinian fall deposits were dispersed concentrically around the vent system and are interbedded in proximal sites by PDC deposits resulting from episodes of column collapse. Explosive activity continued at different vents and preceded extrusion of other lava domes and flows. The Mamaku eruption ended with suspected phreatic (Nairn, 2002) or phreatomagmatic explosions (Smith et al., 2006) at a crater outside the caldera rim, west from the Te Horoa lava dome which separates Lake Okataina from Lake Tarawera (**Fig. 2.4**). A magma volume of ~12 km^3 was estimated for the extruded lavas during the Mamaku eruption. Fallout and PDC deposit totalled a bulk volume of 1.2 km^3. The Mamaku eruption emplaced the largest volume of lava during any single eruptions of the post-25 ka activity of the OVC and, unlike other eruptions from the Haroharo vent

lineament, only a single compositionally homogeneous magma batch was inferred to have fed the eruption.

Whakatane (Nairn, 2002; Kobayashi et al., 2005; Smith et al., 2006). The **5.6 ka cal. BP** Whakatane eruption was the last volcanic event to have occurred from the Haroharo vent lineament, which ultimately shaped the present geometry of the Haroharo dome complex with extrusion of several induvial lava flows and domes. The eruption occurred at five aligned eruptive vents spread over 11 km. Three vent areas are designated as the Makatiti vent area situated in the SW part of the dome complex; the Haroharo-Rotokohu middle vent area; the Pararoa vent at the NE margin of the dome complex, adjacent to the caldera rim. The eruption was characterised by the typical mixed, explosive-effusive, rhyolitic activity of the post 25-ka period of the centre. During the eruption, ~8.5 km^3 DRE of magma was erupted as lava domes and flows while a total of ~2.6 km^3 DRE of magma was erupted explosively forming pyroclastic deposits.

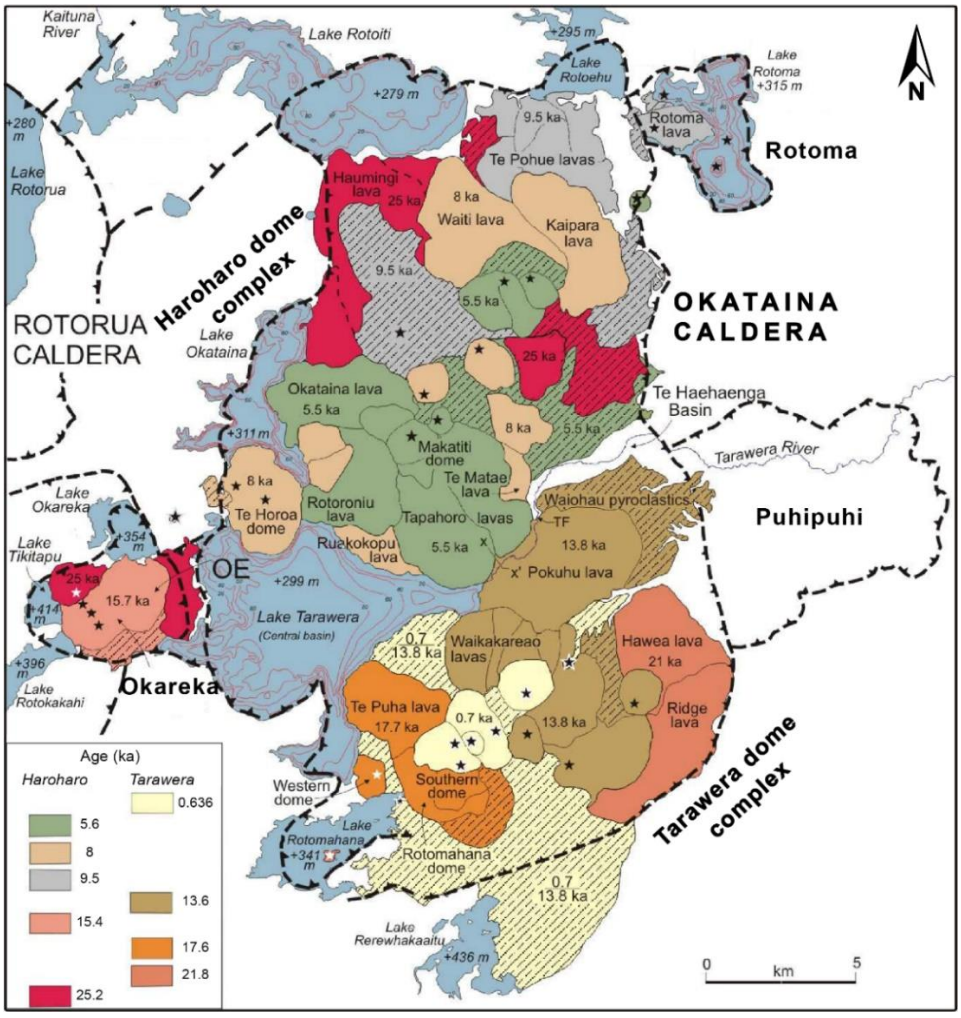

Figure 2.4 – Map of the post-25 ka intra-caldera rhyolitic lavas and domes of the OVC, modified after Villamor et al. (2007).

The eruption sequence comprises explosive and effusive events at each of the three vent areas, some of which have been inferred to have occurred simultaneously. The Whakatane eruption began with two vent-opening explosions at the Haroharo-Rotokohu vent area, generating directed blasts and emplacing multiple coarse lithic-rich beds. These explosions were immediately followed by activity at the Makatiti vent, 6 km SW from the preceding vent, which generated diluted PDCs (depositing fine-grained beds) that preceded the largest explosive phase of the eruption, Plinian in intensity. Plinian columns developed from Makatiti vent, during which tephra were dispersed over a wide area in the north-eastern North Island, with a main dispersal axis toward SW. Repeated column collapses formed PDCs and associated deposits which are found interbedded with the Plinian fall beds. At valleys within 5 km from the source, PDC deposits accumulated up to thicknesses of 50 m. Minor explosions are inferred to have occurred at the same time from the Haroharo-Rotokohu vent area and at Pararoa vent. Explosions at Haroharo-Rotokohu resulted in the formation of a tuff cone. Timing of the initial activity at Pararoa vent is not well constrained, however vent-opening phreatomagmatic explosions are suggested to have produced fine ash deposits bearing ballistic clasts. The main explosive activity at Pararoa vent consisted of Vulcanian explosions through a suggested growing lava dome. These explosions generated and deposited PDCs beds containing dense pumice that further built a small tuff cone around the vent. Further minor phreatomagmatic explosions have been suggested depositing lithic-rich lapilli beds up to 2 km from the vent. The explosive activity at all vents was followed by the extrusion of lava domes and flows. Extrusion of Haroharo, Rotokohu and Pararoa domes, from their respective vents, is inferred to have commenced during the major Plinian events from Makatiti vent. On the other hand, lava flows and domes from the Makatiti vent area were extruded when the Plinian activity had ended. The Makatiti and Pararoa domes continued to grow after all the explosive events had stopped, and they represent the final phase of the Whakatane eruption. Based on the data available, Kobayashi et al. (2005) suggested a probable duration for the entire eruption sequence (explosive and lava activities) of more than ten years, accounting for the growth of the lava domes and associated minor explosions. Plinian events seem to have occurred repeated times during at least two years. This was suggested based on the presence of Plinian deposits underlaying and overlying the dome extruded at the Haroharo crater. Like the Rotoma eruption, the Whakatane eruption tapped three recognised, distinct magma batches, each vent areas erupting a certain magma composition. Most of the magma was erupted from Makatiti vent area as 7.5 km^3 of lava, 2.3 km^3 DRE of the whole Plinian fall deposit and 0.2 km^3 DRE of PDC deposits. Lava flows and domes at Haroharo-Rotokohu and Pararoa have estimated volume of 1 and 0.03 km^3 respectively, and of 0.285 and 0.0065 km^3 DRE of their associated pyroclastic deposit.

2.3.5.1 – Rhyolitic eruptions from the Tarawera vent lineament

Okareka (Nairn, 1992; 2002; Darragh et al., 2006; Shane et al., 2008). The **21.8 ka cal. BP** Okareka eruption marked the beginning of the eruptive activity at the Tarawera vent lineament. The Okareka eruption, despite is misleading name, is not associated with lava flows and domes at the Okareka basin but was erupted form vents within the Tarawera dome complex. Exact locations of the eruptive vents are uncertain as they are buried by younger lavas. The most proximal Okareka pyroclastic deposits can be found at 8 km from an inferred vent area at Kanaka and Ridge domes (**Fig. 2.4**). The eruption was characterised by an initial explosive phase consisting of nine inferred events (units A to I in Darragh et al. 2006) of different style, magnitude, and intensity. The eruption sequence began with a subplinian basaltic scoria event (Unit A), followed by rhyolitic activity (Unit B to I). The rhyolitic activity consisted of: (i) minor phreatomagmatic explosions depositing ash beds containing mingled basalt-rhyolite clasts (Unit B); (ii) a main Plinian event dispersing tephra to the NW from an estimated maximum column height of 19 km (Unit C); (iii) magmatic to phreatomagmatic explosions depositing a finely laminated package of fall, PDC, and co-PDC beds (Unit D, E and F); (iv) a possible subplinian, mainly magmatic, event depositing fall beds (Unit G); (v) activities of non-specified eruptive origins (due to very limited exposures) that emplaced a massive well sorted fine-ash fall deposit (Unit H) and a distinctive orange-brown bed of massive ash with scattered lapilli (Unit I). Further three units (J, K and L) have been found only in one section, consisting of thin ash layers inferred as the result of PDCs deposition and co-PDC ash fallout. The bulk deposit volume is estimated at 11.9 km^3 (termed "non-consolidated" in Darragh et al., 2006). Soon after the explosive activity, the Okareka eruption progressed toward a final effusive phase characterised by the extrusion of 5 km^3 of magma as a lava dome and flows. No evidence has been found for significant erosion or weathering features between the pyroclastic units, suggesting that the explosive phases occurred relatively continuously. By comparison with other post-25 ka eruptions, the duration of the effusive phase is estimated at 2-3 years. Three discrete rhyolitic magma batches were erupted during the Okareka eruption. The basaltic magma erupted at the beginning of the eruption forming subplinian scoria fall deposits is inferred to have intruded at the base of the rhyolitic plumbing system, ultimately reaching the surface (Shane et al., 2008).

Rerewhakaaitu (Nairn, 2002; Darragh et al., 2006; Shane et al., 2007). The **17.6 ka cal. BP** Rerewhakaaitu eruption occurred at the SW end of the Tarawera dome complex, from possibly two separated vents a few km apart. The eruption simultaneously tapped two rhyolitic magmas during most of the eruptive sequence. Extrusion of the Rotomahana dome at the NE present margin of Lake Rotomahana, was suggested by Nairn (2002) to have been the first activity of the Rerewhakaaitu eruption, however eruption initiation needs further investigation. Dome extrusion was followed by explosive activity of different style, magnitude, and intensity. The pyroclastic

sequence was divided into 14 units (A to N) according to Darragh et al. (2006). The initial A unit was emplaced by an early Plinian event, which dispersed fall beds mostly to ENE from eruptive columns of up to 15 km in height. Units B-D consist of stratified, poorly sorted, and lithic-rich ash beds, which have been suggested sourced from phreatomagmatic explosions, marking an abrupt change in the eruption dynamics. Units B-D were widely dispersed around the vent, with lobes to the NE and SE. Units E-J were deposited from 20-25 km high Plinian eruptive columns that dispersed tephra to the SE. The E-J package alternate ash and lapilli beds interpreted as fluctuations in eruption intensity. Unit K consists of fine-grained, well-sorted ash beds, representing a decline in the explosive activity. Deposit of Units L-N have similar characteristic of Units E-J, possibly representing fall beds deposited from a renewed convective column. Explosive activity formed a tuff cone on the eastern margin of the Rotomahana dome. The tuff cone was later overlain by the extrusion of a second lava dome and a lava flow. The total deposit volume is estimated at 7.6 km^3. Lava domes and one flow totalled a magma volume of 5.7 km^3. The eruption is suggested to have lasted for months to years similar to the previous Okareka eruption to account for the explosive and effusive activity. Even if no discrete basaltic deposits have been found within the Rerewhakaaitu pyroclastic sequence, some rhyolitic pumice contain andesitic to rhyodacitic hybrid glass inclusions accompanied by mineral phases typical of basaltic to andesitic magmas (e.g., olivine, calcic plagioclase phases, and magnesium-rich orthopyroxenes). These are inferred to indicate involvement of a basaltic magma during the eruption (Shane et al., 2007).

Waiohau (Nairn, 2002; Speed et al., 2002; Shane et al., 2008). The **13.6 ka cal. BP** Waiohau eruption occurred at possibly two vent areas, ~5 km apart, located at Kanaka and Eastern domes, S and E from the younger Wahanga dome of the present-day Mt Tarawera. Explosive activity possibly occurred only at Kanaka the vent area (Nairn, 2002). The eruption began with the extrusion of Eastern dome, followed by explosive and later effusive activity at Kanaka vent area. The explosive activity was subdivided by Speed et al. (2002) into 15 events each resulting in the deposition of a stratigraphic unit in the Waiohau pyroclastic succession (units A to O). The earliest deposit is a fallout bed of fine lapilli (Unit A), followed by PDC deposits (Unit B). The eruption progressed toward the deposition of fall beds from Plinian and suspected "phreatoplinian" columns (Unit C) dispersed to the SE, and deposition from PDCs (Unit D) radially from Kanaka vent. The eruption continued with a Plinian column reaching heights of ~30 km, dispersing tephra (unit E) into two distinct lobes to the SSW and SE. As the Plinian activity progressed, the vent possibly widened or migrated resulting in the destruction of an obsidian dome/cryptodome or lava built during the same eruption, and emplacing obsidian-bearing lapilli bed (unit F). Immediately after, small explosions and fallout events occurred depositing several pyroclastic beds (units G, H, I and J). The eruption continued with the emplacement of a widespread distinctive thin layer

of poorly sorted, pink ash with abundant lithic clasts and obsidian (unit K) of PDC origin, followed by a new Plinian column. The associated fall deposit (unit L) was dispersed toward the SE, accompanied by the emplacement of thin PDCs (units M). This last Plinian activity (L-M) was followed by a major failure of the NE flanks of the Mt Tarawera. The sector collapse resulted in the emplacement of a thick deposit either as a series of block-and-ash flows, or as one debris avalanche. The collapse possibly induced a sudden decompression of underlying magma, triggering explosions that possibly generated the PDCs of Unit N. The Waiohau eruption ended with the emplacement of lava flows and the extrusion of Kanaka dome. No evidence of significant time breaks is found within the tephra sequence, suggesting the deposition of the pyroclastic succession over a period of days, while the lava flows and domes were possibly emplaced within years. The total volume of magma erupted as lava was 10 km^3 (Shane et al., 2008), while a deposit volume for the whole pyroclastic sequence is estimated at 4.53 km^3 (Speed et al., 2002). The Waiohau eruption, together with the Mamaku eruption from Haroharo dome complex, might have been the only two eruptions of the post-25 ka activity that began with the extrusion of lava as flow or dome. Similarly with the Mamaku eruption, only one magma batch was likely tapped during the Waiohau eruption. No basaltic component is found in the deposits, however Shane et al. (2008) indicated that rare basaltic and andesitic clasts occur within a "rhyolite breccia" deposit erupted from a third vent, near Lake Rotomahana, suggesting the involvement of basaltic magma also for the Waiohau eruption.

Kaharoa eruption, **0.636 ka cal. BP** (**see Section 3.2.2 in Chapter 3**).

2.4 Summary

The OVC is one of the most frequently active, rhyolitic-dominated centres of the modern TVZ (New Zealand). The eruptive activity of the centre possibly started as early as 625 ka with explosive eruptions distributing rhyolitic, cummingtonite-bearing, tephra layers towards the Bay of Plenty and with effusive events emplacing lava domes in the pre-caldera Okataina area.

The volcanic evolution of the centre was punctuated by three very large, caldera-forming eruptions (individual DRE erupted volumes ranged from 90 up to 160 km^3) resulting in the formation of the Okataina caldera system, a complex system of overlapping and nested collapse structures. These eruptions are associated with the emplacement of the Utu, Matahina, and Rotoiti Ignimbrites dated at 557 ka, 322 ka and 54 ka, respectively, giving an average ~250 kyr between consecutive major caldera collapse events.

Volcanism periodically occurred with rhyolitic intra-caldera eruptions during the intervals between each caldera collapse events and continued after the 54 ka Rotoiti/Rotoehu eruption. Although not much data is available on the pre-Rotoiti intra-caldera eruptions, eruptive activity is inferred to have been characterised by periods of repeated Plinian-type eruptions. This type of activity resulted in the formation of packages of pyroclastic deposits interlayered by paleosols that have been grouped into pyroclastic subgroups and sequences (e.g., Murupara and Onuku Subgroups). Eruptive activity during these periods was also characterised by the extrusion of lava domes and flows forming different lava domes complexes (e.g., Moerangi and Tutaeheke dome complexes). Vents for the pre-Rotoiti, intra-caldera eruptions were located both within and outside the caldera margins.

More constraints are available for the eruptive history of the centre following the 54 ka Rotoiti/Rotoehu, caldera-forming eruption. Two periods are conventionally recognised: the (i) 54-31 ka period associated with the Mangaone eruptions and the (ii) post-25 ka period associated with the Haroharo and Tarawera eruptions. The 54-31 ka Mangaone period was characterised by a series of twelve, rhyolitic to rhyodacitic, Plinian-type eruptions whose deposits form the Mangaone Subgroup. Activity during this period developed at inferred vents widely dispersed within the Okataina caldera and at the Puhipuhi basin. The emplacement of the Okataina-sourced Kawerau Ignimbrite (15-50 km^3 deposit volume) was correlated to the Mangaone period, possibly causing a minor caldera collapse event at 33 ka.

The post-25 ka period consisted instead of nine rhyolitic eruptions and two basaltic eruptions, including the 1886 CE basaltic fissure eruption of Tarawera. Contrary to the 54-31 ka Mangaone period, individual post-25 ka rhyolitic eruptions exhibited mixed explosive-and-effusive eruption behaviour. Eruptions typically started with an explosive phase(s) characterised by sustained Plinian-type events and minor ash explosions, followed by the extrusions of lava. Rhyolitic vents during the post-25 ka period are located along two subparallel, NE-trending zones defining the Haroharo and the Tarawera vent lineaments. During individual rhyolitic eruptions, multiple vents were active along one of the two vent lineaments. The effusive phases of each individual eruption from the two lineaments built, over time, the Harharo and the Tarawera intra-caldera dome complexes, which also emplaced lavas at the Okareka and Rotoma basins.

The eruptive history of the OVC records the complex evolution of a silicic caldera system in which up to three cycles of major caldera collapse events and intra-caldera activity can be recognised. This evolution makes the history of the OVC comparable to those of other polycyclic caldera systems both locally and worldwide, with examples at the Taupō (New Zealand), Campi Flegrei (Italy) and Valles-Toledo (USA) caldera systems (Heiken et al., 1990, Barker et al., 2021; Bouvet de Maisonneuve et al., 2021). The intra-caldera eruptive activity can vary largely in

magnitude and eruptive style, from small to moderate scale eruptions (<0.1km^3 DRE), up to moderate to large scale eruptions (0.1–10 km^3 DRE, **Table 1.1**) reaching Plinian intensities and often associated with an effusive phase. At Okataina, in the past 54 kyr following the youngest major caldera-forming eruptions, a total of twenty-one rhyolitic and one basaltic, moderate to large scale eruptions have occurred, erupting individual volumes of >1km^3 DRE of magma, while small to moderate eruptions appear to have been very rare. This seems to differ from the intra-caldera activity at other polycyclic caldera systems, in which smaller scale eruptions (<1km^3 DRE) represent instead the more frequent eruptive activity of the centre following a caldera collapse event (e.g., at Taupō or at Campi Flegrei). The larger magnitude intra-caldera eruptions at Okataina can suggest favourable conditions for the rapid formation and recharge of larger volumes of eruptible magma batches in the shallow crust (Giordano and Cashman, 2014; Sas et al., 2019) possibly aided by the subduction-and-extension tectonic setting in which the Okataina caldera system formed (Seebeck et al., 2014; Sas, 2020) (see also **Chapter 6**). Furthermore, the locations of the post-25 ka eruptive vents along two subparallel linear zones with orientation consistent to that of the Taupō Rift, also suggest magma transfer and eruption along pre-existing regional structures at depth (Nairn, 2002).

[This page intentionally left blank]

Chapter 3

Deposit and stratigraphy of the Kaharoa eruption

3.1 Introduction

Rhyolitic eruptions occur less frequently compared to eruptions fed by intermediate to mafic magmas (White et al., 2006; Crosweller et al., 2012). However, they can generate the most voluminous and catastrophic volcanic explosive events on Earth (Mason et al., 2004; Miller and Wark, 2008; Bryan et al., 2010). Due to the lack of direct observations and monitoring data, the reconstruction of the dynamics and time evolution of rhyolitic eruptions is mostly based on the investigations of the pyroclastic successions and lavas emplaced during these events (e.g., Fierstein and Hildreth, 1992; Wilson and Hildreth, 1997; Nairn et al., 2001; Goto et al., 2018), along with detailed microtextural and geochemical analysis of the erupted juvenile materials (e.g., Smith et al., 2006; Shane et al., 2008; Houghton et al., 2010; Geshi et al., 2020).

Advancements in the understanding of rhyolitic volcanism were made possible by a series of multi-disciplinary studies focused on two very recent rhyolitic eruptions: the 2008-2009 eruption of Chaitén volcano, Chile (Lara, 2009) and at the 2011-2012 eruption of the Puyehue-Cordón Caulle volcanic complex, Chile (Castro et al., 2013). These eruptions offered for the first time a direct observation of the complex and long-lasting eruptive activity associated with moderate- to large-scale (~1 km^3 pyroclastic deposit volume) rhyolitic eruptions and their impacts on modern society (Elissondo et al., 2016; Craig et al., 2016; Forte et al., 2018). Studies conducted on these eruptions highlighted the composite, multiple-phase nature of the explosive sequence of these eruptions, which resulted in the deposition of complex pyroclastic successions (Alfano et al., 2011; Pistolesi et al., 2015; Bonadonna et al., 2015b; 2015c). Furthermore, these studies provided new insights into eruptive dynamics and transition between explosive to effusive-dominated eruption behaviours (Castro et al., 2012a; Saubin et al., 2016; Schipper et al., 2013, 2021).

The study of rhyolitic eruptions is of great relevance in the context of New Zealand volcanology and volcanic hazard scenario planning (Thompson et al., 2015; Stirling et al., 2017). The Taupō Volcanic Zone (TVZ) of New Zealand is one of the most frequently active regions on Earth to have sourced rhyolitic eruptions since the late Quaternary (Wilson et al., 1995; Allan et al., 2008), and hosts two currently active caldera systems at the Okataina and Taupō silicic volcanic centres (Nairn, 2002; Barker et al., 2021). Rhyolitic volcanism in the TVZ is associated with a wide range of eruptive styles and erupted magma volumes, spanning from small to moderate eruptions (0.001 to 0.01 km^3 DRE) dominated by the extrusion of lava-domes (e.g., Leonard, 2003; Kósik et al., 2019) to very large volume (>10 km^3 DRE), up to catastrophic super-eruptions (>450 km^3 DRE) associated with large caldera collapses (e.g., Wilson, 2001) (see **Table 1.1** in **Chapter 1**).

During the past ~50 kyr, in the periods between caldera-collapse events, the eruptive activity of the TVZ's silicic centres was characterised by several intra-caldera explosive to effusive rhyolitic

eruptions, with erupted magma volumes typically ranging from 0.01 to 10 km^3 (Wilson et al., 2009; Leonard et al., 2010). These intra-caldera eruptions emplaced thick, fallout-dominated sequences close to the source and widespread thin ash layers and have been broadly classified as subplinian and Plinian in eruptive styles (Houghton et al., 1995; Lowe et al., 2008). At the Okataina caldera, these pyroclastic deposits display repeated grain size fluctuations and changes in deposit structure within any eruption pyroclastic succession (Nairn, 2002), suggesting complex eruption sequence and deposition mechanisms. A systematic characterisation of the main deposits' features associated with these eruptions is still missing and can provide critical insights to better constrain the eruptive behaviours and hazard potential from intra-caldera rhyolitic eruptions.

This study investigates the pyroclastic succession associated with the explosive phases of the 1314 ± 12 CE Kaharoa eruption sourced from Mt Tarawera, within the Okataina caldera. Through new field observations the existing stratigraphic schemes for the proximal deposits (Nairn et al., 2001) and for the medial-to-distal fallout deposits (Sahetapy-Engel et al., 2014) are revaluated and complemented to characterise in detail the timing of eruptive events and the occurrence of time breaks in the eruption sequence. The in-depth study of the pyroclastic beds in the field is combined with the systematic quantification of the sedimentological and lithological features of the deposits to infer temporal changes in the depositional and eruptive mechanisms during the eruption. This study finally aims to provide a better understanding of moderate to large scale rhyolitic eruptions and their possible intra-eruption scenarios.

3.2 Geological and volcanological background

3.2.1 Geological setting and eruptive history of Okataina and Mt Tarawera

The Okataina Volcanic Centre (OVC) is the northernmost active rhyolitic centre of the TVZ in the North Island of New Zealand and consists mainly in the active Okataina caldera system and extra-caldera lava domes (Wilson et al., 1995; Nairn, 2002; Cole et al., 2010). The Okataina caldera, also referred to as the Haroharo caldera in Nairn (2002), is the most recent source of rhyolitic volcanism in the TVZ, with the CE 1314 ± 12 (or 636 ± 12 cal. yr BP) Kaharoa intra-caldera eruption marking the youngest rhyolitic activity of the region.

The Okataina caldera is a complex of overlapping collapse structures (Nairn, 2002; Spinks et al., 2005; Cole et al., 2014) formed after up to three caldera-forming eruptions, which emplaced large volume ignimbrite deposits (90-160 km^3 DRE) (Cole et al., 2010; Cole et al., 2014). These deposits are dated at ~557 ka (Utu Ignimbrite; Leonard et al., 2010), ~322 ka (Matahina Ignimbrite; Leonard et al., 2010), and at ~54 ka (Rotoiti Ignimbrite; Flude and Storey, 2016. See section 2.3 in Chapter 2 for ages of the Rotoiti Ignimbrite). Presently, the Okataina caldera system consists of a main N-S oriented, 28×16 km collapsed area (the Okataina caldera), resulting in a distinct negative gravity anomaly (Seebeck et al., 2010; Stagpoole et al., 2020), with three additional minor peripheral basins of subsidence (Rotoma, Puhipuhi and Okareka) at the NE, E and W margins of the caldera (**Fig. 3.1**).

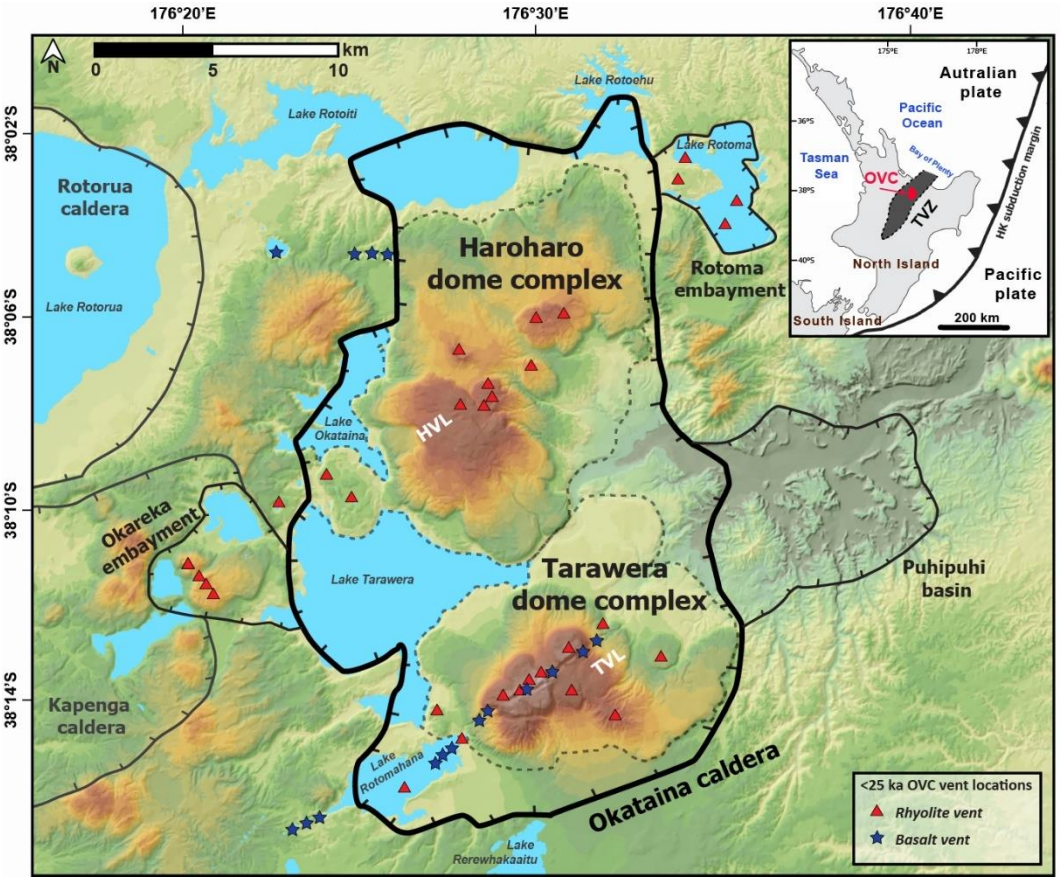

Figure 3.1 – Map of the OVC showing topographic settings, borders of the Okataina caldera and subsidiary basins (Puhipuhi basin, Okareka and Rotoma embayments) and approximate margins of the intra-caldera Haroharo and Tarawera dome complexes. Location of eruptive vents active at the OVC during the past 25 kyr along the Haroharo (HVL) and Tarawera vent lineaments (TVL) are also shown. The OVC structural features and borders of neighbouring calderas are drawn following Nairn (2002). The inset shows tectonic settings of the southern Hikurangi-Kermadec (HK) subduction margin and locations of the OVC in the TVZ within the North Island of New Zealand.

Between caldera collapse events, the eruptive activity of the centre was characterised by repeated explosive eruptions up to Plinian-type in magnitude and intensity, and by the extrusion of rhyolitic lava domes and flows, forming several dome complexes (Nairn, 2002; Cole et al., 2010). After the Rotoiti/Rotoehu eruption, the last major caldera-forming event of the centre (Nairn, 1972, 2002; Schmitz and Smith, 2004), a series of twelve rhyolitic to rhyodacitic Plinian-type eruptions occurred between <54 to 31 ka (Jurado-Chichay and Walker, 2001, Leonard et al., 2010) at various inferred vents within the Okataina caldera and the Puhipuhi basin (Jurado-Chichay and Walker, 2000; Nairn, 2002). Their deposits are collectively referred to as the Mangaone Subgroup (Leonard et al., 2010). No lavas seem to have been emplaced during this eruptive period (Cole et al., 2010). The >15 km^3 Kawerau ignimbrite deposit emplaced at ~33 ka (Unit I in Jurado-Chichay and Walker, 2000) was correlated to the Mangaone Subgroup eruptions, possibly causing some minor collapse in the caldera system (Spinks et al., 2005; Cole et al., 2014).

During the past 25 kyr, following the Mangaone eruptions, a second period of intra-caldera volcanism occurred at the OVC, consisting of nine, moderate- to large-scale, rhyolitic, explosive to dome-forming eruptions. The erupted products of these eruptions formed over time the intra-caldera Haroharo and Tarawera dome complexes (Nairn, 2002) (**Fig. 3.1**). Two basaltic eruptions also occurred during this period: (i) the historical basaltic Plinian fissure eruption of Tarawera in 1886 CE (Walker et al., 1984; Sable et al., 2006; Rowe et al., 2021) and the 3.7 ka, small-volume, maar-forming, Rotokawau eruption (Beanland and Houghton, 1991; Houghton and Smith, 1993; Nairn, 2002). All the <25 ka eruptions (excluding Rotokawau) occurred from multiple aligned vents which define two NE-trending vent lineaments that transect the Okataina caldera in the northern (Haroharo vent lineament) and the southern parts (Tarawera vent lineament) (Nairn, 2002; Cole et al., 2010; Seebeck et al., 2010). The location of the Haroharo and Tarawera vent lineaments is probably related to underlying basement structures (Nairn, 2002), with both vent lineaments having orientation consistent with main active fault trend of the Taupō Rift around the OVC, with a slight offset at an angle of 10-20° clockwise (Villamor et al., 2011). The lavas and pyroclastic sequence from these eruptions at the two vent lineaments are referred to as the Haroharo and Tarawera Subgroups in Leonard et al. (2010).

The intra-caldera Tarawera dome complex (**Fig. 3.2**) was built during four rhyolitic eruptions that occurred along the Tarawera vent lineament: the Okareka (Nairn, 1992; Nairn, 2002; Darragh et al., 2006; Shane et al., 2008), the Rerewhakaaitu (Nairn, 2002; Darragh et al., 2006; Shane et al., 2007), the Waiohau (Nairn, 2002; Speed et al., 2002; Shane et al., 2008) and Kaharoa eruptions (Nairn et al., 2001; Nairn, 2002; Leonard et al., 2002; Nairn et al., 2004; Sahetapy-Engel et al., 2014), dated at 21.8, 17.6, 13.6 and 0.636 cal. kyr BP, respectively (Lowe et al., 2008; 2013). The extrusion of closely spaced and overlapping rhyolitic lava domes and coulees, with intercalated proximal pyroclastic deposits, emplaced during these four eruptions built over time Mt Tarawera,

whose summits consist of the three main lava domes extruded during the Kaharoa eruption (**Fig. 3.2**). The present configuration of Mt Tarawera is affected by the opening of the 17-km-long eruptive fissure during the 1886 CE basaltic eruption (Nairn and Cole, 1981; Carey et al., 2007; Rowe et al., 2021).

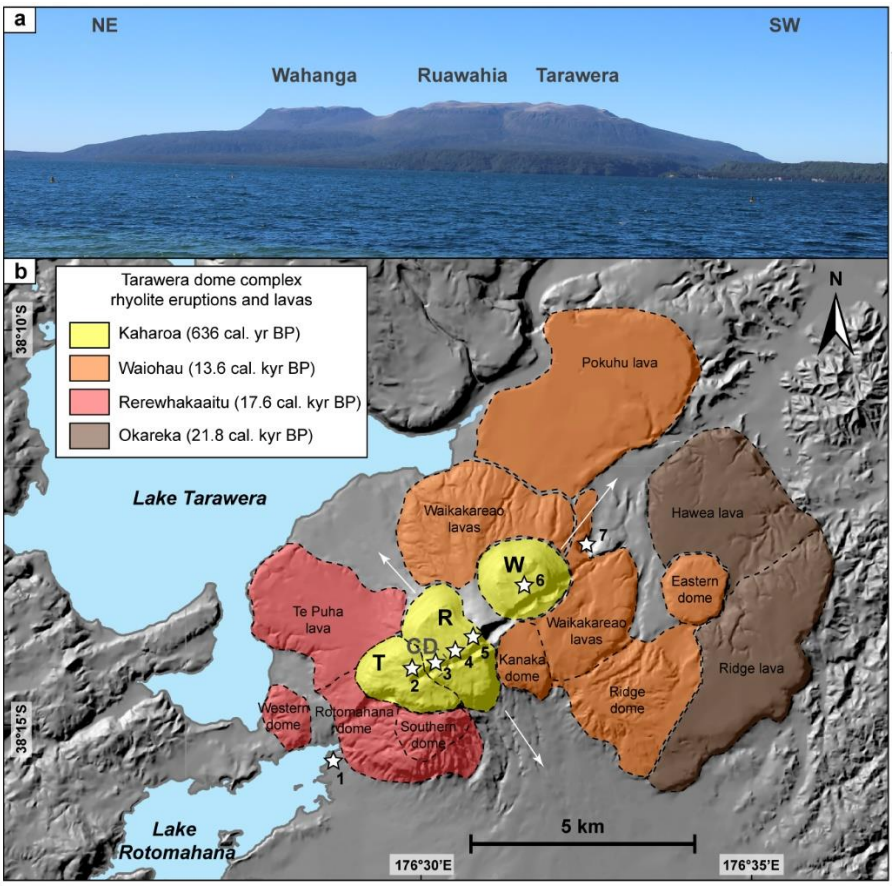

Figure 3.2 – (**a**) Photo of Mt Tarawera with the three summit domes emplaced during the Kaharoa eruption (Wahanga, Ruawahia and Tarawera). The photo is taken from the NW shore of Lake Tarawera. (**b**) Map of the Tarawera dome complex with the distribution of lavas (following Nairn, 2002) erupted during the four rhyolite eruptions that built the dome complex. *W*, *R*, *CD* and *T* indicate Wahanga, Ruawahia, Crater and Tarawera domes (Crater dome is buried beneath Ruawahia and Tarawera domes). Stars show the locations of the inferred seven vents active during the Kaharoa eruption (following Nairn et al. 2001). The vents are numbered from SW to NE (no temporal order is implied): 1 is Green Lake Plug vent, 2 is Tarawera dome vent, 3 is Crater dome vent, 4 is Ruawahia dome vent, 5 is Ruawahia crater vent, 6 is Wahanga dome vent and 7 is Northeast crater. The white arrows indicate the distributions of the Kaharoa block-and-ash flow fans.

Rhyolitic eruptions at Tarawera were characterised by a similar eruptive pattern, characterised by a multiple-vent type of activity and by exhibiting an explosive-to-effusive eruption behaviour, in which the explosive phases were usually followed by the extrusion of lavas. The explosive activity ranged in style within any of these eruptions from minor ash explosions to sustained subplinian

and Plinian events (Nairn, 2002). During each of these four eruptions, the explosive phases emplaced an estimated total pyroclastic deposit volume ranging between 1.2 to 16.5 km^3 (~0.5 to 8 km3 DRE), while the effusive phases erupted between 0.84 to 5 km^3 of lavas as dome and coulees (See **Table 2.2 in Chapter 2**). Although the erupted magma is predominantly rhyolitic in composition, additional subordinate basaltic scoria deposits were associated with the initial explosive phase of the Okareka eruption and evidence of minor basaltic involvement was identified in the erupted magmas of the other Tarawera rhyolitic eruptions (Leonard et al., 2002; Shane et al., 2008).

3.2.2 Previous studies on the Kaharoa eruption

Several studies have been conducted on the Kaharoa eruption for its multiple relevance in understanding rhyolitic volcanism at the TVZ and the Okataina caldera system (e.g., Leonard et al., 2002; Nairn et al. 2004; Shane et al., 2008; Cole et al., 2014; Sahetapy-Engel et al., 2014), and to estimate the associated volcanic hazards of rhyolitic eruptions (e.g., Bonadonna et al., 2005; Jenkins et al., 2008; Thompson et al., 2015). Furthermore, the deposits of the Kaharoa eruption represent an important stratigraphic marker for the late Holocene geological and archaeological record in the norther part of the North Island (e.g., Lowe et al., 1998; Newnham et al., 1998; Shane, 2000; Hogg et al., 2003; Lowe et al., 2011, 2013).

The Kaharoa eruption is the largest eruption to have occurred in New Zealand over the past 1,000 years (Wilson et al., 1995). The deposits of the main explosive activity have been dated at 636 ± 12 cal. yr BP (calendar date 1314 ± 12 CE) during the austral winter, via wiggle-match dating using ^{14}C determination and tree-ring sequences of a carbonised log sampled within the m-thick pyroclastic density currents deposits of a proximal Kaharoa outcrop (Hogg et al., 2003; Lowe et al., 2013).

According to Nairn et al. (2001), the eruption occurred at least at seven vents located along an 8-km-long section of the Tarawera vent lineament at the two extremities of Mt Tarawera, from Green Lake Plug vent in the SW to Northeast crater to the NE (**Fig. 3.2**). The eruption was broadly divided into two main parts: (1) after vent opening explosions, the eruption progressed towards a series of subplinian to Plinian eruptive columns (Nairn et al., 2001; Sahetapy-Engel et al., 2014); (2) after a period of quiescence of uncertain time following the main explosive activity, the eruption continued with the extrusions of lava domes which formed the present-day summit of Mt Tarawera (Nairn et al., 2001) (**Fig. 3.2**).

During the Plinian-type explosive activity, several lapilli fall deposits were dispersed in proximal and medial localities into two main lobes to the SE and N from the Tarawera dome complex, with

deposition of ash beds over a wide SE-NW area, >100 km from the source (**Fig. 3.3**). The bi-lobated distribution of the fall deposits was characterised by Sahetapy-Engel et al. (2014), where individual multiple fall deposit lobes were identified in medial to distal areas. Nairn et al. (2001) suggested that the main explosive activity concluded with the coeval, initial extrusion of a lava dome named Crater Dome (estimated volume 3×10^7 m^3), which was covered by the later domes, named Ruawahia and Tarawera. The total fall deposit volume of the Plinian-type activity was more than doubled at 15.5 km^3 (7.34 km^3 recalculated DRE) by Sahetapy-Engel et al. (2014) compared to previous estimations at ~5 km^3 (Nairn, 2002), making the Kaharoa eruption one of the largest eruptions to have occurred in the post-25 ka eruptive period of the OVC (cf. Nairn, 2002). Individual fall deposit volumes were estimated at between ~0.1 to 2.55 km^3 (0.04 to 1.15 km^3 DRE) (Sahetapy-Engel et al., 2014). In addition, an estimated ~1 km^3 volume of deposits was emplaced during minor ash explosions and pyroclastic density current (PDC) producing events.

The vent location(s) from which the main explosive activity developed is not well constrained due to the lack of very proximal exposures within Mt Tarawera (Sahetapy-Engel et al., 2014). Based on proximal ballistic trajectories and tree trunk alignments, a vent was suggested at Crater Dome vent for the SE dispersed fall deposits (Nairn et al., 2001), while vent location(s) for the N dispersed fall deposits remains more uncertain with sources at either Wahanga (Nairn et al., 2001) or Ruawahia vents (Sahetapy-Engel et al., 2014) (**Fig. 3.2**).

During the dome-forming activity of the eruption, three lava domes (individual dome volume estimated at $2\text{-}4\times10^8$ m^3), Tarawera, Ruawahia and Wahanga, were emplaced from three different aligned vents onto previous pre-Kaharoa lavas (Nairn et al., 2001) (**Fig. 3.2**). Block-and-ash flows (BAFs) accompanied dome growth, and their deposits formed two main fans extending S and SE from Ruawahia and Tarawera Domes and NE from Wahanga Dome (white arrows on **Fig 3.2**), while a smaller BAF fan also extends to the NW from Ruawahia Dome to Lake Tarawera (Nairn et al., 2001; Hanenkamp, 2011). The extrusion of the three domes Tarawera, Ruawahia and Wahanga was shortly preceded by repeated minor explosions building a pyroclastic cone (RC beds in Nairn et al., 2001) around an adjacent vent (vent 5 in **Fig. 3.2**) to Ruawahia Dome vent. The cone was later partially buried by Ruawahia and Wahanga Domes. Ash deposits accumulated in medial sites atop the underlying lapilli deposits were associated with explosions during the pyroclast cone building and lava domes growth (unit M in Nairn et al., 2001; Sahetapy-Engel et al., 2014). A fifth small lava extrusion (estimated volume 5×10^4 m^3) named Green Lake Plug (*Poupoutunoa* in Keam, 2016) also occurred at an uncertain time during the eruption (Nairn et al., 2001) and is located at the SW end of the Kaharoa vent alignment, on the present-day east shore of Lake Rotomahana (vent 1 in **Fig. 3.2**). The total volume of the various lava domes is estimated at 0.84 km^3, with associated block-and-ash deposits volume at 0.16 km^3 (Nairn et al., 2001).

No written historical accounts are available for the Kaharoa eruption (Nairn et al. 2001). The eruption possibly coincides with the first Polynesian settlements in New Zealand (Hogg et al., 2003). Lowe et al. (2002) and Ashwell et al. (2015) report the existence of Māori oral traditions possibly referring to a pre-1886 CE eruption at Mt Tarawera. The total duration of the eruption is estimated at ~4 years based on geological evidence and assumed extrusions rates for the Kaharoa lava domes (Nairn et al., 2001). The duration of the initial main explosive activity only is instead estimated by Sahetapy-Engel et al. (2014) at a minimum of 9-12 days, based on accumulation rate of fall deposits, and up to 40 days according to Nairn et al. (2001).

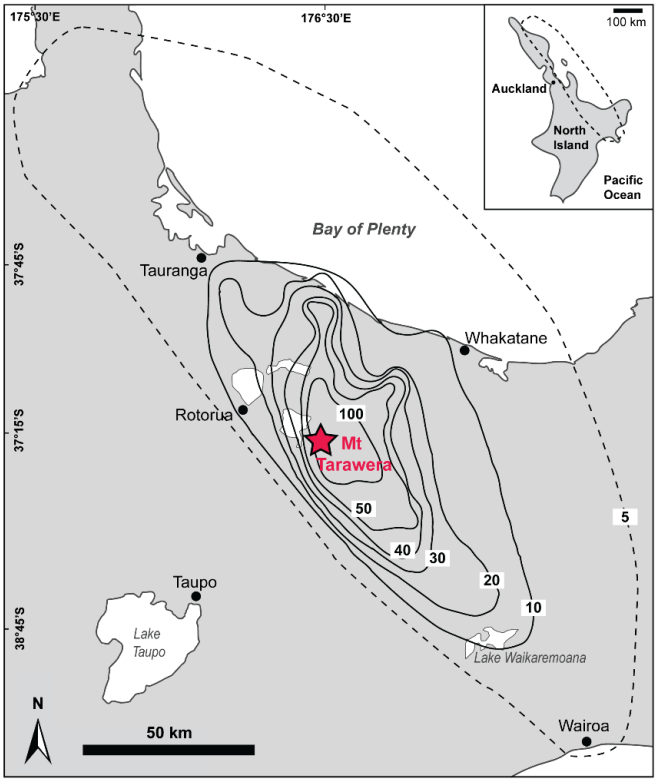

Figure 3.3 – Distribution of the Kaharoa fall deposits in the North Island of New Zealand showing isopach map of the deposits total thickness (in cm) redrawn after Sahetapy-Engel et al. (2014). Individual fall deposit isopach maps are reported in Sahetapy-Engel et al. (2014). Inset show the distribution of the visible distal limit of the Kaharoa deposit reported as ~1-3-cm isopach (Pullar and Birrell,1973).

Repeated basaltic dike injections in the rhyolitic magma body which fed the Kaharoa eruption were inferred as the trigger of the eruption based on the analysis of basaltic clasts scattered in the pyroclastic deposits and basaltic inclusions within the Kaharoa pumice clasts (Leonard et al., 2002). A series of hydrothermal explosions across the Waiotapu-Rotomahana geothermal fields, ~10-20 km SW of Mt Tarawera (e.g., at Lake Okaro), within the Tarawera vent lineament, were linked by Nairn et al. (2005) to the time of the Kaharoa eruption, suggesting the presence of an

active, ~23-km-long basaltic dike system at depth. Associated deposits, crater formation and dynamics of these hydrothermal explosions are also detailed in Montanaro et al. (2020) and in Gallagher er al. (2020).

Nairn et al. (2004) inferred that the eruption sequentially tapped a layered, sill-like magma body formed by two main high-silica, rhyolitic magma compositions (76-77 wt.% SiO_2), named T1 and T2. Erupted materials of T1 magma have slightly higher SiO_2 and K_2O, and lower CaO and Fe_2O_3 bulk compositions than those of T2 magma. The T1 magma was erupted during the main Plinian-type explosive activity and was measured for the deposits dispersed to the SE (Nairn et al., 2004; Sahetapy-Engel et al., 2014). A conduit-derived mingled composition of the two T1 and T2 rhyolitic magmas (named T1+2) was also erupted during the Plinian-type activity and is associated with deposits dispersed to the N (Nairn et al., 2004; Sahetapy-Engel et al., 2014). The T2 magma was erupted instead later as lava domes. All lava domes have T2 composition, excluding the small volume Green Lake Plug lava which has T1 composition (Nairn et al., 2004). Rhyodacite bulk compositions (69-72 wt% SiO_2) were also measured for scattered clasts within the pyroclastic succession and are inferred to derive from the mingling, with some degree of melt mixing, of the high-silica magma in the lower parts of the sill-like magma body with the residual melt from the intruding and crystalising basaltic magmas (Nairn et al., 2004).

3.3 Methods

3.3.1 General field terminology

The terms *proximal*, *medial*, and *distal* are used here to refer to outcrop localities (i) within 5 km from the vent, (ii) between 5 and 20 km from the vent and (iii) beyond 20 km from the vent, respectively. Most of the outcrops studied are found in medial areas (**Fig. 3.4**). In addition, the term *very proximal* is used to refer at areas within the Mt Tarawera domes and their lower slopes, typically up to 3 km from the vent. *Kaharoa deposit* identifies the whole succession of pyroclastic beds emplaced during the explosive phases of the eruption, while *deposit* or *bed* alone is used to refer to any body of volcaniclastic material within the studied outcrops, without any stratigraphic designation or genetic origin. *Pyroclastic deposit* indicates primary volcaniclastic deposit (*sensu* White and Houghton, 2006), whereas deposits formed by syn-eruptive or immediate post-eruptive resedimentation of pyroclastic deposits are referred here as *resedimented volcaniclastic deposit* (*sensu* McPhie et al., 1993).

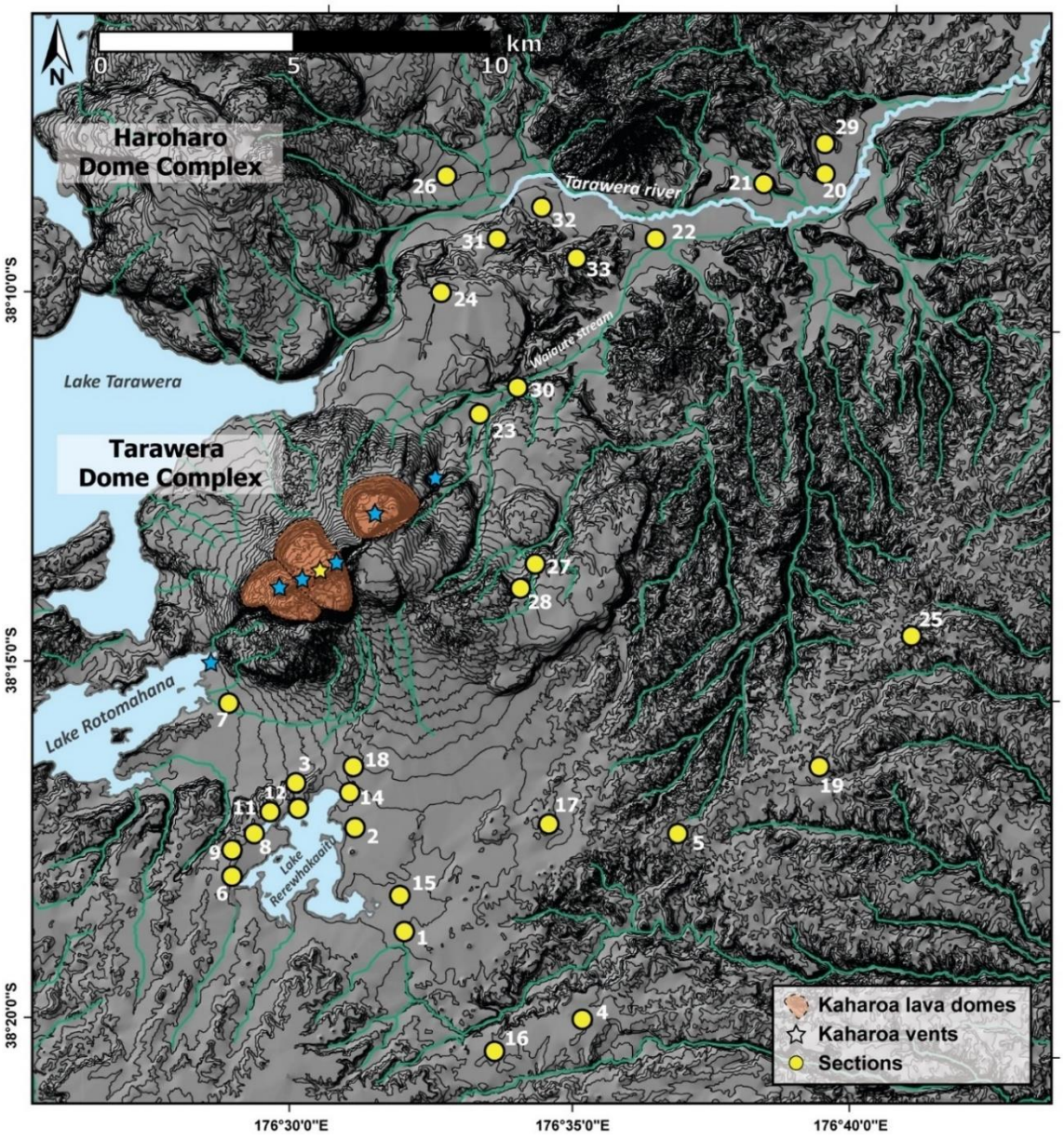

Figure 3.4 – Shaded relief map of the studied area with locations of the investigated stratigraphic sections. Stars indicate the position of the Kaharoa eruptive vents inferred by Nairn et al. (2001), with the yellow start marking the position of Ruawahia vent. The shaded relief map and drainage system of the studied area are obtained from Land Information New Zealand - LINZ, data component of the Topo50 and Topo250 map series (https://data.linz.govt.nz).

3.3.2 Field and interpretation approach

The pyroclastic sequence deposited during the Kaharoa eruption was investigated at 33 sites, mostly south, southeast, and northeast from Mt Tarawera, in proximal to medial areas (**Fig. 3.4**). Coordinates of each site are reported in **Appendix A**. Deposits in very proximal areas were not accessible during this work due to burial by later lava domes extrusion and by block-and-ash flows deposits, and to thick vegetation cover. Accumulation of thick scoria deposits within the

CE 1886 eruptive fissure cutting SW-NE Mt Tarawera (Sable et al., 2006) also prevent detailed observations of the underlying near-vent Kaharoa beds. Field observations were taken at natural and road cuts, quarries and at hand-dug sections. At each site, a detailed stratigraphic log of the pyroclastic succession was measured and described, recording the distinctive lithological and sedimentological characteristics of individual beds. Particular attention was drawn to the contacts between each pyroclastic bed to record evidence of time breaks in the eruptive activity.

As uncertainties remain in the timing and locations of vents active during the eruption, all source-to-outcrop distances reported in this work are measured from Mt Tarawera' summit at Ruawahia Dome (vent 4 in **Fig. 3.2**; vent in yellow in **Fig. 3.4**), if not otherwise specified. The Ruawahia vent, buried by the later dome, is located approximately in the middle of the 8-km-long Kaharoa vents alignment described in Nairn et al. (2001).

The Kaharoa deposit is subdivided in this study into units based on the lithological and sedimentological characteristics observed at the outcrop scale (mean deposit grain size and sorting, clast size grading, particle content, colour and sedimentary structure), as well as based on the units' spatial distribution and stratigraphic position in the pyroclastic succession. The units here identified are therefore intended as lithostratigraphic units (see Lucchi, 2013; Martí et al., 2018). A unit may consist of a single bed or a package of beds, which form a bed-assemblage distinguishable from the over- and underlying units. Abrupt changes in the sedimentary structure of the deposit, grain size characteristics and type and proportion of pyroclasts (componentry), commonly defines boundaries between units.

Units are related to individual depositional events during the eruption sequence (e.g., a fallout event), which are later interpreted in terms of the type of eruptive activity (e.g., a sustained subplinian activity or a transient Vulcanian explosion). Within the pyroclastic succession, units showing similar features are grouped into deposit types (e.g., Houghton et al., 2004; Pardo et al., 2011; Voloschina et al., 2020), suggesting similar transport-depositional mechanisms and eruptive processes at source, occurring at repeated times during the eruption. Vertical variations in sedimentary/lithological characteristics within a unit are related to temporal changes in eruptive and/or environmental conditions influencing the transport and deposition of the pyroclasts forming the unit.

Based on the type of contact between units and on other lines of evidence (e.g., interpreted delayed ash sedimentation from parental eruptive columns) suggesting short time breaks (hours to days) (e.g., Wilson, 2001) the eruption sequence is subdivided in discrete intra-eruption episodes (e.g., Fierstein and Hildreth, 1992). An episode is defined here as an interval of time during the eruption characterised by a relatively continuous eruptive activity bounded by short time breaks and exhibiting a consistent eruptive style. One or more units represent deposition during an intra-

eruption episode. Finally, based on the reconstructed stratigraphy and units' interpretations, the eruption sequence is later organised into eruptive phases, according to the dominant inferred eruptive style (e.g., Cioni et al., 2003; Arce et al., 2005; Saucedo et al., 2010; Torres-Orozco et al., 2018) and/or the identification of prolonged time breaks (a week up to a few months) in the eruptive activity (e.g., Mele et al., 2011; Bebbington and Jenkins, 2019).

3.3.3 Analytical methods

At key sites (sections 2, 18, 24 and 28, **Fig. 3.4**), samples were collected for laboratory analysis to quantify the main sedimentological (grain size distribution) and lithological (componentry of the deposits) features of the pyroclastic succession.

The grain size distribution (GSD) of individual beds was obtained by combining results of manual sieving, conducted on the particle fraction with intermediate diameters ≥63μm (+4 ϕ, with ϕ = $-\log_2$ of the particle diameter in mm) and of laser diffraction techniques for the fraction ≤63μm. Samples were dried for at least 24 h in an oven at T = 100° C and dry sieved down to 63μm, at 0.5ϕ intervals. The fraction coarser than 500μm (+1ϕ) was sieved by hand shaking to minimize artificial breakage of pumice clasts, while the fraction between 500 and 63 μm (+1ϕ and +4ϕ) was dry sieved using a mechanical shaker for a maximum of five minutes. The grain size distribution of the remaining fraction finer than 63μm was characterised down to 1 μm (+10ϕ) via laser diffraction particle analysis, using a laser diffraction particle size analyser, model Partica LA 950V2 of HORIBA, Ltd. at Massey University. The grain size distribution parameters median diameter and sorting coefficients (Mdϕ and σϕ, respectively) are calculated according to Inman (1952). Sorting classes for pyroclastic deposits adopted in this work are modified form Cas and Wright (1987) as follows: very well sorted, σϕ = 0–1; well sorted, σϕ = 1–2; moderately sorted, σϕ = 2–3; poorly sorted, σϕ = 3–4; very poorly sorted, σϕ >4. Sohn and Chough (1989) is referred for grain size nomenclatures. The complete dataset for results from grain size analyses is reported in **Appendix B**.

The relative abundance of clast components was estimated for different individual coarse-grained (coarse ash to lapilli-dominated) units. Typically, one bulk sample was collected when the unit showed no sharp vertical variations in grain size/componentry in the field, whereas two set of samples (one from the bottom and one from the upper parts of the unit) were collected when the unit showed either bedding or had thickness >50 cm. Samples for componentry analysis were collected at the two reference sections, to the north and south of Mt Tarawera (sections 2 and 24, **Fig. 3.4**). These two sites are located at approximately equivalent distance from the vent (6-7 km). Additional samples were collated at section 28 (**Fig. 3.4**) for unit L7S. Different types of

components were recognised and separated by hand picking under a binocular microscope from each grain size class down to ≥1mm or ≥500μm. Components were then counted and weighed, and results are reported in wt.%. For coarse grain sizes, typically ≥4-8 mm, the componentry analysis is performed in the entire particle population of each grain size class (as typically particle populations consisted of less than 250 particles), while for finer grain sizes componentry analysis is performed on aliquots of 300-600 particles (Houghton and Carey, 2015). With respect to the whole-sample weight, the percentage of the sample analysed for componentry was typically >90 wt.% for samples of lapilli-dominated deposits, and 50-80 wt.% for samples of coarse ash deposits. The complete dataset for results from componentry analyses is reported in **Appendix C**. Vesicularity of juvenile clasts reported in the text are descriptive visual estimations; vesicularity is described following Houghton and Wilson (1989). Additional data on bulk clast density and phenocryst content of some juvenile components are reported in this Chapter, however, they are detailed in Chapter 5.

3.4 Results

3.4.1 Deposit features and stratigraphy

3.4.1.1 General characteristics of the Kaharoa deposit

The Kaharoa deposits are mainly distributed into two directions, south and southeast (S sector) and north and northeast (N sector) from Mt Tarawera. To a lesser extent, proximal and medial deposits have been observed also to the east-southeast (sections 25, 27 and 28, **Fig 3.4**). To the southwest, the Kaharoa beds thin rapidly away from the vent and have not been observed west from Lake Tarawera. The proximal-to-medial Kaharoa deposit consists of alternating plane-parallel, cm- to- dm-thick, lapilli-dominated beds and cm-thick ash beds, mantling the paleo-topography, later interpreted as fall deposits. Within the studied area, the succession comprises also topographically controlled, cm- to- m-thick, pumice lapilli-bearing, ash deposits, later interpreted as pyroclastic density current (PDC) deposits.

One of the most notable features of the pyroclastic succession, especially in the S sector, is the repeated stacks of lapilli deposits separated by discrete ash beds (**Fig. 3.5**). These inter-lapilli ash beds are typically few-cm-thick up to medial sites, moderately sorted, with fine ash content (<63 μm) between ~40 and 65 wt.%. Where preserved, the fine ash beds helped in subdividing the

stratigraphy into units and to laterally correlate them among different outcrops. However, lateral correlations are not always straightforward, as the two-fold structure of the pyroclastic succession (lapilli and ash beds pairs) is not maintained at each site in medial areas. This is usually due to the narrower and limited dispersal of the fine ash beds compared to the areal distribution of the lapilli beds.

The lapilli beds within the pyroclastic succession are formed by moderately vesicular, phenocryst-poor, white to yellowish (with typically white interior), sub-angular to sub-rounded pumice clasts (hereafter white pumice) and by subordinate obsidian juvenile and lithic fragments. In addition, the lapilli beds dispersed to the east-southeast and north from Mt Tarawera also contain phenocryst-rich, greyish-coloured pumice clasts whit abundant basaltic inclusions (hereafter grey pumice). Rare basaltic clasts are found scattered throughout the pyroclastic succession.

The contacts between pyroclastic beds in the succession are typically plane-parallel and vary from sharp, marked by the abrupt changing in grain size, to gradual. Erosive surfaces within the pyroclastic sequences are infrequent. The most prominent erosive surface is observed in the S sector, consisting in dm-deep erosional gullies at one stratigraphic horizon (i.e., contact between A3 and L3 units; **Fig. 3.5**). Similar dm-thick erosive gullies are reported also by Sahetapy-Engel et al. (2014) higher in the stratigraphic sequence (i.e., contact between units L6 and A7). No major erosive unconformities or paleosols have been observed in the field at any outcrop, suggesting that the deposition of the different pyroclastic beds occurred without extensive pauses during the eruption (e.g., years long; Isaia et al., 2004).

In medial areas, the Kaharoa deposit is bracketed between a brown paleosol developed atop of the pumice deposits from the 232 ±10 CE Taupō Y eruption (Wilson and Walker, 1985; Lowe, 2016) and a thin black soil underlying the scoria deposits of the CE 1886 Tarawera eruption (Walker et al., 1984; Rowe et al., 2021). The Taupō pumices form either a discrete cm-thick, fine to medium lapilli layer or discontinuous pockets within the pre-Kaharoa paleosol. In the absence of marker beds, the diagnostic biotite phenocrysts content of the Kaharoa pumice clasts was used to distinguish the Kaharoa deposit from other older similar deposits from Mt Tarawera and nearby centres along the Haroharo vent lineament (Nairn et al., 2004; Lowe et al., 2008). At several outcrops in proximal and medial areas, the Kaharoa deposit directly overlies a distinct grey-to-purple-coloured layer consisting in weathered volcanic material, medium to fine ash in size, with scattered lapilli pumice clasts, named P-layer in this work (**Appendix A** for field photos). The contact of the P-layer with the Kaharoa deposit varies from plane-parallel to undulated and is marked by a laterally discontinuous thin black peat horizon (typically few-mm-thick). The P-layer has always been found in the southeast and east outcrops, having a variable thickness (3 up to 20 cm). At northern localities, the P-layer is not well preserved and when observed it fades rapidly

into the underlying brown paleosol. Lowe et al. (2012) and Lowe (2016) refer to this layer as a buried podzol soil with exposed leached E and Bh horizons, occurring on the 232 CE Taupō deposits.

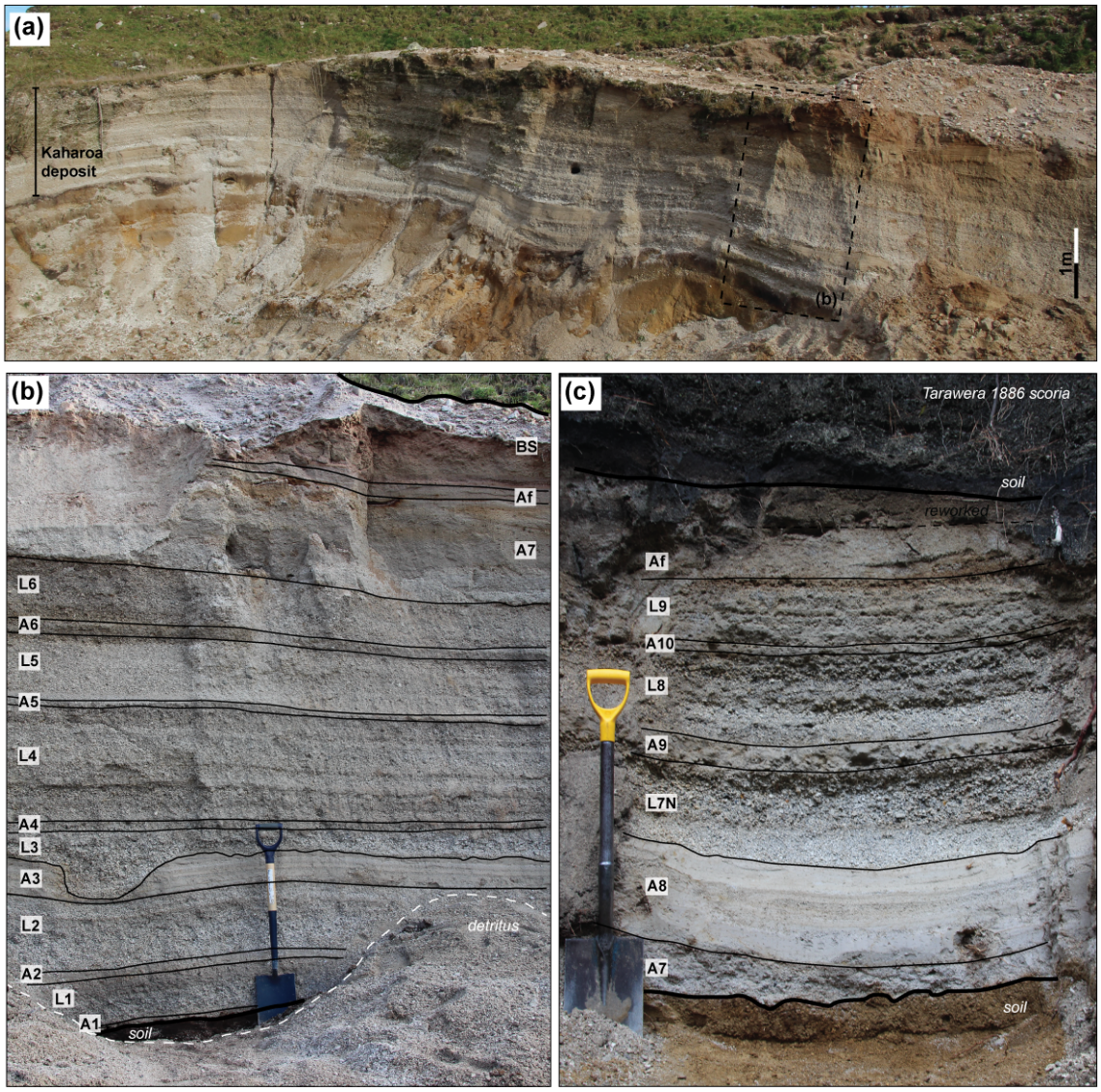

Figure 3.5 – Field photos of the studied pyroclastic succession. (a) Panoramic view of the Kaharoa deposit at reference section 2 (**Fig. 3.4**), at 6.7 km south from the vent. (b) Zoom on section 2. (c) Reference section 24 (**Fig. 3.4**), at 7.4 km north from the vent. Subdivision of the deposit in units (A1 to BS) is indicated in (b) and (c) (spade is 1 m long in both sections). Note erosional gully at the contact between units A3 and L3.

Topographically controlled, lava block-rich and ash-supported deposits from m- up to tens of meters- thick, overlie the lapilli and ash pyroclastic succession both south (at sections 18, 14 and 2) and northeast (at sections 23 and 30 along the Waiaute stream valley) (**Fig. 3.4**). These deposits are interpreted as block-and-ash flows (BAF) occurring during the extrusion of the Kaharoa lava

domes later in the eruption sequence (Nairn et al., 2001; Hanenkamp, 2011). Characteristics of BAF deposits have not been studied in this work, however, brief descriptions are given in **Section 3.4.1.2**. Their deposits are organised into units BS and BN in the proposed stratigraphic scheme and are used for stratigraphic control and lateral correlations. To the NE, beyond the BAF fan, the pyroclastic succession is also overlain by fine-grained, massive to diffusively stratified deposits confined within the Tarawera river floodplains suggesting re-sedimentation processes of the Kaharoa deposit in this area. Two main types of resedimented volcaniclastic deposits can be distinguished and are named RV1 and RV2 (**Section 3.4.1.3** for descriptions).

Although distal deposits were not the focus of our study, it is noteworthy to highlight that Kaharoa fine ash deposition occurred also >100 km far from the volcanic centre, covering a widespread NW-SE area in the northern part of the North Island, approximately from Whangerei (~330 km NW) to Lake Waikaremoana (~80 km SE) (Pullar and Birrell, 1973; Pullar et al., 1977, Sahetapy-Engel et al., 2014) (**Fig. 3.2**). Kaharoa ash deposits have also been observed in marine sediments cores in the Bay of Plenty, ~70 km NE of Mt Tarawera (Kohn and Glasby, 1978). The distal ash deposition records the repeated injection of fine ash into the atmosphere and its distribution by the prevailing winds NW, NE and SE from Mt Tarawera (Sahetapy-Engel et al., 2014).

3.4.1.2 Kaharoa units and deposit types

Giving the repeated alternation of lapilli and ash beds comprising the Kaharoa deposit within the studied area in proximal to medial sites, the pyroclastic succession is subdivided into lapilli and ash units. Similar deposit subdivisions have been used for pyroclastic successions punctuated by numerous beds of contrasting grain sizes at other volcanoes (e.g., Cole et al., 1995, 1999; Cioni et al., 2003; Sulpizio et al., 2005; Mele et al., 2011). Ten lapilli units (unit designation in upward succession: L1 to L9, with L7S and L7N) and twelve ash units (unit designation in upward succession: A1 to Af) are identified for the Kaharoa deposit (**Table 3.1**).

In the S sector the pyroclastic succession consists of units A1, L1, A2, L2, A3, L3, A4, L4, A5, L5, A6, L6, A7, L7S, A11 and Af, with most of the units (excluding L7S) well exposed at reference section 2 (**Fig.3.5**), 6.7 km south form the vent (**Fig. 3.4**). In the N sector, the pyroclastic succession consists instead of units A7, A8, L7N, A9, L8, A10, L9 and Af. The most proximal and complete section is exposed at 7.4 km NE from the vent (section 24, **Fig. 3.4**), and it is used here as a reference section for the northern deposits (**Fig. 3.5**). This subdivision provides the Kaharoa deposit with a new unit stratigraphy nomenclature from the one adopted in Nairn et al. (2001) and Sahetapy-Engel et al. (2014). **Table 3.1** shows tentative correlations between the units proposed in this work and those proposed in the previous studies. In this section the results are presented following the new proposed unit nomenclature and stratigraphic subdivision, while a

comparison and discussion on the major stratigraphic changes from past studies are presented in **Section 3.6.1**.

The Kaharoa units in proximal to medial sites comprise a range of different sedimentary structures and deposit grain size characteristics (**Fig. 3.6**). Based on the observed deposit variability, the units identified in the field can be grouped into seven deposit types (**Table 3.2** for deposit type descriptions). Units of deposit types 1, 2 and 4 formed the majority of the Kaharoa deposit and are repeated throughout the studied pyroclastic succession, while those of type 3, 5, 6 and 7 occur at few or individual stratigraphic positions (**Table 3.2**). Descriptions of individual pyroclastic units in stratigraphic order are provided in the following and are summarised in **Figure 3.7**. Grain size and componentry characteristics are described based on field observations, unless specified otherwise.

Table 3.1 – Tentative correlations between the stratigraphic units of the Kaharoa deposit identified in this study and those proposed in previous works. See **Section 3.6.1** for discussions on the stratigraphic changes adopted in this work compared to previous stratigraphic reconstructions.

This study	**Nairn et al. (2001) and Sahetapy-Engel et al. (2014)**
BS and BN	N-BAFD
Af	M
A11	-
L9	L
A10	K
L8	
A9	I + J
L7N	
L7S	H_{SE}
A8	Cpdc
A7	Hpdc
L6	G
A6	F
L5	
A5	E
L4	
A4	D
L3	
A3	C
L2	B
A2	A1+A
L1	
A1	

Table 3.2 – Summary of the distinctive deposit characteristics of the seven recognised deposit types for the units in the studied pyroclastic succession. Note that unit A3 is placed in both deposit types 3 and 4 as the A3 stratigraphic interval comprises the vertical alternation of beds with characteristics of deposit types 3 and 4.

Deposit type	Unit	Distinctive features
1 – massive lapilli deposit	L1 L2 L3 L7S L7N	Massive, well sorted deposits of fine to coarse lapilli. Vertical grain size changes within the lapilli size fraction or progressive clast-size grading are observed withing these deposits. Units' thickness varies from up to m-thick in proximal sites to dm-to-cm-thick with increasing distance from the vent, along respective main dispersal axes. Units show mantle bedding and clast supported deposit textures.
2 – stratified lapilli deposit	L4 L5 L6 L8 L9	Stratified deposits alternating well sorted medium lapilli beds with poorly sorted fine lapilli to medium ash beds. The unit stratification, expressed by sharp, repeated grain size oscillation, is well preserved in proximal sites, and fades away with increasing distance from the vent. Units' thickness varies from up to m-thick in proximal sites to dm-to-cm-thick with increasing distance from the vent, along respective main dispersal axes. Units show mantle bedding and clast supported deposit textures.
3 – massive, coarse ash deposit	A1 A3 Af	Massive to weakly stratified and well sorted ash deposits of coarse ash, up to fine lapilli in proximal sites. Units show mantle bedding and form distinctive cm to dm thick ash layers within the pyroclastic succession in medial sites.
4 – massive, fine ash deposit	A2 A3 A5 A6 A9	Massive, medium to fine ash beds, with fine ash content between 40 to 65 wt.%. These units vary from moderately to well sorted and have typically a poorly sorted base. They cap both massive and stratified lapilli units at different stratigraphic positions in the pyroclastic succession. Units' thickness is <10 cm in proximal sites and decrease to few-cm in medial area, where preserved. Units' dispersal is overall consistent with those of underlying lapilli units but show narrower distribution.
5 – laterally discontinuous, ash deposit	A4 A10 A11	Poorly to moderately sorted, massive medium ash deposits with scattered lapilli clasts, few cm in thickness. These deposits have a very limited area of distribution, <5 or 10 km from the vent, and typically pinch out laterally. These units are interbedded between lapilli units (A4 and A10) or underlying coarse ash units (A11).
6 – lapilli-bearing ash deposit	A7	Massive to cross-stratified, m-to-dm thick, ash-dominated deposits. The deposit alternates in proximal sites pumice lapilli-bearing, matrix-supported beds with internally cross-laminated ash beds. The unit varies abruptly in thickness from 1-2 m in proximal sites to cm in medial areas and contains charcoal fragments of variable size.
7 – variably consolidated ash deposit	A8	Poorly to moderately sorted, massive to cross-stratified, variably consolidated, ash deposits. The unit alternates beds of moderately consolidated ash with very high fine ash content (up to 80 wt%) and unconsolidated beds of coarse ash. The entire unit displays discontinuous thickness variation at the outcrop scale, and overall decreases from 30- to few-cm- thick away from the vent in medial area.

Unit A1 (deposit type 3) – At several localities in the S sector, the base of the Kaharoa deposit consists of a well sorted, friable, massive bed of coarse ash to fine lapilli. Its thickness is typically of few cm to dm (maximum observed thickness is 14 cm at section 17, **Fig. 3.4; Fig. 3.6h** and **j**). Unit A1 mantles the pre-eruption ground surface with variable contact geometries, from plane-parallel to undulated. The unit is very rich in white pumiceous ash clasts, which make up to ~90 wt.% of the unit (e.g., at section 2, **Fig. 3.4**). Unit A1 displays a SE dispersal (**Fig. 3.8**) and it can be recognized up to 13 km ESE from the vent at section 19 as a distinct bed of coarse ash. South from Mt. Tarawera in medial area, A1 is preserved as trace of medium to coarse ash at the base of unit L1.

Unit L1 (deposit type 1) – Unit L1 is the first lapilli unit found in the S sector, sitting directly atop of unit A1 or the P-layer beyond the A1 dispersal area. The contact between units A1 and L1 is typically gradual in medial sites. Unit L1 consists in a well-sorted, non-graded to locally reversely graded deposits of fine to medium lapilli (**Fig. 3.6j**), composed by white pumices and abundant grey to red lava lithic fragments (>15 wt.%). Towards the top, the unit passes gradually into a massive, poorly sorted bed of lapilli mixed with medium and fine ash (**Fig. 3.6j**). Unit L1 is dispersed SE from Mt Tarawera (**Fig. 3.9**) and is characterised by a rapid thickness decrease towards the east (from 22 cm at section 2 to 9 cm at section 17, **Fig. 3.4**), where the unit passes to a massive layer of fine lapilli, gradually merging into L2 at sections 5 and 19 (**Fig. 3.4**).

Unit A2 (deposit type 4) – It consists of a single massive, moderately to well sorted fine ash bed, 4-cm-thick at section 2 (**Fig. 3.5b; Fig. 3.6j**). Unit A2 has a narrow dispersal directed to the south from the vent (**Fig. 3.8**) and persists as a discrete layer, 0.5-cm-thick, up to 13 km from the source (e.g., section 16, **Fig. 3.4**). Within its narrow dispersal area, A3 always caps the underlying unit L1. The contact is generally gradual due to the mixed lapilli and ash layer forming the top part of L1. The contact with the overlain unit L2 is instead sharp due to the marked contrasting grain size of the two units and is plane-parallel. Only locally (e.g., section 14, **Fig. 3.4)** a mm-thick and faintly laminated layer, laterally discontinuous at the outcrop scale, of fine to coarse ash occurs at the top of unit A2.

Unit L2 (deposit type 1) – L2 consists of two beds up to 10 km from the vent. The bottom one is a well sorted coarse to medium lapilli bed characterised usually by symmetric, reverse-to-normal, grading. The upper bed is normally graded and consists of fine lapilli to very coarse ash. The two beds are separated by a mm-thick, fine-enriched horizon in proximal sites. Beyond 10

km from the vent the unit occurs as a single, massive lapilli bed. The unit has a SE dispersal (**Fig. 3.9**) and decrease in thickness from ~40 to 20 cm from proximal to medial sites (e.g., from section 18 to section 4, **Fig. 3.4**). In medial sites to the ESE where unit A2 is not preserved, unit L1 and L2 tend to merge into a massive deposit of fine to medium lapilli where no clear unit boundary is evident. Unit L2 is composed of white pumices and subordinate grey to red lava lithic fragments (8 wt.%). The contact with the overlying unit A3 is sharp.

Unit A3 (deposit type 3 and 4) – It consists of a markedly distinguishable ash deposit in the pyroclastic succession, south and southeast from Mt Tarawera (**Fig. 3.8**), formed by beds of both types 3 and 4 deposits (**Table 3.2**). The unit is best exposed in medial sites up to 10 km south from the vent (e.g., sections 14, 2, 15, 1, **Fig. 3.4**) where it consists of four to six, cm-thick, ash beds alternating fine and coarse ash. Both fine and coarse ash beds are massive and from moderately to well sorted. The coarse ash beds of unit A3 are typically rich in vesicular juvenile clasts, with a relatively low concentration of lithic fragments (~5 wt.%). At a proximal site (section 18) the unit consists of a 20-cm-thick, weakly stratified coarse ash and fine lapilli beds, bracketed between fine ash beds. Beyond 10 km south form the vent (e.g., sections 16 and 4, **Fig. 3.4**) the unit consist of a massive to faintly stratified, few-cm-thick, deposit of fine to medium ash resulting perhaps from the amalgamation of different coarse and fine ash beds. From proximal to medial sites (from sections 18 to 16, **Fig. 3.4**), south from the vent, the top few cm of unit A3 consist of a dark coloured, fine to medium ash layer (contrasting with the light grey colour of the underlying fine ash beds), laterally discontinuous at the outcrop scale (**Fig. 3.6f**). The bed is poorly sorted and characterised by plane-parallel and low-angle cross-laminations. At section 18, few laminae are notably oxidized (**Fig. 3.6a**). The contact with the overlain unit L3 varies from sharp to erosive. Erosive features consist of (i) cm-sized scours at the top of A3 and in (ii) dm-sized gullies cutting across the whole A3 deposit (**Fig. 3.5b**), filled by coarse lapilli of overlain unit L3 (**Fig. 3.6f**). At section 2 the bottom part of the dm-sized gullies is often filled by dark and dense resedimented volcaniclastic materials, coarse ash in size.

Unit L3 (deposit type 1) – Unit L3 is a well sorted, massive, medium to coarse lapilli bed. The unit is characterised by a southeast dispersal (**Fig. 3.9**) and is the coarsest lapilli unit of the Kaharoa deposit at these localities. At the proximal section 18 (**Fig. 3.4**), unit L3 is 35-cm-thick (**Fig. 3.6a**). In medial sites to the ESE and beyond the distribution of unit A4, units L3 and L4 tend to progressively merge into a single massive medium lapilli deposit. Unit L3 is composed by white pumices and abundant obsidian juvenile fragments (14 wt.%). The unit is notable for the

large amount of angular obsidian fragments observed in the field in the coarser grain size fractions of the bed.

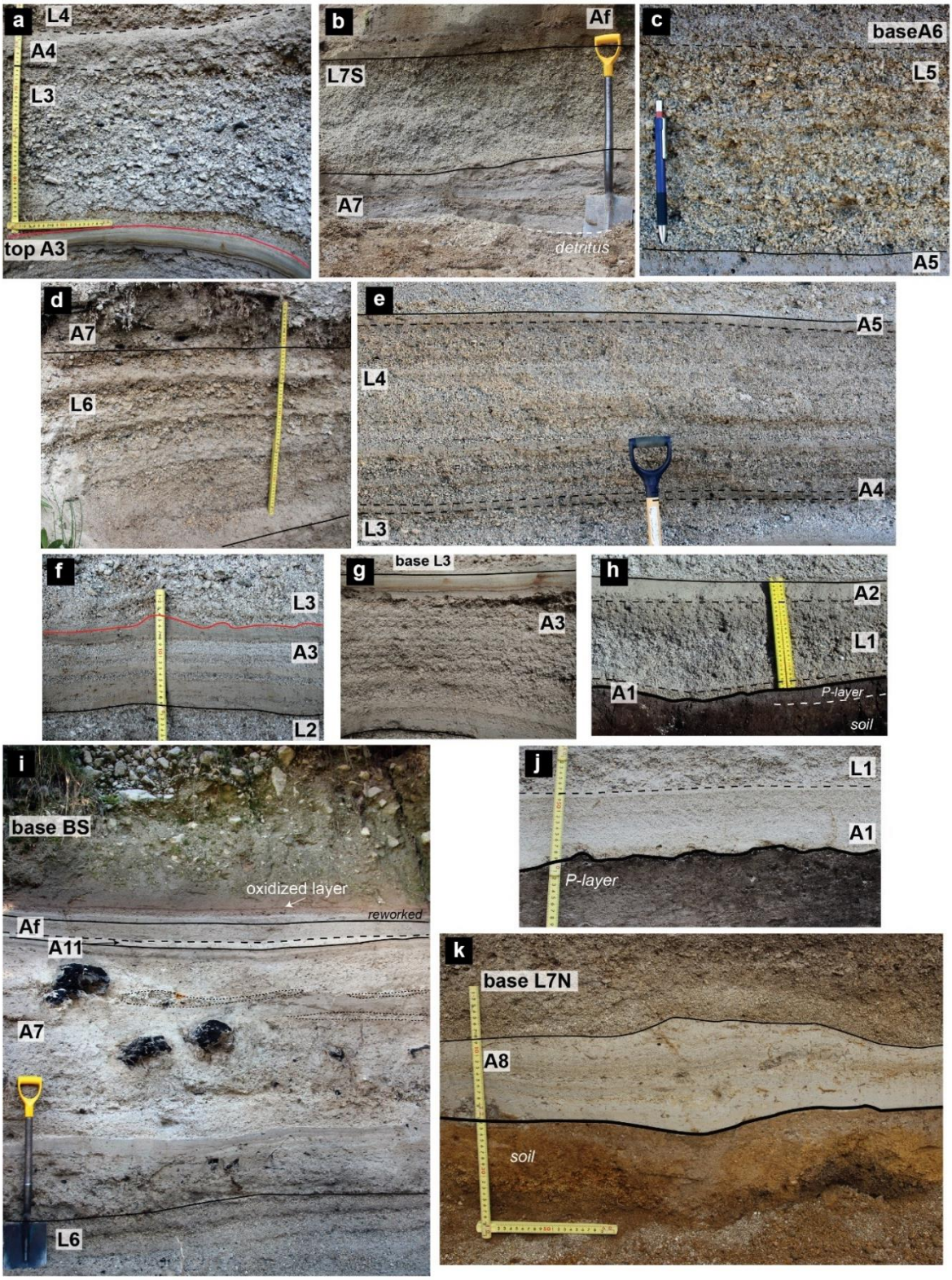

Figure 3.6 – ***caption in next page***.

Figure 3.6 – (***figure in previous page)*** Representative field photos showing the different deposit features of the Kaharoa units at key sections in proximal and medial sites (refer to **Fig. 3.4** for location of outcrops). *Solid red lines* indicate sharp and erosive units contacts; *solid black lines* indicate sharp unit contacts with non to minor erosion/reworking; *dashed black lines* indicate gradual unit contacts; *bold, black lines* indicate the basal contact of the Kaharoa deposit. (**a**) Massive lapilli unit L3 at S18 (*S=stratigraphic section*) south form the vent, overlain by the laterally discontinuous ash unit A4. Note the characteristic features of the top bed of unit A3 in proximal sites having plane-parallel- to cross-laminations (see also **f** and **g**) with few laminae being oxidized. (**b**) Massive lapilli unit L7S at S28, east form the vent. (**c**) Weakly stratified lapilli unit L5 at S1, south from the vent. (**d**) Stratified lapilli unit L6 at S18, south from the vent. The poorly sorted ash beds within L6 deposit have a limited distribution and rapidly fade away from the vent. (**e**) Stratified lapilli unit L4 at S2, south from the vent. (**f**) Deposit features of unit A3 at S2, with alternation of massive, fine to coarse, ash beds. Note the cm-size scours on top of A3 (see also dm-size erosional gullies at A3-L3 contact in **Fig. 3.5**). (**g**) Characteristics of A3 at S18. (**h**) Massive lapilli unit L1 at S2 south from the vent and gradual contact with overlaying massive fine ash unit A2. Note the increase in fine ash content on the top part of unit L1 towards the contact with A2. Basal contact of the pyroclastic succession and underlying P-layer and soil are also shown. (**i**) Top ~3 m of S18, south from the vent with proximal facies of unit A7 lapilli-bearing ash deposits. Note the alternation between massive, dm-thick lapilli-bearing ash beds with dispersed carbonised tree logs and the massive to cross-laminated medium-to-fine, ash beds. Lapilli lenses within A7 are indicated with thin dotted black lines. Unit A7 is overlain by the laterally discontinuous unit A11 and the coarse ash unit Af. The base of the BAF deposit of unit BS is exposed at this section. BS is separated from the underlying units by a thin red, oxidized ash layer. (**j**) Massive coarse ash unit A1 at the base of the Kaharoa deposit at S17. (**k**) Zoom on the variably consolidated unit A8 at S26, north from the vent, showing distinctive very fine ash beds (bottom and top) and cross-stratified, coarser ash beds (middle). Additional field photos are reported in **Appendix A**.

Unit A4 (deposit type 5) – Unit A4 consists of a single, poorly sorted medium ash bed with scattered lapilli clasts (**Fig. 3.6a**). The unit has a limited dispersal area (<10 km from the vent) to the south (**Fig. 3.8**) and was observed at a few sites (sections 18, 14, 2, 9 and 3, **Fig. 3.4**), interbedded between units L3 and L4. Unit A4 is typically laterally discontinuous and varies in thickness from 7 to 2 cm.

Unit L4 (deposit type 2) – L4 is a stratified deposit dispersed to the SE (**Fig. 3.9**), formed by alternating dm- to cm-thick lapilli beds and cm-thick ash-dominated beds (**Fig. 3.6e**). In sites where the unit's stratification is well preserved (e.g., sections 18, 14, 2, 15 and 1, **Fig. 3.4**), the unit can be subdivided into two parts. The lower part is characterised by sharp vertical grain size fluctuations, alternating two moderately sorted medium to coarse lapilli beds and two poorly sorted ash beds. The upper part of the unit comprises one to two well sorted, medium to fine lapilli beds, massive to normally graded, capped by fine enriched thin layers, overlain by a poorly sorted ash bed and a moderately sorted lapilli bed on top. With increasing distance from the vent, the unit passes from ~80cm- to 25-cm-thick (e.g., section 18 to 4, **Fig. 3.4**), and from a stratified to a faintly stratified or massive deposit. L4 is composed by white pumice clasts and grey to red lava lithic fragments. Within the unit are also dispersed rounded greenish, hydrothermally altered,

lithic fragments. The surface of white pumice clasts in unit L4 and in later lapilli unit up to unit L9, tend to have a more yellowish tone compared to white pumice clasts in earlier lapilli units.

Unit A5 (deposit type 4) – A5 consists of a single moderately to well sorted, cm-thick, fine ash bed. At few locations, the base of the unit is characterised by poor sorting resulting from the occurrence of coarse ash clasts at the contact with the underlying unit L4. The unit shows a southeast dispersal (**Fig. 3.8**).

Unit L5 (deposit type 2) – The unit is dispersed to the SE from the vent (**Fig. 3.9**) and is one of the coarsest units in the S sector. South from the vent (sections 18, 14 and 2, **Fig. 3.4**) L5 is stratified and comprises two reverse graded beds of medium to coarse lapilli, underlying a massive well sorted coarse lapilli bed, notably lithic-rich at few outcrops (e.g., section 17 and 5, **Fig. 3.4**). With increasing distance from the vent to the south (e.g., section 15, 9 and 16, **Fig. 3.4**) and east-southeast (e.g., section 5 and 19, **Fig. 3.4**) from the vent, L5 progressively transitions from weakly stratified into a massive deposit. L5 is composed by white pumice clasts and, along with unit L6, contains the largest proportion of lithic fragments observed in the S sector deposits (~20 wt.%), characterised by grey to red lava lithic fragments and minor rounded greenish hydrothermally altered clasts.

Unit A6 (deposit type 4) – This unit consists of a massive, poorly sorted fine ash to coarse ash bottom bed capped by a massive, moderately to well sorted fine ash bed. The unit is dispersed SE, displaying a similar distribution as A5 (**Fig. 3.8**). Unit A6 underlies unit L5 and has a maximum observed thickness of 12 cm at section 17 (**Fig. 3.4**). Beyond 10 km to the south, A6 grades into a single well sorted bed of fine ash in sharp contact with units L5 and L6. In medial position in the southeast (e.g., section 5, **Fig. 3.4**), the unit occurs as a massive poorly sorted bed of fine ash and scattered lapilli, interbedded between unit L5 and L7S (section 5 is beyond the dispersal area of unit L6).

Unit L6 (deposit type 2) – L6 is a stratified unit comprising moderately to well-sorted, fine to medium lapilli beds, from massive to reverse graded, which alternates with poorly sorted ash beds. The ash beds are preserved only at proximal sites (e.g., section 18, **Fig. 3.4**) and the unit becomes faintly stratified to massive with increasing distance from the vent in medial area. The lapilli beds within unit L6 have a narrower distribution compared to the other lapilli units and are dispersed to the south (**Fig. 3.9**), with no evidence of deposition to the east-southeast. The unit

thins from ~30 cm at ~6.5 km from the vent (e.g., section 2) down to 7-cm-thick at 13 km (e.g., section 16). The unit is composed by white pumices and abundant lithic fragments (~20 wt.%). The lithic material is characterised by grey to red lava fragments and minor rounded greenish, hydrothermally altered clasts.

Unit A7 (deposit type 6) – The unit is formed by a succession of massive to cross-stratified beds and is best exposed at sections 18 and 2, within 5 to 6.5 km south from the vent (**Fig. 3.4**). The unit displays a very rapid variation in deposit thickness and internal structures over short distances (within 0.1 to 1 km). The unit passes from 200-170 cm to 40-60 cm thick from sections 18 (**Fig. 3.6i**) to 2 (**Fig. 3.5b**) (**Fig. 3.8**). At section 18 (**Fig. 3.6i**), the unit consists of: (i) dm-thick beds bearing fine to medium lapilli in a matrix of medium ash, (ii) ash beds, and (iii) lenses of coarse lapilli. (i) The matrix supported lapilli beds are massive and moderately sorted, with dispersed large, carbonised logs and cm-size charcoal fragments (**Fig. 3.6i**). These beds are capped by (ii) massive to cross-laminated ash beds, formed by moderately to poorly sorted medium to fine ash. (iii) Open-framework lapilli lenses occur within the matrix supported lapilli bed and rapidly pinch out at the outcrop scale. In medial sites the unit passes from a massive to cross-stratified deposit of medium to coarse ash, with scattered lapilli (e.g., section 2 and 14, **Fig. 3.4**) to a faintly stratified or massive ash deposit with increasing distance from the vent (e.g., section 15, 1, 16 and 4 **Fig. 3.4**). The unit is formed by white pumice clasts, subordinate grey to red lava lithic fragments and abundant obsidian juvenile fragments (17-27 wt.%). The beds associated with unit A7 are distinctive in the field for the large amount of angular obsidian fragments in the coarser grain size (see also unit L3). Scattered grey pumice clats occur within some of the lapilli lenses.

Unit A8 (deposit type 7) – Beyond ~8 km from the vent to the N and NE, the base of the Kaharoa deposit consists of a package of cm-to-dm-thick ash beds forming unit A8 (**Fig. 3.5c; Fig. 3.6k**). The unit displays discontinuous thickness variations at the outcrop scale up to ~10 km from the vent (e.g., section 26), whereas it shows constant deposit thickness at stratigraphic sections located at greater distances (e.g., section 29). The unit typically comprises three beds (**Fig. 3.7**): A8a, A8b and A8c. A8a is a moderately to well sorted, massive fine ash bed (fine ash up to 80 wt.%) moderately consolidated (i.e., unlithified, however forming a compact deposit of cohesive ash, e.g., Austin-Erickson et al., 2008; Van Eaton and Wilson, 2013), with rare soft ash aggregates (mm in size). A8a is in sharp contact with the underlying unit A7 at section 24 (**Fig. 3.4**), while directly overlays a brown paleosol at other localities (e.g., sections 26, 22, 21, 20 and 29, **Fig. 3.4**). A8b is characterised by the alteration of two to three unconsolidated poorly sorted coarse ash to fine lapilli beds capped by thin, medium to fine ash beds, varying from plane-parallel to

cross-stratified. The beds in A8b are typically laterally discontinuous, forming lenses that pinch out at the outcrop scale. A8c shows similar characteristics to A8a, been formed by moderately to well sorted massive fine ash with scattered coarse ash; A8c is however a slightly consolidated deposit, being less compact than A8a. Unit A8 preserved this three-fold internal structure up to 10 km to the N and NE (e.g., section 26 and 32, **Fig. 3.4**). To the NE, beyond 10 km from the vent, the unit thins away more rapidly and consist alternatively of A8a and A8b beds or only the A8a bed.

Units L7S and L7N (deposit type 1) – Units L7S and L7N are two lapilli units sharing very similar deposit features and componentry characteristics. Both units are characterised by the coexistence of white and grey pumice clasts (grey pumice up to 30 wt.%), with scarce obsidian juvenile and lithic fragments. Unit L7S is dispersed to the east-southeast (e.g., section 27, 28, 17, 5, 19 and 25, **Fig. 3.4**), marking a change in the distribution compared to other earlier lapilli units in the S sector, typically dispersed towards the south and southeast (**Fig. 3.9**). The unit consists of a massive, well sorted bed of medium to coarse lapilli (**Fig. 3.6b**), and is best exposed at section 28, ~5 km east from the vent, where is ~60-cm-thick. L7S is absent at reference section 2. Unit L7N is dispersed north from the vent (e.g., section 24, 26, S31, 32 and 33) (**Fig. 3.9**) and is best exposed at the reference section 24 where it overlays in sharp contact unit A8. Unit L7N consists of a bottom bed of massive, well sorted fine to medium lapilli (10-cm-thick at section 24) and by a coarser top bed massive to reverse graded of medium to coarse lapilli (18-cm-thick at section 24) (**Fig. 3.5c**). At section 24, the two lapilli beds of unit L7N are separated by a thin, few-mm-thick, fine-enriched horizon within the lapilli clasts, which thicken into a 5-cm-thick layer of poorly sorted fine lapilli and fine ash at section 26. To the northeast in medial sites unit L7N decreases to a 5-cm-thick coarse ash to fine lapilli massive bed (section 22) and is found as trace underlying unit L8 beyond 15 km form the vent (e.g., section 20, 21 and 29).

Unit A9 (deposit type 4) – The unit consists of a single moderately to well sorted fine ash bed in sharp contact with overlying unit L8. The base of the unit is typically poorly sorted due to sparse lapilli size clasts. The unit is dispersed mainly to the N (**Fig. 3.8**), passing from 10- to 6-cm-thick at section 24 and 26, respectively.

Unit L8 (deposit type 2) – L8 is a stratified unit formed by alternating two moderately sorted coarse ash to fine lapilli beds and two well sorted medium lapilli beds (**Fig. 3.5c**). The unit is dispersed north from the vent and is 30-cm-thick at section 24 (**Fig. 3.9**). With increasing distance from the source, 10 km north from the vent (e.g., section 26), the unit passes into a faintly stratified

25-cm-thick deposit. To the northeast, beyond 10 km from the vent, the beds progressively merge into a single deposit of massive, moderately to well sorted medium lapilli. Unit L8 is formed by white pumices and is characterised by a significant decrease in the abundance of grey pumices compared to the earlier lapilli unit L7N. Distinctive feature of the unit is however the typically high content in grey to red lava lithic fragments (up to ~20 wt.%).

Unit A10 (deposit type 5) – Unit A10 is dispersed north and northeast (**Fig. 3.8**) and is interbedded between unit L8 and L9. The unit has similar deposit characteristics to those observed for unit A4 and consists of a few cm-thick, poorly sorted, fine to medium ash bed with scattered fine lapilli. Beyond section 24, the unit thins rapidly away from the vent towards northeast sites, where A10 is preserved as a discontinuous thin layer, 0.5-cm-thick, of fine to medium ash draping the lapilli clasts of the underlying unit L8 (e.g., sections 33 and 22, **Fig. 3.4**). To the north at section 26, with increasing distance from the vent, the unit has a better sorting and consists predominately of fine ash.

Unit L9 (deposit type 2) – L9 comprises a stratified fine lapilli deposit, 25-cm-thick at the reference section 24, finer-grained compared to other lapilli units in the pyroclastic succession (**Fig. 3.5c**). L9 is formed by moderately sorted fine lapilli beds with scattered medium lapilli, intercalated with moderately to poorly sorted coarse ash beds. The top of the unit consists of a coarser-grained bed, few-cm-thick, of well sorted fine to medium lapilli. The unit slowly thins to 20-cm-thick at section 26, north from Mt Tarawera (**Fig. 3.9**) and preserves overall the same structure observed at section 24, with individual beds gaining a better sorting. To the northeast, beyond 10 km from the vent at outcrops along the Tarawera river valley (sections 22, 21 and 29, **Fig. 3.4**). within the stratigraphic interval of unit L9, the succession increases in thickness up to ~50 cm and consists of a diffusely stratified deposit, dominantly coarse ash clasts in size (see **Section 3.5.2**). The unit is formed by white pumices, minor grey pumices and abundant grey to red lava lithic fragments (15 wt.%). L9 also contains abundant loose crystals.

Unit A11 (deposit type 5) – The unit consists of a characteristic light-grey coloured ash bed, contrasting with the usually darker grey colour of the medium to fine ash bed in the succession (**Fig. 3.6i**). It is ~5-cm-thick, preserved solely at section 18 directly south from the vent (**Fig 3.4**). The bed is massive, poorly to moderately sorted of fine to medium ash and pinches out laterally. The unit is bracketed between A7 at the bottom and Af deposits on top, with the contact with the underlying unit A7 marked by mm- to cm- size scours.

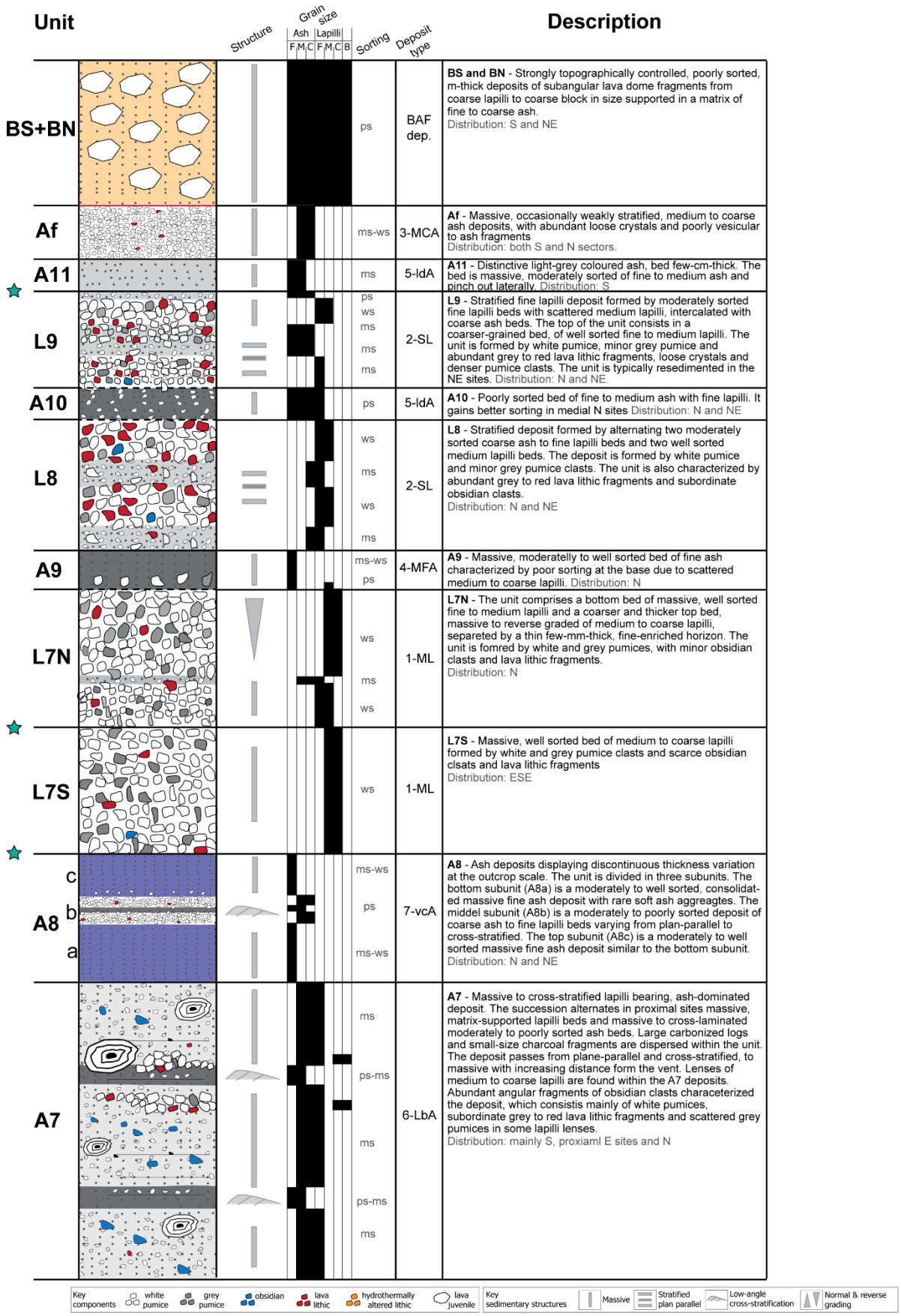

Figure 3.7 – ***figure continues in next page***.

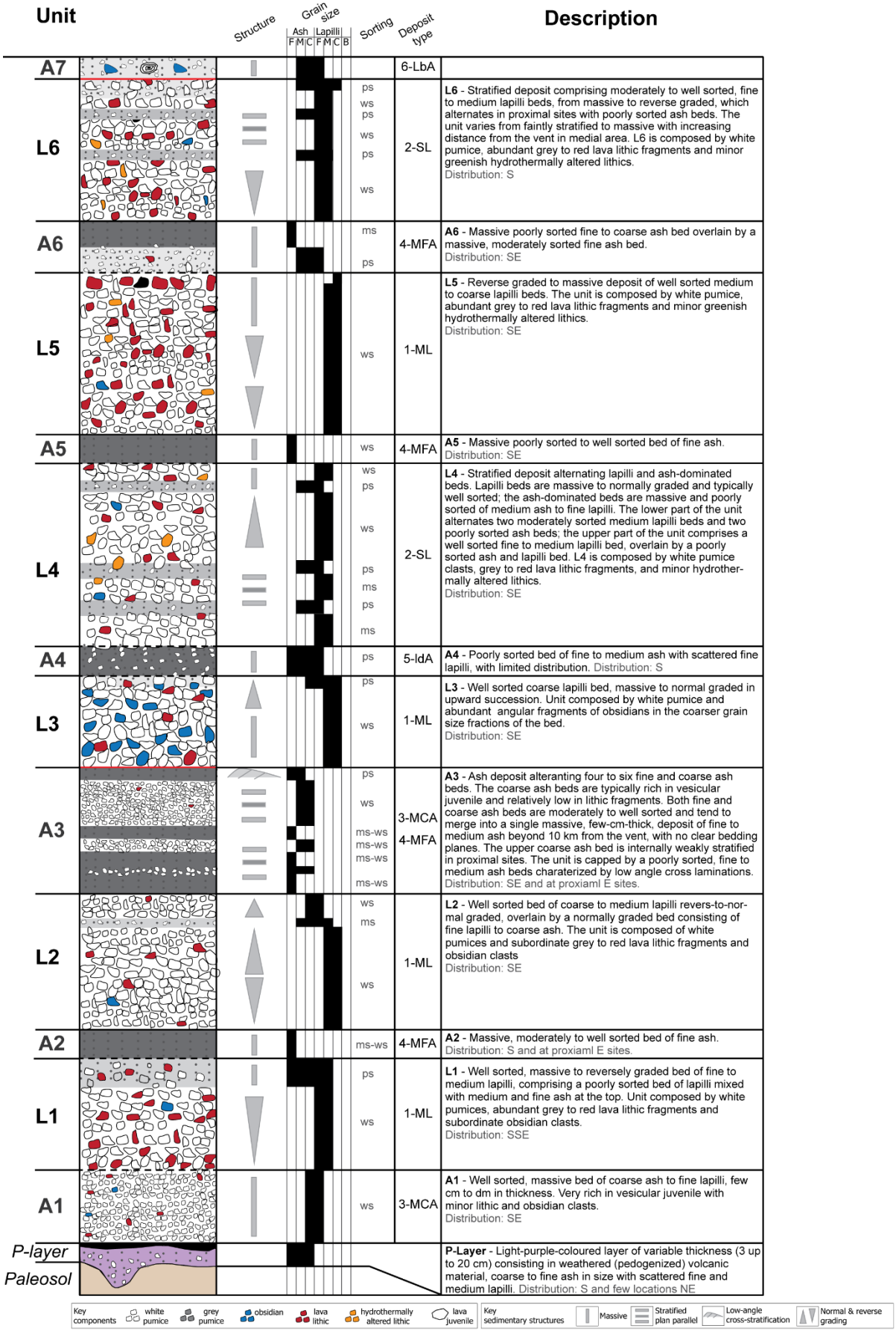

Figure 3.7 – ***caption in next page***.

Figure 3.7 – (***figure in previous page)*** Reconstructed stratigraphy and proposed unit subdivision of the Kaharoa pyroclastic succession. The composite stratigraphic log illustrates the stratigraphic relationship between units and summarized the main sedimentological and lithological features of individual beds. Units' thickness is only representative of main unit differences, and it is not to scale. For each unit the associated deposit type is indicated as follow: *1-ML* is massive lapilli deposit; *2-SL* is stratified lapilli deposit; *3-MCA* is massive coarse ash deposit; *4-MFA* is massive fine ash deposit; *5-ldA* is laterally discontinuous, ash deposit; *6-LbA* lapilli-bearing, ash-supported deposit; *7-vcA* is variably consolidated ash deposit. *Solid red lines* indicate sharp and erosive units contacts (A3-L3 and L6-A7) and contacts marked by thin laterally continuous, oxidized ash layer (Af-BS); *solid black lines* indicate sharp unit contacts with non to minor reworking; *dashed black lines* indicate gradual units contacts. *Stars* indicate reconstructed unit contacts, based on units' correlation among different outcrops. All other unit contacts have been directly observed in the field. Grain size and sorting based on visual estimations on the field: F–fine, M–medium, C–coarse and B–bomb; ws–well sorted, ms–moderately sorted and ps–poorly sorted.

Unit Af (deposit type 3) – The pyroclastic succession in the S and N sectors is capped at several localities S (e.g., sections 18 and 2), SE (e.g., sections 17 and 5), E (e.g., sections 27 and 28) and N (sections 24, 31 and 32) by massive to weakly stratified, medium to coarse ash deposits, which are here collectively refer to as unit Af (**Fig. 3.5**). These deposits show well sorting and have typically abundant loose crystals and poorly vesicular to glassy ash clasts. The unit is ~40-cm-thick in proximal eastern sites (e.g., sections 28, **Fig. 3.4**) and varies between 5 to 30 cm in medial sites (**Fig. 3.8**). Beyond the BAF deposit fan (units BS and BN, see later) the top of unit Af is typically not well preserved due to local reworking, and it gradually passes into a black soil underlying the Tarawera 1886 scoria deposit.

Units BN and BS (BAF deposits) – Very poorly sorted to poorly, sorted matrix-supported lava block deposits with no evident internal structure or subunit boundaries (e.g., **Fig. 3.6i**). Deposits are formed by angular to subangular lava fragments, from coarse lapilli to coarse block in size, occasionally up to m-sized boulders. The coarse lava fragments are supported in a matrix of medium to fine ash. Lava fragments are phenocryst-rich and occur in variable textures, from vesicular (dominant texture) to dense and obsidian-like textures. The deposits are strongly topographically controlled and form two main fans S (unit BS) and NE (unit BN) from the vent, where they overlay the lapilli and ash unit's succession (e.g., **Fig. 3.5b**). BS deposits have thickness of ~5m at section 18 and rapidly thin away from the vent (e.g., section 14 and 2). BN deposits are strongly confined within the Waiaute stream valley (e.g., section 23 and 30, **Fig. 3.4**), forming a succession up to 20-30-m-thick. The observed contact between BS and underlying Af unit is marked by a thin (0.5- 1cm), laterally continuous layer of red oxidized ash (**Fig. 3.6i**).

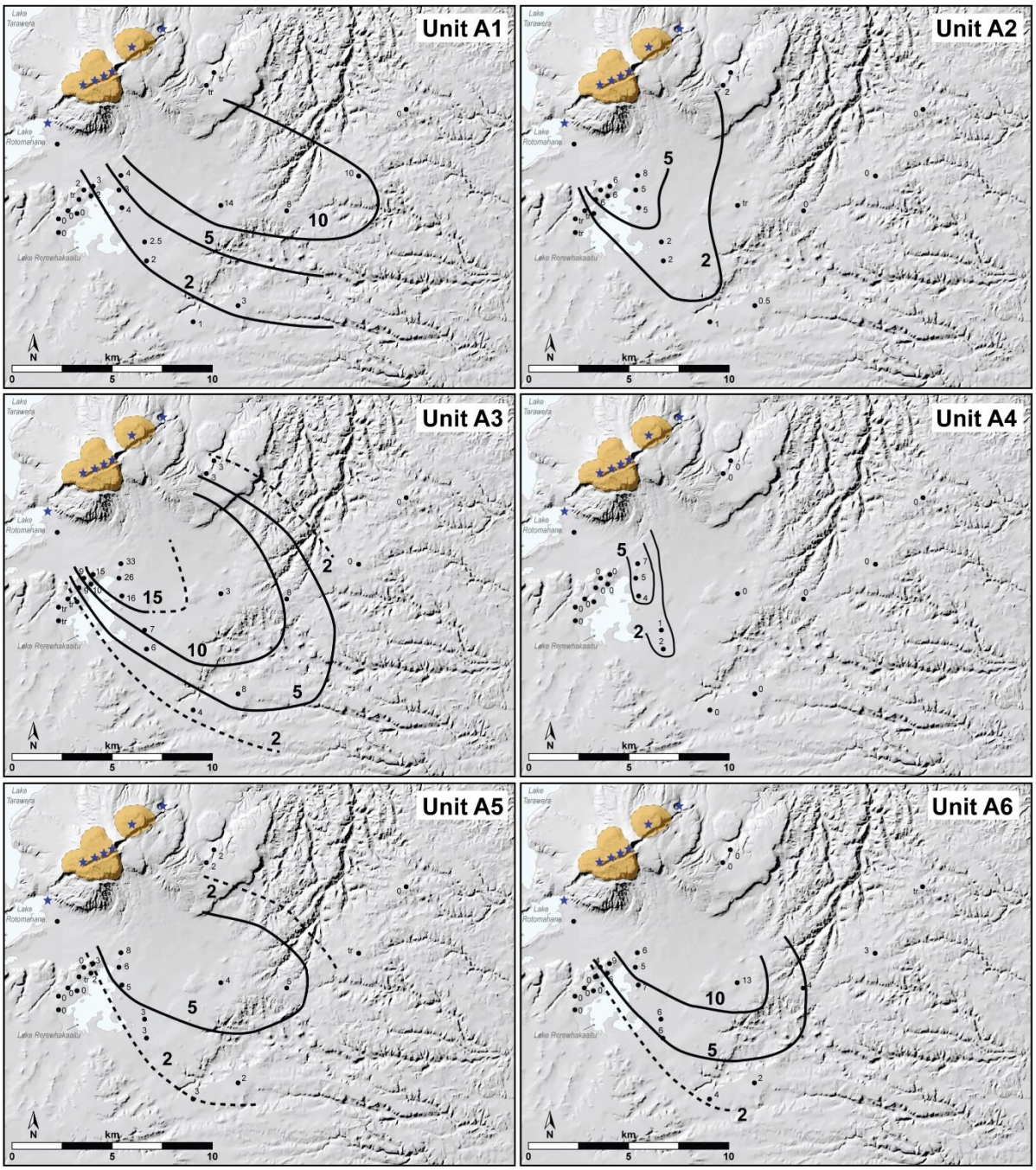

Figure 3.8 – Isopach maps of individual ash units (thickness in centimetres). Black solid lines represent well constrained isopachs, while black dashed lines represent tentative isopachs based on the available thickness data of this study. Thickness measured at each stratigraphic section (value next to black dots) is also reported; *tr* indicates sections where the unit is found as trace. Blue stars indicate the inferred positions of the Kaharoa eruptive vents after Nairn et al. (2001), while the area occupied by the Kaharoa lava domes is highlighted in orange. ***(Figure continues in next page)***.

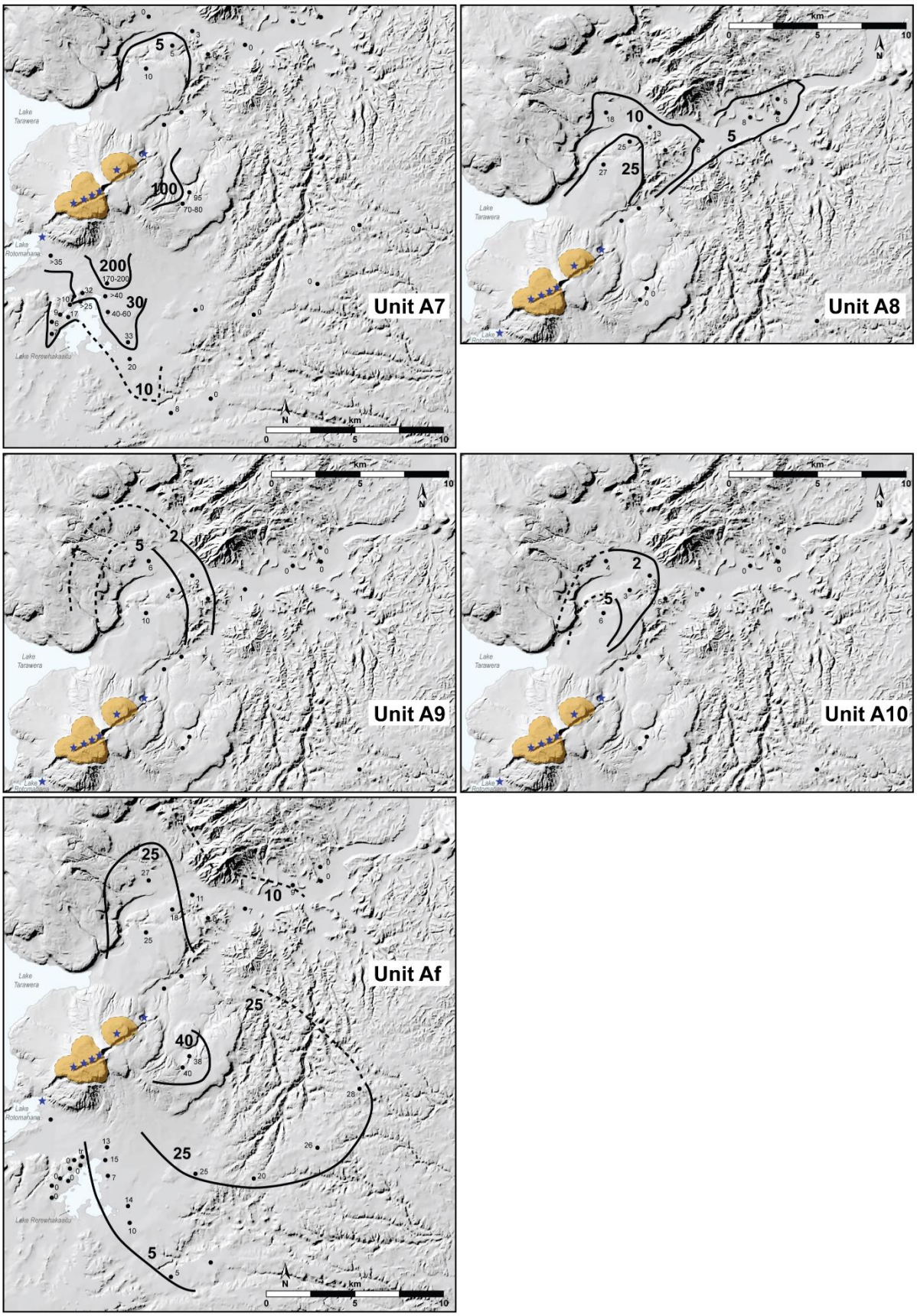

Figure 3.8 – ***(continued)***

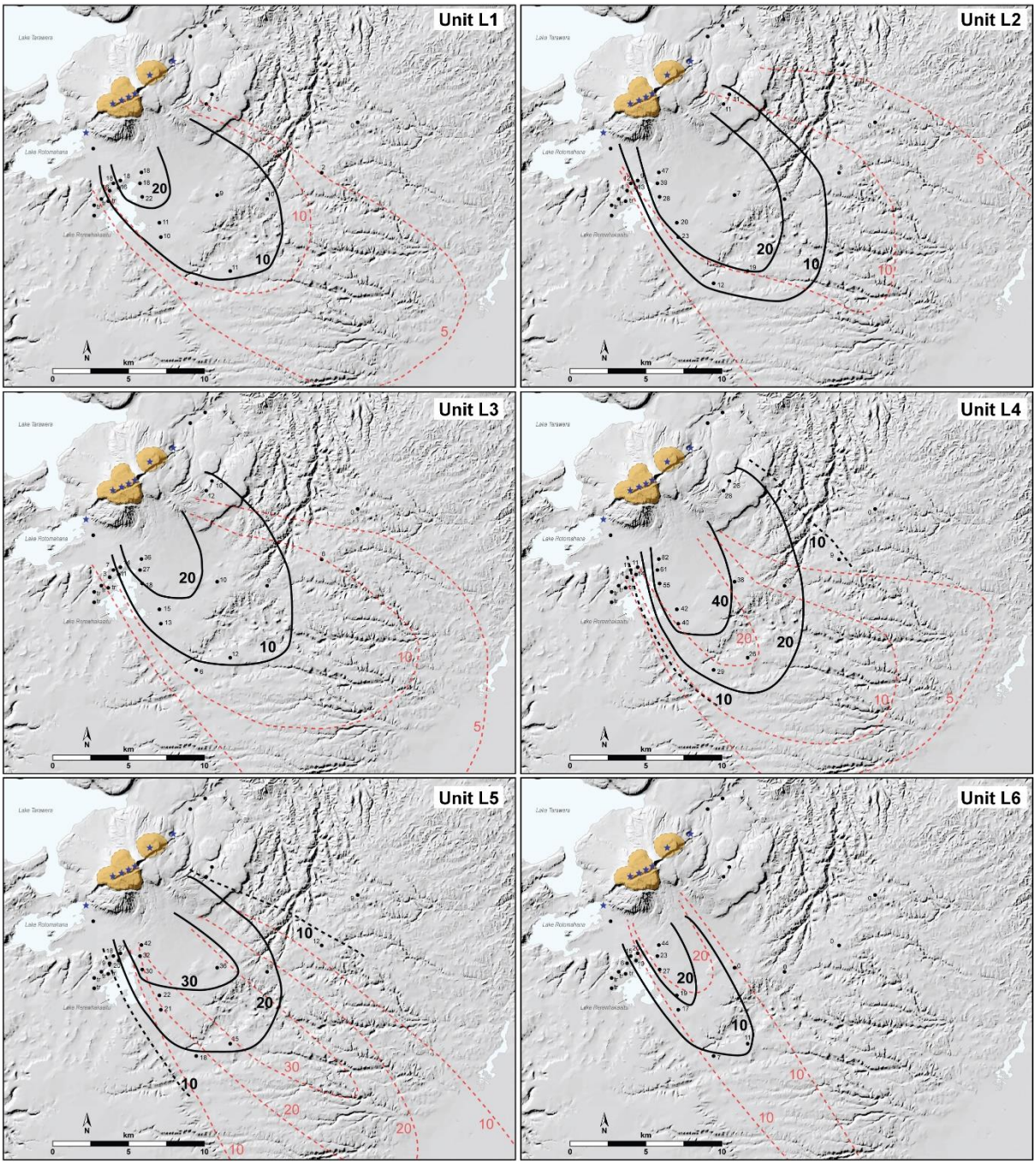

Figure 3.9 – Isopach maps of individual lapilli units (thickness in centimetres). Black solid lines represent well constrained isopachs based on the available thickness data of this study, while black dashed lines represent tentative isopachs. Thickness measured at each stratigraphic section (value next to black dots) is also reported; *tr* indicates sections where the unit is found as trace. Isopachs from Sahetapy-Engel et al. (2014) are shown as red dashed lines for equivalent stratigraphic units (refer to Table 3.1). Blue stars indicate the inferred positions of the Kaharoa eruptive vents after Nairn et al. (2001), while the area occupied by the Kaharoa lava domes is highlighted in orange. ***(Figure continues in next page)***.

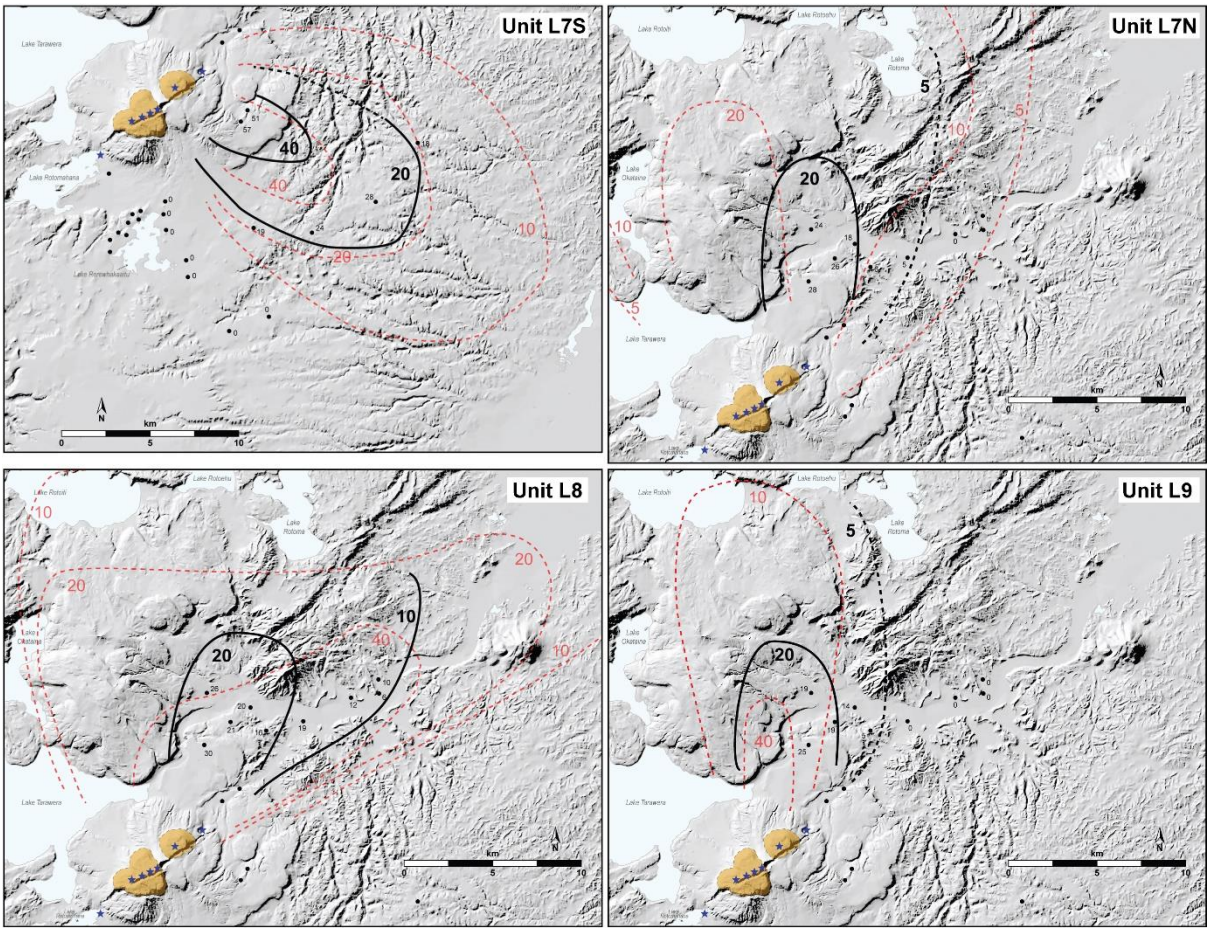

Figure 3.9 – ***(continued)***

3.4.1.3 Resedimented volcaniclastic deposits

RV1 deposit – At medial NE sites along the Tarawera river floodplains (e.g., sections 22, 21, 20 and 29, **Fig. 3.4**), massive to diffusely stratified deposit, 40-60 cm-thick, of moderately to well sorted coarse to very coarse ash, overlie unit L8 (**Fig. 3.10**). The deposit is typically fines-poor, with sporadic alignments of medium lapilli pumices. This deposit produces an evident overthickening of the studied succession downstream and away from the vent (see **Section 3.4.1.4**).

RV2 deposit – It consists of a 50-cm-thick massive deposit, formed by a great variety of vesicular to dense ash clasts and loose crystals, medium to coarse ash in size. The coarsest grain size fractions are dominated by rounded, very vesicular, light-brown clasts. This deposit has been observed only at one location (section 21, **Fig. 3.4**) within the Tarawera river floodplain where it caps the underlying succession of primary and resedimented Kaharoa beds (**Fig. 3.10**). The deposit directly overlies a thin and patchy black peat horizon.

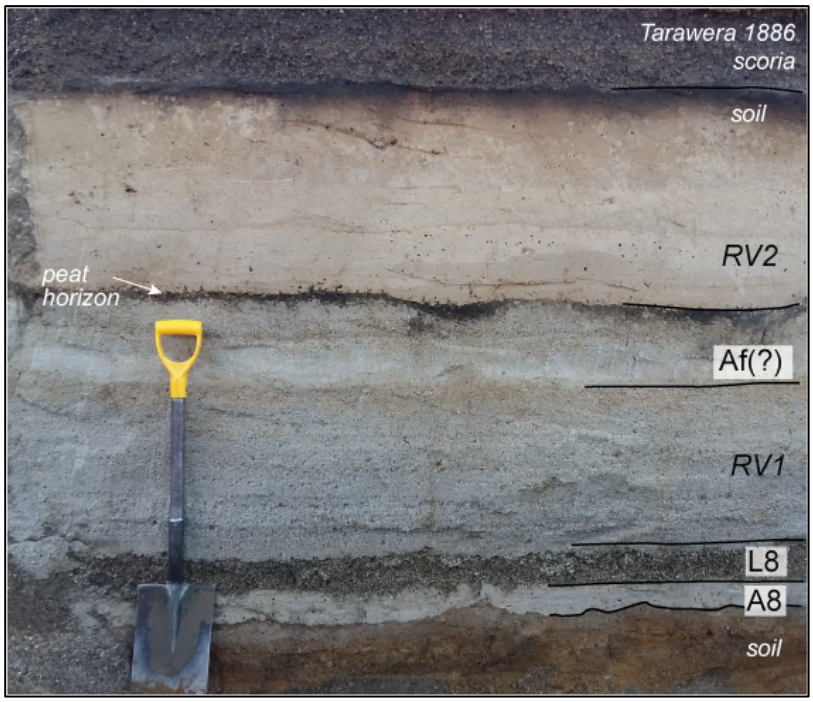

Figure 3.10 – Photograph of section 21 at ~15 km from the vent along the Tarawera river floodplain (see Fig. 3.4), showing deposit features of interpreted RV deposits (RV1 and RV2) and pyroclastic units A8 and L8 at the bottom of the section. A medium ash bed at the top of RV1 is tentatively correlated with unit Af at more proximal sites. Spade 1 m long. Peat horizon might represent accumulation of organic material (e.g., leaves) from the surrounding, partially buried, vegetation.

3.4.1.4 Lateral correlations and spatial distribution

The lapilli and ash units identified in the field have been laterally correlated among proximal and medial outcrops, south to north from Mt Tarawera (**Fig. 3.11**), to record the spatial distribution of the units and to better constrain the eruption stratigraphy. Fine ash deposits served as a guide to correlate the units, as well as units with distinctive lithological features (e.g., obsidian-rich units L3 and A7; lithic-rich units L5 and L8; units L7S and L7N with a bimodal pumice content).

Both ash and lapilli units in the S sector show a main southeast dispersal (**Fig 3.8** and **Fig. 3.9**). The coarse ash units A1, A3 and Af show a wider dispersal compared to the finer ash units A2, A4, A5 and A6, with A4 showing a very narrow area of distribution south from the vent. In medial area, passing from SE to ESE sites (from sections 17, 5, 19 to 25), the ash parting of the deposits becomes progressively less pronounced (**Fig. 3.11**). At these locations, the ash units at lower stratigraphic positions (A2, A3 and A4) have faded away, and the lower Kaharoa sequence consists of fine to medium lapilli beds with no clear unit boundaries (**Fig. 3.11**); only the coarse ash unit A1 is preserved up to these localities as a discrete, 14- to 8-cm-thick bed forming the base of the Kaharoa deposit. Within the upper Kaharoa sequence instead, the ash units A5 and A6 can be recognised towards medial ESE sites, forming few-cm-thick layers or as trace interbedded

between lapilli units. The distinctive lithological features of lapilli units L3 and L5, with high obsidian and high lithic contents, respectively, enable reliable correlations. The topmost bed of the Kaharoa deposit consist in the coarse ash unit Af which shows a more eastern dispersal in the S sector (**Fig 3.8**).

In the N sector, the pyroclastic succession resembles the one exposed in the S sector, alternating lapilli and ash beds. However, the succession in this sector is thinner than the southern counterpart, and a smaller number of units could be identified in the field. Within this area, reliable correlations are provided by means of the distinctive pumice and lithic content of unit L7N and L8, respectively and by the distribution of ash units A9 and A10. Both ash and lapilli fall units are mainly directed to the N of Mt Tarawera (e.g., sections 24, 26, 31, 32 and 33), whereas unit A8 has a more radial distribution from N to NE (e.g., sections 26 to 29) (**Fig 3.8** and **Fig. 3.9**). Valley-confined, m to tens of m thick BAF deposits hindered the observation of underlying lapilli and ash deposits in some proximal NE sites (sections 23 and 30). Beyond the BAF fan, a lapilli bed, 20- to 10-cm-thick with increasing distance from the vent, overlays unit A8 and is correlated to unit L8 due to its high lithic content. Within this NE area, in the topographic lows and floodplains along the Tarawera river, remobilization and re-sedimentation of primary Kaharoa beds is suspected to have occurred and the studied outcrops (e.g., sections 22, 21, 20 and 29) comprise tens of cm thick RV deposits overlaying unit L8 or A10 (**Fig. 3.11**) (see **Section 3.5.2**). The distribution of unit L9 in this area is not well-constrained due to reworking, however the unit appears to be deposited mainly N from the vent as well as unit L7N.

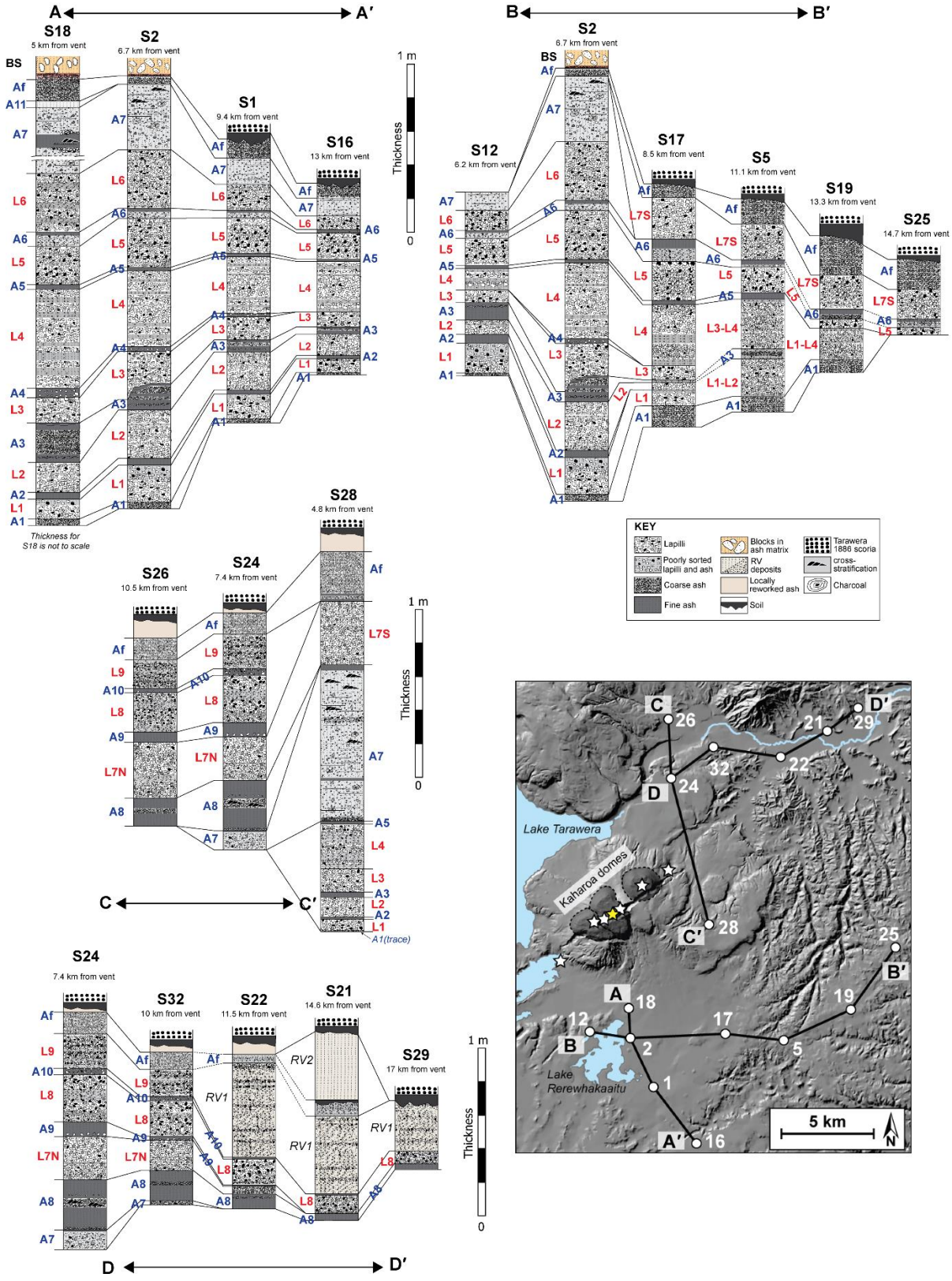

Figure 3.11 – Stratigraphic correlations of Kaharoa units among selected key sections (*S*) along four different transects in both S and N sector. Note that the deposit's thickness in section 18 is not to scale. Reliable correlations are marked with *solid black lines*, while few tentative correlations are marked with *dashed black lines*. Inset shows the locations of key sections (*white dots*) and transects (*AA', BB', CC' and DD'*) relatively to the Kaharoa domes (*dark grey*) and vents (*stars*; the yellow star indicate the reference vent for source-to-outcrop distances).

3.4.2 Grain size

The grain size characteristics of the Kaharoa deposit were quantified from samples collected at the reference sections 2 and 24, at ~7 km south and north from the vent (**Fig. 3.4**). These two sections provided controls on the variation of the grain size distributions (GSDs) of the pyroclastic succession over time and deposit type. Further grain size samples were collected from two additional sites (sections 18, 28, **Fig. 3.4**). Representative grain size results are listed in **Table 3.3**.

The median grain size and sorting of the deposits oscillate vertically through both sections 2 and 24, reflecting the repeated deposition of ash and lapilli beds during the eruption sequence (**Fig. 3.12a** and **b**). The median grain size varies largely from –2.5ϕ (>8mm) to 4-6ϕ (<0.064mm) from medium lapilli beds (e.g., units L3, L7N, L8) to fine ash beds (e.g., units A2, A3, A8) (**Fig. 3.12a** and **b**). The sorting coefficient varies from 1 to 2.5ϕ, occasionally exciding 3ϕ, with ash-dominated deposits having typically sorting >2 (**Fig. 3.12a** and **b**).

GSDs of both massive lapilli units and stratified lapilli units (deposit types 1 and 2) are unimodal (**Fig. 3.12c**), often skewed towards coarse lapilli sizes (e.g., units L2, L3, L4, L5, L8) and are characterised by good sorting (**Fig. 3.13a**). Within the stratified lapilli unit L4, interbedded ash-dominated deposits at section 2 show poor sorting ($\sigma\phi = 3.42$) and have wide and bimodal GSDs (sample K88, **Fig. 3.12c**).

Massive coarse ash units (deposit type 3) have similar unimodal GSDs (**Fig. 3.12c**) and good sorting (**Fig. 3.13a**) to those of lapilli units. In contrast, massive fine ash units (deposit type 4), occurring on the top of lapilli units at both sections, display marked bimodal GSDs, with modes at 2-4ϕ and 6-7ϕ (**Fig. 3.12c**) and have moderate sorting (**Fig. 3.13a**). The fine ash content (F2) of these units is distinctive among other units in the sequence, being between ~40 and 65 wt% (**Fig. 3.13b, Table 3.3**).

Laterally discontinuous ash units (deposit type 5) have typical wide and unimodal GSDs (**Fig. 3.12c**), with minor peaks in the fine ash size and have moderate to poor sorting (**Fig. 3.13a**). Samples collected at various stratigraphic positions from the lapilli-bearing ash deposits of the PDC unit A7 (deposit type 6) at both sections 2 and 24 have wide and unimodal distributions (**Fig. 3.12c**), with mode at 0-1ϕ and sorting at ~2ϕ (**Fig. 3.13a**). GSDs of beds within the variably consolidated ash unit A8 (deposit type 7) are unimodal (**Fig. 3.12c**; see also **Appendix B**). The sorting of this unit at section 24, varies from <2ϕ within the bottom (A8a) and top (A8c) beds formed by massive and cohesive ash (e.g., samples K224 and K226, **Fig. 3.12b**), to 2.5ϕ in the middle bed (A8b) displaying cross-stratifications (K225 **Fig. 3.12b**). The fine ash content (F2) varies within the unit, from 16 wt% (A8b) to >80 wt% (A8a) (**Fig. 3.13b, Table 3.3**).

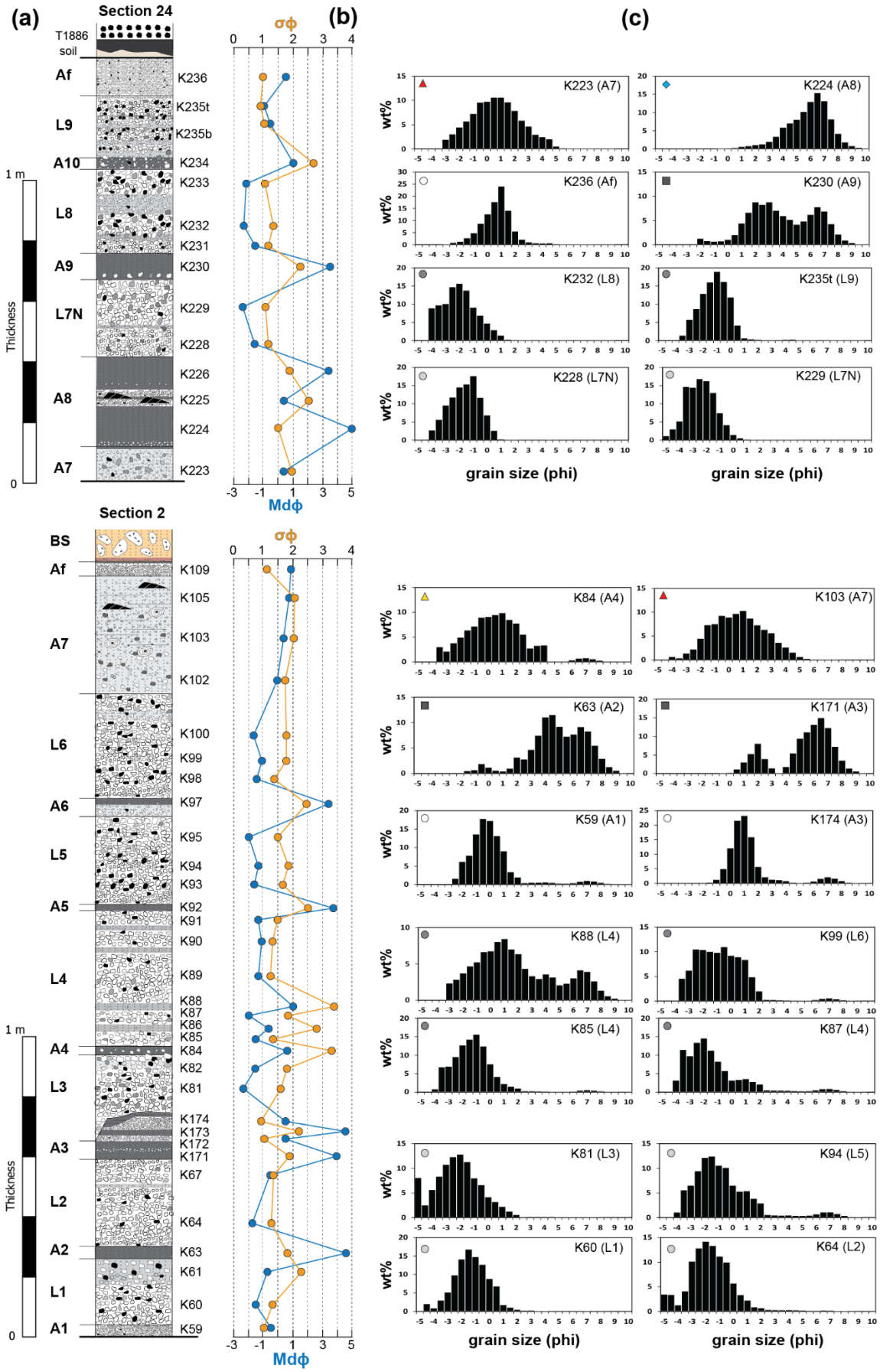

Figure 3.12 – (***caption in next page)***.

Figure 3.12 – (***figure in previous page).*** Grain size characteristics of units at reference sections 2 and 24. (**a**) Stratigraphic logs of the two sections with position and ID of samples (e.g., *K100*). *T1886* in section 24 indicates scoria deposits from the 1886 CE Tarawera eruption. (**b**) Variation with stratigraphic height in median diameter (Mdϕ) and sorting coefficient (σϕ) of individual beds sampled within each unit. (**c**) Selected grain size distributions organized by deposit type (symbol on top left corner of each histogram): massive lapilli deposit (*light grey circles*); stratified lapilli deposit (*dark grey circles*); massive coarse ash deposit (*white circles*); massive, fine ash deposit (*dark grey squares*); laterally discontinuous, ash deposit (*yellow triangles*); lapilli-bearing, ash deposit (*red triangles*); variably consolidated ash deposit (*blue diamonds*).

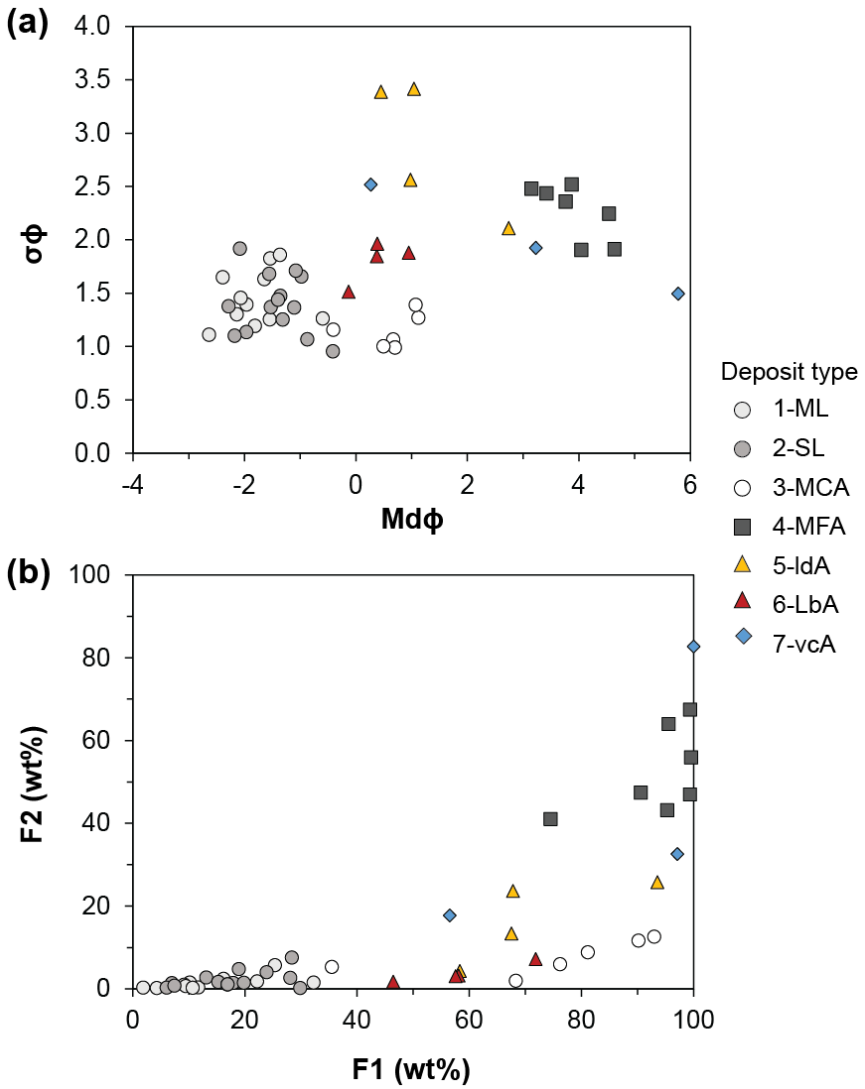

Figure 3.13 – Results of grain size analyses of representative samples analysed in this work plotted as (**a**) median diameter (Mdϕ) versus sorting coefficient (σϕ) and (**b**) as weight % of sample <1 mm (F1) versus weight % of sample <63 μm (F2). Deposit type of individual samples is indicated as follow: *1-ML* is massive lapilli deposit (*light grey circles*); *2-SL* is stratified lapilli deposit (*dark grey circles*); *3-MCA* is massive coarse ash deposit (*white circles*); *4-MFA* is massive, inter-lapilli, fine ash deposit (*dark grey squares*); *5-ldA* is laterally discontinuous, ash deposit (*yellow triangles*); *6-LbA* lapilli-bearing, ash-supported deposit (*red triangles*); *7-vcA* is variably consolidated ash deposit (*blue diamonds*).

Table 3.3 – (***Table continues in next page***) Grain size data of representative samples analysed in this work. Mdϕ and σϕ are the median diameter and sorting coefficient of the obtained grain size distributions, following Inman (1952). F1 and F2 represent the weight % of the sample <1 mm and <63 μm, respectively (Walker, 1971). Deposit type for each unit sampled are abbreviated as follow: (1) massive lapilli deposit; (2) stratified lapilli deposit; (3) massive, coarse ash deposit; (4) massive, fine ash deposit; (5) laterally discontinuous, ash deposit; (6) lapilli-bearing, ash deposit; (7) variably consolidated ash deposit. Location (N=north and S=south) indicates the position of the stratigraphic sections with respect to Mt Tarawera.

Unit	Deposit Type	Sample ID	Section	Location	Dist.(km)	Mdϕ	σϕ	F1	F2
Af	3	K236	24	N	7.4	0.49	1.00	68.26	1.97
Af	3	K109	2	S	6.7	1.07	1.39	90.16	11.66
A11	5	K194	18	S	6.7	2.74	2.11	93.53	25.79
L9	2	K235t	24	N	7.4	-0.87	1.07	20.03	1.82
L9	2	K235b	24	N	7.4	-0.41	0.96	29.80	0.22
A10	5	K234	24	N	7.4	0.98	2.56	70.14	16.00
L8	2	K233	24	N	7.4	-2.18	1.10	5.99	0.34
L8	2	K232	24	N	7.4	-2.29	1.38	7.39	0.77
L8	2	K231	24	N	7.4	-1.97	1.14	6.92	1.40
A9	4	K230	24	N	7.4	3.42	2.44	95.28	43.18
L7N	1	K229	24	N	7.4	-2.64	1.11	1.82	0.34
L7N	1	K228	24	N	7.4	-1.82	1.19	3.81	0.26
L7S	1	K247	28	E	4.8	-2.14	1.30	4.25	0.21
L7S	1	K246	28	E	4.8	-2.39	1.07	1.66	0.22
A8	7	K226	24	N	7.4	3.23	1.92	97.10	32.55
A8	7	K225	24	N	7.4	0.27	2.52	56.52	17.67
A8	7	K224	24	N	7.4	5.79	1.49	100.00	82.72
A7	6	K223	24	N	7.4	0.37	1.85	58.09	3.21
A7	6	K105	2	S	6.7	0.95	1.88	71.85	7.19
A7	6	K103	2	S	6.7	0.38	1.96	57.54	3.06
A7	6	K102	2	S	6.7	-0.13	1.51	46.43	1.72
L6	2	K100	2	S	6.7	-1.56	1.68	16.88	1.11
L6	2	K99	2	S	6.7	-1.08	1.71	28.06	2.66
L6	2	K98	2	S	6.7	-1.40	1.44	17.87	1.44
A6	4	K97	2	S	6.7	3.15	2.48	74.48	41.03
L5	2	K95	2	S	6.7	-2.07	1.46	9.40	0.71
L5	2	K94	2	S	6.7	-1.37	1.86	25.33	5.76
L5	2	K93	2	S	6.7	-1.64	1.63	16.13	2.44
A5	4	K92	2	S	6.7	3.87	2.52	90.59	47.41
L4	2	K91	2	S	6.7	-1.36	1.47	16.82	1.06
L4	2	K90	2	S	6.7	-1.11	1.37	23.82	4.03
L4	2	K89	2	S	6.7	-1.32	1.25	15.22	1.68
L4	5	K88	2	S	6.7	1.04	3.42	67.77	23.64

Unit	Deposit Type	Sample ID	Section	Location	Dist.(km)	Mdϕ	σϕ	F1	F2
L4	2	K87	2	S	6.7	-2.08	1.92	18.87	4.79
L4	2	K86	2	S	6.7	-0.98	2.65	28.33	7.56
L4	2	K85	2	S	6.7	-1.53	1.37	13.07	2.80
A4	5	K84	2	S	6.7	0.45	3.39	58.21	3.34
L3	1	K82	2	S	6.7	-1.54	1.83	22.14	1.82
L3	1	K81	2	S	6.7	-2.39	1.65	9.13	1.04
A3	3	K174	2	S	6.7	0.70	0.99	81.13	8.84
A3	4	K173	2	S	6.7	4.54	2.24	99.53	55.94
A3	3	K172	2	S	6.7	0.67	1.07	76.15	5.98
A3	4	K171	2	S	6.7	4.04	1.91	99.35	67.45
L2	1	K67	2	S	6.7	-0.60	1.26	32.21	1.53
L2	1	K64	2	S	6.7	-1.97	1.39	10.12	1.53
A2	4	K63	2	S	6.7	4.64	1.91	95.53	63.99
L1	1	K61	2	S	6.7	0.08	2.09	52.09	10.05
L1	1	K60	2	S	6.7	-1.55	1.26	11.64	0.39
A1	3	K59	2	S	6.7	-0.41	1.16	35.45	5.30

Table 3.3 – (***continued***)

3.4.3 Componentry

3.4.3.1 Types of components of the Kaharoa deposit

Componentry analysis was performed to quantify the clasts variability observed in the field and to further characterise individual coarse-grained units (coarse ash and lapilli units). The Kaharoa pyroclasts are here subdivided into two main genetic classes as juvenile and lithic (White and Houghton, 2006), and further clast types could be separated from both the juvenile and lithic materials.

According to the clasts' macroscopic textural variability (e.g., colour, external morphology, crystallinity, phenocryst phase, vesicularity) the juvenile material was separated into seven clast types (**Fig. 3.14**): (1) white pumice, (2) grey pumice, (3) banded pumice, (4) dense juvenile, (5) obsidian, (6) loose crystal and (7) basaltic clast. White and grey pumice clasts are differentiated also based on their different whole-rock composition, following Nairn et al. (2004).

Obsidians pyroclasts are here interpreted to be juvenile as (i) they show fresh, unaltered textures with vitreous lustre and (ii) have the same mineral assemblage of pumice clasts, comprising biotite which is a distinctive crystal phase of the Kaharoa eruption (Nairn et al., 2004; Shane et al., 2008; Lowe et al., 2008). In addition, Dunbar and Kyle (1992) showed that obsidian and pumice clasts deposited during the Kaharoa eruption have nearly identical major- and trace-element compositions, further supporting a juvenile origin for the obsidian.

Lithic fragments consist mainly of accessory material (see Fisher and Schmincke, 1984) derived from the conduit walls excavated in the pre-Kaharoa rhyolite lava domes and coulees from the older Tarawera dome complex. Lithics in the Kaharoa deposit are commonly weathered, grey to red in colour depending on the degree of oxidation. Some lithic clasts, typically green in colour, show pervasive alternation textures, interpreted due to hydrothermal modification of the primary mineral phases. In this work lithic material is thereby separated into (i) lava fragments and (ii) hydrothermally altered clasts, based on clasts colour, shape and degree alteration. Additional lithic clasts type, not found in this study, are reported in other works, and consist of lacustrine mudstones found in some very proximal deposits (Nairn et al., 2001) and intrusive rocks sparse in the pyroclastic sequence (Leonard et al., 2002).

3.4.3.2 Characteristics of component types

White pumice (juvenile) – Light-coloured, white to yellowish, with white interiors, moderately vesicular and porphyritic clasts (**Fig. 3.14a**). Lapilli clasts are sub-angular to sub-rounded, dominated by 0.5-2-mm-size vesicles intersecting the external surface of the particles. Surface vesicles shapes range from spherical and elliptic to irregular. Some clasts are characterised by elongated to very elongated, tube-like vesicles oriented along the clast's main axis. White pumice clasts are rhyolitic in whole-rock composition, with SiO_2 content of 76-77 wt.% (Nairn et al., 2004). Phenocryst content is ~10 vol.% (see Chapter 5), comprising plagioclase, quartz, biotite and titanomagnetite, and rare hornblende and orthopyroxene. Occasionally, mm-size basaltic inclusions are found within white pumice clasts. The average clast bulk density is 1095 ±168 kg/m^3 (see Chapter 5; Appendix D).

Grey pumice (juvenile) – Pale-grey, moderately vesicular, porphyritic clasts with abundant mm-size basaltic inclusions (**Fig. 3.14b**). Lapilli clasts are sub-angular to sub-rounded, with surface vesicles varying from 0.5 to >2 mm in coarsely vesicular domains. Vesicle shapes are typically spherical to elliptical, with very elongated and tube-like forms less frequent compared to those observed in white pumice clasts. Grey pumices are common within the larger grain size (lapilli) of the deposits, becoming progressively less abundant in smaller fraction and of difficult discrimination when <1 mm. In the coarse ash fraction, grey pumice grains have a vesicular-fibrous surface texture, marked by the presence of sparse biotite. These clasts have been associated here to the "darker-coloured pumice clasts" described in Leonard et al. (2002) and Nairn et al. (2004), having rhyodacitic whole-rock composition (69 to 72% wt.%. SiO_2). Grey pumice clasts contain the same minerals as white pumice, however, show a larger amount of ferromagnesian and oxide crystals compare to those in white pumices, and have common crystal clots. Phenocryst content is 19 vol.% (see Chapter 5). The average clast bulk density is 1160 ±150 kg/m^3 (see Chapter 5; Appendix D).

Banded pumice (juvenile) – Moderately vesicular, porphyritic clasts composed of dark-grey bands or domains set in a dominant white pumiceous mass (**Fig. 3.14e**). The colour banding appears due to differences in the internal texture between the less vesicular dark bends and the more vesicular white parts, with similar vesicles characteristic to those observed in white pumice. Phenocryst content is identical to those of the white pumice; the composition is assumed to be the same of white pumice. Banded pumice clasts are mainly found in the lapilli fraction of the deposits. Average clast bulk density is 1283 ± 274 kg/m^3 (see Appendix D).

Dense juvenile (juvenile) – Light-toned, grey to translucent, glassy, poorly vesicular, and porphyritic clasts (**Fig. 3.14d**). Lapilli clast are sub-angular to sub-rounded and show dominantly elliptical vesicles, < 0.5 mm in size and usually filled with finer ash grains. Large vesicles (>

2mm) occur sporadically in medium lapilli clasts and are typically elongated to tube-like. Dense juvenile clasts occur throughout all grain size classes and have grain size typically of <4 mm. Overall, dense juvenile clasts show characteristics between vesicular and degassed clasts, representing intermediate members between white pumice and obsidian clasts. Dense juvenile clasts have the same phenocryst content and mineral assemblage of white pumice and are assumed to have the same rhyolitic composition. Dense juvenile clasts have an average bulk density of 1641 ± 59 kg/m^3 (see Appendix D).

Obsidian (juvenile) – Black, dense (incipiently to non-vesicular), porphyritic clast, characterised by evident vitreous lustre and unaltered textures (**Fig. 3.14c**). The broken surfaces of some hand specimen clasts expose oriented mm-sized vesicles (up to 2-3 mm in length) of regular elliptical geometries. Foliation planes are uncommon and when present are orientated parallel to the direction of vesicles elongation. Within the lapilli fraction of the deposits, obsidian clasts occur as black, angular fragments with sharp edges, conchoidal fractures and smooth surfaces. At smaller grain size obsidians became transparent and sub-angular. Obsidian clasts have phenocryst content of 8.5 vol.%, (see Chapter 5), comprising the same mineral assemblage of white pumice and have rhyolitic composition (Dunbar and Kyle, 1992). The average bulk density is 2327 ±72 kg/m^3 (see Appendix D).

Loose crystal (juvenile) – Individual, millimetric to sub-millimetric, crystals dispersed in the deposit. Euhedral to subhedral quartz and plagioclase are the most abundant mineral phases and form nearly the total of the crystals separated during componentry analysis (0.5 to 4 mm in size). Quartz grains are typically bipyramidal in shape. Additional crystals observed in the deposits are biotite, titanomagnetite, hornblende, orthopyroxene, rare cummingtonite, and very rare olivine. The abundance of biotite is far greater compared to these other minerals. However due to their smaller size, commonly < 500-150 μm, these minerals were not accounted during componentry analysis (only biotite occur in the coarse ash fraction as 1-mm grains with pumiceous selvedges).

Basaltic clast (juvenile) – Dark grey to black, non-vesicular to poorly vesicular, porphyritic clasts of basaltic to basaltic-andesite compositions (51-53 wt.% and 53 to 57 wt.% of SiO2, respectively, Leonard et al. 2002). Basaltic material occurs both as individual clasts dispersed in the Kaharoa deposit and as inclusions within white and grey pumice clasts (**Fig. 3.14f**). Individual clasts are usually sub-rounded and are sometimes partially covered by a mm-thick white vesicular coating, resembling white pumice clasts. Basaltic inclusions in pumices are commonly more abundant within grey pumice clasts and are of variable sizes (<0.5 mm up to 1-4 cm in diameter). In white pumices, basaltic inclusions are less abundant but typically of large sizes (up to 5 cm in diameter on lapilli size clasts). The shapes of the mm-to-cm inclusions are usually rounded, ellipsoidal to spheroidal, resembling those of the individual clasts.

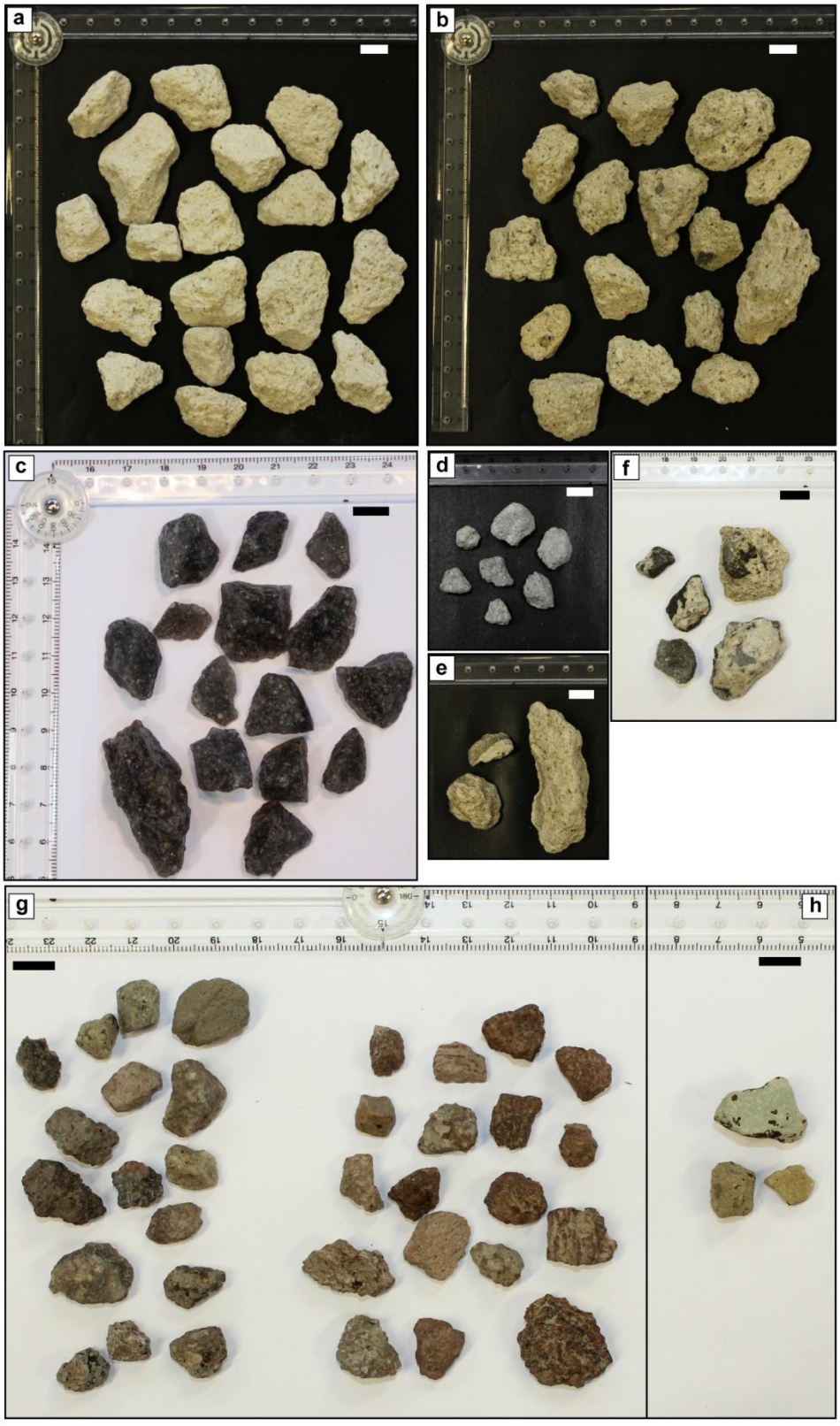

Figure 3.14 – Representative clasts photographs of juvenile (**a** to **f**) and lithic (**g** and **h**) materials of the Kaharoa deposit: (**a**) white pumice; (**b**) grey pumice; (**c**) obsidian; (**d**) dense juvenile: (**e**) banded pumice; (**f**) basaltic material as free clasts and coated with pumice; (**g**) lava fragments with variable degree of oxidation: (**h**) hydrothermally altered clasts. White and black scale bars are 1 cm long in each picture.

Lava fragments (lithic) – Variably altered, sub-angular to sub-rounded fragments of pre-Kaharoa lavas (**Fig. 3.14g**). The fragments are typically devitrified and range from weakly to partially altered, with grey to red colours. Fresh, unaltered textures are typically rare.

Hydrothermally altered clasts (lithic) – Fragments of unspecified original lithologies characterised by a pervasive hydrothermal alteration. Clasts are typically sub-rounded to rounded with distinctive green to cream colours (**Fig. 3.14h**).

3.4.3.3 Componentry variation along the pyroclastic succession

Component analyses of samples collected at key sections 2, 24 and 28 (**Fig. 3.4**) account for all the coarse-grained units of the pyroclastic succession and enable to depict temporal changes in the relative proportion of components during the eruption sequence. Componentry results are shown in **Figure 3.15** and listed in **Table 3.4**.

White pumice clasts form the large majority of the Kaharoa deposit, varying from ~53 to 90 wt.% in abundance in the different units (**Table 3.4**). Grey pumice, obsidian and lithic clasts range individually in abundance from few wt.% up to ~30 wt.%, making alternatively the second most abundant component of the deposits (**Table 3.4**). Elevated abundance of these components are distinctive features of specific stratigraphic intervals and thus units. Dense juvenile clasts are a minor component of the deposit, followed by banded pumice clasts, loose crystals and by sparse, rare basaltic clasts (**Table 3.4**).

A first order variation in the component characteristics of the deposit relates to the presence/absence of grey pumices. Grey pumice clasts are a distinctive component of the upper part of the stratigraphic sequence, encompassing lapilli units L7S, L7N, L8 and L9 (**Fig. 3.15a** and **b**). When present, grey pumice clasts are always subordinate with respect to white pumice clasts. No grey pumice clasts have been found in earlier units (A1 to L6) (**Fig. 3.15a**). Unit L7S is the only lapilli unit in the S sector to contain grey pumice clasts, with grey pumices varying from 9 to 33 wt.%, from base to top of the unit at section 28 (**Table 3.3**). Scattered grey pumice clasts (coarse lapilli in size) have been observed in few lapilli lenses within unit A7 south of Mt Tarawera. In the N sector, grey pumice clasts decrease in abundance vertically toward the top of the sequence, passing from 26, to 9 and 3 wt.% in units L7N, L8 and L9, respectively (**Fig. 3.15b**). Occasional mingled white-grey pumice clasts have been observed during fieldwork at the bottom of unit L7S.

The relative proportion of lithic clasts (lava fragments + hydrothermally altered clasts) oscillated throughout the pyroclastic sequence from 5 to 20 wt.% (**Fig. 3.15c**). Lithic-rich deposits (lithic content ≥15 wt.%) occur at different stratigraphic positions in the pyroclastic sequence and are

associated with lapilli units L1, L5, L6, L8 and L9 (**Table 3.4**). Lava fragments are found throughout the pyroclastic sequence (5 to 15 wt.%), while hydrothermally altered clasts are absent to rare in the deposits. Hydrothermally altered clasts are however characteristic of the stratigraphic interval L4-L5-L6 with relative proportion of ~5 wt.% (**Fig. 3.15; Table 4.4**).

Obsidians are distributed throughout the entire pyroclastic sequence, with typical abundances of <5 wt.%. Two obsidian-rich stratigraphic horizons occur within the Kaharoa deposit and are associated to units L3 in the S sector (14 wt.%) and A7 both in the S and N sectors (17 and 27 wt.%, respectively). These units mark two episodes of sharp increase in the obsidian content during the eruption.

It is noteworthy here to compare the vertical trends in the relative abundance of lithics and obsidians within the pyroclastic sequence. Considering the entire deposit, lithic fragments are always relatively more abundant than juvenile obsidians, except for the obsidian-rich units in which the obsidian: lithic ratio is >1 (**Fig. 3.15c; Table 3.4**). At section 2, no clear correlations between the two components appear evident (**Fig. 3.15a**). Lithic content at this section varies largely at the bottom of the sequence (A1 to A3) and increases progressively in the upper part of the sequence (L3 to L6), whereas obsidian content remains steady at <5 wt.% in most of the units (**Fig. 3.15a** and **c**). In addition, in coincidence of the obsidian-rich units L3 and A7, no sharp increases are observed in the lithic content. On the contrary, in section 24, the vertical changes in the obsidian content of the deposits tend to shadow the one of the lithic (**Fig. 3.15b** and **c**).

The abundance of dense juvenile clasts in the deposit is generally similar to that of obsidian clasts at most stratigraphic intervals and varies from 1 to 5 wt.% (**Table 3.4**). An increase in abundance of dense juvenile clasts is observed in unit L6 (8-9 wt.%) at section 2, prior the obsidian-rich unit A7, and in units L8 and L9 (5-7 wt.%) at section 24. A steeper increase in the dense juvenile content of the deposit is observed in unit Af at the top of both outcrops (**Fig. 3.15a** and **b**).

No significant variations or trends in the abundances of both banded pumice and basaltic clast are observed through the stratigraphy (**Fig. 3.15a** and **b**). The relative proportion of banded pumice clasts is 1 to 4 wt.% in componentry analyses, while basaltic clasts have typical proportion <1 wt.% (**Table 3.4**).

Regarding crystal fraction of the deposit, loose crystals appear to be underrepresented in componentry analyses (which accounts for the grain fraction >0.5 mm of individual beds), having values of typically <1-2 wt.% throughout the pyroclastic sequence. Despite this, a steep increase in the abundance of loose crystals is observed in the top part of the sequence at unit L9 (7.5 wt.%) and unit Af (12.5 wt.%) (**Fig. 3.15; Table 3.4**).

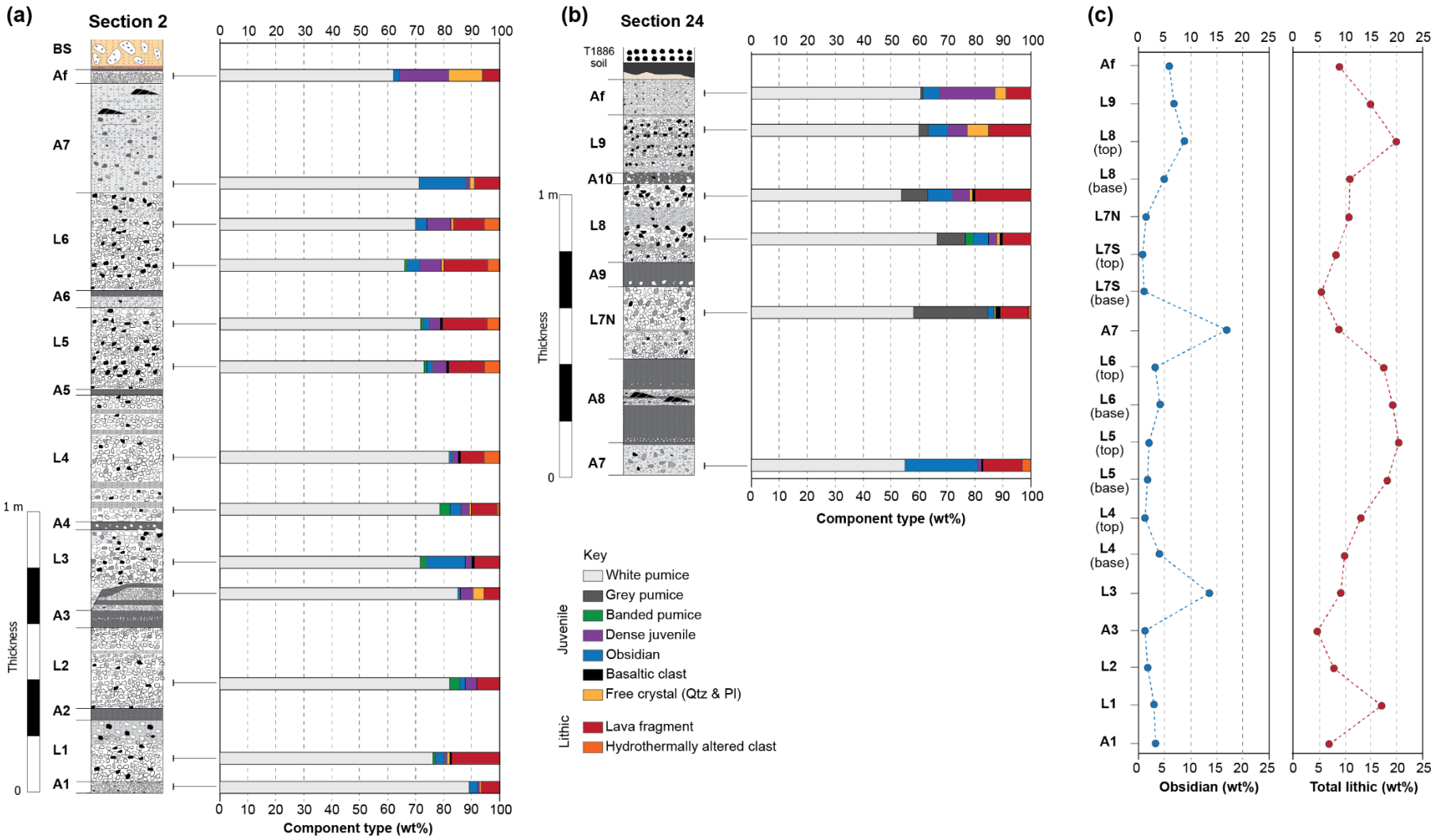

Figure 3.15 – Componentry characteristics of units and variations in the relative abundance of different components with stratigraphic height at reference sections 2 (**a**) and 24 (**b**). In (**c**) are reported the variations in the relative abundance of obsidian and total lithic (lave fragments + hydrothermally altered clasts) through the reconstructed whole pyroclastic sequence.

Table 3.4 – Results of componentry analyses expressed in weight percent of samples collected from coarse-grained units (coarse ash to lapilli units). *H.A.* lithic indicates hydrothermally altered lithic clasts. Deposit type for each unit sampled are abbreviated as follow: (1) massive lapilli deposit; (2) stratified lapilli deposit; (3) massive, coarse ash deposit; (4) massive, fine ash deposit; (5) laterally discontinuous, ash deposit; (6) lapilli-bearing, ash deposit; (7) variably consolidated ash deposit.

Unit	Deposit type	Sample ID	Section	White pumice	Grey pumice	Banded pumice	Obsidian	Dense juvenile	Loose crystal	Basaltic clast	Lava Lithic	H.A. Lithic	Lithic (total)
Af	3	K236	24	61.24	0.00	0.00	5.43	20.13	4.22	0.11	9.04	0.00	9.04
Af	3	K109	2	61.74	0.00	0.00	3.47	16.89	12.58	0.02	5.30	0.00	5.56
L9	2	K235	24	59.93	3.28	0.00	6.94	6.80	7.57	0.51	14.97	0.00	14.97
L8 (top)	2	K233	24	53.64	9.68	0.00	8.97	5.26	0.93	1.20	20.10	0.21	20.32
L8 (base)	2	K232	24	65.70	9.51	4.12	5.34	2.64	1.04	0.55	10.97	0.14	11.11
L7N	1	K229	24	58.36	26.31	0.13	1.50	0.39	0.60	1.92	9.88	0.91	10.79
L7S (top)	1	K247	28	55.96	33.49	0.51	0.69	0.70	0.10	0.48	8.07	0.00	8.07
L7S (base)	1	K246	28	81.08	9.51	1.62	1.17	0.30	0.08	0.45	5.80	0.00	5.80
A7	6	K223	24	56.32	0.00	0.51	26.88	1.64	0.00	0.90	10.98	2.77	13.75
A7	6	K102	2	71.17	0.00	0.31	17.09	1.04	1.45	0.05	8.35	0.54	8.89
L6 (top)	2	K100	2	70.90	0.00	0.30	3.23	9.76	0.67	0.19	13.23	5.84	18.07
L6 (base)	2	K98	2	66.72	0.00	0.05	4.11	8.86	0.64	0.14	14.92	4.57	19.48
L5 (top)	2	K95	2	71.33	0.00	0.43	2.11	3.51	0.73	0.98	15.94	4.97	20.91
L5 (base)	2	K93	2	73.41	0.00	0.55	1.79	4.84	0.07	1.17	13.32	4.84	18.16
L4 (top)	2	K89	2	82.27	0.00	0.38	1.30	2.02	0.23	0.70	7.92	5.17	13.09
L4 (base)	2	K85	2	77.87	0.00	4.18	4.16	2.92	0.74	0.19	8.53	1.40	9.93
L3	1	K81	2	73.06	0.00	2.56	13.98	2.56	0.33	0.68	8.10	0.00	8.10
A3	3	K174	2	85.81	0.00	0.00	1.47	4.13	3.60	0.03	4.78	0.00	4.78
L2	1	K64	2	82.30	0.00	3.83	1.77	3.86	0.21	0.10	7.93	0.00	7.93
L1	1	K60	2	76.34	0.00	1.31	3.11	1.06	0.43	0.67	16.87	0.20	17.08
A1	3	K59	2	88.84	0.00	0.00	3.17	0.72	0.52	0.16	6.60	0.00	6.60

3.5 Interpretations

3.5.1 Eruptive and depositional processes

Within the pyroclastic succession, seven main deposit types can be distinguished for the Kaharoa units (**Table 3.1, Fig. 3.7**), suggesting a range of different transport-depositional processes and eruptive conditions at source. The eruptive and depositional processes emplacing the different units are here interpreted based on the distinctive whole deposit characteristics observed in the field, the units' spatial distribution as well as the quantitative grain size and componentry data. This allows to further constrain the main eruptive styles characterising the explosive phases of the eruption.

Massive and stratified lapilli units (deposit types 1 and 2)

Massive and stratified lapilli units are characterised by good sorting, clast-supported deposit textures, mantle bedding and are formed by pumice clasts as the main component, indicative of fallout deposition from the wind-advected and laterally spreading umbrella region of sustained, convective columns (Sparks et al., 1997; Bonadonna and Philips, 2003). As these types of units are repeated throughout the pyroclastic succession, forming most of the Kaharoa deposit at proximal to medial outcrops, the eruption was therefore dominated by repeated episodes of magma ascent, fragmentation, and development of convective columns. The internal variation in the deposits' characteristics and sedimentary structures of individual lapilli units further suggests that these episodes were characterised by variable evolution in terms of magma discharge (eruptive intensity) and column stability. Massive lapilli units (L1, L2, L3, L7S and L7N) are formed by fine to coarse lapilli deposits and are characterised by minor vertical grain size changes or progressive clast-size grading, and do not display discrete planar beddings (see Houghton and Carey, 2015). These deposit characteristics suggest that the eruptive columns were generally stable; however, magma discharge rate varied during each episode from inception to shutdown of individual columns (e.g., Cioni et al., 2011; Mele et al., 2011; Maeno et al., 2014). On the other hand, stratified lapilli units (L4, L5, L6, L8, L9) are lapilli-dominated deposits characterised by repeated and sharp grain size oscillations, alternating coarser and finer beds. Deposits of unit L6 have also intercalated ash beds having poor sorting (e.g., **Fig. 3.12**) and limited distributions, suggesting deposition from small-volume PDCs, which overlapped with the main fallout lapilli sedimentation. These deposit characteristics of stratified lapilli units suggest instead that magma discharge was overall sustained during each eruptive episode but characterised by repeated, short-time variations, resulting in continuously oscillating eruptive columns, occasionally characterised by partial column collapses (unit L6) (e.g., Cioni et al., 2003; Di Muro et al., 2008; Pardo et al.,

2012; Carazzo et al., 2020). Overall, the sedimentological features of both massive and stratified lapilli units suggest eruptive columns associated with variably unsteady eruptive regimes. This is typical of subplinian eruptive style, as opposed to the quasi-steady eruptive regime typical of Plinian activity (Freundt and Rosi, 1998, Cioni et al., 2015). Subplinian intensity and column heights are also supported by thickness data of fall lapilli units in Sahetapy-Engel et al. (2014) (thickness vs square root of isopach plots) which are comparable to those of other well-studied subplinian events. The eruption, as also suggested by Sahetapy-Engel et al. (2014), might have reached Plinian intensity possibly during the L5 and L7N columns only (their units F and J; **Table 3.1**). Along with these sedimentological features and sedimentary structure, of great interest are also the observed variations, with respect to the deposit type, in the proportion of lithic clasts. Stratified lapilli units are consistently lithic-rich with respect to massive lapilli units (**Fig. 3.15; Table 3.4**). This further suggests that conduit erosion and instabilities of the conduit-vent systems might have contributed to fluctuations in the mass discharge rate and eruptive column behaviours (e.g., Aravena et al., 2018).

Massive coarse ash units (deposit type 3)

The reconstructed stratigraphy of the Kaharoa deposit indicates that the explosive eruption sequence both started and concluded with episodes dominated by ash explosions of much lower eruptive intensity and magnitude compared to the lapilli-producing episodes. This type of activity resulted in the deposition of the coarse ash units A1 and Af. Good to very good sorting, unimodal GSDs, mantle bedding and areal distribution of A1 and Af deposits, indicate that these units were emplaced from low-altitude ash columns. The sedimentological features together with the limited and narrow distribution of unit A1, suggest that A1 resulted from a single, short-lived ash fallout event and that the ash column was sustained (e.g., Miyabuchi et al., 2013). On the contrary, the wider distribution around Tarawera of unit Af (**Fig. 3.8**) possibly suggest fallout and accumulation of ash from repeated, discrete ash columns (e.g., D'Oriano et al., 2011). In this case, ash fallout occurred over prolonged times, during which individual ash plumes were produced and dispersed under different wind conditions. In addition to these field-based interpretations, the steep increase in the relative abundance of both dense juvenile clasts and loose crystals in unit Af (**Fig. 3.15**), further suggest and origin of the Af ash plumes from perhaps Vulcanian-type explosions (e.g., Bonadonna et al., 2002; Miwa et al., 2013; Clarke et al., 2015). This Af activity can be related to the initiation of the dome extrusions during the final phases of the eruption (Nairn et al., 2001) where an increase in the erupted magma crystallinity is also observed (40-60% crystallinity of lava dome products, Ashwell et al., 2015, 2018). Very proximal deposits of unit Af described in Nairn et al. (2001) further imply that ash fallout activity was also accompanied by the generation of near-vent PDCs.

Massive fine ash units (deposit type 4)

Lapilli units are often separated in the pyroclastic succession by massive fine ash beds (units A2, A5, A6, A9), having F2 between ~40 and 65 wt.%. The contacts between massive fine ash units and underlying lapilli units are usually gradual, marked by cm-thick beds of poorly sorted fine lapilli mixed with medium to fine ash (e.g., **Fig 3.6g**), indicative of uninterrupted fallout deposition. According to these sedimentological features and stratigraphic positions, massive fine ash units are related in this work mainly to the delayed sedimentation of fine ash particles which remained suspended in the atmosphere after the parental sustained columns had deposited the preceding lapilli units (a "co-Plinian" origin, e.g., Fierstein and Hildreth, 1992; Barberi et al., 1995; Mele et al., 2011). Fine ash settling likely commenced during the waning of the eruptive columns and continued for prolonged times after the eruptive activity ceased (see also **Section 3.6.2**). Along with a main "co-Plinian" origin, the bimodal GSDs obtained for these massive fine ash units (**Fig. 3.12**) possibly implies additional prosses may have contributed to the injection of ash particles in the atmosphere and later sedimentation. An additional suggested process is here related to events of ash venting that may have followed the subplinian columns, comparably to those documented during other explosive-to-dome-forming rhyolitic eruptions worldwide (e.g., Bonadonna et al., 2002; Schipper et al., 2013; Black et al., 2016). These interpretations on the eruptive and depositional mechanisms of the massive fine ash units are preferred to the exclusively co-PDC origin proposed by Sahetapy-Engel et al. (2014). Supporting evidence are (i) no PDC deposits were observed within these stratigraphic intervals (i.e., A2, A5, A6, A9) at any available proximal outcrops (cf. units A4, A10 and A11 in deposit type 5) and (ii) results from grain size analyses are not directly supportive of sedimentation from exclusively co-PDC plumes. The bimodal GSDs of these units markedly differ from the characteristic unimodal GSD obtained for co-PDC deposits of documented eruptions (Engwell and Eychenne, 2016 and reference therein). Instead, ash deposition from suspected co-PDC plumes generated during the sustained columns may have additionally contributed to the grain size bimodality of the massive fine ash units.

Composite coarse and fine ash unit (alternation of deposit types 3 and 4)

At one stratigraphic interval the pyroclastic succession comprises a complex planar bedded ash deposit identified as unit A3, which shows both features common to deposit types 3 and 4. This deposit overlies unit L2 in the S sector. It is formed by the alternation of discrete massive fine ash beds and coarse ash beds (**Fig. 3.6f** and **g**). In earlier studies it was interpreted as being related to the very proximal deposition from PDCs and medial co-PDC ash fall in the S sector, further correlated to unit A8 deposits in the N sector (see **Section 3.6.1**). Stratigraphic relationships and sedimentological features presented in this work are however suggestive of different eruptive and

depositional processes. The A3 fine ash beds display deposit structure, distribution, and GSD parameters identical to those of units A2, A5, A6, A9 in the deposit type 4 group, suggesting slow settling of ash suspended in the atmosphere from the preceding L2-column. On the other hand, the A3 coarse ash beds shows deposit structure, distribution, and GSD parameters similar to those of units A1 and Af in the deposit type 3 group, supportive instead of fallout events related to ash explosions. These coarse ash beds therefore suggest that fine ash settling after the L2-column was overlapped by deposition of coarse ash from renewed eruptive activity, producing low-altitude ash columns (e.g., Wilson, 2001). In addition to these processes, the top few-cm of unit A3 are characterised, up to <10 km from the vent, by low-angle cross laminations and poor sorting further suggesting that the final, top bed of the unit was transported and deposited from a small-volume PDC.

Laterally discontinuous ash units (deposit type 5)

At few sections, typically at ~5 km from the vent, thin (few-cm-thick) discrete massive ash beds (units A4, A10 and A11) have been observed both interlayered between lapilli units (between L3 and L4, and between L8 and L9) and underlaying coarse ash units (Af at section 18), showing different deposit characteristics compared to other thin ash beds (cf. deposit type 4) in the stratigraphy. These beds vary from moderately to poorly sorted and have wide unimodal GSDs, with modes in the medium ash size range, F2 <25wt.% and contain scattered lapilli clasts. They typically display lateral thickness variation at the outcrop scale and have a narrow dispersal (**Fig. 3.8**). Giving the whole deposit characteristics and restricted areas of deposition these units are related in this work to the transport and deposition from small-volume dilute PDCs. PDCs possibly generated at these intervals in the eruption sequence from either column instabilities and partial collapses of sustained columns (e.g., unit A4 and A10) similar to those inferred for unit L6, or from ash explosions (e.g., unit A11).

Lapilli-bearing ash unit (deposit type 6)

Massive to cross-stratified, m-to-dm-thick, ash-dominated deposits, bearing pumice lapilli clasts were observed in the pyroclastic succession only within unit A7, emplaced after the SE dispersed sequence of fall lapilli units L1-L6. Deposits of unit A7 are widespread around Tarawera and consists, in proximal sites (e.g., sections 18 and 28, **Fig. 3.4**), of repeated beds varying in grain size and structure from thick massive lapilli-bearing, matrix supported beds to thin massive and cross-laminated ash beds (**Fig. 3.6i**). The unit varies abruptly in thickness away from the vent, from 1-2 m in proximal sites to tens of cm in medial areas where the unit consists of a single faintly stratified to massive ash deposit. The deposit characteristics of unit A7 indicate emplacement from PDCs with variable clast concentrations, from concentrated (depositing the matrix supported lapilli-bearing beds) to dilute (depositing ash beds) in proximal sites, and

progressively dilute farther from the vent. Cross-lamination within the ash beds indicates turbulent transport-deposit mechanics, that is consistent with PDCs. The presence of charcoal indicates that the PDCs were hot enough (>250-300°C) to effectively carbonised the vegetation (e.g., Sawada et al., 2000; Pensa et al., 2019). The vertical alteration of beds in proximal sites further indicate that A7 was deposited in response to either (i) multiple, concentrated to dilute, PDCs or (ii) pulses from a single PDC (e.g., Calder et al., 2000; Sulpizio and Dellino, 2008; Sulpizio et al., 2010; Lucchi et al., 2018). In addition, the significant increase of obsidian fragments passing from units L6 to A7 (**Fig. 3.15**), further suggest that the emplacement of unit A7 was not related to the total collapse of the preceding L6-column (e.g., Gillies et al., 2020), but comprises a later discrete eruptive episode. This is further supported by the evidence of a short time break between unit L6 and A7 (see **Section 3.6.3**). Finally, the eruptive processes generating the A7-PDCs are here ascribed to the upwelling at vent and continuous collapse of the erupted gas-particle mixture ("boiling-over" or "pyroclastic fountaining"; Clarke et al., 2002; Branney and Kokelaar, 2002; Sulpizio et al., 2014).

Variably consolidated, ash deposit (deposit type 7)

Further eruptive and depositional processes are interpreted for unit A8 considering its distinctive deposit features within the pyroclastic succession. The unit vertically alternates beds of consolidated ash with very high fine ash content (up to 80 wt.%) and unconsolidated beds of coarse ash. Internally, these beds show both massive structures and cross-stratification, while the whole unit displays discontinuous thickness variation at the outcrop at a few sites <10 km from the vent. These characteristics suggest a dominant transport and deposition of the pyroclast from dilute PDCs generated by possibly minor ash explosions. Beyond 10 km from the vent, where the unit becomes massive, attaining constant thickness at the outcrop scale, deposition was possibly dominated by fallout from concurrent ash plumes. Moreover, the characteristic nature of the A8 deposits with cohesive, variably consolidated ash beds, fine ash content up to 80 wt.% and presences of scattered ash aggregates within the A8 base, is suggestive of variable degree of explosive magma-water interactions in the generation of A8-PDCs (e.g., Barberi et al., 1989; Cole et al., 1995; Giordano, 1998; Houghton et al., 2003; Ellis and Branney, 2010; Austin-Erickson et al., 2011). Although these characteristics do not unequivocally denote phreatomagmatic activity (see White and Valentine, 2016), their combination, together with the differences in sedimentological features of A8 deposits with other ash beds in the pyroclastic succession (e.g., median grain size and GSDs of A8a; **Fig. 3.12, 3.11 and Table 3.3**), suggest a likely phreatomagmatic origin.

3.5.2 Reworking and resedimentation of pyroclastic units

Within the investigated outcrops in medial area in the N sector, the pyroclastic succession is capped by fine-grained, massive to diffusively stratified deposits, showing inconsistent thinning behaviour away from the vent. These deposits occur along the Tarawera river and Waiaute stream floodplains and are interpreted as resedimented volcaniclastic beds of primary Kaharoa deposits. Two types of resedimented volcaniclastic deposits, RV1 and RV2, have been recognised in the field and described in **Section 3.4.1.3**. The occurrence of RV1 deposits confined to topographical lows and floodplains produce an apparent overthickening of the pyroclastic succession away from the vent (**Fig. 3.11**), suggesting syn-eruptive, water-induced resedimentation of primary Kaharoa beds. Particularly, proximal L9 deposits appear to have been significantly interested by remobilisation as result of possibly fluvial and/or torrential rain activity, and downstream resedimentation and accumulation. On the other hand, the RV2 deposit, observed only at section 21 (**Fig. 3.4; Fig. 3.11**), directly overlies a thin and patchy black peat horizon, suggesting post-eruptive resedimentation of pyroclastic beds. The deposit features and location of RV2 deposit within the floodplain suggest overbank deposition originated from a suspected hyperconcentrated mass flow event (e.g., Pierson, 2005) along the Tarawera river channel. The presence of a great variety of clasts within the RV2 deposit further suggest that both Kaharoa and pre-Kaharoa deposits were remobilised during this event. The emplacement of RV2 deposit might also be correlated to the breakout flood event of Lake Tarawera suggested by Hodgson and Nairn (2005) after the main explosive phases of the of the Kaharoa eruption had ceased.

Localised minor reworking appears to have occurred on the top of different ash units in the succession (e.g., unit A2, A11, Af) producing cm-size scours and/or finely laminated, mm-thick layers. The local scouring and reworking resulted from the action of surface running water onto the exposed, deposited pyroclastic bed at different intervals during the eruption sequence (Cutler et al., 2018). Wind remobilisation of dry ash despots (Dominguez et al., 2020) is instead further suspected to have occurred, possibly affecting for prolonged times the Af deposits capping the pyroclastic succession at several sites.

3.5.3 Key stratigraphic relationships and chronology of depositional events

Due to an overall bilobated distribution of the Kaharoa fall units (see also Sahetapy-Engel et al., 2014; **Fig. 3.3**) and the paucity of very proximal outcrops where the south- and north-directed units might have overlapped, crucial stratigraphic relationships between the two main areas of deposition are provided by using a combination of marker units (A7, L7S and L7N). The lateral

correlation and distribution of unit A7 suggests that deposition of north-directed units occurred later in the eruption sequence. Unit A7 is a very distinctive m-to-cm-thick PDC deposits within the pyroclastic succession, characterised by evident cross-stratifications and by a large amount of coarse obsidian fragments. The main area of deposition of unit A7 is directly S from the vent (e.g., sections 18, 14 and 2), with distal massive facies observed >10 km from the vent (e.g., sections 16 and 4) in the same direction (**Fig. 3.8**). The stratigraphic position of unit A7 is well constrained in this area as the unit is always found on top of unit L6, while underlies unit Af and BAF deposits, where preserved. Deposits of massive to cross-stratified, ash-dominated beds with abundant obsidian fragments, occur also ~5 km east from the vent at sections 27 and 28 (**Fig. 3.4**). These deposits are correlated to unit A7, due to the very similar sedimentological and lithological characteristics. At these sites, unit A7 directly overlies a 60-cm-thick sequence comprising A1 to A5 units, while underlies unit L7S (**Fig. 3.11**). In addition, a 10-cm-thick, massive, poorly sorted ash deposit with very abundant obsidian fragments (27 wt.%) has also been observed 7-8 km north from the vent (sections 24, 31 and 32. **Fig. 3.11**). This ash bed forms the base of the Kaharoa deposit at these northern localities, where it underlies unit A8 (**Fig. 3.5c**). This deposit is interpreted to represent a north-dispersed, distal equivalent of unit A7, indicating that PDCs associated with unit A7 were widespread, reaching the N sector at this time of the eruption.

Further evidence of the progression of depositional events from south to north during the eruption are also provided by the distribution and componentry of the fall units L7S and L7N, which enable to place more stratigraphic constrains in correlating deposits in the S and N sectors. Both units have very similar deposit features (deposit type 1, **Table 3.2**) and a distinctive high content of grey pumice clasts (up to ~30 wt.%) (**Table 3.4**). Unit L7S has an ESE dispersal (**Fig. 3.9**) and stratigraphically consists of the topmost lapilli units deposited in the S sector, where it directly overlies unit A7 in proximal E sites (e.g., section 28) and units L5 or A6 in medial ESE sites (e.g., sections 5, 19 and 25; L6 is not preserved at these locations) (**Fig. 3.11**). On the other hand, unit L7N is dispersed N from the vent (**Fig. 3.9**), consisting in the lowermost lapilli unit deposited in the N sector, where it directly overlies unit A8. The characteristic pumice content of these units (white and grey pumice clasts) not observed in earlier lapilli units in the S sector, together with the stratigraphic position of L7S and L7N at the investigated outcrops, further indicate that the north-directed units were deposited later in the eruption sequence. Stratigraphic correlations suggest that unit L7S and L7N were deposited after unit A8, with L7S interpreted to have shortly preceded unit L7N (**Fig. 3.11**), signalling the initiation of the general change in the directions of prevailing winds and associated fallout depositions from the S to the N sectors.

Deposits of L7S and L7N are stratigraphically ascribed in this work to two separate units and depositional events resulting from the formation of two discrete eruptive columns, occurring one after the other (e.g., Sarna-Wojcicki et al., 1981; Cronin et al., 1998; Watt et al., 2008). This

interpretation (i.e., two columns at different times affected by two different dominant wind directions) is here preferred as opposed to the scenario of continuous sedimentation of L7S and L7N pyroclasts from one single and continuously sustained eruptive column affected by a simultaneous shift in wind direction from ESE to N (i.e., one column under an on-going change in atmospheric conditions and wind pattern) (e.g., Pardo et al., 2012; Houghton et al., 2014). The reason for separating the two deposits into two stratigraphic units, although having similar sedimentological and lithological features, is supported by the fact that, during fieldwork, deposits having L7 characteristics have not been found at intermediate eastern to north-eastern proximal and medial localities.

3.6 Discussion

3.6.1 Comparison with previous stratigraphic reconstructions

The stratigraphic reconstruction achieved in this work, aided by the identification and correlation in the field of units with distinctive lithological features (obsidian-rich unit A7; unit L7S and L7N having both white and grey pumice clasts), indicates that the eruption started with explosive activity depositing pyroclastic beds first in the S sector, followed by deposition in the N sector. This reconstruction is in overall agreement with previous studies (Nairn et al. 2001; Sahetapy-Engel et al. 2014). The stratigraphy here presented differs however from the previous ones in the following stratigraphic intervals.

A3 and A8 intervals. Nairn et al. (2001) and Sahetapy-Engel et al. (2014) suggested that the ash units A3 and A8 (units C and Cpdc in their works; **Table 3.1**) deposited in the S and in the N sectors, respectively, correlates to the same stratigraphic interval. Their interpretations indicate deposition of these units from both PDCs and associated co-PDC ash fallout (according to their reconstructions, unit A8 was emplaced from northward-directed PDCs, while unit A3 was emplaced from additional PDCs and from co-PDC ash fallout in the S sector related to the A8-northward-directed PDCs). In this work, the two units represent two distinct times in the eruption sequence, based on both the contrasting deposit characteristics of A3 and A8, and based on the lateral correlation of unit A7 in the S and N sector. The sedimentary structure of the units A3 and A8 are markedly different suggesting two unrelated origins at source. Unit A3 is a planar bedded deposit alternating coarse ash and fine ash beds and shows mantle bedding (only the top few cm of A3 show low-angle cross laminations), while A8 consists of very fine ash beds displaying cross

stratification and discontinuous thickness variations at the outcrop scale (**Section 3.4.2**; **Fig. 3.6**; **Fig. 3.7**). In addition, grain size data (median and sorting coefficient) and the GSDs of beds from units A3 and A8 differs (cf. **Figs. 3.12** and **3.13**), suggesting different main transport/depositional processes. Furthermore, compelling evidence for a co-PDC origin of some fine ash beds in A3 (e.g., unimodal GSD) have not been observed (see also **Section 3.5.1**), excluding a tentative correlation between the two units based on a combined PDC and co-PDC transport and deposition in different sectors.

A7 interval. Nairn et al. (2001) and Sahetapy-Engel et al. (2014) suggested that the PDCs emplacement forming unit A7 (Hpdc in their work) occurred simultaneously with lapilli-fallout from developing sustained convective columns (unit H fall in their work). This interpretation was suggested based on the presence of interbedded lapilli layers within unit A7 PDC deposits to the SE (their section K524, close to section 17 in this work) and to the N (their section K185, equivalent to section 24 in this work). Sahetapy-Engel et al. (2014) mapped these lapilli deposits as unit H_{SE} (dispersed SE) and H_{NW} (dispersed NW) in their stratigraphy. At the available outcrops investigated during this study, no compelling evidence were found to support a coeval PDC and lapilli fallout emplacement. The lapilli layers found in proximal A7 deposits typically do not maintain lateral continuity and occur instead as lenses. Although some of these lapilli layers might have been generated from explosions and/or times during which the ejected particle-gas mixture at vent reached condition for buoyancy and convection forming short-lived plumes, it is here suggested that a sustained column depositing lapilli to the ESE occurred only later in the eruption (unit L7S) after the emplacement of A7. These fall lapilli deposits (unit L7S) are found to overlie PDC deposits of unit A7 (e.g., section 28). Fallout of lapilli from an additional column to the NW (unit H_{NW} in Sahetapy-Engel et al. 2014) during A7 emplacement appear to have not occurred at any available N outcrops (e.g., sections 24, 26, 31; cf. the stratigraphic section K185 of Sahetapy-Engel et al. 2014 with section 24 this work) but cannot be excluded due to the lack of medial-to-distal sites to the NW (see Sahetapy-Engel et al. 2014).

L7N to L9 interval. Sahetapy-Engel et al. (2014) defines four to five lapilli fall units dispersed from individual columns in the N sector (unit I, J, K_{NE} + K_{NW} and L). Based on field evidence, the lapilli deposits in the N sector have been instead here divided into three lapilli fall units (**Table 3.1**). Unit L7N comprises two lapilli beds, a finer at the bottom and coarser one in the upper part of the unit, which tentatively consist of unit I and J of Sahetapy-Engel et al. (2014). These beds have been here grouped together due to their similar deposit features and matching distribution, and since no evidence of time break have been found between the two beds. Further differences with previous proposed stratigraphy lie in the lateral distribution of unit L7N, which in Sahetapy-Engel et al. (2014) (their unit J) is interpreted to extend from NW to NE sites (e.g., section 22). Here unit L7N is proposed to have mainly a N dispersal, while no significant deposition occurred

to the NE (**Fig. 3.11**). In contrast with Sahetapy-Engel et al. (2014), the lapilli bed at the base of most of the NE outcrops (e.g., sections 20, 21, 22, 29) is laterally correlated to unit L8 due to its distinct high lithic and low grey pumice clasts content. Finally, some additional differences with previous works regards the two lapilli units, L8 and L9, consisting in units K and L of Sahetapy-Engel et al. (2014). It is here argued that the dm-thick NE lobe of unit K of Sahetapy-Engel et al. (2014) might have been affected by syn-eruptive reworking of primary Kaharoa beds along the Tarawera river valley and Waiaute stream (**Fig. 3.4**) (e.g., increasing in thickness away from the vent; see RV1 deposit in **Section 3.5.2**).

3.6.2 Constraints on intra-eruption time breaks

No historical written records are available describing the type of activity of the Kaharoa eruption and the timing of the eruptive events. Different lines of evidence from field observations suggest that magma discharge was episodic, resulting in repeated, discrete explosive episodes, separated by short eruptive time breaks of three different proposed time-scales (**Table 3.5**) (e.g., Wilson, 2001; Heinrich et al., 2020). Evidence of the occurrence of short pauses and their possible lengths are here discussed based on the type of contacts between units and delayed fine ash deposition, presence of erosional surfaces and thin oxidized pyroclastic horizons. Furthermore, later in this section, fall units' dispersal and wind patterns are considered to aid in the discussion of time break in the eruptive activity.

Gradual contacts – 3rd order time break

The types of contacts between units vary through the pyroclastic succession from sharp to gradual (**Fig. 3.7**). Gradual contacts occur typically (i) between fall coarse ash units and fall lapilli units (e.g., A1-L1) and (ii) when fall lapilli units are separated by laterally discontinuous, ash units (e.g., L3-A4-L4 and L8-A10-L9). These gradual contacts are suggestive of no to very limited eruptive time breaks (few hours at most) as no evidence of erosion/reworking is observed (**Table 3.5**). Gradual contacts occur in addition (iii) when fall lapilli units pass vertically into massive fine ash units suggesting continuous fallout sedimentation between these units (see also **Section 3.5.1**).

Sharp contacts and delayed ash settling – 2nd order time break

Sharp contacts occur mostly between massive fine ash units and overlying lapilli units (e.g., A2-L2, A5-L5, A6-L6, A9-L8) and are suggestive of the occurrence of short pauses in pyroclastic deposition. Massive fine ash units are interpreted here to result from the delayed sedimentation of fine particles produced during the earlier convective columns, which remained suspended in the atmosphere for longer times before settling (**Section 3.5.1**). The fine ash fallout emplacing

units A2, A5, A6, A9, was the sole depositional process occurring as deposit features do not show sign of contemporary eruptive activity during these times (cf. unit A3). Fallout of medium to fine ash can accumulate on the ground surface forming discrete mm- to cm-thick deposits over several hours to days according to (i) the settling behaviour of fine ash particles and atmospheric conditions, (ii) intrinsic characteristic of the ash particles (e.g., shape and density) and to (iii) the height reached by the parental eruptive column (e.g., Bonadonna et al., 1998; Dellino et al., 2005; Folch,, 2012; Dioguardi et al., 2017; Saxby et al., 2018; Rossi et al., 2021). Sedimentation times of individual Kaharoa fine ash beds have been estimated to vary between 6 and 20 hours by Sahetapy-Engel et al. (2014), using tephra accumulation rate from low-altitude, transient Vulcanian plumes at Soufrière Hills volcano, Monserrat (Bonadonna et al., 2002), to mirror their interpreted co-PDC plumes heights. This dataset provides a first reference for the minimum duration of these "2nd order" pauses in the eruptive activity. Also, it is worth to point out that the following lapilli-producing eruptive episode likely did not begin abruptly after the several hours necessary to accumulate the underlying fine ash unit, since lapilli clast layers are not interbedded within fine ash deposits at any outcrops. Therefore, an additional short hiatus (further hours or days) may have occurred before the deposition of the overlaying lapilli unit (**Table 3.5**). Occurrence of mm-thick, laminated layers within the top of unit A2, indicative of minor reworking, further support that additional time elapsed between the fine ash units and the overlaying lapilli units.

Erosive surfaces and oxidized ash layers – 1st order time break

Prolonged time breaks spanning from a week to possibly a few months might have occurred only at a limited number of intervals during the eruption sequence: between units A3 and L3, between units L6 and A7 and between units Af and BS. The A3-L3 contact is characterised for example by evident erosive surfaces consisting of localised dm-size erosional gullies, intersecting unit A3 for its entire thickness, and by common cm-size scours along the whole units' boundary. The erosional gullies at section 2 have a step-wise profile, perhaps indicating multiple incisions by running surface water (**Fig. 3.5b; Appendix A**). Similar dm-size erosional gullies have also been found in the contact between unit L6 and A7 (Sahetapy-Engel et al., 2014), suggesting similar erosive processes and timescales. Although these characteristics do not denotate unequivocally an extensive pause in the eruptive activity (months), these are suggested to indicate longer time break (a week) compared to other pauses in the eruptive activity identified at the contacts with other units in the succession (**Table 3.5**). This is further supported by the presence of localised oxidized laminae on the top bed of unit A3 (**Fig. 3.6a** and **g**), suggesting time to allow local chemical weathering (e.g., Pistolesi et al., 2017). In addition, at outcrops where the contact between unit BS and underlying unit Af is exposed (e.g., sections 18, 14 and 2. **Fig. 3.4**), a thin, mm-to-cm-thick, oxidized ash layer of red colour separates the two units (**Fig. 3.6i**). This oxidized

laterally continuous thin layer possibly indicates that a prolonged hiatus (weeks to few months) in the deposition occurred before emplacement of the BAF deposits at least in the S sector.

Table 3.5 – Summary of the suggested intra-eruption time breaks and their lengths during the Kaharoa eruption.

Intra-eruption time break	Inferred duration	Evidence	Between units
1st order	Week to few months	Sharp contact between units; dm-size erosional gullies; thin oxidized pyroclast horizon.	A3 and L3; L6 and A7; Af and BS
2nd order	Several hours to days	Sharp contact between units; minor erosion and reworking; delayed fine ash settling from earlier sustained eruptive column.	A2 and L2; A5 and L5; A6 and L6; A7 and L7S; A7 and A8; A8 and L7N; A9 and L8; L9 and Af
3rd order	No time break (abrupt onset of later activity or continuous sedimentation) to time break of few hours	Gradual contact between units; change in type of eruptive activity and depositional processes, and/or main direction of deposition. No evidence for longer time breaks.	A1 and L1; L1 and A2; L2 and A3; L3 and A4; A4 and L4; L4 and A5; L5 and A6; L7S and L7N; L7N and A9; L8 and A10; A10 and L9; A11 and Af

Dispersal of fall units and wind patterns

Considerations on the prevailing wind conditions and main dispersal axes of deposition of the Kaharoa fall units during the eruption sequence can provide further insights to constrain the length of the suggested prolonged 1st order time breaks. The analysis of the wind profiles above Tarawera has been conducted by several authors to model the potential impact of tephra fall from explosive intra-caldera eruptions at Okataina (e.g., Bonadonna et al., 2005; Jenkins et al., 2008; Thompson et al., 2015) as well as to gain insights into the tephra dispersal dynamics of the Kaharoa fall units (Sahetapy-Engel et al., 2014). These analyses assumed that the average wind conditions reported in recent years above Tarawera (i.e., wind speed and direction and their variations with altitude as well as seasons of the year) are comparable to those at the time of the eruption (1314±12 CE, about 700 years ago). Winds above Tarawera, as well as at other active volcanoes in the North Island of New Zealand, blow dominantly to the east (Rhoades et al., 2002; Hurst and Smith, 2010). Wind data reported in both Bonadonna et al. (2005) and Jenkins et al. (2008) further indicate that at altitudes >20km above sea level, seasonal variation in the average wind direction above Tarawera are significantly more pronounced than those observed at lower altitudes. Moreover, the average wind data of Bonadonna et al. (2005), sampled from a 3-year period (Kalnay et al., 1996), indicate that ~50% of wind profiles are characterised by prevalent winds blowing between

0° (North) and 90° (East) and ~40% between 90° (East) and 180° (South), while only 3% have prevailing winds blowing to the west. This is consistent with the distributions of the Kaharoa fall deposits, where individual fall units have been predominantly dispersed in the SE and no deposition is observed to the west of Tarawera. The restricted variation in dispersal axis of fall lapilli units L1 to L6 to the SE suggest that eruptive columns developed under consistent wind conditions (Sahetapy-Engel et al., 2014). Although winds above Tarawera can dominantly blow between 90° and 180° as showed by Bonadonna et al. (2005), such stable wind conditions, with winds blowing consistently SE, can unlikely be maintained for long periods of times (few months). This is due to seasonal variations in the atmospheric conditions and/or due to the occurrence of sudden changes in the weather regimes (Kidson, 2000). This can yield important insights also for estimating the maximum length of the pauses in eruptive activity between consecutive fall units showing very similar dispersal. In fact, to allow a consistent dispersal and fallout deposition in the same confined area, it is unlikely that pauses between these fall units were of long duration (e.g., months). Therefore, considering the inferred 1st order time break between units A3 and L3 based on field evidence at the units' boundary, the pause in eruptive activity after A3 might have not been longer than a week. This timeframe reasonably allows continuation of tephra dispersal under the same stable atmospheric conditions with prevailing SE directed winds.

3.6.3 Insights into the vent system

At least seven aligned vents located along the Tarawera vent lineament and defining and 8-km-long fissure system (**Fig. 3.2**), were inferred by Nairn et al. (2001) to have sourced the Kaharoa eruption. Effusive vents are well constrained by the surface alignments and geomorphology of lava domes (**Fig. 3.2**). On the other hand, due to the scarcity of very proximal pyroclastic outcrops, vent locations for individual pyroclastic units are difficult to reconstruct. Isopach and isopleth maps of Sahetapy-Engel et al. (2014) for the medial-to-distal fall lapilli units are consistent with an overall vent area from Tarawera dome to Wahanga dome (vents 2 to 6 in **Fig. 3.2**). Nairn et al. (2001), suggested vent location beneath Crater dome (vent 3, **Fig. 4.2**) for the south dispersed lapilli units based on impact craters of ballistic blocks and fallen trees alignments at a very proximal section south from Ruawahia dome. More uncertain is the vent location(s) for the north dispersed fall units, with vents suggested around Wahanga dome (Nairn et al., 2001; Sahetapy-Engel et al., 2014).

The temporal changes in componentry of the deposits and stratigraphic relationships presented in this work can provide further insights into the evolution of the Kaharoa conduit-vent system. The relative proportion of lithic fragments oscillate throughout the entire pyroclastic succession (**Fig.**

3.15; Table 3.4). This waxing and waning in lithic content are indicative of continuous instabilities and modifications of the conduit-vent system (e.g., Macedonio et al., 1994; Aravena et al., 2018). Repeated collapses of the conduit-vent walls, and subsequent erosion/clearing and re-establishment of the shallow conduit-to-vent pathways (e.g., Taddeucci and Wohletz, 2001; Jurado-Chichay and Walker, 2001; Carey et al., 2007) are here interpreted to account for the increase in lithics at repeated stratigraphic horizons (e.g., L5-L6, L8-L9). These shallow conduit instabilities likely favoured the opening of new and closely spaced vents along the fissure.

The distribution and stratigraphic correlations of units among the surveyed outcrops indicate a progression of the fallout deposition from south to north, consistent with a change in the main wind pattern during the eruption, also noted by previous studies. Deposition of fall lapilli units in the N sector is however preceded by the emplacement of the PDC units A7 and A8. Deposits of unit A7 are widespread around Mt Tarawera (**Fig. 3.8; Fig. 3.11**), with proximal very thick deposits (up to 2 m) directly south from the vent (e.g., section 18, **Fig. 3.4**), suggesting vents around Tarawera and Crater domes (vents 2 to 3 in **Fig. 3.2**). However, thick (<1m) deposits of this unit also occur at proximal east sites (e.g., sections 28 and 27, **Fig. 3.4**), further suggesting that the active vent area during deposition of unit A7 possibly extended up to Ruawahia crater (vent 5 in **Fig. 3.2**). Following unit A7, the eruption continued with the deposition of unit A8. The distribution and thickness of A8 PDC deposits directed to the N and NE, suggest instead that the unit was sourced from explosions at Wahanga and/or Northeast crater (vents 6 and 7 in **Fig. 3.2**), marking a more prominent shift of vent locations to NE positions.

Although a laterally continuous linear "unzipping" of the 8-km-long vent system is not evident by any field and/or componentry data (cf. Holohan et al., 2008; Geshi et al., 2019; Rowe et al., 2021), the occurrence and distributions of units A7 and later A8 suggest an overall migration of the explosive vents active during the eruption from SW to NE. Following A8, explosive activity might have resumed at more SW area along the vent system (e.g., Smith and Houghton, 1995; Houghton et al., 2010), however since no significant increase in lithic clasts is observed in the later units L7S and L7N, eruptive activity is here suggested to have continued on the NE portion of the vent system (possibly around Ruawahia and/or Wahanga). Overall, earlier units (A1 to L6, including A7) are suggested to have been erupted from a SW vent area around Tarawera domes to Ruawahia crater (vent 2 to 5), and later units (L7 to L9) erupted from a NE vent area around Ruawahia crater and Wahanga domes (vents 5 and 6). This is further supported by the fact that the observed deposits for unit L7S, stratigraphically after unit A8, have maximum observed thickness at proximal eastern sites (section 28, **Fig. 3.4**), indicating a more probable NE vent area, compared to the inferred vent locations for earlier units.

3.6.4 Evolution of the eruption

Based on the combination of stratigraphic correlations, identification of time breaks in the eruptive activity and temporal variation in eruptive styles, the evolution of the eruption can be envisioned as the progression of eleven discrete eruptive episodes (Episode I to XI) grouped into six main eruptive phases (Phase A to F) (**Table 3.6**).

Phase A – Episodes I and II (Units A1, L1, A2, L2, A3) – The Kaharoa eruption started with a low-intensity explosive activity characterised by the deposition of unit A1 from a low-altitude, short-lived, sustained ash column (Episode I). The low proportion of lithic clasts within A1 deposits suggest limited excavation/enlargement of the conduit-vent system during the onset of the eruption. Following deposition of A1 to the SE, the eruption rapidly escalated with the development of the first lapilli-producing, sustained, convective column, which dispersed L1 to the SSE. Units A1 and L1 are grouped in the same Episode I as no evidence of time break is observed (3rd order). The steep increase in the proportion of lithics passing from A1 to L1 deposits indicate that a major event of shallow conduit-vent establishment took place only during the development of the L1-column. The basal "blast and block fall" deposit in Nairn et al. (2001), at 1.3 km south of Crater dome (their "Koa Gully" section), might be linked to very proximal facies of L1. Units A1 and L1 were likely sourced from a vent area around Tarawera dome to Ruawahia crater. During the waning of the L1-column, fine ash suspended in the atmosphere initiated to settle, with slow fine ash settling continuing for longer times after the cessation of the column. Accumulation to the ground formed unit A2. Following a short time break (2nd order), coinciding with the slow fine ash deposition and minor reworking on the top of A2 deposits, the eruption restarted with the development of a second sustained, convective column, which dispersed L2 fall deposits to the SE (Episode II). Grain size characteristics and dispersal suggest that the L2-column was of higher intensity compared to the preceding L1-column. In addition, the relatively low lithic content of unit L2, suggest that no significant modification of the conduit-vent system occurred during this episode, which likely was fed from the same A1-L1 vent. Sharp contact between L2 and overlying A3 units suggest that the L2-column ceased abruptly, and the fine ash suspended in the atmosphere began to settle forming the base of A3. The slow settling of fine ash was however interrupted shortly after by a renew in the eruptive activity characterised by the production of minor, short-lived, sustained ash columns. The coeval sedimentation of fine ash from the preceding L2-column and coarse ash from the resumed eruptive activity formed unit A3. This episode and Phase A concluded with the emplacement of a small-volume dilute PDC (top of A3).

Phase B – Episodes III, IV and V (Units L3, A4, L4, A5, L5, A6, L6) – After a period quiescent of the order of possibly a week (1st order), marked by erosive surfaces between unit A3 and L3

and oxidized horizon on top of A3, the eruption resumed with Phase B, characterised by three explosive episodes. The first episode (Episode III) consisted in the development of two high-intensity convective columns, depositing L3 and L4 fall deposits to the SE. A small-volume dilute PDC (unit A4), possibly generated during the waning of L3-column or at the onset of L4-column, separates the two lapilli units in the field. Time break between the two columns is thought to have been very short (few hours; 3rd order). After deposition of unit L4, delayed fine ash settling (unit A5) began, marking a short time break (hours to days; 2nd order) before the eruption resumed. The eruption continued with two individual episodes, depositing L5 (Episode IV) and L6 (Episode V) to the SE, separated by a short time break (hours to days; 2nd order) during which the fine ash unit A6 was deposited. Phase B was characterised by the repeated alternation of more stable columns (L3) to continuously oscillating (L4 and L5) and, at times partially collapsing columns (L6). Componentry characteristics suggest that Phase B started with the disruption of a suspected degassed magma body in the shallow conduit (e.g., Rust and Cashman, 2007; Davì et al., 2011; see **Chapter 5**) as indicate by the steep increase in obsidian content within unit L3, compared to earlier units in the succession. The relative proportion of lithic fragments increased throughout this phase, culminating in the two lithic-rich units, L5 and L6, suggesting modifications of the conduit-vent system during the phase. The occurrence of rounded, hydrothermally altered lithic clasts within the L4 to L6 stratigraphic interval, further suggest changes in the depth of conduit walls erosion and fragmentation level (Campbell et al., 2013; Druitt, 2014), likely reaching deeper levels. The vent area for the Phase B episodes is thought to have been the same as the Phase A episodes, within Tarawera dome and Ruawahia crater, by the general distribution of the units. However, modification of the conduit-vent system indicated by the variation in the proportion of lithics, suggest that vent positions for individual Phase B episodes might have changed within this SW vent area.

Phase C – Episodes VI and VII (Units: A7 and A8) – Phase C shows a marked change in the eruption dynamics, passing from the repeated production of sustained convective columns and dominantly fallout deposition to a PDC-dominated type of activity. This phase also marks the initiation of a general migration of the vents active during the eruption from SW to NE positions along the inferred fissure system. The onset of Phase C was preceded by a pause in the eruption of possibly a week (1st order) after deposition of unit L6, as evidenced by erosional surfaces between L6 and A7. Lateral stratigraphic correlations and litho-sedimentological characteristics suggest that Phase C began with generation of concentrate to dilute PDCs from the continuous boiling-over at vent of the erupted mixture, which emplaced unit A7 (Episode VI). The main area of PDC inundation was directed to the S, with a runout distance up to ~15 km from Mt Tarawera' summit. Deposits of unit A7 are widespread around Mt Tarawera, with thick deposition in proximal east sites, and thin deposition up to north medial sites, suggesting the vent location

possibly extend up to Ruawahia (vent 4 and 5 in **Fig. 3.2**). Similar to what observed in unit L3, deposits of unit A7 are associated with an elevated content of obsidian clasts, suggesting disruptions of a degassed magma body in the shallow conduit (see **Chapter 5**), possibly formed during the time break between Phase B and C. After a break of possibly several hours at most (2nd order) the eruption continued with ash explosions likely from Wahanga and/or Northeast crater of suspected phreatomagmatic origin (Episode VII). The shift in vent location during this episode likely favoured the supposed interactions of the rising magma with external water. The explosive activity generated directed PDCs and associated minor ash fallout in the N sector, which emplaced unit A8. Opening of new NE vents might be correlated to the very proximal block-rich blast deposits found by Nairn et al. (2001) 1 km from Northeast crater.

Phase D – Episodes VIII and IX (Units: L7S, L7N, A9, L8, A10, L9) – Phase D marks a new phase in the eruption dominated by the production of sustained, convective columns and associated fallout deposition mainly to the N sector. Time break between Phases C and D is supposed to have been no longer than few days (2nd order) from field observations at available outcrops (e.g., sharp contacts with minor erosional scours between units A8 and L7N at north sites; sharp contacts at east sites between unit A7 and L7S with interlayered fine ash settling from A7 co-PDC plumes). Phase D began with the formation of two sustained, convective columns depositing units L7S and L7N to the ESE and N from Tarawera, respectively. The two deposits are correlated to the same episode (Episode VIII) with L7S-column shortly preceding L7N-column, indicating a transition to predominately southerly winds. After a short break (2nd order), during which the delayed fine ash settling of unit A9 occurred on the top of L7N deposits, the eruption resumed with the development of two sustained columns. These dispersed L8 and L9 fall deposits to the N and NE (Episode IX). Similar to the L3-L4 interval, units L8 and L9 are separated in the field by a small-volume dilute PDC (unit A10), suggesting limited time break between the two columns (3rd order). During or immediately after deposition of unit L9, fluvial reworking of L9 deposits occurred along the Tarawera river valley as suggested by deposit characteristics and overthickening of the unit away from the vent to the NE (RV1 deposits). Overall, grain size characteristics suggest that Phase D evolved from relatively stable columns (L7S and L7N) to continuously oscillating columns (L8 and L9) and was characterised by a general progressive waning in eruptive intensity culminating with deposition of the fine lapilli unit L9. The general distribution and componentry features of the L7S to L9 units suggests that the vent area for Phase D episodes was located within the NE section of the of the fissure system (vents 5 and 6 in **Fig. 3.2**). Within this area, individual vent positions for Episodes VIII and IX might have changed following instabilities of the shallow conduit-vent system as suggested by the increase in lithic content from units L7S and L7N to units L8 and L9. This phase is also associated with slight changes in the composition of the erupted magma. Componentry analyses

showed that Phase D is associated with the deposition of grey pumice clasts of rhyodacitic bulk compositions (Nairn et al., 2004), with relatively high abundances in unit L7S and L7N (10-33 wt.%). Furthermore, Nairn et al. (2004) found that white pumices in the north-directed lapilli deposits have a slightly different rhyolitic composition compared to earlier units ("T1+2" compositions. See **Section 3.2.2**).

Phase E – Episodes X (Units A11 and Af) – The explosive sequence concluded with a significant decline in eruptive intensity, passing from sustained, high-intensity (subplinian), convective columns to minor ash explosions. This final explosive phase is characterised by the semi-continuous to intermittent magma discharge producing low-altitude, sustained ash columns to possibly Vulcanian-type plumes and initiation of dome extrusions. Accumulation of ash in different sectors around the volcano formed unit Af. Lateral correlation suggest ash fallout events were preceded by a directed small-volume, dilute PDC south from Tarawera, reaching only proximal sites (e.g., section 18) and emplacing unit A11. Time break with the preceding phase is interpreted to be of days at most (2^{nd} order) to allow fluvial reworking of L9 and minor scouring at the contact between A7 and A11 to the south. Vents for the Phase E units are difficult to constrain due to the limited very proximal exposures and multiple dispersal directions of the ash fallouts. However, Nairn et al. (2001) suggested vent locations at Tarawera dome and Ruawahia crater, with the formation of a pyroclastic cone at Ruawahia crater related to near-vent deposition of Af. Phase E ash explosions possibly accompanied and continued after the extrusion of Crater dome as suggested by evidence of pyroclasts deposits mantling the dome surface (Nairn et al. 2001).

Phase F – Episode XI (main dome extrusions and units BS and BN) – The Kaharoa eruption concluded with the extrusions of three main domes, Tarawera, Ruawahia and Wahanga, which are here placed in the final Phase F. Exact timing of dome extrusions is not clear, however extrusion of Tarawera and Ruawahia domes commenced after Crater dome emplacement, with Nairn et al. (2001) suggesting that Wahanga dome had started to grow as early as during the Af ash explosions. Emplacement of early BAFs to the S forming unit BS initiated at least after a weeks-to-months break in deposition (1^{st} order) as evidenced by a laterally continuous, red-oxidised ash horizon between unit Af and BS. The dome-forming activity of Phase F is assumed to have lasted for ~3 to 4 years based on comparative extrusion rates of historic silicic lava domes (Nairn et al., 2001).

Table 3.6 – Summary of intra-eruption Phases (A to F) and Episodes (I to XI), associated lithostratigraphic units with interpreted eruptive activity and inferred time breaks (1st to 3rd order; see **Table 3.5**).

Phase	Episode	Unit	Time break	Eruptive activity
F	XI	Domes + BS and BN	1st order	Dome growth (Tarawera + Ruawahia + Wahanga domes) and associated collapses with BAFs
E	X	Af	2nd order	Intermittent vulcanian-type ash explosions to sustained ash columns. Dome growth (Crater dome)
		A11	2nd order	Directed, small volume PDC
D	IX	L9	3rd order	Sustained oscillating subplinian column
		A10	3rd order	Small volume, dilute PDC (+ co-PDC fine ash settling)
		L8	2nd order	Sustained oscillating subplinian column
		A9	3rd order	Fine ash settling
	VIII	L7N	3rd order	Sustained stable subplinian column
		L7S	2nd order	Sustained stable subplinian column
C	VII	A8	2nd order	Phreatomagmatic ash explosions. Dilute PDCs and minor ash fallout
	VI	A7	1st order	Concentrated and dilute PDCs from continuous boiling-over (+ co-PDC fine ash settling)
B	V	L6	2nd order	Sustained oscillating and partially collapsing subplinian column
	IV	A6	3rd order	Fine ash settling
		L5	2nd order	Sustained oscillating subplinian column
		A5	3rd order	Fine ash settling
	III	L4	3rd order	Sustained oscillating subplinian column
		A4	3rd order	Small volume, dilute PDC
		L3	1st order	Sustained stable subplinian column
A	II	A3	3rd order	Fine ash settling + ash explosions
		L2	2nd order	Sustained stable subplinian column
		A2	3rd order	Fine ash settling
	I	L1	3rd order	Sustained stable subplinian column
		A1		Sustained ash column

3.7 Conclusions

The stratigraphic reconstruction of the Kaharoa deposit based on new field evidence coupled with quantitative grain size and componentry characterisations of the pyroclastic beds, enabled to gain new insights into a complex moderate- to large-scale, intra-caldera rhyolitic eruption at Okataina.

1) Based on the deposit features at different key outcrops and lateral correlations, up to 24 lithostratigraphic units were established, which together define a new stratigraphic framework for the Kaharoa pyroclastic succession. The identification of units with distinctive component characteristics (e.g., obsidian-rich units, lithic-rich units, units with white and grey pumice clasts) was crucial into providing reliable correlations and timing of eruptive and depositional events.

2) The variable sedimentological characteristics and distribution of the units in the succession imply a range of different transport-depositional mechanisms and eruptive processes occurring during the explosive phases of the eruption. Based on these units' characteristics, seven main deposit types and associated eruptive styles were recognized.

3) Massive and stratified fall lapilli units record repeated episodes of subplinian-style explosive activity, which were characterised by variable degrees of unsteadiness in magma discharge, alternating relatively more stable (massive lapilli units) to continuously oscillating (stratified units) sustained convective columns, occasionally partially collapsing.

4) During the sequence of subplinian columns and fallout-dominated depositions, the eruptive activity transitioned towards a PDC-dominated phase, possibly associated to lateral migration in the active vent. The generation of PDCs resulted from (i) the continuous boiling-over of the erupted gas-particle mixture at vent, leaving widespread lapilli-bearing ash deposits in the N and S sectors, and later from (ii) suspected phreatomagmatic minor explosions emplacing ash deposits to the N and NE of Mt Tarawera.

5) The onset of the eruption was characterised by low-intensity, ash emissions, depositing a cm-thick blanket of coarse ash on the pre-Kaharoa surface in the S sector. Similar ash emission events producing short-lived, sustained ash columns to possibly Vulcanian-type intermittent plumes and depositing massive coarse ash units also occurred within and towards the end of the sequence of subplinian episodes (A3 and later Af). Together with

the A8 PDC-dominated suspected phreatomagmatic activity, these ash-producing episodes indicate that the eruption periodically underwent significant declines in the eruptive intensity.

6) Componentry analysis displayed continuous fluctuations with time in the proportion of lithic fragments of the deposits, suggesting repeated events of shallow conduit walls collapses and re-establishment of the conduit-to-vent pathways. These events probably favoured the opening of new vents along the inferred fissure system. Componentry data, together with the distribution of the units, further suggest a general shift from SW to NE within Mt Tarawera in the position of the active vent from the earlier (Phase A to B) to later (Phase C to D) explosive phases during the eruption.

7) The careful analysis of the pyroclastic succession and units' boundaries indicate that the Kaharoa eruption was characterised by an episodic behaviour during which periods of sustained magma discharge were interrupted by short pauses in the eruptive activity. The intra-eruption time breaks, inferred to span from few hours up to weeks/few months, enabled to identified 10 discrete explosive episodes.

8) Time breaks coupled with the interpreted dominant type of eruptive style further allowed to subdivide the eruption into six main eruptive phases. Three of those are associated with repeated subplinian episodes (Phase A, B, D), one phase comprises the major PDC activity of the eruption (Phase C), while the final two phases (E and F) are associated to activity of ash emission during initiation of lava extrusions and to the following main dome-building sequence of the eruption.

This type of episodic, long-lasting, explosive-to-effusive rhyolitic eruptions, occurring from multiple vents linked to an eruptive fissure appear to have been the dominant type of activity for intra-caldera eruptions at Okataina over the past ~25 kyr (Nairn, 2002; see **Chapter 2**). Similar eruption patterns, subvolcanic settings and associated complex pyroclastic deposits, however involving smaller volume of erupted magma, seem to have occurred repeated times at the Mono-Inyo volcanic chain in USA (e.g., Bursik, 1993, Hildreth, 2004; Nawotniak and Bursik, 2010; Bursik et al., 2014) and might be common at other rhyolitic centres and dome complexes worldwide. The controlling factors of such type of eruptions that result in the spasmodic discharge of rhyolitic magma however capable of producing numerous and powerful subplinian style explosive episodes, remain still poorly understood. The observed variability of juvenile clasts identified in this study for the Kaharoa lapilli units, comprising moderately vesicular pumice clasts with tubular vesicles to completely degassed obsidians, suggest complex ascent and

degassing histories of magma in the conduit. The characterisation of the juvenile microtextures can provide new insights to understand the mechanisms of such pulsatory eruption dynamics.

[This page intentionally left blank]

Chapter 4

An approach to quantify complex and anisotropic vesicle textures in pumice clasts

4.1 Introduction

4.1.1 The importance of microtextural studies of pyroclasts

Vesicles and microlites textures preserved in the erupted and deposited juvenile pyroclasts represent a window into the state of vesiculation and crystallization of the magma in the volcanic conduit prior to fragmentation (Cashman & Blundy 2000, Shea et al. 2010). The spatial arrangement, size, shape and number of vesicles and crystals at the submillimetre scale are characteristics of the microtextures of a pyroclast, and the quantification of these textural features can shed light into the degassing and ascent dynamics of the magma in the conduit prior to explosive eruptions (e.g., Cashman and Mangan, 1994; Gardner et al., 1998; Hammer et al., 1999; Gurioli et al., 2005; D'Oriano et al., 2005; Noguchi et al., 2006; Mastrolorenzo and Pappalardo, 2006; Houghton et al., 2010; Alfano et al., 2012; Pardo et al., 2014; Cashman, 2020; Vona et al., 2020).

Vesicles and vesicle features in pyroclastic rocks are the result of volatile exsolution and expansion due to the decrease in pressure and gas solubility experienced by the ascending magma, which gives way to bubble nucleation and growth (Sparks, 1978; Gonnermann and Manga, 2013; Burgisser and Degruyter, 2015). Bubbles in magmas undergo also processes such as coalescence, deformation (by shear stress and bubble-bubble interactions) and collapse (e.g., Westrich and Eichelberger, 1994; Rust et al., 2003; Rust and Cashman, 2004; Wright and Weinberg, 2009; Castro et al., 2012b; Kennedy et al., 2016). These processes, together with bubble nucleation and growth, determine the continuous evolution of the bubble fraction in the magma while rising to the surface (Sparks et al., 1994; Shea et al. 2010, Cashman and Sparks 2013).

Studies conducted on natural and experimentally derived vesicle textures are a widely used tool in volcanology to understand eruption behaviours. They can be used to provide an estimation on a range of conduit processes and physical conditions of the magma which can impact the eruption dynamics. These include: (1) magma decompression rate in the conduit (e.g., Toramaru, 2006; Shea et al., 2012); (2) mechanisms of bubble nucleation (e.g., Cashman, 2004; Shea et al., 2010; Giachetti et al., 2010; Shea et al., 2017); (3) shear rate and flow type (e.g.,, Rust and Manga, 2002; Rust et al., 2003; Bouvet de Maisonneuve et al., 2009; Wright et al., 2009; Caricchi et al., 2011; Dingwell et al., 2016; Ohashi et al., 2021); (4) magma permeability (e.g.,, Klug and Cashman, 1996; Papale, 1999; Blower, 2001; Rust and Cashman, 2004; Degruyter et al., 2009); (5) fragmentation processes and eruption styles (Gardner et al., 1996; Klug et al., 2002; Gaonac'h et al., 2005; Moitra et al., 2013; Rotella et al., 2015; Giachetti et al., 2021). Selected examples of work on pumice vesicle textures are reported in **Table 4.1**.

Typically, textural studies of vesicles in pumice clasts assume that pyroclasts represent a frozen sample of the magma at fragmentation (Shea et al., 2010). As such, the fragmented and erupted magma particles are thought to experience rapid quenching soon after fragmentation, allowing the conduit-derived vesicles' textures to be preserved in the pyroclasts. However, syn- and post-fragmentation modifications of vesicles shape, size and numbers (e.g., due to relaxation, gas expansion and bubble collapse) can also occur, at least to a certain extent, especially in subaerial explosive eruptions, also of silicic magmas (e.g., Thomas et al., 1994; Gardner et al., 1996; Rotella et al., 2015; Mitchell et al., 2018; Giachetti et al., 2021). These effects must be considered when interpreting the vesicle parameters and the origin of pumice textures to constrain eruption dynamics.

4.1.2 Tube pumice clasts

Among the variety of vesicle textures of pumice clasts, two endmembers can be broadly distinguished according to the vesicles dominant shape and spatial arrangements (Fisher and Schmincke, 1984; McPhie et al., 1993): (1) pumice dominated by subspherical vesicles forming isotropic vesicle texture and (2) pumice dominated by very elongated and oriented vesicles forming anisotropic vesicle texture. The former type can be designated as spherical pumice, while the latter are typically termed tube or woody pumice (Sparks et al., 1994; Martí et al., 1999, Polacci et al., 2003).

Although a univocal definition of *tube pumice* lacks, the term tube pumice is generally used to indicate a type of pumice texture consisting of predominantly parallel, highly elongated vesicles, which form adjacent stacks of tube-like voids, oriented along a preferential direction. Therefore, the use of the term tube pumice should be restricted to textures where the highly elongated, oriented vesicles are pervasively distributed in the clast entire volume rather than localized into bands or zone (e.g., Wright and Weinberg, 2009). This bubble deformation pattern and resulting bubble arrangement can form a unique permeable porous network within the ascending magma (e.g., Wright et al., 2006; Okumura et al., 2008).

Tube vesicles (not to be confused to tube pumice clast as a whole) are defined by Wright et al. (2009) as vesicles stretched to aspect ratio (AR) >5. Vesicle in tube pumice can be characterised by various degree of elongation (see also **Section 4.2**), having moderate (AR = 5 to 10; e.g., the 776 CE Monte Pilato pumice; Wright et al., 2009; Davì et al., 2011) to high aspect ratio (AR > 10; e.g., the ~1314 CE Kaharoa pumice in this study; the Plinian pumice of the ~40ka Campanian Ignimbrite eruption, Rosi et al., 1999, Polacci et al., 2003). Examples of textures were stacked tube vesicles connect forming threads with very high to extremely high aspect ratios (up to >100),

extending through the entire lapilli-to-bomb-size pumice clast, have also been reported (e.g., the 6.6 Ma Ramadas pumices, Dingwell et al., 2016; the 2012 CE Havre pumices, Mitchell et al., 2019).

Tube pumices are commonly found in pyroclastic deposits associated with explosive silicic eruptions of calc-alkaline rhyolitic magmas (e.g., Allen et al., 1999; Houghton et al., 2010), as well as in deposits from alkaline (e.g., Piochi et al., 2021) to peraluminous rhyolitic compositions (e.g., Dingwell et al., 2016). Although they are reported as abundant in deposits of intermediate- up to large-volume ignimbrites (Ohashi et al., 2021), tube pumice clasts are also common product of both smaller volume, lapilli-bearing PDCs deposits and Plinian-type (*sensu lato*, see **Chapter 1**) fall deposits (e.g., Heiken,1978; Heiken and Eichelberger, 1980; Heiken et al., 1986; Martine and White, 2001; Taddeucci and Wohletz, 2001; Polacci et al., 2001; 2003; De Rose et al., 2003; Rosi et al., 2004; Carey et al., 2009; Davì et al., 2011; Pistolesi et al., 2015; Mitchell et al., 2019).

More localized, sheared-derived, highly elongated vesicles are further common (virtually ubiquitous) in the pyroclast population of many silicic explosive eruptions (e.g., Rust et al., 2003; Wright and Weinberg, 2009; Shea et al., 2012; Schipper et al., 2013). They have also been observed in vesicular fragments of rhyolitic lava domes (e.g., Ashwell et al., 2018).

Studies by Martí et al. (1999) and Dingwell et al. (2016) provide supportive evidence that vesicle textures in tube pumice clasts are not affected by significant post-fragmentation modifications. Therefore, the study of tube vesicles can provide important information on the shear stress and deformation history of the magma during ascent in the conduit and on the dynamics of magma degassing/outgassing prior to fragmentation or leading up to lava extrusion (e.g., Okumura et al., 2009).

4.1.3 Study motivations

Textural studies of vesicles in pumice clasts via Scanning Electron Microscope (SEM) imaging and other imaging techniques (e.g., microtomography, see below) in the volcanology literature are predominantly "skewed" toward spherical pumices (i.e., having isotropic vesicles textures with spherical vesicles), while only few studies have been conducted on tube pumices (e.g., Martí et al., 1999; Dingwell et al., 2016). Only fewer of these studies quantified the variation in vesicles features systematically along the investigated pyroclastic succession by sampling tube pumice clasts from different intra-eruption units/phases (e.g., Polacci et al., 2003; – and only recently – Ohashi et al., 2021).

The general lack of quantitative studies on tube pumices appears to be related to the intrinsic complexity of quantifying features of very elongated, tube-like, vesicles such as the size, shape

and number density and to convert the 2D information into 3D distributions using stereological conversions methods (Shea et al., 2010). Stereological conversion techniques assume spherical geometry for the analysed vesicles. By using these techniques, it is possible to convert the area distributions into volume distributions based on the equivalent spherical diameter of the vesicles (the diameter of a sphere having equivalent volume of the irregular object), which is used to correct the original 2D data for the intersection probability effects (Underwood, 1970 and Sahagian and Proussevitch, 1998). This assumption stands for networks of isotropic, spherical to subspherical vesicles, while it remains inadequate for vesicles that have experienced significant deformations and can result in large data uncertainties (see Shea et al., 2010).

Recently Mitchell et al. (2019) quantified the characteristics of submarine tube pumice vesicles by applying a modification to the stereological conversion method of Sahagian and Proussevitch (1998) using prolate geometry assumption. However, Mitchell et al. (2019) further report that accurate volume distributions of vesicles could not be determined after the newly applied 2D-to-3D conversion. Synchrotron X-ray computed microtomography analysis of both natural and experimentally derived samples have been adopted to the study of tube pumices (Degruyter et al., 2010; Dingwell et al. 2016; Ohashi et al., 2020a). Although representing a promising technique to investigate tube vesicles textures, the method to date is very laborious (thus, only a limited number of clasts is generally analysed). Furthermore, it requires a combined approach with traditional 2D textural investigations for more accurate results (e.g., Polacci et al., 2006; Giachetti et al., 2011; Rotella et al., 2014). As a direct outcome of the difficulties in analysing anisotropic vesicle textures, tube pumice clasts are typically discarded from quantitative microtextural analysis when present in the targeted eruption deposit (e.g., Carey et al., 2009; Houghton et al. 2010; Rotella et al. 2014) (**Table 4.1**).

Given these complexities, the study of the 2D features of vesicles in oriented thin sections of natural pumice clasts remains a powerful tool to characterise, both in qualitative and quantitative fashions, the microtextural properties of tube pumice and other complex, heterogeneous pumice clasts (e.g., Polacci et al., 2001; 2003; Trafton and Giachetti, 2021). However, studies designed to evaluate and propose guidelines and standardised methodologies for the 2D quantification of complex and anisotropic vesicle textures have not yet been conducted (cf. Shea et al., 2010). The work presented in this chapter aims to fill this gap by providing first-order recommendations for the quantification of 2D vesicles features (e.g., size, shape, and number density), which can be of help when comparing vesicles characteristics between tube pumices of different eruptions. The workflow presented is developed by investigating the complex vesicle textures of the ~1314 CE Kaharoa pumice clasts (rhyolitic in composition; SiO_2>76wt.% and calc-alkaline), erupted from Mt Tarawera (New Zealand). The Kaharoa pumice microtextures are investigated using BSE (backscattered electron) images obtained via SEM observations of polished clasts thin sections.

Table 4.1 – Summary of studies on pumice vesicle textures. Ref. = references; N. = number; Mag. = microscopy magnification used; n/a = not available; S&P (1998) = Sahagian and Proussevitch (1998); C&L (1983) = Cheng and Lemlich (1983). (***Table continues in next page***)

Ref.	Eruption	Deposit type	Clast type	Clast selection criteria	N. thin section per clasts	N. images	N. Mag.	Imaging Methods	2D-to-3D Conversion	Vesicle parameters quantified	Application
Polacci et al. 2001	Pinatubo 1991	Plinian fallout + PDC	spherical and tube pumices + breadcrust bomb	not applicable (n/a)	3 thin sections per 10 clasts	n/a	3	2D	-	Vesicularity. Number density. Vesicle size. Vesicle shape (deformation parameter).	General conduit dynamic. General conduit stratigraphy
Klug et al. 2002	Mount Mazama 7.7 ka	Plinian fallout + PDC	spherical and tube pumices	density + permeability	n/a	n/a	n/a	2D	S & P (1998)	Vesicle size distributions. Vesicle volume distributions. Cumulative number densities.	Texture origin. Bubble nucleation, growth + coalescence. Magma vesiculation history. Fragmentation processes
Polacci et al. 2003	Campi Flegrei 37ka	Plinian fallout	spherical and tube pumices + reticulites	density + surface features	1-2 thin section per 20 clasts	>7 per thin section	4	2D	n/a	Vesicularity Vesicle number density. Vesicle size. Vesicle coalescence. Vesicle shape (deformation parameter).	General conduit dynamic. General conduit stratigraphy
Gurioli et al. 2005	Vesuvius 79 CE	Plinian and subplinian fallout + PDC	spherical pumice	density distribution	1 thin section per 26 clasts	15 per thin section	n/a	2D	S & P (1998)	Vesicle size distributions. Vesicle volume distributions. Glass wall thickness. Vesicle shape (qualitative).	Relationship vesicles/crystals. eruption model. Transition fallout-PDC.
Giachetti et al. 2010	Soufrière Hills Montserra 1997	volcanian explosions fallout + PDC	spherical pumices + breadcrust bomb	porosity + surface features	1 thin section per 6 clasts	n/a	6	2D	S & P (1998) + C & L (1983)	Vesicle number density. Vesicle volume distributions.	Pre-explosion conduit stratigraphy. Origin of vesicle populations. Bubble nucleation, growth + coalescence. Decompression rate. Eruption model

Houghton et al. 2010	Taupō 232 CE	Plinian fallout + PDC + dome	spherical pumice + lava	density distribution	1 thin section per 40 clasts	14 per thin section	4 to 5	2D	S & P (1998)	Vesicle size distribution. Vesicle volume distribution. Vesicle number density.	Vesicle number density and MDR. Ascent and degassing dynamic per unit. Post-fragmentation role. Eruption model
Alfano et al. 2012	Chaitén 2008	subplinian fallout	spherical pumice	density distribution	2 thin sections per 7 clasts	17 per thin section	4	2D	S & P (1998)	Vesicle volume distribution. Vesicle number density. Vesicle shape (aspect ratio).	Decompression rate. General conduit dynamic. Link to eruptive column dynamic.
Pardo et al. 2014	Ruapehu, 4 erupt. 27-11 cal ka BP	Plinian and subplinian fallout	spherical pumice	porosity + surface features	1 thin section per 3 to 6 clasts per 4 unit	n/a	n/a	2D (+ 3D)	n/a	Vesicle volume distribution. Vesicle number density. 3D volume distribution.	Textures/geochemistry correlation. Bubble nucleation and growth. Decompression rate. Link to eruptive column dynamic/deposit.
Rotella et al. 2014	Raoul, 6 erupt. 3.7-0.37 ka	Plinian and subplinian fallout	spherical pumice	density distribution	1 thin section per 24 clasts	n/a	3 to 5	2D	S & P (1998)	Vesicle volume distribution. Vesicle number density.	Vesiculation processes. Conduit dynamics. Eruption intensity.
Mitchell et al. 2019	Havre 2012	submarine eruption	spherical and tube pumices	density + surface features	1-2 thin section per 13 clasts	16 per thin section	4	2D (+ 3D)	S & P (1998)	Vesicle shape (Circularity. Roundness. Regularity. Solidity). Vesicle size distribution. Vesicle volume distribution. Vesicle number density.	Magma decompression rates. Post-fragmentation expansion Conduit dynamics. Fragmentation

Table 4.1 – (***continued***)

4.2 Materials and methods

4.2.1 Sample selection and description

Pumice samples for this study have been collected from the deposits of the explosive phases of the ~1314 CE Kaharoa eruption of Mt Tarawera (**Chapter 3**). Mt Tarawera is a SW-NE aligned intra-caldera dome complex formed during the past ~20 kyr in the southern end of the Okataina caldera system, in the Taupō Volcanic Zone of New Zealand (Cole, 1970; Nairn, 2002). Tarawera is composed of closely spaced, adjacent and overlapping rhyolite lava domes and coulees, which are intercalated with proximal pyroclastic deposits emplaced during four, multiple-vent and multi-phase, explosive-to-effusive, moderate to large scale rhyolitic eruptions dated at 21.8 cal. kyr BP (Okareka eruption), 17.6 cal. kyr BP (Rerewhakaaitu eruption), 13.6 cal. kyr BP (Waiohau eruption) and 0.636 cal. kyr BP (Kaharoa eruption). Previous studies conducted on these eruptions revealed that the explosive eruptive styles during each eruption ranged from minor transient ash and Vulcanian explosions to sustained Plinian-type events (see **Chapter 2** and references therein).

Representative samples from each lapilli unit identified in the field for the Kaharoa pyroclastic succession have been collected to investigate the physical and textural characteristics of pumice clasts. Samples are collected from reference sections 2 and 24, and the clasts used in this study are the white pumice identified during componentry analyses (refer to **Chapter 3**). The bulk density of the Kaharoa pumices for each individual unit was calculated for approximatively 1300 pumice clasts (~100 per unit). From the mode of the pumice density distributions, three clasts were randomly selected for each unit to produce polished impregnated thin sections for microscopy imaging. As the surface textures of the Kaharoa pumices present anisotropic features, with evident oriented elongated surface vesicles (confirmed also by preliminary petrographic microscope observations) two thin sections were prepared for each clast: parallel (PA) and orthogonal (OR) to vesicle elongation. The pumice microtextures from a total of 60 thin sections were investigated using petrographic microscope and SEM-BSE imaging. Qualitative observations were noted for each of the 60 thin sections over a total of over 800 SEM-BSE images (see **Chapter 5**).

Density and textural variability of pumice clasts with respect to the different lapilli units of the Kaharoa eruptive sequence are addressed in the following chapter (**Chapter 5**). Here the three most different types of microtextures observed during the SEM investigations of the 60 thin section population were selected to test and develop a methodology for quantifying complex

pumice vesicle textures. The three different textural types recognised for the Kaharoa pumices are the following (**Fig. 4.1**):

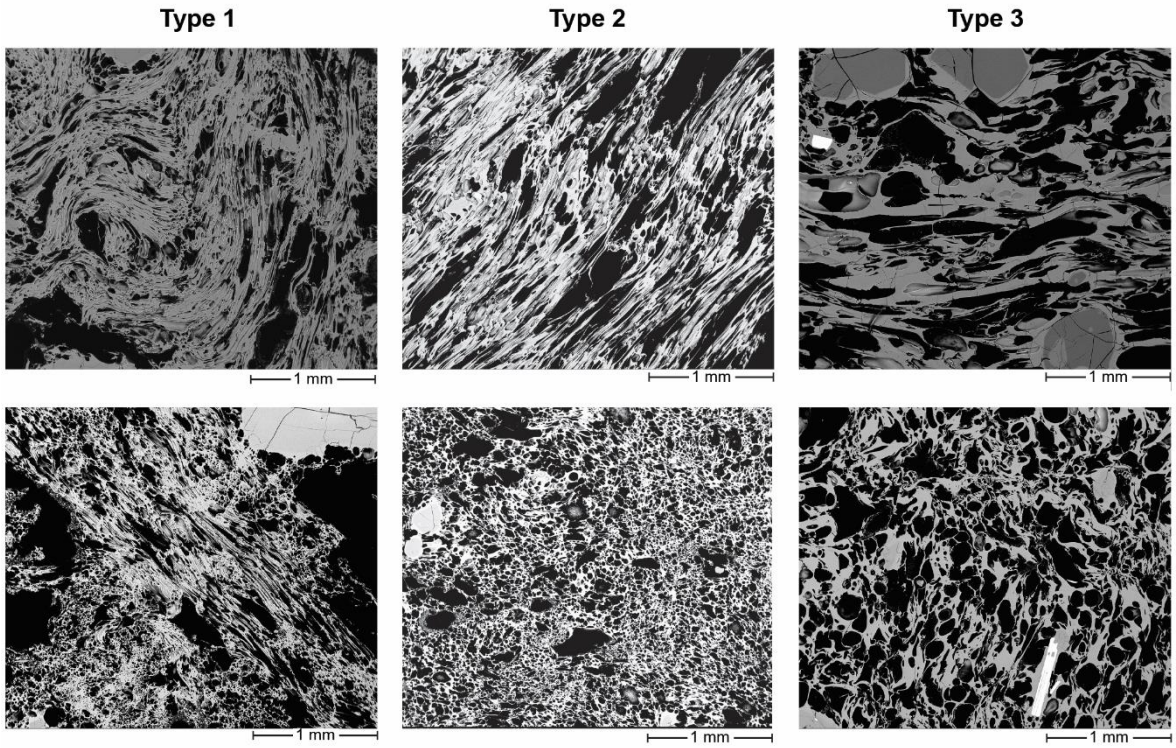

Figure 4.1 – SEM-BSE images at 50× magnification of the three different Kaharoa pumice vesicle textures investigated in this study. Top images are from thin sections parallel (PA) to main vesicle elongation and bottom images are thin sections orthogonal (OR) to main vesicle elongation.

- **Type 1** – Heterogenous textures characterised by vesicles with different shapes and spatial arrangements within the analysed clasts. Deformed vesicles are dominant and have mostly elongated shapes varying from straight tube to irregular-convoluted geometries. Deformed vesicles are predominately stretched along a main direction (the longest axis of the clast) although are sometimes bended/folded into different planes. Tubular and convoluted vesicles occur mainly in PA cuts while are volumetrically less abundant (however present due to apparent folding) in OR cuts, and typically occur in domains or bands. Subspherical vesicles coexist with deformed vesicles within the same plane, however, are more abundant in OR cuts. Dominant vesicles size is <30 μm in equivalent circular diameter.

- **Type 2** – Strongly anisotropic vesicles texture, resembling those reported for classical tube pumice clasts (see **Section 4.1.2**). The texture consists of tube-like vesicles stretched to high aspect ratio, oriented along the longest axis of the clast. OR cuts (perpendicular to vesicle elongation) are characterised by densely packed, small size (few microns to tens of microns),

subspherical vesicles. Dominant vesicles size is <30 μm in equivalent circular diameter as in type 1.

• **Type 3** – Strongly anisotropic vesicles texture similar to type 2 consisting of elongated vesicles, stretched along the longest axis of the clast (PA cuts) and in subspherical vesicles in the perpendicular direction (OR cuts). Vesicles are here markedly larger then type 2, with dominant vesicles size ~100 μm and the texture is characterised by thick vesicles walls and non-vesicular glass area (>50 μm).

4.2.2 Image acquisition

Pumice microtextures were imaged from polished thin sections using a ThermoFisher Scientific™ FEI Quanta 200 Environmental Scanning Electron Microscope operated in Backscattered Electron mode, under accelerating voltage of 25 kV, with a working distance of ~10 mm, at the Massey University's Manawatu Microscopy and Imaging Centre.

To obtain the best SEM-BSE image clarity for tube vesicles, which in the Kaharoa pumice are often characterised by few μm thin glass walls, preliminary tests were made to find an adequate thickness for the clast thin sections. The best image clarity of tube vesicles was obtained at thin sections between 50 and 100 μm in thickness. This thickness range allowed to reduce the number of broken thin glass borders of adjacent vesicles (common in the tested 30μm thin sections) while avoiding excessive 3D effects from the bottom side of the vesicle glass wall (significant for >100μm thin sections) (see also Shea et al. 2010).

As the vesicle population of the Kaharoa pumice clasts span in size over typically four orders of magnitude (0.001 to 1 mm), images were collected at different magnifications from both PA and OR cuts: 20×, 50×, 100× and 200× (**Table 4.2**). Images at different magnification were taken also to test the sensitivity of the vesicle shape and size analysis respect to the magnification selected. Preliminary scan on the entire thin section were made as a map to identified large size heterogeneity in vesicle textures (if any) in the sample.

SEM images were acquired at a high resolution of 4096×3775 pixels for each magnification. This is equivalent to a spatial resolution of 0.6 pixel/μm in 20× images, 1.37 pixel/μm in 50× images, 2.74 pixel/μm in 100× images and 5.5 pixel/μm in 200× images (**Table 4.2**).

Due to the high resolution used, together with the fact that vesicles smaller than 1-2 μm are not abundant in the investigated samples, images at higher magnification (e.g., 500× or more) were not necessary. Following Shea et al. (2010) a minimum area of 80 pixels per vesicles, corresponding to an uncertainty in vesicle size of ~1%, was used as a lower limit for vesicles size

in each magnification (i.e., the pixel density per vesicles is minimum ≥80/1) for later quantification of vesicles size and shape distributions (**Table 4.2**). Thereby, the smallest vesicle analysed have equivalent circular area diameter of 1.84 µm (or equivalent circular area of ~2.64 μm^2) in 200× images (see below Section 4.2.4). Other studies of silicic pumice in the literature report the use of lower resolution SEM images (e.g., 1280×960) as well as minimum area of 5 to 20 pixels per vesicles and typical lower limits of vesicles size analysed >4 µm (see Rotella et al., 2014). In this work vesicle diameter, if not otherwise specified, always refers to the equivalent circular area diameter of the vesicle (Eq.D = 2×[sqrt(area vesicle/π)]),

At least three images were taken at each magnification and additional images were taken for the higher magnifications 100× and 200×. From 12 to 15 images per thin sections (at least three per magnifications) were usually necessary to capture the sample textural variability. OR cuts from texture type 2 and 3 typically required a smaller number of images (10 to 12) to characterise the sample as the textural features are homogeneous across all the thin section (i.e., texture comprise only sub-spherical vesicles, cross-sections of the tube-like vesicles).

Table 4.2 – Summary of the magnifications and resolutions of SEM-BSE images used in this study and minimum vesicle size thresholding applied in quantitative image analyses. Eq.D = equivalent circular diameter of the vesicle. The image widths and heights are 6827µm and 6292µm for 20× images, 2990µm and 2755µm for 50× images, 1495µm and 1378µm for 100× images, and 745µm and 686µm for 200× images. (*****) Due to the large area of 20× images (width of the image is ~7 mm) which would result in extensive manual image editing (see **Section 4.2.3**), the minimum vesicle size for quantitative analyses is set at vesicle area of >700 pixels (i.e., vesicle with Eq.D = 50 µm). Vesicles <50 µm are largely captured by all the other three magnifications. If an 80-pixel vesicle area thresholding was to be also maintained for the 20× images, it would have resulted in a minimum vesicle size of ~17 µm.

SEM-BSE image Magnification	SEM-BSE image pixel/µm	Minimum vesicle size thresholding (pixel)		Minimum Vesicle size thresholding (µm)		Typical upper limit of vesicle size (in Eq.D µm)
		Vesicle area	Vesicle Eq.D	Vesicle area	Vesicle Eq.D	
20×	0.6	~700 (*****)	~30	~1940	~50	>1000
50×	1.37	80	10.09	42.62	7.37	500-1000
100×	2.74	80	10.09	10.66	3.68	500
200×	5.5	80	10.09	2.64	1.84	250

4.2.3 Image adjustments

Usually, prior to vesicles shape and size analyses, the vesicle textures captured by SEM-BSE images required few steps of manual editing to create final binary images with vesicles in black and glass in white. The original SEM-BSE images were edited using Adobe Photoshop. Manual editing is required since, during sample preparation and imaging, original thin vesicles walls are not entirely preserved in the acquired images, thus vesicles walls need to be manually redrawn (see Shea et al., 2010; Heilbronner and Barrett, 2014; Mitchell et al., 2019). Incomplete or broken vesicles walls were manually reconstructed or enhanced following the original vesicles texture.

In this study, interconnected vesicles were "decoalesced" only where vesicles walls showed evidence of partial rupture and/or incomplete wall retraction (i.e., representing very late-stage bubble-bubble coalescences during magma ascent in the conduit and/or immediately post-fragmentation; e.g., Klug et al., 2002). This choice is supported by the fact that extensive manual vesicles decoupling can lead to errors in quantifying vesicle features due to operator bias (see Shea et al., 2010; Gurioli et al., 2015). In **Section 4.4.4**, a further comparison is presented between vesicle data obtained from the decoalescence approach applied in this work (termed minimal decoalescing approach) and from a decoalescence approach where all vesicles showing any signs of interconnections are manually separated (termed maximal decoalescing approach). It is anticipated here that the obtained vesicle size and shape distributions from the two approaches do not show significant discrepancies; however, some differences are reported in the vesicle number density.

In addition to the editing of vesicles walls, manual operations are also necessary to correct for vesicle fillings or vesicles 3D effects to obtain final binary images (i.e., the vesicles area is not black as sometimes the bottom of the vesicles walls has been imaged by the SEM bean current). The problem of vesicles 3D effects is especially significant in PA cuts of texture types 1 and 2, where elongated vesicles are usually thin in the direction perpendicular to the image and bottom glass walls are typically imaged resulting in grey area. The image editing procedures using Adobe Photoshop are similar to what presented in a manual for image processing by Shea et al. (2009) associated to image preparation for the MATLAB®-based FOAMS image analysis programme (Shea e al., 2010).

4.2.4 Image analysis of vesicle features

After the different stages of image adjustment, the high-resolution greyscale images at each magnification are converted into binary images and the vesicle shape and size are quantified with Fiji, a distribution of the open-source software ImageJ (Schneider et al., 2012, Schindelin et al.,

2012). The software, commonly used in volcanology studies of crystals, vesicles and volcanic ash fragments textures (e.g., Liu et al., 2015; Pistolesi et al., 2017; Lormand et al., 2018), allows to measure several dimensional features (e.g., area, perimeters, Feret's diameter, among other) of the target object (vesicles in this study), and calculates several 2D shape parameters, which can be used to quantify the object morphology.

4.2.4.1 Vesicle shape analysis

Among the large number of 2D shape parameters that have been used in volcanology, specially applied for volcanic ash fragments studies (e.g., Dellino and La Volpe, 1996; Leibrandt and Pennec, 2015; Liu et al, 2015; Schmith et al., 2017; Dürig et al., 2018; Edwards et al., 2021; Hantusch et al., 2021), seven non-dimensional parameters are selected in this work to quantify the 2D shapes of vesicles in pumice clasts. The parameters are the following (**Fig. 4.2**):

1) Circularity (C) = Peq-c/P (Leibrandt and Pennec, 2015)

2) Regularity (R) = A/Abest-fit ellipse (this study)

3) Shape Factor (SF) = 4πA/P2 (Shea et al., 2010)

4) Deformation (D) = (sMajor – sMinor)/(sMajor + sMinor) (Polacci et al., 2001)

5) Eccentricity (E) = sqrt (1 – sMinor2/sMajor2) (Shea et al., 2010)

6) Flattening (FLT) = (sMajor – sMinor / sMajor) (Heilbronner and Barrett, 2014)

7) Ellipse Aspect Ratio (AR) = Major/Minor (Liu et al., 2015)

Where P and A are the vesicles perimeter and area, respectively; Peq-c is the perimeter of the circle of the equivalent area of the vesicle; Major and Minor are the long and short axis of the ellipse having the same area, orientation and centroid of the vesicle; sMajor and sMinor are the semi-long and semi-short axis of the same ellipse. With the exception of the AR, the parameters are normalized and vary from 0 to 1.

C, R and SF measure the vesicles complexity or irregularity respect to a reference standard shape being the circle for C and SF and both a circle or an ellipse for R (**Fig. 4.2**). As a result, both C and SF vary also for regular shapes with vesicle elongation (i.e., passing from circular to elliptical shapes; circle has C and SF≈1; ellipse has C and SF <1) while R maintains consistent values for regular circular and elliptical shapes (R≈1). The denomination *shape factor* (3 in previous list)

follows Shea et al. (2010); however, this parameter has been indicated with various names in the volcanological literature, particularly in clasts morphology studies (e.g., roundness, circularity, form factor; Manga et al., 2011; Liu et al., 2015). The R parameter introduced here is similar to the Regularity parameter adopted in Shea et al. (2010). Both parameters can provide a measurement of the vesicle complexity irrespective of vesicle elongation and are based on the comparison between the vesicle area and the area of the vesicle best fit ellipse. However, the two parameters differ in the function used to calculate the object's best fit ellipse. More information is reported in **Appendix F**.

D, E, FLT and AR measure the vesicle degree of elongation or stretching (**Fig. 4.2**). The D parameter is widely used in vesicles studies to quantify the degree of stretching (e.g., Polacci et al., 2001; 2003; Rust et al., 2003; Shea et al., 2010), while E and FLT are useful parameters when describing elliptical shapes and are included in other vesicle shape image analysis programmes (e.g., Shea et al., 2010). Based on the relationship between D and AR illustrate in **Figure 4.3**, vesicles are termed in this study as subspherical, elongated, very elongated, extremely elongated and thread-like.

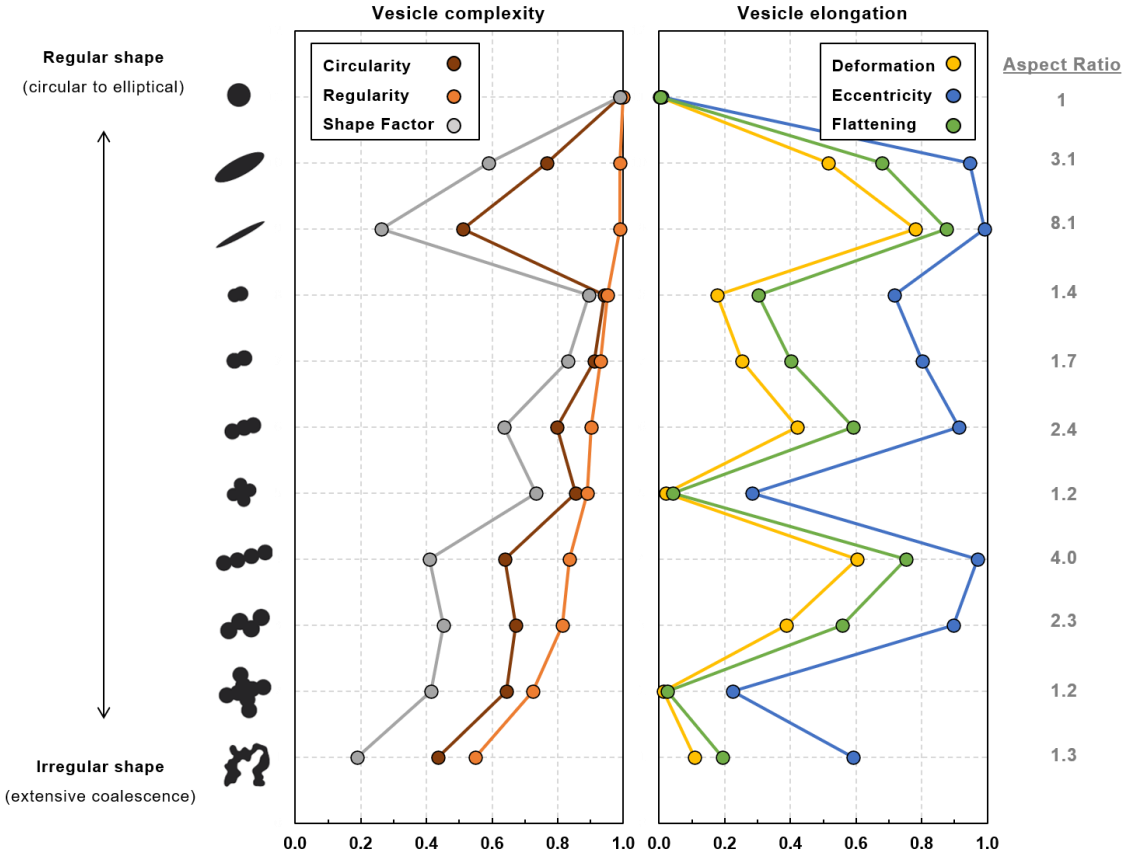

Figure 4.2 – Shape variation captured by the shape parameters used in this study. The eleven hypothetical vesicle geometries are reproduced from Moitra et al. (2013). See text for more details and equations of individual shape parameters.

Although C and SF, as well as D, E and FLT display similar trend with variation in vesicle outlines (**Fig. 4.2**), in this study all parameters are applied together for vesicle shape quantification, since no standardised metrics are to date available. Most of the following discussions are, however, centred around the R and D parameters as they are frequently used in vesicle studies (e.g., Polacci et al., 2003; Rust et al., 2003; Shea et al., 2010; Moitra et al., 2013).

It is important to note also that since the images used are in pixels (not vectors) a given shape parameters approaching the endmember values in the scale is usually approximately equal (≈) rather than equal (=) to 1 or 0 (see also Moitra et al., 2013). Finally, when quantifying shape from different images, only obtained vesicle shape distributions of images at the same magnification from a selected clast sample are averaged (**see Section 4.3.1**).

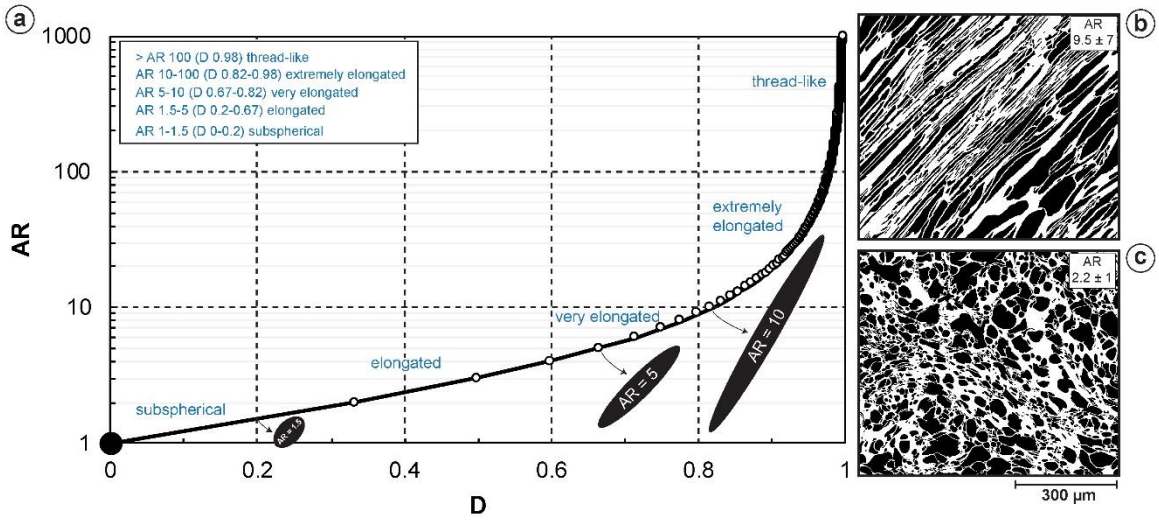

Figure 4.3 – (**a**) Relationship between Aspect Ratio (AR) and Deformation (D) parameters, with nomenclature for elongated vesicles used in this study: *subspherical* (AR = 1 to 1.5 and D = 0 to 0.2), *elongated* (AR = 1.5 to 5 and D = 0.2 to 0.67), *very elongated* (AR = 5 to 10 and D = 0.67 to 0.82), *extremely elongated* (AR = 10 to 100 and D = 0.82 to 0.98) and *thread-like* vesicle (AR > 100 and D > 0.98). Schematic example of vesicles at different elongations are reported in the graph (AR = 1.5, AR = 5, AR = 10, AR = 50 and AR = 100). To the right side, two SEM-BSE images at 200× magnification (processed and binarized) from PA (**b**) and OR cuts (**c**) are reported for comparison, with mean values of AR and ± standard deviation.

4.2.4.2 Vesicle size and number density analysis

Vesicle area and vesicle counts are also quantified in order to determine the following parameters: (1) the 2D vesicularity, which estimates the area fraction of vesicles per melt area in % (here no thresholding area used for vesicle lower limit size); (2) the vesicles number density N_A, which measure the number of vesicles per unit melt area; (3) the vesicles size distribution (VSD) per

melt area. The VSDs are expressed in terms of both N_A (N_A-VSD; number of vesicles of given vesicle size) and area fraction (area-VSD; area occupied by vesicles of given vesicle area), similar to VSDs presented in stereological converted 2D-to-3D data (e.g., Adams et al., 2006; Carey et al., 2009; Rotella et al., 2014). Each parameter is corrected for the presence of crystals (usually phenocrysts) in the image, i.e., the total area of the crystal is removed from later vesicle calculation and the results are always glass (thus melt) referenced (Giachetti et al., 2010). In the VSD, the vesicle sizes are expressed as diameter of the circle of equivalent vesicle area and reported across 30 geometric bin size classes, using a geometric bin factor of $10^{0.1}$ (Sahagian and Proussevitch, 1998), starting from the smallest vesicle diameter measured at 1.84 µm. Following Giachetti et al. (2010) the VSD for each magnification was obtained by averaging the VSD of individual images at the same magnification. To later reconstruct the complete VSD of the sample from images across different magnifications the method proposed in Shea et al. (2010) is used here, where magnification cut-offs are applied using the N_A vs vesicles size curves of images at 20× and 200×magnifications (see **Section 4.4.1**). To reconstruct the total N_A of a thin section sample, the N_A from images at the same magnification are average, then the obtained individual averaged N_A from different magnifications are summed.

4.3 Results

4.3.1 Variability of 2D vesicle shape

The 2D shapes of individual vesicles are quantified using binary SEM-BSE images of the three pumice microtexture types recognised in the deposits of the Kaharoa eruption (**Fig. 4.1**). Both (PA) and orthogonal (OR) cuts to main direction of vesicle elongation are analysed at magnifications of 20×, 50×, 100× and 200× (**Fig. 4.4** and **Table 4.3**). The dataset collated from the vesicle shape analysis is used to estimate the influence of thin section orientation and magnification selection on the resulting shape parameters.

4.3.1.1 Variation of vesicle shape with thin section orientation

The larger variations in vesicle shapes are associated with the thin section orientation. As a result of the anisotropic vesicle structure of the samples, with vesicles stretched along a main direction, the PA cuts predominately contain longitudinal-sections, while OR cut predominately contain

cross-sections of the stretched vesicles. Consequently, the largest differences in vesicle shape with thin sections orientation are observed in the deviation from circular shapes and the degree of elongation. The most elongated vesicles occur in the PA cuts with mean values of D >0.5 in type 2 and type 3 textures and <0.5 in type 1 (**Fig. 4.4**). On the contrary, the least elongated vesicles occur in OR cuts, where mean D values are around 0.35 to 0.25 (**Fig. 4.4**). The FLT parameter also displays high values, >0.6-0.7, in PA cuts and around 0.5 in the OR cuts, whereas the E parameter show narrow ranges close to 1 in the PA cuts and wider ranges in the OR cuts (**Fig. 4.4**). The differences between PA and OR cuts are also evident in the C and SF parameters, showing more circular values in the OR than PA (**Fig. 4.4**).

4.3.1.2 Variation of vesicle shape with magnification and vesicle size

Each individual magnification enables to capture a different vesicle size range (VSR in **Fig. 4.4**; see also **Table 4.2**) and total number of vesicles per analysed images (N in **Fig. 4.4**). The results show that the vesicle shape parameters do not vary significantly within images at high magnification (50×, 100× and 200×) while the most prominent differences are observed between images at 20× and the rest (**Fig. 4.4 and Fig. 4.5**). The 20× images are characterised by overall less elongated (i.e., D, E and FLT, closer to 0; **Fig 4.4**), irregular and complex vesicles (i.e., of C, R, and SF away from 1; **Fig. 4.4**) than the higher magnifications.

Figure 4.5 shows the frequency distributions of the vesicle elongation parameter D and the vesicle shape complexity parameter R. The shape distributions in the 20× images are always skewed towards lower values in both D and R parameters with respect to the distributions at 50×, 100× and 200×. Vesicle shape complexity is sensitive to the magnification change from 20× to higher magnifications, evident in particular in the OR cuts (**Fig. 4.5h** and **k**). Vesicle elongation is less affected by the change in magnification in the OR cuts, where distributions from 20× to 200× are similar (**Fig. 4.5g, j** and **l**), however in the PA cuts 20× and 50× to 200× display different distributions and modes. Within the higher magnification images (50×, 100× and 200×), D and R have nearly matching distributions and modes. However, the frequency of very elongated to extremely elongated vesicles (D>0.7) typically increase passing from 50× to 200× images (**Fig. 4.5a, c, e**), as well as the frequency of very regular vesicle shapes (R>0.9) (**Fig. 4.5d, f, h, k** and **m**).

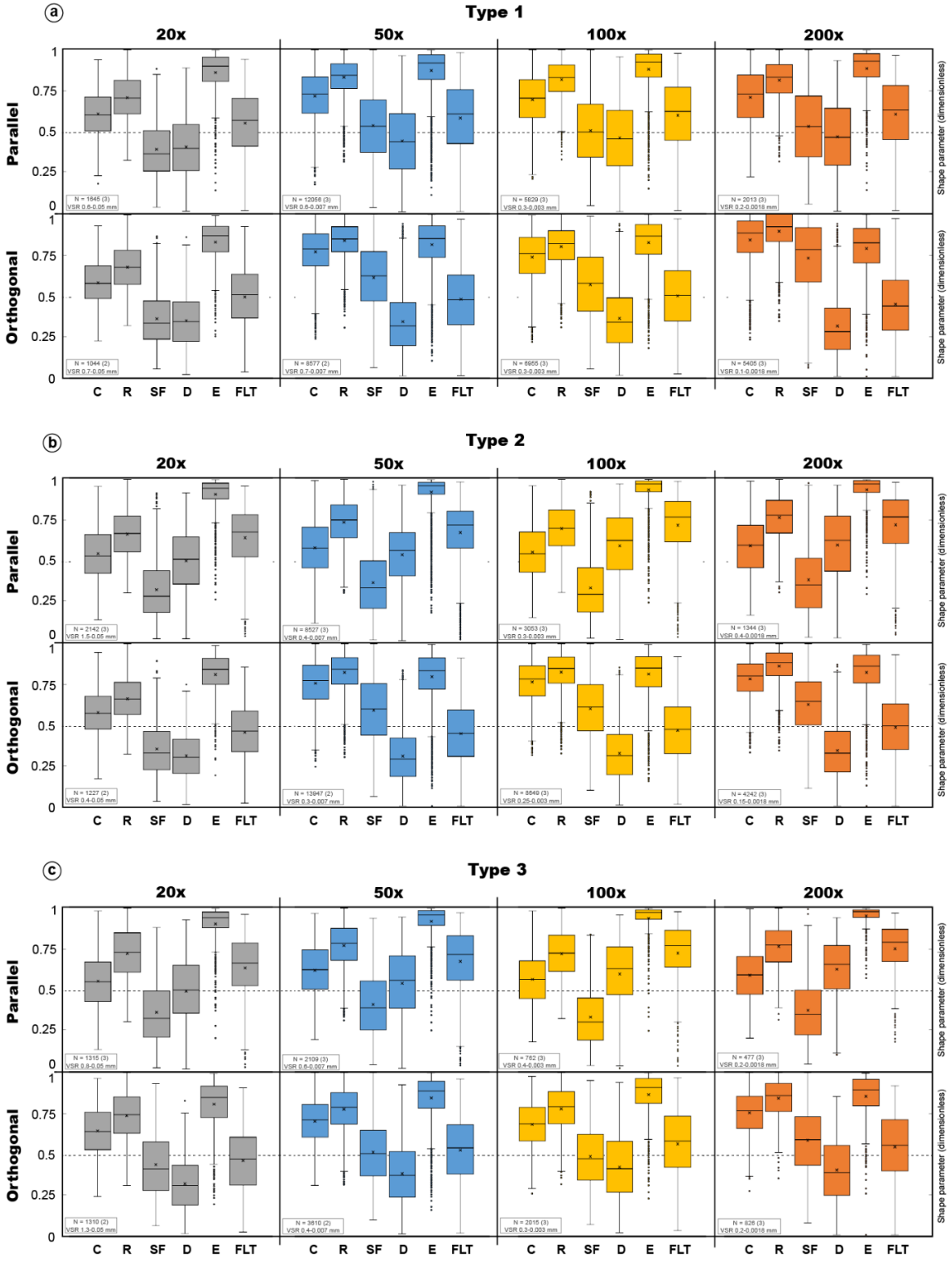

Figure 4.4 – Boxplots of the 2D vesicle shape parameters quantified from images acquired at 20×, 50×, 100× and 200×, along two mutually perpendicular thin sections (PA and OR to main direction of vesicle elongation) in the three vesicle textures analysed: (**a**) Type 1, (**b**) Type 2 and (**c**) Type 3. The shape parameters are dimensionless and are indicated as C = circularity, R = regularity, SF = shape factor, D = deformation, E = eccentricity and FLT = flatness. C, R and SF measure the complexity of the 2D vesicle, while D, E and FLT measure the elongation of the 2D vesicle. See text for shape parameters equations and examples in Fig. 4.2. Inset in each graph indicate the number of vesicles analysed (N), the number of images taken (in brackets) and the vesicle size range (VSR, in mm) per each magnification.

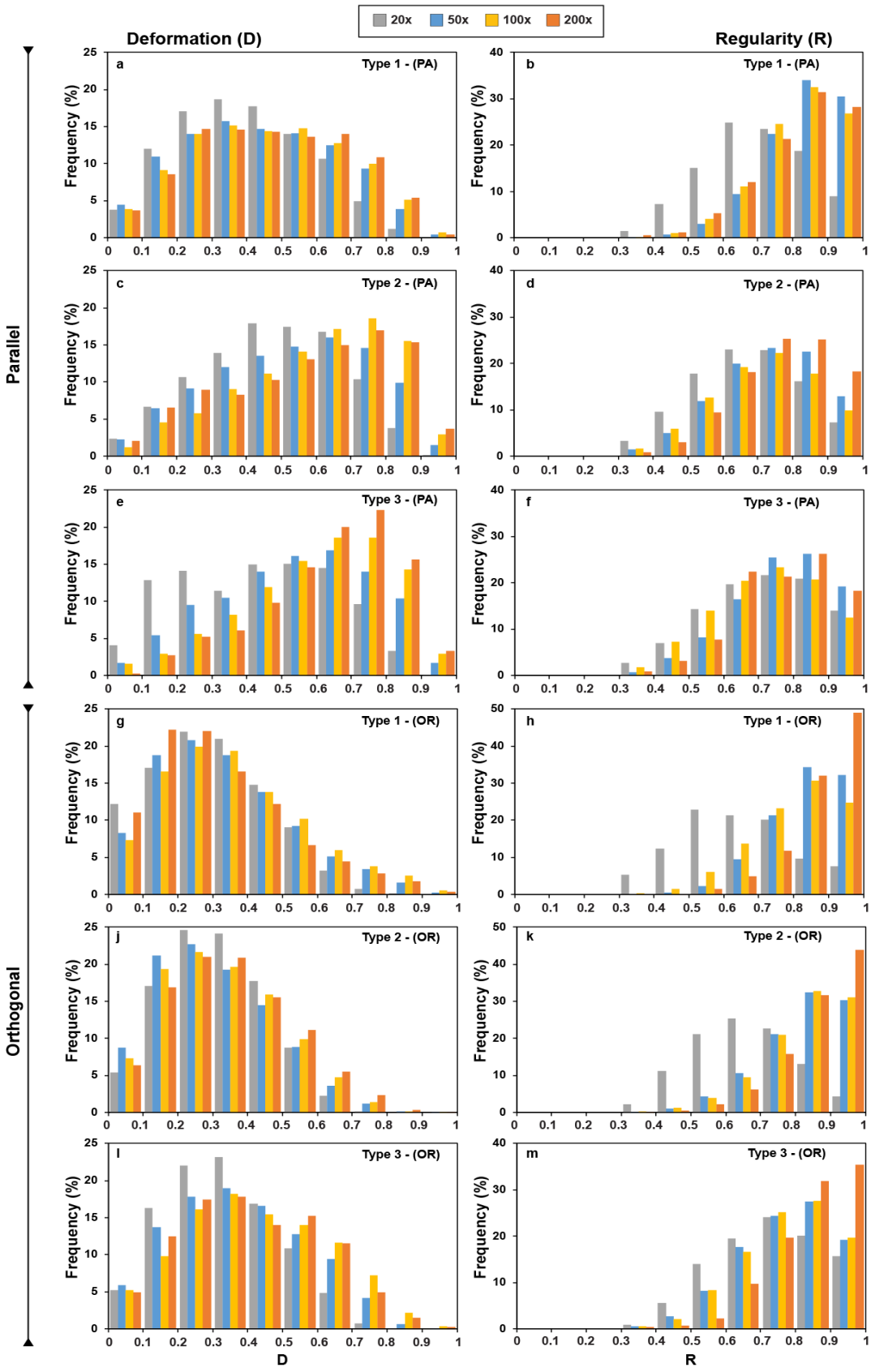

Figure 4.5 – Frequency distributions of the Deformation (D) (vesicle elongation) and Regularity (R) (vesicle complexity) parameters among the vesicle texture types 1, 2 and 3 from both PA and OR cuts to main vesicle elongation. The distributions resulting from the images acquired at 20x, 50x, 100x and 200x are reported in different colours (grey, blue, yellow and orange, respectively) in each graph for comparison.

Table 4.3 – Summary of 2D vesicle shape parameters quantified for the three different pumice microtextures investigated in this study. Results of each thin sections consist of the vesicle shape data collected over 10 (OR thin sections) to 12 (PA thin sections) images acquired at four magnifications (20x, 50x, 100x, 200x). STD = Standard deviation.

Texture type and thin section orientation		Circularity (C)	Regularity (R)	Shape Factor (SF)	Deformation (D)	Eccentricity (E)	Flattening (FLT)	Ellipse Aspect Ratio (AR)
Type 1 PA	Max	1.000	1.000	1.000	0.965	1.000	0.982	56.42
	Min	0.172	0.311	0.029	0.003	0.108	0.006	1.00
	Mean	**0.700**	**0.816**	**0.513**	**0.444**	**0.875**	**0.584**	**3.49**
	STD	0.155	0.124	0.211	0.212	0.131	0.213	2.87
Type 1 OR	Max	1.002	1.000	1.000	0.949	1.000	0.970	38.37
	Min	0.212	0.301	0.045	0.000	0.000	0.000	1.00
	Mean	**0.771**	**0.837**	**0.619**	**0.336**	**0.810**	**0.473**	**2.51**
	STD	0.157	0.128	0.226	0.192	0.153	0.208	2.21
Type 2 PA	Max	0.993	1.000	0.985	0.972	1.000	0.982	70.32
	Min	0.116	0.301	0.013	0.008	0.178	0.016	1.02
	Mean	**0.569**	**0.720**	**0.353**	**0.546**	**0.923**	**0.681**	**5.11**
	STD	0.169	0.149	0.197	0.205	0.101	0.190	4.52
Type 2 OR	Max	1.000	1.000	1.000	0.838	0.996	0.912	11.36
	Min	0.170	0.301	0.029	0.000	0.000	0.000	1.00
	Mean	**0.754**	**0.822**	**0.587**	**0.317**	**0.806**	**0.458**	**2.16**
	STD	0.138	0.126	0.198	0.164	0.144	0.188	1.06
Type 3 PA	Max	0.997	1.002	0.994	0.957	1.000	0.978	45.60
	Min	0.127	0.301	0.016	0.010	0.199	0.020	1.02
	Mean	**0.588**	**0.747**	**0.377**	**0.542**	**0.921**	**0.677**	**4.86**
	STD	0.163	0.149	0.193	0.209	0.102	0.194	4.00
Type 3 OR	Max	1.002	1.000	1.000	0.875	1.000	0.969	15.06
	Min	0.237	0.304	0.056	0.000	0.000	0.000	1.00
	Mean	**0.691**	**0.775**	**0.498**	**0.376**	**0.841**	**0.519**	**2.64**
	STD	0.143	0.139	0.194	0.188	0.141	0.202	1.68

4.3.1.3 Vesicle aspect ratio vs. vesicle size

Vesicle elongation is also estimated using the non-normalized parameter AR, which display the linear variation in elongation according to the ratio between the long to the short axes of the 2D vesicle ellipse (see **Section 4.2.4.1**). The variation in vesicle AR with vesicle size is illustrated in **Figure 4.6**. The AR notably decreases with the increase in vesicle size. Typically, vesicle >150-200 µm are associated with values of AR between 1 and 5. Smaller vesicles are characterised instead by progressively higher AR up to >50 in the PA cuts. The larger variation in vesicle AR is associated with the vesicle population <30 µm, where AR can vary up to one order of magnitude (e.g., 1 to 50 in PA cuts).

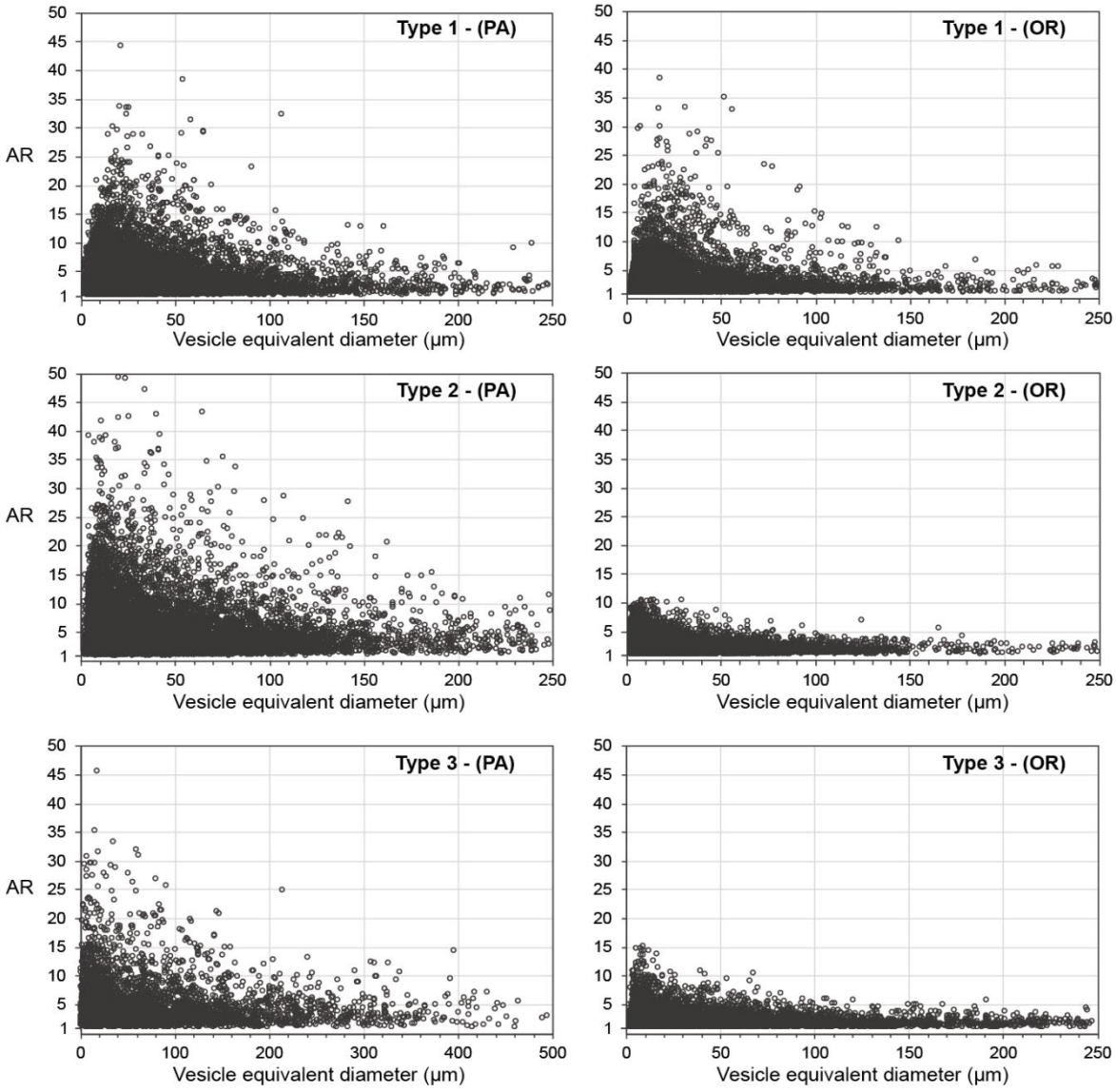

Figure 4.6 – Variation in vesicle AR with vesicle size among the three texture types. To simplify data visualization, upper limits for both vesicle size and vesicle AR are set in each graph to contain >95% of vesicles analysed. For maximum AR values see **Table 4.3**. Vesicles tend to maintain steady AR for size >250 µm.

4.3.1.4 Vesicle shape and texture type

Overall, the difference in vesicle elongation from PA and OR cuts in type 1 is lower than the other texture types (**Fig. 4.4** to **4.6**). This is due to the observed more complex spatial distribution of stretched vesicles and to the whole-clast vesicle heterogeneity (**Section 4.2.1**). In type 1 texture, though to a lesser extent, vesicles are deformed also in the OR cuts and subspherical vesicles are found in the PA cuts (**Fig. 4.1**). This, together with the occurrence of areas of apparently undeformed vesicles in type 1, contributes to a less marked difference from PA and OR vesicle elongation with respect to the results from the strongly anisotropic type 2 and type 3 textures (e.g., **Fig. 4.6**). The changes in the irregularity or shape complexity of the vesicles (expressed by the R parameter) with thin section orientation differs among the different textures. In textures type 2 and 3, the OR thin sections are characterized by lower (i.e., more irregular shape) values of R (means at 0.8-0.75) than what expected for strongly anisotropic textures, where cross-section cuts of elongated vesicles should result in regular subspherical shapes. In other words, the OR sections cut along or close to the plane containing the vesicles' short and intermediate axes, for which circular or low aspect ratio elliptical shapes might be expected (both shapes would have R≈1). The deviation from R≈1 suggests that vesicles within this plane have irregular shapes, which can be produced by the coalescence of originally separated bubbles or by bubbles collapse and bubble walls rupture and wrinkling. SEM observations confirm that lower values from R≈1 are due to bubble coalescence, resulting in irregular vesicle shapes in the preserved pumice microtexture (e.g., **Fig 4.1**). This is best recorded in OR thin section where a larger number of vesicles (and their original bubble interactions perpendicular to bubble stretching) are preserved. Formation of irregular vesicle shapes also influences the overall vesicle elongation in the OR cuts, where the coalescence of more bubbles can produce overall low aspect ratio, however elongated, vesicles shapes, and a less abundant population of subspherical vesicles (see D parameter in **Fig. 4.4**). This effect is also recorded by the FLT parameter which has mean values of 0.4-0.5 (**Fig. 4.4**), associated with more oblate objects.

4.3.2 Variability of 2D vesicle size and number density

Results for 2D vesicularity, number density and vesicle size distribution of the three pumice microtexture types are summarised in **Table 4.4**.

4.3.2.1 Vesicularity

The percentage of vesicle area to glass area is calculated for each analysed image and the results are reported in **Figure 4.7**. The 2D vesicularity appears independent from thin section orientation. This is in agreement with Polacci et al. (2003), where no significant changes in vesicularity were found from two differently oriented thin sections with respect to vesicle elongation. More significant changes are observed between images at different magnifications (**Fig. 4.7**). The vesicularity of the 20× images is lower and with larger ranges (~35 to 50%) than the higher magnification images (~50 to 60%). The difference in vesicularity between 20× and 50-100-200× images is reduced in type 3 samples, which are characterised by overall larger vesicles (**Fig. 4.7**). Within the 50-100-200x images, the difference in vesicularity varies from few % to 10%.

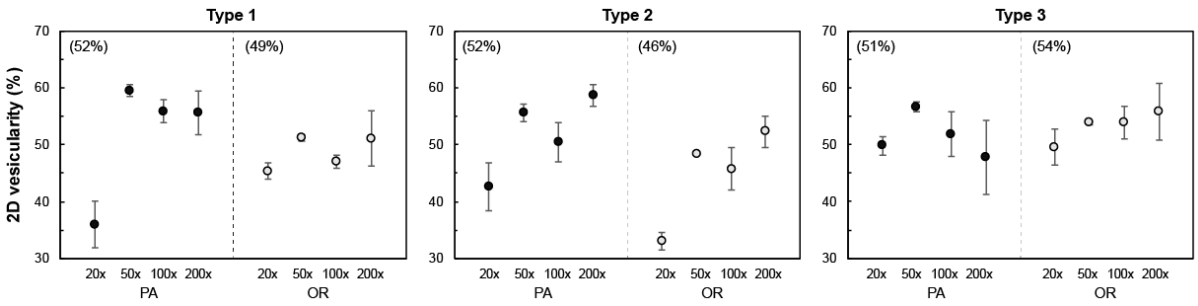

Figure 4.7 – Variation in 2D vesicularity (corrected for crystal content) with image magnification and thin section orientation among the three texture types, type 1 to type 3. Values in brackets indicate the average of 2D vesicularity across all the magnifications per thin sections. Error bars are reported as standard deviation from the results of images at the same magnification.

4.3.2.2 Vesicle number density

Individual N_A are calculated for each bin size class and image at different magnifications. As with increasingly higher magnifications images capture smaller area and resolve progressively smaller vesicles, calculated N_A values vary with magnification selection. **Figure 4.8** shows the variation of N_A as a function of vesicle size for individual magnifications. In the studied samples, the smaller vesicles (~1-30 μm) dominate the N_A distributions. For vesicles <100 μm, individual N_A of images at 200× are always larger than those at lower magnifications (**Fig. 4.8**). The N_A from

200× images contribute to most of the total N_A, up to 95%. The 100× and 50× images display similar N_A trends, having for each given vesicle size similar individual N_A (**Fig. 4.8**). At vesicles <50 µm the N_A of 100× and 50× images are typically half those of the 200× magnification (**Fig. 4.8**). Finally, the images at 20× magnification provide a very small contribution to the total N_A, from 1 to 5% (**Fig. 4.8**).

With respect to thin section orientation, the N_A results of OR cuts are typically two to three times higher than those in the PA counterparts. This effect is reduced for the coarse vesicle fraction at 20× in type 1 and 2 textures, where OR and PA cuts have nearly identical N_A at 20× (**Fig. 4.8; Table 4.4**).

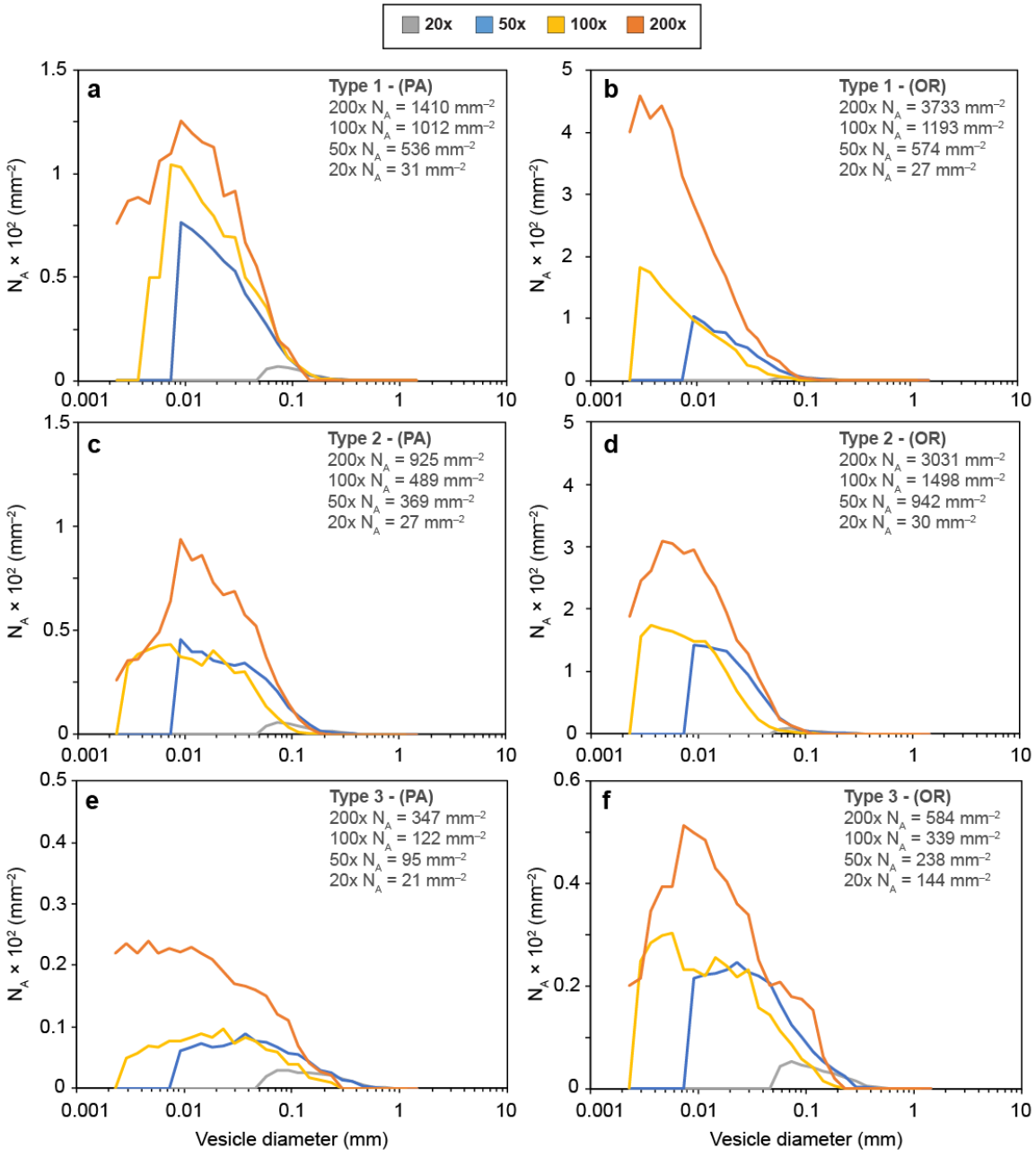

Figure 4.8 – ***(caption in next page)***.

Figure 4.8 – ***(figure in previous page)*** N_A-VSDs. Vesicle number density per area (N_A) as a function of vesicle size (expressed as the diameter of the circle of equivalent area) for the three texture types and thin section cut: (**a**) and (**b**) are type 1, PA and OR cuts, respectively; (**c**) and (**d**) are type 2, PA and OR cuts, respectively; (**e**) and (**f**) are type 3, PA and OR cuts, respectively. The plotted N_A are per melt area as they are corrected for crystal content of individual images. In each graph, N_A vs vesicle size plots resulting from the images acquired at 20×, 50×, 100× and 200× magnifications are displayed in different colours (grey, blue, yellow and orange, respectively) for comparison. The average N_A calculated across individual magnification are reported in each graph. Note the change in the y-axis scale from PA to OR cuts.

4.3.2.3 Vesicle size distribution

The variations in area-VSDs per magnification and thin section orientation are illustrated in **Figure 4.9**. The area-VSDs of 200× and 100× images show unimodal distributions with very similar modes varying from 30 to 65 µm in type 1 and 2, and from 100 to 250 µm in type 3 (**Fig. 4.9**). The 20× images have area-VSDs skewed towards large vesicles and vary among the different samples from unimodal (mode at 100 to 330 µm) to bimodal (second mode at 650 to 1300 µm) distributions. The images at 50×, which capture the largest vesicle size range of the analysed clasts (from vesicle of 7 to about 1000 µm in diameter; **Table 4.2**) show a combined VSDs across 200×-100× to 20× magnifications. The 50× distributions are bimodal in type 1 and type 2 textures, with a primary mode at small vesicle sizes, which coincided with 200× and 100× images, and a second mode at larger vesicle sizes, which coincide to the main mode of the 20× images (**Fig. 4.9**). In type 3, where area-VSDs are typically unimodal in each magnification, the 50× images have and intermediate mode between the one of images at 200×-100× and those at 20× images (**Fig. 4.9**).

The variations in area-VSDs with thin section orientation are not as significant as the one observed in the N_A (**Fig. 4.8**) or for the vesicle shape results (**Fig. 4.4 to 4.6**). The influence of thin section orientation in the strongly anisotropic textures type 2 and type 3 result in a shift of the modes (typically of ~three bin size classes) at each magnification towards smaller vesicles sizes from PA to OR cuts (**Fig. 4.9**). In type 1, where tube vesicles occur, to a lesser extent, also in the OR cuts, area-VSD and modes of PA and OR cuts are very similar. Within type 1, it is to be noted an increase in vesicle area % occupied by smaller vesicles (<30 µm) in OR cuts respect to the PA cuts (**Fig. 4.9**).

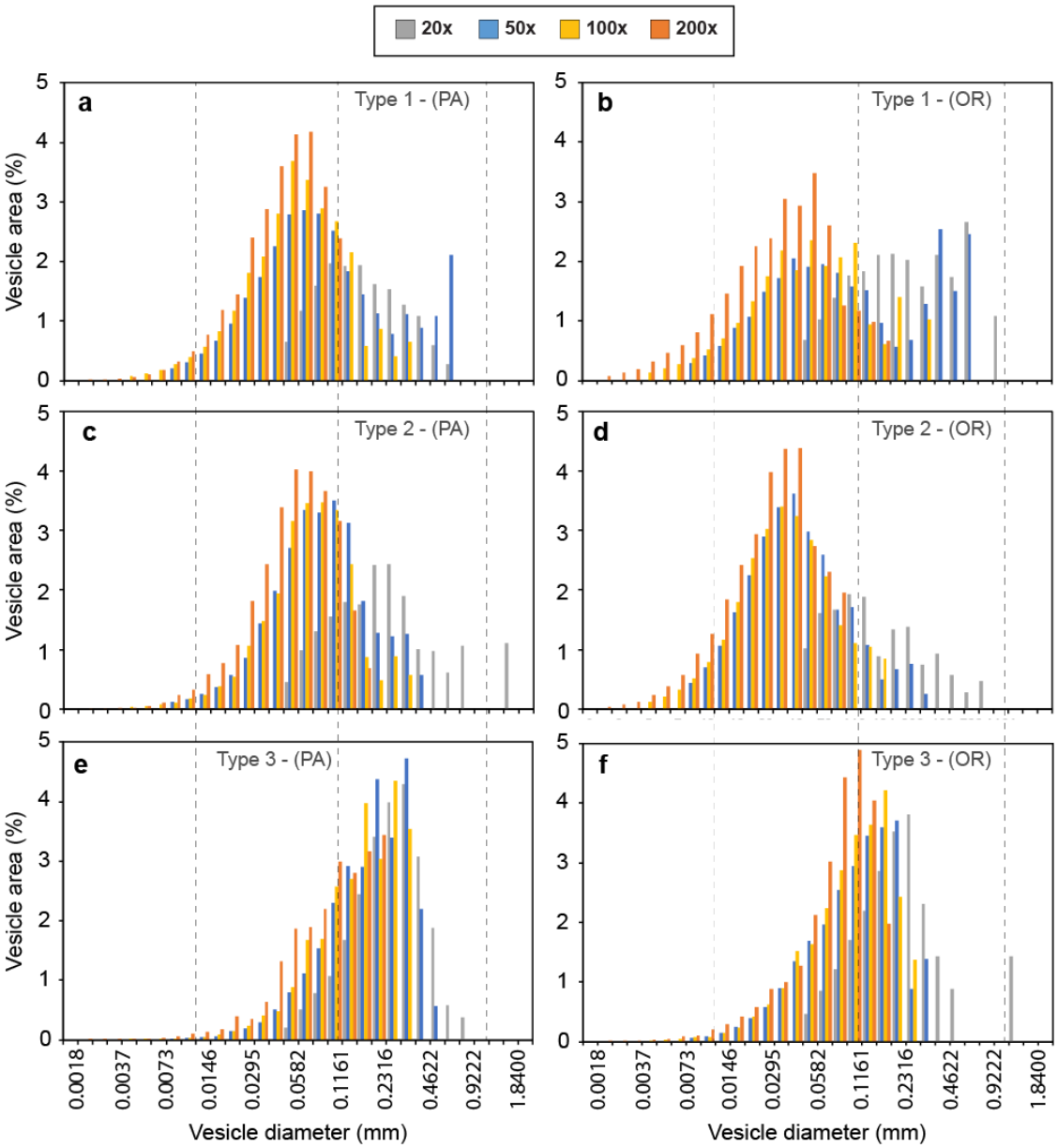

Figure 4.9 – Area-VSDs. Vesicle size distributions per melt area (corrected for crystal content) of images acquired at 20× (grey), 50× (blue), 100× (yellow) and 200× (orange) magnifications. VSDs are plotted for the three texture types and two thin section cuts: (**a**) and (**b**) are type 1, PA and OR cuts, respectively; (**c**) and (**d**) are type 2, PA and OR cuts, respectively; (**e**) and (**f**) are type 3, PA and OR cuts, respectively. Vesicle size (diameter of the circle of equivalent area) are reported across 30 geometric bin size classes (geometric bin factor is 100.1, see text for detail) from 1.84 µm (diameter of smallest vesicle analysed).

Table 4.4 – Summary of 2D vesicularity, number density (N_A) and area vesicle size distribution (area-VSD) quantified for the three different pumice microtextures investigated in this study at PA and OR cuts. Values reported in the table are average of three images per magnification.

Texture Type	Thin section orientation	Mag.	Vesicularity (%)	N_A (mm^{-2})	Area-VSD Mode 1 (μm)	Area-VSD Mode 2 (μm)
1	PA	20x	36	31	165	-
1	PA	50x	60	536	65	655
1	PA	100x	56	1012	65	-
1	PA	200x	56	1410	65	-
1	OR	20x	45	27	165	655
1	OR	50x	51	574	52	655
1	OR	100x	47	1193	52	-
1	OR	200x	51	3733	52	-
2	PA	20x	43	27	261	1628
2	PA	50x	56	369	104	261
2	PA	100x	50	489	65	-
2	PA	200x	59	925	52	-
2	OR	20x	33	30	104	261
2	OR	50x	48	942	41	261
2	OR	100x	46	1498	32	-
2	OR	200x	52	3031	32	-
3	PA	20x	50	21	329	-
3	PA	50x	57	95	239	-
3	PA	100x	52	122	261	-
3	PA	200x	48	347	207	-
3	OR	20x	50	144	261	1310
3	OR	50x	54	238	207	-
3	OR	100x	54	339	165	-
3	OR	200x	56	584	104	-

4.4 Discussion and implications

4.4.1 Representativeness and uncertainties in vesicle textures analysis

Uncertainties in the quantification of vesicle features can be derived from several factors (Gurioli et al., 2015; Saubin et al., 2016), grouped into two main categories: (1) operator bias and (2) data representativeness of natural variability.

Although the textural characterisations of vesicles from pyroclasts have established and generalised practices (e.g., Klug et al., 2002; Shea et al., 2010; Giachetti et al., 2010), operator errors and bias persists and are associated with a number of decisions that have to be taken during the various stages leading to the textural analysis (Shea et al., 2010). These include sample preparation (e.g., thin section orientation), sample imaging strategy (e.g., magnification selection/image resolutions and sample area selection) and image processing (e.g., manual and/or automatic vesicles walls reconstruction and vesicles "decoalescing" approaches). Moreover, uncertainties in textural data can also arise from how well the textural analysis approach used can represent the intrinsic heterogeneity of individual clasts (and/or amongst a set of clasts). The heterogeneities at the clast scale may or may not be fully characterised by quantitative textural analysis, with the risk to represent only a fraction of the natural sample variability.

In anisotropic vesicle textures, such as those in tube pumice clasts, the above-mentioned factors must be taken into careful consideration to provide a more objective and representative characterisation of vesicle shape and size distributions. As the 2D image processing of elongated vesicles can be extensively time-consuming (Polacci et al., 2001; 2003), the challenge in textural analysis is to balance the number of analysis/images required to capture the natural sample heterogeneities within a reasonable working time to obtain consistent and representative results (Shea et al., 2010). The systematic vesicle shape and size quantification of pumice microtextures presented in this study, at different magnifications and among two oriented thin sections, provides further elements to discuss the uncertainties and representativeness of vesicle image analysis.

4.4.2 The importance of thin section orientation

Thin section orientation is a key factor when characterizing vesicles in anisotropic textures (e.g., **Fig. 4.5; Fig. 4.6; Fig. 4.8**). Internal anisotropy in vesicle distribution, deformation and orientation are usually evident from the inspection of the clast's morphological and from the

vesicles intersecting the clast's external surface. However, during sample preparation, it is recommended to perform preliminary thin section tests to ensure slicing the clast along the preferred plane(s). In addition, some subtle internal anisotropies and/or heterogeneity in vesicle properties can be not evident from the clast's external morphology/surface (e.g., Giachetti et al., 2021), thus random pumice cuts should always be avoided to minimise possible sample bias when comparing different clasts.

The PA and OR cuts to the main direction of vesicle elongation enable quantifying different but equally important features of the sample vesicle texture. PA cuts can provide a window into the deformation of vesicles stretched along a main direction. The degree of vesicle elongation can be quantified accordingly in PA cuts using shape parameters such as D and AR, which can be then applied to estimate the shear rate and flow type experienced by the ascending magma (e.g., Dingwell et al., 2016; Ohashi et al., 2018; Ohashi et al., 2020a and b). As the vesicles are not randomly oriented but aligned along a main direction, the OR cuts can provide instead a more accurate estimation of the the number of vesicles per unit area. The 2D vesicle number density in OR cuts can be later used as a basis for the estimation of the number of vesicles per unit volume, in combination with the vesicle elongation data from PA cuts (see Mitchell et al., 2019). If accurate 3D vesicle number densities can be determined, this information can be used as a proxy to infer the decompression rate experienced by the magma prior fragmentation as it has been proposed for vesicle data from spherical pumices (e.g., Toramaru, 2006; Carey et al., 2009; Shea et al., 2012; Myers et al., 2021). In addition, the OR cuts are useful to characterise the degree of interactions of bubbles by coalesce perpendicular to the direction of shear, and to infer whether the elongated vesicles are flattened or have circular shape in cross-sections (see Sparks et al., 1994) if not extensively overprinted by coalescence.

When characterising the vesicle sizes distribution, the area-VSDs preserve the same trends in PA and OR cuts. However, if only one preferential cut is used to quantify vesicle features, it is to be noted that the area-VSD modes can shift to smaller vesicles sizes in the OR cuts respect to PA cuts (the mode shift is of about three bin size classes).

4.4.3 Optimal image magnification(s) for vesicle analysis

The use of images at different magnifications enables the measurements of textural features and heterogeneities at different scale. Results of both vesicle shape and size analyses showed that there is a pronounced difference between vesicle data from 20× and from 50-200× images.

The low magnification images at 20× can adequately resolve vesicles having an equivalent diameter of >50 μm and, in particular, can characterise the very large vesicle population (>1000

μm) typically resulting from protracted coalescence (e.g., Klug et al., 2002; Shea et al., 2010). Thin glass walls (on the order of few μm) and smaller vesicles (<50 μm), cannot instead accurately be resolved at 20× magnification. In the pumice microtextures analysed, the large (>250 μm) and very large vesicles in 20× images are further characterised by less elongated and often irregular shapes, which differ from the shape features observed for smaller vesicles in higher magnification images.

With the increase in pixel density per vesicle and glass walls, images at higher marginations, 50× to 200×, can accurately quantify the shapes of vesicle at progressively smaller sizes. Among the images at 50×, 100× and 200×, there are no significant differences in the distribution of the quantified shape parameters. However, a small increase in vesicle elongation and decrease in vesicle complexity was noted passing from 50× to 200× images (e.g., **Fig. 4.5**). These differences are likely associated with the spatial heterogeneity of the sample at the microscopic scale. By capturing larger sample areas with images at 50× (image width ~3 mm; **Table 4.2**), more spatial heterogeneities in vesicle shape can be included in the imaged sample area, which can result in changes of the mean shape parameters compared to that of 200× images (image width ~0.7 mm). In addition, the inclusion in the imaged area of a greater number of larger vesicles (>250μm) can impact the shape distribution. Within the pumice microtextures analysed, larger vesicles are typically less elongated and have more irregular shape on average (e.g., **Fig. 4.4**). These effects (spatial heterogeneity and inclusion of larger vesicles) can reduce for example the quantified vesicle elongation and increases the vesicle shape irregularity compared to those calculated in higher magnification images.

Some differences from low to high magnification images are also observed in the quantified area-VSDs. The size distributions resulting from images at 100× and 200× are very similar, with modes at 30 to 65 μm (type 1 and 2 textures) and 100 to 250 μm (type 3 texture) varying depending on texture types and thin section orientation, with 20× size distributions skewed at large vesicle sizes (**Table 4.4**). The area-VSDs of images at 50× typically overlap the distributions of both images at 100× to 200× and at 20×, therefore they do not add significant information to the vesicle size characterisation (**Fig. 4.9**).

As vesicles in pumice vary in size over up to four orders of magnitudes, typically pumice textures are imaged with several magnifications (e.g., **Table 4.1**) yielding to an equally large number of images in which perform vesicle analysis. Considering differences and similarities in both vesicle shape and size results among the four magnifications used in this study, a minimum number and an optimal combination of magnifications can be recommended for the quantification of vesicle textures. The results of this study indicate that the combination of high-resolution images

(4096×3775 pixels) at 20× and at 200× magnifications is sufficient to adequately characterize the vesicle features (both shape and size) of the different analysed pumice microtextures (**Fig. 4.10**).

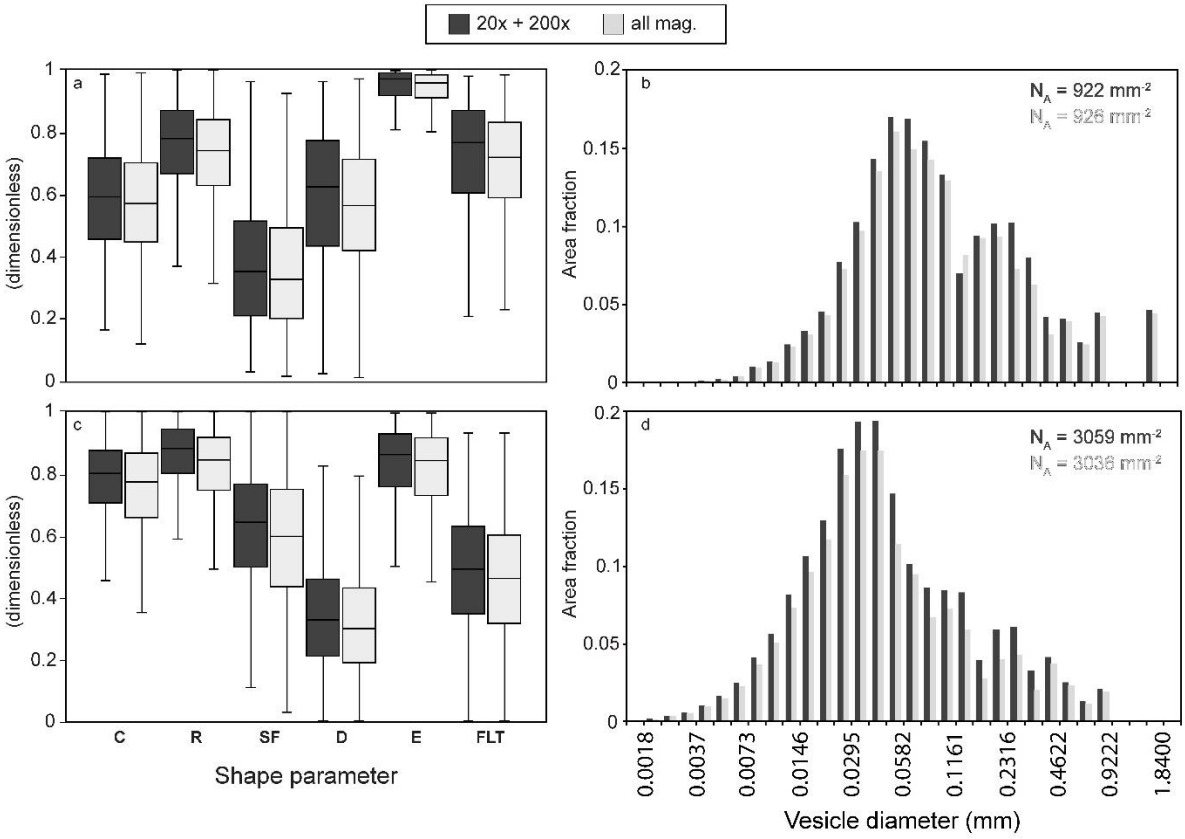

Figure 4.10 – Comparison of vesicle shape and size distributions obtained from the combination of 20× and 200× images (dark grey) and obtained from the combination of images at all magnifications used in this study (light grey), 20×, 50×, 100× and 200×. Texture type 2 is used as an example for the comparison, where (**a**) and (**b**) are vesicles shape and size distributions from the PA cut, while (**c**) and (**d**) are from the OR cut. Boxplots of shape parameters report median, interquartile range and min and max (outliers excluded). The area-VSDs are per melt area express the vesicle area fraction as a function of vesicle equivalent circular diameter in 30 geometric bin size classes. The total N_A resulted from the two magnification combinations are reported in (**b**) and (**d**) for PA and OR cuts, respectively.

The 20× images are essential to capture the very larger vesicle population and reconstruct the sample complete area-VSD. Observation at 20× images can reveal syn-ascent coalescence of large bubbles and/or post fragmentation expansion. Large and small vesicles shape distributions should however be kept separated and not average as they might be the result of different processes (pre-fragmentation or pre- to post-fragmentation). On the other hand, the images at 200× well characterised the smaller vesicle population. They can capture the smallest vesicles at 1.84 µm, while providing an adequate characterisation of vesicle up to 300µm.

As the N_A is primary determined by the contribution of the small vesicle population, the 200× images alone well characterized the N_A of the sample. The 200× images also accurately quantify the vesicle elongation and thus the degree of shearing experienced by the bubble-bearing melt during ascent in the conduit. If very large vesicles are not the target of the study, to reduce the working time spent on manual image editing, the use of high-resolution images at 200× magnification can provide alone an adequate description of vesicle shape, VSDs and total N_A. This is further corroborated by the fact that vesicle of small diameter (<30µm) dominates the vesicle population in silicic pumice clasts (Rotella et al., 2014).

4.4.4 Effects of manual "decoalescence" of interconnected vesicles

Prior to vesicle shape and size analyses, SEM-BSE images often require some steps of manual editing before obtaining the final binary images (**Section 4.2.3**). These steps are required since during sample preparation and imaging, original thin vesicles walls are not entirely preserved in the acquired images, thus vesicles walls need to be manually redrawn. In addition to these necessary manual adjustments, some studies also manually redraw vesicles walls of neighbouring coalescent vesicles, "decoupling" or "decoalescing" vesicles (Giachetti et al., 2010).

This further step can lead to operator bias during manual editing since (i) no standardised guidelines are available and (ii) it is largely dependent on the choices and interpretations of the operator also giving the type of textures and resolution of the images. An associated disadvantage of performing extensive decoupling of vesicles is the increase in the working time on individual images especially for those taken at low magnifications (e.g., Polacci et al., 2003).

In this study, to maintain a consistent approach during image editing only interconnected vesicles showing clear signs of coalesce such as vesicles throats and wall ruptures displaying wrinkling and/or incomplete wall retractions were manually separated (Klug et al., 2002; Mitchell et al., 2019). This is here considered a "minimal decoalescing approach".

To provide some constraints on the influence of manual vesicle decoalescence on the resulting vesicle data, a first-order test was made using images at different magnifications and cuts from seleceted type 2 samples. In these images, interconnected vesicles were first separated using a minimal decoalescing approach (Approach 1 in **Fig. 4.11**) and later using a "maximal decoalescing approach" (Approach 2 in **Fig. 4.11**). In the later, vesicles that show signs of interactions are decoalesed with no restrictions, thus a larger number of vesicles are usually decoalesced depending on the operator interpretations.

Figure 4.11 illustrates the comparison of vesicle data obtained by applying the two different approaches to the same set of images. The comparison shows that no significant changes are

observed in the average vesicle shapes and in the area-VSDs in both PA and OR cuts. Differences occur instead in the vesicle number densities of OR cuts where the total N_A after maximal decoalescing approach is 15% higher than N_A obtain from the minimal decoalescing approach (N_A from the two approaches in PA cuts differ of about 5%) (**Fig. 4.11**).

To reduce the working time on individual images and to reduce eventual operator bias these differences only in the N_A of OR cuts are considered acceptable and the minimal decoalescing approach is preferred. In highly interconnected vesicles textures the choice of one approach respect to the other might have a larger impact in the N_A and both methods should be tested by preliminary analysis and the differences reported (see Gurioli et al., 2015).

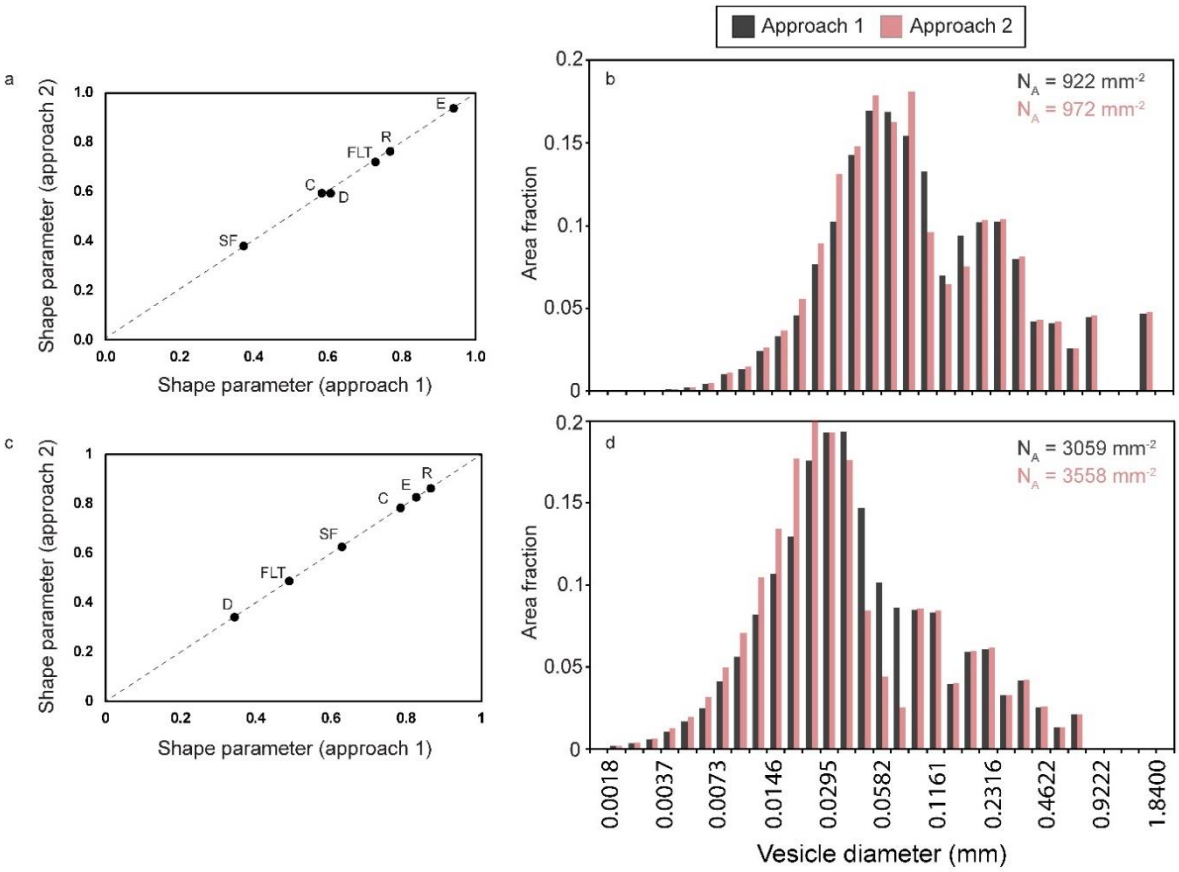

Figure 4.11 – Comparison of vesicle shape and size distributions obtained from the minimal decoalescing approach (Approach 1) and from the maximal decoalescing approach (Approach 2) for images of texture type 2 in PA (**a** and **b**) and OR (**c** and **d**) cuts. See text for more details on the two image editing approaches.

4.4.5 Combination of vesicle shape and size data

Bubbles during magma ascent through a volcanic conduit experience a complex evolution in number, size and shape prior to the eruption, in which many processes occur and overlap, including bubble nucleation, growth, coalescence and collapse (Klug and Cashman, 1996; Klug

et al. 2002; Gonnermann and Manga, 2013). Furthermore, bubble deformation can have an important role in the evolution of the bubble network observed in the final quenched pyroclast texture. For instance, stretching of the bubbles increases bubble coalescence along the direction of bubble elongation (Okumura et al., 2006), which in turn favour the development of a permeable bubble network and the vertical outgassing of volatiles withing the magma column in the conduit (Wright et al., 2006; Wright and Weinberg, 2009; Bouvet de Maisonneuve et al., 2009).

The quantification of the vesicle complexity parameter R in the OR cuts can give an indirect estimation of the degree of coalescence of the bubbles. The estimated R for the pumice samples investigated varies typically between 0.6 and 0.9, suggesting that most of the bubbles have experienced coalescence, also perpendicular to the direction of bubble elongation. This is also confirmed by direct SEM observations (see **Section 4.3.1.4**).

By relating vesicle elongation to vesicle size, it is possible to observe that the smaller vesicles (<30-50 µm) are on average the most elongated (**Fig. 4.5; Fig. 4.6**). In addition, this small-size vesicle population is associated with a larger scatter in elongation from subspherical to extremely elongated shapes. On the contrary, large vesicles (>250 µm) are less elongated but reach more stable values with AR<5 (e.g., **Fig. 4.6**). The larger scatter in vesicles elongation in the small-size vesicle population might by associated with the large number density of small neighbouring vesicles which can influence the shear rate and capillary number of individual vesicles (see also **Section 1.2.4** in **Chapter 1**). The experiments conducted in Ohashi et al. (2020a) suggests in fact that the scatter in the degree of vesicles stretching can results from the inhomogeneous shear field around individual bubbles in a vesiculated magma and to the interaction and coalescence among bubbles, also confirmed by the variation in R values. This is especially true for the strongly anisotropic texture types 2 and 3, while, for texture type 1 the spatial heterogeneity in the distribution of elongated vesicles (i.e., coexistence in the same plane of tube-like and subspherical vesicles) can have further effects.

This study further shows that regardless the type of textures analysed, the average elongation of large vesicles is typically lower when compared to that of smaller vesicles (**Fig. 4.6**). This decrease in vesicle elongation from small to large vesicles suggest that large vesicles formed by a continuous process of bubble growth also after deformation by shearing. This produced vesicles with larger diameters, resulting in an overall progressive decrease in elongation to lower and steady vesicle AR. In the case of the pumice microtextures analysed, this continuous growth of larger bubbles can be ascribed to gas expansion and coalescence with neighbouring bubbles in any directions, hence not aided by shearing along preferential planes.

These findings have an important outcome for studies targeted at estimating the degree of vesicles elongation in pumice clasts. This study shows that quantification of vesicle elongation needs to

be always coupled to vesicle size for an accurate evaluation of the degree of stretching and, in turn, when interpreting magma deformation during ascent.

Recently, a new methodology to quantify vesicle elongation was proposed by Ohashi et al. (2020b) and applied to the tube pumice clasts of the fall and flow deposits of the very large, 232 CE Taupō eruption (Ohashi et al., 2021). The new proposed methodology is based on the use of pumice texture images captured by a digital stereomicroscope with low-angle ring illumination. This instrument enables to image vesicles from unpolished sliced surface of pumice clasts, having the great advantage of cutting down the working time spent on thin section preparation. The authors report that this technique enables to accurately image and reproduce the size and shape distributions of vesicles >50µm, equivalent to the vesicle size range from 20× images in this study. It is here suggested however that for further volcanological interpretations it is important to also incorporate and evaluate the degree of elongation of smaller vesicles. In fact, (i) smaller vesicles (<50µm) can be associated with different degrees of elongation respect to larger vesicles and (ii) larger vesicles might be influenced by coalescence effects overprinting the original (shear-derived) elongation.

4.5 Conclusions

In this study a thorough investigation of the complex and anisotropic vesicle textures was performed using pumice samples from the deposit of a moderate- to large-scale rhyolitic eruption from Tarawera (New Zealand). This study was developed to test the variability of the obtained vesicle data against images magnifications and orientation of prepared polished pumice thin sections. Vesicle shape and size were systematically quantified for three different vesicle textures observed in the ~1314 CE Kaharoa pumices and the influence of magnification selection and thin section orientation to the resulting shape and size distributions was recorded. From this investigation some key finding can be outlined:

1) Thin section orientation is a key factor when characterising the anisotropic vesicle texture of pumice clasts. The PA and OR cuts to the main direction of vesicle elongation enable to quantified different but equally important features of the sample vesicle texture. The PA cuts provide an accurate estimation of the degree of elongation of stretched vesicles. The OR cuts provide instead a more realistic quantification of the sample vesicles number density per unit area. The OR cuts can further provide an estimation of the degree of vesicle interaction and coalescence perpendicular to vesicle elongation, and can allow to

infer the shapes of elongated vesicles in cross-sections if not significantly overprinted by coalescence effects.

2) A minimum number and optimal combination of magnifications was identified for the quantification of vesicle texture in tube pumices. The combination of vesicle size and shape data from 20× and 200× images is adequate to characterise the natural vesicle texture complexity in anisotropic pumices. If large (>250µm) and very large (>1000µm) vesicles are not the target of the study and since in silicic pumices the vesicle population is usually dominated by vesicles <30 µm, vesicle data from high-resolution images at 200× are enough to adequately characterised the pumice vesicle features. This also enables to reduce the working time during image processing by reducing the number of images that must be analysed.

3) The degree of vesicle elongation varies with vesicle size, therefore with the magnification used to image the clast's microtexture. This needs to be considered when using vesicle elongation data to interpret magma dynamic during ascent in the volcanic conduit.

The quantification of vesicle textures in tube pumices has not received as much attention in the past as the more abundant spherical pumice due to the intrinsic complexity of characterising strongly anisotropic vesicle features. After completing the work for this and the following chapter, new studies were published on vesicle texture analyses of tube pumice clasts (Piochi et al., 2021; Ohashi et al., 2021), validating the initial motivations of this study. This work provides guidelines and a reference approach for the 2D quantification of complex and anisotropic vesicle textures, which can be used to infer critical conditions during magma ascent, improving our understanding of conduit processes and eruption dynamics of explosive silicic eruptions.

Chapter 5

Magma conduit dynamics during the explosive phases of the Kaharoa eruption

5.1 Introduction

Eruptions fed by rhyolitic magmas have generated some of Earth's largest explosive volcanic eruptions (>100 km^3 of DRE magma erupted), sourced from caldera volcanoes (Mason et al., 2004; Miller and Wark, 2008). These events can have large impacts, but, on the other hand, they are infrequent compared to smaller-scale eruptions from the same volcanic systems. Rhyolitic volcanism is more frequently characterised by the discharge of 0.01 to 10 km^3 DRE of magma during single eruptions, which are still capable to produce multiple hazards on a regional scale, impacting the environment, infrastructures and human life (e.g., Martin et al., 2009; Elissondo et al., 2016; Craig et al., 2016; Forte et al., 2018).

These moderate- to large-scale rhyolitic eruptions are characterised by complex eruption sequences, comprising repeated eruptive phases of diverse eruption styles, magnitudes and intensities (e.g., Sieh and Bursik 1986; Fierstein and Hildreth 1992; Jurado-Chichay and Walker 2001; Alfano et al., 2011; Pistolesi et al., 2015). Explosive phases characterised by the sustained discharge of magma, forming convective columns of subplinian to Plinian intensity and heights, can alternate with phases of intermittent magma discharge, generating sustained or transient, low-altitude ash-laden plumes. In addition, during rhyolitic eruptions, a transition is often observed in the main eruptive regime, passing from the explosive discharge of fragmented magma to the effusive emplacement of highly viscous domes or lavas (Ogburn et al., 2015; Cassidy et al., 2018). Understanding the mechanisms of these complex eruptions is essential to advance the current knowledge on rhyolitic eruptions' dynamics and to improve volcanic hazard assessments.

Factors controlling temporal changes in eruptive dynamics during an eruption are typically associated with how the magma evolves (i) within the storage region in upper crust (e.g., Petrelli and Zellmer, 2020; Colucci and Papale, 2021) and (ii) within the volcanic conduit during the final ascent to the surface (e.g., Houghton et al., 2010; Cashman and Sparks, 2013). The former evolution pathway determines the initial chemical composition of the erupted magma (uniform or not) and associated initial viscosity, volatile content and saturation conditions (Caricchi and Blundy 2015; Cashman et al., 2017). The latter determines significant changes of the pre-ascent magma properties due to the extensive exsolution of volatiles in response to decompression prior to eruption (Gonnermann and Manga, 2013; Burgisser and Degruyter, 2015). Besides these internal factors, other external factors such as the geometry and mechanical stability of the volcanic conduit system (Wilson et al., 1980; de' Michieli Vitturi et al., 2008; Aravena et al., 2018), as well as possible interactions of the rising magma with available external water (Houghton et al., 2003; Carey et al., 2009) are also critical in controlling eruption behaviours.

Giving an initial set of starting conditions within the magma storage region, assessing how the magma will evolve during ascent in the conduit becomes of primary importance to understand eruptive dynamics (Papale et al., 1998; Cashman and Sparks 2013). Conduit processes can be inferred by studying and quantifying the characteristics of vesicles (and conduit-derived crystals, if present), such as size, shape and number density, frozen in the erupted pyroclasts (e.g., Gurioli et al., 2005; Polacci, 2005; Adams et al., 2006; Giachetti et al., 2010; Alfano et al., 2012; Shea et al., 2012; Moitra et al., 2013; Rotella et al., 2014; Di Piazza et al., 2019; Vona et al., 2020). Under the conditions of minimal post-fragmentation modifications of the erupted magma particles, juvenile textures can be used to derive information on a range of conduit processes (see **Section 4.1, Chapter 4**). Vesicle textures are the results of several sequential and overlapping processes during magma rise in the conduit, which govern how the magmatic gas/bubble faction will evolve over time (Adams et al., 2006; Carey et al., 2009). Process of interest in understanding eruption behaviours are (i) how the magma degasses and bubbles nucleate (Cashman, 2004; Shea, 2017), (ii) how bubbles grow and interact with other bubbles (Castro et al., 2012b; Giachetti et al., 2019), and (iii) how the bubbles-bearing melt respond to shear stresses during flow in the conduit (Rust et al. 2003; Caricchi et al. 2011, Dingwell et al. 2016). In addition to those, the escape of gas from the magma column (outgassing) through the formation of permeable networks of bubbles is a further key process for magma dynamic in the conduit and eruption (Klug and Cashman, 1996; Okumura et al., 2008, 2009: Kennedy et al., 2016; Burgisser et al., 2017; Gonnermann et al., 2017). All these are central factors in governing the evolving magma rheology and ascent rate (Cassidy et al., 2018; Vona et al., 2020).

Vesicular pumice clasts are the volumetrically most abundant juvenile material produced during Plinian-type explosive rhyolitic eruptions (Sparks et al., 1994). Pumices are often characterised by isotropic vesicle textures formed by spherical vesicles (Rotella et al., 2014). However, pumice clasts can also be characterised by anisotropic vesicle textures formed by elongated, tube-like vesicles (**Chapter 4**). Tube pumice clasts have been found associated with numerous pyroclastic deposits of rhyolitic eruptions (e.g., Heiken 1978; Heiken et al., 1986; Allen and Cas, 1998; Martí et al., 1999; Taddeucci and Wohletz, 2001; Carey et al., 2009; Houghton et al., 2010; Schipper et al., 2013) and can provide invaluable information on the shear stress and deformation conditions of the rising magma in the conduit (e.g., Polacci et al., 2003; Dingwell et al., 2016; Ohashi et al., 2021). Alongside pumice clasts, juvenile obsidians are a common, typically subordinate, product of explosive rhyolite eruptions. Assessing their formation mechanisms can further provide additional information on the degassing/outgassing conditions of the magma in the conduit (Rust and Cashman, 2007; Gardner et al., 2017; Giachetti et al., 2020).

This work characterises the complex macro- and micro- textures of pumice clasts emplaced during the explosive phases of the ~1314 CE Kaharoa eruption of Mt Tarawera, within the Okataina

caldera (New Zealand). Pumice vesicle features (size, shape and number density) are systematically quantified for different lapilli-bearing units along the Kaharoa stratigraphy (**Chapter 3**) using Scanning Electron Microscopy (SEM) images. Qualitative and quantitative vesicle texture data are coupled with estimations of the pumice bulk density and deposit componentry data (e.g., proportion of obsidian and lithic clasts) to infer the dominant conduit processes during magma ascent. The dataset collected in this study is further used to evaluate the influence of conduit processes on the diversity of deposit types observed in the Kaharoa pyroclastic succession (**Chapter 3**), providing more details to assess eruption dynamics. Pumice microtextural studies have never been conducted before on rhyolitic eruptions from the Okataina caldera, offering new insights into the eruptive mechanisms of this type of moderate- to large-scale, explosive to effusive eruptions at silicic caldera systems.

5.2 Background

5.2.1 Geological and volcanological settings

The Okataina caldera system is the northernmost active rhyolitic centre of the TVZ, in New Zealand (**Fig. 5.1a**), formed after three, very-large-volume, ignimbrite-forming eruptions and associated caldera collapse events at ~557 ka, ~322 ka and ~54 ka (Leonard et al., 2010; Cole et al., 2014). Following the last major caldera collapse event, the activity of the centre was punctuated by several, mainly intra-caldera, moderate- to large-scale rhyolitic eruptions (Nairn, 2002; Cole et al., 2010; Jurado-Chichay and Walker, 2000). During the past 25 kyr, nine rhyolitic eruptions occurred from several vents along two, subparallel, NE-trending vent lineaments that transect the caldera in the northern and southern parts (Nairn, 2002) defined here as the Haroharo and the Tarawera vent lineaments. These rhyolitic eruptions ranged in volume from ~5 to ~9 km^3 Dense Rock Equivalent (DRE), and displayed similar characteristics (e.g., Nairn, 1996; Nairn et al. 2001; Speed et al., 2002; Kobayashi et al., 2005; Darragh et al., 2006; Smith et al., 2006; Kilgour and Smith, 2008; Sahetapy-Engel et al., 2014) such as: (i) eruptive activity from multiple aligned vents; (ii) transitions from explosive to effusive; (iii) the pulsatory behaviours characterised by multiple repeated explosive events, (iv) the explosive activity ranging in style from sustained Plinian-type events to transient ash explosions (see **Chapter 2**). Four of these eruptions occurred along the southern vent lineament and formed over time the Tarawera dome

complex (**Fig. 5.1**), which comprises several adjacent and overlapping rhyolite lava domes and coulees as well as interbedded, thick, proximal pyroclastic deposits (Nairn, 2002).

5.2.2 General features of the Kaharoa eruption

The 1314 ± 12 CE Kaharoa eruption is a moderate- to large-scale intra-caldera eruption which took place from the Tarawera dome complex, within the Okataina caldera, and it represents the most recent rhyolitic activity of the TVZ of New Zealand (Nairn, 2002; Leonard et al., 2010). Previous field and petrological studies have provided some constraints on the eruptive activity and volume of the erupted magma (Nairn et al., 2001; Hanenkamp, 2011; Sahetapy-Engel et al. 2014), as well as on the possible eruption triggers and characteristics of the magma body feeding the eruption (Leonard et al. 2002; Nairn et al., 2004).

The eruption was sourced from at least seven, aligned vents located along an 8-km-long section of the SW-NE Tarawera vent lineament, across the Tarawera dome complex (**Fig. 5.1**) (Nairn et al., 2001). Based on studies of proximal deposits the eruption sequence was characterised by comprising initial vent opening explosions, followed shortly after by a series of sustained convective columns, broadly described as subplinian to Plinian in eruptive intensity (Nairn et al., 2001). This main explosive activity is thought to have concluded with the initiation of the extrusion of a ~10^7 m^3 lava dome, which was covered by subsequent domes (Nairn et al., 2001). After a period of quiescent of unknown length, the eruption continued with the extrusions of three larger lava domes (individual volumes 2 to 4 × 10^8 m^3), which were preceded by repeated explosions building a pyroclastic cone (Nairn et al., 2001).

During the Plinian-type explosive activity, several lapilli fall beds were deposited from sustained columns distributed into two main directions, SE and later to the N from Mt Tarawera. Sahetapy-Engel et al. (2014), mapped the distribution of the fall deposits and calculated the erupted volumes associated with individual convective columns (ranging from 0.04 to 1.15 km^3 DRE), totalling 7.34 km^3 DRE. Peak column heights were estimated for the most widespread and coarser-grained fall units between 25 and 28 km, while column heights of remaining fall units are suggested within the subplinian range (10-25 km) (Sahetapy-Engel et al. 2014).

Duration of the whole eruption is uncertain. Based on comparative fallout accumulation rates, the high-intensity explosive activity is estimated to have occurred withing a minimum of 9 to 12 days (Sahetapy-Engel et al. 2014). Based on intra-eruption time breaks (**Chapter 3**), the main explosive sequence of the eruption likely lasted for longer times (up to months from onset of the eruption). The extrusion of lava domes is estimated to have occurred over ~4 years based on assumed extrusions rates of silicic lava domes (Nairn et al., 2001).

The eruption was inferred to have been fed from a layered, sill-like magma body at 6-7 km depth, formed by two main high-silica (76-77 wt% SiO_2) rhyolitic magma compositions, T1 and T2 (Nairn et al., 2004). The T1 magma composition is associated with the pyroclastic deposits dispersed to the SE, while a mingled composition of T1 and T2 magmas is associated with pyroclastic deposits dispersed to the N of Tarawera (Nairn et al., 2004). Scattered pumice clasts within the pyroclastic succession have rhyodacitic bulk compositions (69-72 wt% SiO_2), inferred to be formed by the mingling (with some degree of melt mixing) of the high-silica magma with a residual melt from the underlying crystallising basaltic magmas intruded into the rhyolite magma body (Leonard et al., 2002; Nairn et al., 2004). The T2 magma composition was erupted instead during the dome-forming activity of the eruption (Nairn et al., 2004).

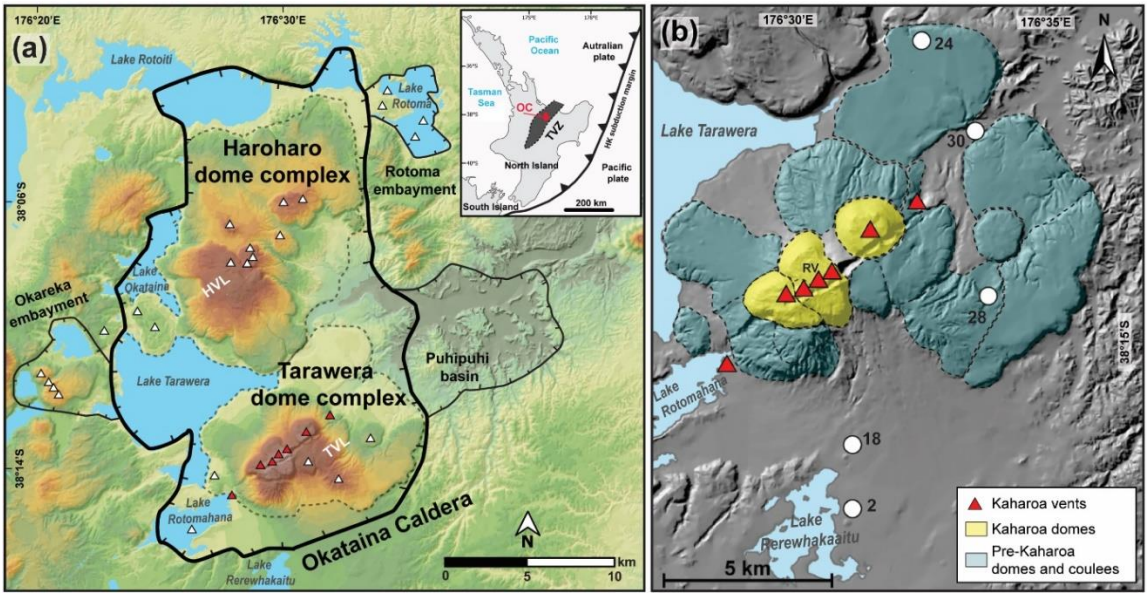

Figure 5.1 – (**a**) Map of the OVC showing topographic settings, borders of the Okataina caldera and subsidiary basins (Puhipuhi basin, Okareka and Rotoma embayments) and approximate margins of the intra-caldera Haroharo and Tarawera dome complexes (dashed lines). Triangles indicates active eruptive vents during the past 25 kyr of the centre, along the Haroharo (HVL) and Tarawera vent lineaments (TVL). Structural features, caldera border and vent location are drawn following Nairn (2002). Inferred vents active during the Kaharoa eruption are indicated with red triangles following Nairn et al. (2001). The inset displays the tectonic settings of the southern Hikurangi-Kermadec (HK) subduction margin and locations of the Okataina caldera (OC) in the Taupō Volcanic Zone (TVZ) within the North Island of New Zealand. (**b**) Zoom in the Tarawera dome complex with distributions of pre-Kaharoa and Kaharoa lavas (following Nairn, 2002) and locations of the outcrops sampled for this work (white dotes). *RV* indicates position of Ruawahia vent.

5.2.3 Deposit features and eruptive phases of the Kaharoa eruption

The study presented in **Chapter 3** enabled to characterise in detail the pyroclastic succession deposited during the Kaharoa eruption, allowing to place more constraints on the timing of different eruptive episodes and on the modalities of transport and deposition of the erupted pyroclasts. This further provided new insights to interpret eruption styles and to propose a subdivision of the eruption into eruptive phases. Here some key characteristics of the Kaharoa deposit are summarised.

The proximal-to-medial Kaharoa pyroclastic sequence consists of a complex fallout-dominated succession punctuated by numerous beds of contrasting grain size (from coarse lapilli to fine ash), alternating cm to dm thick, lapilli-dominated deposits and cm-thick ash-dominated beds. Based on the observed variations of sedimentary structures of the deposit, together with sedimentological and componentry characteristics, the pyroclastic succession was subdivided into ten lapilli and twelve ash units (e.g., **Fig. 3.7** in **Chapter 3**), representing discrete depositional events. These were later organized into ten explosive episodes of magma discharge based on the type of units contact and evidence for eruptive time breaks. The lithostratigraphic units were further grouped into seven main deposit types based on similar deposit features.

Two main types of fall lapilli units were recognized: (1) unit characterised by massive, well sorted deposits of fine to coarse lapilli, with gradual, vertical grain size changes (units L1, L2, L3, L7S and L7N) and (2) units formed by stratified lapilli deposits alternating well sorted medium lapilli beds with poorly sorted fine lapilli to medium ash beds (units L4, L5, L6, L8 and L9). Both deposits are inferred as the result of fallout sedimentation from subplinian, sustained eruptive columns. The first type is interpreted to be the product of fallout from overall stable convective columns, while the latter is the result of fallout from oscillating and at times partially collapsing columns.

Several ash units consist of poorly to well sorted, massive beds, with fine ash content between ~40 to 65 wt.% (units A2, A5, A6, A9). These ash beds cap the numerous lapilli units and are interpreted to be the results of the delayed sedimentation and accumulation of fine particles suspended in the atmosphere after the end of the eruptive activity producing the parental subplinian columns. Other fall ash units are characterised instead by massive to weakly stratified coarse ash beds (units A1 and Af) and by multiple plane-parallel, fine to coarse ash beds (unit A3), produced from low-altitude, weak sustained convective plumes and individual transient ash explosions.

Two main PDC ash deposits were emplaced at proximal to medial sites during the eruption, forming units A7 and A8 in the proposed stratigraphic scheme. Unit A7 is widespread around Tarawera with a main southern area of deposition, and it consists of moderately to poorly sorted, pumice lapilli-bearing, matrix-supported ash deposits, 1 to 2 m thick in proximal sites. Unit A8, directed only to the north of Tarawera, comprises poorly to moderately sorted, massive to cross-stratified, variably consolidated, ash deposits, with very high fine ash content up to 80 wt.% of suggested phreatomagmatic origin.

Other thin, poorly sorted ash beds with limited dispersal area and interbedded between few lapilli units are interpreted as the result from transport and deposition of minor PDCs events (units A4, A10 and A11).

Stratigraphic reconstruction, identification of time breaks in the eruptive activity and temporal variation in eruptive styles, allow to subdivide the eruption in six eruptive phases (A to F) (**Table 3.6** in **Chapter 3**). The first four phases area associated to the main explosive activity of the eruption: Phase A, B and D consist of repeated subplinian episodes, while Phase C comprises the major PDC activity of the eruption taking place before the changes in the main dispersal area of fallout deposition from south to north of Mt Tarawera. The final two Phases E and F are associated to activity of ash emission during initiation of lava extrusions and to the following main dome-building sequence of the eruption.

Field observations and componentry analysis enabled to distinguish two main groups of pumice clasts in the Kaharoa deposit, named white and grey pumice (**Chapter 3**). White pumices are the most abundant clast type in each unit and have rhyolitic composition (Nairn et al., 2004). In contrast, grey pumice clasts occur only in the upper half of the stratigraphic sequence (Phase D units L7S to L9 and scattered within unit A7) and are always subordinate in abundance compared to white pumices (from 3 to ~30 wt.% in samples analysed for componentry). Grey pumices are associated to the rhyodacitic (in bulk composition) clasts of Leonard et al. (2002) and Nairn et al. (2004).

Units also contain subordinate obsidian juvenile clasts and lithic fragments (mainly pre-Kaharoa lava fragments and minor, hydrothermally altered clasts). Obsidian fragments have typical concentrations of ~5 wt.%, however, reach 14 to 27 wt. % in beds from the obsidian-rich fall unit L3 and the PDC unit A7 (**Chapter 3**). The concentration of lithics oscillate throughout the pyroclastic succession, alternating relatively lithic-rich to lithic-poor units, however never exceeding ~20 wt. %. Lithic-rich units (here defined has having ≥15 wt.% of lithic clasts) are consistently associated with stratified lapilli units, whereas massive lapilli units are typically lithic-poor.

5.3 Methods

5.3.1 Sampling and clast frequency

This study is based on pumice clast samples collected from the fall lapilli units L1 to L8 and from the PDC lapilli-bearing unit A7 of the Kaharoa pyroclastic succession (**Chapter 3**). These samples are representative of the three main subplinian, fall-dominated phases (Phase A, B, and D) and of the PDC-dominated phase (Phase C) recognized for the Kaharoa eruption (**Chapter 3**). Samples from these units provide a way to constrain the changes in eruptive style and dynamics during the eruption sequence.

Due to the different main dispersal axis of individual fall units, producing and overall bilobate distribution of the whole Kaharoa deposit, samples were collected at two key sections south (section 2, **Fig. 5.1**; units sampled: L1 to L6 and A7) and north (section 24, **Fig. 5.1**; units sampled: L7N to L8) from Mt Tarawera, at an approximately equivalent distance of 6-7 km from Ruawahia vent (**Fig. 5.1**). Samples for unit L7S were taken instead at section 28, ~5 km east from Ruawahia vent (**Fig. 5.1**), as this unit was not deposited at sections 2 and 24.

Samples were collected to quantify the bulk density of pumice clasts in each unit and to prepare polished thin sections of selected pumice clasts for microtextural investigations of the vesicles content.

Clast sampling for density analysis was performed unit by unit where at least 100 pumice clasts were collected at random, having intermediate diameters between 32- and 16-mm. Samples are typically bulk of the whole fall unit, however if the unit is strongly bedded and/or has thickness >50 cm, two sets of samples from the bottom and upper parts of the unit deposit were also collected. For the PDC unit A7, representative pumice clasts are sampled from the lapilli-bearing, matrix supported beds of the deposit. Since clast density can change due to grain size (e.g., Eychenne and Le Pennec; Gurioli et al., 2015; Pistolesi et al., 2015; Mitchell et al., 2018), unit L9 was not sampled due to its smaller mean grain size (fine lapilli, < 4mm) compared to the rest of the lapilli-bearing units. For consistency during sampling, clasts with evident broken surface (i.e., clasts with an original larger grain size) and clasts showing extensive signs of post-fragmentation vesiculation and expansion (i.e., clasts with unusual large vesicles observed in hand specimen) were excluded to better constrain the density distributions of individual units (e.g., Mitchell et al., 2018; Trafton and Giachetti, 2021).

Macroscopic inspections of the surface textures of each pumice clast in the 100-clasts sample suites were also carried out in order to quantify the relative frequency of clasts showing typical

tube pumice texture (e.g., Taddeucci and Wohletz, 2001; Polacci et al., 2001, 2003; Carey et al., 2009; Houghton et al., 2010; see **Section 4.1.2** in **Chapter 4**), which were previously observed during fieldwork. This enables to later quantify the frequency of two main pumice types (see **Section 5.4.1**).

Additional samples of juvenile obsidian and lava dome fragments (32 to 16 mm in size) were collected for density measurements to characterise the whole density spectrum of the Kaharoa juveniles. A total of 65 obsidian fragments were collected from the obsidian-rich unit L3 and A7 at section 2 (**Fig. 5.1**), whereas two sets of 30 lava dome fragments were collected from block-and-ash flow deposits of units BS and BN at sections 18 and 30, respectively (**Fig. 5.1**). Sampled lava dome fragments have textural features similar to both the "carapace" and "core" facies of Ruawahia dome reported in Ashwell et al. (2018). Finally, few samples within the target size range (32 to 16 mm) of dense juvenile clasts (**Chapter 3**) were found and collected from unit L6 at section 2 for bulk density analysis.

5.3.2 Bulk density and vesicularity measurements

Bulk density quantifications were performed on pumice clasts from the 100-clasts sample suites following Houghton and Wilson (1989). Before performing density measurements, samples were cleaned in distilled water in an ultrasound bath for 5 to 10 min and dried for >24 hours in an oven at T = 100°C. Clasts volumes and densities were estimated by hydrostatic weighing, measuring the weight of the dry clast in air and the weight of the clast submerged in water after applying a cellulose acetate coating to make the clasts impermeable to water. The volume estimation method follows Archimedes principle (Mitchell et al., 2018). The cellulose acetate coating used in this study was obtained by mixing cellulose diacetate and acetone. The clast is immersed in the mixture creating an impermeable film of negligible mass and volume around the clast, effectively sealing the open pores (e.g., Pistolesi et al., 2017; Todde et al., 2017). The increase in mass of the clast after the coating have been measured at 0.5% on average of the original clast mass. Bulk clast vesicularities were further derived from clast density data using an average dense rock equivalent (DRE) density of 2353 kg/m^3 for the Kaharoa magma (**Appendix D**). This average DRE value was determined on powders of crushed pumice clasts (sets of 3 clasts from units L1, L3, L5, L7N, L7S and L8) with a gas pycnometer by Quantachrome, using nitrogen (N_2) as the flowing gas (e.g., Pardo et al., 2014). Bulk vesicularity nomenclature is adopted from Houghton and Wilson (1989). Density measurements are used to provide an estimation of the state of magma degassing/outgassing at the fragmentation level in the conduit during the eruption sequence (e.g., Barker et al., 2012; Vona et al., 2020) and as a filter to select clasts for SEM observations and quantitative vesicle analyses (Houghton et al., 2010).

5.3.3 Image analysis of vesicle textures

To investigate the vesicle textures of pumice clasts and their variability during the eruption sequence, polished thin sections were prepared from three clasts per each lapilli-bearing unit (L1 to L8 and A7, excluding unit L7S) for microscopy imaging. Thin section images of the pumice microtextures were used to qualitatively describe the characteristics of the vesicle network and to quantify the size and shape distributions of vesicles. The methodology used for image acquisition, image adjustments and quantitative analysis follow those detailed in **Chapter 4**.

The three clasts per unit used for microtextural studies were selected from the mode of the obtained pumice density distributions of each investigated unit, which show unimodal trends throughout the stratigraphic sequence (see **Section 5.4.2**). The pumice clasts selected from the density mode are considered representative of the vesiculated magma at fragmentation (Mitchell et al., 2018; Vona et al., 2020). Furthermore, clasts selection from the density mode ensures reliable comparison of vesicle textures between different units in the stratigraphy; accurate estimation of the low- and high- density clasts endmember can be strongly influenced by the number of clasts used for bulk density analysis giving the degree of diversity within the investigated juvenile pumice population (e.g., Houghton and Wilson, 1989; Barker et al., 2012; Gurioli et al., 2015; Mitchell et al., 2018), which could bias vesicle data comparison.

Following results from pumice clast frequency analysis, the clast selected from the density mode cover the spectrum of macroscopic pumice types observed (both pumices with and without pervasive tube pumice fabric are used) (e.g., Pardo et al., 2014). Following the results of deposit componentry analysis (**Chapter 3**), white pumice clasts are used for microtexural analysis since are the most abundant component of the Kaharoa deposit and are found in every unit of the stratigraphy. Three additional representative clasts of grey pumice were also selected from the density mode of unit L7N to characterise the microtextural features and draw comparisons with the ones observed for white pumice clasts. Finally, two additional thin sections were prepared for juvenile obsidian fragments from the obsidian-rich units L3 and A7 to qualitatively describe the obsidian microtextural features.

Since the surface textures of the Kaharoa pumices are typically characterised by elongated vesicles oriented along a preferential direction (parallel to the clast's long axis), two thin sections were made per each clast (60 oriented thin sections in total). Thin sections were prepared from parallel (PA) and orthogonal (OR) cuts to main vesicle elongation.

The polished thin sections were imaged using a Scanning Electron Microscope (SEM) operated in Back-Scattered Electron (BSE) mode. Images were taken at four magnifications, 20×, 50×,

100× and 200×, to record spatial heterogeneity at different scale in the vesicle textures and to cover the range of vesicle sizes which spans from ~0.001 to 1 mm.

Qualitative observations were noted for each PA and OR thin section over a total of over 800 SEM-BSE images (10 to 15 images per thin sections) (see also **Appendix E**). Observations were made for the overall vesicle arrangements, presence of heterogeneity in vesicle size, shape and deformation patterns, vesicle interactions (e.g., coalescence features), characteristics of vesicle walls and crystal-vesicle interactions. This provided essential descriptions on the state of vesiculation of the magma during ascent and eruption.

Quantitative image analyses were conducted to evaluate the variations of vesicle size, shape, and vesicle number density along the stratigraphic sequence. The image vesicle analysis was carried out on three high-resolution SEM-BSE images (4069×3775 pixel) per thin sections taken at 200× from OR cuts. This setting provides an adequate estimation of the vesicle features of the sampled units based on **Chapter 4**. The complete dataset from quantitative vesicle analyses is available in **Appendix F**.

Images at 200× considerably reduce the working time of necessary manual image adjustments compared to those required for larger images at lower magnifications (e.g., 100× and 50×) while providing similar vesicle results (**Chapter 4**). Images at 200× further enable to characterised vesicles from ~1 to ~250 µm in size, consisting of >95 to 99% of the vesicle population in the Kaharoa pumices. Images at 200× provided also a more accurate estimation of the vesicle number density which is primary controlled by small vesicles (<30 µm) and enable characterisation of vesicle size and shape up to ~300µm. Large and very large vesicles (>250 to >1000 µm) possibly originated from protracted vesicle coalescence and/or post-fragmentation effects (e.g., Klug et al., 2002; Giachetti et al., 2010) are not systematically quantified. Although the contribution of these very large bubbles to the vesicle number density is negligible in the investigated samples and in other silicic pumices (e.g., Rotella et al., 2014), it is here reminded that very large vesicles may contribute up to ~15% of the total vesicle area of a sample (area-VSD plots in **Chapter 4**), possibly producing minor secondary peaks in the area-VSD. In this study, when present, very large vesicles have been qualitatively characterised from low magnification images at 20×. Images at 20× were also quantitatively analysed to measure the phenocrysts content (crystallinity) of the samples along the stratigraphy (**Appendix F**). Crystal data are melt-referenced, corrected for the average vesicle content of the 20× images (45% average 2D vesicularity), calculated from images analysed in **Chapter 4**.

Quantification of vesicle features were obtained for only OR cut images throughout the stratigraphy. The use of this type of oriented thin section is preferred in this study as it provides a better constraint on the vesicles number density, which has been usually applied as a proxy for

magma decompression rate in the conduit and eruption style (e.g., Carey et al., 2009; Shea et al., 2012; Myers et al., 2021). Due to the presence of abundant stretched vesicles and their variable degree of elongation, PA cuts can instead underestimate the vesicle number density per unit area.

Following Shea et al. (2010), a minimum area of 80 pixels per vesicle (i.e., 10 pixels in equivalent diameter), corresponding to uncertainty in vesicle size analysis of ~1%, was used as the lower limit for vesicle size. This approach, combined with the high-resolution images at 200× used for this study, enables characterising vesicles down to 1.84 µm in equivalent diameter, extending the arbitrary lower limit of vesicle size usually set at 4 µm in other microtextural studies of rhyolitic pumices (e.g., Adams et al., 2006; Carey et al., 2009; Houghton et al., 2010).

The SEM-BSE images were manually edited using Adobe Photoshop and converted to binary images (vesicles in black and glass in white). Manual adjustments were aimed to (i) reconstruct incomplete vesicle walls and broken/fractured glass (artificially connecting separated vesicles), (ii) to enhance very thin vesicles walls not entirely preserved in the acquired images and (iii) to remove fillings and/or 3D effects inside the vesicles (e.g., Shea et al., 2010; Mitchell et al., 2019). While manually redrawing vesicles walls, interconnected vesicles were separated ("decoalesced") only where vesicle walls exhibited evidence of partial rupture and incomplete bubble wall retraction (see **Chapter 4**).

The binary images were processed using the open-source software Fiji (Schneider et al., 2012, Schindelin et al., 2012). Based on the obtained vesicle dimensional features, the 2D shape characteristics of the vesicles were described and quantified using seven non-dimensional parameters: Circularity (C) (Leibrandt and Pennec, 2015), Regularity (R) (Chapter 4), Shape Factor (SF) (Shea et al., 2010), Deformation (D) (Polacci et al., 2001), Eccentricity (E) (Shea et al., 2010), Flattening (FLT) (Heilbronner and Barrett, 2014) and Ellipse Aspect Ratio (AR) (Liu et al., 2015). The equations of individual shape parameters are reported in Chapter 4 (**Section 4.2.4.1**). Except for AR, the parameters are normalised and vary from 0 to 1. C, R and SF estimate the vesicles shape complexity by measuring the deviation from a reference standard shape (circle for C and SF and an ellipse for R), while D, E, FLT and AR provide a measure of the vesicle elongation (see **Fig. 4.2, Chapter 4**).

Vesicle area data and vesicle counts were used to quantify the 2D vesicularity (total area of vesicles per melt area in %), the vesicle number density N_A (number of vesicles per unit melt area) and the vesicle size distribution (VSD). The VSDs are expressed in terms of both N_A (N_A-VSD) and area fraction (area-VSD) against vesicle size. All parameters are melt-referenced, thus were corrected for the image crystal content (if any). In the VSD plots, the size of vesicles is expressed as diameter of the circle of equivalent vesicle area and binned using a geometric bin factor of $10^{0.1}$ (Sahagian and Proussevitch, 1998), applied in many other vesicle studies of silicic

pumices (e.g., Gurioli et al., 2005; Rotella et al., 2014; Mitchell et al., 2019). The VSD by area fraction are normalized for the measured 2D vesicularity of each image (Shea et al., 2010; Giachetti et al., 2010). Number densities and VSDs are presented in 2D, without 3D stereological volume conversion due to the violation of the spherical geometry assumption by the strongly elongated, tube-like vesicles in the investigated samples (Shea et al., 2010).

Final vesicle data (shape, size, and number density) per each unit are obtained first averaging the result of individual images per sample (thin section), later averaging the results across the clasts selected per each unit. In the later, only vesicle data from the same pumice and microtextures types are averaged.

5.4 Results

5.4.1 Macroscopic observations of pumice clasts

Vesicles exposed along the surface of the Kaharoa pumice clasts, both in white and grey pumices, have variable shapes from subspherical with no apparent orientation, to very elongated and oriented along the clast's main axis. Based on the vesicle surface textures the pumice clasts can be subdivided into two main groups: microvesicular heterogeneous pumice (MHP) and tube pumice (TP) (**Table 5.1**). These surface textures are later found to echo the different microtextural characteristics of the pumice clasts (see **Section 5.4.3**).

MHP clasts (**Fig. 5.2a**) are characterised by surface vesicles varying from spherical to elliptic in shapes, typically <0.5 mm in diameter, with larger (1-2 mm) vesicle having ovoid-like to irregular shapes. Elongated vesicles also occur and are typically aligned in a preferential direction. This texture is common in both white and grey pumice clasts. TP clasts (**Fig. 5.2b**) are characterised instead by a pervasive, anisotropic vesicles structure, consisting of very elongated vesicles, stretched along the longest axis of the clast. Surface vesicles have diameters typically <0.5-1 mm and high aspect ratio (>5-10:1). Vesicles larger than 1 mm also occur and are characterised by less elongated shapes. Perpendicular to vesicle elongation, TP clasts are characterised by densely packed smaller vesicles. These vesicle shapes and spatial vesicle arraignment impart the clast a tube pumice fabric, observed in clasts from other silicic explosive eruptions (see **Section 4.1.2** in **Chapter 4**). This texture is observed mainly in white pumice clasts, while is less common in grey pumice clasts. TP clasts have overall elongated external morphologies with respect to the more equidimensional shapes of the MHP clast

Table 5.1 – Summary of the main features of the Kaharoa pumice clasts, surface texture and vesicle texture types.

Clast type from componentry analysis	Description
White pumice	Light-coloured, white to yellowish, moderately vesicular and porphyritic juvenile pyroclasts of rhyolite whole-rock compositions.
Grey pumice	Pale-grey, moderately vesicular, porphyritic juvenile pyroclasts, with common to abundant mm-size basaltic inclusions of rhyodacite whole-rock compositions.

Pumice type by surface texture	Description
Microvesicular heterogeneous pumice (MHP)	Sub-angular to sub-rounded pumice clasts with equant to elliptical morphologies. Surface vesicles have typical size <0.5 mm, up to 2 mm and have variable shapes (spherical, ovoid-like, irregular and elongated). MHP texture is common in both white and grey pumice clasts.
Tube pumice (TP)	Sub-angular to sub-rounded pumice clasts with predominantly elongated morphologies. Surface vesicles are elongated to very elongated and oriented along the clast's long axis, imparting a clear fabric to the entire clast. Typical vesicle diameter is 0.5-1 mm, with high aspect ratio (>5-10). TP texture is common in white pumice clasts and infrequent in grey pumice clasts.

Pumice vesicle texture (microscopic)	Description
Type 1	Heterogenous assortment of vesicle shape, size and vesicle deformation pattern. Convoluted and tube vesicles occur in domains or bands, coexisting with areas of undeformed, subspherical vesicles. Convoluted and tube vesicles occur mainly in PA cuts, while are less abundant in OR cuts. Type 1 occur in all MHP clasts.
Type 2 and type 3	Strongly anisotropic vesicle texture dominated by a pervasive distributed network of tube vesicles. The tube vesicles are aligned according to a preferred direction of stretching and occur only in PA cuts, while OR cuts display subspherical vesicles. Types 2 and 3 occur in TP clasts. Type 2 is the most common texture observed in TP clasts, while type 3 is rare. The two textures differ in vesicles size, degree of vesicles elongation and vesicle walls thickness.

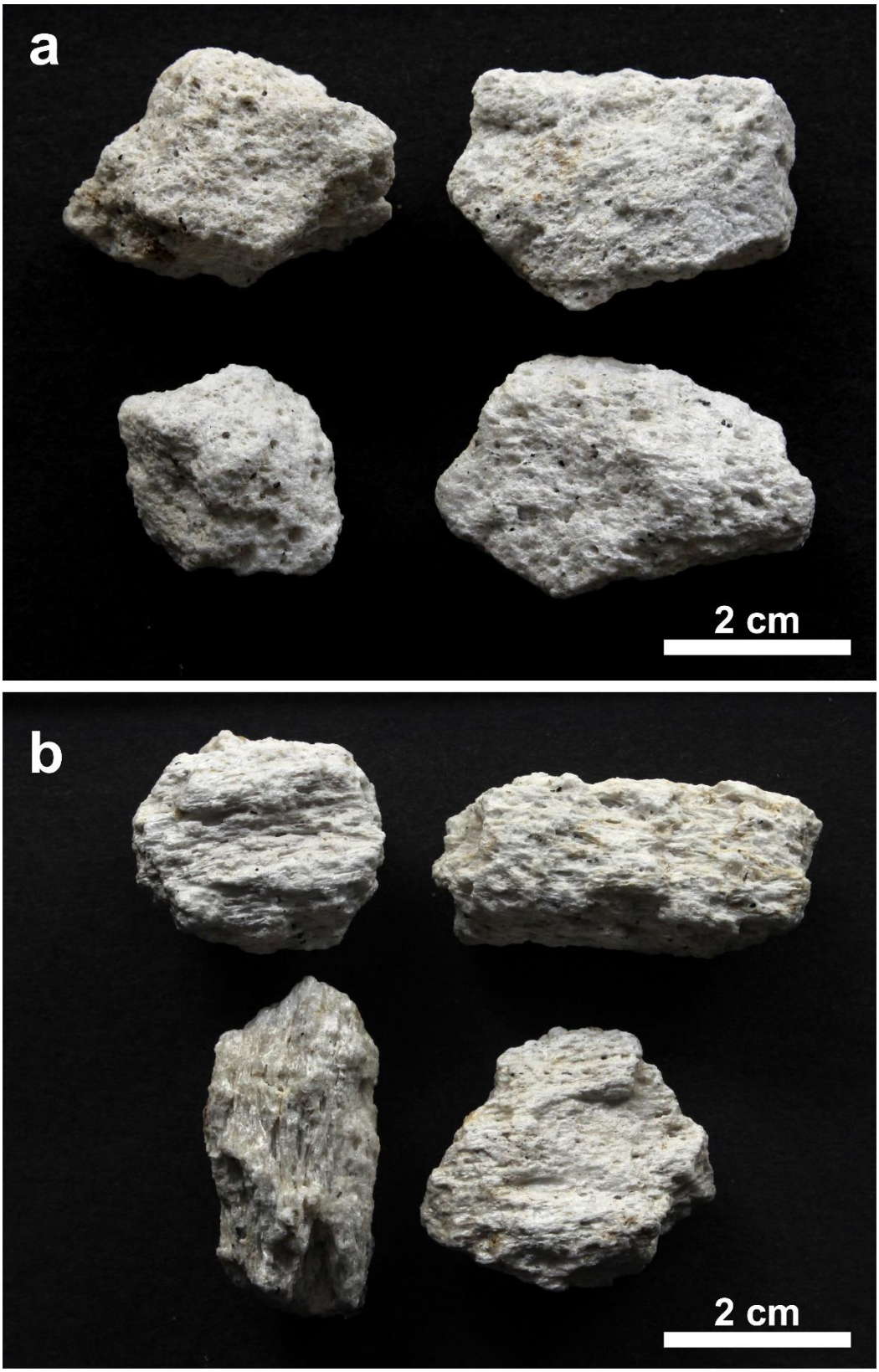

Figure 5.2 – Representative Kaharoa pumice clast typologies according to their vesicle surface textures: (**a**) microvesicular heterogeneous pumice (MHP) and (**b**) tube pumice (TP).

The relative frequency of MHP and TP clasts is assessed from the 100-clast sample suits for each investigated unit along the stratigraphic sequence and is reported in **Figure 5.3**. MHP clasts are the most abundant type of pumice in the analysed fall units, with TP clasts varying typically from 30 to 40%, with a minimum of 20% in unit L1. An exception to this trend in the relative frequency of MHP and TP clasts along the stratigraphy is observed in the PDC unit A7, where TP clasts increase up to 53%.

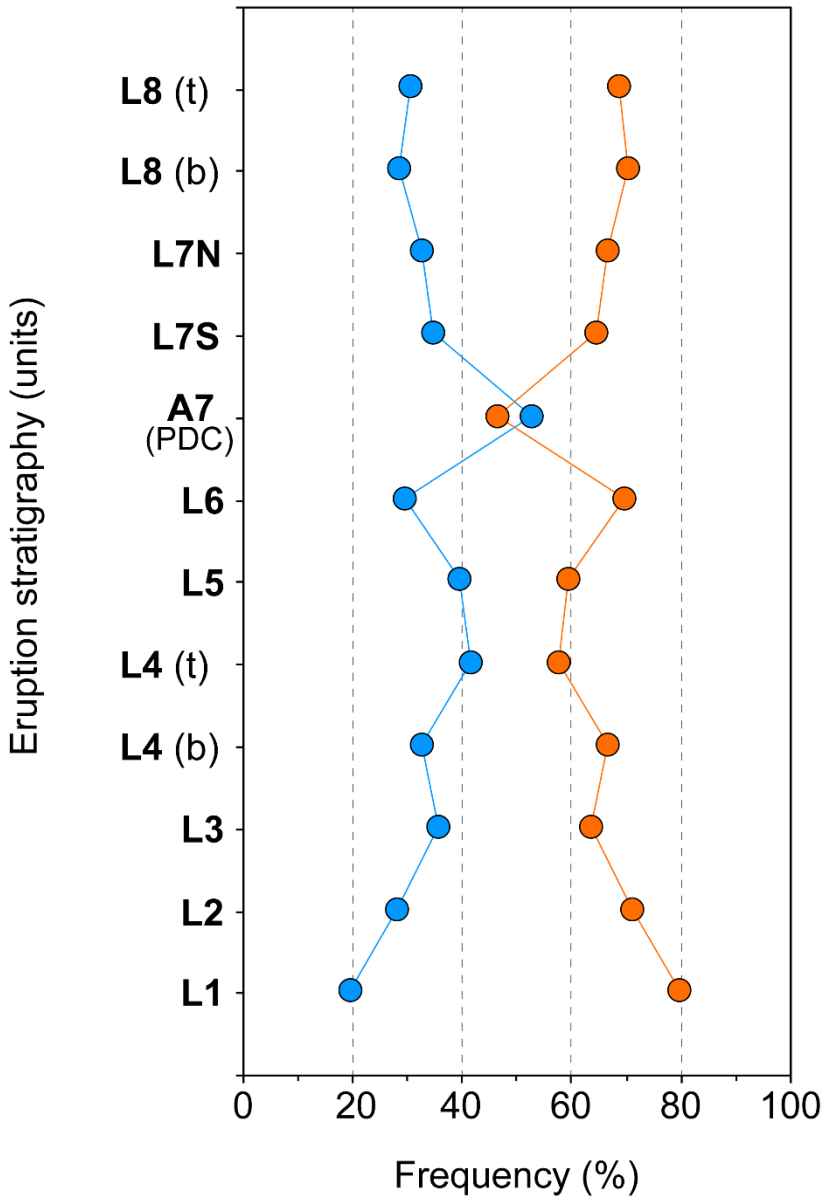

Figure 5.3 – Relative frequency of MHP (orange) and TP (blue) clasts in the studied units in upward succession along the stratigraphic sequence. Pumice type frequency is measured from clasts in the 16-32 mm grain size interval. *(b)* and *(t)* in units L4 and L8 indicate samples collected from the bottom and top parts of the units, respectively.

5.4.2 Bulk density and vesicularity

Pumice clasts in the Kaharoa deposit are typically moderately vesicular (mean vesicularity at 53%), with a mean bulk density of 1100 kg/m^3 across the entire sample population (~1300 clasts). Density distributions for pumice clasts in the different units show unimodal trends, with densities ranging from 700 to 1400 kg/m^3 (70 to 41% vesicularity) and modes varying in a narrow interval from 900-1000 to 1100-1200 kg/m^3 (62-58% to 53-49% vesicularity), (**Fig. 5.4**).

Unimodal distributions are consistent throughout the entire stratigraphic sequence, although density distributions in the initial unit L1 and in the stratified units L4 (base) and L6 display a skewed tail towards higher density with secondary peaks between 1500 and 1700 kg/m^3 (36 and 28% vesicularity) (**Fig. 5.4**). Minor changes in modal densities are observed vertically in the sequence, with most fall units from the early phases of the eruption (Phase A to B, units L1 to L6) having modal densities at 1000-1100 kg/m^3 (58-53% vesicularity), while fall units from the later phases of the eruption (Phase D, units L7S to L8) having modal densities at 1100-1200 kg/m^3 (53-49% vesicularity) (**Fig. 5.4**). Both the two obsidian-rich units L3 and A7 show the lowest modal density values measured among the units in the stratigraphy, being at 900-1000 kg/m^3 (62-58% vesicularity). The PDC unit A7 is also characterised by a narrower density distribution compared to the ones displayed by the fall units (**Fig. 5.4**).

When present in the analysed samples, grey pumice clasts follow the same density distributions of white pumices (**Fig. 5.4**) and have similar mean density values (1160 and 1095 kg/m^3 for grey and white pumice clasts, respectively) (**Table 5.2**).

No significant variations in bulk densities are observed between TP and MHP pumice clasts. Both pumice types have unimodal distributions with modes at 1000-1100 kg/m^3 (58-53% vesicularity) (**Fig. 5.5** and **Table 5.2**). Comparable density distributions between pumice clasts exhibiting typical tube pumice texture and pumice clasts showing no pervasive alignment of stretched vesicles have also been reported for deposits of other silicic eruptions (e.g., Polacci et al., 2003; Houghton et al., 2010).

Bulk density distribution of obsidian fragments collected from units L3 and A7 is narrow with density mode at 2300-2400 kg/m^3 (2 to 0% vesicularity; **Fig. 5.6**). Some obsidian clasts exceed the DRE density value (2353 kg/m^3) measured from powder samples of pumice clasts (**Appendix D**). Lava dome fragments vary from poorly to incipiently vesicular from unit BS to BN with modes at 1600-1700 and 1800-1900 kg/m^3 (32-28% to 24-19% vesicularity), respectively, partially overlapping with the high-density tails measured in pumice clasts (cf. **Fig. 5.4** and **Fig 5.6**). In addition, the average bulk density for the few available dense juvenile clast samples available from unit L6 is 1641±59 kg/m^3 (28±3 % vesicularity) (**Appendix D**).

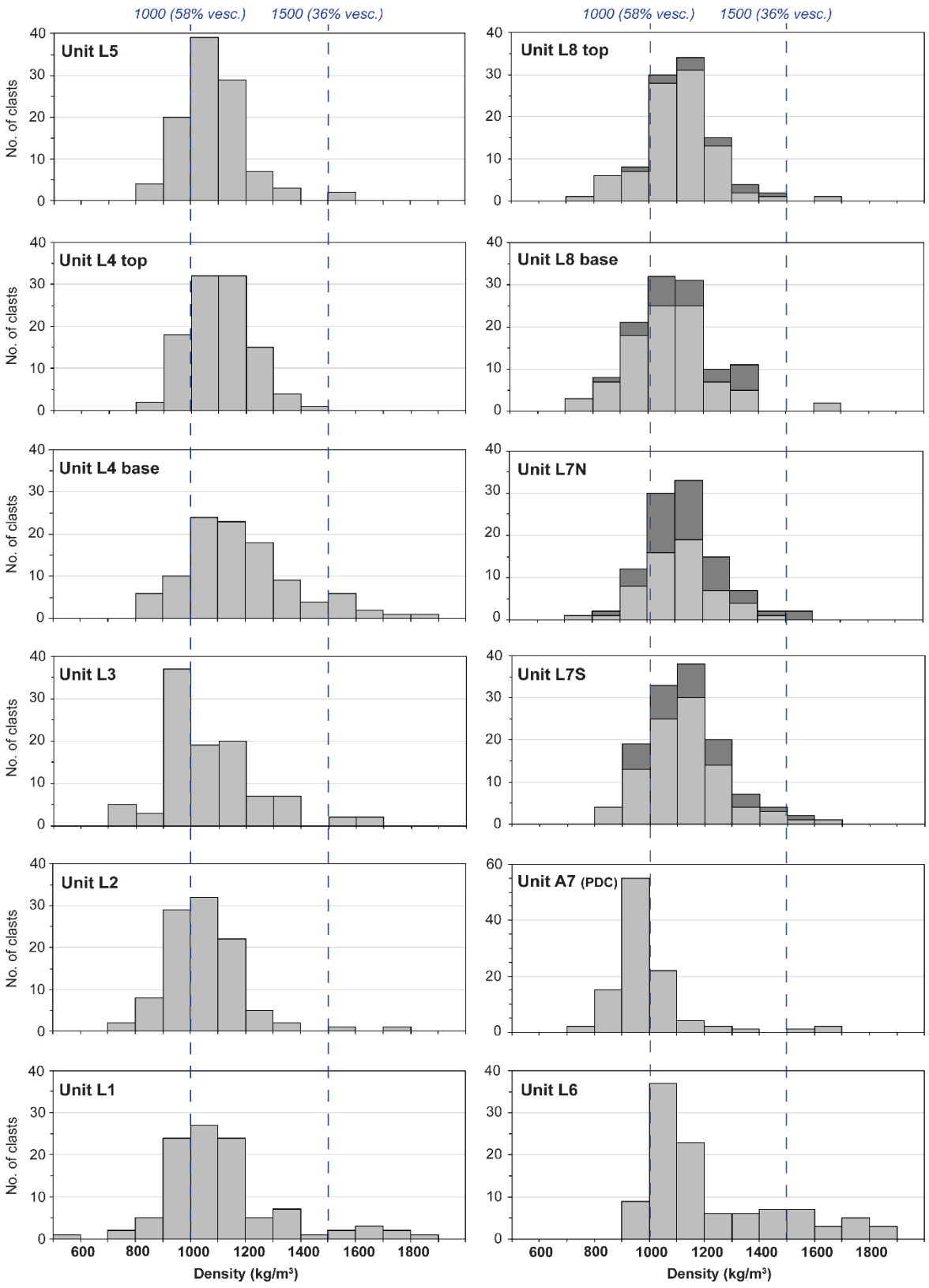

Figure 5.4 – Bulk density distributions of pumice clasts in the investigated units from the Kaharoa deposit. White pumice and grey pumice clasts (the latter occurring only in unit L7S, L7N and L8) are indicated in light and dark grey, respectively. Graphs are in stratigraphic order from left to right panels. Two blue dashed lines at clasts densities of 1000 kg/m^3 and 1500 km/m^3 (corresponding to bulk vesicularity of 58 and 36%, respectively) are reported in the figure to facilitate comparison between units.

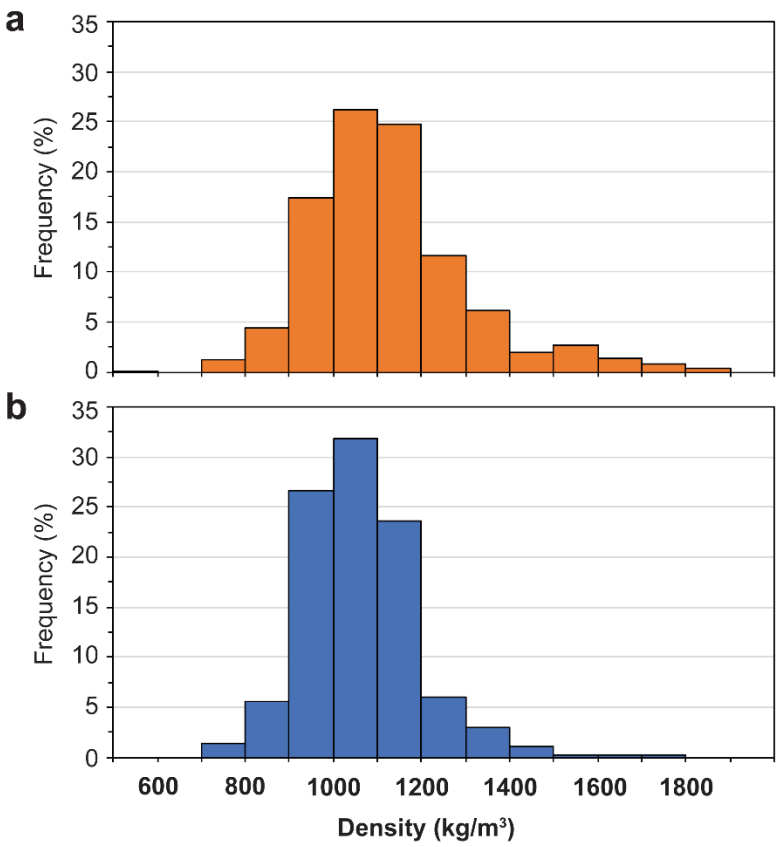

Figure 5.5 – Bulk density distributions for MHP (orange) and TP (blue) clasts from the entire pumice sample collections (~1300 clasts in total).

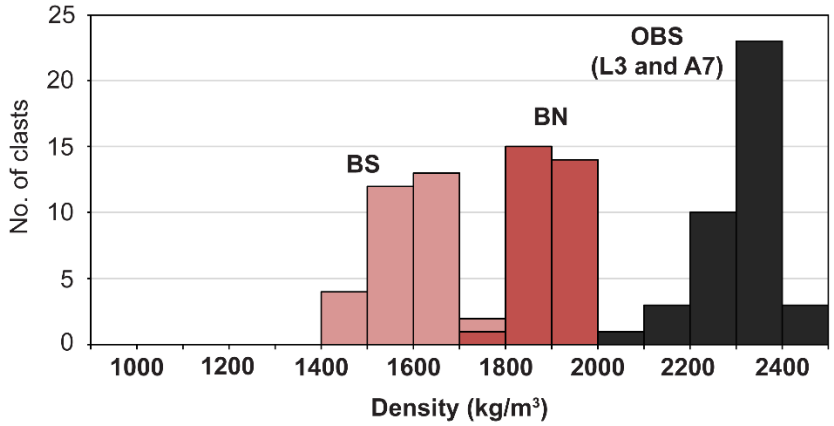

Figure 5.6 – Bulk density distributions for lava dome fragments collected from block-and-ash flow units BS (light red) and BN (dark red) and for obsidian pyroclasts (OBS in black) collected from unit L3 and A7.

Table 5.2 – Bulk density and vesicularity data of pumice clasts from the analysed units (L1 to L8) of the Kaharoa deposit and additional data for juvenile obsidian and lava dome fragments. Data on pumice clast types from the whole sample population are also reported, as well as data on obsidian and lava dome fragments. *(SD)* indicates the standard deviation for mean density and vesicularity values. *Mode 1* indicates the mode of the density and vesicularity distributions, while *Mode 2* indicates secondary, minor peaks in the distributions when present.

	Bulk density (kg/m^3)				**Bulk vesicularity (%)**			
Unit	**Mean (SD)**	**Mode 1**	**Mode 2**	**Range**	**Mean (SD)**	**Mode 1**	**Mode 2**	**Range**
L1	1111 (217)	1000-1100	1600-1700	500-1900	53 (9)	58-53	32-28	79-19
L2	1045 (155)	1000-1100	-	700-1800	56 (7)	58-53	-	70-24
L3	1069 (174)	900-1000	-	700-1700	53 (8)	62-58	-	70-28
L4 (base)	1181 (204)	1000-1100	1500-1600	800-1900	48 (9)	58-53	36-32	66-19
L4 (top)	1108 (110)	1000-1100	-	800-1500	51 (5)	58-53	-	66-36
L5	1083 (125)	1000-1100	-	800-1600	52 (6)	58-53	-	66-32
L6	1214 (239)	1000-1100	1500-1600	900-1900	47 (11)	58-53	36-32	62-19
A7	990 (142)	900-1000	-	700-1700	56 (6)	62-58	-	70-28
L7S	1133 (145)	1100-1200	-	800-1700	52 (6)	53-49	-	66-28
L7N	1124 (138)	1100-1200	-	700-1600	52 (6)	53-49	-	70-32
L8 (base)	1087 (158)	1000-1200	-	700-1700	54 (7)	58-49	-	70-28
L8 (top)	1112 (137)	1100-1200	-	700-1700	53 (6)	53-49	-	70-28
Clast	**Mean (SD)**	**Mode 1**	**Mode 2**	**Range**	**Mean (SD)**	**Mode 1**	**Mode 2**	**Range**
White pumice	1095 (168)	1000-1100	1500-1600	500-1900	53 (7)	58-53	36-32	79-19
Grey pumice	1160 (150)	1100-1200	1500-1600	800-1700	51 (6)	53-49	36-32	66-28
MHP	1125 (184)	1000-1100	1500-1600	500-1900	51 (8)	58-53	36-32	79-19
TP	1060 (131)	1000-1100	-	700-1800	54 (6)	58-53	-	70-24
OBS (L3 and A7)	2327 (72)	2300-2400	-	2000-2450	0.7 (2)	2-0	-	15-0
Lava dome (BS)	1590 (65)	1600-1700	-	1400-1800	32 (3)	32-28	-	41-24
Lava dome (BN)	1885 (56)	1800-1900	-	1700-2000	20 (2)	24-19	-	28-15

5.4.3 Characteristics of vesicle textures in pumice clasts

The most striking feature of the Kaharoa pumice microtextures is the ubiquitous presence of deformed, elongated vesicles regardless the type of pumice clasts and unit in the stratigraphic sequence (**Fig. 5.7**, **5.8** and **5.9**). Deformed vesicles have variable degree of elongation (from elongated to extremely elongated) and are characterised by both convoluted and tubular shapes (tube vesicles hereafter). Convoluted vesicles consist in elongated vesicles affected by one or more secondary folds which impart the vesicles a convoluted or "wavy" outline. As a result of the folding, the vesicle aspect ratio typically does not exceed 5. Tube vesicles form instead when deformed vesicles are not significantly affected by folding/convolution and are stretched for high aspect ratio (AR > 5 up to 50), maintaining continuous tubular shapes along the entire vesicle length. Overall microscopic vesicle textures vary between MHP and TP clasts. According to the shape, size and spatial distribution of vesicles, three main types of vesicle texture can be recognized and are named type 1, type 2 and type 3 (**Table 5.1**). This nomenclature and vesicle texture description follows the same reported in **Chapter 4**. Type 1 and type 2 are the characteristic vesicle textures of MHP and TP clasts, respectively, while type 3 represent a rare texture observed only in few TP clasts.

5.4.3.1 Type 1 texture (MHP clasts)

Type 1 occur in all MHP clasts and display the most complex vesicle texture observed in the investigated samples (**Table 5.1**). Within each given sample, deformed vesicles (convoluted and tube vesicles) coexist with areas of subspherical, apparently undeformed vesicles (**Fig. 5.7**). Deformed vesicles are aligned within a main direction and occur predominately in the PA cuts, while circular vesicles occur mainly in OR cuts (**Fig. 5.7**). Boundaries between domains of convoluted or tube vesicles with domains of undeformed vesicles range from gradual, when separating 10-100 μm-sized areas, (e.g., **Fig 5.7a**) to abrupt, when separating large, mm-sized domains (e.g., **Fig. 5.7c**).

PA cuts are typically dominated by convoluted vesicles, while tube vesicles are localized into bands. Bands of tube vesicles have typically width of 100 to 500 μm and vary in length from ~1 mm (generally interrupted by areas of undeformed vesicles) to >2 mm often extending for the entire thin section (e.g., **Fig 5.7b**). The short axis of deformed vesicles ranges from 5 to 40 μm, with the long axis varying from 50 to 300 μm in convoluted vesicles and from 100 up to 500-1000 μm in tube vesicles, depending on the vesicle's aspect ratio. Tube vesicles are characterised by 3 to 15 μm thick vesicle walls, while convoluted vesicles have vesicle walls varying in thickness from 5 up to 30 μm.

OR cuts are dominated by vesicles having broadly subspherical geometries, varying from regular, circular to elliptical shapes (with aspect ratio up to 2), to irregular-polylobate shapes. Although volumetrically less abundant, convoluted vesicles and tube vesicles bands occasionally occur in OR cuts. Subspherical vesicles have diameters varying from ~1 to 150 μm, typically <50 μm, with the larger vesicles associated with more irregular-polylobate shapes. Large (>250 μm) vesicles are not abundant. Vesicles walls in subspherical vesicles ranges from ~1 to 30 μm.

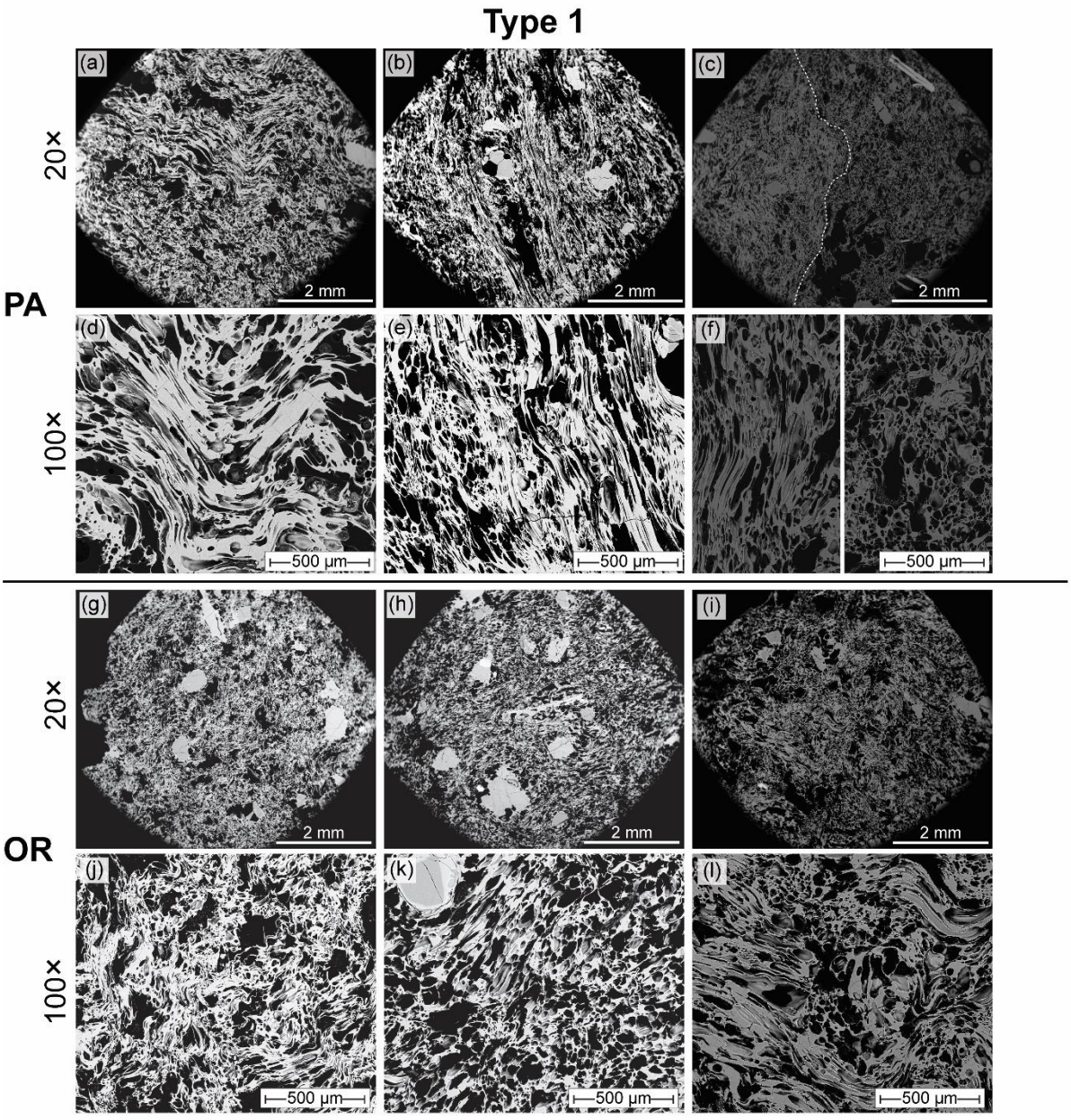

Figure 5.7 – Representative SEM-BSE images at 20× and 100× of vesicle texture type 1 in MHP clasts. (**a**) to (**f**) and are taken from PA cuts (parallel to main direction of vesicle elongation), while (**g**) to (**l**) are taken from OR cuts (perpendicular to main direction of vesicle elongation). Dashed line in (**c**) shows the sharp boundary between texturally different domains having deformed (left in **f**) and undeformed vesicles (right in **f**).

5.4.3.2 Type 2 and 3 textures (TP clasts)

Type 2 and 3 consist in strongly anisotropic vesicle textures, dominated by a pervasive network of tube vesicles (**Fig. 5.8** and **5.9**) (**Table 5.1**). The tube vesicles are aligned according to a preferred direction of stretching and occur only in PA cuts, while OR cuts display subspherical vesicles, being the cross-section of the tubes. Minor areas of subspherical vesicles (~50-200 µm in size) occur sporadically within PA cuts. Type 2 is the most common texture observed in TP clasts, while type 3 has been observed in only two TP clasts. The two textures differ in vesicles size, degree of vesicles elongation and vesicle walls thickness.

Tube vesicles in PA cuts from type 2 have size and elongation similar to those observed in type 1 texture, with the tubes short axis varying from 5 to 30 µm and the long axis varying from 100 up to 500-1000 µm and have vesicles walls between 3 and 15 µm thick (**Fig. 5.8a** to **d**). OR cuts are characterised by a densely packed population of small vesicles (<30 µm), having often circular to elliptical and irregular-polylobate shapes and vesicles walls varying from 1 to 20 µm (**Fig. 5.8e** to **h**). Large vesicles (usually 200-800 µm in diameter) occur sporadically and have elongated shapes parallel to tube vesicles in PA cuts (**Fig. 5.8a**), while have more equant shapes in OR cuts (**Fig. 5.8f**).

In type 3, tube vesicles from PA cuts have markedly coarser sizes (short and long axes of >30-100 µm and >300-1000 µm, respectively) and are less elongated compared to those in type 2 (**Fig 5.9a** to **d**). In OR cuts vesicles have circular to irregular shapes and sizes predominantly in the range of 50 to 150 µm (**Fig. 5.9e** to **h**). Vesicles walls thickness range between 5 and 50 µm. Areas of non-vesicular glass, >50 up to 250 µm thick, between vesicles are widely distributed in both PA and OR cuts.

5.4.3.3 Vesicles interactions and coalescence features

Microtextures in both MHP and TP clasts show extensive evidence of vesicle coalescence. Incipient coalescence features range from thinning of the glass wall (having planar to curvilinear geometries) separating adjacent vesicles, to the rupture and complete failure of the glass wall with subsequent incipient coalescence of the vesicles (**Fig. 5.10**). Remnants of the ruptured glass walls can still be preserved as a thin film (0.5 up to 2-5 µm), which shows typically evidences of retraction and wrinkling (**Fig. 5.10 b**, **c** and **d**). These coalesce features have been commonly observed in pumice clasts from other silicic moderate- to large-scale explosive eruptions (e.g., Klug et al., 2002; Adams et al., 2006; Castro et al., 2012b; Rotella et al., 2014). Evidence of protracted coalescence result in largely irregular vesicle shapes, with vesicles having multiple lobes.

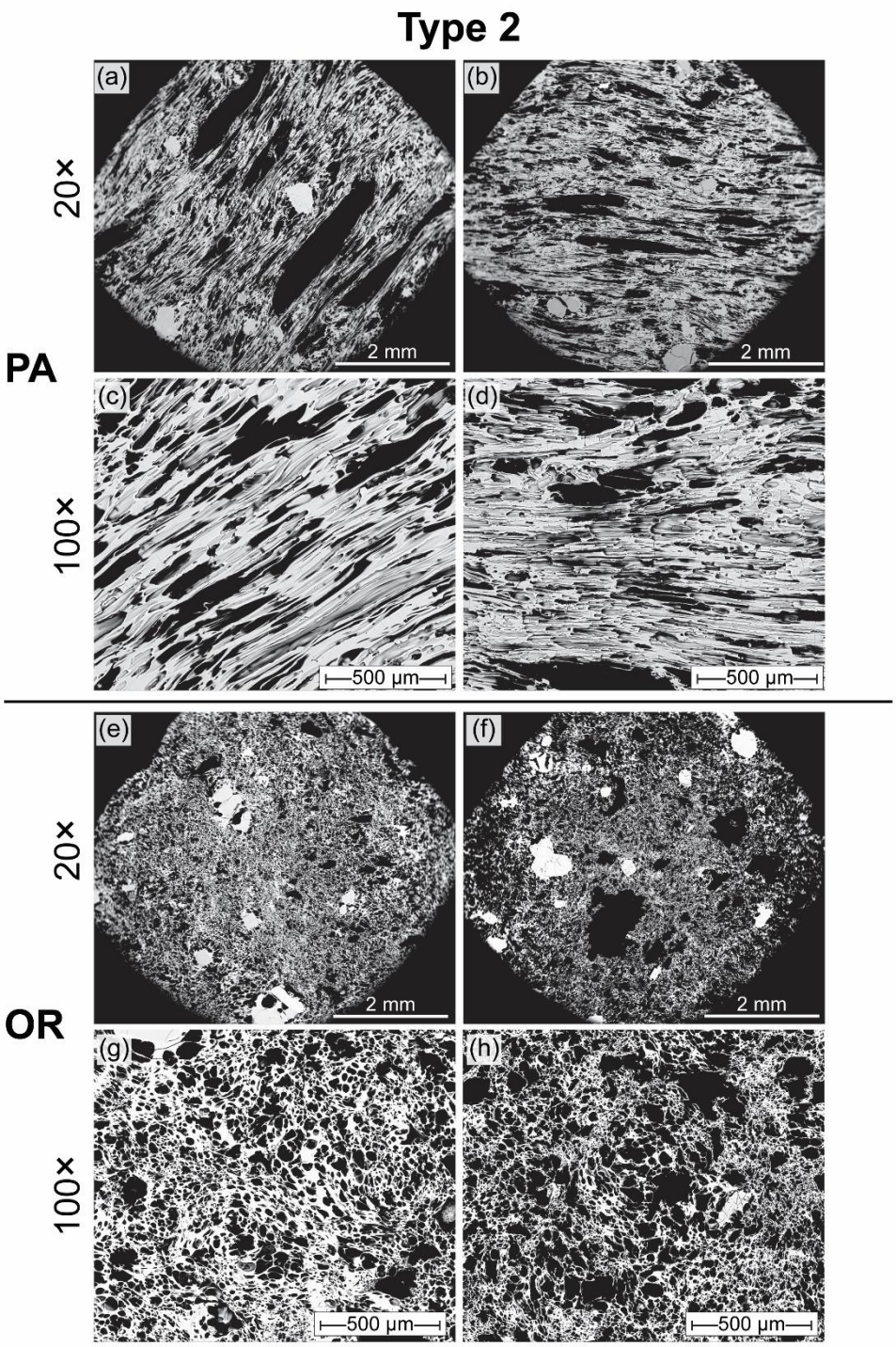

Figure 5.8 – Representative SEM-BSE images at 20× and 100× of vesicle texture type 2 from TP clasts. (**a**) to (**d**) are taken from PA cuts (parallel to main direction of vesicle elongation), while (**e**) to (**h**) are taken from OR cuts (perpendicular to main direction of vesicle elongation).

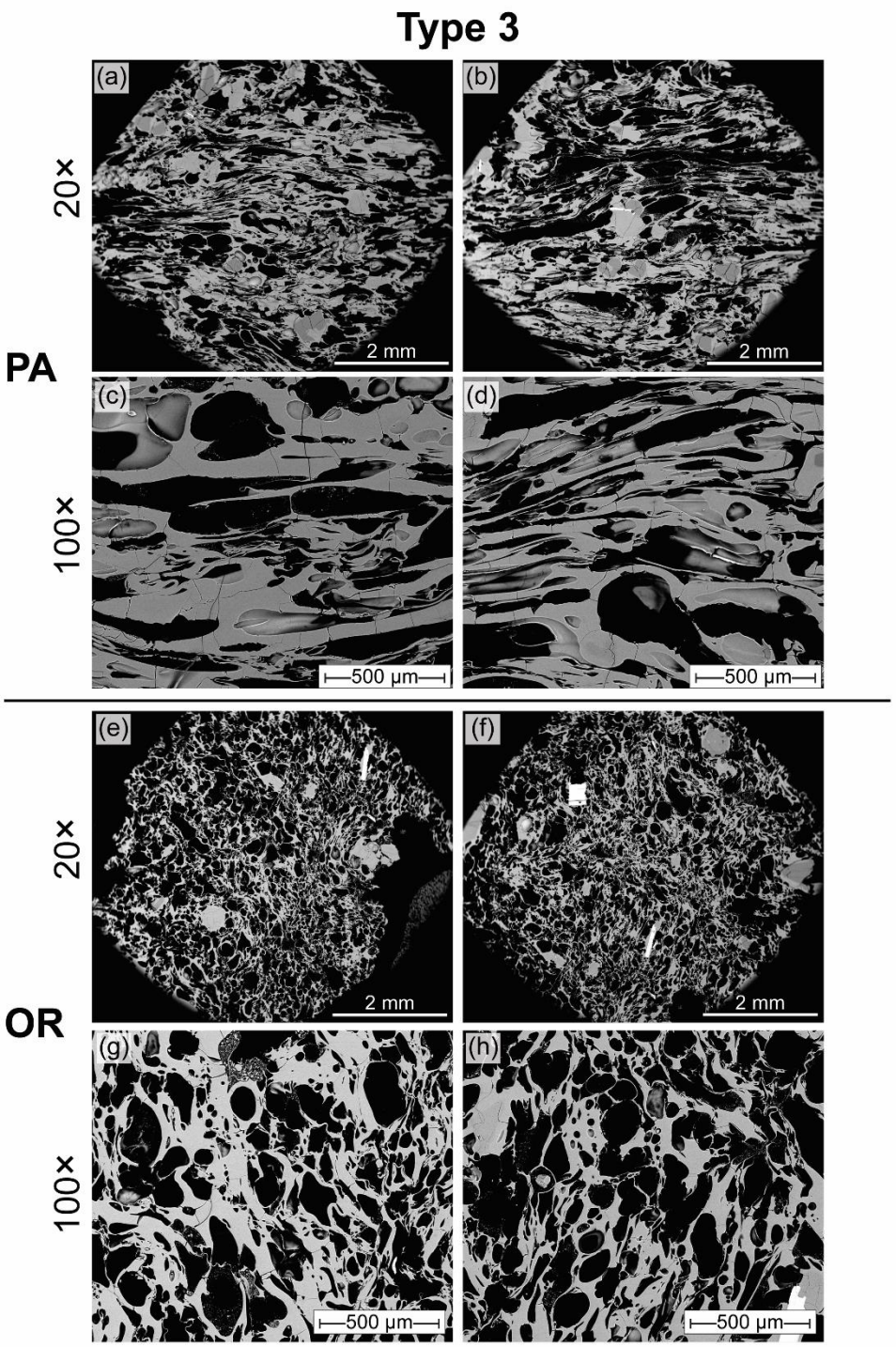

Figure 5.9 – Representative SEM-BSE images at 20× and 100× of vesicle texture type 3 from TP clasts. (**a**) to (**d**) are taken from PA cuts (parallel to main direction of vesicle elongation), while (**e**) to (**h**) are taken from OR cuts (perpendicular to main direction of vesicle elongation).

Incipient coalescence features are mainly observed for circular vesicles, while they are not easily identifiable in the longitudinal sections of tube and convoluted vesicles. This suggest that coalescence in the direction of vesicle elongation (if happened) had already occurred and "healed" prior to magma fragmentation and quenching. Vesicles showing evidence of coalescence have diameter typically >30 up to 300 μm, although smaller vesicles (<30 μm) may merge into larger ones.

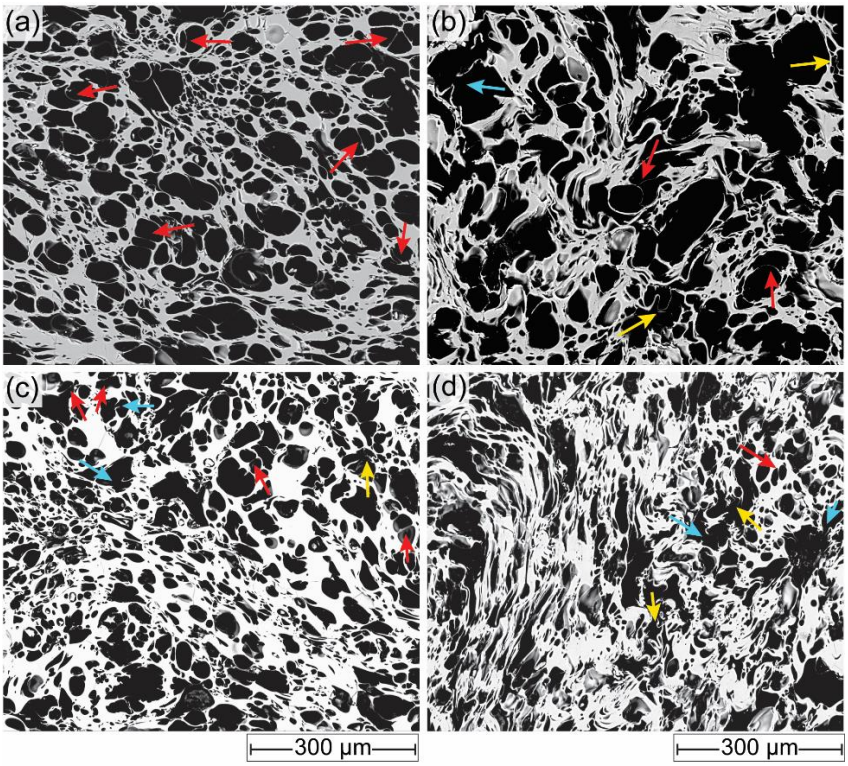

Figure 5.10 – Examples of vesicle coalescence features from SEM-BSE images at 200× from OR cuts of TP (**a** and **c**) and MHP (**b** and **d**) clasts. Red arrows indicate thinning of the glass walls separating adjacent vesicles prior to rupture and coalescence, with the thin walls varying from planar to curvilinear; Blue and yellow arrows indicate retraction and wrinkling, respectively, of glass walls after rupture. Scale for all images is reported at the bottom of (**c**) and (**d**).

5.4.3.4 Qualitative vesicle observations and stratigraphic context

Qualitative observations and comparisons of vesicle textures from different units in the stratigraphic sequence provides some constrains on the consistency/variability on the state of magma vesiculation and deformation during ascent. Overall, the observed Kaharoa pumice microtextures do not vary significantly between units (**Fig. 5.11**). The most significant differences are those observed between MHP and TP clasts and associated vesicles texture (types 1, 2 and 3; cf. **Fig. 5.7**, **5.8** and **5.9**) or within a single clast for few very complex MHP clasts (e.g., **Fig. 5.7 c** and **f**).

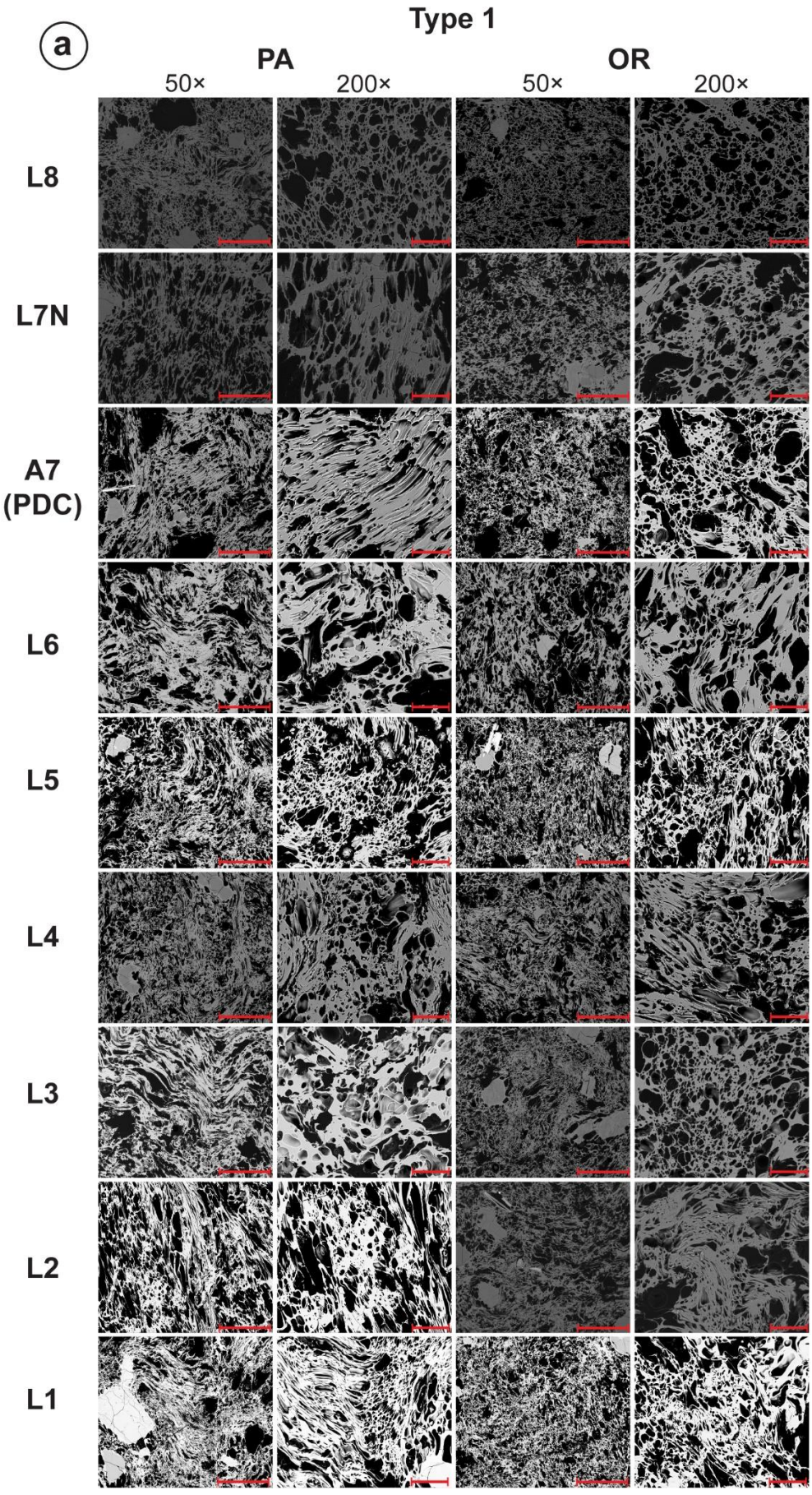

Figure 5.11 (***figure continues in next page***)

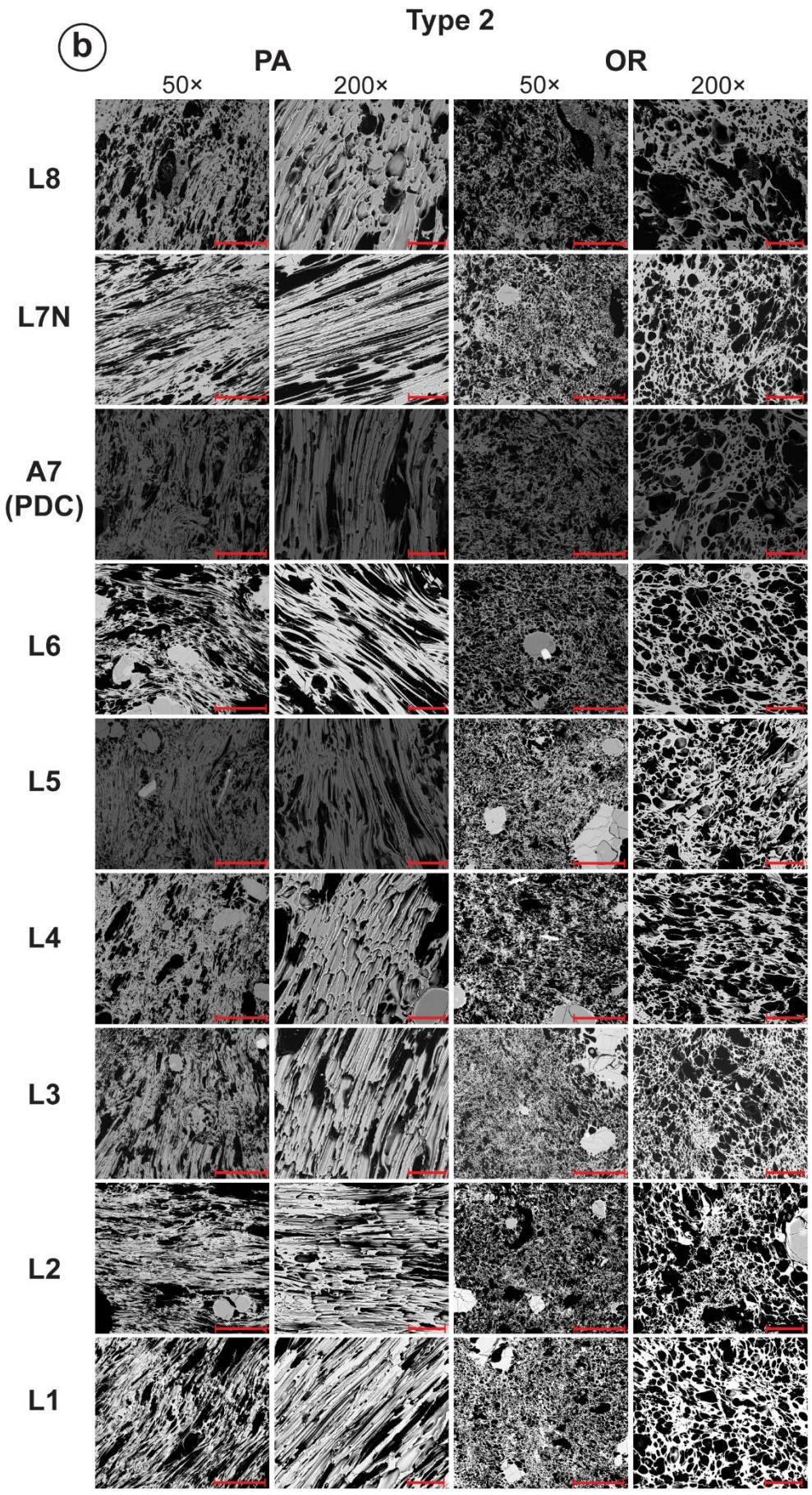

Figure 5.11 (***caption in next page***)

Figure 5.11 (***figure in previous page***) – Representative SEM-BSE images at 50× and 200× of vesicle textures type 1 from MHP clasts (**a**) and type 2 from TP clasts (**b**) for the studied units along the stratigraphic sequence. For the same sample within a unit, both textures from PA and OR cuts are shown. Scale for each image is indicated by a red bar on the bottom right corner, having length of 1 mm and 150 µm for 50× and 200× images, respectively.

5.4.4 Quantitative vesicle data from pumice clasts

Quantification of vesicle size and shape distributions was conducted from set of 200× images acquired from OR cuts of white pumice clasts along the stratigraphic sequence. Results are reported unit by unit and divided according to the two main vesicle textures observed, type 1 and type 2 within MHP and TP clasts. Vesicle size data are also reported for the vesicle texture type 3, observed only in two white pumice samples from unit L5 and L7N. For the sake of comparison, additional vesicle size and shape data were also calculated for two grey pumice samples from unit L7N (see **Section 5.4.4.4**). Results are summarized in **Tables 5.3** and **5.4** for vesicle size and shape, respectively.

5.4.4.1 Vesicle number density and size distribution

Total vesicle number densities per melt area (N_A) range from 1822 to 6119 mm^{-2} with an evident dependency on the sample vesicle textures (**Fig. 5.12a**; **Table 5.3**). In each unit (except for unit L1), N_A obtained from type 2 samples are typically 1.5-2 times larger than type 1 samples. Despite this textural control on N_A, the overall trend of N_A along the stratigraphic sequence are similar for both type 1 and type 2 textures (**Fig. 5.12a**). Obtained N_A increase from units L2 to L5 to than decrease in unit L6 and remain constant in the upper part of the sequence, up to unit L8. The N_A-VSD plots are similar for all units (**Fig. 15b** and **c**). In both type 1 and 2 textures, N_A-VSD are formed by a plateau at high N_A for vesicles <10 µm and by a curved segment for vesicles >10 to 200 µm at progressively smaller N_A. Vesicles <10 um in diameter contribute the most to the final total N_A and therefore to the differences in total N_A between units. Samples from type 3 textures have N_A between 573 and 780 (**Table 5.3**), an order of magnitude smaller than those observed in type 1 and type 2.

5.4.4.2 Area-based vesicle size distribution and 2D vesicularity

The area-VSDs for the Kaharoa pumices are consistently unimodal throughout the units in the stratigraphic sequence, with distribution typically skewed towards larger vesicles size (>30 µm) (**Fig. 5.13**). Vesicle size modes show limited variation with stratigraphic height, with type 1 and

type 2 textures having modes between 21 to 61 µm (typically at 52 µm in type 1 and 41 µm in type 2 µm) (**Table 5.3**). Unimodal distributions are observed also for samples of type 3 texture (**Fig. 5.13**), with modes at 83 and 104 µm (**Table 5.3**). Obtained 2D vesicularity from SEM- BSE images ranges from 49 to 65% (**Table 5.3**) and correlates well with the mean density-based vesicularity (47 to 56%; cf. **Table 5.2**).

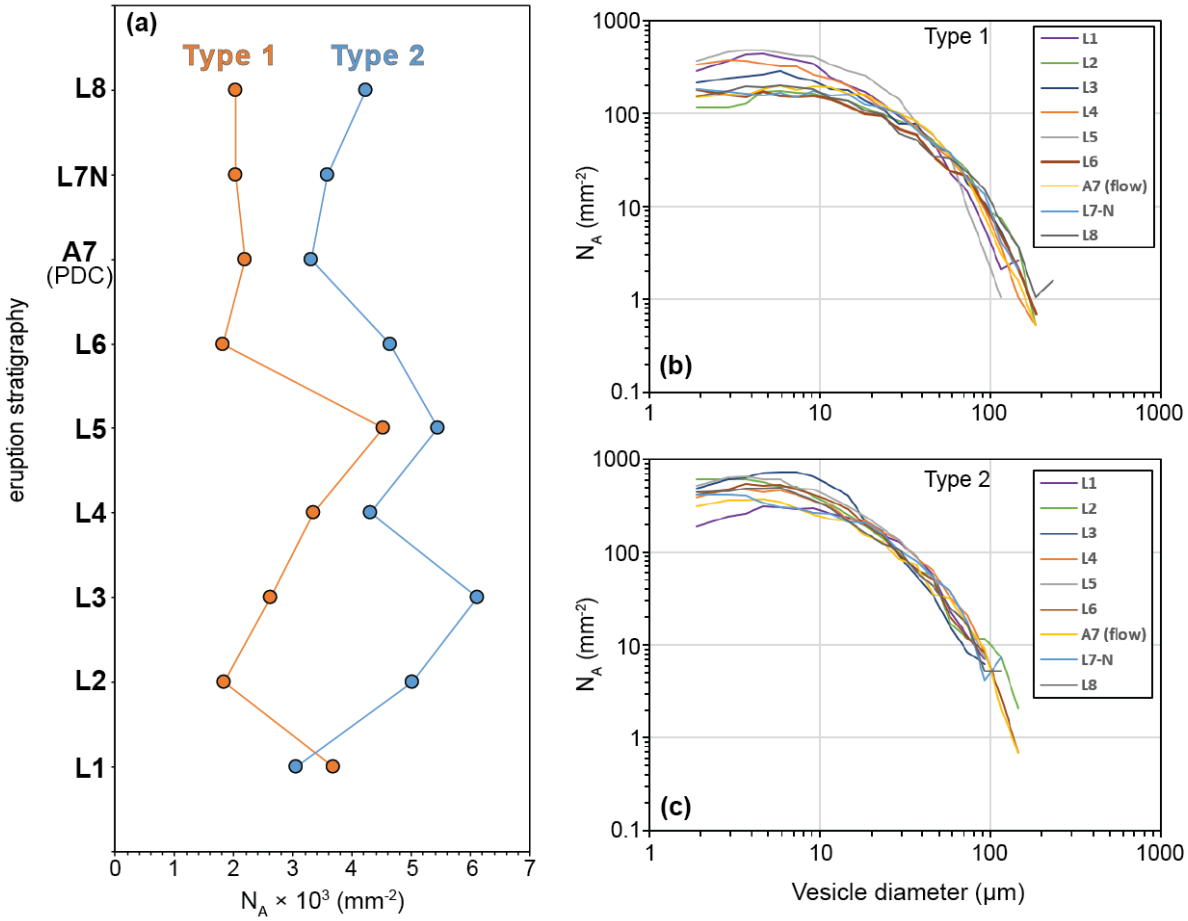

Figure 5.12 – (**a**) Variation of the total vesicle number density per unit area of melt (N_A) of white pumice clasts along the stratigraphic sequence. Total N_A are reported as average results from type 1 texture (orange) and average results from type 2 texture (blue). (**b**) and (**c**) show the distributions of N_A as a function of vesicle size (equivalent diameter in µm) for type 1 texture and for type 2 texture among the different Kaharoa units.

Figure 5.13 (***figure in the following page***) – Vesicle size distributions as area fraction vs vesicle equivalent diameter (in mm) for white pumice clasts from fall lapilli units (L1 to L8) and the PDC unit A7 of the Kaharoa stratigraphy. Vesicle size distributions are obtained from sets of 200× images from OR cuts of three clasts per each unit. Results are corrected for crystal content and normalized for the average 2D vesicularity (value in % on the top right corner of each graph). Vesicle size distributions are plotted as average results from type 1 texture (orange), average results from type 2 texture (blue) and as average results from type 3 textures (dark grey). Two black dashed lines at vesicle size 0.009 and 0.09 mm are reported to facilitate comparison between units in each panel.

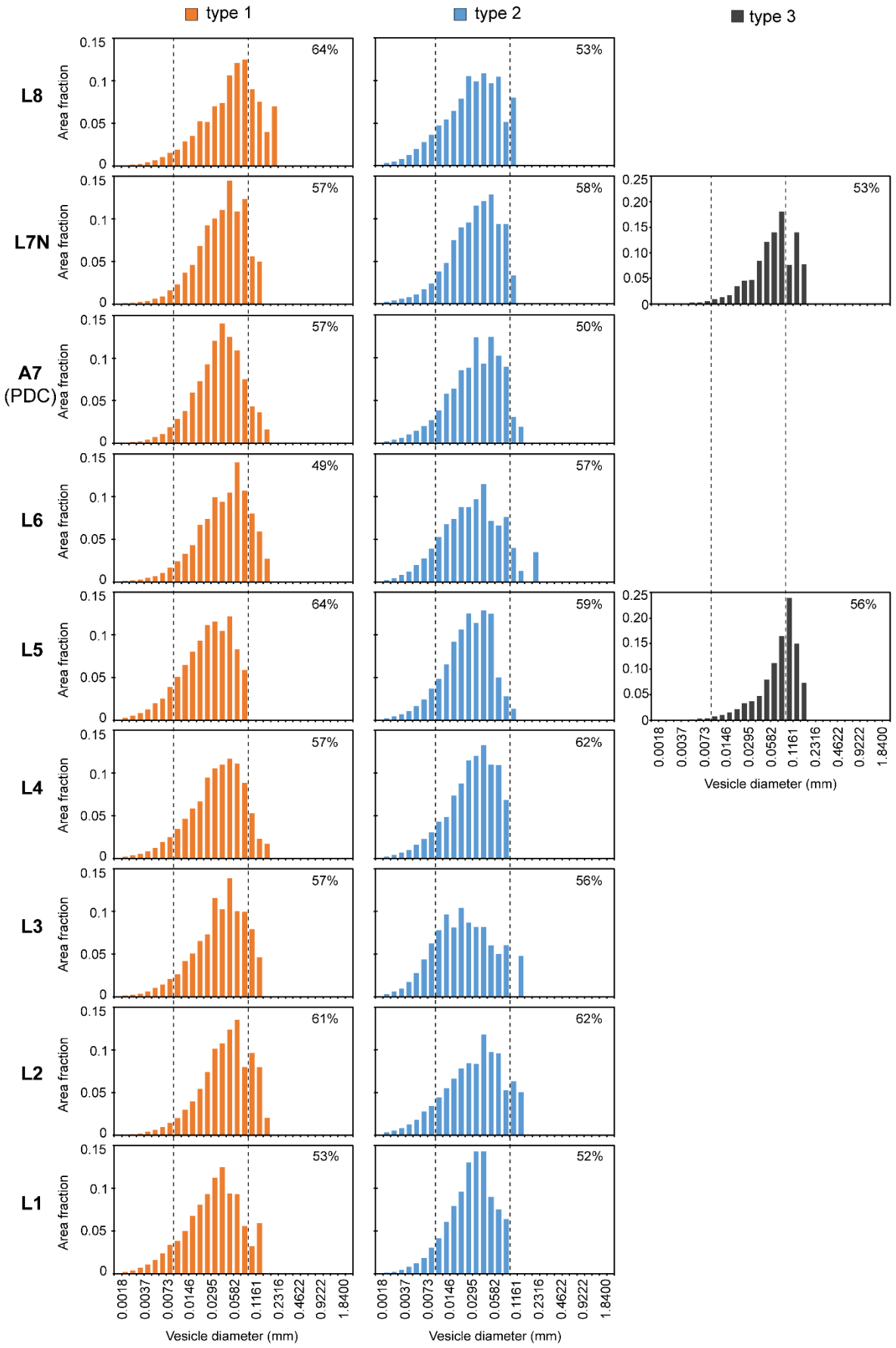

Figure 5.13 (***caption in previous page***)

5.4.4.3 Cumulative vesicle size distribution

Plots of cumulative N_A and cumulative vesicle area fraction are used to further examine and compare vesicle size data between units and vesicle texture types (**Fig. 5.14**). Cumulative number density plots by volume for pumice clasts from Plinian-type eruptions are often characterised by either two linear segments (power-law distribution in log-log plots) with decreasing slopes from large to small vesicles (e.g., Carey et al., 2009) or by a linear segment for large vesicles (>20-50 µm) and an exponential, curved segment (exponential distribution) for smaller vesicles (e.g., Adams et al., 2006; Rotella et al., 2014).

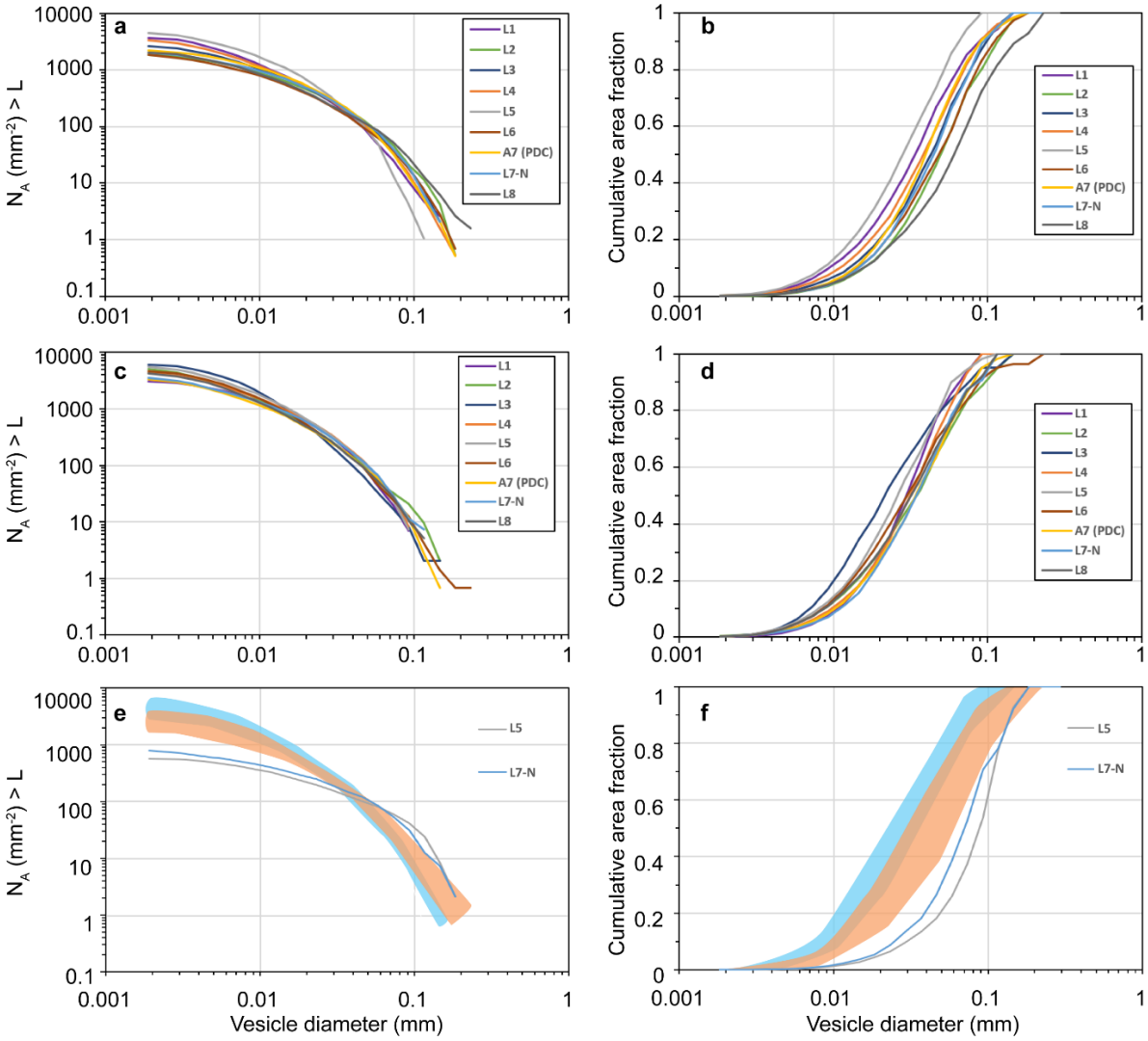

Figure 5.14 – Cumulative vesicle size distributions of white pumice clasts as a function of vesicle number density (number of vesicles per unit area of melt larger than a given vesicle diameter L, left panel) and vesicle area fraction (right panel), corrected for crystal content. Vesicle number densities and area fraction for the different Kaharoa units are plotted as average results from type 1 texture (**a** and **b**), average results from type 2 texture (**c** and **d**) and as average results from type 3 (**e** and **f**; only units L5 and L7N). For comparison, orange and blue fields in **e** and **f** represent ranges of cumulative size distributions for type 1 and type 2 textures.

The cumulative N_A-VSD trends for the Kaharoa pumice clasts with type 1 and 2 textures, although in 2D, can be approximated into two linear segments (**Fig. 5.14a** and **c**). Transition between the two segments typically occur at vesicle size 30-60 μm in type 1 texture and at vesicle size 20-40 μm in type 2 texture, with the larger vesicles size segments characterised by a steeper slope (**Fig. 5.14a** and **c**). By contrast, cumulative N_A-VSD trends for type 3 textures can be better approximated into a linear segment and a curved-exponential segment for large to small vesicles, respectively, with a transition at vesicle sizes ~100 μm (**Fig. 5.14e**).

Cumulative area fraction distributions for the Kaharoa pumices are nearly sigmoidal for texture types 1 and 2, with a well-defined kink at small vesicle sizes, between ~10 to 20 μm, and a second, less pronounced inflection at vesicles approaching 100 μm in diameter (**Fig. 5.14b** and **c**). Cumulative area fraction distributions for the two samples having type 3 texture display only one kink at 30 to 60 μm and a steep constant slop (linear segment) for vesicles > 60 μm.

It is noteworthy to point that small vesicle with diameters <10 μm – despite being significantly more abundant in number (1 to 3 order of magnitude) than larger vesicles in the Kaharoa pumices with type 1 and 2 textures (cf. **Fig. 5.12**) – account only for <10-15% of the total vesicles area fraction (**Fig. 5.14 b** and **d**) and <3% in samples with type 3 texture (**Fig. 5.14f**). Vesicle of size between 10 and 100 μm contribute instead to most of the total vesicle area fraction, up to 80% in the analysed images.

5.4.4.4 Comparison in vesicle size data between white and grey pumices

Vesicle size data obtained for grey pumice clasts of type 1 and type 2 textures are within the range of those observed in white pumice samples (**Table 5.3**). Total N_A for grey pumice clasts varies between 4468 and 5552 mm^{-2} for type 1 and type 2 textures, respectively (**Table 5.3**), consistent with the highest values for total N_A obtained in white pumice clasts (e.g., in units L3 and L5). Area-VSD plots have unimodal distributions with mode at 33 μm for both type 1 and type 2 textures consistent with data from white pumice clasts (**Fig. 5.15a** and **b**; **Tab 5.3**). Finally, cumulative N_A and cumulative vesicle area fraction plots for grey pumice type 1 and type 2 textures follow the same trends of those observed in white pumice samples (**Fig. 5.15c** and **d**).

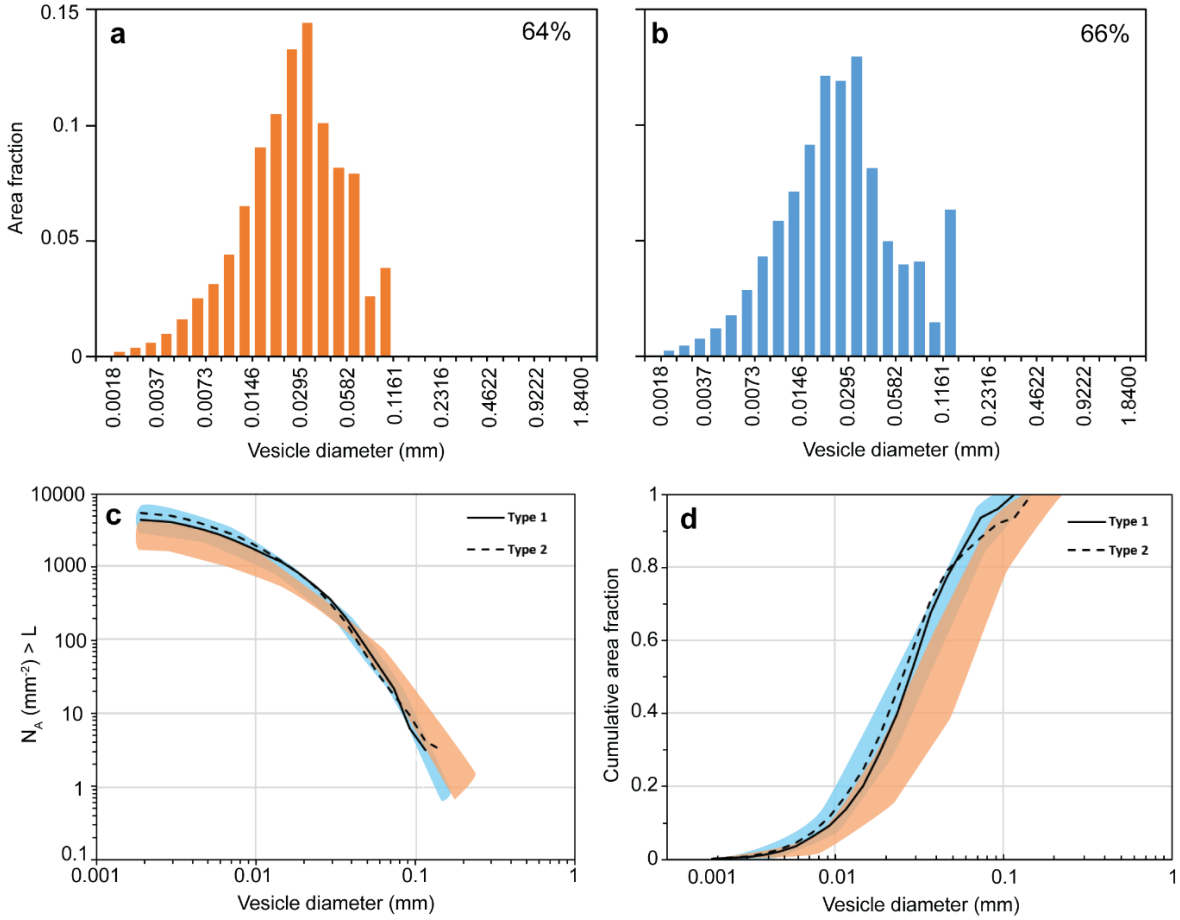

Figure 5.15 – Vesicle size distributions as area fraction vs vesicle equivalent diameter (in mm) for grey pumice clasts in unit L7N for type 1 (**a**) and type 2 (**b**) textures. Results are corrected for crystal content and normalized for the average 2D vesicularity (value in % on the top right corner in **a** and **b**). Cumulative vesicle size distributions as number densities (number of vesicles per unit area of melt larger than a given vesicle equivalent diameter L) and vesicle area fraction are reported in **c** and **d** respectively, for type 1 (solid black line) and type 2 (dashed black line) textures. Orange and blue fields in c and d represent ranges for type 1 and type 2 cumulative size distributions from white pumice clasts in the analysed Kaharoa units.

Table 5.3 – Summary of vesicle size data quantified from set of 200× images acquired from OR cuts of pumice clasts for each unit along the stratigraphic sequence. 2D vesicularity is the average total area of vesicles per melt area; N_A is the total number of vesicles per unit melt area; mode and median vesicle size are derived from the area-VSD and cumulative area-VSD plots, respectively. All parameters are corrected for the image crystal content.

Unit	Pumice	Vesicle texture	2D Vesicularity (%)	N_A total (1/mm^2)	Vesicle size (μm)	
					area-based Mode	area-based Median
L8	white	type 1	64	2029	66	60
	white	type 2	53	4230	41	33
L7N	white	type 1	57	2028	52	46
	white	type 2	58	3588	52	35
	white	type 3	53	780	83	71
	grey	*type 1*	*63*	*4468*	*33*	*30*
	grey	*type 2*	*65*	*5552*	*33*	*25*
A7	white	type 1	57	2191	52	39
	white	type 2	50	3303	33	34
L6	white	type 1	49	1822	66	48
	white	type 2	57	4640	41	31
L5	white	type 1	64	4516	52	28
	white	type 2	59	5454	41	26
	white	type 3	56	573	104	88
L4	white	type 1	57	3340	52	38
	white	type 2	62	4309	41	32
L3	white	type 1	57	2625	52	43
	white	type 2	56	6119	21	22
L2	white	type 1	61	1835	66	50
	white	type 2	62	5012	41	35
L1	white	type 1	53	3687	41	34
	white	type 2	52	3051	41	30

5.4.4.5 Vesicle shape distributions

The 2D shapes of vesicles from OR cuts were quantified using different shape parameters which enabled to estimate the vesicle shape complexity (shape parameters C, R and SF) and the degree of vesicle elongation or stretching (D, E, FLT and AR). The distribution and median of each shape parameters do not vary significantly between different units with stratigraphic height/eruption progression (**Fig. 5.16**; **Table 5.4**). Furthermore, no significant variation in the calculated shape parameters occur between vesicles textures (**Fig. 5.16**; **Table 5.4**) and between samples of white and grey pumice clasts (**Table 5.4**).

Both C and SF have wide distributions skewed towards 1, indicating that vesicles typically tend to approach circular shapes (C and SF median close to 1), however are characterised by irregular outlines, also showed by the deviation of R from 1 (**Fig. 5.16**; **Table 5.4**). The R parameter has a consistently narrower distributions between 0.6-0.5 and 1 in all analysed samples with respect to C and SF, with values rarely below 0.5 (**Fig. 5.16**).

The degree of elongation, D, have median values between 0.3 and 0.4 (**Fig. 5.16**), with corresponding AR median between 1.7 and 2.3 (**Table 5.4**). Distributions for D are wide in all samples, spanning between >0 to 0.8, although skewed towards low D values (**Fig. 5.14**), indicating that vesicles are typically characterised by elongated morphologies with low AR. Wide distributions are also observed for the FLT parameter with median varying between 0.4 and 0.6 (**Fig. 6.19**). The E parameter displays narrow distributions, skewed towards E=1 and median at 0.8-0.9 (**Fig. 5.14**).

Figure 5.16 (***figure in following page***) – Distributions of the vesicle shape parameters quantified from white pumice clasts among the investigated Kaharoa units along the stratigraphic sequence. Boxplots show median and quartiles. Results are from type 1 texture (**a**) and type 2 texture (**b**).

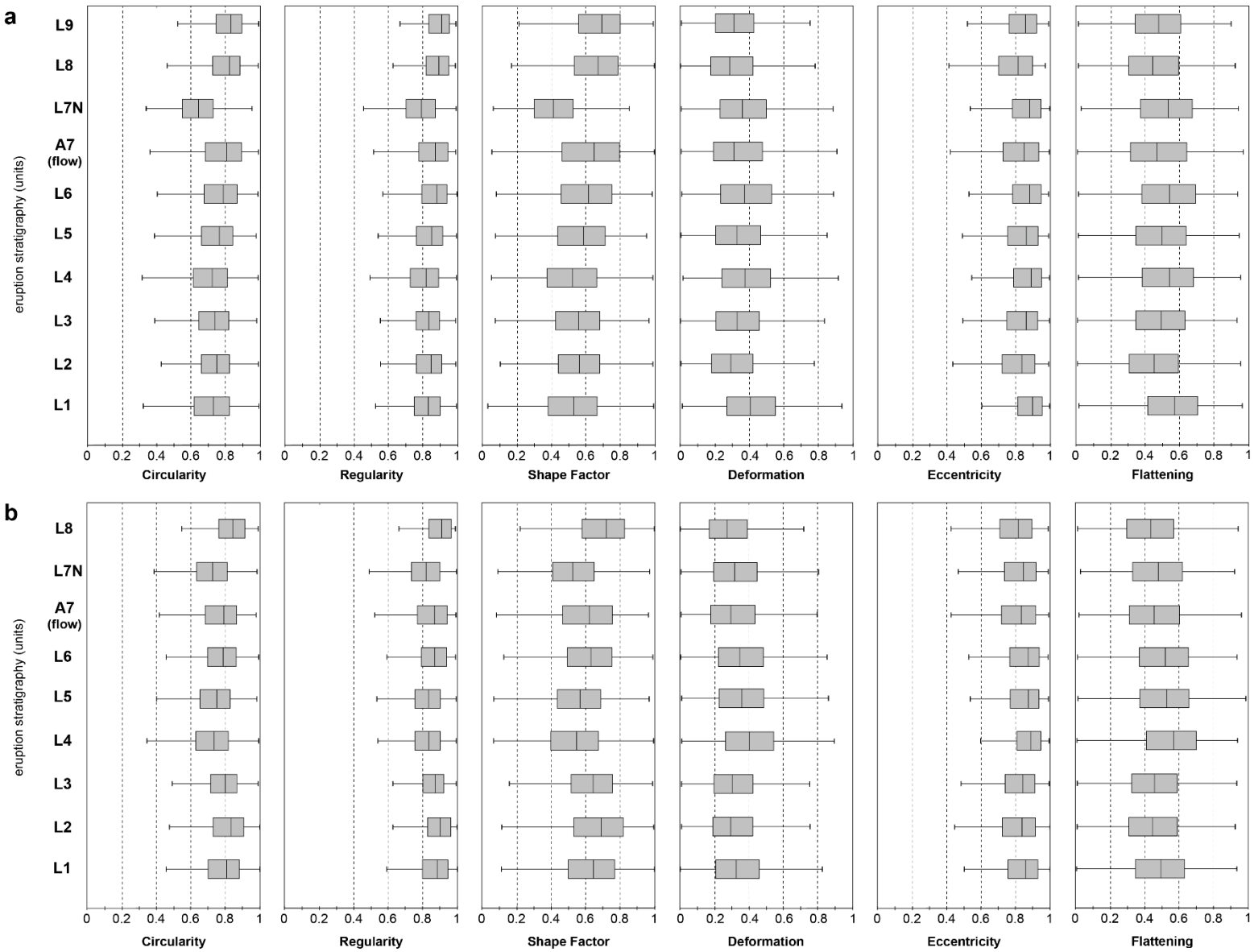

Figure 5.16 – (***caption in previous page***)

Table 5.4 – Median values for the 2D vesicle shape parameters quantified from set of 200x images acquired from OR cuts of pumice clasts for each unit along the stratigraphic sequence.

Unit	Pumice	Vesicle texture	Circularity (C)	Regularity (R)	Shape Factor (SF)	Deformation (D)	Eccentricity (E)	Flattening (FLT)	Ellipse Aspect Ratio (AR)
L8	white	type 1	0.82	0.90	0.68	0.29	0.83	0.45	1.81
	white	type 2	0.85	0.92	0.73	0.27	0.82	0.43	1.75
L7N	white	type 1	0.64	0.79	0.41	0.37	0.89	0.54	2.16
	white	type 2	0.73	0.83	0.53	0.32	0.86	0.48	1.93
	white	type 3	0.66	0.79	0.43	0.40	0.90	0.57	2.33
	grey	*type 1*	*0.73*	*0.83*	*0.53*	*0.28*	*0.83*	*0.44*	*1.78*
	grey	*type 2*	*0.80*	*0.88*	*0.64*	*0.25*	*0.80*	*0.40*	*1.66*
A7	white	type 1	0.86	0.91	0.73	0.27	0.82	0.43	1.75
	white	type 2	0.88	0.92	0.77	0.25	0.80	0.40	1.66
L6	white	type 1	0.79	0.88	0.62	0.37	0.89	0.54	2.19
	white	type 2	0.80	0.88	0.64	0.35	0.88	0.52	2.07
L5	white	type 1	0.77	0.85	0.59	0.33	0.86	0.50	1.98
	white	type 2	0.75	0.84	0.56	0.36	0.88	0.53	2.12
	white	type 3	0.77	0.86	0.59	0.38	0.89	0.55	2.24
L4	white	type 1	0.72	0.82	0.52	0.37	0.89	0.54	2.18
	white	type 2	0.74	0.84	0.55	0.40	0.90	0.57	2.34
L3	white	type 1	0.75	0.84	0.56	0.33	0.86	0.49	1.98
	white	type 2	0.81	0.88	0.65	0.30	0.84	0.46	1.85
L2	white	type 1	0.75	0.85	0.57	0.29	0.84	0.45	1.83
	white	type 2	0.83	0.90	0.69	0.29	0.83	0.45	1.80
L1	white	type 1	0.73	0.83	0.53	0.40	0.90	0.57	2.35
	white	type 2	0.80	0.88	0.64	0.33	0.86	0.49	2.33

5.4.5 Crystal content in pumice clasts

Phenocrysts consist mainly of plagioclase and quartz, subordinate biotite, minor titanomagnetite and rare to absent hornblende and orthopyroxene. Phenocryst content of pumice clasts is calculated from 2D analysis of images at 20×. Variation in crystallinity is observed between compositionally different pumice clasts: white pumices (rhyolite) have average crystallinity of 10% (range between 0.5 and 27% in individual images), while grey pumices (rhyodacite) have average crystallinity of 19% (range between 10 and 36% in individual images) (**Table 5.5**). The calculated average crystallinity of white pumice clasts for each unit remains constant along the entire stratigraphic sequence varying in a narrow range between 9 and 11% (**Table 5.5**).

Large phenocrysts (>1 mm) of plagioclase and quartz distributed in pumice samples often act as areas of "shadow" in the deformation of the bubbles-bearing melt (e.g., Wright and Weinberg, 2009), promoting vesiculation of equant vesicles around the crystals or the formation of large ovoid cavities (**Fig. 5.17**). Large phenocrysts also cause partial bending of tube vesicles, with vesicle overall maintaining the same direction of elongation (i.e., no folding is observed) (**Fig. 5.17**).

Oxides (mainly titanomagnetite) are minor in the Kaharoa pumices (<1%; Nairn et al., 2004) and do not appear to act as significative sites for late-stage nucleation of small bubbles (e.g., Shea, 2017; Burgisser et al., 2020).

SEM observations showed that the groundmass of white pumice clasts is typically microlite-free, while minor to rare microlites (<50 µm) occur within grey pumice clasts.

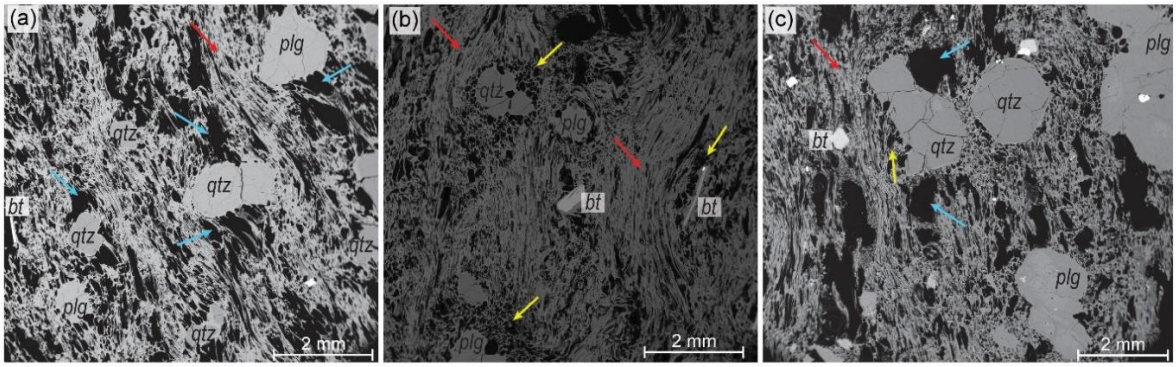

Figure 5.17 – Phenocryst content and crystal-vesicle interactions in SEM-BSE images of white (**a** and **b**) and grey (**c**) pumice clasts. The main crystal phases are indicated as plg, qtz and bt for plagioclase, quartz and biotite crystals, respectively. Arrows in (**a**), (**b**) and (**c**) indicate examples of tube vesicles bend in the proximity of crystals (red arrows), vesiculation of equant vesicles around crystals (yellow arrows) and formation of large cavities around crystals (blue arrows).

5.4.6 General features of obsidian microtextures

Thin sections of two cm-seize obsidian pyroclasts were prepared for samples selected from the obsidian-rich units L3 and A7. The microtexture of the Kaharoa obsidian clasts is characterised by a very low vesicles content (**Fig. 5.18**), with up to ~50 vesicles per unit area in 20× images (1-3% vesicularity; N_A =1.6 mm^{-2}). Vesicles are typically small, with diameters of 10 to 50 µm, have equant to elliptical shapes and occur as isolated individuals with random orientation (e.g., **Fig. 5.18e**) or aligned along a preferred direction (e.g., **Fig 5.18a** and **h**). Few vesicles have larger sizes and elongated shapes, with long axis up to >700 µm and are typically oriented (e.g., **Fig. 5.18a**, **b**, **f**). Obsidians have an identical crystal content to those observed in pumice clasts with plagioclase, quartz, biotite and titanomagnetite, and have average crystallinity of 8.5% (**Table 5.5**). The groundmass is microlite-free, with small microcrysts (>50 µm) of biotite and titanomagnetite scattered within the analysed samples.

Table 5.5 – Summary of crystallinity data as phenocryst content of white pumice clasts in the studied units of the Kaharoa stratigraphic sequence, calculated from 2D analysis of images at 20× (14 to 19 images over 3 clasts per units). Crystallinity for grey pumice clasts were calculated from three selected clasts from unit L7N. Additional crystallinity data are provided for two obsidian pyroclasts from unit L3 and A7.

Unit	Crystallinity (%)	
	average	range
L8	10.9	4.5–27.4
L7N	10.9	5.7–24.3
A7	9.2	0.5–21.6
L6	10.6	3.5–25.9
L5	9.9	5.4–18.9
L4	9.4	3.3–14.4
L3	9.0	3.7–16.0
L2	11.2	3.7–21.6
L1	9.6	3.9–17.9
Clast	**Crystallinity (%)**	
	average	**range**
whole white pumice	10	0.5–27.4
whole grey pumice	19.2	10.2–35.6
Obsidian	8.5	7.8-9.0

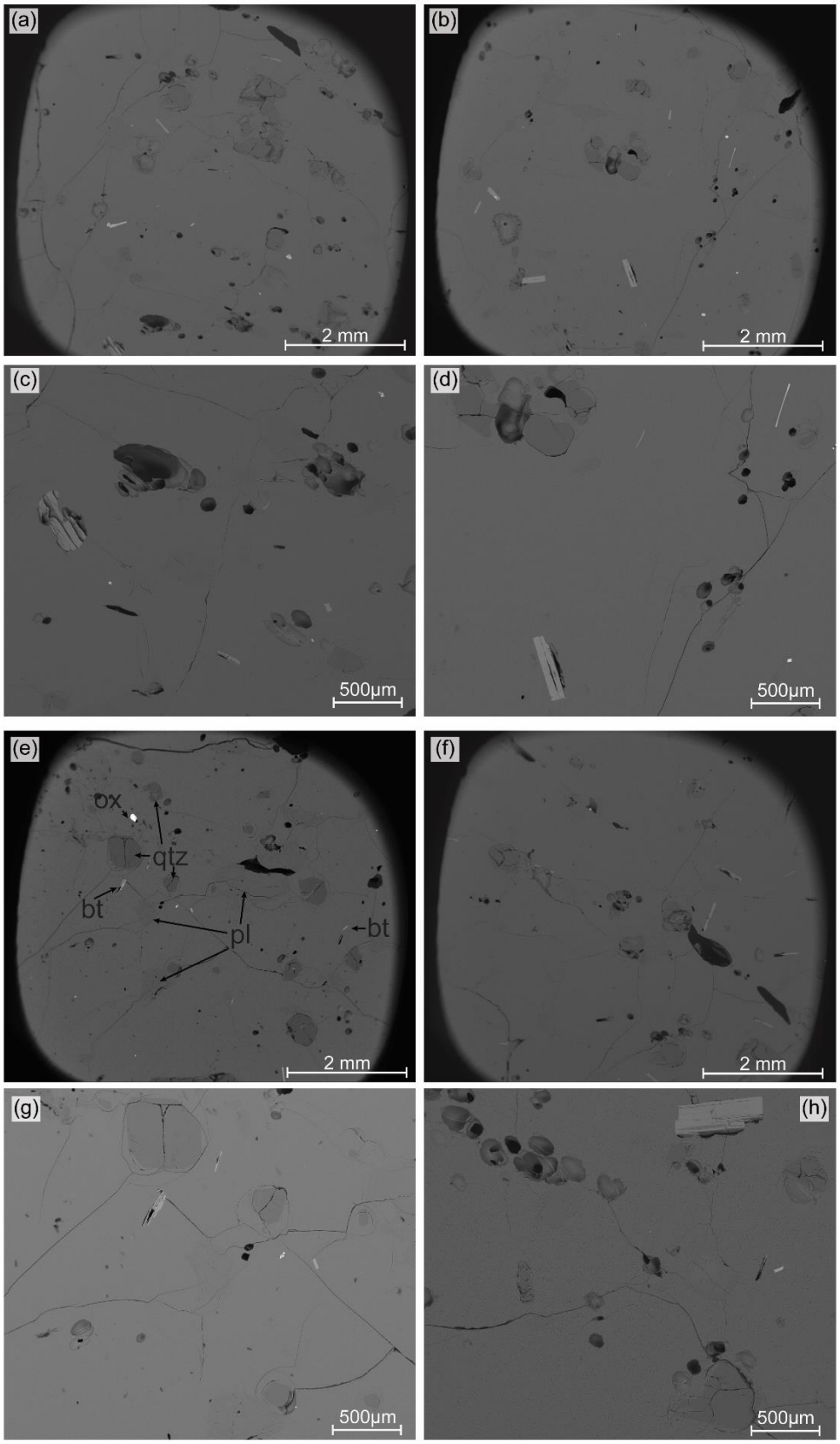

Figure 5.18 – SEM-BSE images of obsidian pyroclast microtexture from unit L3 (**a**, **b**, **c** and **d**) and from unit A7 (**e**, **f**, **g** and **h**). Images are taken at 20× (**a**, **b**, **d** and **e**) and at 50× (**c**, **d**, **g**, and **h**). qtz, pl, bt and ox in (**e**) indicate abbreviations for quartz, plagioclase, biotite and oxides (titanomagnetite) crystals, respectively; the same mineral assemblage is found in the remaining pictures.

5.5 Interpretations and discussion

5.5.1 Insights into conduit processes during magma ascent

Qualitative and quantitative data on pumice microtextures, densities and componentry can provide new insights into conduit processes during magma ascent. The microtextural and physical characteristics of the Kaharoa pumices suggest complex histories of magma degassing and vesiculation (bubble nucleation and growth), outgassing (open-system volatile escape from ascending magma) and shearing (shear stress and deformation of the bubbly melt). These processes can occur at different intervals during magma rise in the conduit (e.g., initial bubble nucleation and growth by diffusion and decompression, followed by bubble growth by coalescence at shallower levels) and/or simultaneously (e.g., continued bubble nucleation and growth, coalescence, shearing and gas escape). The final quenched microtextural features observed in the studied samples represent a combination of these processes (Burgisser and Degruyter, 2015), which are interpreted in the following sections.

5.5.1.1 Bubble nucleation, growth and coalescence

Vesicle size data are of primary importance to understand the formation and evolution of the bubbles within the rising magma in the conduit (e.g., Giachetti et al., 2010). Although total 2D vesicle number densities are sometimes not reported in other vesicle texture studies, the calculated N_A for the Kaharoa pumice clasts are similar to those available for other subplinian and Plinian phases of silicic eruptions. Comparable 2D vesicle number densities have been obtained from pumice samples of the 2008 Chaitén eruption (N_A range = 786 to 2020 mm^{-2}; Alfano et al., 2012), the 1991 Pinatubo eruption (N_A range = 3154 to 9480 mm^{-2}; Polacci et al., 2001), the 1912 Novarupta eruption (N_A range = 1200 to 3800 mm^{-2}, Adams et al., 2006) the ~40ka Plinian phase of the Campanian Ignimbrite eruption (N_A range = 1885 to 3564 mm^{-2}; Polacci et al., 2003).

Data from quantitative vesicle size distributions obtained for the Kaharoa pumices are similar between samples from different units in the stratigraphy, suggesting that processes governing bubble nucleation and growth were consistent during the different phases of the eruption. Furthermore, this appear to be the case also for vesicle textures type 1 and 2, where no large variations are observed in area-VSD, N_A-VSD and cumulative VSD plots (**Figs 5.12, 5.13, 5.14**). Nonetheless, despite these similarities in vesicle size data of pumice sampled from the density mode, the density distributions of individual units (**Fig. 5.5**) indirectly suggest some degree of

variations in the evolving bubble population within the magma to account for the production of pumices within the higher-density tails (**Fig. 5.4**).

Area-VSDs for all the Kaharoa units are unimodal and typically skewed towards larger vesicle sizes (**Fig. 5.13**), which can be interpreted as the result of a continuous process of nucleation and growth of bubbles during ascent, rather than a single event of bubbles nucleation and growth (e.g., Shea et al. 2010). This is also supported by the qualitative observations of vesicles at the SEM, where different size populations of vesicles contribute to form the final pumice microtextures (e.g., **Fig. 5.11**). A protracted process of bubble nucleation during ascent is also supported when both the N_A-VSD (**Fig. 5.12b** and **c**) and cumulative N_A plots are examined (**Fig. 5.13a** and **c**) (e.g., Klug et al., 2002; Adams et al., 2006). In addition, in both plots it is also possible to appreciate the large contribution by number of small vesicles (<10 μm) to the entire vesicle population of individual Kaharoa pumice clasts in each unit. This further suggest that nucleation of bubbles continued during ascent with a substantial late-stage bubble nucleation close to the fragmentation level, next to the continuous growth and evolution of early bubbles. (**Fig. 5.19a**) (e.g., Cluzel et al., 2008; Houghton et al., 2010; Alfano et al., 2012).

Regarding the type of nucleation, two contrasting processes have been proposed for the formation of bubbles in silicic melts (Cashman, 2004; Shea, 2017): (1) homogeneous nucleation, when bubble nucleation occur within the melt without the aid of crystals acting as nucleation sites; (2) heterogeneous nucleation when nucleation of bubbles occur on pre-existing crystals (typically microlites and, in particular, oxides microcrystals provide efficient nucleation sites; Shea, 2017; Burgisser et al., 2020). Although the dominance of homogeneous vs heterogeneous nucleation in silicic eruptions remains an open question (e.g., Shea, 2017), in the case of the Kaharoa eruption it is possible to infer that both mechanisms operated during magma ascent (Mourtada-Bonnefoi and Mader, 2004) as interpreted also in other rhyolitic eruptions (e.g., Adams et al., 2006; Bouvet de Maisonneuve et al., 2009). Though the Kaharoa pumice clasts lack of microlites and have typically low crystallinity (**Table 5.5**) phenocrysts and microcrysts of titanomagnetite and biotite might have acted as sites for early nucleation of bubbles in the volcanic conduit (Mangan et al., 2004; Burgisser et al., 2020). This would have allowed for the heterogeneous nucleation of bubbles to start at relatively lower supersaturations (i.e., at relatively deeper levels in the conduit) and continued during magma ascent (**Fig. 5.19a**). Later, at relatively shallower levels in the conduit, a significant late-stage homogeneous bubble nucleation occurred at high supersaturations resulting in a steep increase in the abundance of newly formed small bubbles in the magma prior to fragmentation (e.g., Klug et al., 2002; Alfano et al., 2012).

Following bubble nucleation, the growth of newly formed isolated bubbles occurs by volatile diffusion and decompression-driven expansion during the early stage of magma vesiculation in

the conduit (Navon and Lyakhovsky 1998; Gonnermann and Manga, 2013). When the magma vesicularity increases to a critical point, the free growth of individual bubbles is then limited by the interactions with neighbouring bubbles, promoting bubble growth by coalescence (**Fig. 5.19a**) (Klug and Cashman, 1996; Castro et al., 2012b; Burgisser et al., 2017; Giachetti et al., 2019). The analysed samples show strong evidence for a significant contribution of bubble coalescence during the evolution of the bubble fractions within the rising magma. Coalescence features can be observed on vesicles of various sizes within the analysed thin sections. These occur mainly on vesicles having equivalent diameters >30 up to 300 µm on OR cuts and to a lesser extent within smaller bubbles (**Fig. 5.10; Fig. 5.11**), suggesting that coalescence was protracted up to fragmentation.

Several studies have also pointed out the importance of bubble shearing and elongation in enhancing bubble coalescence and interconnectivity (e.g., Polacci et al., 2003; Gardner 2007; Okumura et al., 2010; 2013). The extensive presence of bubble deformation in all the vesicle textures observed for the Kaharoa pumice clasts, with tube vesicles localized in bands (MHP clasts, texture type 1; **Fig. 5.7**) or distributed within the entire samples (TP clasts, textures type 2 and 3; **Fig. 5.8** and **Fig. 5.9**), indicates that coalescence of bubbles was a critical process in the ascent dynamic of the Kaharoa magma.

Furthermore, experiments from Burgisser and Gardner (2005) and Okumura et al. (2006; 2008) on rhyolitic melts indicate that shear deformation on bubbles allow bubble coalescence to occur at low magma vesicularity, between ~20-30% (Okumura et al. 2006; 2008) and ~40% (Burgisser and Gardner, 2005). This suggest that for the ascending Kaharoa magma, bubble coalescence (and so possibly bubble deformation; See also **Section 5.5.1.2**) might have started earlier in the conduit at relatively deep levels (**Fig. 5.19a**).

The effects of bubble coalescence can be evaluated also from the quantitative vesicle size and shape data. Despite the vesicle size data quantified here in this study are obtained for oriented thin sections from anisotropic vesicle textures and no 2D to 3D conversion are applied, the cumulative N_A-VSD trends for the Kaharoa pumice clasts can be approximated by two linear segments (**Fig. 6.17a** and **c**). Transition from one segment to the other occur at vesicle size 30-60 µm and 20-40 µm for texture type 1 and 2, respectively. The two segments for the Kaharoa samples can be interpreted as follow: (i) a high rate, late-stage nucleation of bubbles coupled with relatively limited time to grow by coalescence accounting for small vesicles (segment for vesicles <20-30 µm in diameters); (ii) an extended period of growth by coalescence for larger vesicles (segment for vesicles >40-60 µm).

Results from vesicle shape analysis showed that there is a constant deviation from regular, circular or elliptical, shapes to more complex geometries, with vesicles having median values for C, R

and SF between 0.9 to 0.6 (**Fig. 5.16**). This more complex vesicle geometries are here attributed to the effects of bubble coalescence, forming the irregular-polylobate vesicles observed throughout the SEM-BSE images. In addition, the merging of two or more bubbles might have an effect (although difficult to quantify) on the resulting overall vesicle elongation measured, changing the original elongation of individual bubbles (Ohashi et al., 2021). Since no large variations are observed between units for the D, E and FLT parameters, the effect of bubble coalescence on vesicle elongation can be considered constant throughout the eruption.

5.5.1.2 Shear stress, bubble deformation and outgassing

Deformed, elongated vesicles are common in pumice clasts from explosive silicic eruptions and have been interpreted in many studies as the result of shear stresses and strains acting on the vesiculating magma flowing in the conduit (e.g., Martí et al., 1999; Klug et al., 2002; Polacci et al., 2001; 2003; Shea e et al., 2012). A major outcome from this investigation of the Kaharoa pumice microtextures is the ubiquitous and abundant presence of elongated vesicles within all clasts analysed, regardless the stratigraphic position and depositional features of the lapilli-bearing units sampled.

Magma shearing and bubble deformation have several implications for the conduit dynamic, including: (i) enhancing bubble coalescence and magma permeability, thus favouring outgassing (Wright et al., 2006, 2009; Degruyter et al., 2010; Okumura et al., 2013); (ii) promoting brittle fragmentation of the magma as a result of high strain rate (Dingwell, 1996; Papale 1999; Wright and Weinberg 2009); (iii) decreasing the magma relative viscosity in zone of shear (Rust and Manga, 2002; Llewellin et al., 2002; Rosi et al., 2004; Wright and Weinberg 2009); (iv) producing texturally different pyroclasts upon eruption due to spatially variable shear rate within the magma column in the conduit (Polacci et al., 2003; Bouvet de Maisonneuve et al., 2009; Shea et al., 2012; Pardo et al., 2014; Mitchell et al., 2019).

The shear stress to which silicic magmas might undergo during ascent in the conduit has been suggested to be of two main contrasting types, namely simple and pure shear (Rust et al., 2003; Mastin 2005). Simple shear occurs when a lateral velocity gradient develops across the conduit, with higher magma ascent velocities attained towards the conduit's central region and lower ascent velocities attained towards the conduit walls (Polacci et al., 2003; Shea et al., 2012). The resulting magma velocity profile might vary from parabolic to plug-like (Llewellin et al., 2002; Mastin, 2005; Hale and Mühlhaus, 2007; Gonnermann and Manga, 2007; Ohashi et al., 2021). During simple shear, bubbles are typically flattened and elongated at an angle between >0° and 45° to the direction of shear and flow of the magma (Sparks et al., 1994; Rust et al., 2003; Wright

et al., 2009). On the other hand, pure shear is thought to be promoted in response to a fast acceleration and rapid decompression of the magma in the conduit prior to fragmentation, causing a sudden and significant increase in the shear rate of the magma along the conduit (Papale, 1999; Bouvet de Maisonneuve et al., 2009; Ohashi et al., 2020a). The fast acceleration and increase in shear rate will result in the extension and elongation of the bubbles, in this case typically parallel to the direction of shear (Sparks et al., 1994; Rust et al., 2003; Wright et al., 2009).

Both types of shear stresses have been used to explain the deformation of originally spherical bubbles into elongated tubes in both pumice and obsidian clasts. However, the two shearing mechanisms operate at different positions (and hence time) within the magma column in the conduit and discriminate between one or the other type remains a complicated task (Bouvet de Maisonneuve et al., 2009; Dingwell et al., 2016). Rust et al. (2003) proposed that in obsidian fragments (from both lava flow or pyroclastic fall deposits) the shearing mechanism can be qualitatively assessed from the orientation of the elongated vesicles with respect to other indicators of the flow/shear direction such as flow banding structures or microlite alignments. This type of approach cannot however be applied to the Kaharoa obsidian samples as they consist in largely degassed clasts with very few vesicles, and lack in banding structures and microlites (**Fig. 5.18**). Lack of microlites prevent using this technique also in the analysed pumice clasts. Shearing mechanisms can be approximated by the shape of the deformed vesicles (Wright et al., 2009), since simple and pure shear cause flattening (elliptical cross-section section vesicle shape) and extension (circular cross-section vesicle shape) respectively of the bubbles subjected to shear (Sparks et al., 1994). The Kaharoa pumice samples in OR cuts have vesicles with variable shapes from circular to elliptical and are significantly modified by bubble coalescence resulting in more complex and irregular vesicle shapes. Due to the effects of coalescence, quantitative vesicle shape data alone are not conclusive in determining the type of shearing mechanism. Some clearly flattened tube vesicles have however been found in some of the investigated samples (e.g., Fig. E2-12 in **Appendix E**).

Density data can offer further insights into origin of magma shearing in the conduit. The measured pumice clasts densities for the Kaharoa deposit are high when compared to pumice clasts from other dry, Plinian phases of silicic eruptions (e.g., ~232 CE Taupō eruption, Mitchell et al., 2018; 1875 CE Askja eruption, Carey et al., 2009; 1912 CE Novarupta eruption, Adams et al., 2006; 2008 Chaitén eruption, Alfano et al., 2012; 2011 Cordón Caulle eruption, Pistolesi et al., 2015), with density modes varying between 900-1000 and 1100-1200 kg/m^3 (**Fig. 5.4**). The production of such high-density pumice clasts is strongly suggestive, along with microtextural evidence of coalescence and shearing, that the Kaharoa magma experienced a certain degree of permeable outgassing during rise in the conduit. This mechanism permitted the partial escape of exsolved gas, causing a decrease in the magma vesicularity and an increase in magma densification during

ascent (e.g., Okumura et al., 2010; Gonnermann et al., 2017; Colombier et al., 2017; Vona et al., 2020). For gas to decouple and escape from viscous silicic magmas, the development of an interconnected permeable network of bubbles through the magma column in the conduit is required (Klug et al., 1996; Wright et al., 2006, 2009; Degruyter et al., 2010; Castro et al., 2012b; Giachetti et al., 2019). Gas outflow within the Kaharoa magma in the conduit occurred predominantly vertically along the conduit, parallel to the direction of bubbles elongation (e.g., Okumura et al., 2009) rather than through the conduit walls (cf. Jaupart, 1998). Moreover, deformation experiments by Okumura et al. (2009) demonstrated that magma permeability can develop in zones of high strain rate when the magma vesicularity reaches >30%, suggesting onset of magma permeability even at depth of a few thousand meters in the conduit. For these reasons, it is here suggested that shearing of the magma enhancing bubble coalescence might have started at relatively deeper levels in the conduit rather than at very shallow levels immediately before magma fragmentation (**Fig.5.19a**). In this scenario simple shear caused by laterally variable ascent rate in the conduit is suggested as the dominant shearing mechanism during the Kaharoa eruption, enhancing bubble interconnectivity and magma permeability, resulting in the overall high-density of the erupted and deposited pumice clasts. Pure shear caused by the fast acceleration of the magma just prior brittle fragmentation, might have played a minor role in the outgassing dynamic and in the overall ascent dynamics of the Kaharoa magma.

5.5.2 Pyroclast textural heterogeneity

5.5.2.1 Formation of different pumice types and associated vesicle textures

Field investigation of the Kaharoa deposit coupled with clast frequency analysis show that individual lithostratigraphic units are characterised, in the lapilli fraction, by two main texturally different types of pumice – MHP and TP clasts – reflecting different vesicle textures – types 1 and 2 (+ rare type 3 texture) at the submillimetre scale (**Table 5.1**). The presence of both types of pumice at any given units within the pyroclastic succession, with typically constant proportion (60-70% MHP and 40-30% TP) suggest that MHP and TP clasts were continuously produced during the explosive eruption phases and simultaneously transported and deposited (**Fig. 5.3**).

The differences in surface and microscopic textures of the erupted MHP and TP products can therefore be ascribed mainly to spatially variable physical characteristics (flow/deformation conditions) of the ascending magma column in the conduit, as has been proposed for many other eruptions with texturally different clasts (e.g., Polacci et al., 2001, 2003; Rosi et al., 2004; Bouvet de Maisonneuve et al., 2009; Shea et al., 2012; Pardo et al., 2014; Mitchell et al., 2019, Heinrich et al., 2020; Trafton and Giachetti, 2021). Differences in chemical compositions of the magma,

responsible for the simultaneous deposition of white (rhyolite) and grey (rhyodacite) pumice clasts in unit L7 to L9, later in the eruption (Phase D) (**Chapter 3**), appear not to have contribute to significant changes in microtextures (cf. Polacci et al., 2001; Gurioli et al., 2005) since both clasts have very similar vesicle features and bulk densities (**Fig. 5.4** and **5.15**).

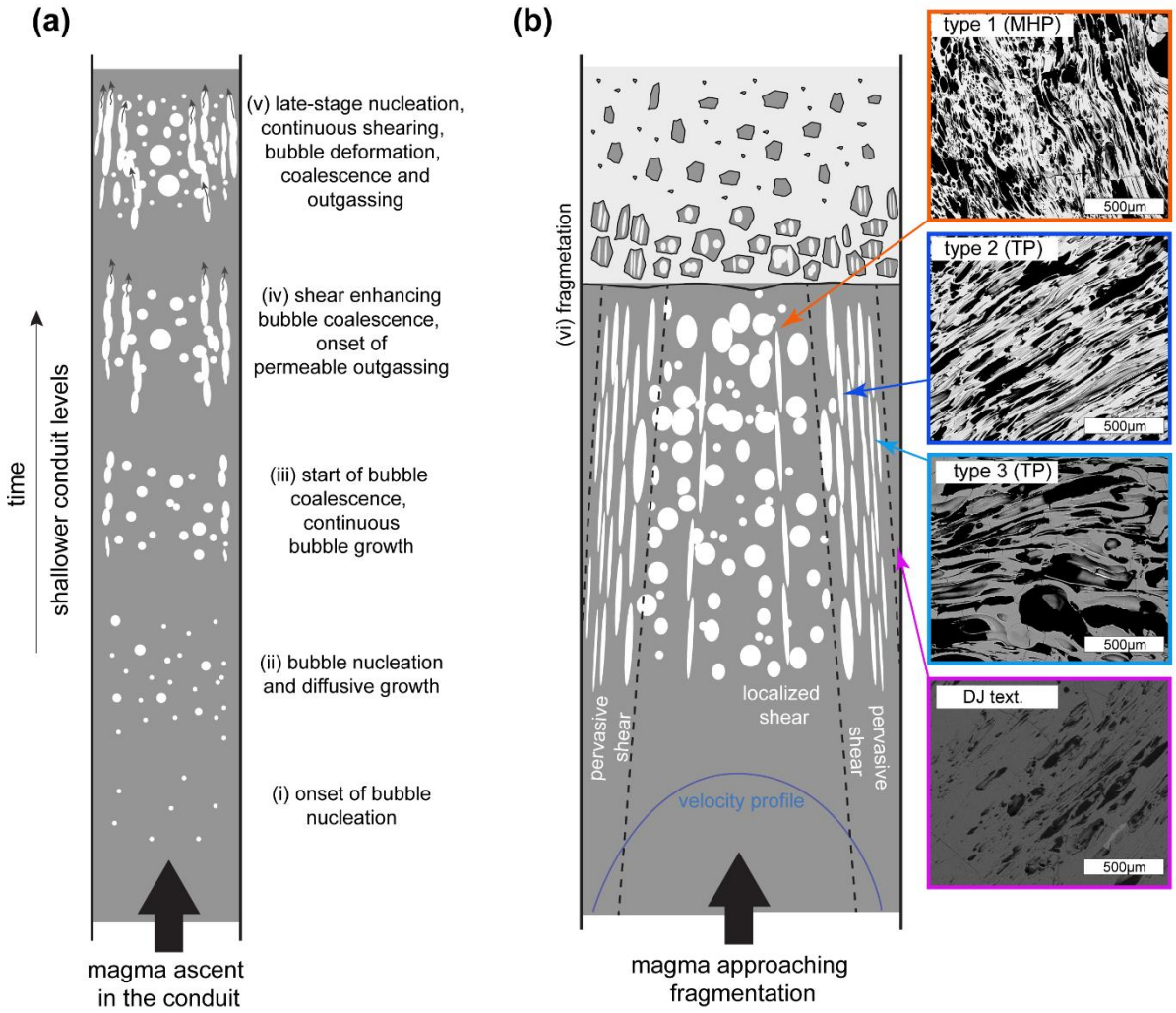

Figure 5.19 – Conceptual model of magma ascent in the conduit through time and origin of different microtextures observed in this study. The conduit width is not to scale, and sizes of bubbles are exaggerated. (**a**) Schematic representation of the evolution of the bubble fraction within the ascending magma column in the conduit at progressively shallower levels and associated sequential and overlapping processes (*i* to *v*). (**b**) Schematic representation of magma in the conduit approaching and at fragmentation (*vi*) during explosive events. The figure shows variation in magma ascent velocity laterally across the conduit leading to the development of areas at different shear. Within the central region of the conduit, magma shearing and bubble deformation is localized in narrow zones. Towards the marginal regions of the conduit, the magma experiences high and pervasive shear with formation of networks of tubular bubbles. Near the conduit walls, longer residence time and efficient outgassing promote collapse of tubular bubbles and magma densification. This model is proposed to explain the origins within the conduit of the different microtextures (indicated by the *arrows*) observed in the later erupted juvenile pyroclasts. SEM-BSE photos are reported as examples; *MHP* is microvesicular heterogeneous pumice, *TP* is tube pumice, and *DJ* is dense juvenile clasts.

Vesicle texture data suggests that the magma column within the conduit was characterised by a lateral (cross-conduit) gradient in ascent velocity promoting simple shear and stretching of the vesicles to tubular shapes. Progressively higher shear rates are reached towards the marginal regions of the conduit (e.g., Mitchell et al., 2019; Trafton and Giachetti, 2021), forming TP clasts upon fragmentation (**Fig. 5.19b**). Towards the central region of the conduit, the lateral magma ascent velocity gradient is reduced, with more uniform velocity possibly resulting in a decrease in shear rate (e.g., Polacci et al., 2003; Bouvet de Maisonneuve et al., 2009), promoting conditions for the formation of MHP clasts (**Fig. 5.19b**). Within this region, high shear was probably only localized into narrower zone (e.g., Wright and Weinberg, 2009; Shea et al., 2012). This permitted the formation of areas in the magma where bubbles are deformed and elongated, and areas where bubbles can instead expand and coalesce without extensive deformation (**Fig. 5.19b**). This can explain the observed spatial heterogeneity of vesicle shapes in the later quenched MHP clasts.

The formation mechanism of MHP textures is largely consistent with what has been recently shown by Piochi et al. (2021). Their study provides an estimation of the spatial variation in capillarity number (i.e., the ratio between viscous stress and surface tension; see **Chapter 1**) measured in SEM-BSE images of thin sections from anisotropic pumice clasts erupted during the Plinian fallout phase of the intra-caldera ~4 ka Agnano Monte Spina eruption of Campi Flegrei (Italy) (trachytic in bulk composition). Their study suggests that significant variations in the capillary number (more than twice in absolute value) can occur at the submillimetre scale, ultimately impacting bubble deformation and resulting in microscopic textural heterogeneities, as also observed for the Kaharoa MHP clasts. More complex MHP clasts with large domains (>1 mm wide) of different textures are explained below (**Section 5.5.2.2**) as different processes might have overlapped in the formation of this texture.

The proposed model of cross-conduit variation in ascent velocity and shear rates also enables the explanation of the main difference in vesicle data between vesicle texture types 1 and 2 in OR cuts. Type 1 samples are characterised by relatively lower N_A and by larger modal vesicle size in the area-VSDs compared to type 2 (**Fig. 5.12** and **5.13; Table 5.3**). Within the central region of the conduit, where magma was less affected by shearing, undeformed bubbles were able to grow also radially by expansion and coalescence. This resulted in the formation of larger bubbles at the expense of smaller ones, causing an overall decrease in bubble number density (e.g., Adams et al., 2006; Rotella et al., 2014), which prompt the formation of texture type 1. In contrast, within the marginal region of the conduit where type 2 texture developed, the higher shear rate (not localized in narrow zones) resulted in bubbles stretching and coalescence vertically along the conduit, allowing to maintain relatively high number density and smaller vesicle size perpendicular to the direction of elongation.

Few TP clasts are characterised by the vesicle texture type 3, formed by a network of tube vesicles similar to type 2, however displaying thicker vesicles walls, vesicle-free glass areas, larger vesicles size and significantly lower N_A (**Fig. 5.13** and **5.14; Table 5.3**). This vesicle texture is here suggested to have formed in response to the slower magma ascent in near proximity of the conduit walls (**Fig. 5.19b**). With longer residence time in the conduit, this portion of magma underwent to protracted bubble coalescence (resulting in larger vesicles) and gas escape by efficient outgassing which led to the initiation of bubble collapse (formation of vesicle-free glass area) (e.g., Adams et al., 2006; Carey et al., 2009; Shea et al., 2012; Kennedy et al., 2016). This process of bubble collapse following extended gas escape is also expected to have dominated in the formation of pumice samples from the high-density tails (**Fig. 5.4**), as well as in the formation of dense juvenile clasts dispersed in the Kaharoa deposit and observed during componentry analysis (**Fig. 5.19b; Fig. 5.20**).

5.5.2.2 Effects of additional syn-ascent and post-fragmentation processes on pumice vesicle textures

Some features observed within the vesicle texture type 1 such as (1) the presence of convoluted, elongated vesicles and (2) the coexistence of contiguous large (mm-size) domains of deformed and apparently undeformed vesicles, cannot be fully explained by a cross-conduit variation in magma ascent and shear rates in the conduit. These features suggest instead the occurrence of additional processes during magma flow in the conduit and/or immediately after fragmentation prior to quenching of the MHP clasts, affecting the final vesicle texture (e.g., Rotella et al., 2014; Giachetti et al., 2021).

(1) Convoluted vesicles suggest that some bubbles underwent different stages of deformation during which the initial bubble stretching by simple shear was followed by folding (e.g., Klug et al., 2002). Folding/convolution of bubbles can result by a series of different processes; however, their contribution to the final convoluted vesicle shapes observed is difficult to constrain from the available data. Few possible mechanisms are here suggested. (i) The formation of convoluted vesicles could have occurred in response to transient, compressional stresses caused by the passage of shock waves during explosive events at magma fragmentation. This process was first hypothesised by Dingwell et al. (2016) to explain the presence of kink bands within the Ramadas tube pumice clasts (Martí et al., 1999) and can be used to describe the multiple deformations of some elongated vesicles in Kaharoa MHP clasts showing "wavy" outlines. (ii) Convoluted vesicles could have been generated by the unconfined expansion of neighbouring subspherical bubbles (during or immediately after fragmentation), which forced the adjacent elongated bubbles to fold (e.g., **Fig. 5.7l**). (iii) Additionally, some of the convoluted vesicles might have formed as

result of protracted simple shear, driving folding of previously formed narrow zones of elongated bubbles. Similar processes have been used to describe the formation of sheath folds in rhyolitic lava flows (e.g., Bullock et al., 2018), but might be of relevance also during magma flow in the conduit, within narrow zones of localized shear (Wright and Weinberg, 2009; Cabrera et al., 2015).

(2) Few MHP clasts are constituted by mm-size texturally different domains (visible under SEM), containing either dominantly tube and convoluted vesicles, or dominantly subspherical vesicles. The domains are separated by typically abrupt boundaries (e.g., **Fig. 5.7c** and **f**). This composite vesicle texture might have been formed from the amalgamation of texturally different magma particles upon fragmentation. Similar processes of sintering/welding of fragmented magma particles have been suggested as important in the formation of small-size obsidian pyroclasts (Gardner et al., 2017; Watkins et al., 2017) and composite volcanic bombs (Schipper et al., 2021). Studies by Trafton and Giachetti (2021) and Giachetti et al. (2021) on rhyolitic juvenile textures from Plinian-type eruptions indicate that amalgamation of magma particles at or above the fragmentation level are largely important in the formation of pumice clasts. Some of the most complex vesicle textures observed in MHP clasts might be the results of this additional process of fragmentation, non-destructive collision, agglomeration, and sinter of magma particles, which individually originated from parts of the ascending magma column which experienced different vesiculation and deformation history before fragmentation (thus having different individual textures) (Giachetti et al., 2021).

5.5.2.3 Insights into the origins and significance of obsidian pyroclasts

The juvenile origin of the Kaharoa obsidian pyroclasts have been discussed in **Chapter 3**. Here, based on the combination of the available textural, componentry and stratigraphic data, diverse processes within the conduit are inferred for the formation of obsidian clasts during the Kaharoa eruption. Formation mechanisms of juvenile obsidians have important implications for conduit processes and eruptive dynamics (e.g., Rust and Cashman, 2007; Schipper et al., 2013; Saubin et al., 2019; Giachetti et al., 2020).

The principal mechanisms that have been postulated for the formation of juvenile obsidians in pyroclastic deposits of rhyolitic eruptions range from the collapse and densification of the ascending permeable magmatic foam in the conduit (Eichelberger et al., 1986; Jaupart and Allègre, 1991; Eichelberger, 1995), to the rapid quenching of magma interacting with groundwater within the conduit (Bursik, 1993). The former can occur when slow magma ascent rates (i.e., longer residence time in the conduit) are attained, enabling an efficient outgassing through the development of permeable bubble networks in the magma column (Okumura et al.,

2013; Kennedy et al., 2016; Cassidy et al., 2018; Giachetti et al., 2020). Recent studies on the microtextures and water content of natural obsidian clast from rhyolitic eruptions (Gardner et al., 2017; Watkins et a., 2017) and on experimentally reproduced obsidians (Gardner et a., 2018, 2019; Wadsworth et a., 2019) have challenged this classical model of obsidian formation via magmatic foam collapse and proposed that obsidian pyroclasts form instead by aggregation and sintering of ash-size magma particles along the conduit walls, above the fragmentation level. The sintered obsidian fragments are then re-incorporated within the erupting gas-magma particles mixture exiting the vent and are deposited together with more vesicular pyroclasts.

Alongside these studies focused on the volatile content and textural features of obsidian, Rust and Cashman (2007) pointed out the importance of quantifying the vertical variation in abundance of obsidians within pyroclastic deposits to rule out multiple origins of obsidian. Within the Kaharoa deposit, obsidian fragments have typical concentration of <5 wt.%, however, reach 14 to 27 wt.% in units L3 (fall deposit) and A7 (PDC deposit) at the start of Phases B and C, respectively (**Fig. 5.20**). These steep increases in obsidian content at two different stratigraphic levels, appears independent from eruption style. Considering the available data, two syn-ascent processes of obsidian formation during the Kaharoa eruption are here proposed:

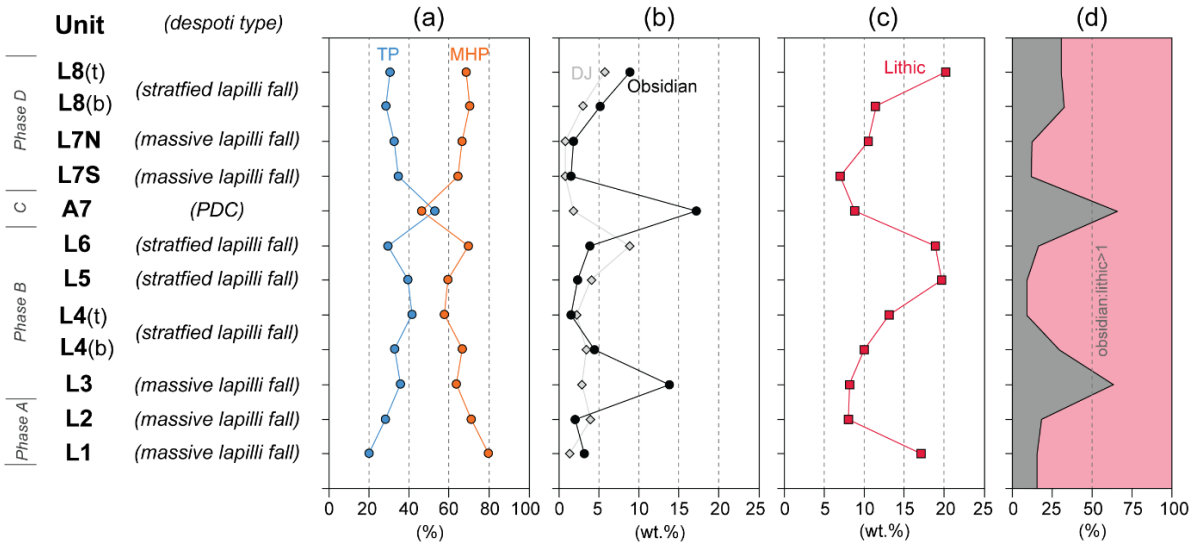

Figure 5.20 – Combined pumice textures and componentry changes throughout the eruption stratigraphy (i.e., time) within the studied units. *(b)* and *(t)* in units L4 and L8 indicate samples collected from the bottom and top parts of the units, respectively. (**a**) Relative frequency of MHP (orange) and TP (blue) clasts. (**b**) and (**c**) relative abundances of dense juvenile (*DJ*, grey), obsidian (black) and lithic clasts in componentry analysis (expressed in weight percent) at sections 2 and 24. Obsidian clasts in unit A7 is up to ~27 wt.% in section 28. (**d**) Proportion of obsidian to lithic clasts.

(1) In most of the Kaharoa units, where obsidian pyroclasts have abundance of <5 wt.% (**Fig. 5.20**), the production of obsidians appeared to have been a constant but limited process. Considering the large evidence of magma shearing and the typically constant population of TP clasts in the investigated units, the formation of obsidians is best explained with bubble collapse and magma densification at the conduit walls (**Fig. 5.19b**) (e.g., Newman et al., 1988; Rust et al., 2004). The unavailability of data on volatile content on the Kaharoa obsidian clasts does not enable however to rule out completely an origin by post-fragmentation sintering of ash, which might had occurred in conjunction with the densification of the magma in zone of high shear and outgassing (Giachetti et al., 2020).

(2) The sharp increase of obsidians in L3 and A7 compared to remainder of the deposits suggest different formation mechanisms of obsidian. Three lines of evidence (*a* to *c*) are reported to propose a different origin.

(a) Textural data. The obsidian sampled from these units are characterised by an identical homogeneous texture, nearly vesicle-free, with the few vesicles present having regular (circular to elliptical) shapes, and no microlites (**Fig. 5.18**). These microtextural features do not match those observed by Gardner et al. (2017) for inferred sintered obsidians (e.g., highly heterogeneous vesicle textures, occurrence of xenoliths, xenocryst bands and distorted vesicles).

(b) Componentry and particle size data. While obsidians in other units are consistently less abundant than lithics, units L3 and A7 are the only intervals in the pyroclastic succession characterised by a higher proportion of obsidian to lithic fragments (obsidian: lithic ratio >1) (**Fig. 5.20**). Obsidian clasts in units L3 and A7 have further overall larger sizes (up to few cm) compared to those of other units (up to few mm) (**Chapter 3**). These results suggest that a wider source region of dense magma from which the obsidian originated was available in the conduit, not only limited to the conduit walls, and was subsequently excavated/fragmented during eruption.

(c) Stratigraphy data. Stratigraphic reconstruction and deposit features indicate that the Kaharoa eruption was episodic, characterised by short pauses in the explosive activity and pyroclast sedimentation in-between each lapilli-bearing unit (**Chapter 3**). Field evidence for erosion is found at the basal contacts of both unit L3 and unit A7 deposits suggesting time breaks of up to a week(s) before deposition of these units. This further suggests that time was available for the magma to slowly ascend and/or stalled and to outgas in the conduit prior to the next explosive episode.

Taken together, the textural, componentry and stratigraphy data suggest that the increase in obsidian content can be linked to the formation of dense, outgassed magma bodies in the shallow conduit prior to both the L3 and A7 explosive episodes. This outgassed magma was either the result of the intrusion of dikes which stalled in the shallow conduit system (e.g., Rust and

Cashman, 2007) or the result of the formation of more laterally confined outgassed plugs (e.g., Rust and Cashman, 2007; Davi' et al., 2011). In both cases, the dense magma obstructing the conduit-vent system was subsequently disrupted in the following explosive episodes and the obsidian plug material was incorporated in the ejected gas-pyroclast mixture and deposited within units L3 and A7. The formation of these two obsidian plugs signal events during which the ascending magma in the conduit underwent to a substantial permeable outgassing. In turn, these events might represent the initiation of an explosive-to-effusive transition period within the explosive-dominated sequence (Phase A to D) of the eruption (e.g., Giachetti et al., 2020). The transition was however "aborted" by the following explosive episodes (L3 and later A7). A complete shift to an effusive-dominated regime was established only later in the eruption during the extrusion of the Kaharoa lava domes (Phase E and F).

Finally, in addition to the formation of conduit-vent plugs as a source for obsidian pyroclasts, a further process might have contributed to the increase in obsidian fragments at least in unit A7. Within the A7 deposits, the increase in obsidian is also accompanied by an increase in the relative proportion of TP clasts respect to other units (**Fig. 5.20**). This suggest that shearing of the ascending magma was enhanced during the A7 event, possibly resulting in a larger portion of obsidian material produced by the high shear rates at the conduit walls, as suggested in point (1).

5.5.3 Implications for conduit geometry

During the Kaharoa eruption, both explosive and effusive activity occurred from multiple vents aligned along the SW-NE Tarawera vent lineament (**Chapter 3** and reference therein). The alignment of vents provides indirect information on the architecture of the shallow feeding system active during the eruption. This vent configuration suggests that each vent might be the topographic representation of a dike-like conduit as opposed to a central, cylindrical conduit system (e.g., Nairn et al., 2005; Houghton et al., 2010). Insights into the conduit geometry can also be gained from the pumice microtextural features and componentry observations acquired throughout this study.

Both Polacci et al. (2003) and Rust and Cashman (2007) proposed that that the production of tube pumice clasts together with obsidians might be favoured in conditions in which exist and a high ratio of conduit surface area to conduit volume (i.e., high ratio of conduit walls to conduit width). These conditions are common for magma rising through a dike-like conduit, where a larger conduit surface area is available, along which shear processes are enhanced (e.g., Pistolesi et al., 2015; Kavanagh, 2018). Moreover, the conduit radius alone is an important factor in increasing the total strain yielded in the magma and hence in the formation of very elongated, stretched

vesicles. Deformation experiments on bubble-bearing rhyolitic melts (Okumura et al., 2009) and conduit modelling of natural rhyolitic eruptions (Mitchell et al., 2019) showed that, for constant volumetric flow, in narrow conduits, a larger portion of the ascending magma can undergo to high shear rate conditions, thus increasing the amount of tube pumice production upon explosive fragmentation.

Further elements in reconstructing the conduit geometry in rhyolitic eruptions might derived from the density and textural variability of the erupted juvenile materials. Both Pistolesi et al. (2015) and Schipper et al. (2021) inferred that the fissure nature of the 2011–2012 Cordón Caulle eruption was a critical factor in driving diverse and complex magma ascent histories which resulted in the formation of a wide density and textural range of the erupted products observed in the associated deposits.

The extensive evidence for (1) magma shearing during the Kaharoa eruption, with production of tube pumice clasts, (2) juvenile material varying in bulk vesicularity/density from moderately vesicular to non-vesicular, and the (3) surface alignment of vents, strongly suggest magma ascent through a dike-like conduit. This resulted in the superficial Kaharoa vent alignment forming a fissure system.

The eruption occurred however through individual active vents along the dike/fissure rather than continuously along the entire fissure length (e.g., Blake and Fink, 1987; Bursik et al., 2014). This channelisation of the magma within the dike during ascent and eruption can occur in response to viscosity increase at the dike-conduit margins and lateral extremities (Bruce and Huppert, 1989; Wylie et al., 1999; Gonnermann and Taisne, 2015; Pansino et al., 2019) and/or in response to irregular widening along the dike strike during initial magma ascent (Acocella, 2021).

5.5.4 Evaluating the role of conduit processes for deposit pattern and eruptive styles

The data presented in this study suggest that the critical processes governing magma dynamics during ascent in the conduit were magma shearing, bubble coalescence and partial outgassing and their interplay. The similarity in vesicle data quantified among different pyroclastic units, further suggest that these main processes were predominant throughout the entire main explosive eruption sequence (Phase A to D) and not confined in specific time-intervals of the eruption. The textural data acquired in this work need to be linked back to the field characteristics and stratigraphy of the Kaharoa deposit (**Chapter 3**) to build a more comprehensive understanding of the inferred changes in eruptive styles.

The deposit characteristics of fall lapilli units vary repeatedly in the succession (within Phases A, B and D) passing from overall massive deposits with limited grain size changes, to stratified deposits characterised by sharp grain size fluctuations. Occasionally, stratified fall lapilli units have interbedded small-volume, poorly sorted PDC beds in more proximal sites (e.g., L6). All these characteristics indicate that deposition of lapilli units changed from more stable sustained columns to continuously oscillating sustained columns. These differences in deposit features are however not equally represented by significant changes in the textures of the erupted pumice clasts (cf. Pardo et al., 2014). Furthermore, the shift from fall lapilli to the lapilli-bearing PDC deposits (Phase B to Phase C), is not accompanied by large variations in vesicle features (e.g., Adams et al., 2006; Carey et al., 2009).

These observations suggest that the changes in the deposit features of lapilli units (between fall units and between fall versus PDC units) might derive from a combination of internal (magmatic) and external (environmental) factors which influenced the transport-depositional patterns and the changes in eruptive styles. These factors did not leave a significant imprint in the microtextures of the erupted pumice clasts which recorded instead the main processes of magma ascent and degassing/outgassing discussed above. Here some of these additional internal and external factors are discussed.

Variation between massive and stratified fall lapilli deposits – The mechanical stability of the conduit-vent system is a chief external factor in controlling the stable versus oscillatory behaviours of rhyolitic explosive eruptions (Aravena et al., 2017). Numerical models by Aravena et al. (2018) suggested that pulsatory explosive events are typically associated with narrow and unstable conduits where wall collapses, and blockages of the conduit-vent can occur, influencing eruption dynamics. This can be observed by the changes in the relative abundance of lithic in the deposit (see Adams et al., 2006). Continuous fluctuations in the proportion of lithic clasts are evident in the Kaharoa pyroclastic succession (**Fig. 5.20**) suggesting repeated episodes of conduit instabilities (**Chapter 3**). This has two important outcomes. On one hand the unstable conduit-vent system could have promoted unsteady magma discharge during an eruptive episode (e.g., Bursik 1993; Cioni et al., 2011). On the other hand, the increase in the production of lithics at fragmentation could have influenced the eruptive column dynamics itself as lithic clasts add mass, but little thermal energy needed to promote and sustain stable column convection conditions (see Mele et al., 2011; Houghton and Carey, 2015). These external factors can explain the production at different times during the eruption of more stable and oscillating columns (**Fig. 5.21**) and the associated deposition of massive (lithic-poor) and stratified (lithic-rich) fall lapilli units (**Fig. 5.20**). In addition, partial column collapses suspected in unit L6 might have been further caused by the fragmentation and incorporation in the exiting eruptive mixtures of a greater proportion of denser pumice clasts (e.g., Shea et al., 2011). This is suggested by the wider L6 pumice density

distribution characterised by a pronounced high-density tail, not observed in other fall lapilli units (**Fig. 5.4**), as well as by the increase in dense juvenile clasts observed in this unit (**Fig. 5.20**).

Shift between fall and PDC lapilli-bearing deposits – Variations in the amount of pumice clast types and obsidians provide some constraints on the changes in eruptive styles and transport-deposition passing from the subplinian fall episodes depositing the L units to the PDC episode emplacing unit A7 (**Fig. 5.20**). Unit A7 is characterised by an increased proportion of TP clasts compare to the lapilli fall units in the succession (**Fig. 5.20**). This increase in TP clasts can be associated to a narrowing of the conduit, where a higher portion of the ascending magma is subjected to high shear rates (e.g., Taddeucci and Wohletz, 2001; Okumura et al., 2009; Mitchell et al., 2019). The decreased conduit width could have further impacted magma ascent and discharge rates compared to those attained during the fall lapilli episodes. In addition, the larger proportion of obsidians in unit A7 resulting from the disruption of the conduit-vent plug (**Section 5.5.2**) further signal an enlargement of the vent area, with the ascending and erupting magma effectively excavating the plug and incorporating a larger portion of obsidian fragments (**Fig. 5.21**) (e.g., Carey et al., 2009). Widening of the vent can result in slower exit velocities, limiting conditions for buoyancy of the ejected gas-pyroclast mixture (Shea et al., 2011). The slower exit velocity favoured instead condition for boiling-over behaviour (continuous collapse of the eruptive mixture at vent; **Chapter 3**) and deposition of PDCs beds as opposed to the formation of buoyant plumes and fallout sedimentation (Clarke et al., 2002; Sulpizio et al., 2014). Finally, similarly to what suggested for partial column collapses of the L6-column, the incorporation of a larger proportion of denser juvenile material in the eruptive mixture (obsidians in this case) might have also contribute to the establishment of continuous collapse conditions at vent (e.g., Shea et al., 2012).

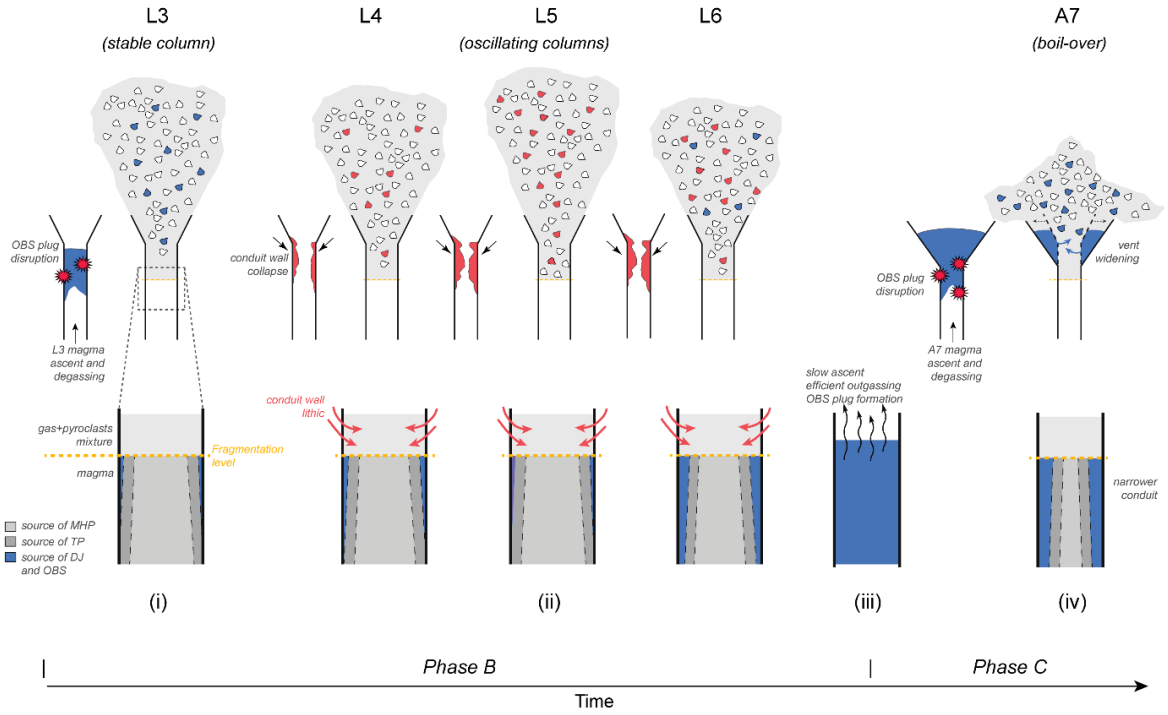

Figure 5.21 – Schematic model illustrating the main changes through time in shallow conduit dynamics and eruption styles with examples for Phases B to C. Development of a laterally stratified magma approaching fragmentation follows Fig. 5.19, with *light grey* indicating the source area of later microvesicular heterogeneous pumice clasts (*MHP*), *dark grey* indicating the source area of tube pumice clasts (*TP*), and *blue* indicating the source area of dense and outgassed magma forming dense juvenile clasts (*DS*) and obsidian plug/clasts (*OBS*). The fragmentation level is kept at the same depth for visualisation purposes; however, it is noted that the depth of the fragmentation zone likely varied during the eruption sequence (e.g., deepening of the fragmentation depth is expected during L4, L5 and L6 episodes). (i) onset of Phase B is characterised by the disruption of a previously formed obsidian plug obstructing the conduit-vent system, with obsidian clasts being incorporated in the L3 column. Efficient clearing of the conduit ensures steady mass discharge rate and stable column leading to deposition of massive lapilli fall deposits. (ii) Conduit-vent instabilities result in repeated wall collapses an incorporation of a higher proportion of lithic clasts in the L4, L5 and L6 plumes, favouring a shift from stable to oscillating eruptive columns and deposition of stratified lapilli fall deposits. Continued partial outgassing during Phase B leads to magma densification at the conduit walls and production of denser juvenile clasts at fragmentation which further impacted the L6 column stability. (iii) The protracted and efficient magma outgassing, and slower ascent rates culminate with the formation of a second obsidian plug, resulting in a pause in the eruption between phases B and C. (iv) Phase C starts with the disruption of the second obsidian plug by the ascending and degassing A7 magma within narrower conduit, leading to an elevated production of TP clasts upon fragmentation. Widening of the vent during eruption favours slower exit velocity of the gas-pyroclast mixture and incorporation of a larger proportion of obsidian clasts. These processes triggered the shift from buoyant plume to boiling-over conditions and production of PDCs.

5.6 Conclusions

The work presented in this chapter offers a first detailed characterisation of the complex vesicle textures of pumice clasts erupted during the explosive phases of the ~1314 CE Kaharoa eruption. Bulk densities and observations of the pumice surface and microscopic textures were coupled with quantitative 2D analysis of vesicle size and shape. This dataset was collected for different lapilli-bearing units along the reconstructed stratigraphy (**Chapter 3**) and provides constraints on the dynamics of magma ascent and degassing within the conduit during the eruption sequence. These observations were coupled to the variation in abundance of obsidian clasts within the pyroclastic succession to provide insights into obsidian formation mechanisms and their implications for conduit dynamics. Furthermore, the textural data were correlated to the deposit structure and componentry characteristics of the investigated units, providing a more comprehensive understanding of the multiple factors controlling changes in eruptive and depositional styles. From the presented study some important outcomes can be drawn:

1) Two main texturally different pumice clast types (MHP and TP clats) have been continuously produced during the explosive phases of the Kaharoa eruption, with relatively uniform ratios within the unit analysed. The two pumice types reflect contrasting vesicle textures at the submillimetre scale characterised by (i) a heterogeneous network of tube and convoluted vesicles coexisting with subspherical vesicles (type 1) and by (ii) a pervasive network of tube vesicles (type 2 and 3). No major variations are observed between units in terms of vesicle features (size, shape and number density), while the most significant differences are observed between pumice and vesicle texture types.

2) The textural variability of pumice clasts is interpreted to result from the fragmentation of a horizontally stratified magma column within the conduit which was subjected to laterally variable ascent rates, promoting simple shear and bubble deformation. Additional syn-ascent and post-fragmentation processes are inferred in controlling the formation of complex microtextural features (convoluted vesicles and coexistence of large domains of deformed and undeformed vesicles) observed within samples of MHP clasts.

3) The Kaharoa pumice microtextures are characterised by highly stretched vesicles, extensive evidence of bubble interaction and bubble interconnectivity. Along with the overall high average bulk densities (modes at 900-1200 kg/m^3) of measured pumice clasts, these features indicates that the main factor controlling the dynamic of magma ascent in the conduit was the interplay between (i) magma shearing, (ii) bubble coalescence and (iii) degree of outgassing. The similarities of quantitative vesicle data obtained for different units in the stratigraphy

indicate that these three main processes did not change significantly during the explosive phases of the eruption.

4) Two main mechanisms for the formation of obsidian pyroclasts were inferred. In most of the lapilli units in the pyroclastic succession, where obsidians abundances are typically <5 wt.%, formation of obsidians was limited to the conduit walls and occurred in response to bubble collapse and densification of the magma due to the high shear rate in this region of the conduit. In the obsidian-rich units, obsidians originated from the formation and subsequent disruption of outgassed magma bodies stalling and obstructing the conduit-vent prior to both the L3 and A7 explosive episodes.

5) The combination of textural and density data of pumice and obsidian clasts provided insights into the efficiency of outgassing during the eruption. While magma shearing facilitated and enhanced bubble coalescence and permeability developments, allowing partial outgassing and magma densification to occur, the exsolved gas could not efficiently decouple from the magma column, leading to brittle magma fragmentation during the numerous explosive events. On the other hand, the magma preceding the L3 and A7 events underwent to substantial and efficient outgassing. These two episodes of magma ascent in the conduit might represent incipient and aborted shift from an explosive- to an effusive-dominated regime, before the main dome-building phase of the Kaharoa eruption.

6) The data acquired during this investigation (e.g., extent of shear-derived microtextures and frequency of TP clasts) together with the evidence for vent surface alignments, suggests that the magma rose through a dike-like conduit system as opposed to a central, cylindrical conduit.

7) This study showed that there is a limited correlation between the different deposit features of the lapilli units observed in the field and the microtextural characteristics of the analysed pumice clasts. Other internal and external factors have been postulated in controlling the changing in the deposit characteristics and eruptive styles, such as: (i) a mechanically unstable conduit-vent system; (ii) the excavation/formation and assimilation of a different proportion of denser clasts (lithic, obsidian, denser pumice) in the eruptive mixture exiting the vent

[This page intentionally left blank]

Chapter 6

Synthesis: an integrated view of intra-caldera, dike-fed, rhyolitic eruptions

6.1 A model for the ascent and degassing dynamics of the Kaharoa magma in the conduit

The integration of the results arising from this research provides new insights into the dynamics of the ascending magma in the conduit during the Kaharoa eruption. A general model is proposed to explain the variations in magma ascent/degassing conditions with respect to the eruption sequence and its different eruptive activity.

6.1.1 The dike nature of the shallow Kaharoa feeding system

The main processes influencing the temporal and spatial evolution of the magma in the conduit are magma shearing, bubble coalescence and partial outgassing (**Chapter 5**). These processes provide bounding conditions for magma rheology and ascent. Shear deformation of silicic magmas in volcanic conduits are enhanced for conduit geometries with a high ratio of surface area to volume (Polacci et al., 2003; Rust and Cashman, 2007; Mitchell et al., 2019). Given the highly stretched vesicle textures of pumice clasts, together with the distribution of individual vents defining a fissure, a dike-shaped conduit as opposed to a cylindrical conduit is inferred to best represent the volcanic conduit architecture beneath Tarawera. This dike conduit system likely formed by the favourable volcano-tectonic settings in which the Tarawera dome complex is located.

The Kaharoa eruption vents are aligned defining a fissure consistent with the orientation of the main active fault trend of the Taupō Rift, indicating a strong control of the Tarawera feeding system related to structures at depths (e.g., pre-existing fractures/weakness facilitating fluid/magma ascent) (Nairn, 2002; Nairn et al., 2005; Seebeck and Nicol, 2009; Villamor et al., 2011; Holden et al., 2015). Furthermore, the diffuse hydrothermal activity associated with Tarawera (Hughes et al., 2019) and adjacent areas along the lineament (de Ronde et al., 2016) might have contributed to the alteration of the subsurface rocks (e.g., Pittarti et al., 2016) forming zone of weakness facilitating dike propagation at shallow depths (e.g., Rivalta et al., 2015).

This geometry of the conduit had a primary control in magma ascent dynamics by providing larger conduit surface area to assist and enhance shear stress and strain of the bubble-bearing melt. This promoted extensive bubble deformation, stretching of bubbles, development of connected networks of bubbles and, ultimately, outgassing (Okumura et al., 2009; 2013; Shea et al., 2012; Mitchell et al., 2019). These physical conditions and conduit geometry also promoted the simultaneous formation of texturally different pumice clasts (MHP and TP) during the eruption, explained by the cross-conduit gradients in magma ascent velocity and shear rate. This spatially

different vesiculation and deformation conditions of the bubble-bearing melt in the conduit is similar to other conceptual models proposed for taking into account the formation of tube pumice clasts (e.g., Polacci et al., 2001; 2003; Rosi et al., 2004; Bouvet de Maisonneuve et al., 2009; Dingwell et al., 2016; Mitchell et al., 2019), or pyroclasts with shear-derived textures (e.g., Shea et al., 2012; Pardo et al., 2014; Heinrich et al., 2020). The difference here is that while these models have been applied to magmas rising into broadly cylindrical conduits, here are applied to narrower and laterally extended dike conduit system which is the most likely feeding system for the Kaharoa and other Tarawera eruptions (see also **Chapter 2** and reference therein). The gradients in magma ascent laterally across the conduit are consequently expected to be accentuated in dikes (e.g., Blake and Fink, 1987; Castro et al., 2013; Kavanagh, 2018). Hence, a larger portion of the magma in the conduit is exposed to high shear rates (e.g., Mitchell et al., 2019). This in turn resulted in the observed copious production of pumice with elongated, deformed vesicles during the eruption and the virtual absence of typical "spherical pumices" with undeformed vesicle textures in the collected sample suites (e.g., **Sections 5.4.1** and **5.4.3** in **Chapter 5**).

6.1.2 Magma dynamics during the subplinian explosive episodes

Both bulk density and vesicle textural data of pumice clasts in lapilli-bearing deposits show similarities throughout the pyroclastic sequence (**Chapter 5**). These similarities suggest that the magma feeding the major explosive episodes of the eruption (e.g., L units and unit A7) underwent comparable evolution in the conduit.

Although permeable volatile escape occurred during magma ascent as evidenced by the interconnected network of deformed vesicles and by the overall high bulk density of the pumice clasts (1100 kg/m^3 on average), magma outgassing did not occur efficiently enough to reduce gas overpressure and prevent explosive fragmentation (e.g., Mueller et al., 2008). As discussed also in Shea et al. (2012) and Castro et al. (2013), the outgassing efficiency is determined by the balance between the rate of magma decompression (i.e., how fast the magma rise to the surface) and the rate of permeable volatiles outflow from the rising magma in the conduit (i.e., how fast the exsolved gas escape from the system).

At the timescales of the considered major explosive episodes, magma ascent occurred slow enough for partial outgassing to take place, but too fast for the magma to reach critical thresholds of efficient gas-melt decoupling before fragmentation. It can then be suggested that: (i) the effect of outgassing (though partial) reducing gas bubble overpressures (Mueller et al., 2008; Okumura et al., 2009) and the (ii) narrow dike-like conduit geometry limiting stable and continuous

conditions for very high magma discharge rate (Melnik et al., 2005; Costa et al., 2009; Aravena et al., 2018) did not allow the rising magmas to attain very fast ascent rates. This precludes/reduces the ability of the eruption to reach very high eruptive intensity (i.e., high-intensity Plinian to ignimbrite styles; e.g., Houghton et al., 2010; Costa et al., 2011; Myers et al., 2016).

Lastly, it is noteworthy to emphasise here the important and dual role of shear stress, and resulting formation of aligned, stretched bubbles in the ascending rhyolitic magmas, for conduit flow dynamics during the subplinian episodes. On one hand bubble deformation can enhance bubble coalescence and outgassing (Okumura et al., 2006; 2008; 2010; 2013; Wright et al., 2006, 2009; Degruyter et al., 2010; Caricchi et al., 2011; Pistone et al., 2012). On the other hand, high strain rate and consequent bubble deformation can reduce magma viscosity by the combined effects of viscous dissipation (Polacci et al., 2001; Rust and Manga, 2002; Mastin, 2005) and by providing free-slip surfaces for the magma to flow (Llewellin and Manga, 2005; Mader et al., 2013). These last effects contributed to the relative rapid rise (within subplinian range) and explosive fragmentation of the otherwise slow-ascending, rhyolitic magmas during the explosive phases of the Kaharoa eruption (e.g., Rosi et al., 2004).

6.1.3 Temporal variations and cyclicity in magma conduit dynamics

Cyclic patterns in deposit features and inferred eruptive intensity can be observed in the Kaharoa eruption sequence (**Chapter 3**). The major explosive phases of the eruption (Phase A to D) periodically concluded with a decline in eruptive intensity, recorded by the decrease in grain size (e.g., Phase A and D; **Section 3.5** and **3.7.5**) and/or concluded with the inferred emplacement of outgassed obsidian plugs in the shallow conduit (e.g., Phase A and B, **Section 5.5.2**), before the start of the next phase. This type of eruptive behaviour continued until the final transition to the dome-building phases (Phase E and F) of the eruption and suggests cyclical patterns in magma degassing/outgassing in the conduit.

Based on the combination of stratigraphic, componentry and textural data, it can be proposed that the protracted partial outgassing of the magma during each explosive phase resulted in a cyclical increase in magma density/viscosity which favoured conditions for slower magma ascent as the eruption progressed (e.g., Vona et al., 2020). This resulted in a lower magma discharge rate, diminishing the overall eruption intensity at the end of a phase (e.g., units A3, L6; L9 in Phases A, B and D, respectively). In addition, in the case of Phases A and B, the final slower magma ascent was such to prompt, as feedback effect, higher levels of gas loss and magma densification which culminated in the stalling of the magma in the shallow conduit and formation of outgassed

plugs. Finally, it is here noted that cyclical waxing and waning of the eruption possibly also occurred at the scale of individual eruptive episodes as suggested by the increase in denser pumice clasts in unit L4 compared to the preceding unit L3.

6.1.4 Obsidian plug formation: aborted transition to effusive activity

The two events of obsidian plug formation in the conduit might represent aborted incipient transitions to an effusive activity (**Chapter 5**). The incipient explosive-to-effusive shift was interrupted by the intrusion of new, gas-rich magmas from the storage region into the conduit system. The degassing of these new ascending magma parcels caused over time gas accumulation beneath the dense, stagnant magma plugs in the conduit. This in turn lead to pressure build-up, ultimately triggering plugs disruption and the start of the following explosive phase (e.g., Platz et al., 2007; Burgisser et al., 2011).

The identified obsidian-rich units (L3 and A7), with obsidian clasts resulting from the disruption of the plugs, are stratigraphically emplaced above erosive surfaces indicative of short eruption time breaks before the start of a new phase. Time is required for the formation of dense obsidian materials through efficient permeable outgassing and foam collapse of the magma in the conduit (Eichelberger et al., 1986; Rust and Cashman, 2004; Giachetti et al., 2020). Although timescales for outgassing and foam collapse/densification are difficult to quantify as the thickness of these dense bodies is unknown along with uncertainties in other variables (e.g., viscosity and permeability of the foam) (e.g., Kennedy et al., 2016), experiments on rhyolitic melts suggests variable duration for this process from >10 to 10^4 hours (Martel and Iacono-Marziano, 2015), which are in overall agreement with the time break duration inferred from the deposit. The formation of these plugs is therefore inferred to have occurred during the end of the preceding phase and/or during the pauses in the eruptive activity between phases (e.g., Rust et al., 2004). The microlite-free textures observed within the analysed obsidian samples is not considered here in contradiction with the expected longer residence time of the magma in the conduit (cf. Hammer et al., 1999). The high viscosity of the melts might have hampered or limited syn-ascent crystallization (Davì et al., 2011; Bain et al., 2019).

Finally, since juvenile obsidian pyroclasts are common products in deposits from rhyolitic eruptions, it is here emphasized that the understanding of their formation mechanisms (Rust and Cashman, 2007; Gardner et al., 2017; Giachetti et al., 2020), together with field evidence, may be used as a proxy to infer breaks in the eruption continuity.

6.1.5 Transition to the final dome-building phase

The transition from explosive activity to lava dome extrusion occurred only after the major explosive phases had ceased. This type of eruptive sequence is one of the most common scenarios expected for moderate- to large-scale explosive (VEI≥4) to dome-forming silicic eruptions worldwide (Ogburn et al., 2015). Although this research was centred on the analysis of the explosive activity and their deposits, factors governing the final transition to the dome-building phase can be suggested and reconciled with proposed models for magma conduit dynamics.

Based on the available data, the explosive to effusive transition might have been facilitated by an increase in volume of the phenocrysts carried by the ascending magmas feeding the dome growth. There is a clear difference between the crystallinity of the pyroclastic products (both pumice and obsidian), at ~10 vol. % DRE (**Chapter 5**), and the crystallinity of the dome materials, at 40-65 vol.% DRE (data from lava samples of Ruawahia dome of Ashwell et al., 2015, 2018). This elevated phenocryst content might have had a significant impact on magma rheology (Costa, 2005; Caricchi et al., 2007; Moitra and Gonnermann, 2015; Kilgour et al., 2016), causing a significant decrease in magma ascent velocities, preventing explosive fragmentation (e.g., Bernard and Bouvet de Maisonneuve, 2020).

The high crystal content was probably a concurrent factor among the many others that have been inferred in driving explosive-effusive transitions (e.g., changes during eruption in pre-ascent magma properties and volatile content, degassing regime in conduit and variation in conduit geometry) (Cassidy et al., 2018 and references therein). Other factors that might have triggered the transition are the rise of the magmas from initially deeper storage regions (Okumura et al., 2009) or through inclined pathways (Castro et al., 2013), both resulting in longer transit time of the magma in the conduit, allowing open-system degassing to prevail. These insights into explosive-to-effusive transition triggers need to be expanded in future studies to incorporate newly developed conceptual model for silicic conduits at shallow levels (Schipper et al., 2021).

6.2 Controlling factors on eruption dynamics

6.2.1 Variation in eruptive style

Overall, the major changes in eruptive activity passing from higher-intensity, subplinian-style episodes to episodes of lower-intensity ash emission and to lava dome extrusion were largely

controlled by the syn-ascent evolution of the magma volatile content, outgassing efficiency and magma rheology. This has been proposed in other studies of moderate- to large-scale silicic eruptions either fed by magmas with relatively uniform geochemical compositions (e.g., Carey et al., 2009; Houghton et al., 2010; Alfano et al., 2012; Di Piazza et al., 2019) or fed by magmas with different compositions (Adams et al., 2006; Shea et al., 2012; Vona et al., 2020). Furthermore, by coupling the temporal variation in deposit features (e.g., componentry and grain size; **Chapter 3**) with density and textural data of juveniles (**Chapter 5**) this research suggests that multiple additional factors, both magmatic and environmental, where crucial to determine the changes in eruptive styles. These are further detailed in the eruption model proposed in **Section 6.3**, while a summary is given in the following.

The cyclical pattern in magma ascent and degassing/outgassing (magmatic "internal" factors) regulated:

(i) The variation in eruptive intensity towards the end of major explosive phases (e.g., units A3, L6; L9; Phases A, B and D).
(ii) The incipient aborted transition to lava extrusions (e.g., obsidian plug formation; end Phases A and B).

Environmental "external" factors such as the mechanical (in)stability and modifications of the conduit-vent system were equally important and acted in concert with the magmatic "internal" factors. These dynamic magma-conduit interactions played an important role in:

(i) The fluctuations in magma discharge during the subplinian episodes resulting in the stable versus oscillating eruptive column behaviours (e.g., the L units), due to conduit-vent instabilities and wall collapses.
(ii) The partial column collapses dynamic due to the combined effects of syn-eruptive magma densification and conduit-vent system instabilities (e.g., L6).
(iii) The shift between a fall-dominated to PDC-dominated activity, due to initially narrower dike conduit width and possible enlargement of the vent area (e.g., unit A7).
(iv) The initial low magma discharge rates at the onset of the eruption due to a poorly developed conduit system (e.g., unit A1).

In addition, the suspected explosive magma-water interactions during A8 might have been triggered by an initial slower magma ascent and by changes in vent position with the rising magma intersecting external available water.

6.2.2 Episodic behaviour of the eruption

Of great interest for both the dynamics of rhyolitic eruptions and the emergency planning/response of future volcanic eruption crises is also the episodic nature of the Kaharoa eruption. The eruption during the explosive sequence underwent repeated pauses in magma discharge, which resulted in an episodic eruption behaviour.

The causes of episodic (or pulsatory) eruption behaviour (i.e., characterised by repeated eruptive episodes or pulses separated by short time breaks) are difficult to constrain since they likely involve the combination of multiple factors across a wide range of depths and timescales, from the magma storage region at mid to shallow crustal depths to the conduit-vent system (see Petrelli and Zellmer, 2020). Hence, processes varying from syn-eruptive changes in the storage region to the variation of the magma properties during ascent in the conduit could determine pulsatory eruption behaviours (Cioni et al., 2011; Cashman and Sparks, 2013).

The pulsatory discharge of magma in discrete eruptive episodes during silicic subplinian eruptions has been credited in a number of studies (e.g., Bursik, 1993; Cioni et al., 2003; Sulpizio et al., 2005; Miyaji et al., 2011) to the imbalance between the *magma supply rate* from storage region to conduit, and the *magma discharge rate* from conduit to surface (Scandone and Malone 1985). This decoupling between magma supply and magma discharge has been theorised to depend on a poorly developed (unconnected) "transport" system (i.e., conduit system) favouring the intermittent intrusion and eruption of individual magma parcels (Scandone et al., 2007). A similar conceptual model could be considered for the Kaharoa eruption, in which the episodic injections of dikes into the conduit system fed individual eruptive episodes. This is further similar to what has been suggested by Mele et al. (2011) for pulsatory Plinian-type eruptions at Somma-Vesuvius. However, even considering this theoretical model, uncertainties remain on the exact causes triggering intermittent magma injections/eruption. Here two views are considered.

(1) Magma degassing and conduit geometry controls on episodic behaviour

The results from componentry and microtextural analyses presented in this research strongly suggests that both magma degassing/outgassing patterns and conduit dike geometries were primary factors in controlling the eruptive styles changes. These factors might have been critical also in modulating the episodic eruption behaviour. By combining the data presented in this study (e.g., variations of lithics abundance in the deposits and juvenile textures) with current numerical models for silicic dike conduits (e.g., Costa et al., 2009; Massaro et al., 2018) it is possible to reconstruct the following conceptual model.

The syn-eruptive exsolution and outgassing of volatiles from the rising magma in the dike conduit during each explosive episode might have contributed to temporarily reducing the overpressure at the top of the magma chamber driving the eruption. This temporary lowering of pressure might have resulted in a discontinuous magma supply into the feeder dike. This in turn caused the closure of the dike from its base and the temporary shutdown of the eruption (end of an episode) (Massaro et al., 2018). This is also consistent with experimental observations on dike propagation in Kavanagh et al. (2018) which show contraction and closure of the dike's tail when the dike reaches the surface. Once a sufficient overpressure is re-established in the storage region, new magma could enter the conduit system and the eruption restart with a new episode. This process likely continued throughout a phase until the stagnation of the magma in the upper conduit. Further modelling by Costa et al. (2009) of magma flow into narrow dikes for explosive silicic eruptions suggests that dike conduits are likely to be very unstable and prone to rapidly close/collapse. This is due to the local (intra-conduit) lower pressure of the magma at the fragmentation depth with respect to the surrounding lithostatic pressure. The continuous conduit-vent instabilities, inferred by the data here presented on wax and wane of lithic clasts in the deposit (**Chapter 3**), might have prevented to maintain a sustained magma discharge for long period of time, causing eruptions to stop and restart.

The usually longer time breaks inferred between eruptive phases compared to those between individual eruptive episodes can be ascribed to: (i) longer time caused by the formation of dense plugs in the upper conduit and subsequent time for pressure to accumulate below the plug until critical values are reached; (ii) a reduced connection of the fractures network in the conduit system due to previous dike closures, hence prolonged time to re-establish connection from storage to vent area; (iii) dike propagation into new zones laterally along the fissure.

(2) Very shallow controls on episodic behaviour by sintering and conduit-vent occlusion

Another possible explanation for the episodic explosive eruption sequence can be suggested by considering a new conceptual model for the very shallow dynamic of rhyolitic conduits developed for the recent Cordón Caulle eruption by Schipper et al. (2021).

Numerous studies have recently emphasised the role of tuffisite veins and viscous sintering of pyroclasts in sealed upper conduits for permeability control and magma outgassing (e.g., Kendrick et al., 2016; Saubin et al., 2016; 2019; Kolzenburg et al., 2019; Heap et al., 2019; Wadsworth et al., 2020). Tuffisite veins consist of small (usually cm-sized) fractures forming in active conduits or lava domes, subsequently filled by variably sintered, ash-size fragmented particles (Tuffen et al., 2003; Castro et al., 2012a; Berlo et al., 2013; Kendrick et al., 2016). Tuffisites have been inferred to act as transient outlets for the vertical escape of gas from magma

at deeper conduit levels, facilitating outgassing and overpressure release (Saubin et al., 2016; Kolzenburg et al., 2019). However, their formation mechanism (fractures opening and clogging by infiltration and sintering of ash) implicates a cyclicity in permeability increases and reductions of the upper conduit (Heap et al., 2019). As a feedback effect, the hampered gas outflow by sintering-driven sealing leads to pressure accumulation until triggering of new explosive outbursts. This process can result in the ejection of tuffisite-hosting volcanic bombs as has been observed for the 2008–2009 Chaitén and the 2011–2012 Cordón Caulle eruptions (Castro et al., 2012a; Saubin et al., 2016; Paisley et al., 2019).

The concepts developed around tuffisite veins and viscous sintering have been extrapolated to a much larger scale by Schipper et al. (2021). The authors, by finding evidence of sintering in texturally composite volcanic bombs at the explosive-effusive transition of the 2011–2012 Cordón Caulle eruption have proposed that rhyolitic conduit act as supersized tuffisites. Their model suggests that magma fragmentation events occurring in the shallow conduit does not result in the complete ejection to the surface of the fragmented pyroclastic material (e.g., Wadsworth et al., 2020) feeding the concurrent eruptive plumes. Instead, the hot and un-expelled pyroclasts of very fine ash in size form a granular suspension in the upper conduit which rapidly undergoes to viscous sintering. This process progressively reduces the upper conduit diameter until conduit-vent occlusion which, in due course, "extinguished explosivity" (Schipper et al., 2021).

Although this model has been proposed to describe the dynamic state of the 2011–2012 Cordón Caulle fissure-conduit at the explosive-effusive transition, it might be of relevance for the interpreted episodic behaviour of the Kaharoa eruption. The shutting down of each subplinian episode might have been aided by the gradual accumulation and sintering of the un-expelled fragmented clasts in the upper conduit. However, the lack of this type of feature in clasts within the studied deposits does not support the mechanism of sintering as a chief control in eruption dynamics. Similarly, the thin section analyses of pumice and obsidian clasts did not reveal the presence of suspected sinter-derived textural features. The only case for a possible role of partial sintering/welding process were found in the very complex microtextures of some MHP clasts which displayed diverse vesicular domains and deformed vesicles oriented in multiple directions. Their origins were here interpreted to result from the immediate post-fragmentation collision and amalgamation of different magma particles before quenching (e.g., Trafton and Giachetti, 2021; Giachetti et al., 2021).

Finally, although a detailed evaluation of the effective extent of viscous sintering during the Kaharoa eruption is still required (e.g., via sampling of near-vent volcanic bombs at the onset and shutdown of subplinian episodes), the combination of the data presented in this research is more supportive of a magma degassing and conduit geometry control on the eruption intermittency.

6.3 Kaharoa eruption model

The reconstructed eruption sequence and observed temporal changes in deposit types and componentry, together with the patterns in magma conduit dynamics inferred from pumice clasts textures can enable to further provide a more comprehensive eruption model (**Fig. 6.1**).

The eruption started with the sustained emission of ash, forming a low-altitude column and associated ash fallout (unit A1). This was followed by a rapid increase in eruptive intensity, with formation of a subplinian convective column reaching higher altitudes and resulting in the deposition of the fall lapilli unit L1. Componentry data (low abundance of lithic clasts within A1 deposits) suggests that the onset of the eruption was not associated with a major event of conduit enlargement, possibly due to an initially poorly connected conduit system (from storage to vent) favouring low mass discharge rate. Conduit erosion and enlargement through excavation of the dike host rock occurred during the production of the L1-column as suggested by the increase in lithic content of the deposit. The enlarged and more stable conduit possibly favoured conditions for higher magma discharge rate which led to the deposition of coarser-grained fall beds and the decrease in lithic clasts as eruption progressed (unit L2). Phase A ended with a decline in eruptive intensity characterised by the production of ash columns and a small-volume PDC (unit A3). This final type of activity is possibly linked to a slower magma ascent rate and the simultaneous increase in the outgassing efficiency of the magma in the shallow conduit, which culminated with the formation of a dense magma plug. This obsidian plug obstructed the shallow conduit and was later disrupted at the onset of the next phase of activity (unit L3, onset of Phase B), with obsidian fragments being contained in the fall unit L3.

After a period of quiescence, the eruption resumed with Phase B, which involved a sequence of up to four subplinian-type columns of similar eruptive intensity to L2, resulting in the deposition of the L3 to L6 fall lapilli units. The phase was characterised by the alternation of more stable (L3) to oscillating (L4 and L5) and at times partially collapsing, eruptive columns (L6) as evidenced by the changes in deposit type of the lapilli units (from massive to stratified) and interbedded poorly sorted ash bed of limited distributions. This dynamic was likely influenced by instabilities within the shallow conduit-vent system. Increase in the proportion of lithic clasts in the deposit after L3, suggests possible collapses of the conduit-vent walls and temporary vent blockages. Increase in the proportion of high-density pumice and other dense juvenile clasts evidenced by bulk density and componentry data further indicate an increase in the outgassing efficiency at the end of the phase (L6), suggesting slower magma ascent and syn-eruptive formation of greater proportions of denser magma in the conduit. The concurrent effects of conduit-vent instabilities and the fragmentation and incorporation of denser pumice clasts as well as lithics in the L6 eruptive column might have favoured conditions for partial column collapses.

Phase B culminated with the formation of a second obsidian plug in the upper conduit which likely started to form during the end of the phase (L6) and continued during the inter-phase time break. The plug was later disrupted at the onset of Phase C (unit A7).

Phase C marked a substantial shift in the eruptive activity from the formation of repeated subplinian columns to the production of PDCs (units A7 and A8). These eruption style changes are associated with conduit modification and magma ascent dynamics for the A7 episode, while it can signal vent migration and suspected magma-water interactions in the case of the A8 episode. Phase C started with the emplacement of unit A7 which is the most widespread and voluminous PDC deposit of the eruption, linked to the continuous boiling-over of the erupted gas-pyroclast mixture at vent. This activity resulted from an initial narrower conduit radius compared to previous subplinian fall-dominated episodes, which promoted higher shear rates as suggested by the increase of TP clasts in A7 deposits. The magma in the dike might have also been erupted from an enlarged vent area resulting in slower exit velocities of the erupted mixtures and the incorporation of a larger portion of dense obsidian fragments from the previous plug. Following a short time break and a vent shift, the eruption continued with weak, suspected phreatomagmatic, ash explosions generating PDCs. In this case the controlling factor determining this type of activity might be related to the migration of the vent to lower elevation along the fissure, which possibly favoured interaction of the rising magma with available external water.

Phase D consists in the last major fall-dominated, explosive phase before transition to ash emission and lava extrusions. Phase D signalled the arrival of new, gas-rich magma parcels having a subtle different rhyolitic composition, together with an additional minor rhyodacitic component (Nairn et al., 2004). The return to a subplinian, fall-dominated activity similar to Phase A and B, does not however appear to be linked to the changes in magma composition, as suggested by the observed similarities in microtextural and bulk density data between compositionally different pumice clasts. Modifications at the conduit system, with magma rising initially through larger dikes, possibly exploiting pre-existing factures network and zone of weakness (e.g., Myers et al., 2021), are inferred for the return to a dominant production of buoyant eruptive columns. As the eruption continued, Phase D progressed from relatively stable (L7S and L7N) to oscillating convective columns (L8 and L9) and was characterised by a final waning in eruptive intensity (L9). The passage from initial stable to final oscillating columns is associated to episodes of conduit-vent instabilities and wall collapses as evidenced by the increase in lithic in the deposits during L8 and L9, and to a relatively lower magma discharge rate towards the end of the phase as evidenced by the decrease in grain size of the deposits and increase in dense juvenile clasts.

The last two phases, E and F shifted from low-intensity ash explosions to dome-growth. Phase E marks a significant decline in the eruptive intensity, with activity characterised by the possible

semi-continuous production of low-altitude, sustained ash columns to Vulcanian-type plumes (unit Af) and initiation of dome extrusion (Crater dome). The final phase F is associated with the extrusion of the three main lava domes (Tarawera, Ruawahia and Wahanga domes). The growth of the lava domes was punctuated by partial collapses and generation of BAFs and might have been accompanied by intermittent ash explosions. The transition of the eruption from explosive to dome-building phases might be related, among other factors, to changes in magma viscosity/rheology due to an increase in the number of phenocrysts carried by the magmas feeding the domes.

Figure 6.1 (***figure in following page***) – Schematic representation of the Kaharoa eruption model and magma dynamics in the conduit.
(**a**) Composite stratigraphic log of the Kaharoa pyroclastic succession with lithostratigraphic units and eruptive phases. The log is not to scale; however, it gives indication on the mean deposit gain size (horizontal axis; finer to coarser is left to right). The colour of each unit in the log are coded according to their deposit type with: 1ML = massive lapilli deposit, 2SL = stratified lapilli deposit, 3MCA = massive coarse ash deposit, 4MFA = massive, fine ash deposit, 5ldA = laterally discontinuous, ash deposit, 6LbA lapilli-bearing, ash-supported deposit, 7vcA = variably consolidated ash deposit; BAF indicates deposit from block-and-ash flows.
(**b**) Schematic visualisation of the seven aligned vents (triangles; positions of vents follow Nairn et al., 2001) active (red triangles) during the eruption, with main distribution of the pyroclastic deposits associated to each eruptive phase. Vent numeration follows Figure 3.2 (D=dome; V=vent).
(**c**) Summary of the eruption timeline with style of eruptive activity and main deposition mechanisms of the erupted products. For the sake of simplicity, the black bars are drawn with equal lengths, however the duration of each activity varied (i.e., activity during Phase E and later F was possibly prolonged for months to years). The subplinian activity is further subdivided to incorporate the observed variations in deposits and interpreted processes: *a* indicates stable sustained columns, *b* indicates oscillating sustained columns, *c* indicates partial column collapses from sustained columns and *d* indicates the fine ash settling mainly occurring when the column had ceased.
(**d**) Schematic visualisation of conduit dynamics. (***d1***) and (***d2***) show variation of conduit characteristics and magma at fragmentation with example for Phase A and Phase B, respectively. The fragmentation level (dashed grey line) is kept at the same depth for visualisation purposes; however, it is here noted that the depth of the fragmentation zone likely varied during the eruption sequence. In (***d1***) the evolution of the conduit is shown for the entire Phase A: in A1 (eruption onset) the conduit paths are poorly connected from bottom to surface; in L1 (first subplinian column) erosion and widening of the conduit walls occur with lithic clasts carried by the eruptive column; in L2, the well-developed conduit ensure stable column condition and higher mass discharge rate; in A3 the outgassing and slower magma ascent result in a low-intensity ash activity with initiation of conduit occlusion by formation of dense magma at the conduit walls; the protracted magma outgassing culminates with the formation of an obsidian plug in the conduit-vent. In (***d2***) two examples are represented: in L3, disruption of the obsidian plug by new gas-rich ascending magma leads to onset of Phase B and subplinian activity; in L5 a case is made for conduit-vent instabilities (wall collapses) leading to oscillating subplinian columns (see text for more details). (***d3***) Illustration of magma ascending through a dike-shaped conduit (modified after Gonnermann and Taisne 2015) showing cross-conduit velocity gradient and magma densification at the conduit walls. (***d4***) Illustration of the inferred variable conduit diameter between eruptive episodes depositing the L fall unit and the A7 PDC unit. The colour gradient gives indication of the areas of magma in the conduit from which MHP and TP clasts are produced at fragmentation. The magma TP portion extends to more central area of the conduit as conduit diameter decrease (e.g., Mitchell et al., 2019).

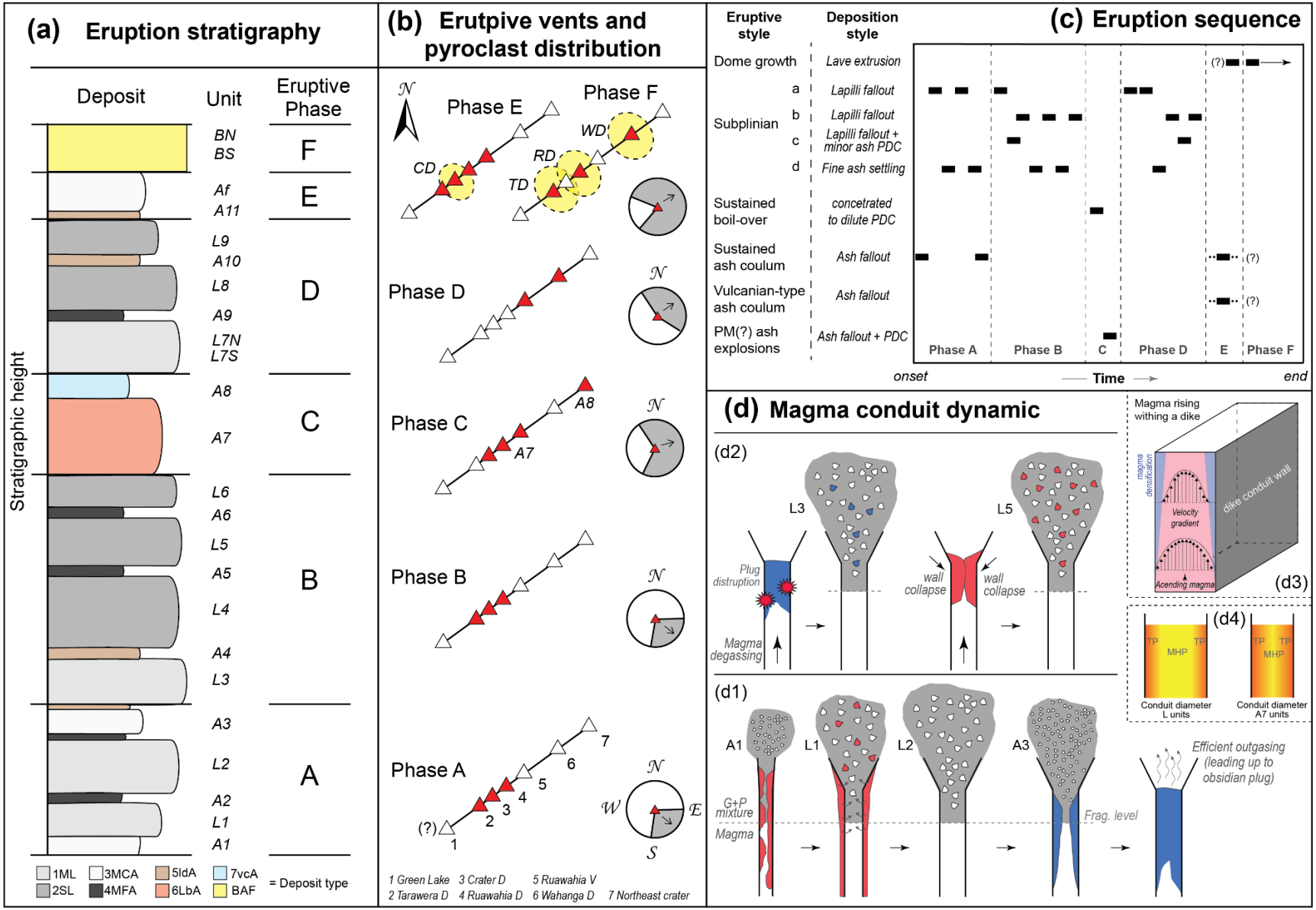
(a) Eruption stratigraphy
Deposit
Unit
Eruptive Phase
Stratigraphic height
BN
BS
F
Af
A11
E
L9
A10
L8
A9
L7N
L7S
D
A8
A7
C
L6
A6
L5
A5
L4
A4
L3
B
A3
L2
A2
L1
A1
A
1ML
2SL
3MCA
4MFA
5ldA
6LbA
7vcA
BAF
= Deposit type
(b) Erutpive vents and pyroclast distribution
Phase E
Phase F
CD
RD
TD
WD
Phase D
Phase C
A8
A7
Phase B
Phase A
1 Green Lake
2 Tarawera D
3 Crater D
4 Ruawahia D
5 Ruawahia V
6 Wahanga D
7 Northeast crater
(c) Eruption sequence
Eruptive style
Deposition style
Dome growth
Lave extrusion
Subplinian
a
Lapilli fallout
b
Lapilli fallout
c
Lapilli fallout + minor ash PDC
d
Fine ash settling
Sustained boil-over
concetrated to dilute PDC
Sustained ash coulum
Ash fallout
Vulcanian-type ash coulum
Ash fallout
PM(?) ash explosions
Ash fallout + PDC
Phase A
Phase B
C
Phase D
E
Phase F
onset
Time
end
(d) Magma conduit dynamic
(d2)
L3
L5
Plug distruption
Magma degassing
wall collapse
wall collapse
(d1)
A1
L1
L2
A3
G+P mixture
Magma
Frag. level
Efficient outgasing (leading up to obsidian plug)
Magma rising withing a dike
magma densification
Velocity gradient
dike conduit wall
Acending magma
(d3)
(d4)
TP
MHP
TP
Conduit diameter L units
Conduit diameter A7 units

6.4 Comparison with similar rhyolitic eruptions

When comparing the Kaharoa eruption to other similar types of moderate- to large- scale rhyolitic eruptions, both locally and globally, some chief characteristics of the studied eruption must be reminded, including: (i) the dike-fed and multiple-vent nature of the eruption, resulting in the alignment of vents and domes at the surface; (ii) the episodic behaviour of the eruption which involved numerous, discrete explosive episodes of sustained magma discharge with each episode producing 0.04 to ~1 km^3 DRE of magma (volume data from Sahetapy-Engel et al., 2014); (iii) the changes in eruptive styles during the explosive phases which alternate between stable to oscillating subplinian eruptive columns, with also episodes of low-intensity ash emission and PDCs emplacement; (iv) the complex magma dynamics in the conduit determining cyclical patterns in outgassing resulting in incipient aborted transitions to lava effusion; (v) A final dome-building phase which involved the extrusion of ~1 km^3 of magma (volume data from Nairn et al., 2001), with dome growth associated with the generation of BAFs.

These eruption characteristics resulted in the formation of a composite succession of pyroclastic beds in proximal to medial sites, with variable sedimentary features and grain size. Transport of pyroclasts and deposition of the fall beds into different wind conditions, together with possible shifts in vent positions, contributed to add complexities to the distribution of pyroclasts and overall deposits architecture. Moreover, physical conditions of the ascending magma as well as conduit geometry contributed to the formation of pumice clasts with moderate to low vesicularity and textural characteristics exhibiting extensive evidence of magma shearing, in addition to the production of completely degassed juvenile obsidians found in variable proportion in the deposit.

6.4.1 Comparison with other eruptions at Okataina

Available data on intra-caldera rhyolitic eruptions and their deposits from the OVC (**Chapter 2** and reference therein), suggest that the above listed characteristics were the typical eruption features of the post-25 ka volcanism at Okataina. Each of the nine rhyolitic eruptions after the Mangaone eruptive period appear to have followed similar sequence and dynamics to those inferred for the Kaharoa eruption and ejected comparable volume of magmas with similar explosive intensities (**Chapter 2**). Some characteristics however varied. For example, the pyroclast to lava (domes and/or coulees) volume ratio (in DRE of magma erupted) at both the Tarawera and the Haroharo vent lineaments changed during each eruption without showing significant temporal trend, however maintaining a general predominance of lava over pyroclasts (**Table 2.2**; **Chapter 2**). According to the most recent erupted volume estimations (Sahetapy-

Engel et al. 2014), the Kaharoa eruption was the most "explosive" eruptions at Okataina with a pyroclast to lava ratio of ~8:1. On the contrary the 8ka cal. BP Mamaku eruption from Haroharo was the most effusive eruption with a pyroclast to lava ratio of >1:10, assuming a converted DRE magma volume of the deposit of ~0.5 km^3 (40% of the reported deposit volume; **Table 2.2**) (see also Nairn, 2002).

In one eruption, the typical explosive-to-effusive progression was inverted, with inferred initial lava dome extrusion preceding intense pyroclastic activity during the 13.6 ka cal. BP Waiohau eruption (Nairn, 2002). Early episode(s) of lava extrusion interspersed within the initial explosive-dominated phases might have occurred at other Okataina eruptions, as suggested by the incipient aborted transitions inferred in this study for the Kaharoa eruptions.

The distance between the multiple aligned vents during individual eruptions varied largely. In some cases, vents were contiguous (few hundred meters apart) to closely spaced (few km apart) (e.g., the Rotorua and the Kaharoa eruptions), while in others, vents were separated by several km (e.g., 20 km apart during the Te Rere eruption). Larger distances between vents likely resulted in different magma ascent pathways and varying eruptive styles, with possible simultaneous eruptive activity (e.g., Kobayashi et al., 2005).

6.4.2 Comparison with post-Oruanui eruptions at Taupō

In the context of the TVZ rhyolitic volcanism, further comparisons can be drawn with the young intra-caldera eruptions from the Taupō caldera system (**Fig. 1.2**). No comparisons are here made with the ~232 CE Taupō "Y" eruption (Wilson and Walker, 1985; Wilson, 1993) as it involved a caldera collapse phase and associated intermediate-volume ignimbrite (*sensu* Giordano and Cas, 2021), which deviate from the studied rhyolitic eruption types.

As remarked by other authors (Barker et al., 2021), the post-Oruanui (<25.5 ka) rhyolitic activity at Taupō differed from that at Okataina for being characterised by numerous (up to 25) but typically smaller volumes (< 0.1 to 1 km^3 DRE) eruptions, only sporadically exciting 1 km^3 DRE (e.g., eruptions E and S). Despite these frequency and magnitude differences between the two volcanic centres, based on the available deposit data and their interpretations (Wilson, 1993), individual Taupō eruptions seems to have shared similar characteristics to those sourced from Okataina. These include (i) eruptive activity from multiple vents along fissures suggesting dike related feeding systems, (ii) eruptive intensity for the major explosive phases broadly classified within the Plinian to subplinian range, and (iii) explosive activity accompanied or followed by dome-forming events (mostly inferred from variation in abundance of juvenile obsidian clasts in the deposits). In addition, at least a few eruptions at Taupō (e.g., eruptions E, V and X) appear to

have been characterised by an episodic behaviour (Wilson, 1993). A larger number of eruptions at Taupō might have been in turn episodic, yet intra-eruption time breaks are complicated to infer for deposits associated to smaller magma volumes.

An important difference however appears to be related to the degree of magma-water interactions during individual Taupō eruptions (Wilson, 1993) compared to those from Okataina (Nairn, 2002). Although minor phreatomagmatic explosions have been suggested for all the post-25 ka Okataina eruptions (**Table 2.2**; **Chapter 2** and reference therein), a larger involvement of external water during the intra-caldera Taupō eruptions might be related to strong environmental controls since eruptive vents typically opened within the older Lake Taupō.

6.4.3 Comparison with similar rhyolitic eruptions worldwide

Comparisons of the Kaharoa eruption with other similar events globally are complicated due to the general low availability of studies focused on moderate-to-large scale rhyolitic eruptions from caldera volcanoes. This is in part due to the overall low frequency of rhyolitic events and the consequently limited availability of historical accounts and instrumental observations. In addition, studies of pyroclastic deposits associated with intra-caldera rhyolitic eruptions are complicated by the limited proximal outcrop exposures due to emplacement of large ignimbrite and/or lavas burring older deposits, together with the subsidence of the caldera floor, typically accompanied by water infilling (Branney and Acocella, 2015).

A preliminary comparison was anticipated in **Chapter 3** with the well-studied rhyolitic eruptions from the Mono-Inyo volcanic chain, an approximately N–S-oriented, 25-km-long lineament of vents and domes starting at the NW corner of Long Valley caldera, in California, USA (Hildreth, 2004; Marcaida et al., 2019). The Mono-Inyo pyroclastic deposits show numerous features in common to the studied Kaharoa deposits, such as the multiple bedded nature of the succession with repeated and strong grain size stratifications resulting from typically subplinian and episodic explosive activities depositing several fall and PDC beds (e.g., Miller et al., 1985; Sieh and Bursik, 1986; Bursik, 1993; Nawotniak and Bursik, 2010; Bursik et al., 2014). These deposits also contain variable amounts of tube pumice clasts and juvenile obsidians and are associated to the emplacement of lava domes and coulees from multiple aligned vents related to intrusion of dikes in the subsurface.

Further comparison can be drawn with other studied eruptions from other silicic caldera systems and volcanic fields in the USA, although less data is available for these eruptions. Rhyolitic eruptions with similar deposit features, dynamics and type of vent and feeding systems are reported for the >130ka intra-caldera volcanism at the Valles-Toledo caldera complex, New

Mexico (Heiken et al., 1986; Heiken et al., 1990; Gardner et al., 2010) and for the recent activity (<1ka) from Glass Mountain and Little Glass Mountain at Medicine Lake volcano, northern California (Heiken, 1978; Donnelly-Nola et al., 1990; Grove et al., 1997).

Finally, other examples of similar rhyolitic activity can be found at La Primavera caldera, Mexico (western Trans-Mexican Volcanic Belt) and at the active Laguna del Maule volcanic field, Chile (Andean Southern Volcanic Zone). Early field studies of Plinian-type deposits associated with lava dome extrusions from the post-caldera activity at La Primavera (~86 to 45ka; Sourisseau et al., 2020) by Walker et al. (1981), suggest that some eruptions (e.g., unit D) underwent to similar dynamics to those inferred for the Kaharoa. Furthermore, the post-glacial (<25 ka), high-frequency (>20 eruptions) rhyolitic activity at Laguna del Maule also appear to have been characterised by similar dike-fed, multiple-vents, explosive-to-effusive eruptions (Hildreth et al., 2010; Singer et al., 2014; Cáceres et al., 2018; Andersen et al., 2019) producing complex pyroclastic sequences (e.g., Contreras Hidalgo, 2020). Comparative studies between eruptions from Okataina and Laguna del Maule would be of great relevance since the recent unrest at the latter volcanic centre (Andersen et al., 2018; Le Mével et al., 2021).

It is important to emphasise that if the available eruption magnitude estimations are accurate (within reasonable uncertainties, e.g., Bonadonna et al., 2015a), the cited similar eruption cases have usually associated smaller volumes of erupted magma compared to those of the intra-caldera rhyolitic activity at Okataina. Each individual post-25ka eruptions at Okataina ejected total magma volumes (as pyroclasts + lavas) within the 5 to 15 km^3 DRE range, whereas eruption volumes for the identified analogues span between <0.1 to 5 km^3 DRE range. These larger volumes might be related to the exceptional subduction-extension tectonic settings in which the Okataina caldera is found within the active Taupō Rift (Wallace et al., 2004; Spinks et al., 2005; Cole et al., 2010; Seebeck et al., 2010; 2014; Sas, 2020). These tectonic settings facilitated magma accumulation and recharge of the silicic magmatic system at mid-shallow crustal levels as inferred by the frequent mafic intrusions from depths (Leonard et al., 2002; Shane et al., 2008; Sas et al., 2019). Furthermore, evidence for storage of silicic magmas in discrete but partially connected batches (Smith et al., 2006; Shane et al., 2007, 2008; Sas, 2020) is supportive of a melt-lens-dominated nature of the magmatic system beneath caldera volcanoes suggested by Cashman and Giordano (2014), which provides favourable conditions for the rapid accumulation of large, eruptible melt bodies.

6.5 Eruption classification

The intra-caldera Okataina eruptions create some problems in terms of traditional eruption classification schemes and terminologies (Bonadonna et al., 2016 for review). The Kaharoa eruption investigated during this research shares the archetypical characteristics of both Plinian and Vulcanian/dome-forming eruption types (see **Chapter 1**).

Plinian-type events are, by definition, sustained volcanic episodes, varying in intensity, magnitude, and degree of eruption unsteadiness (from subplinian to Plinian), with typical durations of few hours to days (Cioni et al., 2015). On the other hand, Vulcanian-type eruptions consist in intermittent, transient, small-volume explosions, typically associated to prolonged period (up to years-long) of cyclical eruptive activity at lava-dome-forming volcanoes (Clarke et al., 2015; Calder et al., 2015).

The intense explosive activity during the Kaharoa eruption falls within the Plinian-type case, however, rather than representing the single climatic phase of the eruption, it consisted of multiple, discrete episodes, repeated over longer durations. This explosive intermittency, the production of moderate-to-low vesicularity pumices together with obsidians, and the association with the extrusion of multiple lava domes, move instead the Kaharoa eruption towards the Vulcanian-type case.

Although also Plinian-type eruptions have long been recognized to consist of multiple phases of contrasting style and intensity, separated or not by short-time breaks (Rosi, 1998; Cioni et al., 2015), the Kaharoa eruption might be more complicated to fit into the traditional categories of eruptions. The Kaharoa and other similar eruptions at Okataina, might represent a particular style of silicic volcanism related to dike-fed eruptions of calc-alkaline rhyolitic magmas. These volcanic events combine Plinian-type eruption intensity to Vulcanian intermittency and extrusion of voluminous lava domes resulting in very complex eruption scenario which can potentially result into multiple volcanic hazards over prolonged time.

[This page intentionally left blank]

Chapter 7

Conclusions and future work

7.1 Research summary

This study focused on the eruptive dynamics of the 1314±12 CE Kaharoa eruption sourced from multiple vents at Tarawera, within the Okataina caldera system in New Zealand. The goals of this research have been achieved through field investigations of the pyroclastic deposits and by the quantification and evaluation of the microtextural characteristics of the erupted juvenile pyroclasts.

Chapter 2 reviewed the eruptive history of the OVC with a particular focus on the rhyolitic activity of the centre following the Rotoiti/Rotoehu major caldera-forming eruption. Based on bibliographic analysis, the main eruption characteristics of the post-25 ka rhyolitic activity from the Tarawera and the Haroharo vent lineaments were outlined.

Chapter 3 presented a detailed field study and quantitative characterisation of the Kaharoa pyroclastic succession. This study enabled the re-evaluation of the stratigraphic sequence and to propose a multi-episode and multi-phase scenario for the eruption. The sedimentary structures of the deposit, together with the main grain size and componentry features, allowed for the recognition of an array of deposit types, which were linked to different eruptive and transport-depositional mechanisms. The reconstructed eruptive sequence suggested complex eruption dynamics whose controlling factors were still poorly understood and required further investigations. The variety of juvenile clasts identified from both fieldwork and componentry analysis, further signalled complex magma ascent and degassing histories in the conduit. Therefore, it was chosen to investigate and quantify the juvenile textural characteristics as a tool to gain a better understanding into the eruption.

Chapter 4 presented an approach to quantify complex and anisotropic vesicle textures in pumice clasts, using SEM-BSE images. Preliminary thin section observations revealed a high degree of complexity of the Kaharoa pumice microtextures, which are characterised by the ubiquitous presence of deformed, convoluted- to tube-like, vesicles. Since a reference methodology to characterise the dimensional features and number densities of tube vesicles was not available from the literature, a new quantitative approach was developed in this chapter.

Chapter 5 presented a thorough characterisation of the vesicle textures of the Kaharoa pumices. The quantitative 2D vesicle analysis was coupled with the estimation of pumice clasts bulk densities and proportion of texturally different pumice types in the deposit. This dataset was collected for the coarse-grained units along the reconstructed stratigraphy and provided constraints on magma conduit dynamics during the explosive phases of the eruption. Furthermore, the textural data were correlated to the deposit types and componentry characteristics to evaluate the role of shallow conduit processes in controlling the eruption dynamics.

Chapter 6 integrated the main findings arising from individual chapters. This provided (i) new insights into magma dynamics in the conduit throughout the eruption sequence, (ii) the definition of the main controls on eruptive style changes and overall eruption dynamics and (iii) to propose of a comprehensive model for the Kaharoa eruption. Furthermore, the studied eruption was compared to other similar rhyolitic volcanic events both locally and globally and its significance in terms of traditional eruption classifications was outlined.

7.2 Objectives and key findings

In **Chapter 1** four specific objectives were defined for the planned research project around the central aim of better understanding the dynamics of rhyolitic eruptions from intra-caldera settings. The key findings emerging from the fulfilment of these research objectives are summarised below.

Objective 1

Characterisation of the pyroclastic succession emplaced during the Kaharoa eruption to define the timing of events and the temporal changes in eruptive and depositional patterns.

Key findings

(1) Eruption stratigraphy. Based on the deposit features at key outcrops and lateral correlations, the investigated pyroclastic succession was subdivided into 24 lithostratigraphic units. This resulted in defining the stratigraphic scheme for the Kaharoa eruption, providing timing for the numerous eruptive and depositional events.

(2) Episodic behaviour. Based on the field evidence of intra-eruption time breaks, the explosive activity was defined as the result of 10 discrete episodes of sustained magma discharge. The pauses between individual explosive episodes are inferred to span from few hours up to weeks.

(3) Changes in eruptive style. The observed variations in the sedimentological and lithological characteristics of the deposits allowed for the establishment of seven main deposit types. The alternation of these deposit types in the stratigraphy defines changes in eruptive style during the eruption sequence. The major explosive episodes consisted in the formation of sustained subplinian eruptive columns. These episodes were characterised by the alternation of stable to continuously oscillating convective columns, at times partially collapsing, which resulted in the formation of massive to stratified lapilli deposits, suggesting fluctuating magma discharge. The

subplinian fallout-dominated activity was interrupted at different times by (i) episodes of low-intensity sustained ash emissions and associated ash fallout, (ii) pyroclastic fountaining producing widespread dilute to concentrated PDCs and (iii) ash explosions (suspected phreatomagmatic) producing dilute PDCs.

(4) Instabilities of the conduit-vent system. Componentry analysis along the stratigraphic sequence showed continuous waxing and waning in the abundance of wall rock lithics. These oscillations are interpreted to represent repeated instabilities of the conduit-vent system, which had implications in the eruptive column stability and dynamic of fallout depositions (e.g., poor connection conduit-to-vent area; increase in volume of lithic clasts in the ejected gas-pyroclast mixture exiting the vent). Lithic-rich units are typically associated with stratified lapilli deposits, whereas lithic-poor units are typically associated with massive lapilli deposits.

(5) Eruption phases. Based on the identification of intra-eruption time breaks and based on the interpreted dominant eruptive activity, six main phases (A to F) were proposed to describe the temporal evolution of the eruption. Three phases are associated with repeated subplinian episodes (Phase A, B, D), one comprises the major PDC activity of the eruption (Phase C), while the final two phases (E and F) are associated to ash emission during the transition to lava extrusions and to the final main dome-building sequence of the eruption.

Objective 2

Development of an approach to quantify complex and anisotropic vesicle textures from pumice clasts using SEM-BSE images.

Key findings

(1) Vesicle datasets from opposite thin section orientations. Parallel (PA) and orthogonal (OR) pumice thin sections to the main direction of vesicle elongation enabled the quantification of different but equally important vesicle features. The PA cuts provide an estimation of the degree of elongation of deformed vesicles. The OR cuts provide instead a more accurate estimation of the 2D vesicle number density and enable to assess the extent of vesicle coalescence perpendicular to shear. Although anisotropies in the vesicle textures are usually evident from the clast's external surface and morphology, preliminary microscopic inspections of pumice thin sections along different orientations are recommended to avoid sample preparation bias on quantitative vesicle analysis.

(2) Optimal image magnification(s) for quantification of vesicle features. The 2D analysis of high-resolution images (4096 × 3775 pixels) taken across four different magnifications (20×, 50×,

100× and 200×), allowed to propose an optimal magnification combination to minimize the working time during image processing. The combination of images taken at 20× and 200× enabled an adequate representation of the natural variability of vesicle size and shape distributions in complex pumice microtextures. Additionally, this study shows that since typically >95% of vesicles have size <100-200 μm in pumice clasts, analysis of high-resolution images at 200× provide alone an adequate estimation of vesicle size and shape distributions.

(3) Vesicle size matters for shape analysis. This study shows a strong dependency of vesicle elongation to vesicle size. Particularly, within the pumice microtextures analysed, vesicles with small diameters (<30-50 μm) have average aspect ratios higher than those of large vesicles (>250 μm to few mm). This size-dependency is a main factor that must be considered in studies dedicated to estimating the degree of vesicle deformation in pumice clasts.

Objective 3

Constrain the dynamics of magma ascent in the shallow conduit and evaluate how conduit processes influenced the observed variations in deposit characteristics and pyroclast textures.

Key findings

(1) Kaharoa pumice texture and density. Based on macroscopic observations coupled with SEM investigations, two main textually different pumice types (MHP and TP clats) were recognized in the lapilli-size fraction. These clasts were continuously produced during each major explosive episode, with relatively uniform proportion in the deposit (usually 60-70% MHP and 30-40% TP clasts). The textual variability reflects different vesicle textures at the submillimetre scale, characterised by: (i) a heterogeneous network of tube and convoluted vesicles coexisting with subspherical vesicles (MHP microtextures), and (ii) a pervasive network of tube vesicles with limited subspherical vesicles (TP microtextures). In terms of clast bulk density, no significant variations were observed between the two pumice types. Overall, the Kaharoa pumices have relatively high average bulk density (1100 kg/m^3) and moderate to low vesicularity (equivalent average vesicularity 53%), generally reported in the literature for silicic, subplinian-style eruptions.

(2) Origin of pumice textural variability. The formation of different pumice types was interpreted as the result of lateral velocity gradients and variable strain rates within the conduit, which exposed the magma to spatially different vesiculation and deformation conditions. These cross-conduit variations are consistent with the obtained differences in quantitative vesicle data between MHP and TP clasts, well represented by parameters such as the total vesicle number density and (to a lesser extent) by vesicle size distributions. Furthermore, additional post-

fragmentation processes were postulated in controlling the formation of very complex microtextures observed within some MHP clasts, characterised by contrasting neighbouring, mm-wide, domains of deformed and subspherical vesicles and by the presence of stretched vesicles showing multiple directions of elongation.

(3) Main conduit processes during magma ascent. The macro- and micro-textural investigations of the Kaharoa pumice clasts showed extensive evidence of deformation and interconnection of bubbles. The textural results, coupled with the obtained high pumice bulk densities and juvenile componentry variations with the stratigraphy, enabled to infer that the main processes regulating magma evolution during ascent in the conduit were: (i) shear stress and deformation of the bubble-bearing melt, (ii) bubble coalesces and (iii) permeable outgassing. These processes, their interplay and extent, provided bounding conditions for magma rheology and ascent, ultimately governing the overall eruption dynamic.

(4) Pumice texture and lapilli deposit correlations. The microtextural characteristics of the analysed pumice clasts are similar throughout the stratigraphy, despite changes in deposits features of the lapilli units (e.g., massive vs. stratified units). This indicates similarities in magma ascent and degassing conditions feeding the subplinian episodes. Variation in deposit types and transport/eruptive modality are inferred to depend on a combination of external (e.g., modifications and instabilities of the conduit-vent system) and internal (e.g., magmatic response to conduit-vent changes) factors. This study further showed correlation between the abundance of lithic clasts, sedimentary features, and the inferred stability of the sustained eruptive columns.

(5) Aborted transition to lava effusion. This study showed evidence for the formation of two obsidian plugs in the conduit during the early explosive phases of the eruption (Phases A and B). These two episodes of obsidian plug formation obstructing the shallow conduit-vent system are related to efficient permeable outgassing and densification of the magma and are interpreted to represent incipient transitions to lava effusions. The transition was aborted due to the arrival and degassing of new magmas in the conduit, which caused pressure build-up and disruptions of the conduit plugs.

(6) Cyclicity in magma conduit dynamic and eruption. The explosive subplinian phases periodically concluded with a decline in eruptive intensity recorded by the decreasing deposit grain size (e.g., Phase A and D). Furthermore, magma densification and emplacement of obsidian plugs in the shallow conduit occurred at the end of Phases A and B. This type of eruptive behaviour indicates cyclical patterns in magma ascent and outgassing in the conduit influencing eruptive intensity and style during the Phase A to D sequence.

(7) Dike geometry of the conduit system. By combining the pumice textural features (e.g., extent of shear-derived microtextures and frequency of TP clasts) with the surface alignment of vents

and domes, defining a fissure, this study suggested that the Kaharoa magmas ascended through a dike-shaped conduit. This conduit geometry limited isotropic expansion and growth of bubbles, promoting instead extensive bubble deformation and coalescence along the direction of shear. This resulted in the development of interconnected anisotropic bubble network and, in turn, facilitated outgassing before fragmentation.

Objective 4

Define the factors controlling the changes in eruptive styles and the overall eruption dynamic to provide a general model for the Kaharoa eruption.

Key findings

(1) Changes in eruptive style controlled by magmatic "internal" factors. While no magmatic factors alone are accredited in causing the observed variability during subplinian episodes (e.g., alternation of stable, oscillating and partially collapsing columns) and/or in the shift to the pyroclastic fountaining PDC episode, the cyclical pattern in magma ascent and outgassing were critical in regulating the intra-phase variation in eruptive intensity and the incipient transitions to lava extrusions. Additional internal controls related to an increase in the amount of phenocryst carried by the ascending magma later in the eruption have been suggested as main control in the final transition to the dome-building phase.

(2) Changes in eruptive style controlled by environmental "external" factors. This research suggests that primary environmental factors in controlling changes in eruptive styles are related to the mechanical (in)stabilities and modification of the conduit-vent system. Together with the magmatic response to conduit-vent changes, these factors played an important role in the variations in magma discharge rate and eruptive column dynamic, as well as in the shift from fall-dominated to pyroclastic fountaining activity. Additional factors related to vent position changes have been associated with ash explosions related to suspected magma-water interactions.

(3) Insights into episodic eruption behaviour. Based on the deposit and pumice textural data presented in this work, together with comparisons with numerical models for silicic dike conduits and experiments on dike propagation dynamics, this research provides some insights into the episodic nature of the Kaharoa eruption. Both magma degassing during ascent and the dike geometry of the conduit are suggested as primary factors in controlling the discontinuous magma discharge to the surface during the explosive phases.

(4) A model for the Kaharoa eruption. Based on the integration of field observations, deposit and pyroclast texture data, this research presented a model for the Kaharoa eruption. This model

provides a reconstruction of the complex intra-eruption sequence of events and combines the inferred eruptive styles to conduit dynamics. The model yields pivotal information for future quantifications of scenario-based volcanic hazard assessments for intra-caldera rhyolitic eruptions at Okataina.

7.3 Broader impact of this research

Detailed studies of moderate- to large-scale rhyolitic eruptions are available only for a very limited number of recent, documented eruptions (e.g., 1875 Askja, 1912 Novarupta, 2008–2009 Chaitén and 2011–2012 Cordón Caulle eruptions; **Chapter 1** and reference therein), for which contemporary accounts and/or geophysical data are also available. Despite these volcanic events offered the rare chance to expand the knowledge on rhyolitic eruptions, the controls and drivers of this type of eruptive activity still remain poorly understood. Using the ~1314 CE Kaharoa eruption of Tarawera as a case study, this research contributes to deepening our current understanding on the dynamics and physical processes of moderate- to large-scale rhyolitic volcanism.

The scenario here depicted for the studied eruption highlights the complex episodic, multi-phase, explosive to dome-forming and long-lasting nature of dike-fed rhyolitic eruptions from intra-caldera settings. Based on the deposit characterisation, stratigraphic reconstruction, and quantification of the physical and textural proprieties of the erupted juveniles, this research defines key internal (magma shearing and outgassing) and external (conduit geometry and mechanical stability) factors in controlling the complex dynamics and eruptive style changes of this type of eruptions. These results provide useful insights that can be applied for the study of other similar eruptions at volcanoes with comparable tectonic settings and shallow feeding systems.

The applied field-based approach of **Chapter 3** (e.g., identifications and characterisation of units and deposit types, together with definition of eruptive episodes and phases) provides a framework to interpret complex pyroclastic successions (e.g., Cioni et al., 2003; Arce et al., 2005; Sulpizio et al., 2005; Saucedo et al., 2010; Pardo et al., 2012; Maeno et al., 2019) associated to dike-fed rhyolitic eruptions at lava dome complexes. The cross-correlation of multiple deposit and pyroclast parameters (e.g., sedimentary structures, grain size, componentry, clast bulk density/vesicularity and pumice textural data) can be used as a proxy to evaluate the roles of internal and external factors in controlling eruptive styles. Pyroclasts density/vesicularity and textures, together with relative proportion in the deposit of obsidian juvenile and different pumice

types can be related to the conditions of the magma in the conduit. Additionally, componentry of lithics can yields important information on intra-eruption conduit-vent modifications. Applications of this multi parametric dataset were provided throughout this research to understand the observed deposit and eruptive variability (e.g., changes in eruptive column dynamics, transition to pyroclastic fountaining, obsidian plug formations).

An important outcome of this research is the dynamic interrelationship between the intrinsic physical properties of the magma and the characteristics of the volcanic conduit (geometry and stability of wall rock) in regulating eruption styles. On one hand, the geometrical constrictions of the conduit impact the modality and extent of magma vesiculation, deformation and outgassing during ascent and decompression to the surface. On the other hand, magma ascent and fragmentation have an impact in the conduit stability, causing intra-conduit pressure drops and causing modification of the conduit-vent system due to erosion/enlargement and wall collapses of the shallow conduit. The evolving magma and conduit properties as eruption initiate are mutually dependent, govern magma discharge (eruptive intensity) and provide source-derived controls to the gas-pyroclasts transport regimes (e.g., eruptive column dynamics and PDC transitions), determining the dominant type of activity.

This study shows that moderate- to large- scale rhyolitic eruptions can undergo intermittent and cyclical behaviours more typical of vulcanian and dome-forming eruptions (e.g., Melnik and Sparks, 2005; Dirksen et al., 2006; Costa et al., 2007; Bain et al., 2021). This manifested at the Kaharoa eruption by (i) the repeated onset and shutdown of discrete explosive episodes and by (ii) the intra-phase variations in eruptive intensity (e.g., decrease in deposit grain size) and magma outgassing efficiency (e.g., formation of obsidian conduit-vent plugs). In addition, the final shift from explosive to dome-building, can be considered an additional cycle occurring over prolonged timescales. The results from this study suggest that while the former two periodicities are controlled by magma conduit dynamics, the latter cycle is suspected to have been primed by changes of the pre-ascent magma properties (e.g., increase in phenocrysts carried by the later magmas).

The Kaharoa eruption exemplified a scenario relevant for volcanic hazard assessments and emergency responses at the Okataina caldera system. Although the modelling to evaluate tephra fallout and vent-opening probabilities have been provided for Plinian-type eruptions at Okataina (Bonadonna et al., 2005; Jenkins et al., 2008; Thompson et al., 2015), studies aimed to forecasts the complex intra-eruption sequence of events have instead not been conducted yet (see Bebbington and Jenkins, 2019). The episodic and multi-phase eruption scenario outlined in this study, provides constraints for building scenario-based event trees for volcanic emergency planning associated to intra-caldera rhyolitic eruptions (e.g., Newhall and Hoblitt, 2002; Cioni et

al., 2008; Torres-Orozco et al., 2018). This can be later expanded to estimate the probability of different types of eruptive events during the eruption sequence (e.g., Neri et al., 2008; Martí et al., 2008; Wright et al., 2019; Tierz et al., 2020; Ang et al., 2020; Tadini et al., 2021). To date, scenario-based hazard assessments and mitigation plans for a Kaharoa-type eruption from the New Zealand's active rhyolitic centres (Okataina and Taupō), have not yet been exhaustively implemented in the national volcanic risk reduction strategies (see Stirling et al., 2017). This needs to be addressed by future volcanological studies and by joint efforts between scientists, civil protections agencies and local authorities and communities.

7.4 Directions for future work

While addressing the specific objectives for this thesis, new research directions for potential future work were identified.

Eruption duration and paleomagnetic studies – Although this study placed some constraints on the intra-eruption time breaks and length of the explosive-dominated sequence (Phase A to D), the total duration of the Kaharoa eruption is still poorly constrained. The development of new techniques able to quantitatively estimate the duration of prehistoric eruption and the length of intra-eruption time breaks, validating with other means field-related time inferences, represent an important future challenge in volcanology. Recently Hasegawa et al. (2018; 2020) proposed a new approach to quantify the total duration of very large and super eruptions based on paleomagnetic secular variation determined in ash samples collected from the targeted pyroclastic sequences. Although to date the resolution of this technique does not appear to resolve eruption duration less than 50-100 years, it might be tested on the Kaharoa deposit. Paleomagnetic studies of the Kaharoa lava domes cited in Nairn et al. (2001) suggest that Crater and Wahanga domes were extruded at similar times. An investigation of the paleomagnetic signature of the Kaharoa ash beds from earlier phases using the Hasegawa et al. approach might help in further constrain the eruption length.

Timing and origin of Green Lake Plug – Green Lake Plug, also known as *Poupoutunoa* (Keam, 2016) or *Baby Volcano* (Thomas, 1888), is thought to represent a small (~50 m high and 100 m long) Kaharoa lava extrusion at the most SW inferred eruptive vent of the eruption (Nairn et al., 2001), located on the eastern termination of Lake Rotomahana (**Fig. 3.2**, **Chapter 3**). Its timing of emplacement is, however, uncertain. Nonetheless it is placed during the early phases of the Kaharoa eruption given its geochemical similarities with the initial Kaharoa pumices (Nairn et al., 2001). A more accurate determination of its timing can be of high relevance in

understanding the dynamic of rhyolitic dike propagation and sequence of vent openings during the eruption. In addition, as very limited field and textural data are available for this near-vertical, coherent rhyolitic body (see Cole, 1966), a study on the formation and emplacement origins (subvolcanic or extrusive?) can add to the knowledge of the eruption.

Kaharoa precursory activity (the P-layer) – During fieldwork conducted for this research, a distinct grey-to-purple-coloured bed was observed underlying the Kaharoa deposit at several southeast and east outcrops in proximal and medial areas. This bed was named the P-layer in the stratigraphy of this study and consists of weathered volcanic material, medium to fine ash in size, with scattered fine and medium lapilli pumice clasts. The layer has variable thickness (3 to 20 cm) and the contact with the overlying Kaharoa deposit is marked by a laterally discontinuous, mm-to-cm-thick black peat horizon. Although Lowe et al. (2012) and Lowe (2016) refer to the P-layer as a buried podzol soil occurring on top of the ~232 CE Taupō Y pumice deposits, the ash and lapilli clasts of the layer could represent an eruptive event sourced from Tarawera, shortly preceding the Kaharoa eruption. A geochemical fingerprint of the clasts in the tephra-soil sequence underlaying the Kaharoa deposit can allow to determine the P-layer origin (volcanic or pedogenic). If a Tarawera volcanic origin is confirmed, the P-layer might in turn represent a precursor event to the Kaharoa eruption.

Modality of near-vent pyroclast depositions and link between vent(s) and medial deposits – Very proximal Kaharoa deposits are difficult to access due to burial by the Kaharoa lava domes and by the later accumulation of the 1886 scoria deposits on the summits of Mt Tarawera. In addition, deposits along the slopes of the dome complex are problematic to access due to dense vegetation cover and local burial by thick block-and-ash flow fans. Despite these complications, future attempts should be made in finding new pyroclastic exposures within Mt Tarawera. This could provide a better understanding of the mechanisms of very proximal pyroclast transport and deposition during explosive-to-effusive rhyolitic eruptions (e.g., Houghton et al., 2004; Carey et al., 2008). In addition, such a study could help to better constraint the locations and timing of explosive vent(s) active during the eruption, linking with more precision the medial beds to the eruptive source area. Access to very proximal exposures of the marker beds identified during this work in proximal to medial sites (**Chapter 3**), could help to better constrain the vent opening sequence.

Explosive to dome-building transition – Based on the available data some factors in controlling the transition to the main dome-building phase of the Kaharoa eruption were proposed in this study (increase in magma phenocryst content). A detailed determination of the causes driving this transition was however beyond the scope of this study, nevertheless it represents an important potential avenue for future work. Future studies should incorporate the traditional

factors reported in the literature and review by Cassidy et al. (2018) in driving explosive-dome-building transition (e.g., changes during eruption in pre-ascent magma properties, magma rheology and conduit flow, degassing regime in conduit and variation in conduit geometry), with the recent conceptual models for silicic conduits developed by Wadsworth et al (2020) and Schipper et al. (2021) (sintering/clastogenic-driven explosive-effusive transitions). In the case of the Kaharoa eruption, textural analysis of juvenile ash fragments from unit Af, together with analysis of near-vent volcanic bombs (if available) preceding the main domes extrusions, could provide new insights into the evolution of the magma in the conduit leading up to the dome-building phase.

Magmatic controls on eruption dynamics and vent openings – The current conceptual model for the magma reservoir feeding the Kaharoa eruption suggests the top-down evacuation of a stratified, sill-like (8-km-long, 1-km-wide) magma chamber at 6-7 km beneath Tarawera, from which two main magma layers were sequentially tapped during the eruption (Nairn et al., 2004). Since the majority of the post-25 ka intra-caldera rhyolitic events at Okataina appear to have been fed by multiple discrete magma bodies during the same eruption (e.g., Rotoma eruption, Smith et al., 2006; Okareka eruption, Shane et al., 2008), it is important that future petrological and isotope geochemistry studies place more constraints on the magma storage region beneath Tarawera (see also Alloway et al., 2015).

Dual shear effects on rhyolitic conduit flow dynamics – This study shows that clasts having tube pumice textures are not only common in ignimbrite deposits associated to caldera-forming eruptions (cf. Ohashi et al., 2021), but are also common in fall and PDCs deposits associated to subplinian-type explosive events. The development of networks of sheared vesicles within the rising magma can represent an important factor to enable fast ascent and explosive fragmentation of otherwise slow-ascending viscous rhyolitic magmas. A future work can be conducted to further understand the dual effects of shear stress and strain on magma conduit flow dynamics (i.e., permeable outgassing and viscous dissipation; see **Section 6.1.2**, **Chapter 6**).

2D to 3D conversion of vesicle data from tube pumices – The approach developed in **Chapter 4** to characterise anisotropic pumice vesicle textures can be fine-tuned in future studies. A challenge is to convert the 2D vesicle data (e.g., size, shape, and number densities) from SEM-BSE images into 3D distributions. This has been done in work dedicated to the characterisation of isotropic pumice vesicle textures (e.g., Shea et al., 2010), but for non-spherical vesicles it remains a challenge. To validate the results from the 2D-alone and 3D-converted vesicle analyses, the use of X-ray computed microtomography to image pumice clasts is suggested for future work (e.g., Giachetti et al., 2011).

Limited deposit and textural data for intra-caldera rhyolitic eruptions – While comparing the studied eruption case with other similar volcanic events worldwide, this research signals a general limited availability of comprehensive datasets (e.g., deposit characteristics, clast-textural features, and deposit- and textural-derived eruption parameters) on intra-caldera rhyolitic eruptions. Expanding the current datasets with investigations of other rhyolitic eruptions needs to be addressed by future works, exploring the deposits of similar eruptions at other volcanic centres also cited in **Chapter 6**.

[This page intentionally left blank]

References

Acocella, V. (2014). Great challenges in volcanology: how does the volcano factory work? Frontiers in Earth Science, 2(4) 10.3389/feart.2014.00004

Acocella, V. (2021). Volcano-Tectonic Processes: Springer International Publishing. doi:10.1007/978-3-030-65968-4

Acocella, V., Spinks, K., Cole, J., & Nicol, A. (2003). Oblique back arc rifting of Taupo Volcanic zone, New Zealand. Tectonics, 22(4)

Acocella, V., Palladino, D. M., Cioni, R., Russo, P., & Simei, S. (2012). Caldera structure, amount of collapse, and erupted volumes: The case of Bolsena caldera, Italy. GSA Bulletin, 124(9-10), 1562-1576. 10.1130/b30662.1

Adams, N. K., Houghton, B. F., Fagents, S. A., & Hildreth, W. (2006). The transition from explosive to effusive eruptive regime: the example of the 1912 Novarupta eruption, Alaska. Geological Society of America Bulletin, 118(5-6), 620-634.

Alfano, F., Bonadonna, C., Volentik, A. C. M., Connor, C. B., Watt, S. F. L., Pyle, D. M., & Connor, L. J. (2011). Tephra stratigraphy and eruptive volume of the May, 2008, Chaitén eruption, Chile. Bulletin of Volcanology, 73(5), 613-630. doi:10.1007/s00445-010-0428-x

Alfano, F., Bonadonna, C., & Gurioli, L. (2012). Insights into eruption dynamics from textural analysis: the case of the May, 2008, Chaitén eruption. Bulletin of Volcanology, 74(9), 2095-2108. 10.1007/s00445-012-0648-3

Alidibirov, M. A. (1994). A model for viscous magma fragmentation during volcanic blasts. Bulletin of Volcanology, 56(6), 459-465. doi:10.1007/bf00302827

Allan, A. S. R., Baker, J. A., Carter, L., & Wysoczanksi, R. J. (2008). Reconstructing the Quaternary evolution of the world's most active silicic volcanic system: insights from an ~1.65Ma deep ocean tephra record sourced from Taupo Volcanic Zone, New Zealand. Quaternary Science Reviews, 27(25), 2341-2360. doi: https://doi.org/10.1016/j.quascirev.2008.09.003

Allen, S. R., & Cas, R. A. F. (1998). Rhyolitic fallout and pyroclastic density current deposits from a phreatoplinian eruption in the eastern Aegean Sea, Greece. Journal of Volcanology and Geothermal Research, 86(1), 219-251. https://doi.org/10.1016/S0377-0273(98)00080-8

Alloway, B., Pearce, N., Villarosa, G., Outes, V., & Moreno, P. (2015). Multiple melt bodies fed the AD 2011 eruption of Puyehue-Cordón Caulle, Chile. Scientific reports, 5, 17589.

Andersen, N. L., Singer, B. S., Costa, F., Fournelle, J., Herrin, J. S., & Fabbro, G. N. (2018). Petrochronologic perspective on rhyolite volcano unrest at Laguna del Maule, Chile. Earth and Planetary Science Letters, 493, 57-70. https://doi.org/10.1016/j.epsl.2018.03.043

Andersen, N. L., Singer, B. S., & Coble, M. A. (2019). Repeated rhyolite eruption from heterogeneous hot zones embedded within a cool, shallow magma reservoir. Journal of Geophysical Research: Solid Earth, 124(3), 2582-2600.

Ang, P. S., Bebbington, M. S., Lindsay, J. M., & Jenkins, S. F. (2020). From eruption scenarios to probabilistic volcanic hazard analysis: An example of the Auckland Volcanic Field, New Zealand. Journal of Volcanology and Geothermal Research, 397, 106871. https://doi.org/10.1016/j.jvolgeores.2020.106871

Aravena, Á., de' Michieli Vitturi, M., Cioni, R., & Neri, A. (2017). Stability of volcanic conduits during explosive eruptions. Journal of Volcanology and Geothermal Research, 339, 52-62. https://doi.org/10.1016/j.jvolgeores.2017.05.003

Aravena, Á., Cioni, R., Vitturi, M. d. M., & Neri, A. (2018). Conduit stability effects on intensity and steadiness of explosive eruptions. Scientific reports, 8(1), 4125.

Arce, J. L., Cervantes, K. E., Macías, J. L., & Mora, J. C. (2005). The 12.1 ka Middle Toluca Pumice: A dacitic Plinian–subplinian eruption of Nevado de Toluca in Central Mexico. Journal of Volcanology and Geothermal Research, 147(1), 125-143. https://doi.org/10.1016/j.jvolgeores.2005.03.010

Ashwell, P. A., Kendrick, J. E., Lavallée, Y., Kennedy, B. M., Hess, K. U., von Aulock, F. W., Wadsworth, F. B., Vasseur, J., & Dingwell, D. B. (2015). Permeability of compacting porous lavas. Journal of Geophysical Research: Solid Earth, 120(3), 1605-1622.

Ashwell, P. A., Kennedy, B. M., Edwards, M., & Cole, J. W. (2018). Characteristics and consequences of lava dome collapse at Ruawahia, Taupo Volcanic Zone, New Zealand. Bulletin of Volcanology, 80(5), 43. 10.1007/s00445-018-1217-1

Avanzinelli, R., Elliott, T., Tommasini, S., & Conticelli, S. (2007). Constraints on the Genesis of Potassium-rich Italian Volcanic Rocks from U/Th Disequilibrium. Journal of Petrology, 49(2), 195-223. 10.1093/petrology/egm076

Austin-Erickson, A., Büttner, R., Dellino, P., Ort, M. H., & Zimanowski, B. (2008). Phreatomagmatic explosions of rhyolitic magma: Experimental and field evidence. Journal of Geophysical Research: Solid Earth, 113(B11), n/a-n/a. 10.1029/2008JB005731

Austin-Erickson, A., Ort, M. H., & Carrasco-Núñez, G. (2011). Rhyolitic phreatomagmatism explored: Tepexitl tuff ring (Eastern Mexican Volcanic Belt). Journal of Volcanology and Geothermal Research, 201(1), 325-341. https://doi.org/10.1016/j.jvolgeores.2010.09.007

Bailey, R. A., & Carr, R. G. (1994). Physical geology and eruptive history of the Matahina Ignimbrite, Taupo Volcanic Zone, North Island, New Zealand. New Zealand Journal of Geology and Geophysics, 37(3), 319-344. doi:10.1080/00288306.1994.9514624

Bain, A. A., Calder, E. S., Cortés, J. A., Cortés, G. P., & Loughlin, S. C. (2018). Textural and geochemical constraints on andesitic plug emplacement prior to the 2004–2010 vulcanian explosions at Galeras volcano, Colombia. Bulletin of Volcanology, 81(1), 1. 10.1007/s00445-018-1260-y

Bain, A. A., Kendrick, J. E., Lamur, A., Lavallée, Y., Calder, E. S., Cortés, J. A., Cortés, G. P., Gómez Martinez, D., & Torres, R. A. (2021). Micro-Textural Controls on Magma Rheology and Vulcanian Explosion Cyclicity. Frontiers in Earth Science, 8(703) 10.3389/feart.2020.611320

Barberi, F., Cioni, R., Rosi, M., Santacroce, R., Sbrana, A., & Vecci, R. (1989). Magmatic and phreatomagmatic phases in explosive eruptions of Vesuvius as deduced by grain-size and component analysis of the pyroclastic deposits. Journal of Volcanology and Geothermal Research, 38(3-4), 287-307.

Barberi, F., Ghigliotti, M., Macedonio, G., Orellana, H., Pareschi, M., & Rosi, M. (1992). Volcanic hazard assessment of Guagua Pichincha (Ecuador) based on past behaviour and numerical models. Journal of Volcanology and Geothermal Research, 49(1-2), 53-68.

Barberi, F., Coltelli, M., Frullani, A., Rosi, M., & Almeida, E. (1995). Chronology and dispersal characteristics of recently (last 5000 years) erupted tephra of Cotopaxi (Ecuador): implications for long-term eruptive forecasting. Journal of Volcanology and Geothermal Research, 69(3), 217-239. https://doi.org/10.1016/0377-0273(95)00017-8

Barker, S. J., Rotella, M. D., Wilson, C. J. N., Wright, I. C., & Wysoczanski, R. J. (2012). Contrasting pyroclast density spectra from subaerial and submarine silicic eruptions in the Kermadec arc: implications for eruption processes and dredge sampling. Bulletin of Volcanology, 74(6), 1425-1443. 10.1007/s00445-012-0604-2

Barker, S. J., Rowe, M. C., Wilson, C. J., Gamble, J. A., Rooyakkers, S. M., Wysoczanski, R. J., Illsley-Kemp, F., & Kenworthy, C. C. (2020). What lies beneath? Reconstructing the primitive magmas fueling voluminous silicic volcanism using olivine-hosted melt inclusions. Geology, 48(5), 504-508.

Barker, S. J., Wilson, C. J., Illsley-Kemp, F., Leonard, G. S., Mestel, E. R., Mauriohooho, K., & Charlier, B. L. (2021). Taupō: an overview of New Zealand's youngest supervolcano. New Zealand Journal of Geology and Geophysics, 1-27.

Barmin, A., Melnik, O., & Sparks, R. S. J. (2002). Periodic behavior in lava dome eruptions. Earth and Planetary Science Letters, 199(1), 173-184. doi:https://doi.org/10.1016/S0012-821X(02)00557-5

Beanland, S., & Houghton, B. (1991). Rotokawau tephra: basaltic maars in Okataina Volcanic Centre, Taupo Volcanic Zone. NZ Geol Surv Rec, 43, 37-43

Beanland, S., & Haines, J. (1998). The kinematics of active deformation in the North Island, New Zealand, determined from geological strain rates. New Zealand Journal of Geology and Geophysics, 41(4), 311-323.

Beavan, J., Moore, M., Pearson, C., Henderson, M., Parsons, B., Bourne, S. Hodgkinson, K. (1999). Crustal deformation during 1994–1998 due to oblique continental collision in the central Southern Alps, New Zealand, and implications for seismic potential of the Alpine fault. Journal of Geophysical Research: Solid Earth, 104(B11), 25233-25255. doi:10.1029/1999JB900198

Beavan, J., & Haines, J. (2001). Contemporary horizontal velocity and strain rate fields of the Pacific-Australian plate boundary zone through New Zealand. Journal of Geophysical Research: Solid Earth, 106(B1), 741-770. doi:10.1029/2000JB900302

Beavan, J., Samsonov, S., Denys, P., Sutherland, R., Palmer, N., & Denham, M. (2010). Oblique slip on the Puysegur subduction interface in the 2009 July MW 7.8 Dusky Sound earthquake from GPS and InSAR observations: implications for the tectonics of southwestern New Zealand. Geophysical Journal International, 183(3), 1265-1286. 10.1111/j.1365-246X.2010.04798.x

Bebbington, M. S. (2020). Temporal-volume probabilistic hazard model for a supervolcano: Taupo, New Zealand. Earth and Planetary Science Letters, 536, 116141. https://doi.org/10.1016/j.epsl.2020.116141

Bebbington, M. S., & Jenkins, S. F. (2019). Intra-eruption forecasting. Bulletin of Volcanology, 81(6), 34. 10.1007/s00445-019-1294-9

Bebbington, M. S., Cronin, S. J., Chapman, I., & Turner, M. B. (2008). Quantifying volcanic ash fall hazard to electricity infrastructure. Journal of Volcanology and Geothermal Research, 177(4), 1055-1062. https://doi.org/10.1016/j.jvolgeores.2008.07.023

Bellamy, S. (1991). Some studies of the Te Wairoa ignimbrites and the associated volcanic geology of the SW Okataina volcanic centre, Taupo Volcanic Zone. Unpublished MSc thesis, University of Waikato, Hamilton, New Zealand.

Belousov, A., Voight, B., & Belousova, M. (2007). Directed blasts and blast-generated pyroclastic density currents: a comparison of the Bezymianny 1956, Mount St Helens 1980, and Soufrière Hills, Montserrat 1997 eruptions and deposits. Bulletin of Volcanology, 69(7), 701. doi:10.1007/s00445-006-0109-y

Benson, T. W., Illsley-Kemp, F., Elms, H. C., Hamling, I. J., Savage, M. K., Wilson, C. J. N., Mestel, E. R. H., & Barker, S. J. (2021). Earthquake Analysis Suggests Dyke Intrusion in 2019 Near Tarawera Volcano, New Zealand. Frontiers in Earth Science, 8(604) 10.3389/feart.2020.606992

Berlo, K., Tuffen, H., Smith, V. C., Castro, J. M., Pyle, D. M., Mather, T. A., & Geraki, K. (2013). Element variations in rhyolitic magma resulting from gas transport. Geochimica et Cosmochimica Acta, 121, 436-451. https://doi.org/10.1016/j.gca.2013.07.032

Bernard, O., & Bouvet de Maisonneuve, C. (2020). Controls on eruption style at Rabaul, Papua New Guinea – Insights from microlites, porosity and permeability measurements. Journal of Volcanology and Geothermal Research, 406, 107068. https://doi.org/10.1016/j.jvolgeores.2020.107068

Biass, S., Todde, A., Cioni, R., Pistolesi, M., Geshi, N., & Bonadonna, C. (2017). Potential impacts of tephra fallout from a large-scale explosive eruption at Sakurajima volcano, Japan. Bulletin of Volcanology, 79(10), 73. 10.1007/s00445-017-1153-5

Bibby, H. M., Caldwell, T. G., Davey, F. J., & Webb, T. H. (1995). Geophysical evidence on the structure of the Taupo Volcanic Zone and its hydrothermal circulation. Journal of Volcanology and Geothermal Research, 68(1), 29-58. doi:https://doi.org/10.1016/0377-0273(95)00007-H

Black, B. A., Manga, M., & Andrews, B. (2016). Ash production and dispersal from sustained low-intensity Mono-Inyo eruptions. Bulletin of Volcanology, 78(8), 1-13.

Blake, S., & Fink, J. H. (1987). The dynamics of magma withdrawal from a density stratified dyke. Earth and Planetary Science Letters, 85(4), 516-524. https://doi.org/10.1016/0012-821X(87)90145-2

Blower, J. (2001). Factors controlling permeability–porosity relationships in magma. Bulletin of Volcanology, 63(7), 497-504. 10.1007/s004450100172

Blundy, J., & Cashman, K. (2008). Petrologic reconstruction of magmatic system variables and processes. Reviews in Mineralogy and Geochemistry, 69(1), 179-239.

Bonadonna, C., & Phillips, J. C. (2003). Sedimentation from strong volcanic plumes. Journal of Geophysical Research: Solid Earth, 108(B7) https://doi.org/10.1029/2002JB002034

Bonadonna, C., & Costa, A. (2013). Plume height, volume, and classification of explosive volcanic eruptions based on the Weibull function. Bulletin of Volcanology, 75(8), 742. 10.1007/s00445-013-0742-1

Bonadonna, C., Ernst, G., & Sparks, R. (1998). Thickness variations and volume estimates of tephra fall deposits: the importance of particle Reynolds number. J Volcanol Geotherm Res, 81 10.1016/s0377-0273(98)00007-9

Bonadonna, C., Mayberry, G., Calder, E., Sparks, R., Choux, C., Jackson, P., Lejeune, A., Loughlin, S., Norton, G., & Rose, W. I. (2002). Tephra fallout in the eruption of Soufrière Hills Volcano, Montserrat. Geological Society, London, Memoirs, 21(1), 483-516.

Bonadonna, C., Connor, C. B., Houghton, B., Connor, L., Byrne, M., Laing, A., & Hincks, T. (2005). Probabilistic modeling of tephra dispersal: Hazard assessment of a multiphase rhyolitic eruption at Tarawera, New Zealand. Journal of Geophysical Research: Solid Earth, 110(B3)

Bonadonna, C., & Costa, A. (2013). Plume height, volume, and classification of explosive volcanic eruptions based on the Weibull function. Bulletin of Volcanology, 75(8), 742. 10.1007/s00445-013-0742-1

Bonadonna, C., Biass, S., & Costa, A. (2015a). Physical characterization of explosive volcanic eruptions based on tephra deposits: Propagation of uncertainties and sensitivity analysis. Journal of Volcanology and Geothermal Research, 296, 80-100. https://doi.org/10.1016/j.jvolgeores.2015.03.009

Bonadonna, C., Cioni, R., Pistolesi, M., Elissondo, M., & Baumann, V. (2015b). Sedimentation of long-lasting wind-affected volcanic plumes: the example of the 2011 rhyolitic Cordón Caulle eruption, Chile. Bulletin of Volcanology, 77(2), 13. doi:10.1007/s00445-015-0900-8

Bonadonna, C., Pistolesi, M., Cioni, R., Degruyter, W., Elissondo, M., & Baumann, V. (2015c). Dynamics of wind-affected volcanic plumes: The example of the 2011 Cordón Caulle eruption, Chile. Journal of Geophysical Research: Solid Earth, 120(4), 2242-2261. doi:10.1002/2014JB011478

Bonadonna, C., Cioni, R., Costa, A., Druitt, T., Phillips, J., Pioli, L., . . . Wallenstein, N. (2016). MeMoVolc report on classification and dynamics of volcanic explosive eruptions. Bulletin of Volcanology, 78(11), 84. 10.1007/s00445-016-1071-y

Boudon, G., Villemant, B., Komorowski, J.-C., Ildefonse, P., & Semet, M. P. (1998). The hydrothermal system at Soufriere Hills Volcano, Montserrat (West Indies): Characterization and role in the on-going eruption. Geophysical Research Letters, 25(19), 3693-3696. doi:10.1029/98GL00985

Bouvet de Maisonneuve, C., Bachmann, O., & Burgisser, A. (2009). Characterization of juvenile pyroclasts from the Kos Plateau Tuff (Aegean Arc): insights into the eruptive dynamics of a large rhyolitic eruption. Bulletin of Volcanology, 71(6), 643. 10.1007/s00445-008-0250-x

Bouvet de Maisonneuve, C., Forni, F., & Bachmann, O. (2021). Magma reservoir evolution during the build up to and recovery from caldera-forming eruptions – A generalizable model? Earth-Science Reviews, 218, 103684. https://doi.org/10.1016/j.earscirev.2021.103684

Branca, S., & Del Carlo, P. (2004). Eruptions of Mt Etna during the past 3.200 years: a revised compilation integrating the Historical and stratigraphic records. In Mt. Etna: volcano laboratory: AGU.

Branney, M. J., & Kokelaar, B. P. (2002). Pyroclastic density currents and the sedimentation of ignimbrites. Geological Society, London, Memoir 27.

Branney, M., & Acocella, V. (2015). In H. Sigurdsson (Ed.), The Encyclopedia of Volcanoes (Second Edition) (pp. 299-315). Amsterdam: Academic Press. https://doi.org/10.1016/B978-0-12-385938-9.00016-X

Brooker, M. R., Houghton, B. F., Wilson, C. J. N., & Gamble, J. A. (1993). Pyroclastic phases of a rhyolitic dome-building eruption: Puketarata tuff ring, Taupo Volcanic Zone, New Zealand. Bulletin of Volcanology, 55(6), 395-406. 10.1007/BF00301999

Brown, R. J., & D. M. Andrews, G. (2015). Chapter 36 - Deposits of Pyroclastic Density Currents A2 - Sigurdsson, Haraldur. In The Encyclopedia of Volcanoes (Second Edition) (pp. 631-648). Amsterdam: Academic Press.

Brown, S. K., Crosweller, H. S., Sparks, R. S. J., Cottrell, E., Deligne, N. I., Guerrero, N. O., Hobbs, L., Kiyosugi, K., Loughlin, S. C., Siebert, L., & Takarada, S. (2014). Characterisation of the Quaternary eruption record: analysis of the Large Magnitude Explosive Volcanic Eruptions (LaMEVE) database. Journal of Applied Volcanology, 3(1), 5. 10.1186/2191-5040-3-5

Bryan, S. E., Peate, I. U., Peate, D. W., Self, S., Jerram, D. A., Mawby, M. R., Marsh, J. S., & Miller, J. A. (2010). The largest volcanic eruptions on Earth. Earth-Science Reviews, 102(3), 207-229. https://doi.org/10.1016/j.earscirev.2010.07.001

Bullock, L. A., Gertisser, R., & O'Driscoll, B. (2018). Emplacement of the Rocche Rosse rhyolite lava flow (Lipari, Aeolian Islands). Bulletin of Volcanology, 80(5), 1-19.

Burgisser, A., & Gardner, J. E. (2005). Experimental constraints on degassing and permeability in volcanic conduit flow. Bulletin of Volcanology, 67(1), 42-56.10.1007/s00445-004-0359-5

Burgisser, A., Arbaret, L., Druitt, T. H., & Giachetti, T. (2011). Pre-explosive conduit conditions of the 1997 Vulcanian explosions at Soufrière Hills Volcano, Montserrat: II. Overpressure and depth distributions. Journal of Volcanology and Geothermal Research, 199(3), 193-205. https://doi.org/10.1016/j.jvolgeores.2010.11.014

Burgisser, A., & Degruyter, W. (2015). Magma ascent and degassing at shallow levels. In The encyclopedia of volcanoes (pp. 225-236): Elsevier.

Burgisser, A., Chevalier, L., Gardner, J. E., & Castro, J. M. (2017). The percolation threshold and permeability evolution of ascending magmas. Earth and Planetary Science Letters, 470, 37-47. https://doi.org/10.1016/j.epsl.2017.04.023

Burgisser, A., Arbaret, L., Martel, C., Forien, M., & Colombier, M. (2020). The role of oxides in the shallow vesiculation of ascending magmas. Journal of Volcanology and Geothermal Research, 406, 107072. https://doi.org/10.1016/j.jvolgeores.2020.107072

Bursik, M. (1993). Subplinian eruption mechanisms inferred from volatile and clast dispersal data. Journal of Volcanology and Geothermal Research, 57(1), 57-70. https://doi.org/10.1016/0377-0273(93)90031-L

Bursik, M. (2001). Effect of wind on the rise height of volcanic plumes. Geophysical Research Letters, 28(18), 3621-3624. doi:10.1029/2001GL013393

Bursik, M. I., Sparks, R. S. J., Gilbert, J. S., & Carey, S. N. (1992). Sedimentation of tephra by volcanic plumes: I. Theory and its comparison with a study of the Fogo A plinian deposit, Sao Miguel (Azores). Bulletin of Volcanology, 54(4), 329-344. doi:10.1007/bf00301486

Bursik, M., Sieh, K., & Meltzner, A. (2014). Deposits of the most recent eruption in the Southern Mono Craters, California: Description, interpretation and implications for regional marker tephras. Journal of Volcanology and Geothermal Research, 275, 114-131. https://doi.org/10.1016/j.jvolgeores.2014.02.015

Burt, R. M., Brown, S. J. A., Cole, J. W., Shelley, D., & Waight, T. E. (1998). Glass-bearing plutonic fragments from ignimbrites of the Okataina caldera complex, Taupo Volcanic Zone, New Zealand: remnants of a partially molten intrusion associated with preceding eruptions. Journal of Volcanology and Geothermal Research, 84(3), 209-237. https://doi.org/10.1016/S0377-0273(98)00039-0

Cabrera, A., Weinberg, R. F., & Wright, H. M. (2015). Magma fracturing and degassing associated with obsidian formation: the explosive–effusive transition. Journal of Volcanology and Geothermal Research, 298, 71-84.

Cáceres, F., Castruccio, Á., & Parada, M. A. (2018). Morphology, Effusion Rates, and Petrology of Postglacial Lavas of Laguna del Maule Volcanic Field, Chilean Andes, and Implications for Their Plumbing System. Geochemistry, Geophysics, Geosystems, 19(12), 4925-4944. https://doi.org/10.1029/2018GC007817

Cáceres, F., Wadsworth, F. B., Scheu, B., Colombier, M., Madonna, C., Cimarelli, C., Hess, K.-U., Kaliwoda, M., Ruthensteiner, B., & Dingwell, D. B. (2020). Can nanolites enhance eruption explosivity? Geology, 48(10), 997-1001.

Calder, E. S., Sparks, R. S. J., & Gardeweg, M. C. (2000). Erosion, transport and segregation of pumice and lithic clasts in pyroclastic flows inferred from ignimbrite at Lascar Volcano, Chile. Journal of Volcanology and Geothermal Research, 104(1), 201-235. https://doi.org/10.1016/S0377-0273(00)00207-9

Calder, E. S., Lavallée, Y., Kendrick, J. E., & Bernstein, M. (2015). Chapter 18 - Lava Dome Eruptions A2 - Sigurdsson, Haraldur. In The Encyclopedia of Volcanoes (Second Edition) (pp. 343-362). Amsterdam: Academic Press.

Campbell, M. E., Russell, J. K., & Porritt, L. A. (2013). Thermomechanical milling of accessory lithics in volcanic conduits. Earth and Planetary Science Letters, 377-378, 276-286. https://doi.org/10.1016/j.epsl.2013.07.008

Carazzo, G., Tait, S., Michaud-Dubuy, A., Fries, A., & Kaminski, E. (2020). Transition from stable column to partial collapse during the 79 cal CE P3 Plinian eruption of Mt. Pelée volcano (Lesser Antilles). Journal of Volcanology and Geothermal Research, 392, 106764. https://doi.org/10.1016/j.jvolgeores.2019.106764

Carey, R. J., Houghton, B. F., Sable, J. E., & Wilson, C. J. N. (2007). Contrasting grain size and componentry in complex proximal deposits of the 1886 Tarawera basaltic Plinian eruption. Bulletin of Volcanology, 69(8), 903-926. 10.1007/s00445-007-0117-6

Carey, R. J., Houghton, B. F., & Thordarson, T. (2008). Contrasting styles of welding observed in the proximal Askja 1875 eruption deposits II: Local welding. Journal of Volcanology and Geothermal Research, 171(1), 20-44. https://doi.org/10.1016/j.jvolgeores.2007.11.017

Carey, R. J., Houghton, B. F., & Thordarson, T. (2009). Abrupt shifts between wet and dry phases of the 1875 eruption of Askja Volcano: Microscopic evidence for macroscopic dynamics. Journal of Volcanology and Geothermal Research, 184(3), 256-270. https://doi.org/10.1016/j.jvolgeores.2009.04.003

Carey, R. J., Houghton, B. F., & Thordarson, T. (2010). Tephra dispersal and eruption dynamics of wet and dry phases of the 1875 eruption of Askja Volcano, Iceland. Bulletin of Volcanology, 72(3), 259-278. 10.1007/s00445-009-0317-3

Carey, S., & Sigurdsson, H. (1989). The intensity of plinian eruptions. Bulletin of Volcanology, 51(1), 28-40. doi:10.1007/bf01086759

Carey, S., & Bursik, M. (2015). Chapter 32 - Volcanic Plumes A2 - Sigurdsson, Haraldur. In The Encyclopedia of Volcanoes (Second Edition) (pp. 571-585). Amsterdam: Academic Press.

Caricchi, L., Burlini, L., Ulmer, P., Gerya, T., Vassalli, M., & Papale, P. (2007). Non-Newtonian rheology of crystal-bearing magmas and implications for magma ascent dynamics. Earth and Planetary Science Letters, 264(3), 402-419. https://doi.org/10.1016/j.epsl.2007.09.032

Caricchi, L., Pommier, A., Pistone, M., Castro, J., Burgisser, A., & Perugini, D. (2011). Strain-induced magma degassing: insights from simple-shear experiments on bubble bearing melts. Bulletin of Volcanology, 73(9), 1245-1257. 10.1007/s00445-011-0471-2

Caricchi, L., & Blundy, J. (2015). The temporal evolution of chemical and physical properties of magmatic systems. Geological Society, London, Special Publications, 422, SP422. 411.

Carrigan, C. R., Schubert, G., & Eichelberger, J. C. (1992). Thermal and dynamical regimes of single- and two-phase magmatic flow in dikes. Journal of Geophysical Research: Solid Earth, 97(B12), 17377-17392. doi:10.1029/92JB01244

Cas, R., & Wright, J. V. (1987). Volcanic successions modern and ancient: A geological approach to processes, products and successions: Springer Science & Business Media.

Cashman, K. V. (1992). Groundmass crystallization of Mount St. Helens dacite, 1980–1986: a tool for interpreting shallow magmatic processes. Contributions to Mineralogy and Petrology, 109(4), 431-449. doi:10.1007/bf00306547

Cashman, K. V. (2004). Volatile controls on magma ascent and eruption. The state of the planet: Frontiers and challenges in geophysics, 109-124.

Cashman, K., & Blundy, J. (2000). Degassing and crystallization of ascending andesite and dacite. Philosophical Transactions of the Royal Society of London A: Mathematical, Physical and Engineering Sciences, 358(1770), 1487-1513.

Cashman, K. V., & Sparks, R. S. J. (2013). How volcanoes work: A 25 year perspective. Bulletin, 125(5-6), 664-690.

Cashman, K., & Biggs, J. (2014). Common processes at unique volcanoes—a volcanological conundrum. Frontiers in Earth Science, 2(28) 10.3389/feart.2014.00028

Cashman, K. V., & Giordano, G. (2014). Calderas and magma reservoirs. Journal of Volcanology and Geothermal Research, 288, 28-45. https://doi.org/10.1016/j.jvolgeores.2014.09.007

Cashman, K. V., & Scheu, B. (2015). Chapter 25 - Magmatic Fragmentation A2 - Sigurdsson, Haraldur. In The Encyclopedia of Volcanoes (Second Edition) (pp. 459-471). Amsterdam: Academic Press.

Cashman, K. V., Mangan, M. T., & Newman, S. (1994). Surface degassing and modifications to vesicle size distributions in active basalt flows. Journal of Volcanology and Geothermal Research, 61(1-2), 45-68.

Cashman, K. V., Sparks, R. S. J., & Blundy, J. D. (2017). Vertically extensive and unstable magmatic systems: a unified view of igneous processes. Science, 355(6331), eaag3055.

Cassidy, M., Manga, M., Cashman, K., & Bachmann, O. (2018). Controls on explosive-effusive volcanic eruption styles. Nature Communications, 9(1), 2839. 10.1038/s41467-018-05293-3

Castro, J. M., Cordonnier, B., Tuffen, H., Tobin, M. J., Puskar, L., Martin, M. C., & Bechtel, H. A. (2012a). The role of melt-fracture degassing in defusing explosive rhyolite eruptions at volcán Chaitén. Earth and Planetary Science Letters, 333-334, 63-69. https://doi.org/10.1016/j.epsl.2012.04.024

Castro, J. M., Burgisser, A., Schipper, C. I., & Mancini, S. (2012b). Mechanisms of bubble coalescence in silicic magmas. Bulletin of Volcanology, 74(10), 2339-2352. 10.1007/s00445-012-0666-1

Castro, J. M., Schipper, C. I., Mueller, S. P., Militzer, A. S., Amigo, A., Parejas, C. S., & Jacob, D. (2013). Storage and eruption of near-liquidus rhyolite magma at Cordón Caulle, Chile. Bulletin of Volcanology, 75(4), 702. 10.1007/s00445-013-0702-9

Charlier, B. L. A., Peate, D. W., Wilson, C. J. N., Lowenstern, J. B., Storey, M., & Brown, S. J. A. (2003). Crystallisation ages in coeval silicic magma bodies: 238U–230Th disequilibrium evidence from the Rotoiti and Earthquake Flat eruption deposits, Taupo Volcanic Zone, New Zealand. Earth and Planetary Science Letters, 206(3), 441-457. doi:https://doi.org/10.1016/S0012-821X(02)01109-3

Cheng, H.C., Lemlich, R., 1983. Errors in the measurement of bubble-size distribution in foam. Ind. Eng. Chem. Fundam. 22, 105–109.

Christiansen, R. L. (2001). The quaternary and pliocene Yellowstone Plateau volcanic field of Wyoming, Idaho, and Montana (Vol. 729). US Department of the Interior, US Geological Survey.

Christiansen, R. L., & Peterson, D. W. (1981). Chronology of the 1980 eruptive activity. US Geol. Surv. Prof. Pap, 1250, 17-30.

Cioni, R., Marianelli, P., & Sbrana, A. (1992). Dynamics of the AD 79 eruption: stratigraphic, sedimentologic and geochemical data on the successions of the Somma-Vesuvius southern sector. Acta Vulcanologica, 2, 109-123.

Cioni, R., Sulpizio, R., & Garruccio, N. (2003). Variability of the eruption dynamics during a Subplinian event: the Greenish Pumice eruption of Somma–Vesuvius (Italy). Journal of Volcanology and Geothermal Research, 124(1), 89-114. https://doi.org/10.1016/S0377-0273(03)00070-2

Cioni, R., Bertagnini, A., Santacroce, R., & Andronico, D. (2008). Explosive activity and eruption scenarios at Somma-Vesuvius (Italy): Towards a new classification scheme. Journal of Volcanology and Geothermal Research, 178(3), 331-346. doi:https://doi.org/10.1016/j.jvolgeores.2008.04.024

Cioni, R., Bertagnini, A., Andronico, D., Cole, P. D., & Mundula, F. (2011). The 512 AD eruption of Vesuvius: complex dynamics of a small scale subplinian event. Bulletin of Volcanology, 73(7), 789-810. 10.1007/s00445-011-0454-3

Cioni, R., Pistolesi, M., Bertagnini, A., Bonadonna, C., Hoskuldsson, A., & Scateni, B. (2014). Insights into the dynamics and evolution of the 2010 Eyjafjallajökull summit eruption (Iceland) provided by volcanic ash textures. Earth and Planetary Science Letters, 394, 111-123. https://doi.org/10.1016/j.epsl.2014.02.051

Cioni, R., Pistolesi, M., & Rosi, M. (2015). Chapter 29 - Plinian and Subplinian Eruptions A2 - Sigurdsson, Haraldur. In The Encyclopedia of Volcanoes (Second Edition) (pp. 519-535). Amsterdam: Academic Press

Cioni, R., Pistolesi, M., Pompilio, M., & Scaillet, B. (2021). In P. Papale (Ed.), Forecasting and Planning for Volcanic Hazards, Risks, and Disasters (Vol. 2, pp. 285-328): Elsevier. https://doi.org/10.1016/B978-0-12-818082-2.00007-X

Clarke, A. (2013). Unsteady explosive activity: Vulcanian eruptions. Fagents SA, Tracy KP G, Rosaly MC L (eds) Modeling Volcanic Processes: The Physics and Mathematics of Volcanism. Cambridge University Press, England, 129-152.

Clarke, A., Voight, B., Neri, A., & Macedonio, G. (2002). Transient dynamics of vulcanian explosions and column collapse. Nature, 415(6874), 897-901.

Clarke, A. B., Esposti Ongaro, T., & Belousov, A. (2015). Chapter 28 - Vulcanian Eruptions A2 - Sigurdsson, Haraldur. In The Encyclopedia of Volcanoes (Second Edition) (pp. 505-518). Amsterdam: Academic Press.

Cluzel, N., Laporte, D., Provost, A., & Kannewischer, I. (2008). Kinetics of heterogeneous bubble nucleation in rhyolitic melts: implications for the number density of bubbles in volcanic conduits and for pumice textures. Contributions to Mineralogy and Petrology, 156(6), 745-763. 10.1007/s00410-008-0313-1

Cole, J.W. (1966). Tarawera volcanic complex. PhD thesis, Victoria University of Wellington.

Cole, J. W. (1970). Structure and eruptive history of the Tarawera Volcanic Complex. New Zealand Journal of Geology and Geophysics, 13(4), 879-902. 10.1080/00288306.1970.10418208

Cole, J. W. (1990). Structural control and origin of volcanism in the Taupo volcanic zone, New Zealand. Bulletin of Volcanology, 52(6), 445-459. doi:10.1007/bf00268925

Cole, J. W., & Spinks, K. D. (2009). Caldera volcanism and rift structure in the Taupo Volcanic Zone, New Zealand. Geological Society, London, Special Publications, 327(1), 9-29.

Cole, J. W., Darby, D. J., & Stern, T. A. (1995). Taupo Volcanic Zone and Central Volcanic Region Backarc Structures of North Island, New Zealand. In B. Taylor (Ed.), Backarc Basins: Tectonics and Magmatism (pp. 1-28). Boston, MA: Springer US.

Cole, J. W., Milner, D., & Spinks, K. (2005). Calderas and caldera structures: a review. Earth-Science Reviews, 69(1-2), 1-26. https://doi.org/10.1016/j.earscirev.2004.06.004

Cole, J. W., Spinks, K. D., Deering, C. D., Nairn, I. A., & Leonard, G. S. (2010). Volcanic and structural evolution of the Okataina Volcanic Centre; dominantly silicic volcanism associated with the Taupo Rift, New Zealand. Journal of Volcanology and Geothermal Research, 190(1), 123-135. https://doi.org/10.1016/j.jvolgeores.2009.08.011

Cole, J. W., Deering, C. D., Burt, R. M., Sewell, S., Shane, P. A. R., & Matthews, N. E. (2014). Okataina Volcanic Centre, Taupo Volcanic Zone, New Zealand: A review of volcanism and synchronous pluton development in an active, dominantly silicic caldera system. Earth-Science Reviews, 128, 1-17. https://doi.org/10.1016/j.earscirev.2013.10.008

Cole, P. D., Queiroz, G., Wallenstein, N., Gaspar, J. L., Duncan, A. M., & Guest, J. E. (1995). An historic subplinian/phreatomagmatic eruption: the 1630 AD eruption of Furnas volcano, Sa˜o Miguel, Azores. Journal of Volcanology and Geothermal Research, 69(1), 117-135. https://doi.org/10.1016/0377-0273(95)00033-X

Cole, P. D., Guest, J. E., Queiroz, G., Wallenstein, N., Pacheco, J. M., Gaspar, J. L., . . . Duncan, A. M. (1999). Styles of volcanism and volcanic hazards on Furnas volcano, São Miguel, Azores. Journal of Volcanology and Geothermal Research, 92(1), 39-53. https://doi.org/10.1016/S0377-0273(99)00066-9

Cole, P. D., Calder, E. S., Sparks, R. S. J., Clarke, A. B., Druitt, T. H., Young, S. R., Norton, G. E. (2002). Deposits from dome-collapse and fountain-collapse pyroclastic flows at Soufrière Hills Volcano, Montserrat. Geological Society, London, Memoirs, 21(1), 231-262. doi:10.1144/gsl.mem.2002.021.01.11

Cole, P.D., Smith, P., Stinton, A., Odbert, H., Bernstein, M., Komorowski, J., & Stewart, R. (2014). Vulcanian explosions at Soufrière Hills Volcano, Montserrat between 2008 and 2010. Geological Society, London, Memoirs, 39(1), 93-111.

Colucci, S., & Papale, P. (2021). Deep Magma Transport Control on the Size and Evolution of Explosive Volcanic Eruptions. Frontiers in Earth Science, 9(436) 10.3389/feart.2021.681083

Colombier, M., Wadsworth, F. B., Gurioli, L., Scheu, B., Kueppers, U., Di Muro, A., & Dingwell, D. B. (2017). The evolution of pore connectivity in volcanic rocks. Earth and Planetary Science Letters, 462, 99-109. https://doi.org/10.1016/j.epsl.2017.01.011

Contreras Hidalgo, C. (2020). Silicic Eruptive Transitions of Laguna Del Maule. PhD thesis, the University of Bristol.

Coombs, M. L., & Gardner, J. E. (2001). Shallow-storage conditions for the rhyolite of the 1912 eruption at Novarupta, Alaska. Geology, 29(9), 775-778.

Costa, A. (2005). Viscosity of high crystal content melts: Dependence on solid fraction. Geophysical Research Letters, 32(22) https://doi.org/10.1029/2005GL024303

Costa, A., Melnik, O., & Sparks, R. S. J. (2007). Controls of conduit geometry and wallrock elasticity on lava dome eruptions. Earth and Planetary Science Letters, 260(1), 137-151. https://doi.org/10.1016/j.epsl.2007.05.024

Costa, A., Sparks, R. S. J., Macedonio, G., & Melnik, O. (2009). Effects of wall-rock elasticity on magma flow in dykes during explosive eruptions. Earth and Planetary Science Letters, 288(3), 455-462. https://doi.org/10.1016/j.epsl.2009.10.006

Costa, A., Gottsmann, J., Melnik, O., & Sparks, R. S. J. (2011). A stress-controlled mechanism for the intensity of very large magnitude explosive eruptions. Earth and Planetary Science Letters, 310(1), 161-166. https://doi.org/10.1016/j.epsl.2011.07.024

Costa, F. (2008). Residence times of silicic magmas associated with calderas. Developments in volcanology, 10, 1-55.

Craig, H., Wilson, T., Stewart, C., Outes, V., Villarosa, G., & Baxter, P. (2016). Impacts to agriculture and critical infrastructure in Argentina after ashfall from the 2011 eruption of the Cordón Caulle volcanic complex: an assessment of published damage and function thresholds. Journal of Applied Volcanology, 5(1), 7. 10.1186/s13617-016-0046-1

Cronin, S. J., Hedley, M. J., Neall, V. E., & Smith, R. G. (1998). Agronomic impact of tephra fallout from the 1995 and 1996 Ruapehu Volcano eruptions, New Zealand. Environmental Geology, 34(1), 21-30.

Crosweller, H. S., Arora, B., Brown, S. K., Cottrell, E., Deligne, N. I., Guerrero, N. O., . . . Venzke, E. (2012). Global database on large magnitude explosive volcanic eruptions (LaMEVE). Journal of Applied Volcanology, 1(1), 4. 10.1186/2191-5040-1-4

Cutler, N. A., Streeter, R., Marple, J., Shotter, L., Yeoh, J., & Dugmore, A. (2018). Tephra transformations: variable preservation of tephra layers from two well-studied eruptions. Bulletin of Volcanology, 80(11), 77.

Cutler, N. A., Streeter, R. T., Engwell, S. L., Bolton, M. S., Jensen, B. J. L., & Dugmore, A. J. (2020). How does tephra deposit thickness change over time? A calibration exercise based on the 1980 Mount St Helens tephra deposit. Journal of Volcanology and Geothermal Research, 399, 106883. https://doi.org/10.1016/j.jvolgeores.2020.106883

D'Oriano, C., Poggianti, E., Bertagnini, A., Cioni, R., Landi, P., Polacci, M., & Rosi, M. (2005). Changes in eruptive style during the A.D. 1538 Monte Nuovo eruption (Phlegrean Fields, Italy): the role of syn-eruptive crystallization. Bulletin of Volcanology, 67(7), 601-621. doi:10.1007/s00445-004-0397-z

D'Oriano, C., Cioni, R., Bertagnini, A., Andronico, D., & Cole, P. D. (2011). Dynamics of ash-dominated eruptions at Vesuvius: the post-512 AD AS1a event. Bulletin of Volcanology, 73(6), 699-715. 10.1007/s00445-010-0432-1

Danišík, M., Shane, P., Schmitt, A. K., Hogg, A., Santos, G. M., Storm, S, Lindsay, J. M. (2012). Re-anchoring the late Pleistocene tephrochronology of New Zealand based on concordant radiocarbon ages and combined 238U/230Th disequilibrium and (U–Th)/He zircon ages. Earth and Planetary Science Letters, 349-350, 240-250. doi:https://doi.org/10.1016/j.epsl.2012.06.041

Darragh, M., Cole, J., Nairn, I., & Shane, P. (2006). Pyroclastic stratigraphy and eruption dynamics of the 21.9 ka Okareka and 17.6 ka Rerewhakaaitu eruption episodes from Tarawera Volcano, Okataina Volcanic Centre, New Zealand. New Zealand Journal of Geology and Geophysics, 49(3), 309-328. doi:10.1080/00288306.2006.9515170

Davì, M., De Rosa, R., Donato, P., & Sulpizio, R. (2011). The Lami pyroclastic succession (Lipari, Aeolian Islands): A clue for unravelling the eruptive dynamics of the Monte Pilato rhyolitic pumice cone. Journal of Volcanology and Geothermal Research, 201(1), 285-300. https://doi.org/10.1016/j.jvolgeores.2010.09.010

Davy, B. W., & Caldwell, T. G. (1998). Gravity, magnetic and seismic surveys of the caldera complex, Lake Taupo, North Island, New Zealand. Journal of Volcanology and Geothermal Research, 81(1), 69-89. doi:https://doi.org/10.1016/S0377-0273(97)00074-7

de' Michieli Vitturi, M., Clarke, A. B., Neri, A., & Voight, B. (2008). Effects of conduit geometry on magma ascent dynamics in dome-forming eruptions. Earth and Planetary Science Letters, 272(3), 567-578. https://doi.org/10.1016/j.epsl.2008.05.025

de Ronde, C. E. J., Walker, S. L., LeBlanc, C., Davy, B. W., Fornari, D. J., Tontini, F. C., Scott, B. J., Seebeck, H., Stewart, T. J., Mazot, A., Nicol, A., & Tivey, M. A. (2016a). Reconstruction of the geology and structure of Lake Rotomahana and its hydrothermal systems from high-resolution multibeam mapping and seismic surveys: Effects of the 1886 Tarawera Rift eruption. Journal of Volcanology and Geothermal Research, 314, 57-83. https://doi.org/10.1016/j.jvolgeores.2016.02.002

de Ronde, C. E. J., Fornari, D. J., Ferrini, V. L., Walker, S. L., Davy, B. W., LeBlanc, C., Caratori Tontini, F., Kukulya, A. L., & Littlefield, R. H. (2016b). The Pink and White Terraces of Lake Rotomahana: what was their fate after the 1886 Tarawera Rift eruption? Journal of Volcanology and Geothermal Research, 314, 126-141. https://doi.org/10.1016/j.jvolgeores.2016.02.003

de Ronde, C. E., Caratori Tontini, F., & Keam, R. F. (2019). Where are the Pink and White Terraces of Lake Rotomahana?. Journal of the Royal Society of New Zealand, 49(1), 36-59.

de Silva, S., & Lindsay, J. M. (2015). In H. Sigurdsson (Ed.), The Encyclopedia of Volcanoes (Second Edition) (pp. 273-297). Amsterdam: Academic Press. https://doi.org/10.1016/B978-0-12-385938-9.00015-8

Decker, R. (1990). How often does a Minoan eruption occur. Thera and the Aegean world III, 2, 444-452.

Deering, C. D. (2009). Cannibalization of an amphibole-rich andesitic progenitor induced by caldera-collapse during the Matahina eruption: Evidence from amphibole compositions. American Mineralogist, 94(8-9), 1162-1174.

Deering, C. D., Cole, J. W., & Vogel, T. A. (2011). Extraction of crystal-poor rhyolite from a hornblende-bearing intermediate mush: a case study of the caldera-forming Matahina eruption, Okataina volcanic complex. Contributions to Mineralogy and Petrology, 161(1), 129-151. doi:10.1007/s00410-010-0524-0

Degruyter, W., Bachmann, O., & Burgisser, A. (2010). Controls on magma permeability in the volcanic conduit during the climactic phase of the Kos Plateau Tuff eruption (Aegean Arc). Bulletin of Volcanology, 72(1), 63. 10.1007/s00445-009-0302-x

Degruyter, W., Bachmann, O., Burgisser, A., & Manga, M. (2012). The effects of outgassing on the transition between effusive and explosive silicic eruptions. Earth and Planetary Science Letters, 349-350, 161-170. https://doi.org/10.1016/j.epsl.2012.06.056

Del Negro, C., Cappello, A., & Ganci, G. (2016). Quantifying lava flow hazards in response to effusive eruption. Bulletin, 128(5-6), 752-763.

Deligne, N. I., Horspool, N., Canessa, S., Matcham, I., Williams, G. T., Wilson, G., & Wilson, T. M. (2017). Evaluating the impacts of volcanic eruptions using RiskScape. Journal of Applied Volcanology, 6(1), 1-21. https://doi.org/10.1186/s13617-017-0069-2

Dellino, P., Mele, D., Bonasia, R., Braia, G., La Volpe, L., & Sulpizio, R. (2005). The analysis of the influence of pumice shape on its terminal velocity. Geophysical Research Letters, 32(21) doi:10.1029/2005GL023954

Dellino, P., Gudmundsson, M. T., Larsen, G., Mele, D., Stevenson, J. A., Thordarson, T., & Zimanowski, B. (2012). Ash from the Eyjafjallajökull eruption (Iceland): Fragmentation processes and aerodynamic behavior. Journal of Geophysical Research: Solid Earth, 117(B9), n/a-n/a. doi:10.1029/2011JB008726

DeMets, C., Gordon, R. G., Argus, D. F., & Stein, S. (1994). Effect of recent revisions to the geomagnetic reversal time scale on estimates of current plate motions. Geophysical Research Letters, 21(20), 2191-2194. doi:10.1029/94GL02118

Devine, J. D., Rutherford, M. J., & Gardner, J. E. (1998). Petrologic determination of ascent rates for the 1995–1997 Soufriere Hills Volcano andesitic magma. Geophysical Research Letters, 25(19), 3673-3676. doi:10.1029/98GL00912.

Di Genova, D., Brooker, R. A., Mader, H. M., Drewitt, J. W., Longo, A., Deubener, J., Neuville, D. R., Fanara, S., Shebanova, O., & Anzellini, S. (2020). In situ observation of nanolite growth in volcanic melt: A driving force for explosive eruptions. Science advances, 6(39), eabb0413.

Di Muro, A., Neri, A., & Rosi, M. (2004). Contemporaneous convective and collapsing eruptive dynamics: The transitional regime of explosive eruptions. Geophysical Research Letters, 31(10), n/a-n/a. doi:10.1029/2004GL019709

Di Muro, A., Rosi, M., Aguilera, E., Barbieri, R., Massa, G., Mundula, F., & Pieri, F. (2008). Transport and sedimentation dynamics of transitional explosive eruption columns: the example of the 800 BP Quilotoa Plinian eruption (Ecuador). Journal of Volcanology and Geothermal Research, 174(4), 307-324.

Di Piazza, A., Vona, A., Mollo, S., De Astis, G., Soto, G. J., & Romano, C. (2019). Unsteady magma discharge during the “El Retiro” subplinian eruption (Turrialba volcano, Costa Rica): Insights from textural and petrological analyses. Journal of Volcanology and Geothermal Research, 371, 101-115. https://doi.org/10.1016/j.jvolgeores.2019.01.004

Dingwell, D. B. (1996). Volcanic Dilemma--Flow or Blow? Science, 273(5278), 1054-1055.

Dingwell, D. B., Lavallée, Y., Hess, K. U., Flaws, A., Marti, J., Nichols, A. R. L., Gilg, H. A., & Schillinger, B. (2016). Eruptive shearing of tube pumice: pure and simple. Solid Earth, 7(5), 1383-1393. 10.5194/se-7-1383-2016

Dioguardi, F., Mele, D., Dellino, P., & Dürig, T. (2017). The terminal velocity of volcanic particles with shape obtained from 3D X-ray microtomography. Journal of Volcanology and Geothermal Research, 329, 41-53. https://doi.org/10.1016/j.jvolgeores.2016.11.013

Dirksen, O., Humphreys, M. C. S., Pletchov, P., Melnik, O., Demyanchuk, Y., Sparks, R. S. J., & Mahony, S. (2006). The 2001–2004 dome-forming eruption of Shiveluch volcano, Kamchatka: Observation, petrological investigation and numerical modelling. Journal of Volcanology and Geothermal Research, 155(3), 201-226. https://doi.org/10.1016/j.jvolgeores.2006.03.029

Di Vito, M. A., Acocella, V., Aiello, G., Barra, D., Battaglia, M., Carandente, A., Del Gaudio, C., de Vita, S., Ricciardi, G. P., Ricco, C., Scandone, R., & Terrasi, F. (2016). Magma transfer at Campi Flegrei caldera (Italy) before the 1538 AD eruption. Scientific reports, 6(1), 32245. 10.1038/srep32245

Dominguez, L., Bonadonna, C., Forte, P., Jarvis, P. A., Cioni, R., Mingari, L., Bran, D., & Panebianco, J. E. (2020). Aeolian Remobilisation of the 2011-Cordón Caulle Tephra-Fallout Deposit: Example of an Important Process in the Life Cycle of Volcanic Ash. Frontiers in Earth Science, 7(343) 10.3389/feart.2019.00343

Donnelly-Nolan, J. M., Champion, D. E., Miller, C. D., Grove, T. L., & Trimble, D. A. (1990). Post-11,000-year volcanism at Medicine Lake Volcano, Cascade Range, northern California. Journal of Geophysical Research: Solid Earth, 95(B12), 19693-19704.

Druitt, T. H. (2014). New insights into the initiation and venting of the Bronze-Age eruption of Santorini (Greece), from component analysis. Bulletin of Volcanology, 76(2), 794. 10.1007/s00445-014-0794-x

Druitt, T. H., & Kokelaar, B. P. (2002). The eruption of Soufrière Hills volcano, Montserrat, from 1995 to 1999.

Druitt, T., Young, S., Baptie, B., Bonadonna, C., Calder, E., Clarke, A., Cole, P., Harford, C., Herd, R., & Luckett, R. (2002). Episodes of cyclic Vulcanian explosive activity with fountain collapse at Soufrière Hills Volcano, Montserrat. Memoirs-Geological Society of London, 21, 281-306.

Dufek, J., Esposti Ongaro, T., & Roche, O. (2015). Chapter 35 - Pyroclastic Density Currents: Processes and Models A2 - Sigurdsson, Haraldur. In The Encyclopedia of Volcanoes (Second Edition) (pp. 617-629). Amsterdam: Academic Press.

Dunbar, N. W., & Kyle, P. R. (1992). Volatile contents of obsidian clasts in tephra from the Taupo Volcanic Zone, New Zealand: Implications to eruptive processes. Journal of Volcanology and Geothermal Research, 49(1), 127-145. https://doi.org/10.1016/0377-0273(92)90009-3

Dürig, T., Bowman, M. H., White, J. D., Murch, A., Mele, D., Verolino, A., & Dellino, P. (2018). PARTIcle Shape ANalyzer PARTISAN–an open source tool for multi-standard two-dimensional particle morphometry analysis. Annals of Geophysics, 61, 31.

Edmonds, M., Oppenheimer, C., Pyle, D. M., Herd, R. A., & Thompson, G. (2003). SO2 emissions from Soufrière Hills Volcano and their relationship to conduit permeability, hydrothermal interaction and degassing regime. Journal of Volcanology and Geothermal Research, 124(1), 23-43. doi:https://doi.org/10.1016/S0377-0273(03)00041-6

Edmonds, M., Cashman, K. V., Holness, M., & Jackson, M. (2019). Architecture and dynamics of magma reservoirs. In: The Royal Society Publishing.

Edwards, M. J., Eychenne, J., & Pioli, L. (2021). Formation and Dispersal of Ash at Open Conduit Basaltic Volcanoes: Lessons From Etna. Frontiers in Earth Science, 9(757) 10.3389/feart.2021.709657

Eichelberger, J. C. (1995). Silicic Volcanism: Ascent of Viscous Magmas from Crustal Reservoirs. Annual Review of Earth and Planetary Sciences, 23(1), 41-63. doi:10.1146/annurev.ea.23.050195.000353

Eichelberger, J. C., Carrigan, C. R., Westrich, H. R., & Price, R. H. (1986). Non-explosive silicic volcanism. Nature, 323, 598. 10.1038/323598a0

Elissondo, M., Baumann, V., Bonadonna, C., Pistolesi, M., Cioni, R., Bertagnini, A., Biass, S., Herrero, J. C., & Gonzalez, R. (2016). Chronology and impact of the 2011 Cordón Caulle eruption, Chile. Nat. Hazards Earth Syst. Sci., 16(3), 675-704. 10.5194/nhess-16-675-2016

Ellis, B., & Branney, M. J. (2010). Silicic phreatomagmatism in the Snake River Plain: the Deadeye Member. Bulletin of Volcanology, 72(10), 1241-1257. 10.1007/s00445-010-0400-9

Ellis, S., Heise, W., Kissling, W., Villamor, P., & Schreurs, G. (2014). The effect of crustal melt on rift dynamics: case study of the Taupo Volcanic Zone. New Zealand Journal of Geology and Geophysics, 57(4), 453-458.

Engwell, S., & Eychenne, J. (2016). In S. Mackie, K. Cashman, H. Ricketts, A. Rust, & M. Watson (Eds.), Volcanic Ash (pp. 67-85): Elsevier. https://doi.org/10.1016/B978-0-08-100405-0.00007-0

Fierstein, J., & Hildreth, W. (1992). The plinian eruptions of 1912 at Novarupta, Katmai National Park, Alaska. Bulletin of Volcanology, 54(8), 646-684. doi:10.1007/bf00430778

Fink, J. H. (1990). Lava Flows and Domes. Emplacement Mechanisms and Hazard Implications. IAVCEI Proceedings in Volcanology (Berlin; Heidelberg: Springer).

Fink, J. H., & Anderson, S. W. (2000). Lava domes and coulees. Encyclopedia of volcanoes, 307-319.

Fink, J. H., Malin, M. C., & Anderson, S. W. (1990). Intrusive and extrusive growth of the Mount St Helens lava dome. Nature, 348, 435. doi:10.1038/348435a0

Fisher, R. V., & Schmincke, H.-U. (1984). Pyroclastic rocks: Springer Science & Business Media.

Flude, S., & Storey, M. (2016). 40Ar/39Ar age of the Rotoiti Breccia and Rotoehu Ash, Okataina Volcanic Complex, New Zealand, and identification of heterogeneously distributed excess 40Ar in supercooled crystals. Quaternary Geochronology, 33, 13-23. https://doi.org/10.1016/j.quageo.2016.01.002

Folch, A. (2012). A review of tephra transport and dispersal models: Evolution, current status, and future perspectives. Journal of Volcanology and Geothermal Research, 235-236, 96-115. https://doi.org/10.1016/j.jvolgeores.2012.05.020

Formenti, Y., Druitt, T. H., & Kelfoun, K. (2003). Characterisation of the 1997 Vulcanian explosions of Soufrière Hills Volcano, Montserrat, by video analysis. Bulletin of Volcanology, 65(8), 587-605. doi:10.1007/s00445-003-0288-8

Forni, F., Degruyter, W., Bachmann, O., De Astis, G., & Mollo, S. (2018). Long-term magmatic evolution reveals the beginning of a new caldera cycle at Campi Flegrei. Science advances, 4(11), eaat9401.

Forte, P., Domínguez, L., Bonadonna, C., Gregg, C. E., Bran, D., Bird, D., & Castro, J. M. (2018). Ash resuspension related to the 2011–2012 Cordón Caulle eruption, Chile, in a rural community of Patagonia, Argentina. Journal of Volcanology and Geothermal Research, 350, 18-32. https://doi.org/10.1016/j.jvolgeores.2017.11.021

Freundt, A., & Rosi, M. (1998). From magma to tephra (modelling physical processes of explosive volcanic eruptions). ELSEVIER, 1-318.

Froggatt, P. C., & Lowe, D. J. (1990). A review of late Quaternary silicic and some other tephra formations from New Zealand: Their stratigraphy, nomenclature, distribution, volume, and age. New Zealand Journal of Geology and Geophysics, 33(1), 89-109. 10.1080/00288306.1990.10427576

Gabrielsen, H., Procter, J., Rainforth, H., Black, T., Harmsworth, G., & Pardo, N. (2017). Reflections from an indigenous community on volcanic event management, communications and resilience. In Observing the volcano world (pp. 463-479): Springer.

Gallagher, A., Montanaro, C., Cronin, S., Scott, B., Dingwell, D. B., & Scheu, B. (2020). Hydrothermal eruption dynamics reflecting vertical variations in host rock geology and geothermal alteration, Champagne Pool, Wai-o-tapu, New Zealand. Bulletin of Volcanology, 82(12), 77. 10.1007/s00445-020-01414-3

Gaonac'h, H., Lovejoy, S., & Schertzer, D. (2005). Scaling vesicle distributions and volcanic eruptions. Bulletin of Volcanology, 67(4), 350-357. 10.1007/s00445-004-0376-4

Gardner, C. A., Cashman, K. V., & Neal, C. A. (1998). Tephra-fall deposits from the 1992 eruption of Crater Peak, Alaska: implications of clast textures for eruptive processes. Bulletin of Volcanology, 59(8), 537-555. 10.1007/s004450050208

Gardner, J. E. (2007). Bubble coalescence in rhyolitic melts during decompression from high pressure. Journal of Volcanology and Geothermal Research, 166(3), 161-176. https://doi.org/10.1016/j.jvolgeores.2007.07.006

Gardner, J. E., & Denis, M.-H. (2004). Heterogeneous bubble nucleation on Fe-Ti oxide crystals in high-silica rhyolitic melts1 1Associate editor: J. K. Russell. Geochimica et Cosmochimica Acta, 68(17), 3587-3597. https://doi.org/10.1016/j.gca.2004.02.021

Gardner, J. E., Thomas, R. M. E., Jaupart, C., & Tait, S. (1996). Fragmentation of magma during Plinian volcanic eruptions. Bulletin of Volcanology, 58(2), 144-162. 10.1007/s004450050132

Gardner, J. E., Hilton, M., & Carroll, M. R. (1999). Experimental constraints on degassing of magma: isothermal bubble growth during continuous decompression from high pressure. Earth and Planetary Science Letters, 168(1-2), 201-218.

Gardner, J. N., Goff, F., Kelley, S., & Jacobs, E. (2010). Rhyolites and associated deposits of the Valles-Toledo caldera complex. New Mexico Geology, 32(1), 3-18.

Gardner, J. E., Llewellin, E. W., Watkins, J. M., & Befus, K. S. (2017). Formation of obsidian pyroclasts by sintering of ash particles in the volcanic conduit. Earth and Planetary Science Letters, 459, 252-263. https://doi.org/10.1016/j.epsl.2016.11.037

Gardner, J. E., Wadsworth, F. B., Llewellin, E. W., Watkins, J. M., & Coumans, J. P. (2018). Experimental sintering of ash at conduit conditions and implications for the longevity of tuffisites. Bulletin of Volcanology, 80(3), 23. 10.1007/s00445-018-1202-8

Gardner, J. E., Wadsworth, F. B., Llewellin, E. W., Watkins, J. M., & Coumans, J. P. (2019). Experimental constraints on the textures and origin of obsidian pyroclasts. Bulletin of Volcanology, 81(4), 22. 10.1007/s00445-019-1283-z

Geshi, N., & Nakagawa, M. (2018). Overview of the Special Issue "Progress of Studies on Caldera-forming Eruptions and Future Problems". Journal of Geography (Chigaku Zasshi), 127(2), 103-105. doi:10.5026/jgeography.127.103

Geshi, N., Ruch, J., & Acocella, V. (2014). Evaluating volumes for magma chambers and magma withdrawn for caldera collapse. Earth and Planetary Science Letters, 396, 107-115. https://doi.org/10.1016/j.epsl.2014.03.059

Geshi, N., Németh, K., Noguchi, R., & Oikawa, T. (2019). Shift from magmatic to phreatomagmatic explosions controlled by the lateral evolution of a feeder dike in the Suoana-Kazahaya eruption, Miyakejima Volcano, Japan. Earth and Planetary Science Letters, 511, 177-189. https://doi.org/10.1016/j.epsl.2019.01.038

Geshi, N., Yamada, I., Matsumoto, K., Nishihara, A., & Miyagi, I. (2020). Accumulation of rhyolite magma and triggers for a caldera-forming eruption of the Aira Caldera, Japan. Bulletin of Volcanology, 82(6), 44. 10.1007/s00445-020-01384-6

Giachetti, T., Druitt, T. H., Burgisser, A., Arbaret, L., & Galven, C. (2010). Bubble nucleation, growth and coalescence during the 1997 Vulcanian explosions of Soufrière Hills Volcano, Montserrat. Journal of Volcanology and Geothermal Research, 193(3), 215-231. https://doi.org/10.1016/j.jvolgeores.2010.04.001

Giachetti, T., Burgisser, A., Arbaret, L., Druitt, T. H., & Kelfoun, K. (2011). Quantitative textural analysis of Vulcanian pyroclasts (Montserrat) using multi-scale X-ray computed microtomography: comparison with results from 2D image analysis. Bulletin of Volcanology, 73(9), 1295-1309.

Giachetti, T., Gonnermann, H. M., Gardner, J. E., Burgisser, A., Hajimirza, S., Earley, T. C., Truong, N., & Toledo, P. (2019). Bubble Coalescence and Percolation Threshold in Expanding Rhyolitic Magma. Geochemistry, Geophysics, Geosystems, 20(2), 1054-1074. 10.1029/2018gc008006

Giachetti, T., Hudak, M. R., Shea, T., Bindeman, I. N., & Hoxsie, E. C. (2020). D/H ratios and H2O contents record degassing and rehydration history of rhyolitic magma and pyroclasts. Earth and Planetary Science Letters, 530, 115909. https://doi.org/10.1016/j.epsl.2019.115909

Giachetti, T., Trafton, K. R., Wiejaczka, J., Gardner, J. E., Watkins, J. M., Shea, T., & Wright, H. M. (2021). The products of primary magma fragmentation finally revealed by pumice agglomerates. Geology

Giggenbach, W., Sheppard, D., Robinson, B., Stewart, M., & Lyon, G. (1994). Geochemical structure and position of the Waiotapu geothermal field, New Zealand. Geothermics, 23(5-6), 599-644.

Gillies, J., Kennedy, B., Gravley, D., Leonard, G., & Cowlyn, J. (2020). Identifying Pyroclastic Density Currents From Partial Outcrop Exposure on Mt. Ruapehu, New Zealand. Frontiers in Earth Science, 8(402) 10.3389/feart.2020.542932

Giordano, D., Russell, J. K., & Dingwell, D. B. (2008). Viscosity of magmatic liquids: A model. Earth and Planetary Science Letters, 271(1), 123-134. https://doi.org/10.1016/j.epsl.2008.03.038

Giordano, G. (1998). Facies characteristics and magma–water interaction of the White Trachytic Tuffs (Roccamonfina Volcano, southern Italy). Bulletin of Volcanology, 60(1), 10-26. 10.1007/s004450050213

Giordano, G., & Cas, R. A. F. (2021). Classification of ignimbrites and their eruptions. Earth-Science Reviews, 103697. https://doi.org/10.1016/j.earscirev.2021.103697

Gonnermann, H. M. (2015). Magma fragmentation. Annual Review of Earth and Planetary Sciences, 43, 431-458.

Gonnermann, H. M., & Manga, M. (2003). Explosive volcanism may not be an inevitable consequence of magma fragmentation. Nature, 426, 432. doi:10.1038/nature02138

Gonnermann, H. M., & Manga, M. (2007). The Fluid Mechanics Inside a Volcano. Annual Review of Fluid Mechanics, 39(1), 321-356. doi:10.1146/annurev.fluid.39.050905.110207

Gonnermann, H., & Houghton, B. (2012). Magma degassing during the Plinian eruption of Novarupta, Alaska, 1912. Geochemistry, Geophysics, Geosystems, 13(10)

Gonnermann, H., & Gardner, J. (2013). Homogeneous bubble nucleation in rhyolitic melt: Experiments and nonclassical theory. Geochemistry, Geophysics, Geosystems, 14(11), 4758-4773

Gonnermann, H. M., & Manga, M. (2013). Dynamics of magma ascent in the volcanic conduit. In R. M. C. Lopes, S. A. Fagents, & T. K. P. Gregg (Eds.), Modeling volcanic processes: The physics and mathematics of volcanism (pp. 55-84). Cambridge: Cambridge University Press.

Gonnermann, H., & Taisne, B. (2015). In H. Sigurdsson (Ed.), The Encyclopedia of Volcanoes (Second Edition) (pp. 215-224). Amsterdam: Academic Press. https://doi.org/10.1016/B978-0-12-385938-9.00010-9

Gonnermann, H. M., Giachetti, T., Fliedner, C., Nguyen, C. T., Houghton, B. F., Crozier, J. A., & Carey, R. J. (2017). Permeability During Magma Expansion and Compaction. Journal of Geophysical Research: Solid Earth, 122(12), 9825-9848. 10.1002/2017JB014783

Goto, Y., Suzuki, K., Shinya, T., Yamauchi, A., Miyoshi, M. Danhara, T., and Tomiya, A., (2018). Stratigraphy and lithofacies of the Toya ignimbrite in Southwestern Hokkaido, Japan: Insights into the caldera-forming eruption at Toya caldera. Jour. Geogr., 127, 191–227.

Grange, L. I. (1937). The geology of the Rotorua-Taupo subdivision. NZ Geol Survey Bull 37:138p

Grobys, J. W. G., Gohl, K., & Eagles, G. (2008). Quantitative tectonic reconstructions of Zealandia based on crustal thickness estimates. Geochemistry, Geophysics, Geosystems, 9(1) https://doi.org/10.1029/2007GC001691

Grove, T. L., Donnelly-Nolan, J. M., & Housh, T. (1997). Magmatic processes that generated the rhyolite of Glass Mountain, Medicine Lake volcano, N. California. Contributions to Mineralogy and Petrology, 127(3), 205-223.

Groppelli, G., Principe, C., & Sulpizio, R. (2019). Geological data in volcanology: Collection, organisation and applications. Journal of Volcanology and Geothermal Research, 385, 1-2. https://doi.org/10.1016/j.jvolgeores.2019.106694

Gurioli, L., Houghton, B. F., Cashman, K. V., & Cioni, R. (2005). Complex changes in eruption dynamics during the 79 AD eruption of Vesuvius. Bulletin of Volcanology, 67(2), 144-159. doi:10.1007/s00445-004-0368-4

Gurioli, L., Andronico, D., Bachelery, P., Balcone-Boissard, H., Battaglia, J., Boudon, G., . . . Thordarson, T. (2015). MeMoVolc consensual document: a review of cross-disciplinary approaches to characterizing small explosive magmatic eruptions. Bulletin of Volcanology, 77(6), 49. 10.1007/s00445-015-0935-x

Hale, A. J., & Mühlhaus, H.-B. (2007). Modelling shear bands in a volcanic conduit: Implications for over-pressures and extrusion-rates. Earth and Planetary Science Letters, 263(1), 74-87. https://doi.org/10.1016/j.epsl.2007.08.026

Hale, A. J., & Wadge, G. (2008). The transition from endogenous to exogenous growth of lava domes with the development of shear bands. Journal of Volcanology and Geothermal Research, 171(3), 237-257. doi:https://doi.org/10.1016/j.jvolgeores.2007.12.016

Hamling, I. J., Hreinsdóttir, S., & Fournier, N. (2015). The ups and downs of the TVZ: Geodetic observations of deformation around the Taupo Volcanic Zone, New Zealand. Journal of Geophysical Research: Solid Earth, 120(6), 4667-4679. https://doi.org/10.1002/2015JB012125

Hammer, J. E. (2008). Experimental studies of the kinetics and energetics of magma crystallization. Reviews in Mineralogy and Geochemistry, 69(1), 9-59.

Hammer, J. E., Cashman, K. V., Hoblitt, R. P., & Newman, S. (1999). Degassing and microlite crystallization during pre-climactic events of the 1991 eruption of Mt. Pinatubo, Philippines. Bulletin of Volcanology, 60(5), 355-380. 10.1007/s004450050238

Hanenkamp, E. (2011). Decoupling processes in block-and-ash flows: field evidence and analogue modelling. PhD Thesis. University of Canterbury.

Hantusch, M., Lacanna, G., Ripepe, M., Montenegro, V., Valderrama, O., Farias, C., Caselli, A., Gabellini, P., & Cioni, R. (2021). Low-Energy Fragmentation Dynamics at Copahue Volcano (Argentina) as Revealed by an Infrasonic Array and Ash Characteristics. Frontiers in Earth Science, 9(92) 10.3389/feart.2021.578437

Harris, A. J., Rose, W. I., & Flynn, L. P. (2003). Temporal trends in lava dome extrusion at Santiaguito 1922–2000. Bulletin of Volcanology, 65(2), 77-89. doi:10.1007/s00445-002-0243-0

Hasegawa, T., Mochizuki, N., & Oiwane, H. (2018). Methods of estimating the durations of super large eruptions based on pyroclastic deposits. Journal Of Geography-Chigaku Zasshi, 127(2), 273-288. (in Japanese with English abstract)

Hasegawa, T., Mochizuki, N., Gravley, D., Kusu, C., Okada, M., Geshi, N., Kósik, S., Kaneda, Y., & Shibata, S. (2020). Evaluation on the durations of large-scale caldera-forming eruptions based on paleomagnetic method: Examples from Aira caldera, Japan and Mamaku/Ohakuri Ignimbrites, New Zealand.

Healy, J. (1962). Structure and volcanism in the Taupo volcanic zone, New Zealand: Wiley Online Library.

Heap, M. J., Tuffen, H., Wadsworth, F. B., Reuschlé, T., Castro, J. M., & Schipper, C. I. (2019). The Permeability Evolution of Tuffisites and Implications for Outgassing Through Dense Rhyolitic Magma. Journal of Geophysical Research: Solid Earth, 124(8), 8281-8299. https://doi.org/10.1029/2018JB017035

Heiken, G. (1978). Plinian-type eruptions in the Medicine Lake highland, California, and the nature of the underlying magma. Journal of Volcanology and Geothermal Research, 4(3), 375-402. https://doi.org/10.1016/0377-0273(78)90023-9

Heiken, G., & Wohletz, K. (1987). Tephra deposits associated with silicic domes and lava flows. Geol Soc Am Spec Pap, 212, 55-76.

Heiken, G., Goff, F., Stix, J., Tamanyu, S., Shafiqullah, M., Garcia, S., & Hagan, R. (1986). Intracaldera volcanic activity, Toledo caldera and embayment, Jemez Mountains, New Mexico. Journal of Geophysical Research: Solid Earth, 91(B2), 1799-1815.

Heiken, G., Goff, F., Gardner, J. N., Baldridge, W., Hulen, J., Nielson, D. L., & Vaniman, D. (1990). The Valles/Toledo Caldera Complex, Jemez Volcanic Field, New Mexico. Annual Review of Earth and Planetary Sciences, 18(1), 27-53.

Heilbronner, R., & Barrett, S. (2014). Image Analysis in Earth Sciences. Microstructures and Textures of Earth Materials. Springer, Berlin, Heidelberg. doi:10.1007/978-3-642-10343-8

Heinrich, M., Cronin, S. J., & Pardo, N. (2020). Understanding multi-vent Plinian eruptions at Mt. Tongariro volcanic complex, New Zealand. Bulletin of Volcanology, 82(3), 1-29. https://doi.org/10.1007/s00445-020-1369-7

Heinrich, M., Cronin, S. J., Torres-Orozco, R., Colombier, M., Scheu, B., & Pardo, N. (2020). Micro-porous pyroclasts reflecting multi-vent basaltic-andesite Plinian eruptions at Mt. Tongariro, New Zealand. Journal of Volcanology and Geothermal Research, 401, 106936. https://doi.org/10.1016/j.jvolgeores.2020.106936

Henrys, S., Reyners, M., & Bibby, H. (2003). Exploring the plate boundary structure of the North Island, New Zealand. Eos, Transactions American Geophysical Union, 84(31), 289-295. doi:10.1029/2003EO310002

Hildreth, W. (2004). Volcanological perspectives on Long Valley, Mammoth Mountain, and Mono Craters: several contiguous but discrete systems. Journal of Volcanology and Geothermal Research, 136(3), 169-198. https://doi.org/10.1016/j.jvolgeores.2004.05.019

Hildreth, W., & Fierstein, J. (2012). The Novarupta-Katmai eruption of 1912: largest eruption of the twentieth century: centennial perspectives: Geological Survey.

Hildreth, W., Godoy, E., Fierstein, J., Singer, B.S., (2010). Laguna del Maule volcanic field: eruptive history of a Quaternary basalt to rhyolite distributed volcanic field on the Andean range crest in central Chile. Servicio Nacional de Geología y Minería-Chile, Boletin 63.

Hogg, A. G., Higham, T. F., Lowe, D. J., Palmer, J. G., Reimer, P. J., & Newnham, R. M. (2003). A wiggle-match date for Polynesian settlement of New Zealand. Antiquity, 77(295), 116-125.

Holden, L., Wallace, L., Beavan, J., Fournier, N., Cas, R., Ailleres, L., & Silcock, D. (2015). Contemporary ground deformation in the Taupo Rift and Okataina Volcanic Centre from 1998 to 2011, measured using GPS. Geophysical Journal International, 202(3), 2082-2105.

Holden, L., Cas, R., Fournier, N., & Ailleres, L. (2017). Modelling ground deformation patterns associated with volcanic processes at the Okataina Volcanic Centre. Journal of Volcanology and Geothermal Research, 344, 65-78.

Holohan, E. P., Troll, V. R., van Wyk de Vries, B., Walsh, J. J., & Walter, T. R. (2008). Unzipping Long Valley: An explanation for vent migration patterns during an elliptical ring fracture eruption. Geology, 36(4), 323-326.

Holt, W. E., & Haines, A. J. (1995). The kinematics of northern South Island, New Zealand, determined from geologic strain rates. Journal of Geophysical Research: Solid Earth, 100(B9), 17991-18010. doi:10.1029/95JB01059

Houghton, B. F., & Wilson, C. J. N. (1989). A vesicularity index for pyroclastic deposits. Bulletin of Volcanology, 51(6), 451-462. doi:10.1007/bf01078811

Houghton, B. F., & Nairn, I. A. (1991). The 1976–1982 Strombolian and phreatomagmatic eruptions of White Island, New Zealand: eruptive and depositional mechanisms at a 'wet' volcano. Bulletin of Volcanology, 54(1), 25-49. 10.1007/bf00278204

Houghton, B. F., & Smith, R. T. (1993). Recycling of magmatic clasts during explosive eruptions: estimating the true juvenile content of phreatomagmatic volcanic deposits. Bulletin of Volcanology, 55(6), 414-420. 10.1007/bf00302001

Houghton, B. F., Wilson, C., McWilliams, M., Lanphere, M., Weaver, S., Briggs, R., & Pringle, M. (1995). Chronology and dynamics of a large silicic magmatic system: Central Taupo Volcanic Zone, New Zealand. Geology, 23(1), 13-16.

Houghton, B. F., Hobden, B., Cashman, K., Wilson, C., & Smith, R. (2003). Large-scale interaction of lake water and rhyolitic magma during the 1.8 ka Taupo eruption, New Zealand. Washington DC American Geophysical Union Geophysical Monograph Series, 140, 97-109.

Houghton, B. F., Wilson, C. J. N., Fierstein, J., & Hildreth, W. (2004). Complex proximal deposition during the Plinian eruptions of 1912 at Novarupta, Alaska. Bulletin of Volcanology, 66(2), 95-133. 10.1007/s00445-003-0297-7

Houghton, B. F., Carey, R. J., Cashman, K. V., Wilson, C. J. N., Hobden, B. J., & Hammer, J. E. (2010). Diverse patterns of ascent, degassing, and eruption of rhyolite magma during the 1.8ka Taupo eruption, New Zealand: Evidence from clast vesicularity. Journal of Volcanology and Geothermal Research, 195(1), 31-47. https://doi.org/10.1016/j.jvolgeores.2010.06.002

Houghton, B. F., & Carey, R. J. (2015). In H. Sigurdsson (Ed.), The Encyclopedia of Volcanoes (Second Edition) (pp. 599-616). Amsterdam: Academic Press. https://doi.org/10.1016/B978-0-12-385938-9.00034-1

Hughes, E. C., Mazot, A., Kilgour, G., Asher, C., Michelini, M., Britten, K., Chardot, L., Feisel, Y., & Werner, C. (2019). Understanding Degassing Pathways Along the 1886 Tarawera (New Zealand) Volcanic Fissure by Combining Soil and Lake CO2 Fluxes. Frontiers in Earth Science, 7(264) 10.3389/feart.2019.00264

Hui, H., & Zhang, Y. (2007). Toward a general viscosity equation for natural anhydrous and hydrous silicate melts. Geochimica et Cosmochimica Acta, 71(2), 403-416. doi:https://doi.org/10.1016/j.gca.2006.09.003

Hunt, T., Glover, R., & Wood, C. (1994). Waimangu, Waiotapu, and Waikite geothermal systems, New Zealand: background and history. Geothermics, 23(5-6), 379-400.

Hurst, T., & Smith, W. (2010). Volcanic ashfall in New Zealand–probabilistic hazard modelling for multiple sources. New Zealand Journal of Geology and Geophysics, 53(1), 1-14.

Hurwitz, S., & Navon, O. (1994). Bubble nucleation in rhyolitic melts: Experiments at high pressure, temperature, and water content. Earth and Planetary Science Letters, 122(3), 267-280. https://doi.org/10.1016/0012-821X(94)90001-9

Hutchison, W., Fusillo, R., Pyle, D. M., Mather, T. A., Blundy, J. D., Biggs, J., Yirgu, G., Cohen, B. E., Brooker, R. A., Barfod, D. N., & Calvert, A. T. (2016). A pulse of mid-Pleistocene rift volcanism in Ethiopia at the dawn of modern humans. Nature Communications, 7(1), 13192. 10.1038/ncomms13192

Illsley-Kemp, F., Barker, S. J., Wilson, C. J. N., Chamberlain, C. J., Hreinsdóttir, S., Ellis, S., Hamling, I. J., Savage, M. K., Mestel, E. R. H., & Wadsworth, F. B. (2021). Volcanic Unrest at Taupō Volcano in 2019: Causes, Mechanisms and Implications. Geochemistry, Geophysics, Geosystems, 22(6), e2021GC009803. https://doi.org/10.1029/2021GC009803

Imura, R. (1998). Reconstruction of the sequence of the An-ei eruption of Sakurajima volcano (AD 1779-1782) using the historical records. Bull Volcanol. Soc. Japan, 43 (5), 373-383. (in Japanese with English abstract).

Inman, D. L. (1952). Measures for describing the size distribution of sediments. Journal of Sedimentary Research, 22(3), 125-145.

Isaia, R., D'Antonio, M., Dell'Erba, F., Di Vito, M., & Orsi, G. (2004). The Astroni volcano: the only example of closely spaced eruptions in the same vent area during the recent history of the Campi Flegrei caldera (Italy). Journal of Volcanology and Geothermal Research, 133(1), 171-192. https://doi.org/10.1016/S0377-0273(03)00397-4

Isaia, R., Di Giuseppe, M. G., Natale, J., Tramparulo, F., Troiano, A., & Vitale, S. (2021). Volcano-tectonic setting of the Pisciarelli Fumarole Field, Campi Flegrei caldera, southern Italy: insights into fluid circulation patterns and hazard scenarios. Tectonics, 40, e2020TC006227Jaupart, C. (1998). Gas loss from magmas through conduit walls during eruption. Geological Society, London, Special Publications, 145(1), 73-90.

Jaupart, C., & Allègre, C. J. (1991). Gas content, eruption rate and instabilities of eruption regime in silicic volcanoes. Earth and Planetary Science Letters, 102(3), 413-429. https://doi.org/10.1016/0012-821X(91)90032-D

Jenkins, S., Magill, C., McAneney, J., & Hurst, T. (2008). Multistage volcanic events: Tephra hazard simulations for the Okataina Volcanic Center, New Zealand. Journal of Geophysical Research: Earth Surface, 113(F4) 10.1029/2007jf000787

Jenkins, S., Komorowski, J. C., Baxter, P. J., Spence, R., Picquout, A., Lavigne, F., & Surono. (2013). The Merapi 2010 eruption: An interdisciplinary impact assessment methodology for studying pyroclastic density current dynamics. Journal of Volcanology and Geothermal Research, 261, 316-329. doi:https://doi.org/10.1016/j.jvolgeores.2013.02.012

Jurado-Chichay, Z., & Walker, G. P. L. (2000). Stratigraphy and dispersal of the Mangaone Subgroup pyroclastic deposits, Okataina Volcanic Centre, New Zealand. Journal of Volcanology and Geothermal Research, 104(1), 319-380. https://doi.org/10.1016/S0377-0273(00)00210-9

Jurado-Chichay, Z., & Walker, G. P. L. (2001). Variability of plinian fall deposits: examples from Okataina Volcanic Centre, New Zealand. Journal of Volcanology and Geothermal Research, 111(1), 239-263. https://doi.org/10.1016/S0377-0273(01)00229-3

Kalnay, E., et al. (1996), The NCEP/NCAR 40-year reanalysis project, Bull. Am. Meteorol. Soc., 77(3), 437–471.

Kaneko, T., Wooster, M. J., & Nakada, S. (2002). Exogenous and endogenous growth of the Unzen lava dome examined by satellite infrared image analysis. Journal of Volcanology and Geothermal Research, 116(1), 151-160. doi: https://doi.org/10.1016/S0377-0273(02)00216-0

Kavanagh, J. L. (2018). Mechanisms of magma transport in the upper crust—dyking. In S. Burchardt (Ed.), Volcanic and Igneous Plumbing Systems (pp. 55-88): Elsevier. https://doi.org/10.1016/B978-0-12-809749-6.00003-0

Kavanagh, J. L., Burns, A. J., Hilmi Hazim, S., Wood, E. P., Martin, S. A., Hignett, S., & Dennis, D. J. C. (2018). Challenging dyke ascent models using novel laboratory experiments: Implications for reinterpreting evidence of magma ascent and volcanism. Journal of Volcanology and Geothermal Research, 354, 87-101. https://doi.org/10.1016/j.jvolgeores.2018.01.002

Keam, R.F. (1988). Tarawera: The volcanic eruption of 10 June 1886. Auckland, New Zealand, ISBN 0473004445 (hbk.). 472 p.

Keam, R. F. (2016). The Tarawera eruption, Lake Rotomahana, and the origin of the Pink and White Terraces. Journal of Volcanology and Geothermal Research, 314, 10-38. https://doi.org/10.1016/j.jvolgeores.2015.11.009

Kendrick, J. E., Lavallée, Y., Varley, N. R., Wadsworth, F. B., Lamb, O. D., & Vasseur, J. (2016). Blowing Off Steam: Tuffisite Formation As a Regulator for Lava Dome Eruptions. Frontiers in Earth Science, 4(41) 10.3389/feart.2016.00041

Kennedy, B., Spieler, O., Scheu, B., Kueppers, U., Taddeucci, J., & Dingwell, D. B. (2005). Conduit implosion during Vulcanian eruptions. Geology, 33(7), 581-584.

Kennedy, B., Wilcock, J., & Stix, J. (2012). Caldera resurgence during magma replenishment and rejuvenation at Valles and Lake City calderas. Bulletin of Volcanology, 74(8), 1833-1847.

Kennedy, B. M., Wadsworth, F. B., Vasseur, J., Schipper, C. I., Jellinek, A. M., von Aulock, F. W., ... & Dingwell, D. B. (2016). Surface tension driven processes densify and retain permeability in magma and lava. Earth and Planetary Science Letters, 433, 116-124.

Kennedy, B. M., Holohan, E. P., Stix, J., Gravley, D. M., Davidson, J. R. J., & Cole, J. W. (2018). Magma plumbing beneath collapse caldera volcanic systems. Earth-Science Reviews, 177, 404-424. https://doi.org/10.1016/j.earscirev.2017.12.002

Kidson, J. W. (2000). An analysis of New Zealand synoptic types and their use in defining weather regimes. International Journal of Climatology: A Journal of the Royal Meteorological Society, 20(3), 299-316.

Kilgour, G. N., & Smith, R. T. (2008). Stratigraphy, dynamics, and eruption impacts of the dual magma Rotorua eruptive episode, Okataina Volcanic Centre, New Zealand. New Zealand Journal of Geology and Geophysics, 51(4), 367-378. 10.1080/00288300809509871

Kilgour, G. N., Mader, H. M., Blundy, J. D., & Brooker, R. A. (2016). Rheological controls on the eruption potential and style of an andesite volcano: A case study from Mt. Ruapehu, New Zealand. Journal of Volcanology and Geothermal Research, 327, 273-287. https://doi.org/10.1016/j.jvolgeores.2016.08.001

Kilgour, G., Kennedy, B., Scott, B., Christenson, B., Jolly, A., Asher, A., Rosenberg, M., & Saunders, K. (2021). Whakaari/White Island: a review of New Zealand's most active volcano. New Zealand Journal of Geology and Geophysics, 64

King, P. R. (2000). Tectonic reconstructions of New Zealand: 40 Ma to the Present. New Zealand Journal of Geology and Geophysics, 43(4), 611-638. doi:10.1080/00288306.2000.9514913

Klug, C., & Cashman, K. V. (1996). Permeability development in vesiculating magmas: implications for fragmentation. Bulletin of Volcanology, 58(2), 87-100. doi:10.1007/s004450050128

Klug, C., Cashman, K., & Bacon, C. (2002). Structure and physical characteristics of pumice from the climactic eruption of Mount Mazama (Crater Lake), Oregon. Bulletin of Volcanology, 64(7), 486-501. 10.1007/s00445-002-0230-5

Kobayashi, T., Nairn, I., Smith, V., & Shane, P. (2005). Proximal stratigraphy and event sequence of the c. 5600 cal. yr BP Whakatane rhyolite eruption episode from Haroharo volcano, Okataina Volcanic Centre, New Zealand. New Zealand Journal of Geology and Geophysics, 48(3), 471-490. 10.1080/00288306.2005.9515127

Kobayashi, T., Morishita, Y., & Munekane, H. (2018). First detection of precursory ground inflation of a small phreatic eruption by InSAR. Earth and Planetary Science Letters, 491, 244-254. https://doi.org/10.1016/j.epsl.2018.03.041

Kohn, B. P.; Glasby, G. P. (1978). Tephra distribution and sedimentation rates in the Bay of" Plenty, New Zealand. New Zealand Journal of Geology and Geophysics 21: 49-70.

Kolzenburg, S., Ryan, A. G., & Russell, J. K. (2019). Permeability evolution during non-isothermal compaction in volcanic conduits and tuffisite veins: Implications for pressure monitoring of volcanic edifices. Earth and Planetary Science Letters, 527, 115783. https://doi.org/10.1016/j.epsl.2019.115783

Kósik, S. (2018). Small-volume volcanism associated with polygenetic volcanoes, Taupo Volcanic Zone, New Zealand. PhD thesis, Massey University.

Kósik, S., Németh, K., Lexa, J., & Procter, J. N. (2019). Understanding the evolution of a small-volume silicic fissure eruption: Puketerata Volcanic Complex, Taupo Volcanic Zone, New Zealand. Journal of Volcanology and Geothermal Research https://doi.org/10.1016/j.jvolgeores.2017.12.008

Kósik, S., Bebbington, M., & Németh, K. (2020). Spatio-temporal hazard estimation in the central silicic part of Taupo Volcanic Zone, New Zealand, based on small to medium volume eruptions. Bulletin of Volcanology, 82(6), 50. 10.1007/s00445-020-01392-6

Koyaguchi, T., Scheu, B., Mitani, N. K., & Melnik, O. (2008). A fragmentation criterion for highly viscous bubbly magmas estimated from shock tube experiments. Journal of Volcanology and Geothermal Research, 178(1), 58-71. doi:https://doi.org/10.1016/j.jvolgeores.2008.02.008

Kushnir, A. R. L., Martel, C., Champallier, R., & Arbaret, L. (2017). In situ confirmation of permeability development in shearing bubble-bearing melts and implications for volcanic outgassing. Earth and Planetary Science Letters, 458, 315-326. https://doi.org/10.1016/j.epsl.2016.10.053

Lamarche, G., & Lebrun, J.-F. (2000). Transition from strike-slip faulting to oblique subduction: active tectonics at the Puysegur Margin, South New Zealand. Tectonophysics, 316(1), 67-89. https://doi.org/10.1016/S0040-1951(99)00232-2

Lamarche, G., Barnes, P. M., & Bull, J. M. (2006). Faulting and extension rate over the last 20,000 years in the offshore Whakatane Graben, New Zealand continental shelf. Tectonics, 25(4), n/a-n/a. 10.1029/2005TC001886

Lara, L. E. (2009). The 2008 eruption of the Chaitén Volcano, Chile: a preliminary report. Andean Geology, 36(1), 125-129.

Larsen, J. F. (2008). Heterogeneous bubble nucleation and disequilibrium H2O exsolution in Vesuvius K-phonolite melts. Journal of Volcanology and Geothermal Research, 175(3), 278-288.

Lavallée, Y., Varley, N. R., Alatorre-Ibargüengoitia, M. A., Hess, K. U., Kueppers, U., Mueller, S., Richard, D., Scheu, B., Spieler, O., & Dingwell, D. B. (2012). Magmatic architecture of dome-building eruptions at Volcán de Colima, Mexico. Bulletin of Volcanology, 74(1), 249-260. 10.1007/s00445-011-0518-4

Le Mével, H., Córdova, L., Cardona, C., & Feigl, K. L. (2021). Unrest at the Laguna del Maule volcanic field 2005–2020: renewed acceleration of deformation. Bulletin of Volcanology, 83(6), 39. 10.1007/s00445-021-01457-0

Lebrun, J.-F., Lamarche, G., Collot, J.-Y., & Delteil, J. (2000). Abrupt strike-slip fault to subduction transition: The Alpine Fault-Puysegur Trench connection, New Zealand. Tectonics, 19(4), 688-706. doi:10.1029/2000TC900008

Leibrandt, S., & Le Pennec, J.-L. (2015). Towards fast and routine analyses of volcanic ash morphometry for eruption surveillance applications. Journal of Volcanology and Geothermal Research, 297, 11-27. https://doi.org/10.1016/j.jvolgeores.2015.03.014

Leonard, G. S. (2003). The evolution of Maroa Volcanic Centre, Taupo Volcanic Zone, New Zealand. PhD thesis, University of Canterbury.

Leonard, G. S., Cole, J. W., Nairn, I. A., & Self, S. (2002). Basalt triggering of the c. AD 1305 Kaharoa rhyolite eruption, Tarawera Volcanic Complex, New Zealand. Journal of Volcanology and Geothermal Research, 115(3), 461-486. https://doi.org/10.1016/S0377-0273(01)00326-2

Leonard, G. S., Begg, J. G., & Wilson, C. J. N. (2010). Geology of the Rotorua Area: Institute of Geological & Nuclear Sciences 1: 250,000 Geological Map 5. 1 Sheet+ 102p. GNS Science, Lower Hutt, New Zealand (compilers).

Leonard, G. S., Cole, R. P., Christenson, B. W., Conway, C. E., Cronin, S. J., Gamble, J. A., Hurst, T., Kennedy, B. M., Miller, C. A., Procter, J. N., Pure, L. R., Townsend, D. B., White, J. D. L., & Wilson, C. J. N. (2021). Ruapehu and Tongariro stratovolcanoes: a review of current understanding. New Zealand Journal of Geology and Geophysics, 64(2-3), 389-420. 10.1080/00288306.2021.1909080

Lesher, C. E., & Spera, F. J. (2015). In H. Sigurdsson (Ed.), The Encyclopedia of Volcanoes (Second Edition) (pp. 113-141). Amsterdam: Academic Press. https://doi.org/10.1016/B978-0-12-385938-9.00005-5

Lipman, P. W. (1997). Subsidence of ash-flow calderas: relation to caldera size and magma-chamber geometry. Bulletin of Volcanology, 59(3), 198-218. 10.1007/s004450050186

Lipman, P.W. (2000). Calderas. In: Sigurdsson, H. (Ed.), Encyclopedia of Volcanoes. Academic Press, San Francisco, pp. 643– 662.

Liu, E. J., Cashman, K. V., & Rust, A. C. (2015). Optimising shape analysis to quantify volcanic ash morphology. GeoResJ, 8, 14-30. https://doi.org/10.1016/j.grj.2015.09.001

Llewellin, E., Mader, H., & Wilson, S. (2002). The constitutive equation and flow dynamics of bubbly magmas. Geophysical Research Letters, 29(24), 23-21-23-24

Llewellin, E. W., & Manga, M. (2005). Bubble suspension rheology and implications for conduit flow. Journal of Volcanology and Geothermal Research, 143(1), 205-217. doi:https://doi.org/10.1016/j.jvolgeores.2004.09.018

Lowe, D. J. (2008). Polynesian settlement of New Zealand and the impacts of volcanism on early Maori society: an update. In: Lowe, D.J. (editor) Guidebook for Pre-conference North Island Field Trip A1 ‘Ashes and Issues’ (28-30 November 2008). Australian and New Zealand 4th Joint Soils Conference, Massey University, Palmerston North (1-5 Dec. 2008). New Zealand Society of Soil Science. Pp.142-147. ISBN 978-0-473-14476-0

Lowe, D. J. (2016). Introduction to tephra-derived soils, North Island, New Zealand: University of Waikato and University of Wisconsin-Platteville post-conference Andisol excursion, 21-23 December, 2016.

Lowe, D. J., McFadgen, B. G., Higham, T. F., Hogg, A. G., Froggatt, P. C., & Nairn, I. A. (1998). Radiocarbon age of the Kaharoa Tephra, a key marker for late-Holocene stratigraphy and archaeology in New Zealand. The Holocene, 8(4), 487-495.

Lowe, D., J., Keam, R. F., Lee, D. E. (2001). How many deaths were caused by the Tarawera eruption? Geol. Soc. N. Z. Newsl. 124, 31–33.

Lowe, D. J., Newnham, R., & McCraw, J. (2002). Volcanism and early Maori society in New Zealand. Natural disasters and cultural change, 45, 126-161

Lowe, D. J., Shane, P. A. R., Alloway, B. V., & Newnham, R. M. (2008). Fingerprints and age models for widespread New Zealand tephra marker beds erupted since 30,000 years ago: a framework for NZ-INTIMATE. Quaternary Science Reviews, 27(1), 95-126. https://doi.org/10.1016/j.quascirev.2007.01.013

Lowe, D.J., Lanigan, K.M., Palmer, D.J. (2012). Where geology meets pedology: Late Quaternary tephras, loess, and paleosols in the Mamaku Plateau and Lake Rerewhakaaitu areas. In: Pittari, A. (compiler). Field Trip Guides, Geosciences 2012 Conference, Hamilton, New Zealand. Geoscience Society of New Zealand Miscellaneous Publication 134B, pp. 2.1−2.45

Lowe, D. J., Blaauw, M., Hogg, A. G., & Newnham, R. M. (2013). Ages of 24 widespread tephras erupted since 30,000 years ago in New Zealand, with re-evaluation of the timing and palaeoclimatic implications of the Lateglacial cool episode recorded at Kaipo bog. Quaternary Science Reviews, 74, 170-194. https://doi.org/10.1016/j.quascirev.2012.11.022

Lube, G., Breard, E. C. P., Esposti-Ongaro, T., Dufek, J., & Brand, B. (2020). Multiphase flow behaviour and hazard prediction of pyroclastic density currents. Nature Reviews Earth & Environment, 1(7), 348-365. 10.1038/s43017-020-0064-8

Lucchi, F. (2013). Stratigraphic methodology for the geological mapping of volcanic areas: insights from the Aeolian archipelago (southern Italy). Geological Society, London, Memoirs, 37(1), 37-53.

Lucchi, F., Francalanci, L., De Astis, G., Tranne, C. A., Braschi, E., & Klaver, M. (2018). Geological evidence for recurrent collapse-driven phreatomagmatic pyroclastic density currents in the Holocene activity of Stromboli volcano, Italy. Journal of Volcanology and Geothermal Research https://doi.org/10.1016/j.jvolgeores.2018.10.024

Macedonio, G., Dobran, F., & Neri, A. (1994). Erosion processes in volcanic conduits and application to the AD 79 eruption of Vesuvius. Earth and Planetary Science Letters, 121(1), 137-152. https://doi.org/10.1016/0012-821X(94)90037-X

Mackie, S., Cashman, K., Ricketts, H., Rust, A., & Watson, M. (2016). Volcanic ash: hazard observation: Elsevier.

Mader, H. M., Llewellin, E. W., & Mueller, S. P. (2013). The rheology of two-phase magmas: A review and analysis. Journal of Volcanology and Geothermal Research, 257, 135-158. https://doi.org/10.1016/j.jvolgeores.2013.02.014

Maeno, F., Nagai, M., Nakada, S., Burden, R. E., Engwell, S., Suzuki, Y., & Kaneko, T. (2014). Constraining tephra dispersion and deposition from three subplinian explosions in 2011 at Shinmoedake volcano, Kyushu, Japan. Bulletin of Volcanology, 76(6), 823. 10.1007/s00445-014-0823-9

Maeno, F., Nakada, S., Yoshimoto, M., Shimano, T., Hokanishi, N., Zaennudin, A., & Iguchi, M. (2019). A sequence of a plinian eruption preceded by dome destruction at Kelud volcano, Indonesia, on February 13, 2014, revealed from tephra fallout and pyroclastic density current deposits. Journal of Volcanology and Geothermal Research, 382, 24-41. https://doi.org/10.1016/j.jvolgeores.2017.03.002

Mangan, M., & Sisson, T. (2000). Delayed, disequilibrium degassing in rhyolite magma: decompression experiments and implications for explosive volcanism. Earth and Planetary Science Letters, 183(3-4), 441-455.

Mangan, M., Mastin, L., & Sisson, T. (2004). Gas evolution in eruptive conduits: combining insights from high temperature and pressure decompression experiments with steady-state flow modeling. Journal of Volcanology and Geothermal Research, 129(1), 23-36. https://doi.org/10.1016/S0377-0273(03)00230-0

Manning, D. A. (1995). Late Pleistocene tephrostratigraphy of the eastern Bay of Plenty region, New Zealand. PhD thesis, Victoria University of Wellington.

Manning, D. A. (1996). Middle-Late Pleistocene tephrostratigraphy of the eastern Bay of Plenty, New Zealand. Quaternary International, 34-36, 3-12. doi:https://doi.org/10.1016/1040-6182(95)00064-X

Manville, V. (2010). An overview of break-out floods from intracaldera lakes. Global and Planetary Change, 70(1), 14-23. https://doi.org/10.1016/j.gloplacha.2009.11.004

Marcaida, M., Vazquez, J. A., Stelten, M. E., & Miller, J. S. (2019). Constraining the Early Eruptive History of the Mono Craters Rhyolites, California, Based on 238U-230Th Isochron Dating of Their Explosive and Effusive Products. Geochemistry, Geophysics, Geosystems, 20(3), 1539-1556. https://doi.org/10.1029/2018GC008052

Marra, F., Castellano, C., Cucci, L., Florindo, F., Gaeta, M., Jicha, B. R., Palladino, D.M., Sottili, G., Tertulliani, A., & Tolomei, C. (2020). Monti Sabatini and Colli Albani: the dormant twin volcanoes at the gates of Rome. Scientific reports, 10(1), 1-17.

Martel, C., Dingwell, D. B., Spieler, O., Pichavant, M., & Wilke, M. (2000). Fragmentation of foamed silicic melts: an experimental study. Earth and Planetary Science Letters, 178(1), 47-58. https://doi.org/10.1016/S0012-821X(00)00062-5

Martel, C., & Iacono-Marziano, G. (2015). Timescales of bubble coalescence, outgassing, and foam collapse in decompressed rhyolitic melts. Earth and Planetary Science Letters, 412, 173-185. https://doi.org/10.1016/j.epsl.2014.12.010

Martí, J., Soriano, C., & Dingwell, D. (1999). Tube pumices as strain markers of the ductile–brittle transition during magma fragmentation. Nature, 402(6762), 650.

Martí, J., Aspinall, W. P., Sobradelo, R., Felpeto, A., Geyer, A., Ortiz, R., Baxter, P., Cole, P., Pacheco, J., Blanco, M. J., & Lopez, C. (2008). A long-term volcanic hazard event tree for Teide-Pico Viejo stratovolcanoes (Tenerife, Canary Islands). Journal of Volcanology and Geothermal Research, 178(3), 543-552. https://doi.org/10.1016/j.jvolgeores.2008.09.023

Martí, J., Groppelli, G., & Brum da Silveira, A. (2018). Volcanic stratigraphy: A review. Journal of Volcanology and Geothermal Research, 357, 68-91. https://doi.org/10.1016/j.jvolgeores.2018.04.006

Martin, J. (1888). The Terraces of Rotomahana, New Zealand. Martin, Auckland ((ii) 15).

Martin, R. S., Watt, S. F. L., Pyle, D. M., Mather, T. A., Matthews, N. E., Georg, R. B., Day, J. A., Fairhead, T., Witt, M. L. I., & Quayle, B. M. (2009). Environmental effects of ashfall in Argentina from the 2008 Chaitén volcanic eruption. Journal of Volcanology and Geothermal Research, 184(3), 462-472. https://doi.org/10.1016/j.jvolgeores.2009.04.010

Martin-Del Pozzo, A. L., González-Morán, T., Espinasa-Pereña, R., Butron, M. A., & Reyes, M. (2008). Characterization of the recent ash emissions at Popocatepetl Volcano, Mexico. Journal of

Volcanology and Geothermal Research, 170(1), 61-75. https://doi.org/10.1016/j.jvolgeores.2007.09.004

Marzocchi, W., Sandri, L., Gasparini, P., Newhall, C., & Boschi, E. (2004). Quantifying probabilities of volcanic events: The example of volcanic hazard at Mount Vesuvius. Journal of Geophysical Research: Solid Earth, 109(B11) https://doi.org/10.1029/2004JB003155

Mason, B. G., Pyle, D. M., & Oppenheimer, C. (2004). The size and frequency of the largest explosive eruptions on Earth. Bulletin of Volcanology, 66(8), 735-748. doi:10.1007/s00445-004-0355-9

Massaro, S., Costa, A., & Sulpizio, R. (2018). Evolution of the magma feeding system during a Plinian eruption: The case of Pomici di Avellino eruption of Somma–Vesuvius, Italy. Earth and Planetary Science Letters, 482, 545-555. https://doi.org/10.1016/j.epsl.2017.11.030

Mastin, L. G. (2005). The controlling effect of viscous dissipation on magma flow in silicic conduits. Journal of Volcanology and Geothermal Research, 143(1), 17-28. https://doi.org/10.1016/j.jvolgeores.2004.09.008

Mastin, L. G., Guffanti, M., Servranckx, R., Webley, P., Barsotti, S., Dean, K., Durant, A., Ewert, J. W., Neri, A., Rose, W. I., Schneider, D., Siebert, L., Stunder, B., Swanson, G., Tupper, A., Volentik, A., & Waythomas, C. F. (2009). A multidisciplinary effort to assign realistic source parameters to models of volcanic ash-cloud transport and dispersion during eruptions. Journal of Volcanology and Geothermal Research, 186(1), 10-21. https://doi.org/10.1016/j.jvolgeores.2009.01.008

Mastrolorenzo, G., & Pappalardo, L. (2006). Magma degassing and crystallization processes during eruptions of high-risk Neapolitan-volcanoes: evidence of common equilibrium rising processes in alkaline magmas. Earth and Planetary Science Letters, 250(1-2), 164-181.

Matsumoto, A., & Nakagawa, M. (2019). Reconstruction of the eruptive history of Usu volcano, Hokkaido, Japan, inferred from petrological correlation between tephras and dome lavas. Island Arc, 28(3), e12301.

Matthews, S. J., Gardeweg, M. C., & Sparks, R. S. J. (1997). The 1984 to 1996 cyclic activity of Lascar Volcano, northern Chile: cycles of dome growth, dome subsidence, degassing and explosive eruptions. Bulletin of Volcanology, 59(1), 72-82. doi:10.1007/s004450050176

Mayer, K., Scheu, B., Gilg, H. A., Heap, M. J., Kennedy, B. M., Lavallée, Y., Letham-Brake, M., & Dingwell, D. B. (2015). Experimental constraints on phreatic eruption processes at Whakaari (White Island volcano). Journal of Volcanology and Geothermal Research, 302, 150-162. https://doi.org/10.1016/j.jvolgeores.2015.06.014

McGimsey, R. G., Neal, C. A., & Riley, C. M. (2001). Areal distribution, thickness, mass, volume, and grain size of tephra-fall deposits from the 1992 eruptions of Crater Peak vent, Mt. Spurr Volcano, Alaska (Report No. 01-370). Anchorage, AK. Retrieved from http://pubs.er.usgs.gov/publication/ofr01370

McPhie, J., Doyle, M., & Allen, R. (1993). Volcanic textures. A guide to the interpretation of textures in volcanic rocks. Tasmanian Government Printing Office, Tasmania, 196

Mele, D., Sulpizio, R., Dellino, P., & La Volpe, L. (2011). Stratigraphy and eruptive dynamics of a pulsating Plinian eruption of Somma-Vesuvius: the Pomici di Mercato (8900 years B.P.). Bulletin of Volcanology, 73(3), 257-278. 10.1007/s00445-010-0407-2

Melhuish, A., Sutherland, R., Davey, F. J., & Lamarche, G. (1999). Crustal structure and neotectonics of the Puysegur oblique subduction zone, New Zealand. Tectonophysics, 313(4), 335-362. https://doi.org/10.1016/S0040-1951(99)00212-7

Melnik, O., & Sparks, R. S. J. (2005). Controls on conduit magma flow dynamics during lava dome building eruptions. Journal of Geophysical Research: Solid Earth, 110(B2), n/a-n/a. 10.1029/2004JB003183

Melnik, O., Barmin, A. A., & Sparks, R. S. J. (2005). Dynamics of magma flow inside volcanic conduits with bubble overpressure buildup and gas loss through permeable magma. Journal of Volcanology and Geothermal Research, 143(1), 53-68. https://doi.org/10.1016/j.jvolgeores.2004.09.010

Mercalli, G. (1907). Vulcani Attivi della Terra: Morfologia—Dinamismo—Prodotti Distribuzione Geografica—Cause. Pp. viii + 421; illustrated. Milano: Ulrico Hoepli.

Miller, C. D. (1985). Holocene eruptions at the Inyo volcanic chain, California: Implications for possible eruptions in Long Valley caldera. Geology, 13(1), 14-17.

Miller, C. F., & Wark, D. A. (2008). Supervolcanoes and their explosive supereruptions. Elements, 4(1), 11-15.

Miller, T. P., & Chouet, B. A. (1994). The 1989–1990 eruptions of Redoubt Volcano: an introduction. Journal of Volcanology and Geothermal Research, 62(1), 1-10. doi:https://doi.org/10.1016/0377-0273(94)90025-6

Mitchell, S. J., Biass, S., Houghton, R., Anderson, A., Bonny, E., Walker, B., Mintz, B., Turner, N., Frank, D., & Carey, R. (2018). The interplay among clast size, vesicularity, postfragmentation expansion, and clast breakage: An example from the 1.8 ka Taupo eruption.

Mitchell, S. J., Houghton, B. F., Carey, R. J., Manga, M., Fauria, K. E., Jones, M. R., Soule, S. A., Conway, C. E., Wei, Z., & Giachetti, T. (2019). Submarine giant pumice: a window into the shallow conduit dynamics of a recent silicic eruption. Bulletin of Volcanology, 81(7), 42. 10.1007/s00445-019-1298-5

Miwa, T., Geshi, N., & Shinohara, H. (2013). Temporal variation in volcanic ash texture during a vulcanian eruption at the Sakurajima volcano, Japan. Journal of Volcanology and Geothermal Research, 260, 80-89. https://doi.org/10.1016/j.jvolgeores.2013.05.010

Miyabuchi, Y. (1999). Deposits associated with the 1990–1995 eruption of Unzen volcano, Japan. Journal of Volcanology and Geothermal Research, 89(1), 139-158. https://doi.org/10.1016/S0377-0273(98)00129-2

Miyabuchi, Y., Ikebe, S.-i., & Watanabe, K. (2008). Geological constraints on the 2003–2005 ash emissions from the Nakadake crater lake, Aso Volcano, Japan. Journal of Volcanology and Geothermal Research, 178(2), 169-183. https://doi.org/10.1016/j.jvolgeores.2008.06.025

Miyabuchi, Y., Hanada, D., Niimi, H., & Kobayashi, T. (2013). Stratigraphy, grain-size and component characteristics of the 2011 Shinmoedake eruption deposits, Kirishima Volcano, Japan. Journal of Volcanology and Geothermal Research, 258, 31-46. https://doi.org/10.1016/j.jvolgeores.2013.03.027

Miyaji, N., Kan'no, A., Kanamaru, T., & Mannen, K. (2011). High-resolution reconstruction of the Hoei eruption (AD 1707) of Fuji volcano, Japan. Journal of Volcanology and Geothermal Research, 207(3), 113-129. https://doi.org/10.1016/j.jvolgeores.2011.06.013

Moitra, P., Gonnermann, H. M., Houghton, B. F., & Giachetti, T. (2013). Relating vesicle shapes in pyroclasts to eruption styles. Bulletin of Volcanology, 75(2), 691. 10.1007/s00445-013-0691-8

Moitra, P., & Gonnermann, H. M. (2015). Effects of crystal shape- and size-modality on magma rheology. Geochemistry, Geophysics, Geosystems, 16(1), 1-26. 10.1002/2014gc005554

Molloy, L., & Acland, J. (2006). Our world heritage: a tentative list of New Zealand cultural and natural heritage sites. A Report to the Department of Conservation by the Cultural and Natural Heritage Advisory Groups, Department of Conservation. ISBN: 0-478-14113-0

Montanaro, C., Scheu, B., Gudmundsson, M.T., Vogfjörd, K., Reynolds, H.I., Dürig, T., Strehlow, K., Rott, S., Reuschlé, T., and Dingwell, D.B. (2016), Multidisciplinary constraints of hydrothermal explosions based on the 2013 Gengissig Lake events, Kverkfjöll volcano, Iceland: Earth and Planetary Science Letters, v. 434, p. 308–319, https://doi.org/10.1016/j.epsl.2015.11.043.

Montanaro, C., Cronin, S., Scheu, B., Kennedy, B., & Scott, B. (2020). Complex crater fields formed by steam-driven eruptions: Lake Okaro, New Zealand. Bulletin, 132(9-10), 1914-1930.

Mortimer, N., Rattenbury, M. S., King, P. R., Bland, K. J., Barrell, D. J. A., Bache, F., Begg, J. G., Campbell, H. J., Cox, S. C., Crampton, J. S., Edbrooke, S. W., Forsyth, P. J., Johnston, M. R., Jongens, R., Lee, J. M., Leonard, G. S., Raine, J. I., Skinner, D. N. B., Timm, C., Townsend, D. B., Tulloch, A. J., Turnbull, I. M., & Turnbull, R. E. (2014). High-level stratigraphic scheme for New Zealand rocks. New Zealand Journal of Geology and Geophysics, 57(4), 402-419. 10.1080/00288306.2014.946062

Mortimer, N., Campbell, H. J., Tulloch, A. J., King, P. R., Stagpoole, V. M., Wood, R. A., Rattenbury, M. S., Sutherland, R., Adams, C. J., & Collot, J. (2017). Zealandia: Earth's hidden continent. GSA Today, 27(3), 27-35.

Mortimer, N., & Scott, J. M. (2020). Volcanoes of Zealandia and the Southwest Pacific. New Zealand Journal of Geology and Geophysics, 63(4), 371-377. 10.1080/00288306.2020.1713824

Mourtada-Bonnefoi, C., & Laporte, D. (2002). Homogeneous bubble nucleation in rhyolitic magmas: an experimental study of the effect of H2O and CO2. Journal of Geophysical Research: Solid Earth, 107(B4), ECV 2-1-ECV 2-19.

Mourtada-Bonnefoi, C. C., & Laporte, D. (2004). Kinetics of bubble nucleation in a rhyolitic melt: an experimental study of the effect of ascent rate. Earth and Planetary Science Letters, 218(3-4), 521-537.

Mueller, S., Scheu, B., Spieler, O., & Dingwell, D. B. (2008). Permeability control on magma fragmentation. Geology, 36(5), 399-402. 10.1130/g24605a.1

Mulas, M., Cioni, R., Andronico, D., & Mundula, F. (2016). The explosive activity of the 1669 Monti Rossi eruption at Mt. Etna (Italy). Journal of Volcanology and Geothermal Research, 328, 115-133. https://doi.org/10.1016/j.jvolgeores.2016.10.012

Myers, M. L., Wallace, P. J., Wilson, C. J. N., Morter, B. K., & Swallow, E. J. (2016). Prolonged ascent and episodic venting of discrete magma batches at the onset of the Huckleberry Ridge supereruption, Yellowstone. Earth and Planetary Science Letters, 451, 285-297. https://doi.org/10.1016/j.epsl.2016.07.023

Myers, M. L., Druitt, T. H., Schiavi, F., Gurioli, L., & Flaherty, T. (2021). Evolution of magma decompression and discharge during a Plinian event (Late Bronze-Age eruption, Santorini) from multiple eruption-intensity proxies. Bulletin of Volcanology, 83(3), 18. 10.1007/s00445-021-01438-3

Nairn, I. A. (1972). Rotoehu ash and the Rotoiti Breccia Formation, Taupo Volcanic zone, New Zealand. New Zealand Journal of Geology and Geophysics, 15(2), 251-261. doi:10.1080/00288306.1972.10421958

Nairn, I. A. (1980). Source, age, and eruptive mechanisms of Rotorua Ash. New Zealand Journal of Geology and Geophysics, 23(2), 193-207. 10.1080/00288306.1980.10424206

Nairn, I. A. (1981). Some studies of the geology, volcanic history, and geothermal resources of the Okataina Volcanic Centre, Taupo Volcanic Zone, New Zealand. PhD thesis, Victoria University of Wellington.

Nairn, I. A. (1992). The Te Rere and Okareka eruptive episodes — Okataina Volcanic Centre, Taupo Volcanic Zone, New Zealand. New Zealand Journal of Geology and Geophysics, 35(1), 93-108. 10.1080/00288306.1992.9514503

Nairn, I. A. (2002). Geology of the Okataina Volcanic Centre, scale 1: 50 000. Institute of Geological and Nuclear Sciences geological map 25. 1 sheet+ 156 p. Institute of Geological and Nuclear Sciences Ltd.

Nairn, I. A., & Kohn, B. P. (1973). Relation of the Earthquake Flat Breccia to the Rotoiti Breccia, Central North Island, New Zealand. New Zealand Journal of Geology and Geophysics, 16(2), 269-279. doi:10.1080/00288306.1973.10431457

Nairn, I. A., & Self, S. (1978). Explosive eruptions and pyroclastic avalanches from Ngauruhoe in February 1975. Journal of Volcanology and Geothermal Research, 3(1), 39-60. doi:https://doi.org/10.1016/0377-0273(78)90003-3

Nairn, I. A., & Wiradiradja, S. (1980). Late quaternary hydrothermal explosion breccias at Kawerau Geothermal Field, New Zealand. Bulletin Volcanologique, 43(1), 1-13. 10.1007/BF02597607

Nairn, I. A., & Cole, J. W. (1981). Basalt dikes in the 1886 Tarawera Rift. New Zealand Journal of Geology and Geophysics, 24(5-6), 585-592. doi:10.1080/00288306.1981.10421534

Nairn, I. A., & Beanland, S. (1989). Geological setting of the 1987 Edgecumbe earthquake, New Zealand. New Zealand Journal of Geology and Geophysics, 32(1), 1-13. doi:10.1080/00288306.1989.10421383

Nairn, I. A., Self, S., Cole, J. W., Leonard, G. S., & Scutter, C. (2001). Distribution, stratigraphy, and history of proximal deposits from the c. AD 1305 Kaharoa eruptive episode at Tarawera Volcano, New Zealand. New Zealand Journal of Geology and Geophysics, 44(3), 467-484. 10.1080/00288306.2001.9514950

Nairn, I. A., Shane, P. R., Cole, J. W., Leonard, G. J., Self, S., & Pearson, N. (2004). Rhyolite magma processes of the ~AD 1315 Kaharoa eruption episode, Tarawera volcano, New Zealand. Journal of Volcanology and Geothermal Research, 131(3), 265-294. https://doi.org/10.1016/S0377-0273(03)00381-0

Nairn, I. A., Hedenquist, J. W., Villamor, P., Berryman, K. R., & Shane, P. A. (2005). The ~AD1315 Tarawera and Waiotapu eruptions, New Zealand: contemporaneous rhyolite and hydrothermal eruptions driven by an arrested basalt dike system? Bulletin of Volcanology, 67(2), 186-193. 10.1007/s00445-004-0373-7

Nakada, S., Miyake, Y., Sato, H., Oshima, O., & Fujinawa, A. (1995). Endogenous growth of dacite dome at Unzen volcano (Japan), 1993–1994. Geology, 23(2), 157-160.

Navon, O., & Lyakhovsky, V. (1998). Vesiculation processes in silicic magmas. Geological Society, London, Special Publications, 145(1), 27-50. 10.1144/gsl.sp.1996.145.01.03

Nawotniak, S. E. K., & Bursik, M. (2010). Subplinian fall deposits of Inyo Craters, CA. Journal of Volcanology and Geothermal Research, 198(3), 433-446. https://doi.org/10.1016/j.jvolgeores.2010.10.005

Neri, A., & Dobran, F. (1994). Influence of eruption parameters on the thermofluid dynamics of collapsing volcanic columns. Journal of Geophysical Research: Solid Earth, 99(B6), 11833-11857. doi:10.1029/94JB00471

Neri, A., Papale, P., Del Seppia, D., & Santacroce, R. (2003). Coupled conduit and atmospheric dispersal dynamics of the AD 79 Plinian eruption of Vesuvius. Journal of Volcanology and Geothermal Research, 120(1), 141-160. doi:https://doi.org/10.1016/S0377-0273(02)00381-5

Neri, A., Aspinall, W. P., Cioni, R., Bertagnini, A., Baxter, P. J., Zuccaro, G., Andronico, D., Barsotti, S., Cole, P. D., Esposti Ongaro, T., Hincks, T. K., Macedonio, G., Papale, P., Rosi, M., Santacroce, R., & Woo, G. (2008). Developing an Event Tree for probabilistic hazard and risk assessment at Vesuvius. Journal of Volcanology and Geothermal Research, 178(3), 397-415. https://doi.org/10.1016/j.jvolgeores.2008.05.014

Newhall, C. G., & Self, S. (1982). The volcanic explosivity index (VEI) an estimate of explosive magnitude for historical volcanism. Journal of Geophysical Research: Oceans, 87(C2), 1231-1238.

Newhall, C. G., & Melson, W. G. (1983). Explosive activity associated with the growth of volcanic domes. Journal of Volcanology and Geothermal Research, 17(1), 111-131. doi:https://doi.org/10.1016/0377-0273(83)90064-1

Newhall, C. G., & Hoblitt, R. (2002). Constructing event trees for volcanic crises. Bulletin of Volcanology, 64(1), 3-20. 10.1007/s004450100173

Newman, S., Epstein, S., & Stolper, E. (1988). Water, carbon dioxide, and hydrogen isotopes in glasses from the ca. 1340 A.D. eruption of the Mono Craters, California: Constraints on degassing phenomena and initial volatile content. Journal of Volcanology and Geothermal Research, 35(1), 75-96. https://doi.org/10.1016/0377-0273(88)90007-8

Newnham, R. M., Lowe, D. J., McGlone, M. S., Wilmshurst, J. M., & Higham, T. F. G. (1998). The Kaharoa Tephra as a Critical Datum for Earliest Human Impact in Northern New Zealand. Journal of Archaeological Science, 25(6), 533-544. https://doi.org/10.1006/jasc.1997.0217

Ngāti Rangitihi Trust. (2017). Ngāti Rangitihi Story. Chapter One: Te Ao Tawhito & Chapter Two: Whenua Hou. In ngatirangitihi.iwi.nz, from https://ngatirangitihi.iwi.nz/cultural-resources/rangitihi-story/

Noguchi, S., Toramaru, A., & Shimano, T. (2006). Crystallization of microlites and degassing during magma ascent: Constraints on the fluid mechanical behavior of magma during the Tenjo Eruption on Kozu Island, Japan. Bulletin of Volcanology, 68(5), 432-449. 10.1007/s00445-005-0019-4

Norris, R. J., Koons, P. O., & Cooper, A. F. (1990). The obliquely-convergent plate boundary in the South Island of New Zealand: implications for ancient collision zones. Journal of Structural Geology, 12(5), 715-725. doi:https://doi.org/10.1016/0191-8141(90)90084-C

Norris, R. J., & Cooper, A. F. (2001). Late Quaternary slip rates and slip partitioning on the Alpine Fault, New Zealand. Journal of Structural Geology, 23(2), 507-520. doi:https://doi.org/10.1016/S0191-8141(00)00122-X

Ogburn, S. E., Loughlin, S. C., & Calder, E. S. (2015). The association of lava dome growth with major explosive activity (VEI ≥ 4): DomeHaz, a global dataset. Bulletin of Volcanology, 77(5), 40. 10.1007/s00445-015-0919-x

Ohashi, M., Ichihara, M., & Toramaru, A. (2018). Bubble deformation in magma under transient flow conditions. Journal of Volcanology and Geothermal Research, 364, 59-75. https://doi.org/10.1016/j.jvolgeores.2018.09.005

Ohashi, M., Ichihara, M., Takeda, S., Hirota, K., Sato, S., Kuwano, O., & Kameda, M. (2020a). Formation of tube-pumice structure under pure shear: Insights from extension tests of solidifying foam. Journal of Volcanology and Geothermal Research, 106772.

Ohashi, M., Ichihara, M., Maeno, F., Kennedy, B., & Gravley, D. (2020b). Quantitative measurement of bubble textures in pumice clasts using a digital stereo microscope with low-angled ring illumination. Earth, Planets and Space, 72(1), 185. 10.1186/s40623-020-01320-0

Ohashi, M., Ichihara, M., Kennedy, B., & Gravley, D. (2021). Comparison of Bubble Shape Model Results With Textural Analysis: Implications for the Velocity Profile Across a Volcanic Conduit. Journal of Geophysical Research: Solid Earth, 126(6), e2021JB021841. https://doi.org/10.1029/2021JB021841

Okumura, S., Nakamura, M., & Tsuchiyama, A. (2006). Shear-induced bubble coalescence in rhyolitic melts with low vesicularity. Geophysical Research Letters, 33(20)

Okumura, S., Nakamura, M., Tsuchiyama, A., Nakano, T., & Uesugi, K. (2008). Evolution of bubble microstructure in sheared rhyolite: Formation of a channel-like bubble network. Journal of Geophysical Research: Solid Earth, 113(B7)

Okumura, S., Nakamura, M., Takeuchi, S., Tsuchiyama, A., Nakano, T., & Uesugi, K. (2009). Magma deformation may induce non-explosive volcanism via degassing through bubble networks. Earth and Planetary Science Letters, 281(3), 267-274. https://doi.org/10.1016/j.epsl.2009.02.036

Okumura, S., Nakamura, M., Nakano, T., Uesugi, K., & Tsuchiyama, A. (2010). Shear deformation experiments on vesicular rhyolite: Implications for brittle fracturing, degassing, and compaction of magmas in volcanic conduits. Journal of Geophysical Research: Solid Earth, 115(B6) https://doi.org/10.1029/2009JB006904

Okumura, S., Nakamura, M., Uesugi, K., Nakano, T., & Fujioka, T. (2013). Coupled effect of magma degassing and rheology on silicic volcanism. Earth and Planetary Science Letters, 362, 163-170.

Paisley, R., Berlo, K., Whattam, J., Schipper, C. I., & Tuffen, H. (2019). Degassing-induced chemical heterogeneity at the 2011-2012 Cordón Caulle eruption. Volcanica, 2(2), 211-237.

Paladio-Melosantos, M. L. O., Solidum, R. U., Scott, W. E., Quiambao, R. B., Umbal, J. V., Rodolfo, K. S., Tubianosa, B. S., Delos Reyes, P., Alonso, R. A., & Ruelo, H. B. (1996). Tephra falls of the 1991 eruptions of Mount Pinatubo. Fire and mud, 12000, 12030.

Pallister, J. S., Diefenbach, A. K., Burton, W. C., Muñoz, J., Griswold, J. P., Lara, L. E., Valenzuela, C. E. (2013). The Chaitén rhyolite lava dome: Eruption sequence, lava dome volumes, rapid effusion rates and source of the rhyolite magma. Andean Geology, 40(2).

Pansino, S., Emadzadeh, A., & Taisne, B. (2019). Dike channelization and solidification: time scale controls on the geometry and placement of magma migration pathways. Journal of Geophysical Research: Solid Earth, 124(9), 9580-9599. https://doi.org/10.1029/2019JB018191

Papale, P. (1999). Strain-induced magma fragmentation in explosive eruptions. Nature, 397, 425. 10.1038/17109

Papale, P., Neri, A., & Macedonio, G. (1998). The role of magma composition and water content in explosive eruptions: 1. Conduit ascent dynamics. Journal of Volcanology and Geothermal Research, 87(1), 75-93. https://doi.org/10.1016/S0377-0273(98)00101-2

Pardo, N., Cronin, S. J., Palmer, A. S., & Németh, K. (2011). Reconstructing the largest explosive eruptions of Mt. Ruapehu, New Zealand: lithostratigraphic tools to understand subplinian–plinian eruptions at andesitic volcanoes. Bulletin of Volcanology, 74(3), 617-640. 10.1007/s00445-011-0555-z

Pardo, N., Cronin, S., Palmer, A., Procter, J., & Smith, I. (2012). Andesitic Plinian eruptions at Mt. Ruapehu: quantifying the uppermost limits of eruptive parameters. Bulletin of Volcanology, 74(5), 1161-1185. 10.1007/s00445-012-0588-y

Pardo, N., Cronin, S. J., Wright, H. M. N., Schipper, C. I., Smith, I., & Stewart, B. (2014). Pyroclast textural variation as an indicator of eruption column steadiness in andesitic Plinian eruptions at Mt. Ruapehu. Bulletin of Volcanology, 76(5), 822. 10.1007/s00445-014-0822-x

Pardo, N., Avellaneda, J. D., Rausch, J., Jaramillo-Vogel, D., Gutiérrez, M., & Foubert, A. (2020). Decrypting silicic magma/plug fragmentation at Azufral crater lake, Northern Andes: insights from fine to extremely fine ash morpho-chemistry. Bulletin of Volcanology, 82(12), 79. 10.1007/s00445-020-01418-z

Parson, L. M., & Wright, I. C. (1996). The Lau-Havre-Taupo back-arc basin: A southward-propagating, multi-stage evolution from rifting to spreading. Tectonophysics, 263(1), 1-22. doi:https://doi.org/10.1016/S0040-1951(96)00029-7

Pensa, A., Capra, L., & Giordano, G. (2019). Ash clouds temperature estimation. Implication on dilute and concentrated PDCs coupling and topography confinement. Scientific reports, 9(1), 5657. 10.1038/s41598-019-42035-x

Pierson, T. C. (2005). Hyperconcentrated flow—transitional process between water flow and debris flow. In Debris-flow hazards and related phenomena (pp. 159-202). Springer, Berlin, Heidelberg.

Piochi, M., Polacci, M., Arzilli, F., & Ventura, G. (2021). Microscale textural heterogeneity and tip-streaming instability in alkaline magmas: Evidence in tube pumices from Campi Flegrei, Italy. Journal of Volcanology and Geothermal Research, 413, 107200.

Pistolesi, M., Cioni, R., Bonadonna, C., Elissondo, M., Baumann, V., Bertagnini, A., Chiari L, Gonzales R, Rosi M, Francalanci, L. (2015). Complex dynamics of small-moderate volcanic events: the example of the 2011 rhyolitic Cordón Caulle eruption, Chile. Bulletin of Volcanology, 77(1), 3. 10.1007/s00445-014-0898-3

Pistolesi, M., Isaia, R., Marianelli, P., Bertagnini, A., Fourmentraux, C., Albert, P. G., Tomlinson, E. L., Menzies, M. A., Rosi, M., & Sbrana, A. (2016). Simultaneous eruptions from multiple vents at Campi Flegrei (Italy) highlight new eruption processes at calderas. Geology, 44(6), 487-490

Pistolesi, M., Bertagnini, A., Di Roberto, A., Isaia, R., Vona, A., Cioni, R., & Giordano, G. (2017). The Baia–Fondi di Baia eruption at Campi Flegrei: stratigraphy and dynamics of a multi-stage caldera reactivation event. Bulletin of Volcanology, 79(9), 67. 10.1007/s00445-017-1149-1

Pittari, A., Briggs, R. M., & Bowyer, D. A. (2016). Subsurface geology, ancient hydrothermal systems and crater excavation processes beneath Lake Rotomahana: Evidence from lithic clasts of the 1886AD Rotomahana Pyroclastics. Journal of Volcanology and Geothermal Research, 314, 110-125. https://doi.org/10.1016/j.jvolgeores.2015.10.009

Pittari, A., Prentice, M. L., McLeod, O. E., Yousef Zadeh, E., Kamp, P. J., Danišík, M., & Vincent, K. A. (2021). Inception of the modern North Island (New Zealand) volcanic setting: spatio-temporal patterns of volcanism between 3.0 to 0.9 Ma. New Zealand Journal of Geology and Geophysics, 1-23.

Platz, T., Cronin, S. J., Cashman, K. V., Stewart, R. B., & Smith, I. E. M. (2007). Transition from effusive to explosive phases in andesite eruptions — A case-study from the AD1655 eruption of Mt. Taranaki, New Zealand. Journal of Volcanology and Geothermal Research, 161(1), 15-34. https://doi.org/10.1016/j.jvolgeores.2006.11.005

Polacci, M. (2005). Constraining the dynamics of volcanic eruptions by characterization of pumice textures. Annals of Geophysics

Polacci, M., Papale, P., & Rosi, M. (2001). Textural heterogeneities in pumices from the climactic eruption of Mount Pinatubo, 15 June 1991, and implications for magma ascent dynamics. Bulletin of Volcanology, 63(2), 83-97. 10.1007/s004450000123

Polacci, M., Pioli, L., & Rosi, M. (2003). The Plinian phase of the Campanian Ignimbrite eruption (Phlegrean Fields, Italy): evidence from density measurements and textural characterization of pumice. Bulletin of Volcanology, 65(6), 418-432. 10.1007/s00445-002-0268-4

Polacci, M., Baker, D. R., Mancini, L., Tromba, G., & Zanini, F. (2006). Three-dimensional investigation of volcanic textures by X-ray microtomography and implications for conduit processes. Geophysical Research Letters, 33(13) 10.1029/2006gl026241

Poland M. (2019). A personal commentary: Why I dislike the term "supervolcano" (and what we should be saying instead). Yellowstone Caldera Chronicles, https://www.usgs.gov/center-news/a-personal-commentary-why-i-dislike-term-supervolcano-and-what-we-should-be-saying

Price, R. C., Gamble, J. A., Smith, I. E. M., Maas, R., Waight, T., Stewart, R. B., & Woodhead, J. (2012). The Anatomy of an Andesite Volcano: a Time–Stratigraphic Study of Andesite Petrogenesis and Crustal Evolution at Ruapehu Volcano, New Zealand. Journal of Petrology, 53(10), 2139-2189. doi:10.1093/petrology/egs050

Pullar, W. A., & Nairn, I. A. (1972). Matahi Basaltic Tephra member, Rotoiti Breccia Formation. New Zealand Journal of Geology and Geophysics, 15(3), 446-450. doi:10.1080/00288306.1972.10422342

Pullar, W. A., & Birrell K.S. (1973) Age and distribution of late Quaternary pyroclastic and associated cover deposits of the Rotorua and Taupo area, North Island, New Zealand. NZ Soil Surv Rept 1 & 2, Explanatory notes:32 p

Pullar, W. A., Birrell, K. S., & Heine, J. C. (1973). Named tephras and tephra formations occurring in the Central North Island, with notes on derived soils and buried paleosols. New Zealand Journal of Geology and Geophysics, 16(3), 497-518. 10.1080/00288306.1973.10431374

Pullar, W., Kohn, B., & Cox, J. (1977). Air-fall Kaharoa ash and Taupo Pumice, and sea-rafted Loisels Pumice, Taupo Pumice, and Leigh Pumice in northern and eastern parts of the North Island, New Zealand. New Zealand Journal of Geology and Geophysics, 20(4), 697-717.

Pyle, D. M. (1989). The thickness, volume and grainsize of tephra fall deposits. Bulletin of Volcanology, 51(1), 1-15. doi:10.1007/bf01086757

Pyle, D. M. (2015). Chapter 13 - Sizes of Volcanic Eruptions A2 - Sigurdsson, Haraldur. In The Encyclopedia of Volcanoes (Second Edition) (pp. 257-264). Amsterdam: Academic Press.

Rampino, M. R. (2002). Supereruptions as a Threat to Civilizations on Earth-like Planets. Icarus, 156(2), 562-569. https://doi.org/10.1006/icar.2001.6808

Rhoades, D. A., Dowrick, D. J., & Wilson, C. J. N. (2002). Volcanic hazard in New Zealand: scaling and attenuation relations for tephra fall deposits from Taupo Volcano. Natural Hazards, 26(2), 147-174.

Rhodes, E., Kennedy, B. M., Lavallée, Y., Hornby, A., Edwards, M., & Chigna, G. (2018). Textural insights into the evolving lava dome cycles at Santiaguito lava dome, Guatemala. Frontiers in Earth Science, 6, 30.

Rivalta, E., Taisne, B., Bunger, A. P., & Katz, R. F. (2015). A review of mechanical models of dike propagation: Schools of thought, results and future directions. Tectonophysics, 638, 1-42. https://doi.org/10.1016/j.tecto.2014.10.003

Rivalta, E., Corbi, F., Passarelli, L., Acocella, V., Davis, T., & Di Vito, M. A. (2019). Stress inversions to forecast magma pathways and eruptive vent location. Science advances, 5(7), eaau9784.

Robertson, R., Cole, P., Sparks, R. S. J., Harford, C., Lejeune, A. M., McGuire, W. J., Miller, A. D., Murphy, M. D., Norton, G., Stevens, N. F., & Young, S. R. (1998). The explosive eruption of

Soufriere Hills Volcano, Montserrat, West Indies, 17 September, 1996. Geophysical Research Letters, 25(18), 3429-3432. 10.1029/98GL01442

Rogan, M. (1982). A geophysical study of the Taupo Volcanic Zone New Zealand. Journal of Geophysical Research: Solid Earth, 87(B5), 4073-4088. doi:10.1029/JB087iB05p04073

Roggensack, K., Williams, S. N., Schaefer, S. J., & Parnell, R. A. (1996). Volatiles from the 1994 eruptions of Rabaul: Understanding large caldera systems. Science, 273(5274), 490-493.

Rosi, M. (1996). Quantitative reconstruction of recent volcanic activity: a contribution to forecasting of future eruptions. In Monitoring and Mitigation of Volcano Hazards (pp. 631-674): Springer.

Rosi, M. (1998). Plinian eruption columns: particle transport and fallout. From magma to tephra. Elsevier, Amsterdam, 139-172. In Freundt, A., & Rosi, M. From magma to tephra (modelling physical processes of explosive volcanic eruptions).

Rosi, M., Principe, C., & Vecci, R. (1993). The 1631 Vesuvius eruption. A reconstruction based on historical and stratigraphical data. Journal of Volcanology and Geothermal Research, 58(1), 151-182. https://doi.org/10.1016/0377-0273(93)90106-2

Rosi, M., Paladio-Melosantos, M., Di Muro, A., Leoni, R., & Bacolcol, T. (2001). Fall vs flow activity during the 1991 climactic eruption of Pinatubo Volcano (Philippines). Bulletin of Volcanology, 62(8), 549-566. doi:10.1007/s004450000118

Rosi, M., Landi, P., Polacci, M., Di Muro, A., & Zandomeneghi, D. (2004). Role of conduit shear on ascent of the crystal-rich magma feeding the 800-year-b.p. Plinian eruption of Quilotoa Volcano (Ecuador). Bulletin of Volcanology, 66(4), 307-321. 10.1007/s00445-003-0312-z

Rossi, E., Bagheri, G., Beckett, F., & Bonadonna, C. (2021). The fate of volcanic ash: premature or delayed sedimentation? Nature Communications, 12(1), 1303. 10.1038/s41467-021-21568-8

Rotella, M. D., Wilson, C. J. N., Barker, S. J., Cashman, K. V., Houghton, B. F., & Wright, I. C. (2014). Bubble development in explosive silicic eruptions: insights from pyroclast vesicularity textures from Raoul volcano (Kermadec arc). Bulletin of Volcanology, 76(8), 826. 10.1007/s00445-014-0826-6

Rowe, M. C., Carey, R. J., White, J. D., Kilgour, G., Hughes, E., Ellis, B., Rosseel, J.-B., & Segovia, A. (2021). Tarawera 1886: an integrated review of volcanological and geochemical characteristics of a complex basaltic eruption. New Zealand Journal of Geology and Geophysics, 1-24.

Rust, A. C., & Manga, M. (2002). Effects of bubble deformation on the viscosity of dilute suspensions. Journal of non-newtonian fluid mechanics, 104(1), 53-63.

Rust, A. C., Manga, M., & Cashman, K. V. (2003). Determining flow type, shear rate and shear stress in magmas from bubble shapes and orientations. Journal of Volcanology and Geothermal Research, 122(1-2), 111-132.

Rust, A. C., & Cashman, K. V. (2004). Permeability of vesicular silicic magma: inertial and hysteresis effects. Earth and Planetary Science Letters, 228(1), 93-107. https://doi.org/10.1016/j.epsl.2004.09.025

Rust, A. C., Cashman, K., & Wallace, P. (2004). Magma degassing buffered by vapor flow through brecciated conduit margins. Geology, 32(4), 349-352

Rust, A. C., & Cashman, K. V. (2007). Multiple origins of obsidian pyroclasts and implications for changes in the dynamics of the 1300 B.P. eruption of Newberry Volcano, USA. Bulletin of Volcanology, 69(8), 825-845. 10.1007/s00445-006-0111-4

Rust, A. C., & Cashman, K. V. (2011). Permeability controls on expansion and size distributions of pyroclasts. Journal of Geophysical Research: Solid Earth, 116(B11), n/a-n/a. doi:10.1029/2011JB008494

Rutherford, M. J., & Hill, P. M. (1993). Magma ascent rates from amphibole breakdown: An experimental study applied to the 1980–1986 Mount St. Helens eruptions. Journal of Geophysical Research: Solid Earth, 98(B11), 19667-19685. doi:10.1029/93JB01613

Rymer, H., Sparks, S., Self, S., Grattan, J., Oppenheimer, C., & Pyle, D. (2005). Super-eruptions: global effects and future threats. Geological Society of London.

Sable, J. E., Houghton, B. F., Wilson, C. J. N., & Carey, R. J. (2006). Complex proximal sedimentation from Plinian plumes: the example of Tarawera 1886. Bulletin of Volcanology, 69(1), 89. 10.1007/s00445-006-0057-6

Sahagian, D. L., & Proussevitch, A. A. (1998). 3D particle size distributions from 2D observations: stereology for natural applications. Journal of Volcanology and Geothermal Research, 84(3), 173-196. https://doi.org/10.1016/S0377-0273(98)00043-2

Sahetapy-Engel, S., Self, S., Carey, R. J., & Nairn, I. A. (2014). Deposition and generation of multiple widespread fall units from the c. AD 1314 Kaharoa rhyolitic eruption, Tarawera, New Zealand. Bulletin of Volcanology, 76(8), 836. 10.1007/s00445-014-0836-4

Sandri, L., Tierz, P., Costa, A., & Marzocchi, W. (2018). Probabilistic Hazard From Pyroclastic Density Currents in the Neapolitan Area (Southern Italy). Journal of Geophysical Research: Solid Earth, 123(5), 3474-3500. https://doi.org/10.1002/2017JB014890

Sarna-Wojcicki, A. M., Shipley, S., Waitt Jr, R. B., Dzurisin, D., & Wood, S. H. (1981). Areal distribution, thickness, mass, volume, and grain size of air-fall ash from the six major eruptions of 1980.

Sas, M., (2020). Isotopic and geochemical records of magmatic processes captured in crystals from rhyolites at Okataina volcano. PhD thesis, The University of Auckland.

Sas, M., Kawasaki, N., Sakamoto, N., Shane, P., Zellmer, G. F., Kent, A. J. R., & Yurimoto, H. (2019). The ion microprobe as a tool for obtaining strontium isotopes in magmatic plagioclase: A case study at Okataina Volcanic Centre, New Zealand. Chemical Geology, 513, 153-166. https://doi.org/10.1016/j.chemgeo.2019.03.016

Sas, M., Shane, P., Kuritani, T., Zellmer, G. F., Kent, A. J. R., & Nakagawa, M. (2021). Mush, melts and metasediments: A history of rhyolites from the Okataina Volcanic Centre, New Zealand, as captured in plagioclase. Journal of Petrology 10.1093/petrology/egab038

Sato, H., Fujii, T., & Nakada, S. (1992). Crumbling of dacite dome lava and generation of pyroclastic flows at Unzen volcano. Nature, 360(6405), 664.

Saubin, E., Tuffen, H., Gurioli, L., Owen, J., Castro, J. M., Berlo, K., McGowan, E. M., Schipper, C. I., & Wehbe, K. (2016). Conduit Dynamics in Transitional Rhyolitic Activity Recorded by Tuffisite Vein Textures from the 2008–2009 Chaitén Eruption. Frontiers in Earth Science, 4(59) 10.3389/feart.2016.00059

Saubin, E., Kennedy, B., Tuffen, H., Villeneuve, M., Davidson, J., & Burchardt, S. (2019). Comparative field study of shallow rhyolite intrusions in Iceland: emplacement mechanisms and impact on country rocks. Journal of Volcanology and Geothermal Research, 106691. https://doi.org/10.1016/j.jvolgeores.2019.106691

Saucedo, R., Macías, J. L., & Bursik, M. (2004). Pyroclastic flow deposits of the 1991 eruption of Volcán de Colima, Mexico. Bulletin of Volcanology, 66(4), 291-306. doi:10.1007/s00445-003-0311-0

Saucedo, R., Macías, J. L., Gavilanes, J. C., Arce, J. L., Komorowski, J. C., Gardner, J. E., & Valdez-Moreno, G. (2010). Eyewitness, stratigraphy, chemistry, and eruptive dynamics of the 1913 Plinian eruption of Volcán de Colima, México. Journal of Volcanology and Geothermal Research, 191(3), 149-166. https://doi.org/10.1016/j.jvolgeores.2010.01.011

Sawada, Y., Sampei, Y., Hyodo, M., Yagami, T., & Fukue, M. (2000). Estimation of emplacement temperatures of pyroclastic flows using H/C ratios of carbonized wood. Journal of Volcanology and Geothermal Research, 104(1), 1-20. https://doi.org/10.1016/S0377-0273(00)00196-7

Saxby, J., Beckett, F., Cashman, K., Rust, A., & Tennant, E. (2018). The impact of particle shape on fall velocity: Implications for volcanic ash dispersion modelling. Journal of Volcanology and Geothermal Research, 362, 32-48. https://doi.org/10.1016/j.jvolgeores.2018.08.006

Scandone, R., & Malone, S. D. (1985). Magma supply, magma discharge and readjustment of the feeding system of mount St. Helens during 1980. Journal of Volcanology and Geothermal Research, 23(3), 239-262. https://doi.org/10.1016/0377-0273(85)90036-8

Scandone, R., Cashman, K. V., & Malone, S. D. (2007). Magma supply, magma ascent and the style of volcanic eruptions. Earth and Planetary Science Letters, 253(3), 513-529. doi:https://doi.org/10.1016/j.epsl.2006.11.016

Scarpati, C., Sparice, D., & Perrotta, A. (2014). A crystal concentration method for calculating ignimbrite volume from distal ash-fall deposits and a reappraisal of the magnitude of the Campanian Ignimbrite. Journal of Volcanology and Geothermal Research, 280, 67-75. https://doi.org/10.1016/j.jvolgeores.2014.05.009

Schindelin, J., Arganda-Carreras, I., Frise, E., Kaynig, V., Longair, M., Pietzsch, T., Preibisch, S., Rueden, C., Saalfeld, S., Schmid, B., Tinevez, J.-Y., White, D. J., Hartenstein, V., Eliceiri, K., Tomancak, P., & Cardona, A. (2012). Fiji: an open-source platform for biological-image analysis. Nature Methods, 9(7), 676-682. 10.1038/nmeth.2019

Schipper, C. I., Castro, J. M., Tuffen, H., James, M. R., & How, P. (2013). Shallow vent architecture during hybrid explosive–effusive activity at Cordón Caulle (Chile, 2011–12): Evidence from direct observations and pyroclast textures. Journal of Volcanology and Geothermal Research, 262, 25-37. doi:https://doi.org/10.1016/j.jvolgeores.2013.06.005

Schipper, C. I., Castro, J. M., Kennedy, B. M., Tuffen, H., Whattam, J., Wadsworth, F. B., Paisley, R., Fitzgerald, R. H., Rhodes, E., Schaefer, L. N., Ashwell, P. A., Forte, P., Seropian, G., & Alloway, B. V. (2021). Silicic conduits as supersized tuffisites: Clastogenic influences on shifting eruption styles at Cordón Caulle volcano (Chile). Bulletin of Volcanology, 83(2), 11. 10.1007/s00445-020-01432-1

Schmith, J., Höskuldsson, Á., & Holm, P. M. (2017). Grain shape of basaltic ash populations: implications for fragmentation. Bulletin of Volcanology, 79(2), 14. 10.1007/s00445-016-1093-5

Schmitz, M. D., & Smith, I. E. (2004). The petrology of the Rotoiti eruption sequence, Taupo Volcanic Zone: an example of fractionation and mixing in a rhyolitic system. Journal of Petrology, 45(10), 2045-2066.

Schneider, C. A., Rasband, W. S., & Eliceiri, K. W. (2012). NIH Image to ImageJ: 25 years of image analysis. Nature Methods, 9(7), 671-675.

Schwarzkopf, L. M., Schmincke, H.-U., & Cronin, S. J. (2005). A conceptual model for block-and-ash flow basal avalanche transport and deposition, based on deposit architecture of 1998 and 1994 Merapi flows. Journal of Volcanology and Geothermal Research, 139(1), 117-134. doi:https://doi.org/10.1016/j.jvolgeores.2004.06.012

Scott, B. J., & Travers, J. (2009). Volcano monitoring in NZ and links to SW Pacific via the Wellington VAAC. Natural Hazards, 51(2), 263-273. 10.1007/s11069-009-9354-7

Seebeck, H., & Nicol, A. (2009). Dike intrusion and displacement accumulation at the intersection of the Okataina Volcanic Centre and Paeroa Fault zone, Taupo Rift, New Zealand. Tectonophysics, 475(3), 575-585. https://doi.org/10.1016/j.tecto.2009.07.009

Seebeck, H., Nicol, A., Stern, T. A., Bibby, H. M., & Stagpoole, V. (2010). Fault controls on the geometry and location of the Okataina Caldera, Taupo Volcanic Zone, New Zealand. Journal of Volcanology and Geothermal Research, 190(1), 136-151. doi:https://doi.org/10.1016/j.jvolgeores.2009.04.011

Seebeck, H., Nicol, A., Villamor, P., Ristau, J., & Pettinga, J. (2014). Structure and kinematics of the Taupo Rift, New Zealand. Tectonics, 33(6), 1178-1199.

Self, S., & Sparks, R. S. J. (1978). Characteristics of widespread pyroclastic deposits formed by the interaction of silicic magma and water. Bulletin Volcanologique, 41(3), 196. doi:10.1007/bf02597223

Shane, P. (2000). Tephrochronology: a New Zealand case study. Earth-Science Reviews, 49(1), 223-259. https://doi.org/10.1016/S0012-8252(99)00058-6

Shane, P., Smith, V. C., & Nairn, I. A. (2005). High temperature rhyodacites of the 36 ka Hauparu pyroclastic eruption, Okataina Volcanic Centre, New Zealand: change in a silicic magmatic system following caldera collapse. Journal of Volcanology and Geothermal Research, 147(3-4), 357-376.

Shane, P., Martin, S. B., Smith, V. C., Beggs, K. F., Darragh, M. B., Cole, J. W., & Nairn, I. A. (2007). Multiple rhyolite magmas and basalt injection in the 17.7 ka Rerewhakaaitu eruption episode from Tarawera volcanic complex, New Zealand. Journal of Volcanology and Geothermal Research, 164(1), 1-26. https://doi.org/10.1016/j.jvolgeores.2007.04.003

Shane, P., Smith, V. C., & Nairn, I. (2008). Millennial timescale resolution of rhyolite magma recharge at Tarawera volcano: insights from quartz chemistry and melt inclusions. Contributions to Mineralogy and Petrology, 156(3), 397-411. doi:10.1007/s00410-008-0292-2

Shane, P., Nairn, I. A., Smith, V. C., Darragh, M., Beggs, K., & Cole, J. W. (2008). Silicic recharge of multiple rhyolite magmas by basaltic intrusion during the 22.6 ka Okareka Eruption Episode, New Zealand. Lithos, 103(3), 527-549. https://doi.org/10.1016/j.lithos.2007.11.002

Shea, T. (2017). Bubble nucleation in magmas: A dominantly heterogeneous process? Journal of Volcanology and Geothermal Research, 343, 155-170. https://doi.org/10.1016/j.jvolgeores.2017.06.025

Shea, T., Houghton, B. F., Gurioli, L., Cashman, K. V., Hammer, J. E., Hobden, B. J., Stovall, W., & Carey, R., J. (2009). SEM image processing with Photoshop. On:< http://www2. hawaii. edu/~ tshea/methodsimrec. html.

Shea, T., Houghton, B. F., Gurioli, L., Cashman, K. V., Hammer, J. E., & Hobden, B. J. (2010). Textural studies of vesicles in volcanic rocks: An integrated methodology. Journal of Volcanology and Geothermal Research, 190(3), 271-289. https://doi.org/10.1016/j.jvolgeores.2009.12.003

Shea, T., Gurioli, L., Houghton, B. F., Cioni, R., & Cashman, K. V. (2011). Column collapse and generation of pyroclastic density currents during the AD 79 eruption of Vesuvius: the role of pyroclast density. Geology, 39(7), 695-698

Shea, T., Gurioli, L., & Houghton, B. F. (2012). Transitions between fall phases and pyroclastic density currents during the AD 79 eruption at Vesuvius: building a transient conduit model from the textural and volatile record. Bulletin of Volcanology, 74(10), 2363-2381

Sherburn, S., Bannister, S., & Bibby, H. (2003). Seismic velocity structure of the central Taupo Volcanic Zone, New Zealand, from local earthquake tomography. Journal of Volcanology and Geothermal Research, 122(1), 69-88. doi:https://doi.org/10.1016/S0377-0273(02)00470-5

Sheridan, M. F., & Wohletz, K. H. (1983). Hydrovolcanism: Basic considerations and review. Journal of Volcanology and Geothermal Research, 17(1), 1-29. doi:https://doi.org/10.1016/0377-0273(83)90060-4

Siebert, L. (1984). Large volcanic debris avalanches: Characteristics of source areas, deposits, and associated eruptions. Journal of Volcanology and Geothermal Research, 22(3), 163-197. doi:https://doi.org/10.1016/0377-0273(84)90002-7

Siebert, L., Cottrell, E., Venzke, E., & Andrews, B. (2015). In H. Sigurdsson (Ed.), The Encyclopedia of Volcanoes (Second Edition) (pp. 239-255). Amsterdam: Academic Press. https://doi.org/10.1016/B978-0-12-385938-9.00012-2

Sieh, K., & Bursik, M. (1986). Most recent eruption of the Mono Craters, eastern central California. Journal of Geophysical Research: Solid Earth, 91(B12), 12539-12571.

Sigurdsson, H., & Sparks, R. S. J. (1981). Petrology of Rhyolitic and Mixed Magma Ejecta from the 1875 Eruption of Askja, Iceland. Journal of Petrology, 22(1), 41-84. 10.1093/petrology/22.1.41

Silleni, A., Giordano, G., Isaia, R., & Ort, M. H. (2020). The Magnitude of the 39.8 ka Campanian Ignimbrite Eruption, Italy: Method, Uncertainties and Errors. Frontiers in Earth Science, 8(444) 10.3389/feart.2020.543399

Singer, B. S., Andersen, N. L., Le Mével, H., Feigl, K. L., DeMets, C., Tikoff, B., Thurber, C. H., Jicha, B. R., Cardona, C., & Córdova, L. (2014). Dynamics of a large, restless, rhyolitic magma system at Laguna del Maule, southern Andes, Chile. GSA Today, 24(12), 4-10.

Smith, A., Roobol, M., Schellekens, J., & Mattioli, G. (2007). Prehistoric stratigraphy of the Soufriere Hills–South Soufriere Hills volcanic complex, Montserrat, West Indies. The Journal of Geology, 115(1), 115-127.

Smith, I. E. M., & Price, R. C. (2006). The Tonga–Kermadec arc and Havre–Lau back-arc system: Their role in the development of tectonic and magmatic models for the western Pacific. Journal of Volcanology and Geothermal Research, 156(3), 315-331. doi:https://doi.org/10.1016/j.jvolgeores.2006.03.006

Smith, V. C., Shane, P., & Smith, I. E. M. (2002). Tephrostratigraphy and geochemical fingerprinting of the Mangaone Subgroup tephra beds, Okataina Volcanic Centre, New Zealand. New Zealand Journal of Geology and Geophysics, 45(2), 207-219. doi:10.1080/00288306.2002.9514969

Smith, V. C., Shane, P., & Nairn, I. A. (2004). Reactivation of a rhyolitic magma body by new rhyolitic intrusion before the 15.8 ka Rotorua eruptive episode: implications for magma storage in the Okataina Volcanic Centre, New Zealand. Journal of the Geological Society, 161(5), 757-772.

Smith, V. C., Shane, P., & Nairn, I. A. (2005). Trends in rhyolite geochemistry, mineralogy, and magma storage during the last 50 kyr at Okataina and Taupo volcanic centres, Taupo Volcanic Zone, New Zealand. Journal of Volcanology and Geothermal Research, 148(3), 372-406.

Smith, V. C., Shane, P., Nairn, I. A., & Williams, C. M. (2006). Geochemistry and magmatic properties of eruption episodes from Haroharo linear vent zone, Okataina Volcanic Centre, New Zealand during the last 10 kyr. Bulletin of Volcanology, 69(1), 57. doi:10.1007/s00445-006-0056-7

Sohn, Y. K., & Chough, S. K. (1989). Depositional processes of the Suwolbong tuff ring, Cheju Island (Korea). Sedimentology, 36(5), 837-855.

Sourisseau, D., Macías, J. L., García Tenorio, F., Avellán, D. R., Saucedo Girón, R., Bernal, J. P., . . . Tinoco Murillo, Z. (2020). New insights into the stratigraphy and 230Th/U geochronology of the post-caldera explosive volcanism of La Primavera caldera, Mexico. Journal of South American Earth Sciences, 103, 102747. https://doi.org/10.1016/j.jsames.2020.102747

Sparks, R. S. J. (1978). The dynamics of bubble formation and growth in magmas: A review and analysis. Journal of Volcanology and Geothermal Research, 3(1), 1-37. https://doi.org/10.1016/0377-0273(78)90002-1

Sparks, R. S. J. (1986). The dimensions and dynamics of volcanic eruption columns. Bulletin of Volcanology, 48(1), 3-15. doi:10.1007/bf01073509

Sparks, R. S. J. (1997). Causes and consequences of pressurisation in lava dome eruptions. Earth and Planetary Science Letters, 150(3), 177-189. doi:https://doi.org/10.1016/S0012-821X(97)00109-X

Sparks, R. S. J., & Young, S. (2002). The eruption of Soufrière Hills Volcano, Montserrat (1995-1999): overview of scientific results. Geological Society, London, Memoirs, 21(1), 45-69.

Sparks, R. S. J., Wilson, L., & Hulme, G. (1978). Theoretical modeling of the generation, movement, and emplacement of pyroclastic flows by column collapse. Journal of Geophysical Research: Solid Earth, 83(B4), 1727-1739. doi:10.1029/JB083iB04p01727

Sparks, R. S. J., Wilson, L., & Sigurdsson, H. (1981). The pyroclastic deposits of the 1875 eruption of Askja, Iceland. Philosophical Transactions of the Royal Society of London. Series A, Mathematical and Physical Sciences, 299(1447), 241-273.

Sparks, R. S. J., Bursik, M. I., Ablay, G. J., Thomas, R. M. E., & Carey, S. N. (1992). Sedimentation of tephra by volcanic plumes. Part 2: controls on thickness and grain-size variations of tephra fall deposits. Bulletin of Volcanology, 54(8), 685-695. doi:10.1007/bf00430779

Sparks, R.S.J., Barclay, J., Jaupart, C., Mader, H.M., & Phillips, J.C. (1994). Physical aspects of magmatic degassing: I. Experimental and theoretical constraints on vesiculation, in Carrol, M.R., and Holloway, J.R., eds., Volatiles in Magmas: Washington, D.C., Mineralogical Society of America, Reviews in Mineralogy, v. 30, p. 413–446, https://doi.org/10.1515/9781501509674-017.

Sparks, R. S. J., Bursik, M. I., Carey, S. N., Gilbert, J. S., Glaze, L., Sigurdsson, H., & Woods, A. W. (1997). Volcanic plumes: John Wiley and Sons, Inc.

Sparks, R. S. J., Annen, C., Blundy, J., Cashman, K., Rust, A., & Jackson, M. (2019). Formation and dynamics of magma reservoirs. Philosophical Transactions of the Royal society A, 377(2139), 20180019

Speed, J., Shane, P., & Nairn, I. (2002). Volcanic stratigraphy and phase chemistry of the 11 900 yr BP Waiohau eruptive episode, Tarawera Volcanic Complex, New Zealand. New Zealand Journal of Geology and Geophysics, 45(3), 395-410. 10.1080/00288306.2002.9514981

Spinks, K. D. (2005). Rift architecture and caldera volcanism in the Taupo Volcanic Zone, New Zealand. PhD thesis, University of Canterbury.

Spinks, K. D., Acocella, V., Cole, J. W., & Bassett, K. N. (2005). Structural control of volcanism and caldera development in the transtensional Taupo Volcanic Zone, New Zealand. Journal of Volcanology and Geothermal Research, 144(1), 7-22. https://doi.org/10.1016/j.jvolgeores.2004.11.014

Stagpoole, V., Miller, C., Caratori Tontini, F., Brakenrig, T., & Macdonald, N. (2021). A two million-year history of rifting and caldera volcanism imprinted in new gravity anomaly compilation of the Taupō Volcanic Zone, New Zealand. New Zealand Journal of Geology and Geophysics, 1-14.

Stirling, M., Bebbington, M., Brenna, M., Cronin, S., Christophersen, A., Deligne, N., . . . Wilson, T. (2017). Conceptual Development of a National Volcanic Hazard Model for New Zealand. Frontiers in Earth Science, 5(51) 10.3389/feart.2017.00051

Stix, J., Torres, R. C., Narváez M, L., Cortés J, G. P., Raigosa, J. A., Gómez M, D., & Castonguay, R. (1997). A model of vulcanian eruptions at Galeras volcano, Colombia. Journal of Volcanology and Geothermal Research, 77(1), 285-303. doi:https://doi.org/10.1016/S0377-0273(96)00100-X

Sulpizio, R., & Dellino, P. (2008). Chapter 2 Sedimentology, Depositional Mechanisms and Pulsating Behaviour of Pyroclastic Density Currents. In J. Gottsmann, Mart, iacute, & Joan (Eds.), Developments in volcanology (Vol. 10, pp. 57-96): Elsevier. https://doi.org/10.1016/S1871-644X(07)00002-2

Sulpizio, R., Mele, D., Dellino, P., & Volpe, L. L. (2005). A complex, Subplinian-type eruption from low-viscosity, phonolitic to tephri-phonolitic magma: the AD 472 (Pollena) eruption of Somma-Vesuvius, Italy. Bulletin of Volcanology, 67(8), 743-767. 10.1007/s00445-005-0414-x

Sulpizio, R., Bonasia, R., Dellino, P., Mele, D., Di Vito, M. A., & La Volpe, L. (2010). The Pomici di Avellino eruption of Somma–Vesuvius (3.9 ka BP). Part II: sedimentology and physical volcanology of pyroclastic density current deposits. Bulletin of Volcanology, 72(5), 559-577. 10.1007/s00445-009-0340-4

Sulpizio, R., Dellino, P., Doronzo, D., & Sarocchi, D. (2014). Pyroclastic density currents: state of the art and perspectives. Journal of Volcanology and Geothermal Research, 283, 36-65

Sutherland, R. (1999). Cenozoic bending of New Zealand basement terranes and Alpine Fault displacement: A brief review. New Zealand Journal of Geology and Geophysics, 42(2), 295-301. doi:10.1080/00288306.1999.9514846

Sutherland, R., Barnes, P., & Uruski, C. (2006). Miocene-Recent deformation, surface elevation, and volcanic intrusion of the overriding plate during subduction initiation, offshore southern Fiordland, Puysegur margin, southwest New Zealand. New Zealand Journal of Geology and Geophysics, 49(1), 131-149. doi:10.1080/00288306.2006.9515154

Sutton, A. N., Blake, S., Wilson, C. J., & Charlier, B. L. (2000). Late Quaternary evolution of a hyperactive rhyolite magmatic system: Taupo volcanic centre, New Zealand. Journal of the Geological Society, 157(3), 537-552.

Swanson, D., Dzurisin, D., Holcomb, R., Iwatsubo, E., Chadwick Jr, W., Casadevall, T., Ewert, J., & Heliker, C. (1987). Growth of the lava dome at Mount St. Helens, Washington (USA). The emplacement of silicic domes and lava flows, Geological Society of America, Boulder, Special Paper, 212, 1-16.

Taddeucci, J., & Wohletz, K. H. (2001). Temporal evolution of the Minoan eruption (Santorini, Greece), as recorded by its Plinian fall deposit and interlayered ash flow beds. Journal of Volcanology and Geothermal Research, 109(4), 299-317. https://doi.org/10.1016/S0377-0273(01)00197-4

Tadini, A., Roche, O., Samaniego, P., Azzaoui, N., Bevilacqua, A., Guillin, A., . . . Pique, M. (2021). Eruption type probability and eruption source parameters at Cotopaxi and Guagua Pichincha volcanoes (Ecuador) with uncertainty quantification. Bulletin of Volcanology, 83(5), 35. 10.1007/s00445-021-01458-z

Tait, S., Jaupart, C., & Vergniolle, S. (1989). Pressure, gas content and eruption periodicity of a shallow, crystallising magma chamber. Earth and Planetary Science Letters, 92(1), 107-123. doi:https://doi.org/10.1016/0012-821X(89)90025-3

Thomas, N., Jaupart, C., & Vergniolle, S. (1994). On the vesicularity of pumice. Journal of Geophysical Research: Solid Earth, 99(B8), 15633-15644. 10.1029/94jb00650

Thomas, S. A. P. W. (1888). Report on the eruption of Tarawera and Rotomahana, New Zealand. Government Print.

Thompson, B. (1974). Geology of the Rotorua geothermal district. Geothermal Resource Survey, Rotorua Geothermal District. Dep. Sci. Ind. Res.(NZ) Geotherm. Rep(6), 10-36.

Thompson, M. A., Lindsay, J. M., Sandri, L., Biass, S., Bonadonna, C., Jolly, G., & Marzocchi, W. (2015). Exploring the influence of vent location and eruption style on tephra fall hazard from the Okataina Volcanic Centre, New Zealand. Bulletin of Volcanology, 77(5), 38. 10.1007/s00445-015-0926-y

Tibaldi, A. (2015). Structure of volcano plumbing systems: A review of multi-parametric effects. Journal of Volcanology and Geothermal Research, 298, 85-135. https://doi.org/10.1016/j.jvolgeores.2015.03.023

Todde, A., Cioni, R., Pistolesi, M., Geshi, N., & Bonadonna, C. (2017). The 1914 Taisho eruption of Sakurajima volcano: stratigraphy and dynamics of the largest explosive event in Japan during the twentieth century. Bulletin of Volcanology, 79(10), 72. doi:10.1007/s00445-017-1154-4

Toramaru, A. (2006). BND (bubble number density) decompression rate meter for explosive volcanic eruptions. Journal of Volcanology and Geothermal Research, 154(3), 303-316. https://doi.org/10.1016/j.jvolgeores.2006.03.027

Trafton, K. R., & Giachetti, T. (2021). The morphology and texture of Plinian pyroclasts reflect their lateral sourcing in the conduit. Earth and Planetary Science Letters, 562, 116844. https://doi.org/10.1016/j.epsl.2021.116844

Tuffen, H., Dingwell, D. B., & Pinkerton, H. (2003). Repeated fracture and healing of silicic magma generate flow banding and earthquakes? Geology, 31(12), 1089-1092.

Tuffen, H., James, M. R., Castro, J. M., & Schipper, C. I. (2013). Exceptional mobility of an advancing rhyolitic obsidian flow at Cordón Caulle volcano in Chile. Nature Communications, 4(1), 1-7.

Ui, T., Matsuwo, N., Sumita, M., & Fujinawa, A. (1999). Generation of block and ash flows during the 1990–1995 eruption of Unzen Volcano, Japan. Journal of Volcanology and Geothermal Research, 89(1), 123-137. doi:https://doi.org/10.1016/S0377-0273(98)00128-0

Underwood, E.E., 1970. Quantitative stereology. Addison-Wesley, Reading. 274 pp.

Van Dissen, R., & Yeats, R. S. (1991). Hope fault, Jordan thrust, and uplift of the seaward Kaikoura Range, New Zealand. Geology, 19(4), 393-396.

Van Eaton, A. R., & Wilson, C. J. N. (2013). The nature, origins and distribution of ash aggregates in a large-scale wet eruption deposit: Oruanui, New Zealand. Journal of Volcanology and Geothermal Research, 250, 129-154. https://doi.org/10.1016/j.jvolgeores.2012.10.016

Van Eaton, A., Herzog, M., Wilson, C., & McGregor, J. (2012). Ascent dynamics of large phreatomagmatic eruption clouds: The role of microphysics. Journal of Geophysical Research: Solid Earth, 117(B3)

Vandergoes, M. J., Hogg, A. G., Lowe, D. J., Newnham, R. M., Denton, G. H., Southon, J., Barrell, D. J. A., Wilson, C. J. N., McGlone, M. S., Allan, A. S. R., Almond, P. C., Petchey, F., Dabell, K., Dieffenbacher-Krall, A. C., & Blaauw, M. (2013). A revised age for the Kawakawa/Oruanui tephra, a key marker for the Last Glacial Maximum in New Zealand. Quaternary Science Reviews, 74, 195-201. https://doi.org/10.1016/j.quascirev.2012.11.006

Villamor, P., & Berryman, K. (2001). A late Quaternary extension rate in the Taupo Volcanic Zone, New Zealand, derived from fault slip data. New Zealand Journal of Geology and Geophysics, 44(2), 243-269. doi:10.1080/00288306.2001.9514937

Villamor, P., Nairn, I., & Seebeck, H. (2007) Geological Society of New Zealand & New Zealand Geophysical Society Joint Annual Conference Tauranga 2007 - Fieldtrip Guides Compiled by Ursula Cochran and Annie Cervelli. Geological Society of New Zealand Miscellaneous Publication 123B. ISBN 0-908678-09-6

Villamor, P., Berryman, K., Nairn, I., Wilson, K., Litchfield, N., & Ries, W. (2011). Associations between volcanic eruptions from Okataina volcanic center and surface rupture of nearby active faults, Taupo rift, New Zealand: Insights into the nature of volcano-tectonic interactions. Bulletin, 123(7-8), 1383-1405.

Vitale, S., & Isaia, R. (2014). Fractures and faults in volcanic rocks (Campi Flegrei, southern Italy): insight into volcano-tectonic processes. International Journal of Earth Sciences, 103(3), 801-819. 10.1007/s00531-013-0979-0

Voight, B., Komorowski, J.-C., Norton, G. E., Belousov, A. B., Belousova, M., Boudon, G., Francis, P. W., Franz, W., Heinrich, P., Sparks, R. S. J., & Young, S. R. (2002). The 26 December (Boxing Day) 1997 sector collapse and debris avalanche at Soufrière Hills Volcano, Montserrat. Geological Society, London, Memoirs, 21(1), 363-407. 10.1144/gsl.mem.2002.021.01.17

Voloschina, M., Lube, G., Procter, J., Moebis, A., & Timm, C. (2020). Lithosedimentological and tephrostratigraphical characterisation of small-volume, low-intensity eruptions: The 1800 years Tufa Trig Formation, Mt. Ruapehu (New Zealand). Journal of Volcanology and Geothermal Research, 402, 106987. https://doi.org/10.1016/j.jvolgeores.2020.106987

Voloschina, M., Bebbington, M., Lube, G., & Procter, J. (2021). Probabilistic modelling of multi-phase eruptions found in geological records: An example from Mt. Ruapehu, New Zealand. Journal of Volcanology and Geothermal Research, 107273. https://doi.org/10.1016/j.jvolgeores.2021.107273

Vona, A., Ryan, A. G., Russell, J. K., & Romano, C. (2016). Models for viscosity and shear localization in bubble-rich magmas. Earth and Planetary Science Letters, 449, 26-38. https://doi.org/10.1016/j.epsl.2016.05.029

Vona, A., Romano, C., Giordano, G., & Sulpizio, R. (2020). Linking magma texture, rheology and eruptive style during the 472 AD Pollena Subplinian eruption (Somma-Vesuvius). Lithos, 370, 105658.

Vucetich, C., & Pullar, W. (1963). Ash beds and soils in the Rotorua district. Paper presented at the Proceedings (New Zealand Ecological Society).

Vucetich, C., & Pullar, W. (1964). Stratigraphy of Holocene ash in the Rotorua and Gisborne districts. New Zealand Geological Survey Bulletin, 73, 43-88.

Vucetich, C., & Pullar, W. (1969). Stratigraphy and chronology of late Pleistocene volcanic ash beds in central North Island, New Zealand. New Zealand Journal of Geology and Geophysics, 12(4), 784-837.

Wadge, G., Voight, B., Sparks, R., Cole, P., Loughlin, S., & Robertson, R. (2014). An overview of the eruption of Soufriere Hills Volcano, Montserrat from 2000 to 2010. Geological Society, London, Memoirs, 39(1), 1-40.

Wadsworth, F. B., Vasseur, J., Schauroth, J., Llewellin, E. W., Dobson, K. J., Havard, T., Scheu, B., von Aulock, F. W., Gardner, J. E., Dingwell, D. B., Hess, K.-U., Colombier, M., Marone, F., Tuffen, H., & Heap, M. J. (2019). A general model for welding of ash particles in volcanic systems validated using in situ X-ray tomography. Earth and Planetary Science Letters, 525, 115726. https://doi.org/10.1016/j.epsl.2019.115726

Wadsworth, F. B., Llewellin, E. W., Vasseur, J., Gardner, J. E., & Tuffen, H. (2020). Explosive-effusive volcanic eruption transitions caused by sintering. Science advances, 6(39), eaba7940.

Walcott, R. I. (1984). The kinematics of the plate boundary zone through New Zealand: a comparison of short-and long-term deformations. Geophysical Journal of the Royal Astronomical Society, 79(2), 613-633. doi:10.1111/j.1365-246X.1984.tb02244.x

Walcott, R. I. (1987). Geodetic strain and the deformational history of the North Island of New Zealand during the late Cainozoic. Phil. Trans. R. Soc. Lond. A, 321(1557), 163-181.

Walker, G. P. L. (1971). Grain-size characteristics of pyroclastic deposits. The Journal of Geology, 79(6), 696-714.

Walker, G. P. L. (1973). Explosive volcanic eruptions — a new classification scheme. Geologische Rundschau, 62(2), 431-446. doi:10.1007/BF01840108

Walker, G. P. L. (1979). A volcanic ash generated by explosions where ignimbrite entered the sea. Nature, 281(5733), 642.

Walker, G. P. L. (1980). The Taupo pumice: Product of the most powerful known (ultraplinian) eruption? Journal of Volcanology and Geothermal Research, 8(1), 69-94. doi: https://doi.org/10.1016/0377-0273(80)90008-6

Walker, G. P. L. (1981). Plinian eruptions and their products. Bulletin Volcanologique, 44(3), 223. doi:10.1007/bf02600561

Walker, G. P. L., Wright, J. V., Clough, B. J., & Booth, B. (1981). Pyroclastic geology of the rhyolitic volcano of La Primavera, Mexico. Geologische Rundschau, 70(3), 1100-1118. 10.1007/bf01820184

Walker, G. P. L., Self, S., & Wilson, L. (1984). Tarawera 1886, New Zealand — A basaltic plinian fissure eruption. Journal of Volcanology and Geothermal Research, 21(1), 61-78. https://doi.org/10.1016/0377-0273(84)90016-7

Wallace, L. M., Beavan, J., McCaffrey, R., & Darby, D. (2004). Subduction zone coupling and tectonic block rotations in the North Island, New Zealand. Journal of Geophysical Research: Solid Earth, 109(B12), n/a-n/a. doi:10.1029/2004JB003241

Watkins, J., Gardner, J., & Befus, K. (2017). Nonequilibrium degassing, regassing, and vapor fluxing in magmatic feeder systems. Geology, 45(2), 183-186.

Watt, S. F. L., Pyle, D. M., Mather, T. A., Martin, R. S., & Matthews, N. E. (2009). Fallout and distribution of volcanic ash over Argentina following the May 2008 explosive eruption of Chaitén, Chile. Journal of Geophysical Research: Solid Earth, 114(B4) 10.1029/2008jb006219

Westrich, H. R., & Eichelberger, J. C. (1994). Gas transport and bubble collapse in rhyolitic magma: an experimental approach. Bulletin of Volcanology, 56(6), 447-458. doi:10.1007/bf00302826

White, J. D., & Houghton, B. (2006). Primary volcaniclastic rocks. Geology, 34(8), 677-680.

White, J. D., & Valentine, G. A. (2016). Magmatic versus phreatomagmatic fragmentation: Absence of evidence is not evidence of absence. Geosphere, 12(5), 1478-1488.

White, S. M., Crisp, J. A., & Spera, F. J. (2006). Long-term volumetric eruption rates and magma budgets. Geochemistry, Geophysics, Geosystems, 7(3).

Whittington, A. G., Hellwig, B. M., Behrens, H., Joachim, B., Stechern, A., & Vetere, F. (2009). The viscosity of hydrous dacitic liquids: implications for the rheology of evolving silicic magmas. Bulletin of Volcanology, 71(2), 185-199. 10.1007/s00445-008-0217-y

Wilson, C. J. N. (1985). The Taupo eruption, New Zealand I. General aspects. Phil. Trans. R. Soc. Lond. A, 314(1529), 199-228.

Wilson, C. J. N. (1993). Stratigraphy, chronology, styles and dynamics of late Quaternary eruptions from Taupo volcano, New Zealand. Phil. Trans. R. Soc. Lond. A, 343(1668), 205-306.

Wilson, C. J. N. (1996). Taupo's atypical arc. Nature, 379(6560), 27.

Wilson, C. J. N. (2001). The 26.5ka Oruanui eruption, New Zealand: an introduction and overview. Journal of Volcanology and Geothermal Research, 112(1), 133-174. https://doi.org/10.1016/S0377-0273(01)00239-6

Wilson, C. J. N. (2008). Supereruptions and supervolcanoes: processes and products. Elements, 4(1), 29-34.

Wilson, C. J. N., & Walker, G.P.L. (1985). The Taupo eruption, New Zealand I. General aspects. Phil. Trans. Roy. Soc. Lond. A314, 199–228.

Wilson, C. J. N., & Hildreth, W. (1997). The Bishop Tuff: new insights from eruptive stratigraphy. The Journal of Geology, 105(4), 407-440

Wilson, C. J. N., & Hildreth, W. (1998). Hybrid fall deposits in the Bishop Tuff, California: A novel pyroclastic depositional mechanism. Geology, 26(1), 7-10.

Wilson, C. J. N., & Rowland, J. V. (2016). The volcanic, magmatic and tectonic setting of the Taupo Volcanic Zone, New Zealand, reviewed from a geothermal perspective. Geothermics, 59, 168-187. https://doi.org/10.1016/j.geothermics.2015.06.013

Wilson, L., Sparks, R. S. J., & Walker, G. P. L. (1980). Explosive volcanic eruptions — IV. The control of magma properties and conduit geometry on eruption column behaviour. Geophysical Journal International, 63(1), 117-148. doi:10.1111/j.1365-246X.1980.tb02613.x

Wilson, C. J. N., Houghton, B. F., McWilliams, M. O., Lanphere, M. A., Weaver, S. D., & Briggs, R. M. (1995). Volcanic and structural evolution of Taupo Volcanic Zone, New Zealand: a review. Journal of Volcanology and Geothermal Research, 68(1), 1-28. https://doi.org/10.1016/0377-0273(95)00006-G

Wilson, C. J. N., Rhoades, D. A., Lanphere, M. A., Calvert, A. T., Houghton, B. F., Weaver, S. D., & Cole, J. W. (2007). A multiple-approach radiometric age estimate for the Rotoiti and Earthquake Flat eruptions, New Zealand, with implications for the MIS 4/3 boundary. Quaternary Science Reviews, 26(13), 1861-1870. doi:https://doi.org/10.1016/j.quascirev.2007.04.017

Wilson, C. J. N., Gravley, D., Leonard, G., & Rowland, J. (2009). Volcanism in the central Taupo Volcanic Zone, New Zealand: tempo, styles and controls. Studies in volcanology: the legacy of George Walker. Special Publications of IAVCEI, 2, 225-247.

Wilson, G., Wilson, T. M., Deligne, N. I., & Cole, J. W. (2014). Volcanic hazard impacts to critical infrastructure: A review. Journal of Volcanology and Geothermal Research, 286, 148-182. https://doi.org/10.1016/j.jvolgeores.2014.08.030

Wolfe EW, Hoblitt RP (1996) Overview of the eruptions. Fire and Mud: eruptions and lahars of Mount Pinatubo, Philippines, pp 3–20

Woods, A. W. (1988). The fluid dynamics and thermodynamics of eruption columns. Bulletin of Volcanology, 50(3), 169-193. doi:10.1007/bf01079681

Woods, A. W. (1995). The dynamics of explosive volcanic eruptions. Reviews of Geophysics, 33(4), 495-530. doi:10.1029/95RG02096

Woods, A. W., & Koyaguchi, T. (1994). Transitions between explosive and effusive eruptions of silicic magmas. Nature, 370, 641. doi:10.1038/370641a0

Wright, H. M. N., Roberts, J. J., & Cashman, K. V. (2006). Permeability of anisotropic tube pumice: Model calculations and measurements. Geophysical Research Letters, 33(17) 10.1029/2006gl027224

Wright, H. M. N., Cashman, K. V., Rosi, M., & Cioni, R. (2007). Breadcrust bombs as indicators of Vulcanian eruption dynamics at Guagua Pichincha volcano, Ecuador. Bulletin of Volcanology, 69(3), 281-300. doi:10.1007/s00445-006-0073-6

Wright, H. M. N., & Weinberg, R. F. (2009). Strain localization in vesicular magma: Implications for rheology and fragmentation. Geology, 37(11), 1023-1026.

Wright, H. M. N., Cashman, K. V., Gottesfeld, E. H., & Roberts, J. J. (2009). Pore structure of volcanic clasts: Measurements of permeability and electrical conductivity. Earth and Planetary Science Letters, 280(1), 93-104. https://doi.org/10.1016/j.epsl.2009.01.023

Yasui, M., & Koyaguchi, T. (2004). Sequence and eruptive style of the 1783 eruption of Asama Volcano, central Japan: a case study of an andesitic explosive eruption generating fountain-fed lava flow, pumice fall, scoria flow and forming a cone. Bulletin of Volcanology, 66(3), 243-262. 10.1007/s00445-003-0308-8

List of appendices

All the appendices compiled for this work and listed in the following section are available at *Massey Research Online*, the open access digital archive of the research and scholarship of Massey University.

Appendix A – Field (.pdf file)

A1) Location of the investigated stratigraphic sections and units exposed.

A2) Additional field photos

Appendix B – Grain size (.pdf and .xlsx files)

B1) Additional information on grain size analysis

B2) Sampling sites and sample position in stratigraphy

B3) Grain size data

Appendix C – Componentry (.xlsx file)

C1) Additional information on componentry analysis

C2) Componentry data

Appendix D – Clast bulk density/vesicularity and clast DRE density (.xlsx file)

D1) Clast bulk density/vesicularity data

D2) Clast DRE density data

Appendix E – SEM-BSE images of juvenile clasts (.pdf file)

E1) Additional images of white and grey pumice clasts

E2) Representative images of other types of juvenile clasts

Appendix F – Image analysis of juvenile textures (.pdf and .xlsx files)

F1) Shape parameter Regularity: metrics, ImageJ script and comparisons with similar parameters

F2) Sample size for image analysis and example of binary images

F3) Vesicle shape data Chapter 4

F4) Vesicle size and number density Chapter 4

F5) Vesicle shape data Chapter 5

F6) Vesicle size and number density Chapter 5

F7) Phenocryst content

Appendix G – Massey University DRC16 forms on statements of originality and contribution (.pdf file)

G1) Statement of originality and contribution to Chapters 3

G2) Statement of originality and contribution to Chapters 4

G3) Statement of originality and contribution to Chapters 5

G1) Statement of originality and contribution to Chapters 3

DRC 16

MASSEY UNIVERSITY
TE KUNENGA KI PŪREHUROA
UNIVERSITY OF NEW ZEALAND

GRADUATE RESEARCH SCHOOL

STATEMENT OF CONTRIBUTION
DOCTORATE WITH PUBLICATIONS/MANUSCRIPTS

We, the candidate and the candidate's Primary Supervisor, certify that all co-authors have consented to their work being included in the thesis and they have accepted the candidate's contribution as indicated below in the *Statement of Originality*.

Name of candidate:	Andrea Todde
Name/title of Primary Supervisor:	Jonathan N. Procter
In which chapter is the manuscript /published work:	Chapter 3

Please select one of the following three options:

○ The manuscript/published work is published or in press

- Please provide the full reference of the Research Output:

○ The manuscript is currently under review for publication – please indicate:

- The name of the journal:

- The percentage of the manuscript/published work that was contributed by the candidate: 100.00

- Describe the contribution that the candidate has made to the manuscript/published work:

Andrea Todde performed field work and laboratory analysis, sampling, data acquisition, data interpretation, and wrote the manuscript and prepared the figures.

◉ It is intended that the manuscript will be published, but it has not yet been submitted to a journal

Candidate's Signature:	Andrea Todde Digitally signed by Andrea Todde Date: 2021.09.08 15:15:38 +12'00'
Date:	08-Sep-2021
Primary Supervisor's Signature:	Jonathan Procter Digitally signed by Jonathan Procter Date: 2021.09.14 10:46:19 +12'00'
Date:	14-Sep-2021

This form should appear at the end of each thesis chapter/section/appendix submitted as a manuscript/ publication or collected as an appendix at the end of the thesis.

GRS Version 5 – 13 December 2019
DRC 19/09/10

G2) Statement of originality and contribution to Chapters 4

DRC 16

MASSEY UNIVERSITY
TE KUNENGA KI PŪREHUROA
UNIVERSITY OF NEW ZEALAND

GRADUATE RESEARCH SCHOOL

STATEMENT OF CONTRIBUTION
DOCTORATE WITH PUBLICATIONS/MANUSCRIPTS

We, the candidate and the candidate's Primary Supervisor, certify that all co-authors have consented to their work being included in the thesis and they have accepted the candidate's contribution as indicated below in the *Statement of Originality*.

Name of candidate:	Andrea Todde
Name/title of Primary Supervisor:	Jonathan N. Procter
In which chapter is the manuscript /published work:	Chapter 4

Please select one of the following three options:

○ The manuscript/published work is published or in press

- Please provide the full reference of the Research Output:

○ The manuscript is currently under review for publication – please indicate:

- The name of the journal:

- The percentage of the manuscript/published work that was contributed by the candidate: 95.00

- Describe the contribution that the candidate has made to the manuscript/published work:

Andrea Todde designed the methodology, collected the samples, performed the analysis, interpreted the data, and wrote the manuscript and prepared the figures.

◉ It is intended that the manuscript will be published, but it has not yet been submitted to a journal

Candidate's Signature:	Andrea Todde Digitally signed by Andrea Todde Date: 2021.09.08 15:16:49 +12'00'
Date:	08-Sep-2021
Primary Supervisor's Signature:	Jonathan Procter Digitally signed by Jonathan Procter Date: 2021.09.14 10:46:56 +12'00'
Date:	14-Sep-2021

This form should appear at the end of each thesis chapter/section/appendix submitted as a manuscript/ publication or collected as an appendix at the end of the thesis.

GRS Version 5 – 13 December 2019
DRC 19/09/10

G3) Statement of originality and contribution to Chapters 5

DRC 16

MASSEY UNIVERSITY
TE KUNENGA KI PŪREHUROA
UNIVERSITY OF NEW ZEALAND

GRADUATE RESEARCH SCHOOL

STATEMENT OF CONTRIBUTION
DOCTORATE WITH PUBLICATIONS/MANUSCRIPTS

We, the candidate and the candidate's Primary Supervisor, certify that all co-authors have consented to their work being included in the thesis and they have accepted the candidate's contribution as indicated below in the *Statement of Originality*.

Name of candidate:	Andrea Todde
Name/title of Primary Supervisor:	Jonathan N. Procter
In which chapter is the manuscript /published work:	Chapter 5

Please select one of the following three options:

○ The manuscript/published work is published or in press

- Please provide the full reference of the Research Output:

○ The manuscript is currently under review for publication – please indicate:

- The name of the journal:
- The percentage of the manuscript/published work that was contributed by the candidate: 100.00
- Describe the contribution that the candidate has made to the manuscript/published work:

Andrea Todde collected the samples, performed the analysis, interpreted the data, and wrote the manuscript and prepared the figures.

◉ It is intended that the manuscript will be published, but it has not yet been submitted to a journal

Candidate's Signature:	Andrea Todde Digitally signed by Andrea Todde Date: 2021.09.08 15:17:56 +12'00'
Date:	08-Sep-2021
Primary Supervisor's Signature:	Jonathan Procter Digitally signed by Jonathan Procter Date: 2021.09.14 10:47:23 +12'00'
Date:	14-Sep-2021

This form should appear at the end of each thesis chapter/section/appendix submitted as a manuscript/ publication or collected as an appendix at the end of the thesis.

GRS Version 5 – 13 December 2019
DRC 19/09/10